Max-Planck-Institut für extraterrestrische Physik
Garching bei München

Star Groups and their Nucleosynthesis

Moritz M. M. Pleintinger

Vollständiger Abdruck der von der Fakultät für Physik der Technischen Universität München zur Erlangung des akademischen Grades eines

Doktors der Naturwissenschaften

genehmigten Dissertation.

Vorsitzender:		Prof. Dr. Alejandro Ibarra
Prüfer der Dissertation:	1.	apl. Prof. Dr. Roland Diehl
	2.	Prof. Dr. Lothar Oberauer

Die Dissertation wurde am 10.08.2020 bei der Technischen Universität München eingereicht und durch die Fakultät für Physik am 02.11.2020 angenommen.

Kurzfassung

Aktuell stattfindende Nukleosynthese in der Milchstraße wurde durch die Messung hochauflösender Spektren der 1,8 MeV-Emission von interstellarem ^{26}Al mithilfe eines Gammastrahlenteleskops untersucht. Die Neuproduktion von Atomkernen findet in Sterngruppen statt und wurde durch galaxieweite Modellierung der zugrunde liegenden Prozesse analysiert. Erhöhte Mengen von ^{26}Al wurde in Blasen um diese Sterngruppen entlang der Spiralarme und in der nahegelegenen Umgebung des Sonnensystems gefunden.

Abstract

Ongoing nucleosynthesis in the Milky Way was investigated by measuring high-resolution spectra of the 1.8 MeV emission from interstellar ^{26}Al with a space gamma-ray telescope. Enrichment with new nuclei is closely related to massive star groups and was analysed through galaxy-wide modelling of the underlying processes. Enhanced amounts of ^{26}Al were found in bubbles along the spiral arms as well as surrounding the Solar System.

Contents

List of Figures

List of Tables

List of Acronyms

ACS	anti-coincidence shield
AGB	asymptotic giant branch
AGN	active galactic nucleus
AMS	accellerator mass spectrometry
ANU	Australian National University
B+19	binary model calculations by Brinkman et al. (2019)
BGO	$Bi_4Ge_3O_{12}$ bismuth germanate
C05	stellar IMF following Chabrier (2005)
ccSN	core collapse supernova
CDF	cumulative distribution function
CFR	cluster formation rate
CGRO	Compton Gamma Ray Observatory
CMF	initial core mass function
CNM	cold neutral medium
COMPTEL	Compton Telescope
COSI	Compton Spectrometer and Imager
CRIS	Cosmic Ray Isotope Spectrometer
DIRBE	Diffuse Infrared Background Experiment
ECMF	embedded cluster mass function
ESA	European Space Agency
ESO	European Southern Observatory
F+18	galaxy simulation by Fujimoto et al. (2018)
FRANEC	Frascati Raphson Newton Evolutionary Code
FWHM	full width at half maximum
GLIMPSE	Galactic Legacy Infrared Mid-Plane Survey Extraordinaire
GMC	giant molecular cloud
GRB	gamma-ray burst
GRIS	Gamma-Ray Imaging Spectrometer
HEAO 3	High Energy Astrophysical Observatory 3
HEXAGONE	High Energy X-ray And Gamma-ray Observatory for Nuclear Emissions

HIM	hot ionised medium
HRD	Hertzsprung-Russell diagram
IAU	International Astronomical Union
IBIS	Imager on-Board the INTEGRAL Satellite
IGIMF	integrated galactic initial mass function
IMF	initial mass function
INTEGRAL	International Gamma Ray Astrophysics Laboratory
IR	infrared
IRF	image response function
ISDC	INTEGRAL's Science Data Centre
ISM	interstellar medium
J12	explodability model by Janka (2012)
JEM-X	Joint European X-Ray Monitor
K01	stellar IMF following Kroupa (2001)
LAT	Large Area Telescope
LC06	stellar models by Limongi & Chieffi (2006)
LC18	stellar models by Limongi & Chieffi (2018)
LCC	Lower Centaurus Crux
LMC	Large Magellanic Cloud
MASSCLEAN	Massive Cluster Evolution and Analysis package
MC	Monte Carlo
MCMC	Markov chain Monte Carlo
MESA	Modules for Experiments in Stellar Astrophysics
MHD	magneto-hydrodynamic
NASA	National Aeronautics and Space Administration
OMC	Optical Monitoring Camera
PopSyn	population synthesis model by Voss et al. (2009)
PSYCO	galactic population synthesis code
R+19	galaxy simulation by Rodgers-Lee et al. (2019)
RGB	red giant branch
RMF	redistribution matrix file
ROI	region of interest
S+16	explodability model by Sukhbold et al. (2016)
S09	explodability model by Smartt (2009)
S55	stellar IMF following Salpeter (1955)

SDSS	Sloan Digital Sky Survey
SFR	star formation rate
SLUG	Stochastically Light Up Galaxies package
SMC	Small Magellanic Cloud
SMM	Solar Maximum Mission
SN	supernova explosion
SNR	supernova rate
SPI	Spectrometer on INTEGRAL
UCL	Upper Centaurus Lupus
UNM	thermally unstable neutral medium
USco	Upper Scorpius
UV	ultraviolet
VLBA	Very Long Baseline Array
WIM	warm ionised medium
WMAP	Wilkinson Microwave Anisotropy Probe
WNM	warm neutral medium
WR	Wolf-Rayet
ZAMS	zero-age main sequence

Danksagung

Als erstes danke ich meinem Doktorvater Roland Diehl, dass er mir diese Arbeit ermöglicht hat. Er hat mich wissenschaftliches und eigenständiges Denken und Arbeiten gelehrt und meine persönliche Entwicklung durch eine Vielzahl internationaler Erfahrungen aktiv befördert. Für all das bin ich sehr dankbar.
Darüber hinaus danke ich meinem Kollegen, Mentor und lieben Freund Thomas Siegert. Die unzähligen Gespräche und Diskussionen mit ihm sind unvergesslich und haben mich und mein Leben enorm bereichert. Lieber Thomas, ich danke Dir und Deinem Gehirn für alles, was wir in dieser Zeit erlebt haben, Deinen unermüdlichen Beistand und vor allem Deine Freundschaft.
Ich bedanke mich bei Jochen Greiner, der mir oft mit guten Ratschlägen zur Seite stand. Außerdem danke ich meinen Kollegen Christoph Weinberger, Björn Biltzinger und Michael Burgess, durch die ich die Freude an der Arbeit nicht verloren habe. Ich danke Tanja Kreitenweis für ihren ausdauernden Beistand und viele Ratschläge, insbesondere in der letzten Phase dieser Arbeit.
Großer Dank gilt meinen Freunden Martin Kauschinger, Ralph Schiffner und Daniel Bastan, die mir stets bei meiner persönlichen Entwicklung zur Seite standen und bei denen ich jenseits des akademischen Umfeldes oft Kraft schöpfen durfte. Ich bedanke mich auch insbesondere bei meiner großartigen Familie, deren Rückhalt mich immer begleitet und bestärkt hat; mein Bruder Michael Pleintinger war mir dabei immer ein besonderes Vorbild.
Ich danke meinem ehemaligen Lehrer Ernst Schütz. Er hat mich durch fordernde und aufrichtige Erziehung in meiner Persönlichkeitsentwicklung maßgeblich geprägt und mich so zu akademischen Leistungen angespornt.
Der größte Dank gebührt dem wichtigsten und liebsten Menschen in meinem Leben, Corinna Sommermann. Ihre liebevolle Unterstützung, ihr treuer Beistand und ihr Glaube an mich haben mir Halt und Motivation gegeben, ohne welche ich die letzten Jahre so nicht durchgestanden hätte. Liebste Corinna, ich danke Dir, dass Du an meiner Seite bist und immer an mich geglaubt hast.

Für meine Mutter

1 Introduction

Scientific thought has inflicted three deep narcissistic wounds on humanity: a cosmological, a biological, and a psychological. This is the diagnosis made by the psychoanalyst Sigmund Freud (1917). It corresponds to the general impression that each scientific revolution seems to have driven mankind further out of the bright centre of the cosmos and banished it into a dark and barren Universe. In order to try a treatment attempt for this alienation, one can take a structuralist perspective on reality. In this way one finds, that the scientific revolutions have actually deeply interwoven humanity with nature. The collective unconscious proposed by Carl Gustav Jung (1954) connects the individual psyche intimately with all humans beyond generational limits. The evolutionary process discovered by Charles Darwin (1859) links humans with the biological diversity of all living creatures on Earth. And finally, also on cosmic scale the Earth is embedded in a progressing cycle of emergence and decay: The cosmic cycle of matter.
Stars form in groups from giant gas clouds in galaxies. In their interiors they fuse light nuclei to heavier elements. The newly formed nucleosynthesis products are ejected via massive star winds or supernova explosions (SNe) into the surroundings where they mix with the interstellar medium (ISM). When the next generation of stars emerges from this material, it has a different elemental composition. This continuing loop of nucleosynthesis feedback from mainly massive stars drives galactic nuclear enrichment and thus also the chemical evolution of our Milky Way. In order to cure or at least alleviate the pain of the cosmological wound, it is essential to understand these overarching and transforming processes and especially our place in them.

Nuclear fusion reactions in stars, SNe, and violent merger events are the fundamental drivers of chemical evolution. They fuel the progression from the primordial element abundance, which consists only of hydrogen, helium, and small amounts of lithium and beryllium, into the variety of currently 118 known elements and over 3300 different isotopes, of which about 3000 are radioactive (Firestone et al. 1999; Audi et al. 2003). When radioactivity was discovered serendipitously by Conrad Röntgen (1895) and Henri Becquerel (1896), it quickly became clear that this radiation provides a unique window to subatomic processes. Its fundamental importance for astrophysics dawned when Sir Arthur Eddington (1920) proposed such processes as energy sources of stars; this was later confirmed as nuclear fusion reactions by Mark Oliphant et al. (1934a,b). Finally, Fred Hoyle (1946a,b,c, 1954) combined all these findings to a groundbreaking theory of nucleosynthesis in stars. According to this, stars continuously enrich galaxies with nuclei heavier than hydrogen, many of which are radioactive. That would mean we live in a radioactive Galaxy? Indeed, William A. Mahoney et al. (1982, 1984) reported the first detection of a gamma-ray line from interstellar radioactivity using the High Energy Astrophysical Observatory 3 (HEAO 3) spectrometer; it was a line emitted during the decay of ^{26}Al with photon energies of 1.809 MeV. This nucleus is produced mostly in massive stars, and to a

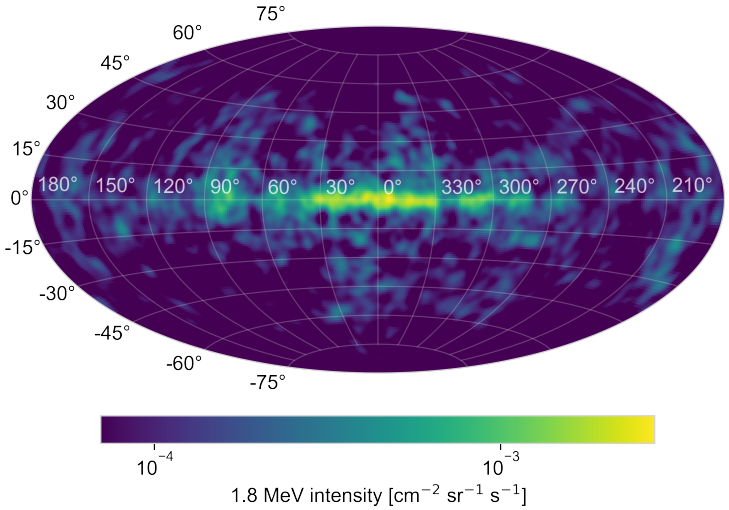

Figure 1.1: Full-sky map of the 1.809 MeV emission from ^{26}Al decay by COMPTEL (Plüschke et al. 2001; Plüschke 2001).

lesser extent in asymptotic giant branch (AGB) stars and novae (Diehl et al. 2018a, 431–454). It decays with a half-life time of ~ 0.7 Myr to ^{26}Mg*, which transitions to its ground state by emission of a gamma-ray photon at 1.809 MeV. The Galactic ^{26}Al full-sky emission was mapped later by the Compton Telescope (COMPTEL) aboard the Compton Gamma Ray Observatory (CGRO), which uncovered its unique astrophysical potential (Oberlack et al. 1996; Plüschke et al. 2001, see Fig. 1.1). On the one hand, the lifetime of ^{26}Al is long enough to escape from the star where it is produced in both stellar winds and SNe, filling the previously blown large cavities surrounded by shells of neutral hydrogen gas of a few hundred pc. On the other hand, the lifetime is short enough to not be completely homogenised in the Galaxy before it decays (Kretschmer et al. 2013; Krause et al. 2015; Fujimoto et al. 2018; Rodgers-Lee et al. 2019). This makes it an ideal tracer of the dynamics of ongoing nucleosynthesis in the Galaxy. Thus, in combination with the measurement of other radioisotopes, gamma-ray astrophysics has the exceptional opportunity to observe a direct signal from the nexus between nuclear processes and large-scale dynamics in the ISM. For example, with lifetimes from days to years, ^{56}Ni (Diehl et al. 2014, 2015), ^{56}Co (Tueller et al. 1990), or ^{44}Ti (Iyudin et al. 1998; Grefenstette et al. 2017) carry the signature of explosive nucleosynthesis from the innermost core of a SN. With lifetimes up to a few Myr ^{26}Al, ^{60}Fe, or ^{244}Pu track the dynamics of these nucleosynthesis products on the galactic scale and how they are mixed into the ISM to enrich the Galaxy with the variety of elements that is present today e.g. in the Solar System (Diehl et al. 2006; Wallner et al. 2015, 2016; Wang et al. 2020).

This thesis is ultimately based on four fundamental questions of nuclear astrophysics: Why is a plethora of elements available everywhere in the Milky Way? Where do these elements originate? How do they distribute throughout the Galaxy? And what is the particular chemical history of the Solar System?
In order to address these questions, the nuclear feedback from massive star groups and their nucleosynthesis is discussed in the framework of the Galactic ^{26}Al emission. In the attempt to acquire knowledge about such processes on astronomical scales, one necessarily faces a fundamental epistemic challenge inherent to astrophysics in general. One can not change the experimental setup or start the experiment again. There is one Universe, one Milky Way, and one Solar System with all their chemical

and morphological peculiarities; and it is about 13.8 billion years too late to directly observe how all of it came into being (Planck-Collaboration et al. 2014). Thus, astrophysics has to rely heavily on numerical simulations and model calculations in order to test the physical understanding of the cosmic and galactic history. Such tests can only be performed in comparison with empirical data. This is particularly challenging if the observationally accessible targets are rare because a single instantiation of a generic simulation is usually not expected to exactly match the specific properties of a unique observed object.
This fundamental epistemic challenge is discussed with respect to measurements and models of the Galactic ^{26}Al emission in order to understand the properties of star groups and their nucleosynthesis. On the one hand gamma-ray measurements of ^{26}Al with the spectrometer aboard the International Gamma Ray Astrophysics Laboratory (INTEGRAL) satellite, the Spectrometer on INTEGRAL (SPI), are exploited. On the other hand a newly developed galactic population synthesis code (PSYCO) is used to make predictions about the emission morphology and spatial distribution of ^{26}Al in the Milky Way for different model assumptions. This is the first approach to forward model the Galactic ^{26}Al distribution using a broad variety of simulations based on individual star groups. The theoretical and observational fields are brought together with a newly devised approach for morphological comparison in order to investigate the nucleosynthesis history of the Milky Way and the Solar System. In particular, global estimates of the star formation rate (SFR), supernova rate (SNR), and the total mass of ^{26}Al and ^{60}Fe are modelled and tested. The morphological study of gamma-ray measurements will provide insight into local nucleosynthesis contributions as well as the Galactic chemical enrichment dynamics in superbubbles, spiral arms, and Galactic outflows.
Overall, this work thus aims to answer the condensed research question: How does nucleosynthesis feedback from massive star groups affect the chemical evolution of the Milky Way and the Solar System?

This thesis is structured as follows: In Ch. 2 the physics of nucleosynthesis and chemical evolution is outlined on three major scales; from the evolution of individual stars to the cumulative effects of stellar groups up to the large-scale chemical evolution of the entire Galaxy. Ch. 3 presents an overview over measurements of cosmic gamma-rays with the INTEGRAL satellite and SPI. A detailed description is given of how self-consistent modelling of the instrumental background and estimation of emission models are used to measure diffuse and point-like sources with SPI with an emphasis on ^{26}Al line emission. The presentation of the observational approach is followed by a discussion of theoretical predictions and nucleosynthesis calculations for single stars as well as stellar groups in Ch. 4. Here, the newly developed PSYCO modelling routine is presented and described. This tool extends population synthesis calculations of star groups to the galactic scale in order to model the distribution and yields of nucleosynthesis ejecta in the entire Milky Way. In Ch. 5 a comparison of the theoretical modelling approach and the gamma-ray measurements is performed for all three stellar feedback scales: for the nearby Wolf-Rayet star γ^2-Vel as individual source, the Perseus OB1 association as stellar group, and the full-sky emission from the entire Milky Way. This is essential for the aim to draw a coherent picture of nucleosynthesis feedback from massive star groups. Finally, Ch. 6 summarises the results and open questions towards understanding our place in the radioactive Galaxy.

2 Nucleosynthesis and Massive Stars in Our Galaxy

"Was du ererbt von deinen Vätern hast
Erwirb es um es zu besitzen."
— Johann Wolfgang v. Goethe (1808)

2.1 Nucleosynthesis Feedback and the Cycle of Matter

Physical feedback is the mechanism by which a process loop alters itself. While the main system stays the same procedurally with every iteration, feedback describes an inherent sub-loop of self-driven change in process parameters. In other words, feedback is the mechanism underlying any kind of evolution.
Such a kind of evolution must have taken place on cosmic scale. Big Bang Nucleosynthesis produced a primordial element abundance of basically only hydrogen and helium. The amount of metals, i.e. nuclei heavier than He relative to H was less than 10^{-9} (Steigman 2007; Cyburt et al. 2016). Today, about 13.8 Gyr later, however, the material in the Solar System and its vicinity consists of 73.8% H and 1.4% metals (Asplund et al. 2009). This means that the primordial element abundance of the Universe must have been processed into a more metal-rich material in our Galaxy (cf. Fig. 2.1). The main agents of the Galactic evolution are stars, especially massive stars with initial masses of $M_* \geq 8\,\mathrm{M}_\odot$. From their formation, over different

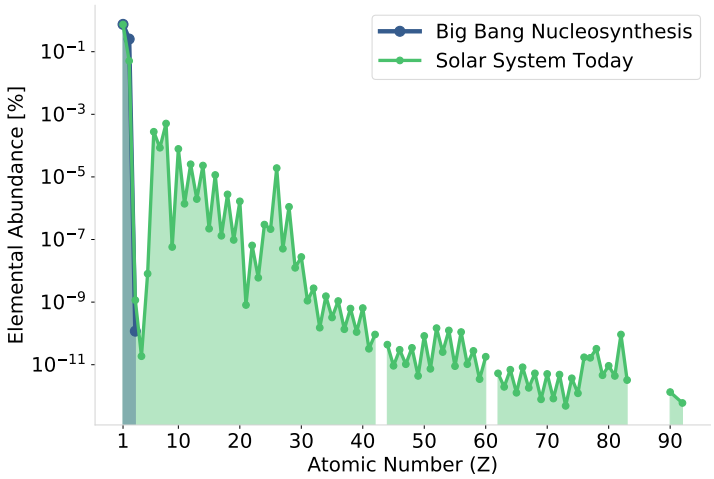

Figure 2.1: Elemental abundances in the Universe after primordial nucleosynthesis (data from Coc 2016, *blue*) and in the Solar System today (data from Palme et al. 2014, *green*).

stages of stellar evolution, up to their partly violent terminal phases, they shape the gas in their host galaxy dynamically, thermally, and chemically. The main process comprising all these effects can be described as cosmic Cycle of Matter (see Fig. 2.2).

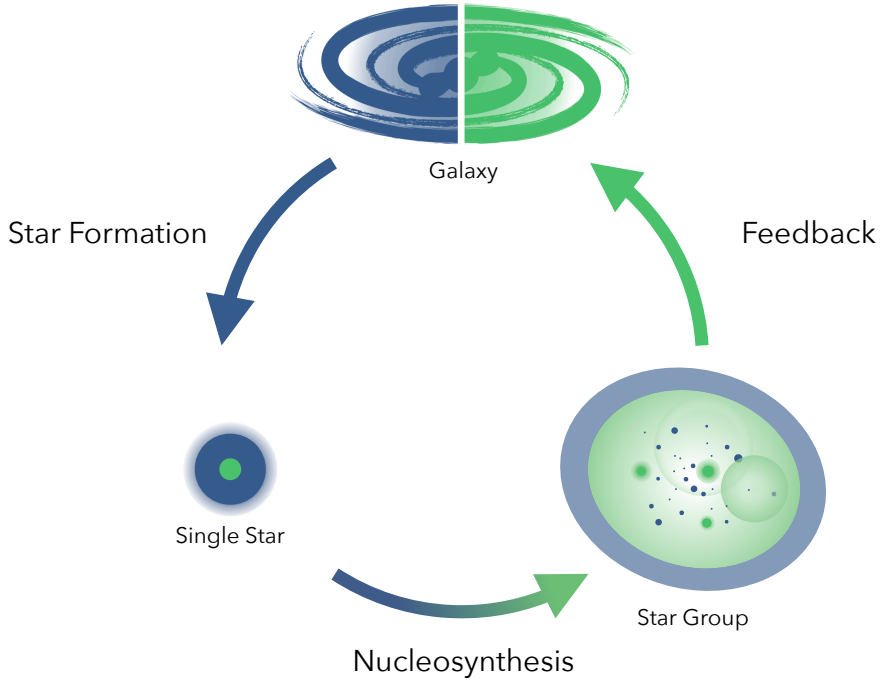

Figure 2.2: Schematic representation of the cosmic Cycle of Matter with metallicity symbolically increasing from *blue* to *green*. The cycle progresses basically in three fundamental steps over three major scales. (1) Single stars emerge from the ISM on galactic scale. (2) In the interior of these stars nucleosynthesis occurs and produces more heavy nuclei. (3) The more metal-rich material is ejected from individual stars in stellar winds and SNe and mixes back into the ISM in superbubble structures around massive star groups. This closes the cycle by an overall enrichment of the galactic ISM with heavier elements.

Star Formation Turbulence and gravitational instabilities mostly inside the spiral arms lead to large-scale fragmentation of the diffuse ISM into giant molecular clouds (GMCs). The latter have masses of $\sim 10^6\,\mathrm{M}_\odot$ and diameters of a few hundred pc (Shu et al. 1987; McKee & Ostriker 2007). Internal turbulence leads to sub-fragmentation of clouds into denser regions which become self-gravitating bound cores. When the latter exceed a critical mass, they collapse under further accretion. This leads to a net star formation efficiency of $\epsilon_{\mathrm{SF}} \sim 1/3$ in an individual core. The outward angular momentum transport of the collapsing core leads to the formation of a rotating disk. Stars form in the mass range between 10^{-1} and $10^2\,\mathrm{M}_\odot$, with massive stars forming predominantly form highly turbulent cores. This process will be described in detail in Sec. 2.2.
The massive and luminous stars ionise the surrounding gas in bubble-like structures. These cavities expand with $v_{\mathrm{exp}} \sim 10\,\mathrm{km\,s^{-1}}$ which is accompanied by injection of energy and turbulence to the surrounding ISM. This cumulative process from multiple stars disperses the host GMC due to photoevaporation and the GMC gas returns into the diffuse phase of the ISM. In the course of this cycle only $\sim 5\%$ of the total mass of the original GMC has been transformed into stars (McKee & Ostriker 2007). The other part of the material remains unprocessed.

Nucleosynthesis The gas confined inside the stars is exposed to high temperature and gravitative pressure. As a consequence, it undergoes fusion reactions to heavier nuclei. This nucleosynthesis processes release radiative energy corresponding to the difference in binding energy between the nuclei before and after the fusion. The thermal and radiative energy counteracts the inwardly directed gravitational collapse of the material and the star reaches a stable equilibrium state. Besides stars, nucleosynthesis reactions occur also in other astrophysical sites of high temperature and density, novae, thermonuclear or core collapse supernovae (ccSNe), merger events, or due to cosmic ray interactions.
Newly produced material up to the Fe-group resides in the stellar interior until the star reaches the terminal phases of its evolution. If the star finally undergoes a SN or stellar merger, the energy release during the collapse leads to production of nuclei with mass numbers beyond the Fe-group elements in explosive nucleosynthesis. Fundamental nucleosynthesis processes will be outlined in Sec. 2.2.3. Despite their importance for the understanding of the cosmogenic history, currently none of these sites can be considered as sufficiently understood in order to draw a complete picture of nucleosynthesis (Diehl 2018).

Feedback If the freshly produced nuclei would stay where they were created, nucleosynthesis would be a discontinuous process restricting chemical enrichment to distinct astrophysical sites. This happens mostly in low-mass stars which end their evolution as cooling white dwarfs. But some nucleosynthesis products are ejected from their production sites. Stellar winds carry dredged up material from the stellar surface into the surroundings. When the star terminates in a SN and is entirely disrupted, the full variety of newly produced elements is ejected with high velocities.
The surrounding gas and previously ejected material is swept up cumulatively in shells around groups of massive stars, which reside in huge superbubble structures filled with hot and thin gas heated by expelled gas and strong ultraviolet (UV) radiation. As these shells cool, processed stellar material is mixed in turbulent flows with unprocessed cold gas of the host GMC. Thus, the surrounding gas is enriched with heavier elements and dispersed or compressed by the injected kinetic energy. As this process occurs in many places in a galaxy, the entire diffuse ISM is thereby chemically enriched and infused with turbulent flows. These turbulences again lead to fragmentation and self-gravitational instabilities in the ISM. This means that the next generation of stars forms and one iteration of the galactic Cycle of Matter is completed. The loop of stellar material starts anew with a different initial elemental composition.

Essentials

Nucleosynthesis feedback is the mechanism underlying galactic chemical evolution. The overarching process in which nucleosynthesis feedback occurs is the cosmic Cycle of Matter.

- How do individual stars form? ⟶ Sec. 2.2.1
- Why does nucleosynthesis occur in stars? ⟶ Sec. 2.2.3
- What are the different aspects of stellar feedback? ⟶ Sec. 2.2.5
- What is the effect of nucleosynthesis feedback in star groups? ⟶ Sec. 2.3
- How does single star feedback affect the entire Galaxy? ⟶ Sec. 2.4

2.2 Single Stars

First and foremost in human history, stars are among the key objects that excited and fostered natural philosophy and later scientific thought. A major insight for mankind has been that stars do evolve, rather than being eternal objects in an unchanging cosmos. This evolution shows processes much larger and longer than what is related to biology on Earth. One of the longest direct research enterprises of one object follows SN 1054 since its first mentioning in 1054 in Chinese scripture. This event marked the gravitational collapse of a 8–10 $M_\odot$ star and the research that tried to understand its origin and aftermath (Smith 2013). Historically, such events set the previously static cosmos in a motion of emergence and decay. Thus, until today, we study stars as primary tracers of the content and evolution of the Universe.

2.2.1 Formation

Molecular Clouds Star formation is a gravitationally driven and hierarchically structured process that transforms gas from the ISM into stars. One individual star formation event is defined here as process in which mostly H I, i.e. atomic hydrogen gas, in a spatial range of $\sim 1\,\mathrm{pc}$ is transformed into a star in $\sim 1\,\mathrm{Myr}$ (Kroupa et al. 2013). The original molecular gas has a mass density of the order of $10^{-20}\,\mathrm{g\,cm^{-3}}$. This collapses into stars with densities of the order $1\,\mathrm{g\,cm^{-3}}$ (Bonnell & Larson 2007). What is usually defined as molecular clouds is where the extinction is high enough to form molecules. This is typically the case for hydrogen column densities of $N_\mathrm{H} \gtrsim 2 \times 10^{21}\,\mathrm{cm^{-2}}$ (Bohlin et al. 1978; Lombardi et al. 2014). Embedded in this gas, there are GMCs with a higher mean column density of $N_\mathrm{H} = (1.5 \pm 0.3) \times 10^{22} R_\mathrm{pc}^{0.0\pm0.1}\,\mathrm{cm^{-2}}$ weakly dependent on the galactocentric radius R_pc in units of pc (McKee & Ostriker 2007). They can form due to large-scale gravitational instabilities (e.g. McKee & Holliman 1999) or large-scale colliding galactic flow motions (e.g. Heitsch et al. 2005). In either case, cold H I clouds merge due to Jeans instabilities caused by differential gravity in the galactic plane (Jeans 1902)

or, to a lesser extent, due to large-scale Parker instabilities along galactic magnetic field lines (Parker 1966) that quench the gas until the gravitational mass of a GMC is reached (Elmegreen 1979). The Jeans mass of a cloud is the mass of an object that is necessary to be gravitationally bound against its thermal outward pressure. Thus, in the simplified case of a uniform sphere of gas, the equilibrium condition for gravitation and thermal energy is, according to the virial theorem, $2E_{\mathrm{kin}} = -E_{\mathrm{pot}}$. This can be expressed as (Unsöld & Bascheck 2002, 379–380)

$$\frac{3k_{\mathrm{B}}T}{\mu m_{\mathrm{u}}}M = -\frac{3}{5}\frac{GM^2}{R}, \tag{2.1}$$

with Boltzmann's constant k_{B}, gas temperature T, molecular weight of the gas particles μ, atomic mass constant m_{u}, gravitational constant G, and the mass $M = (4\pi/3)\rho R^3$ of the gas with density ρ inside the radius R. This implies a characteristic length scale, the Jeans radius, for the gravitational fragmentation of a molecular cloud (Jeans 1902)

$$R_{\mathrm{Jeans}} = \sqrt{\frac{15k_{\mathrm{B}}T}{4\pi G\rho\mu m_{\mathrm{u}}}}. \tag{2.2}$$

This is the critical radius at which thermal energy and gravity of a cloud are equilibrated. The critical mass inside this radius is then

$$M_{\mathrm{Jeans}} = \left(\frac{4\pi}{3}\rho\right)^{-\frac{1}{2}}\left(\frac{1}{5}\frac{k_{\mathrm{B}}T}{G\mu m_{\mathrm{u}}}\right)^{\frac{3}{2}} \approx 3.82\times10^{-9}\ \rho^{-\frac{1}{2}}\left(\frac{T}{\mu}\right)^{\frac{3}{2}}\mathrm{M}_{\odot}, \tag{2.3}$$

with temperature in units of K and density in units of $\mathrm{kg\,m^{-3}}$. For cold molecular gas clouds with densities in the range between 10^{-21} and $10^{-18}\,\mathrm{kg\,m^{-3}}$ and temperatures from about 10 to 100 K the Jeans mass is of the order of 10^2 to $10^5\,\mathrm{M}_{\odot}$. Impinging ionizing cosmic rays provide a continuous heating source, even in dense cloud cores, which prevents molecular gas from cooling significantly below ~ 10 K. The critical mass estimation serves as theoretical lower mass limit for a cloud to collapse under its own gravity.

While numerically most clouds have low masses, 80% of the molecular gas is contained in clouds more massive than $10^5\,\mathrm{M}_{\odot}$ (Stark & Lee 2006). The overall distribution of molecular gas in the Milky Way can be traced by CO emission lines and is depicted in Fig. 2.3.

Masses of star-forming bound clouds are typically a few times the Jeans mass (Kim et al. 2002). Larson (1981) assigned as main physical feature of such GMCs that they are supersonically turbulent, which is the source of star formation. Nevertheless, most of the gas in a GMC is unbound and is not converted into stars because feedback from the first-born stars is counteracting the global collapse as well (Clark et al. 2005). This mechanism will be explained in more detail in Sec. 2.2.5.

In general, star formation is a cloud internal process and inherent gravitational Jeans instabilities are mostly induced in spiral arms and centres of galaxies. These are the regions where consequently most star formation occurs (Elmegreen 1994; Kim & Ostriker 2002). Stars that are formed within clouds constitute the main source of feedback via UV radiation. As the cloud gains energy from this internal stellar feedback, it loses mass. The dominant destruction mechanism of clouds is therefore photoevaporation by H II regions, i.e. sites of ionised hydrogen gas (McKee & Ostriker 2007). This can especially disrupt smaller clouds and leads overall to a theoretically estimated lifetime of about $20 - 30$ Myr for clouds with masses

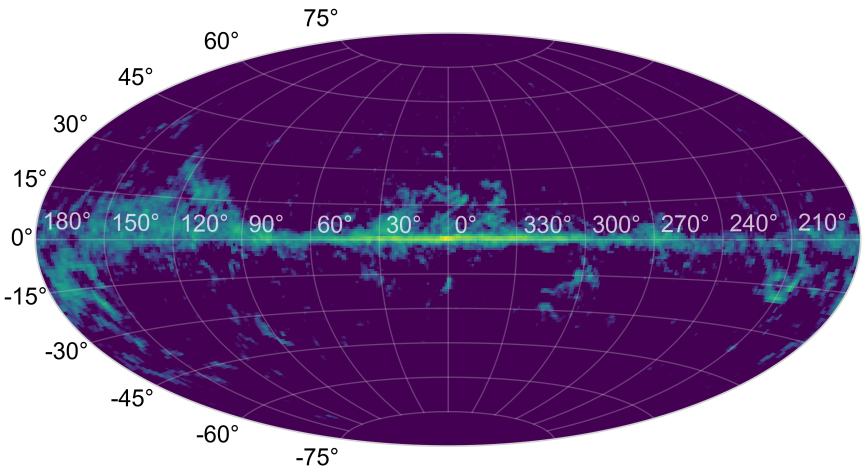

Figure 2.3: All-sky map of CO $J = 1 \rightarrow 0$ (857 GHz) dust emission measured by the *Planck* satellite.

$\sim 10^6\,\mathrm{M}_\odot$(Matzner 2002; Krumholz et al. 2006).
The large GMCs are not homogeneous but hierarchically sub-structured in clumps with densities of $n_\mathrm{H} \approx (3-12)\times 10^3\,\mathrm{cm}^{-3}$ (Liszt 1993; Sanders et al. 1993). That are those parts of the cloud which become Jeans unstable. Because of these structures stars do not form individually but in groups of stars (Lada & Lada 2003). These will be discussed in detail in Sec. 2.3. Clumps are again sub-structured in cores which will finally form stars (Ward-Thompson et al. 2007). Overall, this means that a collapsing cloud follows a hierarchical process sketched in Fig. 2.4, with clumps forming star groups and cores being the birthplaces of individual or, in the case of fragmentation, binary stars (McKee & Ostriker 2007; Shu et al. 1987; Kennicutt & Evans 2012).

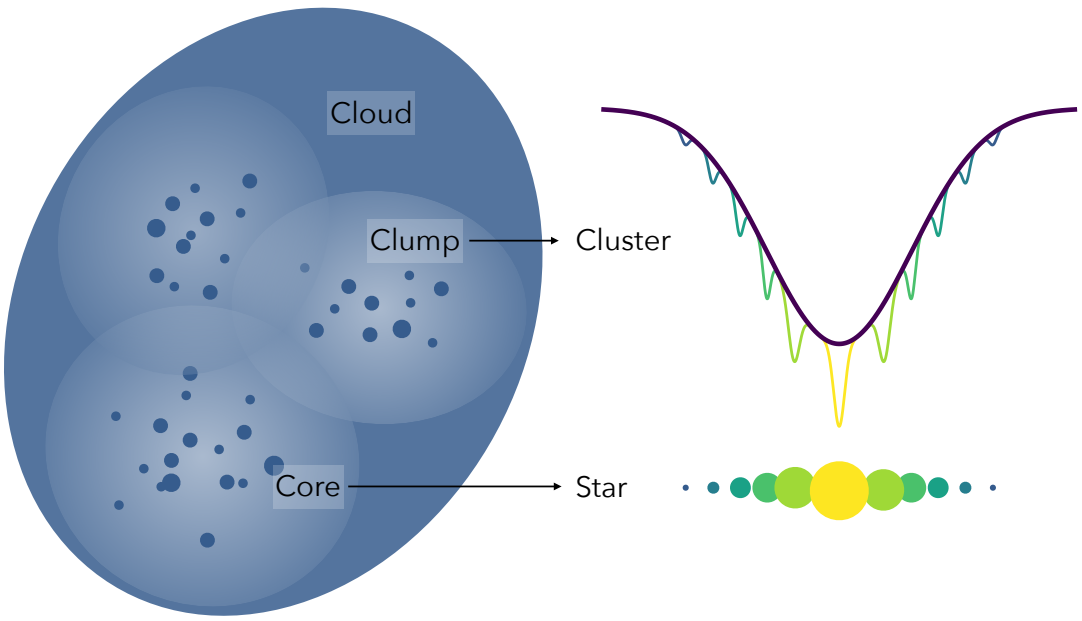

Figure 2.4: *Left:* Hierarchical structure of molecular clouds. They are sub-structured into clumps, which form star groups, and these into cores, which form stars. *Right:* Schematic diagram of the cluster forming potential of a clump. Gas flows globally inwards and fragments into the overlaid funnels of star forming cores. The inflow of gas in the potential well leads to higher accretion on star forming cores in the centre than in the outer regions. This leads to a stellar masses formed in the cluster as depicted schematically on the lower right (adopted from Bonnell & Larson 2007).

When a core significantly heats up due to gravitational collapse, it is referred to as protostar. This is defined as a hydrostatic object with $M > 0.012\,\mathrm{M}_\odot$ not yet undergoing nuclear burning processes. The time in which the protostar gravitationally contracts until nuclear burning starts is determined by the Kelvin-Helmholtz time scale $\tau_{\mathrm{KH}} = GM_*^2/RL$. This is the time in which the kinetic energy in the total gas mass of the star M_* is radiated away with a given luminosity L and stellar radius R. With $L \propto M^{3.5}$ this gives the relation $\tau_{\mathrm{KH}} \propto M_*^{-2.5}$ (Kippenhahn et al. 2012, 328). This implies that lower-mass protostars contract slower than higher-mass stars, i.e. lower-mass stars form slower than stars with higher masses. Herbig (1962) proposed bimodal star formation with different mechanisms to be responsible for the formation of high- and low-mass stars. The latter are usually defined as having masses $M_* < 0.8\,\mathrm{M}_\odot$, whereas high-mass stars have masses $M_* \geq 8\,\mathrm{M}_\odot$. This defines intermediate-mass stars in the mass range $0.8\,\mathrm{M}_\odot < M_* < 8\,\mathrm{M}_\odot$. Classifications of stars according to their masses are summarised in Tab. 2.1.

Table 2.1: Classification of stars by their mass. Nucleosynthesis characteristics are conserved from low to high masses and only stepwise additional or changing characteristics are mentioned. For H-burning the dominant process is indicated in superscript for either pp-chain or CNO-cycle.

Class	Sub-class	Mass [$\mathrm{M}_\odot$]	Nucleosynthesis characteristics
Low-mass			
	(Sub-dwarf)	4×10^{-3}–$0.012^{(a)}$	collapse faster than cooling
	Brown dwarf	0.012–$0.075^{(b)}$	deuterium burning
	Red dwarf	0.075–$0.2^{(c)}$	core H^{pp}-burning
Intermediate-mass			
	M-type	0.2–$0.8^{(d)}$	shell H^{pp}-burning
	K-type	0.8–$1.1^{(d)}$	core He-burning
	G-type	1.1–$1.5^{(d)}$	core He-burning
	F-type	1.5–$3^{(d)}$	core $\mathrm{H}^{\mathrm{CNO}}$-burning
	A-type	3–$6^{(d)}$	He-shell burning
	Late B-type	6–$8^{(d)}$	hot bottom burning
High-mass			
	Early B-type	8–$16^{(e)}$	C-, Ne-, O-, and Si-burning
	Late O-type	16–$32^{(e)}$	C-, Ne-, O-, and Si-burning
	Early O-type	32–$64^{(e)}$	C-, Ne-, O-, and Si-burning
	O/WR-type	$\geq 64^{(e)}$	C-, Ne-, O-, and Si-burning

Adopted from $^{(a)}$ Low & Lynden-Bell (1976), $^{(b)}$ Luhman (2012), $^{(c)}$ McKee & Ostriker (2007), $^{(d)}$ Unsöld & Bascheck (2002, 291), and $^{(e)}$ Zinnecker & Yorke (2007).

If the core mass lies significantly above the thermal Jeans mass, a protostar that forms with an accretion disk and an infalling gas envelope. If the continuous accretion from the parental cloud is not halted by proto-stellar feedback, a massive star forms.

IMF The mass distribution of the star formation process was empirically described as the stellar initial mass function (IMF) by Salpeter (1955) as a single slope power-law

$$\xi(M_*) = \frac{dN_{\mathrm{star}}}{dM} = kM_*^{-\alpha}, \tag{2.4}$$

with an exponent $\alpha = 2.35$ for stellar mass M_* in units of $\mathrm{M}_\odot$ and a normalisation constant k. It gives the number of stars dN_{star} in the mass interval between M and $M + dM$. As stars are the fundamental agents of most astrophysical processes this

is one of the most important astrophysical distribution functions. The observational basis for the IMF is provided by measuring the stellar census of many dense clusters, such as e.g. R136 in the 30 Dor region of the LMC, NGC 346 in the SMC, h and χ Persei, NGC 604 in M33, NGC 1960, NGC 2194, or NGC 6611; an overview of recent observational cases probing the IMF can be found e.g. in Elmegreen (2009), Weidner et al. (2010), Kirk & Myers (2011), or Dib (2014). The IMF itself is not a directly measurable quantity because no individual stellar population can be followed for its entire dynamical history. A proof of this IMF unmeasurability theorem can be found in Kroupa et al. (2013, 129). The main challenge arises from the fact that only the present-day distribution is observable but many stars with lifetimes shorter than the age of the Galaxy have disappeared from the initial distribution (Scalo 1986). Thus, in order to infer the IMF from the present-day distribution the main assumption is temporal invariance (Elmegreen & Scalo 2006). Another challenge is that most massive stars form in binary systems with lower mass companions. If these companion stars are not resolved this means an observational bias that changes the IMF significantly (Kroupa 2001; Maíz-Apellániz 2008). Particularly at the low mass end of the IMF objects are very faint and therefore rather difficult to measure (Covey et al. 2005). This causes major observational biases in the low-mass realm of the distribution. However, the shapes of the IMF inferred from observations of field stars, star forming regions, and open clusters agree. This indicates that the systematic errors down to masses $\sim 0.02\,\mathrm{M}_\odot$ are reasonably taken into account and corrected because observations of different stages in age of stellar groups yield consistent IMF slopes (Luhman & Potter 2006). As a rule of thumb to illustrate the IMF, there should be over 10^6 solar-type stars for every $100\,\mathrm{M}_\odot$ star. Although the IMF is a necessary tool in modelling and understanding star formation processes it remains a problematic field that requires further research (Krumholz 2014).
The relation in Eq. 2.4 was later refined by Miller & Scalo (1979) with a flatter $\alpha = 1$ distribution below $1\,\mathrm{M}_\odot$. In the Solar Neighbourhood this flattening for low-mass objects was found to occur only at even lower masses $< 0.5\,\mathrm{M}_\odot$ (Chabrier 2001; Reid et al. 2002; Covey et al. 2008; Bochanski et al. 2010). Kroupa (2001) adjusted the slope of the IMF to the standard IMF as multiple-broken power-law

$$\xi_{\mathrm{Kroupa}}(M_*) = k_i M_*^{-\alpha} \quad \text{with} \quad \begin{cases} \alpha = 0.3 & \text{for } M_* \leq 0.08 \\ \alpha = 1.3 & \text{for } 0.08 < M_* \leq 0.5\,, \\ \alpha = 2.3 & \text{for } M_* > 0.5 \end{cases} \tag{2.5}$$

with a normalisation constant k_i in each of the three mass regimes depending on the local star formation rate and ensuring continuity. The IMF estimated by Chabrier (2003) follows a very similar shape below $1\,\mathrm{M}_\odot$ in a smoother log-normal formulation

$$\xi_{\mathrm{Chabrier}}(M_*) = \begin{cases} \frac{a}{M_* \log(10)} \exp\left(-\frac{[\log(M_*)-\log(\mu)]^2}{2\sigma^2}\right) & \text{if } M_* \leq 1 \\ k_{\mathrm{Chabrier}} M_*^{-2.3} & \text{if } M_* > 1 \end{cases}, \tag{2.6}$$

with normalisation constant $k_{\mathrm{Chabrier}} = 1/\log(10)\exp\left[-(\log(\mu)^2/2\sigma^2)\right]$. The log-normal parameters are amplitude $a = 0.158$, mean $\mu = 0.079$, and width $\sigma = 0.69$. These values have been revised by Chabrier (2005) to $a = 0.086$, $\mu = 0.2$, and $\sigma = 0.55$. The different IMFs are shown graphically in Fig. 2.5 for a star formation event with a total mass of $10^6\,\mathrm{M}_\odot$.
If the IMF is assumed to be continuous without confinement to higher masses, statistical random sampling would predict stars to be observable up to a mass of

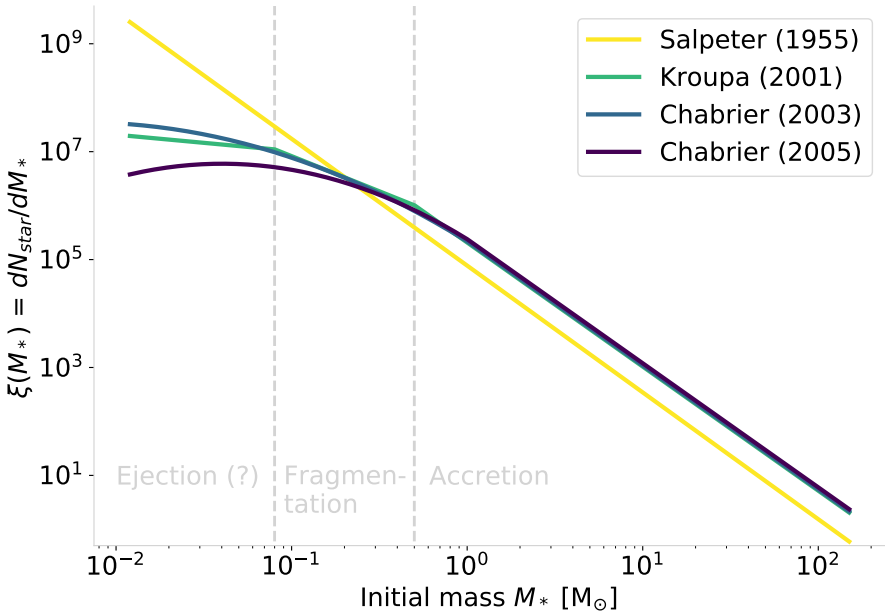

Figure 2.5: Different shapes of the stellar IMF in the mass range between 0.012 and 150 $M_\odot$ for a stellar cluster with a total mass of 10^6 $M_\odot$. The different shapes are estimated by Salpeter (1955), Kroupa (2001), Chabrier (2003), and Chabrier (2005). Star formation mechanisms are ascribed to different mass regimes following Bonnell & Larson (2007).

4×10^5 $M_\odot$ (Elmegreen 2000). However, there is an empirical upper mass limit of ~ 150 $M_\odot$ (Weidner & Kroupa 2004; Oey & Clarke 2005; Figer 2005). It is discussed whether this is a physical limit or due to observational biases; or if it is due to statistical reasons of too few stars sampled at very high masses to be observed (e.g. Elmegreen 1997; Massey 2003).

There is discussion whether in the early Universe there might have been no cutoff allowing for supermassive stars (Bond et al. 1984; Bromm et al. 2001) or a general time-dependence of the IMF (Bastian et al. 2010; Dib 2014). In particular, there are indications that the IMF in the early Universe was skewed compared to today, producing less low-mass stars and more massive stars (Jerabkova et al. 2018). For low-mass stars a theoretical limit has been proposed but so far without observational confirmation (McKee & Ostriker 2007). The lowest physical limit for star formation is set by the condition that the contraction time has to be shorter than the cooling time. This limit is set by the Eddington limit or slightly lower by the minimum Jeans mass to 3–10 Jupiter masses (Low & Lynden-Bell 1976; Rees 1976; Boyd & Whitworth 2005).

The detailed processes occurring early in star formation were reviewed e.g. by (Bonnell & Larson 2007), finding that the effects of feedback and magnetic fields on the origin of the IMF are still largely unclear. Nevertheless, the shape of the IMF can be interpreted to reflect three regimes governed by different main processes: fragmentation of dense filaments and disks, early ejection from these dense environments, or continued accretion in the cluster environment for high-mass stars. Accretion generally denotes the rate of mass inflow onto an object. Note that it is neither the rate of mass gain of an object nor mass gain itself.

Low-mass stars originate from gravitational fragmentation due to turbulence and the filamentary structure inherent to molecular clouds (Bate et al. 2002). The re-

sulting self-gravity is very sensitive to ionisation and thermal processes, which are in turn influenced by the metallicity and density of the gas, as well as its dust grain properties. Stars initially have the composition of the ISM they formed out of. In contrast, planets forming from the circumstellar disc have a higher metallicity than the ambient ISM. Very low mass protostars and very young low mass stars are actually expected to gain from accretion and become more massive because of their mass beyond the Jeans mass. However, a large number of brown dwarfs (cf. Tab. 2.1) is observed. In order to explain their abundance, they must have been ejected or accelerated away from the environment where they have been born due to stellar feedback. This process halts accretion and allows for stars remaining at very low masses (Padoan & Nordlund 2004). Stars at the high mass side of the IMF build up their high mass due to continued accretion of gas from the dense cluster environment. The generally accepted explanation for this process is that the cluster potential (cf. right side of Fig. 2.4) facilitates higher accretion rates for the stars in the cluster centre. This is in agreement with the observed mass segregation in young stellar clusters (Bonnell & Larson 2007). The stellar feedback in the star formation process does affect both, the star itself and also its environment. It includes jets, outflows, winds, ionisation and radiation pressure. All these processes affect the shape of the IMF in a complex way which is difficult to model (Li & Nakamura 2005) and which will be discussed in more detail in Sec. 2.2.5.

High-Mass Star Formation The formation of massive stars happens in a time longer than t_{KH} (Kahn 1974; Unsöld & Bascheck 2002), which means that nuclear fusion reactions occur already during the accretion phase. In addition, the radiative stellar feedback affects already the formation phase of the star itself. As can be seen from the schematic structure of the cluster potential in Fig. 2.4, high-mass stars occur preferentially in the dense central part of a cluster, which affects the gas evolution and protostars in their surroundings. High-mass star formation takes place in cold gas clumps with temperatures between 10 and 30 K which have a low level of turbulence with smooth velocity dispersion and gradients in the range between 5 and $10\,\mathrm{km\,s^{-1}\,pc^{-1}}$ (Bihr et al. 2015). The characteristic density of the material is of the order of $10^{-3}\,\mathrm{M_\odot}$ (Larson 1969; Bate 2000). During the infall of the material the size scale decreases from $\sim 0.1\,\mathrm{pc}$ by about 6 orders of magnitude. This process carries significant momentum to the star and forms a rotating disk around it (Zinnecker & Yorke 2007). Due to radiative feedback, the birth cloud is usually disrupted. Because of the quick infall of gas and the early onset of H burning, the ionising radiation decreases accretion but does usually not reduce it to zero (Krumholz et al. 2005). Simulations suggest that radiative feedback can set an upper limit to accretion. This sets the maximum stellar mass achievable via accretion to about $40\,\mathrm{M_\odot}$ (Yorke & Sonnhalter 2002; Edgar & Clarke 2004). Nevertheless, observational evidence suggests that stars exist up to a mass of the order of $150\,\mathrm{M_\odot}$ (Massey & Hunter 1998; Weidner & Kroupa 2004; Figer 2005). The circumvention of the proposed limit is likely due to a combination of Rayleigh-Taylor instabilities in the inflowing gas or stellar collisions and merger (Bonnell & Bate 2005; Krumholz et al. 2005; Bonnell & Larson 2007). A theoretical upper mass limit for stars is determined by the condition that if the star has a very high mass, it can generate energy at such a high rate, that the inside-out radiative pressure dominates and overcomes the counteracting gravitational pressure P_{grav}. In that case the star disperses. The radiative pressure inside a star can be determined as

(Kippenhahn et al. 2012)

$$\frac{dP_{\mathrm{rad}}(r)}{dr} = \frac{\kappa\rho(r)L(r)}{4\pi r^2 c}, \tag{2.7}$$

with opacity κ, luminosity $L(r)$, and the gas density $\rho(r)$. Hydrostatic equilibrium, which will be discussed in more detail in Eq. 2.11 in the following Sec. 2.2.2, is broken if

$$\begin{aligned}\frac{dP_{\mathrm{grav}}(r)}{dr} + \frac{dP_{\mathrm{rad}}(r)}{dr} &= \rho(r)\frac{GM(r)}{r^2}\left(1 - \frac{\kappa L(r)}{4\pi c^2 GM(r)}\right) \\ &= \rho(r)\frac{GM(r)}{r^2}(1-\Gamma_{\mathrm{E}}) < 0.\end{aligned} \tag{2.8}$$

This means that the outwardly acting radiative pressure exceeds the counteracting gravitational pressure. Consequently, the star disperses. The following Sec. 2.2.2 will underpin the understanding of this process with a detailed outline of the underlying stellar structure. The condition in Eq. 2.8 is fulfilled if $\Gamma_{\mathrm{E}} > 1$. For stellar mass M_*, this implies the critical Eddington luminosity

$$L_{\mathrm{E}} = \frac{4\pi c G M_*}{\kappa} \tag{2.9}$$

at which Eq. 2.8 is right equal to zero. In hot and massive stars, electron scattering dominates the opacity. In this case the Eddington luminosity can be approximated as

$$\frac{L_{\mathrm{E}}}{L_\odot} = 3.824 \times 10^4 \frac{M_*}{M_\odot}, \tag{2.10}$$

given a hydrogen fraction of 0.7. This means that massive main-sequence stars with $M_* \gtrsim 200\,\mathrm{M}_\odot$ are not stable and disperse due their high radiative pressure. Thus, it can be taken as approximation of the upper mass limit of stars. This constitutes an important boundary condition for the normalisation of the IMF.

2.2.2 Stellar Structure

Basics and Fundamental Equations Stars are spheres of gas with mass M_* and radius R_* in hydrostatic equilibrium. At each volume element at radius r from the centre, gravity acts inwards corresponding to the mass $M(r)$ inside radius r. This is equilibrated by the outwards acting gas pressure $P = P_{\mathrm{th}} + P_{\mathrm{rad}}$, which is the sum of thermal and radiative pressure. The gravitational pressure can be formalised as (e.g. Heger et al. 2000; Hurley et al. 2000; Unsöld & Bascheck 2002, 280–289)

$$\frac{dP(r)}{dr} = -\rho(r)\frac{GM(r)}{r^2}, \tag{2.11}$$

where mass conservation

$$\frac{dM(r)}{dr} = 4\pi r^2 \rho(r) \tag{2.12}$$

holds. In a first order approximation the gas inside a regular star can be assumed to be an ideal gas dominated by thermal pressure only. Therefore, its equation of state is

$$P_{\mathrm{th}} = \rho\frac{k_{\mathrm{B}}T}{\mu m_{\mathrm{u}}}. \tag{2.13}$$

Stars release energy in their interior due to nuclear reactions and gravitational collapse. In order to stay in equilibrium, internally at radius r with rate $\epsilon(r)$ generated energy has to escape from the star. Therefore, it has to be transported from the central regions to the surface, which implies an outwards flow of energy

$$\frac{dL(r)}{dr} = 4\pi r^2 \rho(r) \epsilon(r) \tag{2.14}$$

through a differential shell between r and $r + dr$. The energy transport inside the star happens radiatively as well as convectively. The internal stellar temperature distribution is determined by (2.13). With the equation for radiative transport and spherical integration over the internal radiation field, the radiative component of energy transport

$$\frac{dT(r)}{dr} = \frac{3\kappa\rho}{4acT^3} \frac{L(r)}{4\pi r^2} \tag{2.15}$$

can be obtained. It is dependent on metallicity, which in turn affects opacity κ as well as density ρ. In addition to radiative transport, there occur large convective flows of hot plasma inside a star, which transport energy outwards by large scale motions of material between regions. This causes a much more complex temperature gradient in convection zones. A convection zone is a region where the convective energy transport outweighs the radiative energy transport. The relation between temperature and pressure of an ideal gas is given by $T \propto P^{1-\frac{1}{\gamma}}$, with the adiabatic constant γ. This determines the temperature gradient

$$\frac{dT(r)}{dr} = \left(1 - \frac{1}{\gamma}\right) \frac{T}{P} \frac{dP(r)}{dr}. \tag{2.16}$$

This is based on simplified assumptions, invoking only the radial dimension, and can only serve as a rough description of otherwise highly complex convection zones. The mechanism of convection mixes fresh material into different stellar burning regions and thereby influences nucleosynthesis, as will be described in more detail later in Sec. 2.2.4. There are other external factors that influence the stellar structure significantly, such as rotation (Maeder & Meynet 2000) or binary interactions. Overall, if we combine Eq. 2.11 for hydrostatic equilibrium with the relation of mass and central temperature $T_c \propto \mu M/R$, we obtain the fundamental relation (Lugaro & Chieffi 2018)

$$L_* \propto \mu^4 M_*^3 \tag{2.17}$$

between luminosity L_* and stellar mass M_* along the main sequence. Since temperature and pressure determine nuclear fusion processes going on in the star, their radial gradient leads to a shell like structure of burning processes as depicted schematically in Fig. 2.6. This is also supported by the gravitational sedimentation of heavier elements at smaller stellar radii.

Mixing In the above mentioned picture stellar structure appears to be rather static. If that were the case, freshly synthesised nuclei would reside in the centres of stars and there would be no trace of nucleosynthesis other than from after the disruption of massive stars in SNe. But already during their earlier evolution enrichment in heavy elements and isotopes is observed on stellar surfaces. This is because other than the simplified picture of the aforementioned hierarchical shell structure and equilibria suggest, the matter inside a star is not stationary. Instead, mixing of

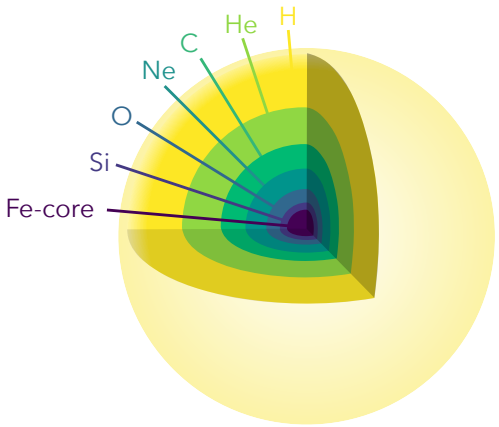

Figure 2.6: Scheme of the burning shell structure of a 25 $M_\odot$ star. Concentric shells arrange so that heavier nuclides are processed closer to the stellar centre. This is a simplified picture where shells are not to scale and mixing between shells has been neglected.

different layers on large scales can occur. In order to have large scale motions inside a star the Schwarzschild criterion must be overcome, i.e. the radiative temperature gradient exceeds the adiabatic gradient. In this case, stochastic motion of matter is amplified, and leads to growing large scale motions (Lugaro & Chieffi 2018, 107). Thus, in order for large scale convection to occur, a steep temperature gradient must be present. This is the case either close to nuclear burning sites where energy is produced and highly concentrated in small areas, or in regions with high opacity, i.e. environments with a short mean free path for photons. In either case, convection becomes an effective way of energy transport because convective turbulences have a large mean free path compared to that of photons. Along with the mixing of material with different thermal states occurs mixing of material with different chemical compositions. This mechanism transports nucleosynthesis products away from their production sites.

Internal effects due to stellar rotation also influence the mixing processes. On the one hand, additional advection and turbulent diffusion occurs to transport angular momentum (e.g. Endal & Sofia 1978; Heger et al. 2000). On the other hand, these motions are oriented preferably horizontally, i.e. inside a shell at a certain radius. If this effect becomes very large, it inhibits radial advection. While angular momentum is still transported outwards, the radial transport of chemical enriched material is largely reduced to diffusion (Chaboyer & Zahn 1992). Thus, the characteristic mixing time for chemical elements inside a rotating star is (Maeder & Meynet 2000)

$$t_{\mathrm{mix}} \approx \frac{R^2}{D_{\mathrm{mix}}}, \tag{2.18}$$

with the coefficient D_{mix} being the sum of the turbulent and non-turbulent diffusion coefficients. Since rotation can reduce D_{mix}, chemical mixing can also be slower in rotating stars. This explains the reduced effects on surface metallicity observed in some rotating intermediate-mass stars (e.g. Pinsonneault et al. 1991; Chaboyer et al. 1995; Heger et al. 2000).

In the massive star regime, anomalies related to rotation can occur. These anomalies override the before mentioned mechanism of attenuating chemical diffusion and instead foster extensive deep mixing. This process is particularly difficult to constrain observationally because in massive stars the surface abundances are also strongly

affected by mass loss from the outer layers. Since energy generation in massive stars happens largely in convective cores, convection is able to penetrate the entire star. This can disperse the shell structure completely and lead to fully mixed evolution in $\sim 15\%$ of the most massive stars. In general, mixing is comparable or reduced in lower-mass stars compared to high-mass stars (Maeder 1987). With a special focus on massive stars, this can be roughly summarised as follows: The more massive a star and the faster it is rotating, the more mixing is occurring (Pinsonneault 1997)

2.2.3 Nucleosynthesis

The theory of stellar nucleosynthesis describes the formation of elements from less massive nuclei in stars. Since its pioneering foundation by Fred Hoyle (1946b,c), it is subject to extensive studies in order to explain the history of the isotopic abundances we observe today. This history starts basically with hydrogen as the fundamental building block for two reasons. First, Big Bang Nucleosynthesis (cf. Fig. 2.1) produced a primordial abundance of hydrogen as the most abundant element and only a fraction of $\sim 10^{-9}$ less heavier elements (Steigman 2007; Cyburt et al. 2016). Second, the proton is the simplest stable nuclide, since neutrons decay with a mean lifetime of $\sim 880\,\mathrm{s}$ (Beringer et al. 2012; Tanabashi et al. 2018). This stellar nucleosynthesis was studied extensively in a seminal paper by Burbidge et al. (1957).
Energy release Q due to nuclear fusion reactions $0 \rightarrow 1$ is based on the fundamental energy-mass equivalence principle $Q = mc^2$ (Einstein 1905a) and the difference in mass between parent nuclei and daughter nucleus. For the foremost in stars occurring fusion of four ^{1}H atoms to one ^{4}He atom this is (e.g. Iliadis 2015, 353–354)

$$\begin{aligned} Q &= (m_0 - A_0 m_\mathrm{u})c^2 - (m_1 - A_1 m_\mathrm{u})c^2 \\ &= 4m_{^1\mathrm{H}}c^2 - m_{^4\mathrm{He}}c^2 = 26.731\,\mathrm{MeV}, \end{aligned} \tag{2.19}$$

where A_i is the mass number and m_i the atomic mass of the reactants, which are distinguished by the index i. This energy difference is due to the fact that nuclei in the ^{4}He are more tightly bound than protons in ^{1}H atoms. Thus, Q represents a release of binding energy in the form of gamma-rays or kinetic energy of the products.
On the one hand, the efficiency of nuclear reactions depends on the abundance of the reactants. On the other hand, it depends on their cross section $\sigma(E)$ and their relative velocities v. The distribution of particle velocities in stellar plasma corresponds to their thermal motions and can be described by the Maxwell-Boltzmann distribution in energy space (e.g. Wolf 1965)

$$P(E)dE = \sqrt{\frac{4E}{\pi(k_\mathrm{B}T)^3}}e^{-E/k_\mathrm{B}T}dE \tag{2.20}$$

for $E = mv^2/2$, temperature T, and the reduced mass $m = \frac{m_0 m_1}{m_0+m_1}$ of projectile and target nuclei. The Maxwellian-averaged reaction rate is then obtained by the product of cross section and velocity integrated over the energy

$$N_\mathrm{A}\langle\sigma v\rangle = \sqrt{\frac{8N_\mathrm{A}^2}{\pi m(k_\mathrm{B}T)^3}}\int_0^\infty E\sigma(E)e^{-E/k_\mathrm{B}T}dE. \tag{2.21}$$

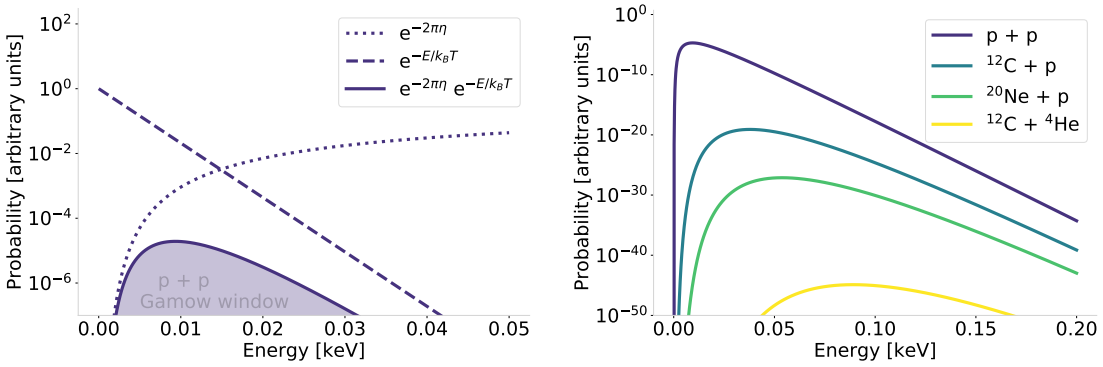

Figure 2.7: *Left:* Gamow window for the p + p reaction at $T = 30\,\mathrm{MK}$ as composed of the Gamow factor $e^{-2\pi\eta}$ and the Maxwell-Boltzmann factor $e^{-E/k_\mathrm{B}T}$. *Right:* Gamow peaks for different reactions from hydrogen burning at $T = 20\,\mathrm{MK}$; p + p from the pp chain, $^{12}\mathrm{C} + \mathrm{p}$ from the CNO cycle, and $^{12}\mathrm{C} + ^4\mathrm{He}$ from the NeNaMgAl cycle. Note that at this temperature the $^{12}\mathrm{C} + ^4\mathrm{He}$ reaction for helium burning has a 20–45 orders of magnitude lower maximum probability compared to the other shown cases.

The multiplication with the Avogadro number N_A is typically done to translate the quantity into physically useful units of $\mathrm{cm}^3\,\mathrm{mol}^{-1}\,\mathrm{s}^{-1}$. For fusion reactions, high velocities are required because the positively charged nuclei build a large Coulomb barrier that has to be overcome. The transmission probability to tunnel through the barrier can be approximated as

$$\tau(E) \approx \exp\left(-\frac{2\pi}{\hbar}\sqrt{\frac{m}{2E}}Z_0 Z_1 e^2\right) \coloneqq e^{-2\pi\eta}, \tag{2.22}$$

with charge numbers Z_0 and Z_1 of projectile and target and the charge of an electron e. The factor $e^{-2\pi\eta}$ is called the Gamow factor and includes the Sommerfeld parameter $\eta \propto E^{-1/2}$. Thus, the cross section can be rescaled as the astrophysical S-factor

$$S(E) \coloneqq \sigma(E)\frac{E}{e^{-2\pi\eta}} \tag{2.23}$$

in order to re-parametrise the E^{-1} dependence. Compared to the cross section, the S-factor is only weakly dependent on energy and it can be approximated as a constant $S(E) = S_0$ (Angulo et al. 1999). The nonresonant nuclear reaction rate is then calculated as

$$N_A\langle\sigma v\rangle = \sqrt{\frac{8N_\mathrm{A}^2}{\pi m(k_\mathrm{B}T)^3}}S_0\int_0^\infty e^{-2\pi\eta}e^{-E/k_\mathrm{B}T}dE, \tag{2.24}$$

which is called the Gamow window. For the p + p $\rightarrow d$ reaction at a typical temperature of 30 MK in an intermediate-mass star it is shown in the left panel of Fig. 2.7. The maximum of the probability distribution is referred to as Gamow peak which is obtained by taking the derivative of the integrand

$$\frac{d}{dE}\left[-2\pi\eta - \frac{E}{k_\mathrm{B}T}\right]_{E=E_0} = \frac{\pi}{\hbar}Z_0 Z_1 e^2\sqrt{\frac{m}{2}}E_0^{-3/2} - \frac{1}{k_\mathrm{B}T} = 0, \tag{2.25}$$

which gives

$$E_0 = \left(\frac{\pi Z_0 Z_1 e^2 k_\mathrm{B}T}{\hbar}\right)^{2/3}\left(\frac{m}{2}\right)^{1/3}. \tag{2.26}$$

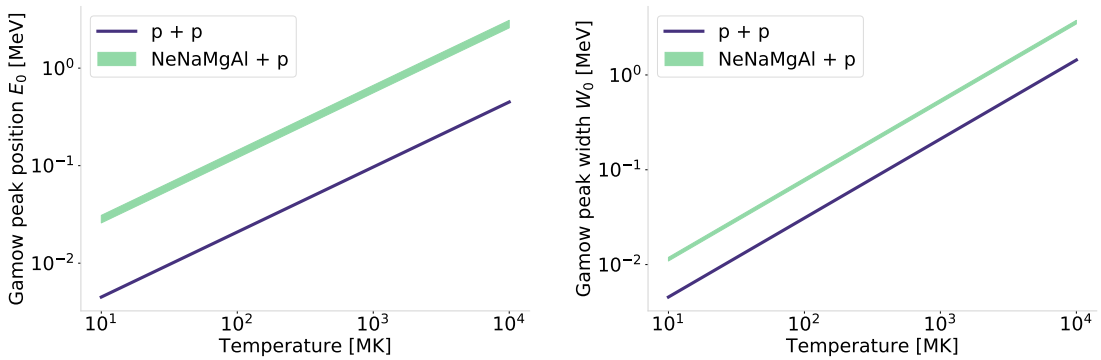

Figure 2.8: *Left:* Gamow peak positions. *Right:* Gamow peak widths. The green shaded region shows the area within which all proton capture reactions in the NeNaMgAl cycle fall.

Note that E_0 is usually much smaller than the height of the Coulomb barrier. Thus, tunnelling is a necessary to fuse charged nuclei. Gamow peaks for different reactions at $T = 30\,\mathrm{MK}$ are shown in the right panel of Fig. 2.7. For more advanced burning stages involving nuclei of higher charge number, it shifts towards higher energies and the Gamow window decreases in amplitude. For example, in such an environment, the $^{12}\mathrm{C} + ^4\mathrm{He}$ reaction has more than 20 orders of magnitude lower probability in the Gamow peak than $^{20}\mathrm{Ne} + \mathrm{p}$ from the NeNaMgAl burning cycle. This shows that central He-burning does not occur in intermediate-mass stars with such a temperature, while H-burning does occur. Using a Gaussian approximation, the width of the Gamow peak can be estimated as

$$W_0 = 4\sqrt{\frac{1}{3}E_0 k_\mathrm{B} T} \propto T^{5/6}. \tag{2.27}$$

With higher temperatures the Gamow peak shifts towards higher particle energies and the width of the window increases. This behaviour is shown in Fig. 2.8 for the comparison of a $\mathrm{p} + \mathrm{p}$ reaction with the proton capture reactions in the NeNaMgAl cycle. For stellar masses $0.075\,\mathrm{M}_\odot < M_* < 1.7\,\mathrm{M}_\odot$, the central temperature is (1–2) $\times\, 10^7\,\mathrm{K}$ and hydrostatic H-burning progresses mainly via the proton-proton (pp) chain. The temperature dependence of this reaction channel is shown in Fig. 2.9 in comparison with the competing CNO cycle. Different reactions and reaction cycles

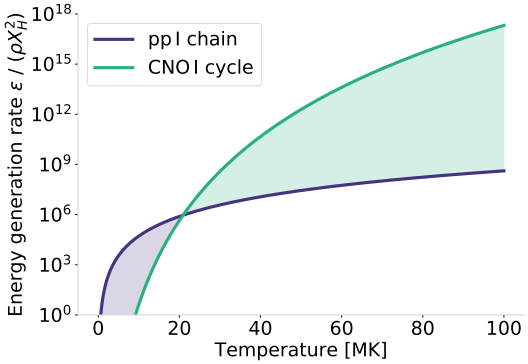

Figure 2.9: Equilibrium energy generation rate in pp I chain and CNO I cycle normalised to density and hydrogen abundance of the stellar material. The purple and green shaded regions indicate temperature regimes in which the pp I chain or the CNO I cycle dominate the stellar energy generation rate respectively. Reproduced following Iliadis (2015, 377).

Table 2.2: Hydrogen burning reactions. The production channel of the observationally important short-lived radioisotope ^{26}Al is highlighted in green, while its destruction channels are marked in blue.

pp I chain	pp II chain	pp III chain	
$p(p,e^+\nu)^2H$	$p(p,e^+\nu)^2H$	$p(p,e^+\nu)^2H$	
$^2H(p,\gamma)^3He$	$^2H(p,\gamma)^3He$	$^2H(p,\gamma)^3He$	
$^3He(^3He,2p)^4He$	$^3He(^4He,\gamma)^7Be$	$^3He(^4He,\gamma)^7Be$	
	$^7Be(e^-,\nu)^7Li$	$^7Be(p,\gamma)^8B$	
	$^7Li(p,^4He)^4He$	$^8B(\beta^+\nu)^8Be$	
		$^8Be(^4He)^4He$	
CNO I	CNO II	CNO III	CNO IV
$^{12}C(p,\gamma)^{13}N$	$^{14}N(p,\gamma)^{15}O$	$^{15}N(p,\gamma)^{16}O$	$^{16}O(p,\gamma)^{17}F$
$^{13}N(\beta^+\nu)^{13}C$	$^{15}O(\beta^+\nu)^{15}N$	$^{16}O(p,\gamma)^{17}F$	$^{17}F(\beta^+\nu)^{17}O$
$^{13}C(p,\gamma)^{14}N$	$^{15}N(p,\gamma)^{16}O$	$^{17}F(\beta^+\nu)^{17}O$	$^{17}O(p,\gamma)^{18}F$
$^{14}N(p,\gamma)^{15}O$	$^{16}O(p,\gamma)^{17}F$	$^{17}O(p,\gamma)^{18}F$	$^{18}F(\beta^+\nu)^{18}O$
$^{15}O(\beta^+\nu)^{15}N$	$^{17}F(\beta^+\nu)^{17}O$	$^{18}F(\beta^+\nu)^{18}O$	$^{18}O(p,\gamma)^{19}F$
$^{15}N(p,\alpha)^{12}C$	$^{17}O(p,\alpha)^{14}N$	$^{18}O(p,\alpha)^{15}N$	$^{19}F(p,\alpha)^{16}O$
NeNa	(NeNa)MgAl		
$^{20}Ne(p,\gamma)^{21}Na$	$^{23}Na(p,\gamma)^{24}Mg$		
$^{21}Na(\beta^+\nu)^{21}Ne$	$^{24}Mg(p,\gamma)^{25}Al$		
$^{21}Ne(p,\gamma)^{22}Na$	$^{25}Al(\beta^+\nu)^{25}Mg$		
$^{22}Na(\beta^+\nu)^{22}Ne$	$^{25}Mg(p,\gamma)^{26}Al$		
$^{22}Ne(p,\gamma)^{23}Na$	$^{26}Al(\beta^+\nu)^{26}Mg$		
$^{23}Na(p,\alpha)^{20}Ne$	$^{26}Al(p,\gamma)^{27}Si$		
	$^{26}Mg(p,\gamma)^{27}Al$		
	$^{27}Si(\beta^+\nu)^{27}Al$		
	$^{27}Al(p,\gamma)^{28}Si$		
	$^{27}Al(p,\alpha)^{24}Mg$		

Adopted from Iliadis (2015, 354) and Lugaro & Chieffi (2018).

commonly referred to as hydrogen burning are summarised in Tab. 2.2.
Because ^{3}He(p,$\beta^+\nu$)^{4}He has a very low cross section, hydrogen burning via the pp chain requires a sufficient build-up of ^{3}He abundance. Below $M \approx 1.5\,M_\odot$ the pp-chain is dominant, above the CNO-cycle (Iliadis 2015, 15). At central temperatures of ~ 20 MK the pp chain and the CNO cycle are equally effective in terms of energy production. Above that temperature the CNO cycle dominates the stellar energy production in hydrogen burning while the pp chain is predominant below. The CNO cycle is a catalytic cycle progressing through carbon, nitrogen, and oxygen via subsequent proton captures and β^+-decays. The net process of the pp chain and the CNO cycle is always $4\,H \rightarrow {}^4He + 2e^+ + 2\nu$. For temperatures above 25 MK the CNO cycle reaches a quasi-equilibrium state at which the abundance of the involved nuclei settles at steady states. The reaction $^{14}N(p,\gamma)^{15}O$ is the slowest in the cycle and therefore determines its total energy generation rate. For temperatures above 50 MK another reaction cycle adds, the NeNaMgAl cycle. In the latter ^{26}Al is produced, a short-lived radioisotope which is, along with ^{60}Fe, of great importance for the study of nucleosynthesis feedback in the Milky Way and which is of major concern for this thesis. This isotopes will be discussed in more detail in the following paragraphs.
As temperature and pressure rise the energy becomes increasingly sufficient to overcome the Coulomb barriers between heavier elements and to process them by fusion reactions. A summary of such advanced burning reactions is given in Tab. 2.3. After hydrogen, the stable element with the next higher charge number is helium. It will be consumed by He-burning. In massive star environments this is subsequently

Table 2.3: Advanced hydrostatic burning reactions.

He-burning	C-burning	Ne-burning	O-burning	Si-burning
^{4}He($\alpha\alpha$,γ)^{12}C	^{12}C(^{12}C,p)^{23}Na	^{20}Ne(γ,α)^{16}O	^{16}O(^{16}O,p)^{31}P	^{28}Si(γ,p)^{27}Al
^{12}C(α,γ)^{16}O	^{12}C(^{12}C,α)^{20}Ne	^{20}Ne(α,γ)^{24}Mg	^{16}O(^{16}O,2p)^{30}Si	^{28}Si(γ,α)^{24}Mg
^{16}O(α,γ)^{20}Ne	^{12}C(^{12}C,n)^{23}Mg	^{24}Mg(α,γ)^{28}Si	^{16}O(^{16}O,α)^{28}Si	^{28}Si(α,γ)^{32}S
^{20}Ne(α,γ)^{24}Mg	^{12}C(α,γ)^{16}O		^{16}O(^{16}O,2α)^{24}Mg	^{32}S(α,γ)^{36}Ar
			^{16}O(^{16}O,d)^{30}P	^{36}Ar(α,γ)^{40}Ca
			^{16}O(^{16}O,n)^{31}S	^{40}Ca(α,γ)^{44}Ti
				^{44}Ti(α,γ)^{48}Cr
				^{48}Cr(α,γ)^{52}Fe
				^{52}Fe(α,γ)^{56}Ni

Adopted from Iliadis (2015, 390, 400, 408, 413, 420–432) and Siegert (2017) following Karakas & Lattanzio (2014), Lugaro & Chieffi (2018) and Thielemann et al. (2018).

followed by C-, Ne-, and O-burning. The last hydrostatic burning phase in a star is Si-burning, which is a special case because it proceeds mostly via photodisintegration and alpha-capture. The astrophysical implications of these burning stages will be discussed in Sec.2.2.4. Hydrostatic burning is fundamentally based on an increase in binding energy from parent to daughter nuclei. In Fig. 2.10 the binding energy per nucleon is given for mass numbers $A = 1$ to $A = 270$, i.e. ^{1}H to ^{270}Ds. The binding energy per nucleon reaches a maximum value of 8.79 MeV for ^{56}Fe.

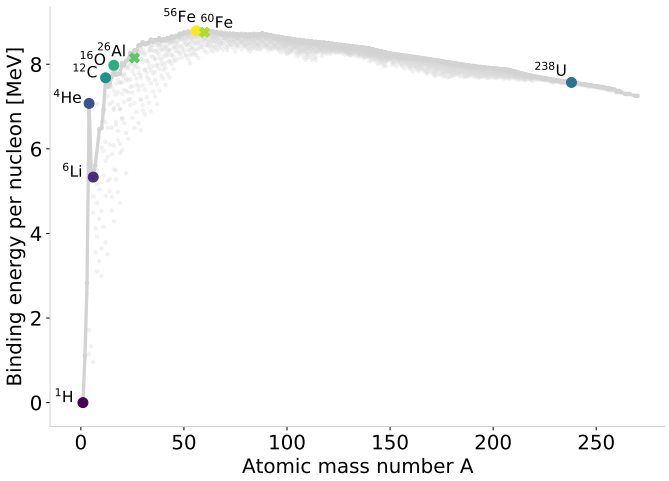

Figure 2.10: Nuclear binding energies per nucleon (*grey*) for mass isotopes with numbers $A = 1$ to $A = 270$, which corresponds to the elements ^{1}H to ^{270}Ds respectively. Some prominent nuclei are denoted in colours representing their hierarchy in binding energy. Radioactive ^{26}Al and ^{60}Fe are shown as crosses due to their particular relevance in the context of this thesis. Data from Audi et al. (2003)

This means that nuclear fusion by hydrostatic burning can not reach significantly beyond isotopes around this iron peak, as such reactions would consume energy and not release it. Thus, hydrostatic burning ceases after Si-burning and populating elements up to the iron peak. Nucleosynthesis exceeding this point requires high energy input from astrophysical events.

Explosive Nucleosynthesis Nuclear fusion processes occur also under explosive conditions (Hoyle & Fowler 1960; Woosley et al. 1973). In such environments, high

temperatures, densities, and particle fluxes are available on a short timescale. In a stellar explosion, high fluxes of protons, neutrons, electrons, and neutrinos sweep through the previously processed stellar material. Thus, especially ^{12}C, ^{16}O, ^{20}Ne, ^{24}Mg, and ^{28}Si are the feedstock for explosive nucleosynthesis (Thielemann et al. 2018).
The large flux of neutrons induces the r-process, which is characterised by rapid neutron-capture reactions. This is in contrast to the s-process, i.e. slow neutron-capture reaction process, which proceeds more slowly and is governed by the β-decay timescale of neutron-rich nuclei. The r-process, on the other hand, populates neutron-rich isotopes of the heavy elements quicker than their β-decay timescale. This leads to formation of isotopes that are far from stability and very neutron-rich up to the neutron drip line. When isotopes reach this limit, they subsequently β-decay back to stability and form the elemental zoo beyond ^{56}Fe.
The first layer hit by an outward moving SN shock consists mainly of ^{28}Si. It is subsequently heated to temperatures of $\sim 5 \times 10^9$ K. In combination with a high neutron flux, this destroys the silicon and produces elements around the iron peak, favourably ^{56}Ni. At lower densities also other species are produced in this process, such as ^{44}Ti, which is a prominent gamma-ray emitter and also important as tracer of massive star physics. As the shock propagates further outwards, it reaches the next layer, mainly composed of ^{16}O, and induces explosive oxygen burning at temperatures of 3.5–4 $\times 10^9$ K and densities around $10^6\,\mathrm{g\,cm^{-3}}$. Here, ^{16}O is destroyed, producing elements around the iron peak in the silicon region. The final stage is explosive neon-carbon burning. At a reduced temperature of about 2.5×10^9 K and density around $3.2 \times 10^5\,\mathrm{g\,cm^{-3}}$, it produces mainly ^{16}O and ^{28}Si (Iliadis 2015, 445–451).

^{26}Al The short-lived radioisotope ^{26}Al is an ideal tracer of ongoing nucleosynthesis in the Milky Way and of great importance for the understanding of the Galaxy's history. The nuclear characteristics of ^{26}Al are summarised extensively e.g. in Iliadis et al. (2011) and Diehl et al. (2018a). This paragraph deals with its nuclear properties, however the astrophysical implications associated with ^{26}Al form the main thread throughout the entire thesis.
As shown in Tab. 2.2, ^{26}Al is produced by the proton capture reaction $^{25}\mathrm{Mg(p,\gamma)^{26}Al}$. This reaction occurs in the NeNaMgAl-cycle and is part of hydrogen burning. The initial isotope is ^{26}Mg that is mostly present already since the formation of the star. This makes ^{26}Al production sensitive to the initial metallicity. Nevertheless, there are also destruction channels consuming ^{26}Al. The most prominent are via neutron capture through $^{26}\mathrm{Al(n,p)^{26}Mg}$ and $^{26}\mathrm{Al(n,\alpha)^{23}Na}$. Destruction via proton capture $^{26}\mathrm{Al(p,\gamma)^{27}Si}$ is of less importance because the high Coulomb barrier of ^{26}Al reduces this channel (Parikh et al. 2014). A summary of reaction and destruction channels of ^{26}Al is shown in Fig. 2.11. ^{26}Al is radioactive and unstable against β^+-decay to the first excited state of ^{26}Mg with spin parity $J^\pi = 2^+$ and a lifetime of 1.04×10^6 yr. This decay is followed by a de-excitation of ^{26}Mg to its ground state (0^+) in only 109 ms by emission of a gamma-ray photon with an energy of 1809 keV. The energy levels of ^{26}Al and ^{26}Mg are shown in Fig. 2.12. This emission is of outstanding importance for measurements of nucleosynthesis ejecta in ISM which is the topic of this thesis (cf. Sec. 3.4.3). The transition from the ^{26}Al ground state (5^+) to the ^{26}Mg ground state (0^+) is forbidden. In hot environments, this can be circumvented via the population of the excited levels at 228 keV (0^+), 417 keV (3^+), or 1058 keV

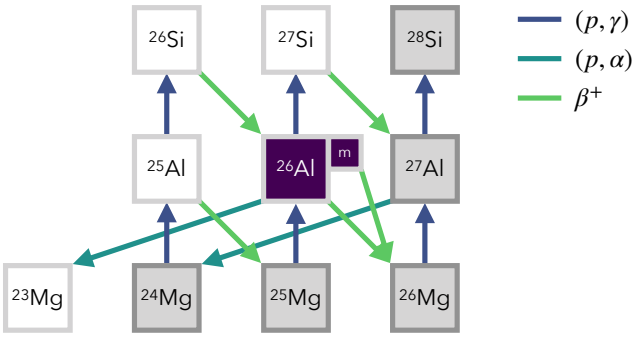

Figure 2.11: Nuclear production and destruction channels of ^{26}Al (*purple*). Production occurs mainly due to proton capture on ^{25}Mg, and destruction proceeds mostly via neutron capture. Stable isotopes are marked in *dark grey*. Adopted from Diehl et al. (2018a) following Prantzos & Diehl (1996)

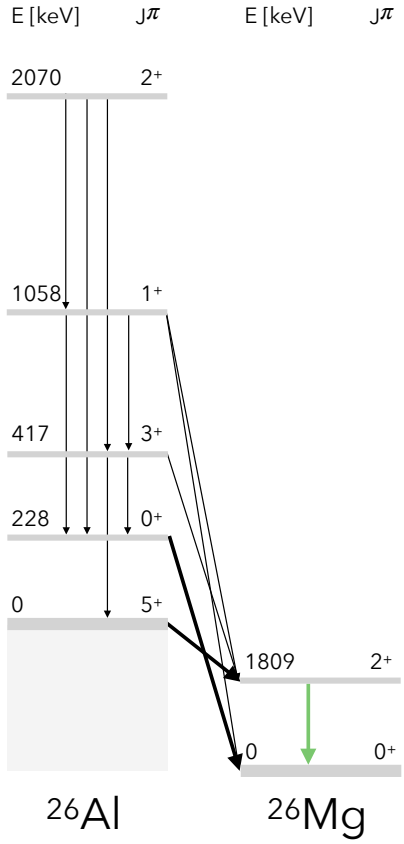

Figure 2.12: Nuclear energy level scheme of ^{26}Al. Transitions associated with observationally relevant gamma-ray emission are marked in *green*. Adopted from Iliadis et al. (2011) following Endt (1990)

(1^+) followed by a subsequent decay.
According to its lifetime against β^+-decay, ^{26}Al establishes an equilibrium abundance in this reaction network. This is strongly temperature dependent and its abundance is comparable to that of Mg isotopes. This is shown for an intermediate-mass asymptotic giant branch (AGB) star in Fig. 2.13.
The abundance ratio $Y_{^{26}\mathrm{Al}}/Y_{^{27}\mathrm{Al}}$ is between 0.03 and 0.8 for central stellar temperatures of 60 and 100 MK respectively. If ^{26}Al is excited to 228 keV it forms a metastable isomeric state, denoted $^{26}\mathrm{Al}^m$, that decays with a half-life of $T_{1/2} = 6.34\,\mathrm{s}$ to the ^{26}Mg ground state. At temperatures $T \geq 0.1 \times 10^9\,\mathrm{K}$ this destruction channel becomes important and at $T \geq 0.45 \times 10^9\,\mathrm{K}$ the ground and isomeric states are in thermal equilibrium. This temperature sensitivity results in an additional impor-

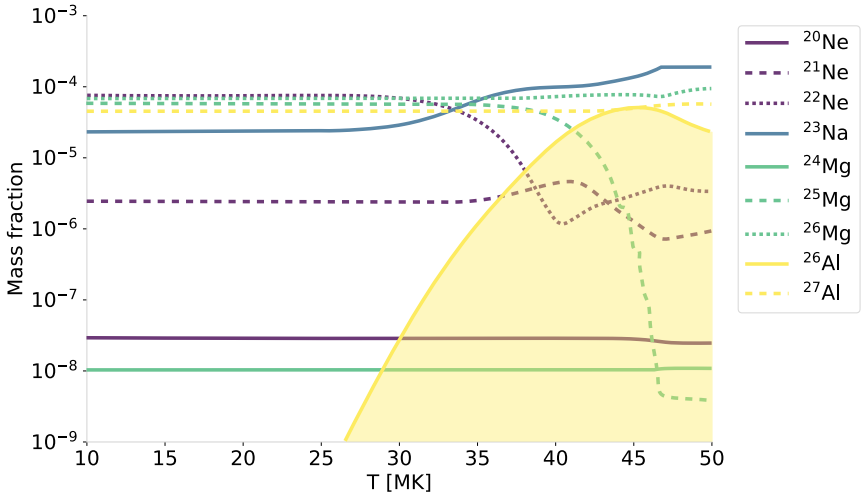

Figure 2.13: Temperature dependence of element abundances in the NeNaMgAl cycle in an intermediate-mass AGB star. Special emphasis is put on the abundance of ^{26}Al as *yellow* shaded region. Since temperature decreases towards larger stellar radii, the x-axis can also be read as radial information with hotter regions being closer to the stellar centre. Data from Lugaro & Chieffi (2018).

tance of astrophysical processes.
On the one hand, rapid convective transport away from hot regions avoids destruction via the thermally excited meta-stable state and allocates more ^{26}Mg as ^{26}Al-fuel to H-burning regions. On the other hand, further heating during advanced burning stages or the enhanced neutron flux in SN shocks increase the decay. But there is also an explosive burning component in the production of ^{26}Al. A SN shock wave releases protons along with a huge neutrino flux. While the protons undergo capture reactions on the abundant ^{25}Mg this can be processed further to ^{26}Al via neutrino interaction due to their high flux. This occurs in novae and ccSNe. While the precise properties of such neutrino induced nucleosynthesis reactions are still debated, it was estimated that this process may enhance ^{26}Al production by 20–30% (Sieverding et al. 2017; Diehl et al. 2018a). Another explosive burning component of ^{26}Al occurs via $^{24}\mathrm{Mg}(\mathrm{n},\gamma)^{25}\mathrm{Mg}(\mathrm{p},\gamma)^{26}\mathrm{Al}$ during explosive Ne/C-burning. The time evolution of elemental abundances during this stage are shown in Fig. 2.14. Overall, this produces an ^{26}Al stellar mass fraction of 3×10^{-5} on average.

^{60}Fe Another radioisotope that traces massive star nucleosynthesis feedback is ^{60}Fe with a half-life time of 2.6 Myr (Rugel et al. 2009). With a slightly longer lifetime than ^{26}Al, it is of similar importance for studying the chemical evolution of the ISM. As opposed to ^{26}Al, ^{60}Fe is only produced by the *s*-process in the neutron-capture chain $^{58}\mathrm{Fe}(\mathrm{n},\gamma)^{59}\mathrm{Fe}(\mathrm{n},\gamma)^{60}\mathrm{Fe}$ on already existing Fe isotopes. This means that ^{26}Al and ^{60}Fe both originate from massive stars but from slightly different mechanisms. This makes especially the ratio $^{60}\mathrm{Fe}/^{26}\mathrm{Al}$ an important measure for these underlying nucleosynthesis processes (Timmes et al. 1995; Limongi & Chieffi 2006). Since ^{59}Fe has a half-life of only 44.5 d, ^{60}Fe production by the *s*-process during convective core He-burning is prevented by the faster β-decay of ^{59}Fe. During shell C-burning, neutron densities reach values on the order of $10^{11}\,\mathrm{cm}^{-3}$. This is sufficient for the (n,γ) rate to dominate over the ^{59}Fe β-decay and result in efficient ^{60}Fe production (Tur et al. 2010; Uberseder et al. 2014; Diehl et al. 2018a;

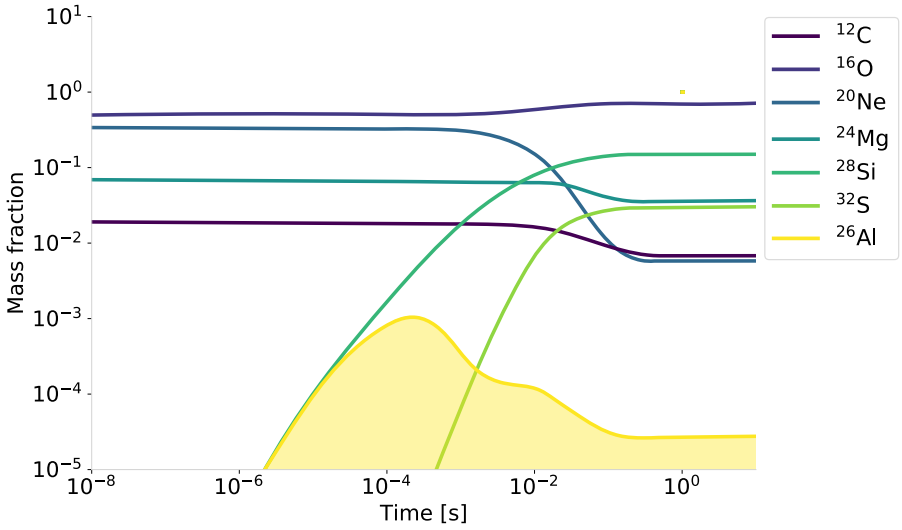

Figure 2.14: Elemental abundance evolution during explosive nucleosynthesis. Special emphasis is put on the abundance of ^{26}Al as *yellow* shaded region. Data from Iliadis (2015, 448).

Thielemann et al. 2018). Destruction of ^{60}Fe also proceeds via neutron capture, namely the reaction $^{60}\mathrm{Fe}(\mathrm{n},\gamma)^{61}\mathrm{Fe}$ (Uberseder et al. 2009; Heftrich et al. 2015). The production and destruction channels of ^{60}Fe are summarised in Fig. 2.15. The decay chain of ^{60}Fe which proceeds by two β^--decays via $^{60}\mathrm{Fe} \rightarrow {}^{60}\mathrm{Co} \rightarrow {}^{60}\mathrm{Ni}$ can be followed in the level scheme in Fig. 2.16. In a first step, ^{60}Fe decays to the first excited state (2^+) of its daughter nucleus ^{60}Co. This de-excites to the ground state (5^+) primarily via internal conversion. In less than 2% of the transitions this proceeds by emission of a gamma-ray photon with 58.6 keV. Because of this low yield of photons, this transition is below the sensitivity of current gamma-ray instruments. A second β^--decay transforms ^{60}Co into ^{60}Ni. The latter emerges at an excited level at 2505 keV (4^+). The subsequent de-excitation follows a two step cascade through an energy level at 1332.5 keV (2^+) and via the immediate emission of two gamma-ray photons at 1173.2 keV and 1332.5 keV (Diehl et al. 2018a). These can be detected as their flux is about 50 times larger than that of the 58 keV line. Thus, the cumulative flux of these nuclear emission lines is a very important tracer of massive star nucleosynthesis in the Galaxy.

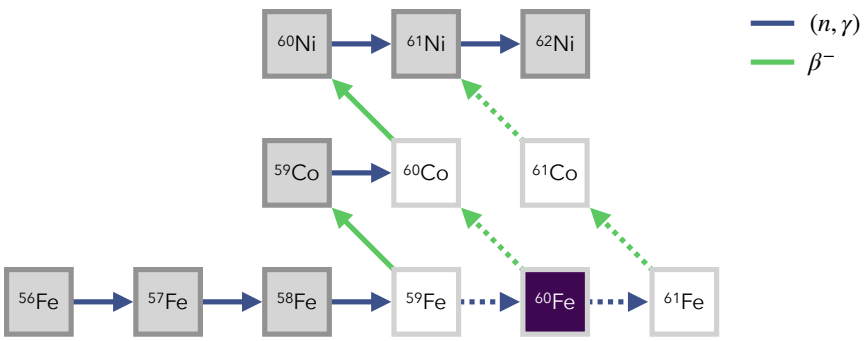

Figure 2.15: Nuclear production and destruction channels of ^{60}Fe (*purple*). Both mainly occurs via neutron capture reactions. Stable isotopes are marked in *dark grey*. Adopted from Heftrich et al. (2015)

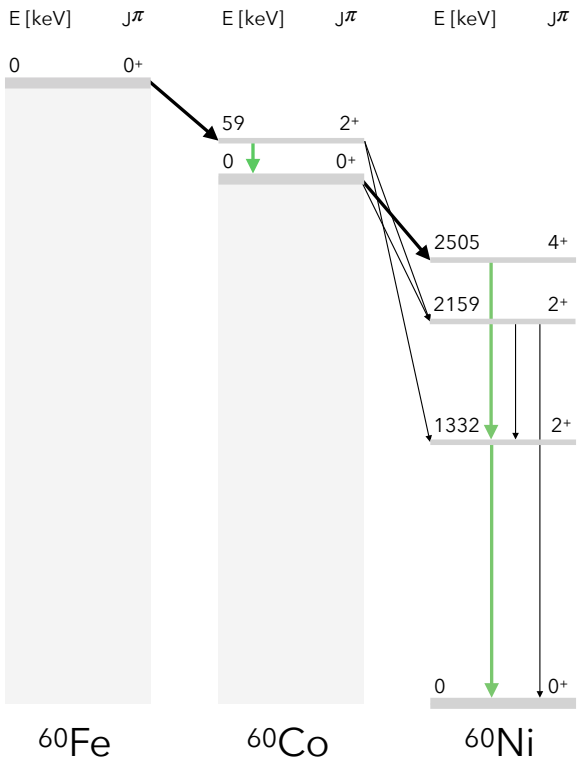

Figure 2.16: Level scheme of ^{60}Fe. Transitions associated with observationally relevant gamma-ray emission are marked in *green*. Adopted from Rugel et al. (2009).

2.2.4 Stellar Evolution

Herzsprung-Russell Diagram To visualise stellar evolution, the luminosity L of a star is typically shown in a relation to its effective surface temperature T_{eff} in a Hertzsprung-Russell diagram (HRD). A schematic example is shown in Fig. 2.17. Stars do not scatter randomly in such a diagram but show clear correlations that represent specific stellar properties and evolutionary stages. Most stars are found to inhabit the diagonal main sequence relation. Stars in this region fuse hydrogen to helium in core H-burning and follow the the stable mass-luminosity relation $L_* \propto M_*^3$. In the HRD, this corresponds to $L_* \sim T_{\text{eff}}^7$. Because this is the dominant process for most of a star's lifetime, in astronomical observations, stars accumulate in the main sequence in observations of star groups and globular clusters. After a star has formed on the main sequence with a certain zero-age main sequence (ZAMS) mass it evolves structurally, energetically, and chemically along an evolutionary track characteristic for its initial mass, metallicity, and rotation. As a general rule of thumb, the more massive a star the greater its core temperature, the higher its luminosity, and the faster its evolution. With higher mass, the pressure in the central regions increases and the hydrogen fuel is burnt more quickly. The timescales of different stellar burning processes are summarised in Tab. 2.4.
When the hydrogen fuel in the centre is exhausted and a star is more massive than $0.8\,\mathrm{M}_\odot$, H-burning continues in in a shell around the core. Because nuclear fusion energy, which counteracts gravitational pressure, is reduced, the star contracts. Subsequently, the star leaves the main sequence and the contraction leads to an increase of central temperature and pressure (Sackmann et al. 1993). If the star is massive enough, core He-burning to carbon and oxygen ignites. As the gas in the core is usu-

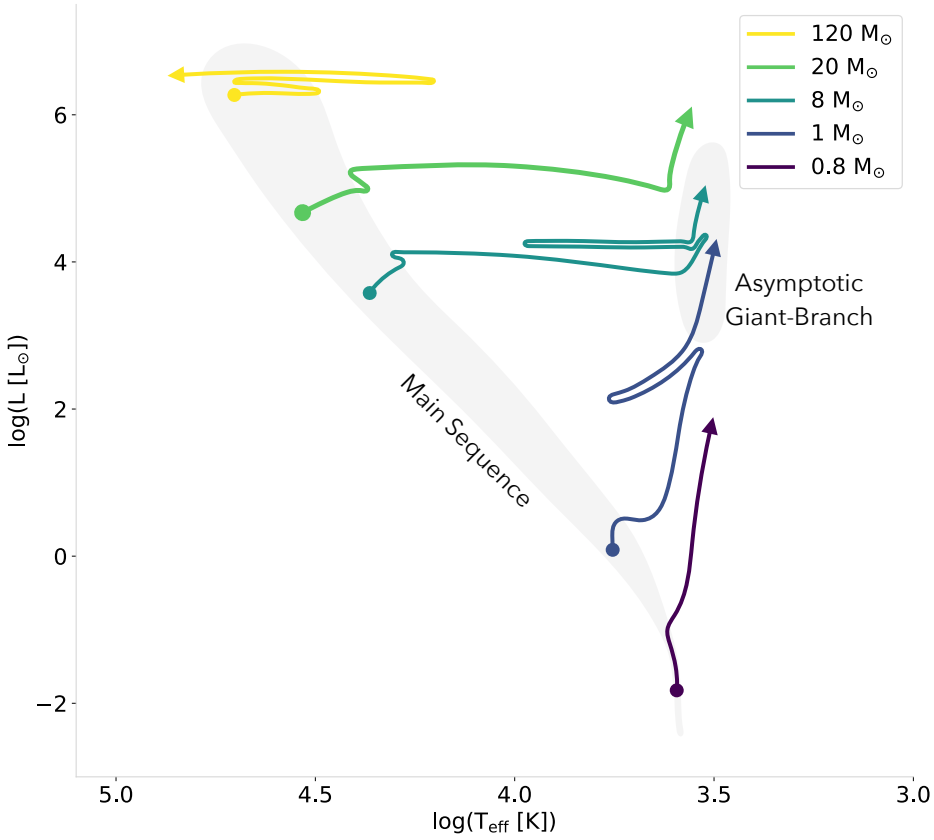

Figure 2.17: Schematic example of an HRD with evolutionary tracks for five stars with different initial mass M_{ZAMS} at ZAMS. Regimes of main sequence and AGB stars are highlighted as grey regions. Stellar evolutionary tracks tend to evolve from the main sequence towards the upper right, i.e. towards higher luminosity and lower surface temperature. Note that surface temperature decreases from left to right.

Table 2.4: Time scales of nuclear burning processes in stars with solar metallicity and different initial masses M_{ZAMS}.

	1 $M_\odot$	13 $M_\odot$	15 $M_\odot$	20 $M_\odot$	25 $M_\odot$	75 $M_\odot$
H	1.1 Gyr	13.5 Myr	11.1 Myr	8.13 Myr	6.70 Myr	3.16 Myr
He	110 Myr	2.67 Myr	1.97 Myr	1.17 Myr	840 kyr	450 kyr
C	-	2.82 kyr	2.03 kyr	980 yr	520 yr	1.01 kyr
Ne	-	120 d	270d	220 yr	320 d	210 d
O	-	4.77 yr	2.58 yr	1.25 yr	150 d	320 d
Si	-	17.8 d	18.3 d	11.5 d	16.8 h	1.09 d

Adopted from (Woosley et al. 2002).

ally degenerate, the additional nuclear energy release increases the temperature but does not affect the pressure. The continuously increasing pressure and temperature lead to a thermonuclear runaway of He-burning in the core until the energy release is enough to lift the electron degeneracy in the gas and enable expansion. When helium in the core is exhausted, He-burning moves into a shell and the star ascends the AGB. In this phase, thermal pulses in the He-burning shell can cause significant mass loss via stellar winds. In that case, stars move horizontally to the left on the HRD and the hotter inner layers are revealed and leave ionised planetary nebulae of ejected hydrogen gas in the ISM. This phase will be explained in further detail in a separate following paragraph, because it leaves an important observable signature of nucleosynthesis. Finally, stars above 8 $M_\odot$ undergo more advanced burning

stages and the evolutionary tracks on the HRD become increasingly complex. The evolution of such massive stars will be discussed in more detail below.

Low- and Intermediate-Mass Stars In this thesis, low-mass stars are defined as having masses in the range between the deuterium burning limit of $\sim 0.012\,\mathrm{M}_\odot$ and $0.2\,\mathrm{M}_\odot$(cf. Tab. 2.1). As represented by the IMF, these are the most abundant stellar objects in the Galaxy. However, stellar mass categories are not uniformly defined in literature. Some authors define the lower mass limit of low-mass stars at the hydrogen burning limit of $\sim 0.075\,\mathrm{M}_\odot$ (Luhman 2012). Others define it as $4 \times 10^{-3}\,\mathrm{M}_\odot$, above which an object becomes opaque to the radiation it emits due to energy release in self-gravitational collapse (Low & Lynden-Bell 1976; Whitworth et al. 2007). Deuterium burning has negligible effects on stellar structure (Chabrier et al. 2000, 2007). Nevertheless, it is adopted here as determinant for the lower mass limit of stars, because it fulfils a basic condition for being a star, namely undergoing nuclear fusion reactions at all.
Brown dwarfs are stars at the low-mass extreme of stars between the He- and H-burning limits (Burrows et al. 1997; Luhman 2012). Above $\sim 0.06\,\mathrm{M}_\odot$ at temperatures of $\sim 3000\,\mathrm{K}$ Li-burning occurs in these objects via the process $^7\mathrm{Li} + \mathrm{p} \rightarrow 2\,^4\mathrm{He}$ in addition to He-burning (Chabrier et al. 1996). Since burning processes occur dominantly in the centre of stars, this is the region where also chemical enrichment is concentrated. Because of the large temperature sensitivity of the CNO cycle, the concentration of hydrogen burning in the stellar centre is strongly correlated with the overall stellar mass. This changes when the core becomes convective and mixing to regions further out from the centre occurs. This is generally the case for most intermediate-mass stars with masses $\gtrsim 2\,\mathrm{M}_\odot$ and makes those stars evolve similarly on the main sequence. The time a star spends on the main sequence decreases with increasing mass as $\tau_\mathrm{H}(M) \propto M^{-2.8}$. This accounts for about 95–97% of its entire evolution (Kippenhahn et al. 2012). Overall, the time a star undergoes nuclear fusion is much longer than the Kelvin-Helmholtz timescale. Thus, an equilibrium state during this phase is plausible. If the hydrogen fuel in the centre is depleted, the star has a helium core surrounded by a hydrogen envelope.
For a star with $M_* = 2\,\mathrm{M}_\odot$ the helium core has about $0.18\,\mathrm{M}_\odot$ and a temperature of around 22 MK. Right on top of the isothermal helium core and at the bottom of the envelope, the temperature and pressure are such that hydrogen fusion is still going on in that shell region.
If the star's mass is above $6\,\mathrm{M}_\odot$, the core does not reach a isothermal state before the ignition of helium burning. The ongoing production of helium leads to growth of the core and finally an expansion of the envelope. For a $5\,\mathrm{M}_\odot$ star the radius increases during this phase by a factor of about 15. This is the red giant phase of the star, in which envelope and core develop in opposite directions. In this phase, the star moves to lower temperatures in the HRD and then up the red giant branch (RGB) close to the Hayashi line. This almost vertical line in the HRD between $3\text{–}5 \times 10^3\,\mathrm{K}$ marks the border beyond which a fully convective star can not be in equilibrium. When the contracting core reaches a temperature of $\sim 10^8\,\mathrm{K}$ and a density of the order of $10^3\,\mathrm{g\,cm^{-3}}$ helium fusion in the core ignites (Woosley et al. 2002). The internal structure evolution of a $5\,\mathrm{M}_\odot$ star, which proceeds through a He-burning phase in the centre, is shown in Fig.2.18.
At about the same time, while the star enters the RGB, the hydrogen envelope cools due to the expansion. This causes the star to ascend the RGB and at the same time

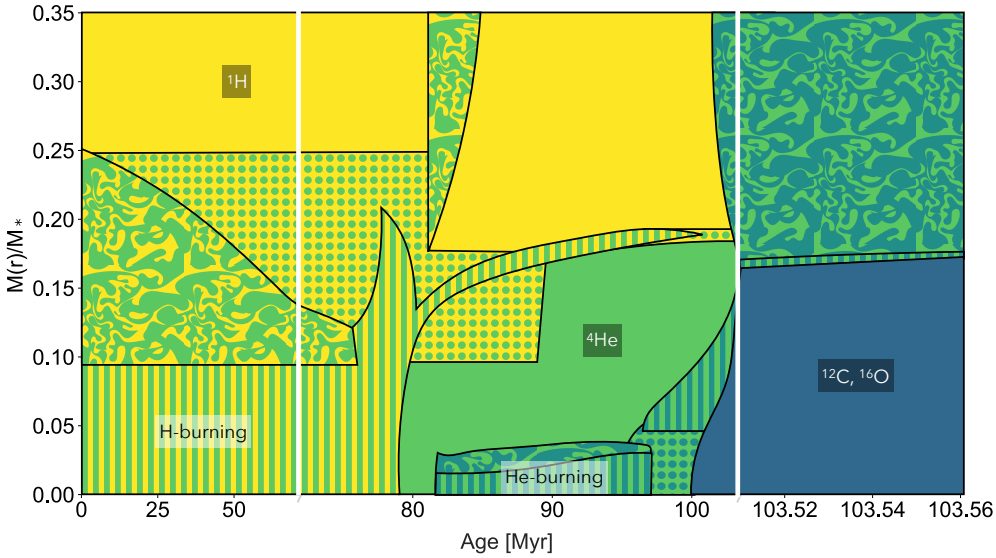

Figure 2.18: Schematic evolution of the structure of a $5\,M_\odot$ star. The early evolution is similar to a Solar-type star. During H-burning (*green* and *yellow* hatched region) in a shell, He-burning (*blue* and *green* hatched region) in the centre evolves. This also moves finally into a shell around a core mainly consisting of ^{12}C and ^{16}O (*blue*). Convective regimes (swirling structured regions) that transport nucleosynthesis products radially develop after $\sim 80\,Myr$, i.e. first dredge-up, and during the end of the evolution. Adopted from Kippenhahn et al. (2012, 369).

makes the convection zone grow deeper. When the convection zone reaches down to the hydrogen burning shell, in a first dredge-up, processed material is mixed up to the surface. As the star reaches the top of the RGB, its core is highly degenerate with a density of the order of $10^6\,g\,cm^{-3}$. In this case, helium burning ignites in a violent nuclear instability. The high energy generation rate in this helium flash drives a second convective layer which merges with the outer envelope. This causes a dip in luminosity until non-degenerate helium burning brightens the star again. Its HRD track ascends in the AGB which asymptotically approaches the first RGB (Acero et al. 2009). This happens after about 80 Myr in Fig. 2.18. Thus, the elemental abundances on the surface change and fresh nucleosynthesis products are lifted out of the stellar core for the first time. In the context of this thesis, this constitutes an important process because thereby ^{26}Al reaches the stellar surface. This will be discussed in more detail in the following paragraph.
In a conceptual picture, helium burns to carbon, oxygen, and neon, which accumulates in the core. Its particular isotopic ratio is strongly dependent on temperature. When the helium fuel in the core is exhausted, helium burning continues also in a shell. The core is continuously fed with ashes from this burning shell and contracts. All advanced burning stages follow in principle this sequence in core evolution, which is shown in Fig. 2.19: undergoing nuclear burning, exhaustion of nuclear fuel, and self-gravitational core contraction, which heats the core up to the stage where the next burning phase starts. In massive stars, advanced burning stages occur simultaneously in multiple layers.

AGB Stars As schematically illustrated in Fig. 2.19, the previously described shift from core to shell burning repeats for helium burning. During this phase, the stars with masses of 3–$5\,M_\odot$ comprise two burning shells, i.e. a helium burning shell

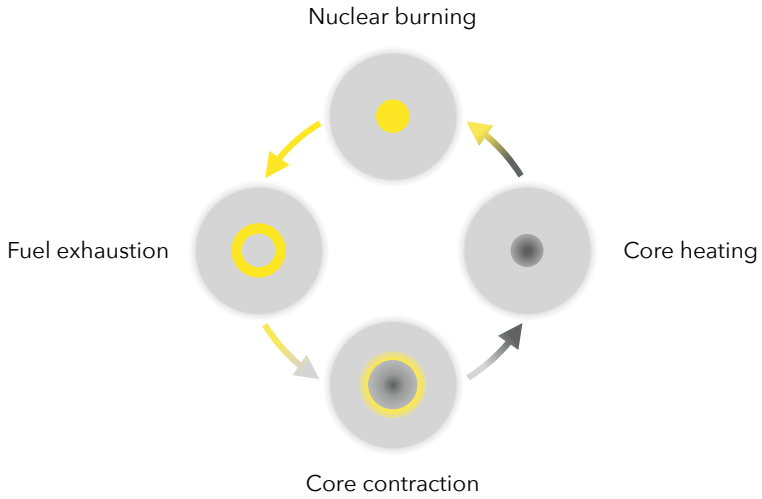

Figure 2.19: Schematic cycle of stellar core evolution which is repeatedly iterated evolving through different nuclear burning stages. It proceeds via four main steps: (1) nuclear fuel is burnt in the stellar core. (2) The fuel is exhausted in the centre and the burning stage is shifted into a shell. (3) The core continues to accumulate burning ashes and contracts due to the mass gain. (4) The core contraction leads to central heating until the next burning stage ignites in the centre. Adopted from Kippenhahn et al. (2012, 439).

around the core as well as hot bottom burning at the innermost boundary of the convective hydrogen envelope. The shell helium burning occurs at temperatures between (4.5–10) $\times 10^7$ K (Shingles et al. 2015). The star follows a track in the HRD that asymptotically approaches the first RGB. This is characteristic for the AGB phase. It is accompanied by an expansion of the envelope with convection growing larger in the star until it comprises up to $\sim 80\%$ of the entire stellar mass. This establishes a convective connection through both burning shells all the way down to the helium core and up to the stellar surface. In this second dredge-up period ^{4}He, ^{12}C, ^{14}N, and all the isotopes of the advanced burning stage, including also in particular ^{26}Al, appear at the surface.
The hydrogen burning shell continuously produces more and more helium. In the regions in which hydrogen is exhausted, nitrogen is the second-most abundant element, since it accumulates in the bottle-neck reaction of the CNO cycle. The helium burning shell leaves behind a core, consisting mostly of carbon and oxygen, with neon being the third most abundant element. If the mass of the CO core is below 1.1 $M_\odot$ electron degeneracy sustains against gravity and no further contraction occurs. This is the case for stars with initial mass $M_* \lesssim 8\,M_\odot$. Thus, the characteristic structure of an AGB star consists of three dynamic layers as depicted in Fig. 2.20: An electron degenerate CO core surrounded by a helium rich inter-shell layer within a mostly convective hydrogen-rich mantle. Here, it is important to note that hydrogen and helium burning are occurring at different times during the evolution. Instead, freshly produced helium piles up in the inter-shell region due to hot-bottom hydrogen burning. This accretion dominates the rather steep temperature and density profile of the helium rich layer. Due to the huge temperature dependence of the triple-α reaction, helium burning ignites in a thermal runaway. The large energy injection of $\sim 10^{48}$ erg in a short time during each pulse induces convection, penetrating the entire inter-shell region and establishes a convective connection between the two burning shells. As this occurs repeatedly, the star undergoes a series of convective periods and freshly synthesised material is mixed onto the surface. Because the core in more massive stars is not electron-degenerate, smooth core helium burning occurs. This makes AGB stars an observationally special case and par-

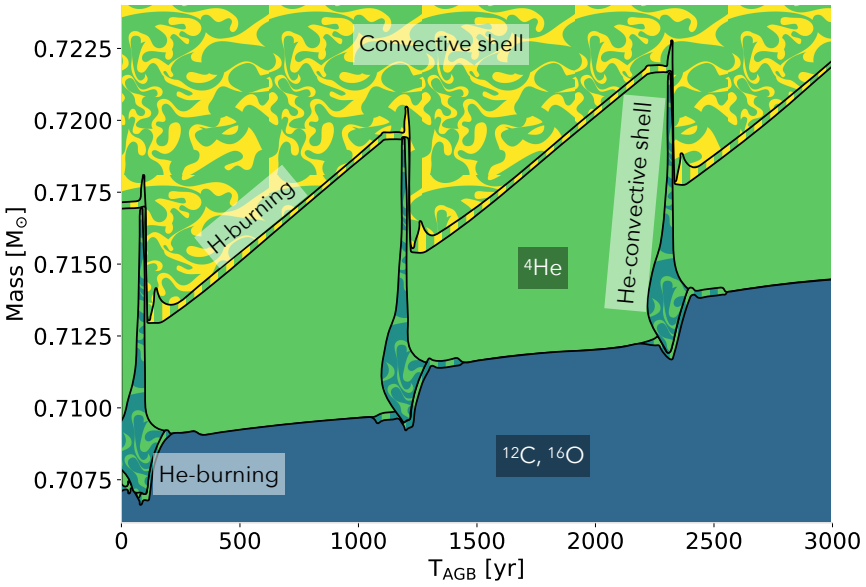

Figure 2.20: Schematic evolution of the internal burning structure of AGB stars. Shown is the course of three subsequent thermal pulses during the time T_{AGB} on the AGB; these are indicated by the occurrence of a He convective shell shown in *blue/green* swirling regions, which have been widened by a factor of 100 in time in order to increase the readability of the figure. It reaches from the hydrogen burning shell (*green/yellow* hatched) down to the He burning shell (*blue/green* hatched). If the star is not thermally pulsing, these shells are separated by an inter-shell region (*green*). This is framed outwards by a convective hydrogen shell (*yellow/green* swirling) and inwards by a carbon oxygen core (*blue*). Adopted from Lugaro & Chieffi (2018).

ticularly interesting from a nucleosynthesis perspective, especially with regard to ^{26}Al measurements, because of their enhanced and deep mixing. The convective period flattens the temperature gradient in the inter-shell and therefore transfers to a quiescent helium shell burning phase. On the other hand, the thermal pulse forces the outer hydrogen layer to expand. This leads to cooling and termination of hydrogen-burning. Thus, the temperature gradient steepens again and the helium-burning shell runs out of power. After the subsequent contraction of the hydrogen layer, hydrogen burning re-ignites and the thermal pulse cycle is completed. The structural behaviour during three such pulses is schematically shown in Fig. 2.20 (Lugaro & Chieffi 2018).

During each convective pulse the metallicity of the outer regions increases significantly. As discussed already in Sec. 2.2.2, this increases the opacity and thereby the outward radiation pressure. The latter increases until the mass-loss reaches up to $10^{-4}\,\mathrm{M}_{\odot}\,\mathrm{yr}^{-1}$ and is high enough to entirely strip off the hydrogen rich envelope (Höfner & Olofsson 2018). This leaves the bare core as terminal state of an AGB star which has thus evolved into a CO white dwarf. From a nucleosynthesis perspective, the latter are still important because they potentially yield further processed material in nova explosions. Because of the high mass-loss and the enhanced mixing, the AGB phase itself is of particular interest for the investigation of nucleosynthesis as it is expected to carry a direct signal of these processes.

High-Mass Stars Massive stars exhibit high surface temperatures and therefore high luminosities. Referring to the respective spectral classes they are also defined as O and B stars. In terms of structural evolution, stars that initiate C-burning are

termed massive, which constitutes another type of definition. These stars generally have a mass of $M_* \gtrsim 8$, which is sufficient to produce a ccSN (Zinnecker & Yorke 2007; Smartt 2009).
Massive stars are major sources of heavy elements and UV radiation in the Universe. They evolve into Wolf-Rayet (WR) stars, neutron stars, or black holes and their main modes of feedback occur via expanding H II regions, winds, massive outflows, and supernova explosions. They are the main agents driving mixing, heating, and turbulence in the ISM and thus predominantly shape the structure and evolution of their host galaxy.
Due to their high mass, most of these stars do not enter a phase of electron degeneracy in the core after hydrogen and helium burning. Thus, the core evolution cycle in Fig. 2.19 continues and they enter further nuclear burning phases after hydrogen- and helium-burning. As they progress through carbon-, neon-, oxygen-, and silicon-burning, massive stars develop the entire hierarchy of the shell structure in Fig. 2.6. This simplified picture is intended as a support for a clearer comprehension. Actually, mixing and shell merging processes destroy such a clear structure. Additionally, the high mass generates extreme conditions inside the star in terms of temperature and density. In Fig. 2.21 the change in core parameters throughout the whole sequence of nuclear burning stages is shown for different initial stellar masses. This accelerates the nuclear burning processes and leads to short lifetimes of the

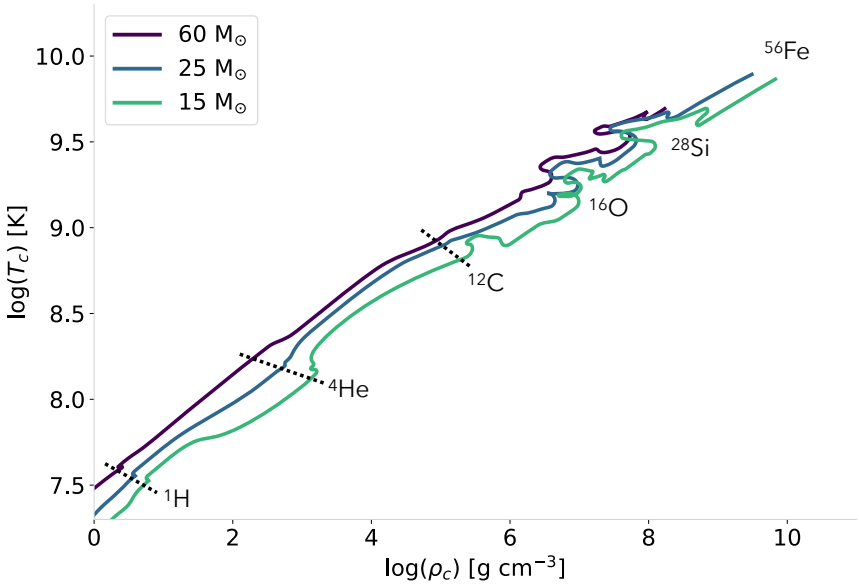

Figure 2.21: Core evolution of massive stars. The onset of different core burning stages are marked as dashed lines. Adopted from Hirschi et al. (2004) and Woosley et al. (2002).

order of 10^{-3} times the age of the Universe (cf. Tab. 2.4). Consequently, if a massive star is observed, it must have formed recently on astronomical time scales (Larson 2003). The fast evolution and the comparatively low number of observational cases makes it difficult to study them at greater distances. This bias can be overcome by gamma-ray observations, e.g. of the ^{26}Al decay radiation, which basically have no distance limitation in the Galaxy. An important side note is that the energy loss due to neutrino emission exceeds the radiative losses during the advanced burning stages. This implies that the core decouples from the evolution of the stellar enve-

lope (Janka 2012), which is of importance for the discussion of terminal phases later in this section.
The main reactions in advanced burning stages beyond hydrogen burning have been summarised in Tab. 2.3. Helium-burning mainly accumulates ^{12}C and ^{16}O. Subsequently, for stellar masses above $8\,M_\odot$, carbon-burning ignites at $T = (6\text{–}8) \times 10^8\,K$ via the reaction $^{12}C + {}^{12}C$ because of the lower Coulomb barrier compared to ^{16}O. The ashes of this stage are predominantly ^{16}O, ^{20}Ne, and ^{24}Mg. Since ^{16}O has double magic number $Z = N = 8$, ^{20}Ne is consumed first after carbon-burning at $T = (1.2\text{–}1.5) \times 10^9\,K$. At this point, photodisintegration starts as an important process. When the central temperature reaches $T = 1.9 \times 10^9\,K$, oxygen-burning occurs via $^{16}O + {}^{16}O$ through a variety of channels. The final nuclear burning stage, which is silicon-burning, sets in at about $3.3 \times 10^9\,K$ and produces mainly ^{52,56}Fe, ^{56}Ni, ^{48,52}Cr, and ^{44,48}Ti (Maeder 2009, 719–725). As described in Sec. 2.2.3, ^{26}Al is expected to emerge from massive stars through both winds and SNe. These mechanisms will be discussed in more detail in Sec. 2.2.5. In this thesis, the gamma-ray emission of ^{26}Al from massive stars is thus used as observational tracer to study the connection of these nucleosynthesis processes occurring in massive stars with the large-scale enrichment of the ISM.

WR Stars The particularly high temperature and luminosity of O-type stars can lead to strong radiatively driven winds (Cassinelli 1979; Abbott 1982). The underlying mechanism is that the radiation generated in the interior scatters with the gas inside a star. Thereby, momentum is transferred from the radiation field to the stellar matter. Especially in regions close to the surface, this mechanism can accelerate the gas beyond the escape velocities of about 600–800 $km\,s^{-1}$ which is thus ejected as stellar wind. The latter often give rise to planetary nebulae around the respective sources (Conti 1978). Massive stars exhibiting enhanced winds are classified as WR stars due to the original documentation of their spectroscopic peculiarities by Wolf & Rayet (1867). The physical explanation of the respective properties due to continuous mass loss was suggested later by Beals (1929). The initial wind velocities can reach up to $4 \times 10^3\,km\,s^{-1}$ (Chiosi & Maeder 1986; Howarth & Prinja 1989; Puls et al. 2008) and decelerate in the surroundings to terminal velocities of $\sim 100\,km\,s^{-1}$ (Dale 2015). This leads to a mass loss rate for WR stars exceeding $\dot{M}_* \gtrsim 10^{-6}\,M_\odot\,yr^{-1}$. The most massive stars $\geq 60\,M_\odot$ experience a mass-loss during their red supergiant phase that entirely removes the envelope and continue their evolution as bare helium cores after the main sequence. The stellar structure evolution of a $60\,M_\odot$ star including mass-loss is shown in Fig. 2.22. The mass-loss depends on the chemical composition of the star and increases for metallicity $(Z/Z_\odot) \gtrsim 10^{-3}$. Due to an enhancement in intermediate mass elements such as carbon or nitrogen, WR stars typically have a ten times higher mass-loss rate than more quiet O-stars of comparable luminosity, typically in the range $1 \times 10^{-5} \leq \dot{M}_* \leq 4 \times 10^{-5}\,M_\odot\,yr^{-1}$ but can reach even up to $10^{-3}\,M_\odot\,yr^{-1}$ (Abbott 1982; Vink & de Koter 2005; Dale 2015). OB stars often show fast rotation with an average of $190\,km\,s^{-1}$ (Huang & Gies 2006). An isolated treatment of O-stars gives a slightly lower average of $\sim 100\,km\,s^{-1}$ (Glebocki & Gnacinski 2005, cf. Sec. 4.2.3). This leads to additional rotational mixing and an enhanced mass-loss rate. The increased convection transports nucleosynthesis products from the central regions to the surface. Thus, ^{26}Al, along with other freshly produced elements, is ejected with the strong stellar winds.

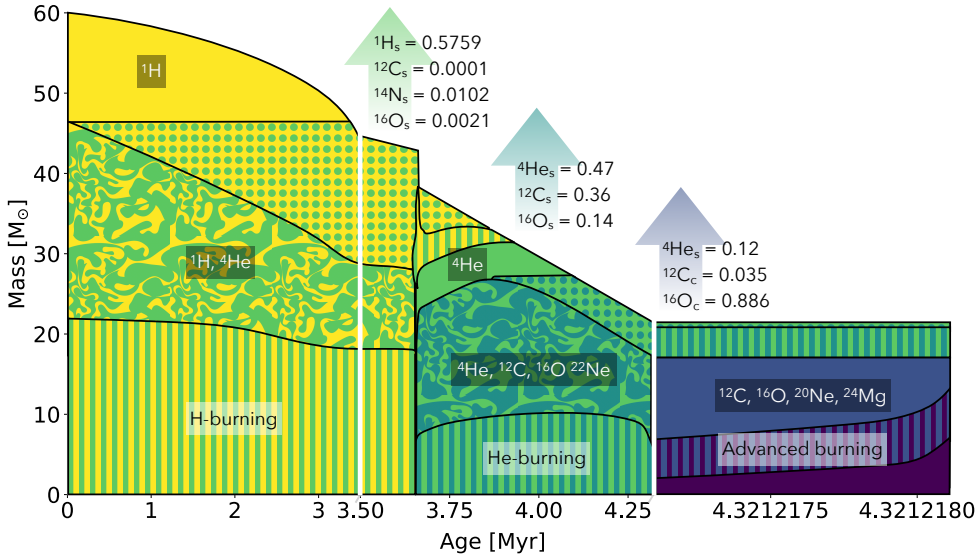

Figure 2.22: Schematic evolution of the structure of a 60 $M_\odot$ star. Wind compositions at different stages are denoted in vertical arrows. These become more and more enriched in heavy elements as the evolution progresses. Surface and central abundances are indexed with s and c respectively. The internal evolution proceeds much faster but in the beginning similar to Fig. 2.18. Due to significant mass loss, later stages of the stellar evolution go on as bare He-core which produces the zoo of advanced burning products in its core (*purple*). Adopted from Maeder (2009, 692).

Terminal Phases There are two main scenarios for explosive end stages of stars: a thermonuclear runaway disrupting the star, or a self-gravitative implosion of the star. The former characterises type Ia SNe which occur in accreting white dwarfs, and the latter describes core collapse supernovae (ccSNe) of type II or type Ib/c (Hoyle & Fowler 1960; Janka 2012; Burrows et al. 2018) which is characteristic for stars with mass $M_* \geq 8\,M_\odot$. Depending on the initial mass of a star, such events leave white dwarfs, neutron stars or black holes as remnants, if the star is not entirely disrupted. This is summarised graphically in Fig. 2.23. Considering nucleosynthesis feedback from massive stars, ccSNe constitute a highly relevant event type in the context of this thesis because they are expected to yield large amounts of ^{26}Al and ^{60}Fe.

Stars with mass $M_* \sim 9\,M_\odot$ reach electron degeneracy in a Ne-O-Mg core before Ne-burning. In that case, an increase of the electron Fermi energy facilitates electron capture reactions. This leads to a decrease in pressure and collapse in an electron-capture SN. In more massive stars, further burning stages reach up to ^{56}Fe (cf. Fig. 2.10). An Fe core develops, which heats up to temperatures $T \approx 10^{10}$ K. At these temperatures, a substantial amount of photons is absorbed in photodisintegration reactions and the elemental abundances are governed by nuclear statistical equilibrium. Thus, the overall radiative pressure decreases. At this point, the core becomes dynamically unstable and starts to collapse (Kippenhahn et al. 2012, 461–462). The onset of contraction increases the density and induces electron capture reactions, which in turn boosts the collapse. This accelerating inward motion halts when the density reaches $\rho \sim 10^{14}\,\mathrm{g\,cm^{-3}}$. This marks the transition of the core to homogeneous nuclear matter in which the short-range nuclear forces dominate the adiabatic index. Overshooting of the infalling core is believed to abruptly reverses the collapse. The back bouncing core collides in a supersonic outward motion with the still infalling layers above. In this clash, shock fronts establish that ultimately

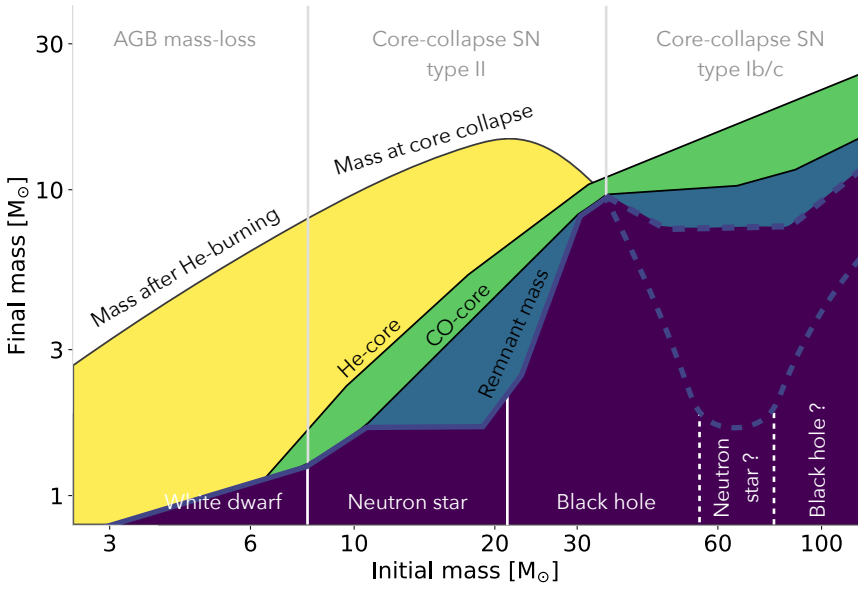

Figure 2.23: Remnant masses for given initial stellar masses (*purple*). Coloured regions above the remnant mass denote the additional material that is present during terminal phases. This consists of mostly H (*yellow*), He (*green*), or CO (*blue*), and is lost due to AGB mass-loss or the SN blast wave as assigned in the upper part. For the more massive stars a large amount of the initial mass is absent at the onset of core collapse due to previously occurring WR winds. Adopted from Maeder (2009, 740) following Heger et al. (2003).

disrupt the star in an iron-core SN.

For the most massive stars with $M_* \gtrsim 100\,\mathrm{M}_\odot$ a third scenario of pair-instability SNe is plausible. In this mass range, a substantial amount of high-energy photons forms e^+e^- pairs at $T \approx 10^9\,\mathrm{K}$ already after C-burning as a consequence of the high energy tail of the Maxwell-Boltzmann distribution. This reduces the thermal energy significantly, which leads to gravitational core instability and triggers a core collapse.

A canonical assumption is that stars with $M_* \geq 8\,\mathrm{M}_\odot$ experience a ccSN at the end of their evolution and thereby inject an energy in the range between 10^{50}–10^{51} erg along with a plethora of elements into the surroundings (Arnett et al. 1989; Smartt 2009; Janka et al. 2012; Wanajo et al. 2018). In recent years, it is considered that not all of these stars actually stable and instead fully collapse into black holes. This has strong implications for the energetic as well as chemical feedback from massive stars. Some models suggest that the immediate collapse to black holes happens for all initial masses $M \geq 25\,\mathrm{M}_\odot$ (Limongi & Chieffi 2018), or alternatively for stars in the mass range $100\,\mathrm{M}_\odot \leq M_* \leq 140\,\mathrm{M}_\odot$ (Janka 2012). Three-dimensional hydrodynamic SN simulations indicate that the explodability of massive stars shows a more complex profile with rather irregular islands and gaps, especially for initial stellar masses $M_* \geq 20\,\mathrm{M}_\odot$ (e.g. Ugliano et al. 2012; Sukhbold et al. 2016; Wanajo et al. 2018; Burrows et al. 2020; Ertl et al. 2020). This is still a matter of debate and, especially because of the low frequency of such events in the Milky Way, difficult to address observationally. A possible approach to solving this problem by modelling the cumulative nucleosynthesis signature of ccSNe will be discussed in Ch. 4.

Binarity Many stars form in multiple star systems, most of which are binary systems, rather than in isolation as single stars. The interaction with one or more companion stars is expected to affect the stellar evolution. Very low-mass stars $\leq 0.1\,\mathrm{M}_\odot$ have a binary fraction of only 0.1–0.3%. These systems are infrequently occurring but of very similar kind. A fraction of 93% of them have separations smaller than 20 AU and in 77% of the cases near-equal mass ratios $q = M_2/M_1 \geq 0.8$ (Burgasser et al. 2007). The mass ratio in a binary system is defined as $q = M_2/M_1$, where M_1 is the mass of the primary, i.e. the more massive star, and M_2 the lower mass of its companion. For massive stars, the binary fraction is much higher and most of them are found in binaries (Duchêne & Kraus 2013). For O-stars, i.e. stars with masses above $\sim 16\,\mathrm{M}_\odot$, the binary fraction is even more than 70%, which preferentially happen to have close separations (Sana et al. 2012). This can lead to mass exchange when stellar material overflows the critical gravitational equipotential around the donor and enters the gravitational catchment area of its companion. The size of this Roche-lobe can be approximated by (Eggleton 1983)

$$R_{\text{Roche-lobe}} = \frac{0.49q^{\frac{2}{3}}}{0.6q^{\frac{2}{3}} + \ln(1 + q^{\frac{1}{3}})}. \tag{2.28}$$

Binary models suggest that in a Roche-lobe overflow, only $\sim 10\%$ of the material is actually transferred between the companions. However, a proportion of $\sim 90\%$ of the mass ejected by one of the stars leaves the system (Petrovic et al. 2005). This means that a Roche-lobe overflow may especially influence the formation of WR stars and enhanced mass-loss may be the dominant feedback effect seen from binary interaction (Vanbeveren et al. 2007). But the overall importance of this effect for massive star evolution is still rather unclear (cf. Maeder 2009, 713). A recent study of WR stars and binaries in the Small Magellanic Cloud (SMC) and Large Magellanic Cloud (LMC) indicates that the effect of increased metallicity might dominate the formation of WR stars compared to binary interactions (Shenar et al. 2020). Also the effect of enhanced winds on SN progenitors due to binary interaction is still subject to recent research and debates (Brinkman et al. 2019; Ertl et al. 2020). In Ch. 4, an estimation of these effects using population synthesis calculations will be given.

2.2.5 Stellar Feedback

In Sec. 2.2.1, the formation of stars from cooling and collapsing GMCs was presented. Once stars have formed inside these clouds, the processes of cooling and collapse can be compensated or turned around due to the effects of especially young, massive, and luminous stars on their surroundings. This damps star formation to an overall efficiency of the order of $\epsilon_{\text{SF}} \sim 10\%$. From the moment of formation on, throughout their evolution, until their final explosions, these stars determine the energetics and chemistry of the ISM. This mechanism is summarised in the term massive star feedback. There are three main physical phenomena that drive this process: radiation, stellar winds, and SNe. In the absence of these feedback mechanisms, nothing prevents gas from self-gravitational collapse and all the gas from a cloud would collapse into stars, i.e. star formation efficiency would be one. In that case, there would be no ISM in the Galaxy left. In the following these feedback components are summarised (cf. e.g. Krumholz et al. 2014; Dale 2015).

Radiation Inside a GMC, molecules are destroyed due to the irradiation from embedded stars. Radiative heating is caused primarily by far-UV photons through photo-effect on dust. An additional form of radiative feedback comes from the direct force of radiation. Far-UV radiation can diffuse dust into the gas phase and directly push gas as well as dust. In opaque regions, the infrared (IR) part of the radiation field can be absorbed and reprocessed on dust particles and therefore contributes to the thermal energy budget of a region. The gas component itself is also heated by photoionisation, giving rise to large H II regions. As soon as a star of sufficient mass forms, it emits ionising photons with a total rate

$$Q(\mathrm{H}^0) = \int_{E_0}^{\infty} \frac{L(E)}{2\pi\hbar E}\, dE, \tag{2.29}$$

with luminosity $L(E)$ for a given photon energy E above the photoionisation threshold E_0. For a typical O-star this is of the order of $\sim 10^{49}\,\mathrm{s}^{-1}$. For B-stars, this decreases to $\sim 10^{45}\,\mathrm{s}^{-1}$. This decrease by four orders of magnitude shows that the photoionisation process is entirely dominated by the contribution of the most massive O-type stars (Osterbrock & Ferland 2006). On the one hand, the ionising photons impinge with intensity $I(E)$ on neutral hydrogen atoms with density $n(\mathrm{H}^0)$ and ionisation cross section $\alpha_{\mathrm{ion}}(\mathrm{H}^0, E)$. On the other hand, free electrons and protons with respective densities n_e and n_p recombine according to the recombination cross section $\alpha_{\mathrm{rec}}(\mathrm{H}^0, T)$, which is also dependent on the gas temperature T. Since the intensity decreases with increasing distance from the radiation source, there is a certain radius at which ionisation is balanced with recombination. This equilibrium can be approximated for the case of a mono-atomic hydrogen cloud as

$$n(\mathrm{H}^0) \int_{E_0}^{\infty} \frac{2\, I(E)}{\hbar E}\, \alpha_{\mathrm{ion}}(\mathrm{H}^0, E)\, dE = n_e\, n_p\, \alpha_{\mathrm{rec}}(\mathrm{H}^0, T), \tag{2.30}$$

with the left side describing the number of ionisations and the right side giving the number of recombinations. This radius corresponds to an ionisation front and defines the boundary of a Strömgren sphere. Accordingly, the fully ionised and heated interior has a volume of

$$\frac{4\pi}{3} R_{\mathrm{S}}^3 = \frac{Q(\mathrm{H}^0)}{n_{\mathrm{H}} \alpha_{\mathrm{rec}}(\mathrm{H}^0, T)}, \tag{2.31}$$

with the Strömgren radius R_{S} and a homogenous total hydrogen density $n_{\mathrm{H}} = n(\mathrm{H}^0) + n_p$. It is surrounded by a rather thin transition zone with thickness

$$d \approx \frac{1}{\xi n_{\mathrm{H}} \alpha_{\mathrm{rec}}(\mathrm{H}^0)}, \tag{2.32}$$

where ξ denotes the fraction of neutral H^0 outside the H II region. Overall, the photoionisation rate scales with $Q(\mathrm{H}^0)$ and the size of the cloud. A schematic picture of an idealised H II region is shown in Fig. 2.24 for the case of a fully embedded and a blister region. Since the gas inside the sphere is ionised and heated, the interior of the sphere is overpressured compared to the neutral gas in the surrounding. This means in particular that the Strömgren radius sets the density rather than the other way around. Overall, this leads to an overall expansion of the H II region that is proportional to the number of ionising photons per unit time (Kim et al. 2016). In terms of luminosity there are generally more non-ionising than ionising photons.

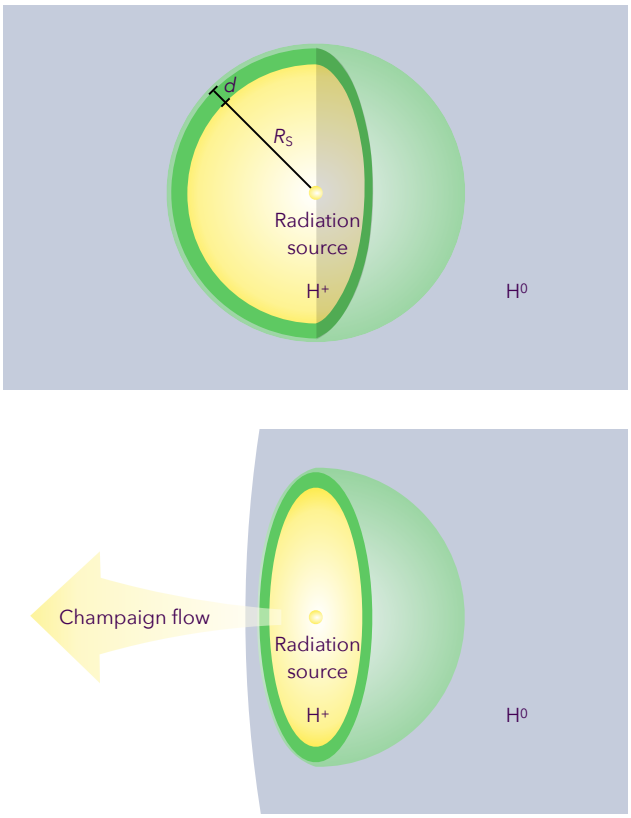

Figure 2.24: Schematic picture of H II regions. The fully ionised interior of the H II region with Strömgren radius R_S is shown in *yellow*. It is separated by a transition zone (*green*) of thickness d from the neutral surroundings (*blue*). *Upper:* Radiation source fully surrounded by neutral neutral hydrogen with an embedded H II region. *Lower:* Radiation source in the outer region of a cloud causing a blister H II region.

Thus, it is also important to take the effect of non-ionising photons into account. These lower energetic photons can rearrange the material within the Strömgren sphere with a gradient from radiation pressure dominated in the central region to gas pressure dominated in the outer part. If the H II region expands enough, it can completely disrupt the cloud in which the star formation event took place on timescales of 1–10 Myr. The dispersal time is shorter and of the order of only a few Myr. The basic correlation here is, that the higher the surface density of the cloud, the higher star formation efficiency is needed to disrupt the cloud (Murray et al. 2010; Fall et al. 2010). The first order approximation of a spherical cloud with an isotropically expanding H II region is of course rarely found in reality. Actually most of the time stars form in outer regions of a cloud and form blister H II regions with the radiation being incident only on a part of the cloud that is exposed to the outside (Krumholz & Matzner 2009). Gas that is photo-evaporated from that surface can escape in flows comparable to the sound speed which is of the order of $10\,\mathrm{km\,s^{-1}}$; this effect is sometimes also called champaign-flow (cf. lower panel in Fig. 2.24). On the other side, there is a back reaction pushing the neutral gas, which increases the pressure in that cloud region comparable to what occurs in the case of a full Strömgren sphere. Since the gas around ionising sources is not homogenous and the sources are not always fully embedded, on average about 40% of the photons escape and do not contribute to the radiation pressure (Kim et al. 2019). Nevertheless, as will be discussed in Sec. 2.3, the radiative effects are of major importance for the overall feedback on large scales.

Stellar Winds A second source of stellar feedback is the mass loss due to stellar winds that was briefly mentioned in the discussion of AGB, WR, and massive stars in Sec. 2.2.4. For the first time, Norman & Silk (1980) suggested stellar outflows as important source of energy injection in GMCs and proposed that these outflows blow large cavities and thereby govern the dynamics and structure of clouds. Lower-mass stars contribute mainly by magnetocentrifugally driven winds and jets to this form of feedback. Because the terminal velocities of these winds is only 10–100 $\mathrm{km\,s^{-1}}$, they are overall of less importance. Nevertheless, massive stars contribute also with strong line-driven winds and circumstellar disk winds which have a much larger effect. Stellar winds can be approximated as steady flowing fluid (Cassinelli 1979)

$$\dot{M} = 4\pi\rho\ vr^2 = \text{const.}, \tag{2.33}$$

with momentum conservation

$$v\frac{dv}{dr} + \frac{1}{\rho}\frac{dp}{d\rho} + \frac{GM}{r^2} + g_{\mathrm{rad}} = 0, \tag{2.34}$$

with the radial velocity v of the outflowing material of density ρ. The pressure of the gas is p and the acceleration due to radiation pressure g_{rad}. The latter can be split into its line and continuum components

$$g_{\mathrm{rad}} = \frac{\kappa L(r)}{4\pi c^2 r^2} + \sum_l g_{\mathrm{l}}, \tag{2.35}$$

whith the continuum mean opacity κ and the acceleration g_{l} that caused by spectral line l. Applied to Eq. 2.34, this obtains

$$v\frac{dv}{dr} + \frac{1}{\rho}\frac{dp}{d\rho} + \frac{GM}{r^2}(1-\Gamma_{\mathrm{E}}) + \sum_l g_{\mathrm{l}} = 0, \tag{2.36}$$

with the Eddington parameter Γ_{E} as defined in Eq. 2.8. This reproduces $\Gamma_{\mathrm{E}} \leq 1$ with the critical Eddington luminosity L_{E} (cf. Eq. 2.9) as condition for net inward acceleration inside the star and $\Gamma_{\mathrm{E}} > 1$ for outward wind acceleration. The latter implies deposition of radiative and mechanical energy, as well as momentum in the ISM.

The terminal wind velocities of OB stars are of the order of $10^3\,\mathrm{km\,s^{-1}}$ with a mass-loss rate in the range $10^{-5}\,\mathrm{M_\odot\,yr^{-1}}$ to $10^{-4}\,\mathrm{M_\odot\,yr^{-1}}$. The steady outflow leads to the emergence of wind bubbles around AGB or massive stars. This is shown schematically in Fig. 2.25. After the wind is accelerated in a turbulent shock phase, it forms a stable outflow, that pushes the surrounding gas outwards. As it runs into the cold ISM, it is decelerated to velocities of $\sim 100\,\mathrm{km\,s^{-1}}$. In the most extreme case with all mechanical energy being retained in the bubble, it expands adiabatically with $R(t) = (L/\rho)^{\frac{1}{5}} t^{\frac{3}{2}}$. This is based on very simplified assumptions and is sensitive to the detailed thermodynamics and especially the cooling efficiency of the gas in the bubble interior (Dale 2015). But it is important to note that the dependence on stellar luminosity L and the ISM density ρ is rather weak. A more holistic picture with combined feedback effects will be given in the context of larger-scale superbubbles in Sec. 2.3.

Fig. 2.26 shows the wind yields for different remnant types from particular initial stellar mass regimes as a variation of Fig. 2.23, now focussing explicitly on stellar wind ejection. While the integrated kinetic energy that is injected into the sur-

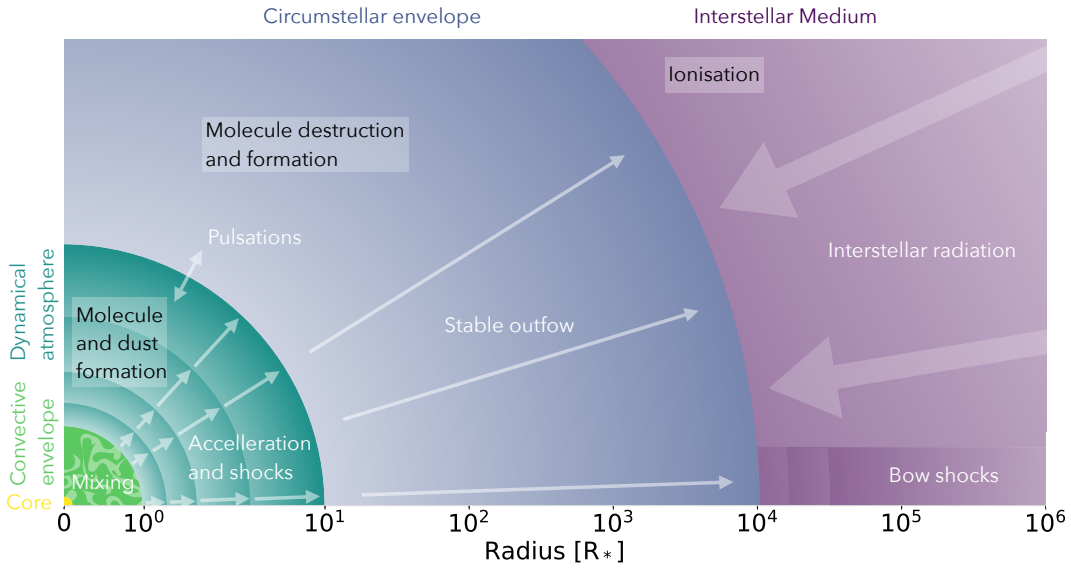

Figure 2.25: Schematic feedback from AGB stars. Flow properties in different regimes are denoted in *white* and chemical characteristics are annotated in *black*. Adopted from Höfner & Olofsson (2018).

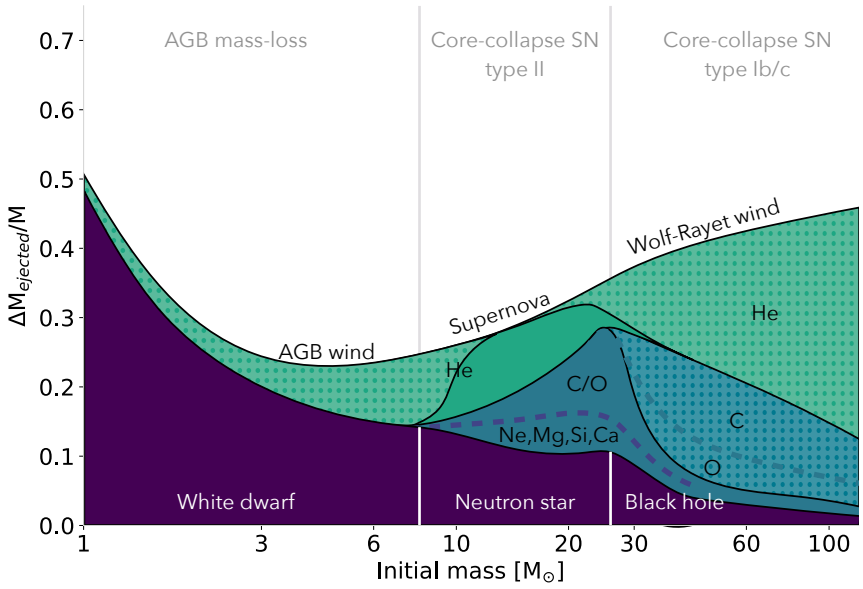

Figure 2.26: Stellar wind yields for different stellar remnants and initial mass regimes. The ejected mass with varying composition is shown above the remnant mass (*purple*) and wind types are assigned to different regimes. Reproduced following Maeder (1992).

roundings by stellar winds is comparable to that by SNe, observations suggest that a substantial amount of the wind energy is lost from the surrounding bubble. A possible scenario is that turbulent small-scale mixing between the hot bubble interior and the cold surrounding gas or bulk leakage of hot gas in H II region Champaign-flows remove a substantial amount of the kinetic energy injected by massive star winds. Such mechanisms could limit the importance of stellar winds as contributors to feedback on the cold ISM significantly (Rosen et al. 2014).

Supernova Explosions At the end of their evolution, massive stars explode in ccSNe and thereby energy on order of $\sim 10^{51}$ erg during a few seconds (cf. Sec. 2.2.4). This launches a blast wave with with a velocity of the order of 3000–5000 km s^{-1} that first sweeps through the stellar envelope itself, then the surroundings, which may consist of a wind-blown cavity, and then runs into the surrounding molecular gas (Janka 2012; Dale 2015). In the simplified picture of expansion in a homogenous medium, the SN blast wave can be described as going through three phases: In the first phase, the surrounding ISM pressure is negligible and has no effect on the expansion. This means the radius of the shock scales as

$$R_{\text{free}}(t) = v_{\text{ej}} t, \tag{2.37}$$

according to the velocity of the ejecta v_{ej}. As the ejecta are freely streaming spherically outwards, ISM gas is accumulated in a shock front. The accumulation of material leads to the build-up of a reverse shock. When the shocked material about equals the ejected material in mass, the reverse shock starts to slow down the expansion. This marks the end of the free-expansion phase. With the inward propagation of the reverse shock, this starts the second phase, i.e. the Sedov-Taylor phase of a pressure-driven explosion. Here, the radius of the shock evolves with (Dale 2015)

$$R_{\text{Sedov-Taylor}}(t) \propto \left(\frac{E_{\text{SN}}}{\rho_0}\right)^{\frac{1}{5}} t^{\frac{2}{5}}, \tag{2.38}$$

with the total energy of the SN E_{SN} and the un-shocked homogenous ISM density ρ_0. In the final snowplough phase, matter is continuously swept up in the expanding shell. (Klessen & Glover 2016)

$$R_{\text{snowplough}}(t) \propto \left(\frac{\mu}{\rho_1}\right)^{\frac{1}{4}} t^{\frac{1}{4}}, \tag{2.39}$$

with the total momentum of the expanding shell μ and the increased density in the swept-up shell ρ_1. The evolution through these three phases is shown schematically in the left panel of Fig. 2.27. The picture becomes more complicated when turbulences are taken into account. When the blast wave runs into the denser ISM, Rayleigh-Taylor instabilities establish. Additionally, inhomogeneities and pre-existing bubbles in the ISM interact with the blast wave to form discontinuities,

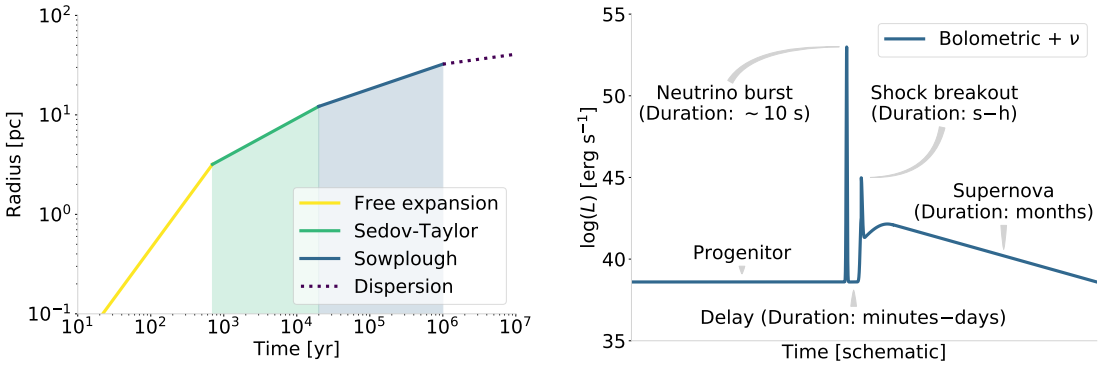

Figure 2.27: *Left:* Schematic stages of the expansion of a ccSN. It starts expanding freely (Eq. 2.37, *yellow*), experiences deceleration in the Sedov-Taylor phase (Eq. 2.38, *green*), and finally reaches the snowplough phase (Eq. 2.39, *blue*), which is dominated by the pressure of the ambient material. *Right:* Schematic of the characteristic luminosity course in a ccSN time sequence. Adopted following Adams et al. (2013).

vortices, or protrusions (Jun et al. 1996; Blondin et al. 2001). The time sequence of a ccSN blast is depicted schematically in the right panel of Fig. 2.27. It is shown that the largest part of energy is released in a neutrino burst, that lasts only on the order of $\sim 10\,\mathrm{s}$. Magneto-hydrodynamic (MHD) simulations indicate that large fractions of this energy escapes the cloud due to the low cross section for neutrino interaction and therefore do not affect the dynamics of a molecular cloud. Nevertheless, SNe are the dominant energy sources in the diffuse ISM (Mac Low & Klessen 2004). Multiple SNe are cumulatively able to inject approximately $10^{43}\,\mathrm{g\,cm\,s^{-1}}$ of momentum per event into the surroundings (Geen et al. 2016; Kim et al. 2017). This makes SNe particularly important for feedback processes on the larger scale. A single SN can not contribute significantly to the collapse of a molecular cloud because of the high density difference between the diffuse ISM and the molecular cloud gas. In that case, the energy is mostly reflected from the cloud which is dominated by the turbulences inherited from its GMC formation (Elmegreen 1999; Heitsch & Burkert 2002). The cumulative effect from multiple sources will be discussed in the following Sec. 2.3.

Nucleosynthesis Feedback Besides its thermal and kinetic aspects, stellar evolution is also accompanied by a chemical change of the surrounding ISM. This is referred to as nucleosynthesis feedback. As long as the freshly produced nuclei reside at their production sites inside stars, there is no such feedback. It requires stellar winds or SNe to transport the nucleosynthesis products into the surroundings. This means nucleosynthesis feedback has two main aspects: dynamics and yields of nucleosynthesis products. While the former essentially resembles the dynamic ejection properties of the respective source, the latter refers to the amount of an isotope that emerges from a source.

Except for neutrino measurements from the Sun, the nuclear processes inside stars are observationally not directly accessible and our understanding of them therefore empirically barely testable. Thus, calculations of nucleosynthesis yields are an important tool of theoretical astrophysics as it addresses an immediate as well as potentially observable effect of these processes. In that respect, the yields of radioisotopes such as the previously mentioned ^{26}Al, ^{60}Fe, or ^{44}Ti are of particular interest because they are directly observable by their gamma-ray line emission. Observations of stable isotopes are necessarily biased according to certain thermal or ionisation conditions, and therefore do not trace the distribution of nucleosynthesis products directly but instead general physical conditions of the surroundings. From such observations information about nucleosynthesis feedback can only be inferred according to certain assumptions about density, temperature, ionisation, or velocity. Nevertheless, nuclear line emission from radioisotopes is less biased by such environmental conditions and offers a uniquely direct window to the dynamics of chemical enrichment of the ISM. As reviewed by Diehl et al. (2018a), model calculations of nucleosynthesis yields including radioisotopes have been and still are subject to intense studies. ^{26}Al yields were initially investigated by e.g. Woosley & Weaver (1995), (Timmes et al. 1995), Thielemann et al. (1996), Palacios et al. (2005), or Limongi & Chieffi (2006). Newer stellar yield models take especially the influence of rotation and metallicity into account (Meynet et al. 2006; Ekström et al. 2012; Chieffi & Limongi 2013; Pignatari et al. 2016; Limongi & Chieffi 2018). Most of these models are concerned with the emission from massive stars in the range 10–120 $\mathrm{M}_\odot$. Also yields from novae (Jose & Hernanz 1998; Gehrz et al. 1998) and

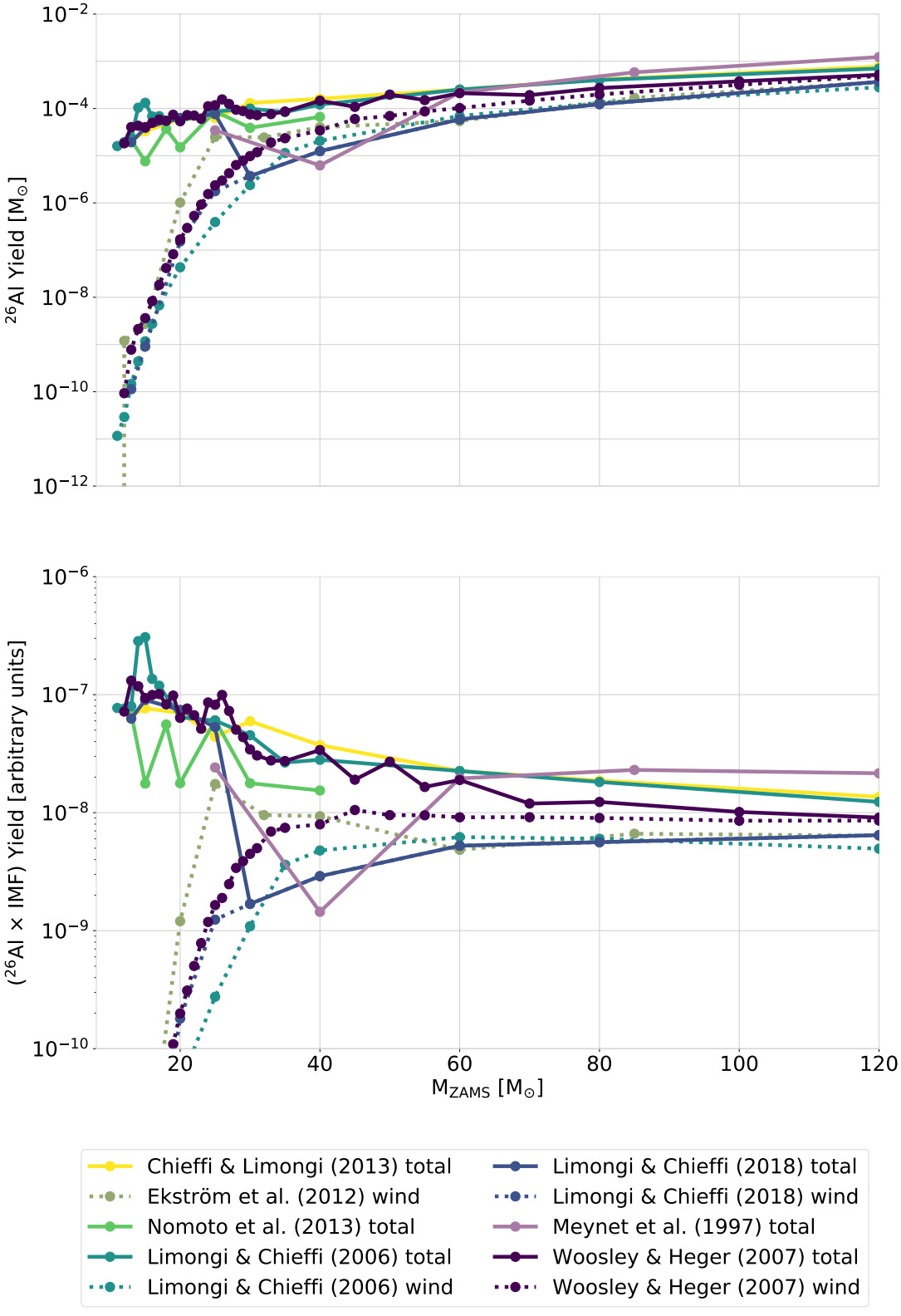

Figure 2.28: ^{26}Al single star yields per initial stellar zero-age main sequence (ZAMS) mass from non-rotating stellar models with Solar metallicity by Meynet et al. (1997), Limongi & Chieffi (2006), Woosley & Heger (2007), Ekström et al. (2012), Chieffi & Limongi (2013), and Limongi & Chieffi (2018). *Upper:* Total ^{26}Al yields of combined wind and SN contribution (solid lines) and isolated contribution due to stellar winds only (dotted lines). *Lower:* Effective ^{26}Al yields weighted by the IMF (Eq. 2.5). This gives effective contribution of different stellar mass regimes by taking their formation frequency into account.

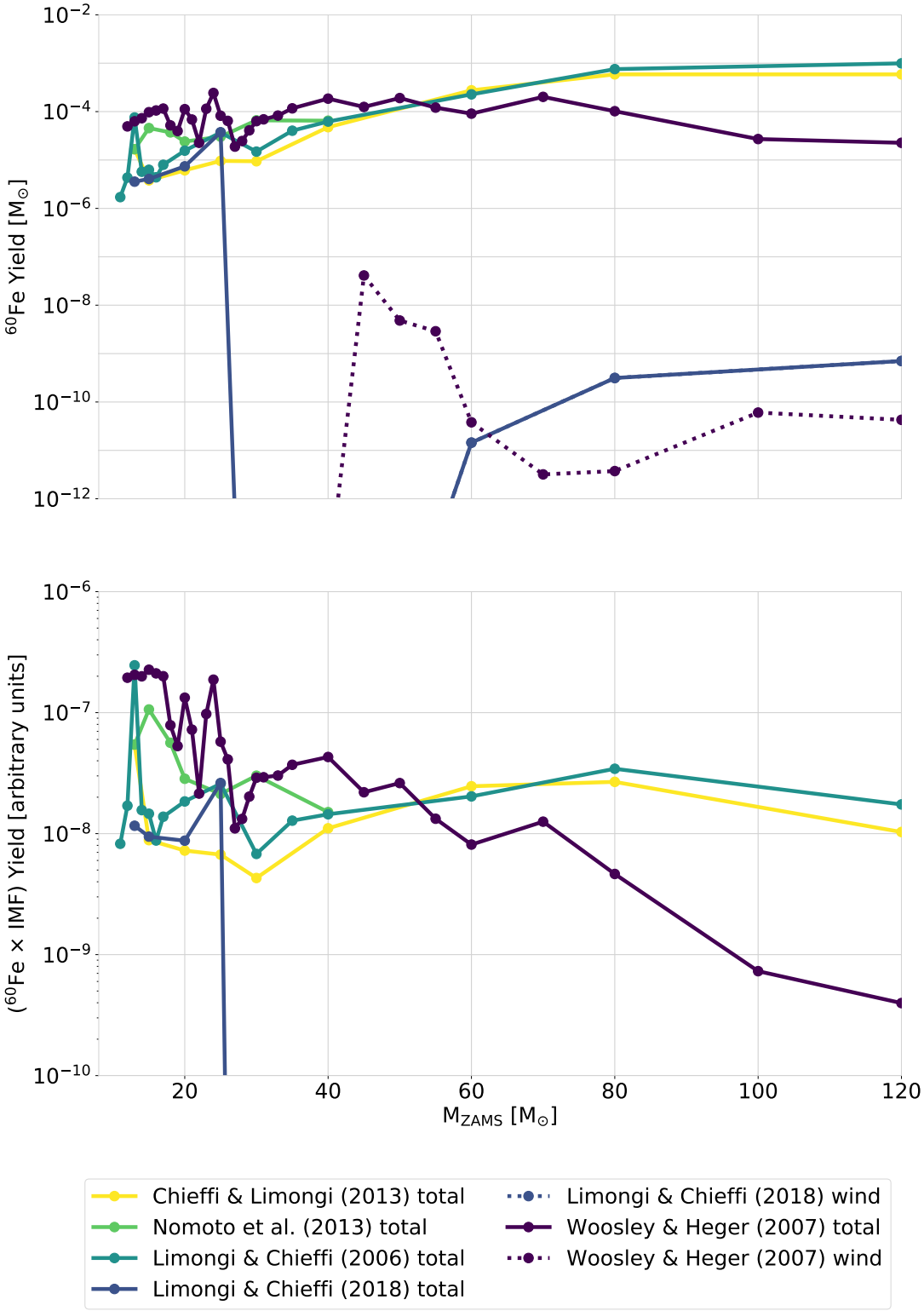

Figure 2.29: Same as Fig.2.28 for ^{60}Fe.

lower-mass AGB stars have been provided (Bazan et al. 1993; Meynet et al. 1997; Mowlavi & Meynet 2000; Karakas & Lattanzio 2014). A summary of total ^{26}Al and ^{60}Fe yields from different theoretical model calculations of non-rotating stars with Solar metallicity are given in Fig. 2.28 and Fig. 2.29, respectively.
A massive star ejects on average on the order of $10^{-4}\,M_\odot$ of ^{26}Al as well as ^{60}Fe. An AGB star of about $4\,M_\odot$ is expected to eject less, i.e. $\sim 5 \times 10^{-5}\,M_\odot$, of ^{26}Alas estimated by Bazan et al. (1993). The results for different stellar models show a spread of about one order of magnitude in yields. The amount ejected by SNe seems to outweigh the wind component over the whole mass range. Models by Limongi & Chieffi (2018) constitute a special case because they assume an immediate collapse into a black hole for stellar masses $M_{\mathrm{ZAMS}} \geq 25\,M_\odot$. This reduces nucleosynthesis feedback in this mass range to only a wind component. In general, individual stars with very high mass $M_{\mathrm{ZAMS}} \geq 60\,M_\odot$ eject more ^{26}Al than less massive stars. Nevertheless, for the overall contribution to nucleosynthesis feedback, their difference in formation frequency has to be taken into account. The lower panel in Fig. 2.28 shows the effective ^{26}Al yields weighted with the standard IMF which reflects this dependence on the formation frequency of stars in a certain mass range. This shows an overall larger contribution of ^{26}Al in the ISM due to stars with $M_{\mathrm{ZAMS}} \leq 30\,M_\odot$.
^{60}Fe is produced mainly in shell C/Ne-burning. This only occurs at late evolutionary stages and far from the surface deep inside of massive stars. In that phase, stellar evolution proceeds on timescales of a few kyr at most. Convective transport is neither quick enough nor does it reach deep enough in order to dredge up a significant amount of ^{60}Fe before the star explodes. Thus, ^{60}Fe is only released when the entire star is disrupted in a SN. This is shown by the negligible wind contributions in Fig. 2.29. The disagreement among models for ^{60}Fe yields spans about two orders of magnitude. The above mentioned explodability included in Limongi & Chieffi (2018) yields shows a much larger effect for ^{60}Fe since it is only expelled during an explosion. This makes the contribution of stars with mass $M_{\mathrm{ZAMS}} \geq 25\,M_\odot$ to ^{60}Fe in the ISM negligible in this model. Additionally, this underlines the particular sensitivity of ^{60}Fe production to metallicity assumptions.
Overall, the main contributors to ^{26}Al are winds from AGB, massive, and WR stars as well as SN ejecta. This marks an important difference to ^{60}Fe, which is only ejected in SNe. Thus, ^{26}Al and ^{60}Fe are expected to emerge from slightly different ejection mechanisms. In a sufficiently small region, where the ISM does not reach equilibrium between injection and decay of these isotopes, the ^{60}Fe/^{26}Al ratio is therefore not expected to be constant. Instead, a variation on the order of the time delay between the different ejection mechanisms should occur.
For simplicity, the following explanations are mainly restricted to the models by Limongi & Chieffi (2006) (LC06) and Limongi & Chieffi (2018) (LC18) because they are shown to reflect two rather extreme cases at the upper and lower boundaries of the spread between models (cf. Fig. 2.28 and Fig. 2.29).
LC06 use the Frascati Raphson Newton Evolutionary Code (FRANEC), a one-dimensional stellar evolution code with nuclear burning coupled to convective mixing. In order to describe the chemical evolution of matter, the nuclear generation rate is computed with cross sections for a full nuclear network from neutrons to ^{98}Mo (Limongi & Chieffi 2003). The wind mass-loss was calculated via Monte Carlo (MC) ray tracing, i.e. by following the momentum transfer of a large number of photons that are released from below the surface to the outflowing material (Vink et al. 2000; Nugis & Lamers 2000). After central fuel exhaustion, the explosion is started by instantaneously injecting an initial velocity v_0 at a mass cut of $\sim 1\,M_\odot$ inside

the iron core of the pre-SN model. The boundary condition for the choice of this mass cut is to finally obtain $0.1\,M_\odot$ ^{56}Ni. Since ^{26}Al and ^{60}Fe are produced further out in the mantle, the mass cut choice is expected to have no huge effect on their yields. It is important to note that v_0 is chosen in a way that all the mass above the iron core is actually ejected. The subsequent shock propagation is calculated by an hydrodynamic explosion simulation code. In order to follow the explosive nucleosynthesis in this phase, the nuclear network is coupled to the hydrodynamic equations. This way, the nucleosynthesis feedback is modelled for non-rotating single stars with metallicity $Z = 0.02$ in the mass range 11–120 $M_\odot$.

LC18 includes a grid of pre-SN models with different metallicities and rotation velocities. The metallicites range from Solar [Fe/H] = 0, i.e. $Z = 1.345 \times 10^{-2}$ (Asplund et al. 2009), to [Fe/H] = −3, i.e. $Z = 3.236 \times 10^{-5}$. Here, $[X/Y]$ denotes the abundance ratio defined as $[X/Z] = \log(X/Y) - \log(X/Y)_\odot$. Included steps of initial rotation velocities are 0, 150, and 300 $\mathrm{km\,s^{-1}}$. This induces instabilities affecting two convection coefficients for meridional circulation and shear instability. In order to include the multi-dimensional effects of stellar rotation into the one-dimensional evolution code, the rotation-induced mixing efficiency is normalised by adjusting the enhanced surface nitrogen abundance in a $20\,M_\odot$ star at core hydrogen depletion to the value observed in the LMC (Heger et al. 2000; Maeder & Meynet 2000). The stellar evolution up to the SN stage is calculated with an updated version of the FRANEC code, coupled to a reaction network that is extended to ^{209}Bi (Chieffi & Limongi 2013). The main improvements in stellar evolution calculations compared to LC06 concern a more detailed treatment of momentum transport in the stellar envelope, triggered mass-loss effects near the Eddington limit, and angular momentum loss during wind phases. Additionally, the nuclear cross-sections and weak interaction rates are updated following the STARLIB database (Sallaska et al. 2013). The impact of rotation on pre-SN stellar evolution scales inversely with the initial mass of the star. That means, for a given rotational velocity the rotation-induced effects decrease as the initial stellar mass increases (Maeder & Meynet 2000). The main effect of rotation at the end of the pre-SN stage in LC18 are enhanced He and CO core masses. The finally produced elemental yields mainly cause an overproduction of weak *s*-components but it is overall not strongly affected by rotation. The mass cut condition for SN ejection is adjusted to the mixing and fallback scheme by Umeda & Nomoto (2002). In order to obtain explosive nucleosynthesis yields this is combined with the assumption that stars initially more massive than $25\,M_\odot$ fully collapse into black holes. The latter assumptions is subsequently denoted as the explodability model following LC18.

This explodability assumption strongly affects the SN yields of ^{26}Al and ^{60}Fe. A comparison of SN yields in LC18 and LC06 is shown in Fig. 2.30. Other explodability models investigated in this thesis are summarised in Tab. 2.5. Their effect on SN nucleosynthesis yields from LC06 is shown in the lower panels of Fig. 2.30.

Table 2.5: Explodability models and the respective acronyms used in this thesis. M_* denotes the initial stellar mass in units of $M_\odot$.

Source	Acronym	Exploding stellar models
Smartt (2009)	S09	$M_* \geq 8$
Janka (2012)	J12	$8 \leq M_* \leq 100$ and $140 \leq M_* \leq 260$
Sukhbold et al. (2016)	S+16	Irregular islands and valleys of explodability
Limongi & Chieffi (2018)	LC18	$8 \leq M_* \leq 25$

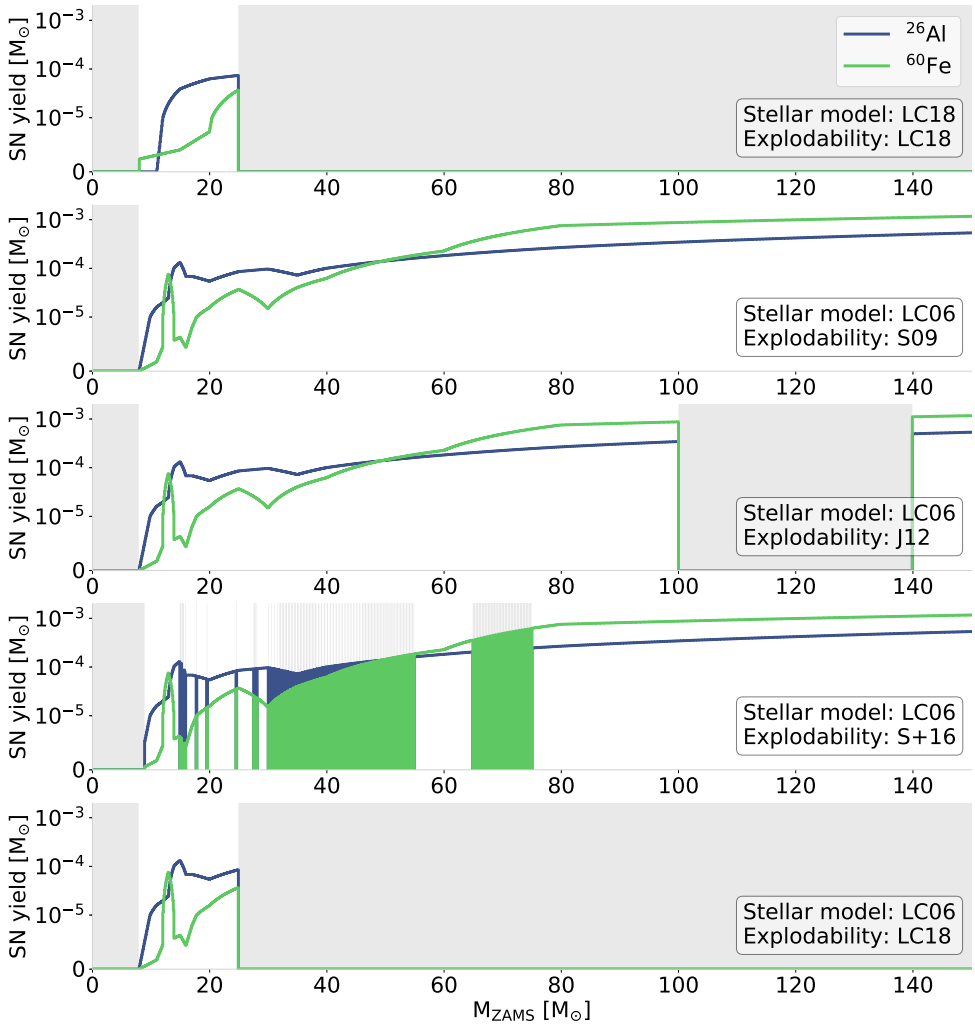

Figure 2.30: SN yields of ^{26}Al and ^{60}Fe from stellar evolution models by Limongi & Chieffi (2006) (LC06) and Limongi & Chieffi (2018) (LC18). The panels give the yields additionally for different explodability models following LC18, Smartt (2009) (S09), Janka (2012) (J12), and Sukhbold et al. (2016) (S+16). Grey shaded regions indicate initial stellar masses for which no ccSNe occur in a given explodability study.

It should be mentioned in this context that the explodability model by Sukhbold et al. (2016) is a special case as its irregular islands of explodability are based on one-dimensional hydrodynamic explosion simulations of a set of pre-SN models. If not mentioned otherwise, LC06 is combined with explodability S09. The global effects of the different explodability assumptions will be discussed further in Sec. 2.3 and Ch. 4.

The overall difference in time evolution of nucleosynthesis feedback between LC06 and the updated LC18 is shown in Fig. 2.31.

Here, wind and SN contributions are combined for non-rotating single star models with Solar metallicity. If there is a stellar wind component, ^{26}Al is emerging from the source prior to ^{60}Fe. This means that the former completely dominates in the pre-SN phase. If there is any ^{60}Fe in the SN ejecta, it will at some point come to dominate the ^{60}Fe/^{26}Al ratio after the explosion due to its longer half-life time of 2.6 Myr (Rugel et al. 2009). For LC06 and LC18 this occurs between 5–18 Myr and 16–30 Myr after the formation, depending on the initial mass of the source (cf. lower

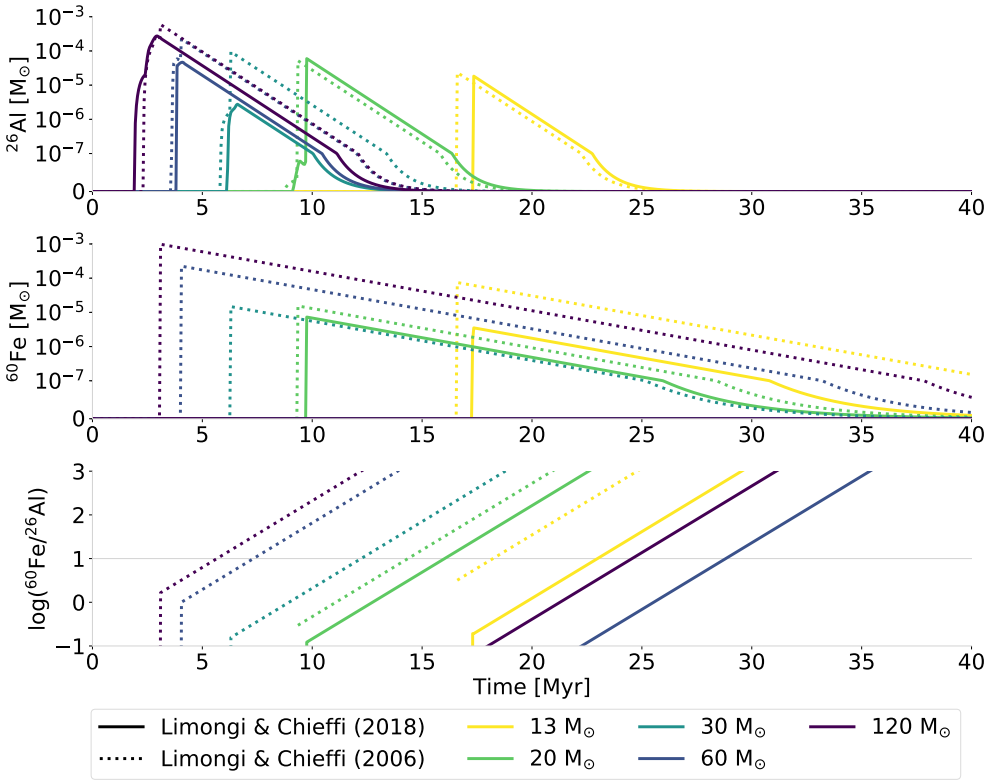

Figure 2.31: Time profiles for ^{26}Al ejecta (*upper*), ^{60}Fe ejecta (*middle*), and their ratio (*lower*) as obtained from stellar models by Limongi & Chieffi (2006) (LC06) in solid and stellar models by Limongi & Chieffi (2018) (LC18) in dotted lines. Colours denote different initial stellar masses.

panel in Fig. 2.31). This indicates a strong model sensitivity of the ^{60}Fe/^{26}Al and makes this ratio an important touchstone for testing different stellar evolution models.

The two main parameters that are introduced in LC18 compared to LC06 are a grid of metallicities [Fe/H] and rotational velocities $v_{\rm rot}$. The effect of these parameters on ^{26}Al and ^{60}Fe yields in LC18 are depicted in Fig. 2.32, in which the left side shows variations with $v_{\rm rot}$ and the right side gives the effect of variations in [Fe/H]. Since the amount of ^{26}Al produced through ^{26}Mg(p, γ)^{26}Al largely depends on the amount of ^{26}Mg that is present when the star forms, its final abundance is sensitive to metallicity. The same is valid for ^{60}Fe production due to its dependence on the initially available amount of mainly ^{56}Fe. Thus, the overall effect seen in the right side of Fig. 2.32 is a reduction in ^{26}Al and ^{60}Fe yields with decreasing metallicity. This goes along with a decrease in opacity due to a lower electron scattering cross-section. According to Eq. 2.35 this decreases the radiative wind acceleration and therefore reduces the stellar wind contribution for lower-metallicity stars.

Higher rotation velocity shows three main effects: enhanced yields, increased lifetime, and earlier and stronger wind contributions (cf. left panel in Fig. 2.32). As discussed in Sec. 2.2.2, stellar rotation increases mixing and expedites convection. This means that freshly produced ^{26}Al is transported more quickly from hot regions, such as in hot bottom burning or shell C-burning, into cooler regions which avoids its decay via the thermally populated isomeric state ^{26}Al^m. Rotation also mixes neutron-rich material and leads to an enlargement of convective regions in which C/Ne-burning produces ^{60}Fe and therefore also enhances the yield of this isotope. The increased lifetime of rotating models is due to enlarged stellar cores as a conse-

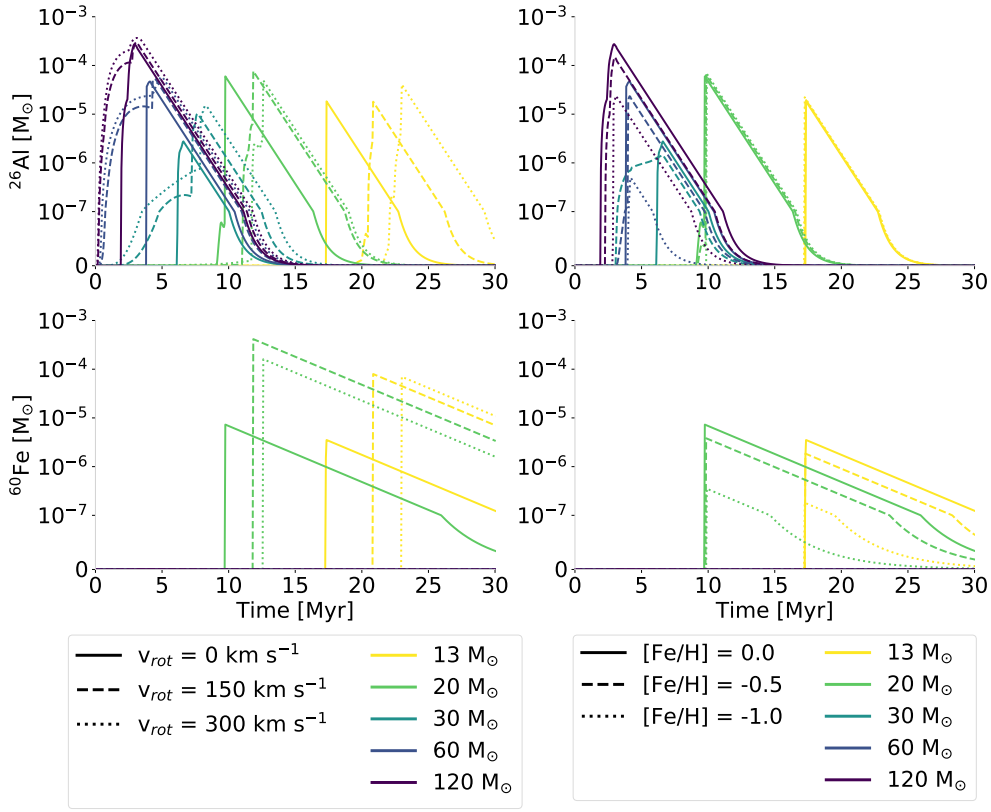

Figure 2.32: Rotation (*left*) and metallicity (*right*) effects on ^{26}Al (*upper*) and ^{60}Fe (*lower*) ejection time profiles in LC18. In the *left* panels only models with Solar metallicity are shown. In the *right* panels evolution models of non rotating stars are compared. Colours denote different initial stellar masses.

quence of rotation. With a constant core mass, this slows down the nuclear burning processes. The dependence on the mass-loss rate on rotational velocity $v_{\rm rot}$ follows the relation (Langer 1998; Heger & Langer 1998)

$$\dot{M}(v_{\rm rot}) = \dot{M}_0 \left(1 - \frac{v_{\rm rot}}{v_{\rm crit}}\right)^{-0.43}, \tag{2.40}$$

where $\dot{M}_0$ is the mass-loss rate at $v_{\rm rot} = 0\,{\rm km\,s^{-1}}$ and the critical velocity $v_{\rm crit} = \sqrt{(GM)/R}$. From this it can be seen that higher $v_{\rm rot}$ also results in a higher mass-loss rate $\dot{M}$. Thus, the wind component is enhanced in faster spinning models due to increased centrifugal forces. A more extensive grid of nucleosynthesis feedback profiles for different metallicities and rotational velocities can be found in Fig. A.1 for ^{26}Al and in Fig. A.2 for ^{60}Fein the appendix.

In the models considered so far, only isolated single stars were discussed. In Sec. 2.2.4, it has already been mentioned that another property, that may enhance the stellar wind, is a potential interaction with a companion. This is currently a highly debated uncertainty factor with respect to nucleosynthesis contributions (Isern et al. 2018). Thus, the ^{26}Al ejection from binary systems was addressed only recently in binary model calculations by Brinkman et al. (2019) (B+19) using Modules for Experiments in Stellar Astrophysics (MESA). With this one-dimensional stellar evolution code, the authors compute the effect of binary mass transfer on ^{26}Al wind yields in non-rotating models in the mass range $10\,{\rm M}_\odot \leq M_{\rm ZAMS} \leq 80\,{\rm M}_\odot$ with Solar metallicity $Z = 0.014$. In addition to initial mass, metallicity, and rotation, also the mass ratio q as well as the orbital period p are important parameters for stellar evolution

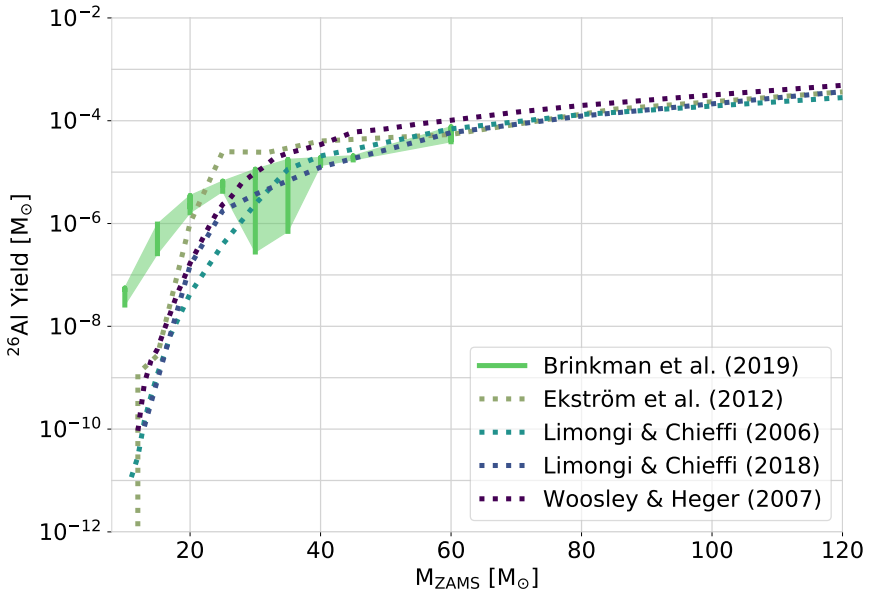

Figure 2.33: ^{26}Al wind yields with the green regions indicating enhanced wind yields due to binary interactions by Brinkman et al. (2019). Dotted lines denote single star models. The vertical green lines span between models with identical initial mass but different orbital periods ranging from a few days up to ~ 100 days. Generally, models with shorter periods, i.e. closer separation, show more mass-loss and lie at the upper boundary of the green region. The binary models include non-rotating stars with mass ratio $q = 0.9$ and a mass-loss efficiency of $\beta = 1$.

in binary systems. In order to limit the parameter space to a calculable size, the authors have fixed q to a value of 0.9 in all their models. The nuclear network contains all relevant reaction rates in the context of ^{26}Al production as well as destruction based on Angulo et al. (1999). According to Kepler's third law, the orbital period p of the stars is proportional to their separation, which determines the strength of gravitational interaction. This in turn affects convection and mixing inside the star as well as the mass exchange between the companions. This is taken into account in MESA following the mass-loss scheme by Schootemeijer & Langer (2018). The yield calculations were done for a set of orbital periods between a few days and up to ~ 100 days in a semi-numerical approach by entirely stripping the star of its envelope in the case of Roche-lobe overflow (cf. Eq. 2.28). The fraction of overflowing material that is accreted by the companion is described by the mass-loss efficiency β. In order to constrain an upper limit for the effect on ^{26}Al feedback $\beta = 1$ had been chosen by the authors, i.e. fully non-conservative mass transfer with all the mass overflowing the Roche-lobe being ejected from the system. The corresponding ^{26}Al wind yields are shown in Fig. 2.33 in comparison to single star wind yield calculations. It can be seen that especially in stars with masses $M_{\mathrm{ZAMS}} \leq 20\,\mathrm{M}_\odot$ show enhanced wind contribution in ^{26}Al compared to single star models by up to a factor of ~ 100. For more massive stars the binary interaction seems to have basically no effect on the wind yields. The green region in Fig. 2.33 gives an upper limit of this effect on nucleosynthesis feedback because observations indicate that actual mass-transfer efficiencies are below one, i.e. some mass fraction ~ 0.2 is accreted by the companion and therefore stays in the system (Pols et al. 1991; de Mink et al. 2007; Schootemeijer & Langer 2018). Also the mass removed from the primary will be usually lower than in the semi-numerical approach of an entirely stripped envelope. A discussion of the global effects of binary interactions on nucleosynthesis feedback on the level of massive star groups will be given in Sec. 4.2.2 on the basis of the

yield calculations by Brinkman et al. (2019).

Essentials

Massive stars are the main agents driving galactic chemical enrichment. Their thermal and kinetic feedback is mainly due to UV radiation, stellar winds, and SNe. Their nucleosynthesis feedback can be traced by radioactive isotopes, such as ^{26}Al and ^{60}Fe. The former is produced in massive stars in hydrostatic core H-burning, convective shell C-burning, and explosive Ne/C-burning and it is ejected via stellar winds and SNe. The latter is produced in massive stars in convective shell C/Ne-burning and ejected only in SN outflows.

- How does massive star nucleosynthesis affect larger scales?
  ⟶ Ch. 4
- How can stellar model yields be tested observationally?
  ⟶ Sec. 4.1
- What is the global effect of binary interaction to nucleosynthesis feedback?
  ⟶ Sec. 4.2.2
- Can individual sources of nucleosynthesis be observed directly?
  ⟶ Sec. 5.2

2.3 Massive Star Groups

It was discovered quite early on in modern astrophysics that massive stars in the Milky Way are not randomly distributed but accumulated in larger aggregations of stars (Kapteyn 1914). Due to their hierarchical formation process from GMCs outlined in Sec. 2.2.1, stars emerge in groups embedded in molecular clouds (McKee & Williams 1997; Lada & Lada 2003; Portegies Zwart et al. 2010). Such assemblies of physically related stars make coherent units of cumulative feedback in the Galaxy and therefore constitute the conceptual nexus between single star feedback and galactic evolution. In this thesis, stellar groups are of particular interest because they frame the highly complex process of nucleosynthesis feedback.

2.3.1 Clusters and Associations

The general condition for individual stars to constitute a stellar group is to be physically related. This can be specified by the conceptual subdivision into clusters and associations. Classifications of clusters, associations, and respective subgroups are manifold in literature, however not fully canonical. The definitions adopted in this thesis are summarised in Tab. 2.6 and mostly follow Lada & Lada (2003).
In the context of stellar feedback, star groups containing young and massive stars are of particular relevance. The following explanations will focus mainly on embedded clusters, young massive clusters, and OB associations.

Table 2.6: Classifications of different types of star groups. (Kholopov 1959; van den Bergh 1966; Lada & Lada 2003; Böker et al. 2004; Portegies Zwart et al. 2010; Gratton et al. 2019)

Class	Sub-class	Physical Characteristics
Cluster		Stable against tidal disruption, $\rho_* \geq 1.0\,\mathrm{M_\odot/pc^{-3}}$
	Embedded	Partially or fully embedded in GMCs, youngest groups
	Exposed	Little or no ISM gas within the boundaries
	Bound	Negative total kinetic and potential energy
	Unbound	Positive total kinetic and potential energy
	Open	Bound, exposed, mass $\lesssim 10^3\,\mathrm{M_\odot}$, in Galactic disk
	Young Massive	Age $\lesssim 100\,\mathrm{Myr}$, mass $\gtrsim 10^4\,\mathrm{M_\odot}$
	Nuclear	Age $\leq 300\,\mathrm{Myr}$, mass 10^5–$10^6\,\mathrm{M_\odot}$, in Galactic centre
	Globular	Age $\gtrsim 10\,\mathrm{Gyr}$, mass $\gtrsim 10^3\,\mathrm{M_\odot}$, size 3–5 pc, in Galactic halo
Association		Unstable against tidal disruption, $\rho_* < 1.0\,\mathrm{M_\odot/pc^{-3}}$
	OB	Age $\lesssim 50\,\mathrm{Myr}$, high density of O- and B-type stars
	T	Age $\lesssim 10\,\mathrm{Myr}$, high density of T Tauri stars
	R	Associated with reflection nebula

Star groups preferentially form in gas that is shocked when entering a spiral arm (Roberts 1969). This means that their distribution is linked to larger-scale dynamics and is key to understanding the Galactic structure. This is an important aspect, that will be carried on especially in Sec. 2.4.4 and Sec. 4.3. During their earliest evolutionary phase, all stellar groups emerge as embedded clusters. In this stage, the stellar aggregation is still fully or at least partially embedded in the cloud where the star formation event occurs. These objects form with a rate of about 2–$4\,\mathrm{Myr^{-1}\,kpc^{-2}}$, which implies a SFR inside each cluster of $\sim 3\times10^3\,\mathrm{M_\odot\,Myr^{-1}\,kpc^{-2}}$. Observationally, it is difficult to constrain the radii of stellar clusters. In general, massive star clusters are approximately spherically symmetric and a typical measure of their extent is the virial radius (Lada & Lada 2003; Krumholz et al. 2019)

$$R_{\mathrm{vir}} = \frac{GM_{\mathrm{cl}}^2}{2|U|}, \tag{2.41}$$

where M_{cl} is the entire cluster mass with the total potential energy $U = -M_{\mathrm{cl}}\langle v^2\rangle$ according to the virial theorem. This radius encloses about 80% of the total luminosity (Plummer 1911) and will be adopted as measure of the spatial extent of star groups throughout this thesis.

Embedded clusters form with an initial radial extent between 0.5–5 pc (Pfalzner 2009). Since these are the youngest groups of stars, they are expected to encompass a relatively high number of young and also massive stars. Overall, $\sim$ 96% of all O-type stars form inside a cluster (Portegies Zwart et al. 2010). Thus, massive star feedback is strongly coupled to star group environments. In each star group, usually around five star formation episodes happen over $\sim 20\,\mathrm{Myr}$ (Blaauw 1964; McKee & Williams 1997). This reflects the substructure inherited from the birth cloud and an intrinsically fractal structure of star groups emerges. However, their dynamical evolution tends to a smoother and concentric sub-structure (Daffern-Powell & Parker 2020). The main physical parameters that determine the further evolution of a stellar group as cluster or association are the velocity dispersion, the gas fraction, and the timescale on which stellar feedback removes interstellar gas from the group (Verschueren & David 1989; Brown et al. 1999). If the total kinetic and potential energy is negative, the aggregation is bound by its own gravity. If the kinetic energy is larger than the potential energy, the cluster is unbound and evolves into a loose stellar asso-

ciation. About 90% of all star clusters dissolve within $\sim 10\,\mathrm{Myr}$ after their formation due to gas removal during the formation process (Whitmore et al. 2007; Fall et al. 2005). Overall, associations have stellar densities of $\rho_* < 1.0\,\mathrm{M}_\odot\,\mathrm{pc}^{-3}$, which is too low to gravitationally cohere its members against galactic tidal forces (Bok 1934). Clusters on the other hand can sustain their structure against such forces due to a higher density $\rho_* \geq 1.0\,\mathrm{M}_\odot\,\mathrm{pc}^{-3}$. Although associations and unbound clusters disperse over time, $70\% - 80\%$ of all O stars reside still in the stellar groups which they were born in (Gies 1987; Neugent & Massey 2011). This means, the dispersal time is longer than the lifetime of massive stars and massive star feedback is closely linked to the host group. The more intense this feedback is, the faster the remaining interstellar gas content will be evaporated and removed from the group, making it an exposed or open cluster. For the Galactic census of open clusters, current estimates include a total number of about 23,000–37,000 with an average age of $\sim 250\,\mathrm{Myr}$ (Piskunov et al. 2006). After the removal of interstellar gas, it takes on the order of $\sim 100\,\mathrm{Myr}$ for mass loss and large scale tidal shocks to disperse the cluster. Only $\sim 10\%$ of groups can sustain their aggregation as open clusters (Krumholz et al. 2019). The cumulative effect of stellar feedback mechanisms described in Sec. 2.2.5 induces gas removal from the cluster as well as its dissipation. This drives the evolution of the remaining 90% to loose associations. The mechanism that is mainly causing the dispersal of the group varies with its total mass. In the smallest clusters with masses $M_\mathrm{cl} \lesssim 100\,\mathrm{M}_\odot$, protostellar outflows mainly drive the overall relevant feedback since more massive stars with stronger feedback mechanisms are mostly absent. In more massive clusters with $M_\mathrm{cl} \leq 10^4\,\mathrm{M}_\odot$, photoionisation dominates stellar feedback effects. This happens because the thermal pressure of photoionised gas exceeds the radiative pressure and it sets in instantaneously, unlike stellar winds or SNe. The more massive a stellar group gets, the more important the latter mechanisms become. Only the most massive clusters with $M_\mathrm{cl} \sim 10^5\,\mathrm{M}_\odot$ have a deep enough gravitational potential to persist beyond the cumulative effect of multiple SNe (Krumholz et al. 2019). Once stars have escaped the sphere of influence of their original group they are classified as field stars.

OB associations The term OB association was coined by Ambartsumian (1949) and later refined by Blaauw (1964) as a gravitationally unbound group of stars with an enhanced density of O-type stars (cf. Tab. 2.1). This distinguishes OB associations from T and R associations. The former have a high density of young and less massive T Tauri stars and the latter give rise to prominent reflection nebulae (Kholopov 1959; van den Bergh 1966). Because of their large number of massive stars, OB associations constitute a particularly relevant class of star groups with respect to stellar feedback. Since OB associations are also quite young with an age of about 50 Myr, they are generally located near molecular clouds, which makes them especially intriguing laboratories of ongoing chemical enrichment processes in the Galaxy (Brown et al. 1999). In about 90% of the observed cases, their spatial extent ranges from 5–100 pc, with the remaining 10% extending up to 500 pc (Blaha & Humphreys 1989; Brown et al. 1999). Their median stellar mass is $9 \times 10^3\,\mathrm{M}_\odot$ (Melnik & Dambis 2017a). It is important to note that despite the nomenclature focussing on their O- and B-type members, OB associations contain the entire range of masses, formed according to the IMF. Especially the distribution of the large number of lower mass stars in OB associations shows that they are also hierarchically structured in subgroups. These substructures have a typical age spread on the

order of $\sim 10\,\mathrm{Myr}$ (Briceño et al. 2007). This is lower than the average age spread of clusters, which indicates that the feedback driving the development of a cluster into an unbound association generally also tends to suppress star formation. The vast majority of massive stars are found in OB associations (Miller & Scalo 1978; Briceño et al. 2007). This is the case because the strong massive star feedback is causing quick gas removal from embedded clusters as well as their dispersal. Therefore, also the internal velocity dispersion is $\sim 3\,\mathrm{km\,s^{-1}}$ or $3\,\mathrm{pc\,Myr^{-1}}$ (de Zeeuw et al. 1999), which is rather high compared to bound clusters. Nevertheless, this means that even the longest-lived massive stars with $M_* \sim 8\,\mathrm{M_\odot}$ travel during their main-sequence lifetime of $\sim 35\,\mathrm{Myr}$ a maximum of about $100\,\mathrm{pc}$ from their site of origin. This is not far enough to escape the birth association. Thus, ccSNe occur within a $100\,\mathrm{pc}$ radius inside associations (Higdon & Lingenfelter 2013). The expansion velocity of OB associations is typically $v_{\mathrm{exp}} \approx 6\,\mathrm{km\,s^{-1}}$(Melnik & Dambis 2017a). This means that a kinematic age can be assigned according to their size, which will be used in Sec. 4.2 for spatial modelling of star groups.

2.3.2 Embedded Cluster Mass Function

In Sec. 2.2.1 star formation was described as hierarchically proceeding collapse of GMCs with clumps being the progenitors of clusters (McKee & Ostriker 2007). Thus, star groups generally originate as embedded clusters. For these, an embedded cluster mass function (ECMF) can be formulated to describe the probability distribution function for their formation in a particular mass regime (Lada & Lada 2003; Kroupa & Boily 2002; Kroupa & Weidner 2003; Weidner & Kroupa 2005); this is similar to the initial core mass function (CMF) for pre-stellar cores or the IMF for individual stars. For similar reasons as already discussed with respect to the IMF (cf. Sec. 2.2.1), this can only be inferred from an observational necessarily under-determined basis. In this respect, the argument by Kroupa & Weidner (2003) for the determination of the ECMF is adopted in the following.
Looking a galaxy as a whole, the entire stellar content reflects all star formation processes that took place separately in the individual clusters formed in one consistent epoch. This can be formulated as the integrated galactic initial mass function (IGIMF) of single stars. The star-formation process in each cluster in turn follows the IMF. This means, these are related via (Kroupa & Weidner 2003)

$$\xi_{\mathrm{IG}}(M_*) = \int_{M_{\mathrm{EC,\,min}}}^{M_{\mathrm{EC,\,max}}} \xi(M_* \leq M_{*,\,\mathrm{max}})\ \xi_{\mathrm{EC}}(M_{\mathrm{EC}})\ dM_{\mathrm{EC}}, \tag{2.42}$$

where ξ is IMF for single stars with mass M_*, ξ_{EC} is the ECMF for clusters with mass M_{EC}, and ξ_{IG} is the IGIMF.
Now the argumentation branches off according to two conceptual premises. One ansatz is that star formation is an inherently stochastic process sampling the IMF and therefore entirely probabilistic (Approach A, according to Kroupa et al. 2013, 124). A second ansatz is that star formation is in fact a self-regulatory process which produces overall deterministically a mass distribution following the IMF as outcome (Approach B, according Kroupa et al. 2013, 124–125). Following Approach A, the IGIMF and the IMF would be identical, because stochastic processes do not influence each other and temporal or spatial groupings or other boundary condi-

tions have no effect on the global result; Following Approach B, the IGIMF can be different from the IMF, because varying boundary conditions in individual clusters favour the IMF in restricted mass ranges.
The stellar feedback described in Sec. 2.2.5 and its larger scale effect on star formation mentioned in Sec. 2.3.1 indicate that star formation is a self-regulatory process rather than purely stochastic. In star groups, gas dispersion, gas removal as well as star-formation efficiency seems to vary particularly with the total mass. Furthermore, it seems plausible that a large number of small star forming regions produces in total fewer massive stars than a single massive cluster with the same total mass in one large star formation event. This becomes clear when star formation events with a small total mass of e.g. up to $\sim 100\,\mathrm{M}_\odot$ are assumed. No higher stellar mass could form. Overall, this thought experiment also underlines the importance of the correct subdivision of star formation events. In addition to such a logical lower limit, there are also strong indications for an observational upper mass limit of $\sim 150\,\mathrm{M}_\odot$ for a single star (Weidner & Kroupa 2004; Figer 2005; Oey & Clarke 2005; Koen 2006; Maíz-Apellániz et al. 2007). The mass of the most massive star $M_{*,\,\mathrm{max}}$ formed in an individual region appears to vary with the total cluster mass M_{EC}. The relation can be approximated by

$$\log(M_{*,\,\mathrm{max}}) = 2.56\log(M_{\mathrm{EC}})\left\{3.821^{\lambda} + [\log(M_{\mathrm{EC}})]^{\lambda}\right\}^{-\frac{1}{\lambda}} - 0.38, \tag{2.43}$$

with $\lambda = 9.17$ (Pflamm-Altenburg et al. 2007; Kroupa et al. 2013). Eq. 2.43 is shown graphically in the left panel in Fig. 2.34. This relation again emphasises a linkage

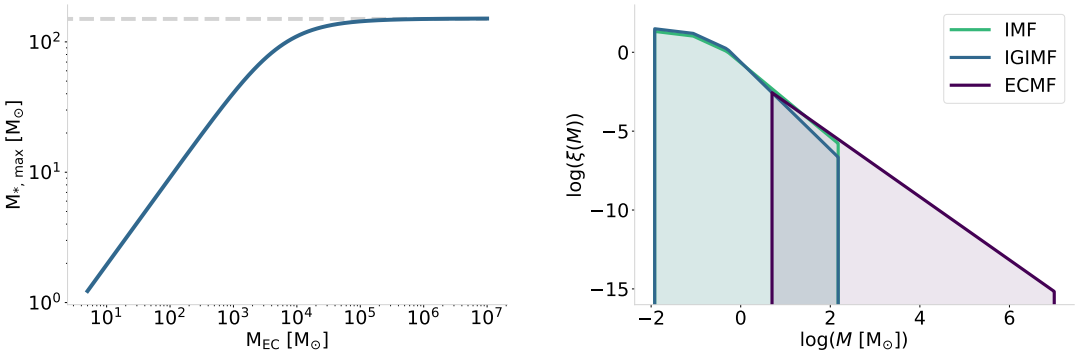

Figure 2.34: *Left:* Mass of the most massive star formed within a cluster with total mass of $5\,\mathrm{M}_\odot \leq M_{\mathrm{EC}} \leq 10^7\,\mathrm{M}_\odot$ according to Eq. 2.43. The dashed grey line indicates the overall physical mass limit for single stars of $150\,\mathrm{M}_\odot$ (following Pflamm-Altenburg et al. 2007). *Right:* Probability distributions for the formation of single stars determined as initial mass function (IMF) or integrated galactic initial mass function (IGIMF), and for star groups, i.e. embedded cluster mass function (ECMF). The x-axis refers to the initial mass of the respective object class and the functions are given in Eq. 2.5, Eq. 2.42, and Eq. 2.44 respectively. All functions are normalised to one. The power-law exponents above $1\,\mathrm{M}_\odot$ are $\alpha_{\mathrm{IMF}} = 2.35$, $\alpha_{\mathrm{IGIMF}} = 2.77$, and $\alpha_{\mathrm{ECMF}} = 2$.

between the cluster mass and a self-regulated star formation process. This is also in line with the finding in Sec. 2.2.5 that the most massive star dominates the instantaneous radiative feedback. It implies that if a star forms above a certain mass limit the radiative feedback disperses the birth cloud an therefore suppresses higher mass star formation. Finally, it was found observationally that the IGIMF in fact shows a different slope than the IMF and varies with SFR and metallicity (Kroupa & Weidner 2003; Weidner & Kroupa 2005; Pflamm-Altenburg & Kroupa 2008; Weidner et al. 2013; Yan et al. 2017; Jerabkova et al. 2018). All the above-mentioned indications therefore support Approach B of a self-regulatory star formation pro-

cess. Thus, the remaining argumentation in this thesis follows this ansatz. This will be of particular importance for the application of the optimal sampling approach in Sec. 4.2.1 in order to calculate the global ejecta of ^{26}Al and ^{60}Fe from stellar associations.
Because during their initial phase star groups are embedded in a dense cloud environment, the ECMF is observationally possibly even more biased than the IMF. Thus, it is generally inferred from the galaxy-wide IGIMF (cf. Eq. 2.42). The IGIMF in the Milky Way is found to follow the standard IMF in the low-mass regime with a steeper decrease with $\alpha_{\mathrm{IGIMF}} = 2.77$ above $1\,\mathrm{M}_\odot$ (Kroupa & Weidner 2003; Weidner & Kroupa 2005). Both, the IMF and IGIMF, are determined on the basis of observations. The ECMF derived according to Eq. 2.42 follows approximately a power law (Krumholz et al. 2019)

$$\xi_{\mathrm{EC}}(M_{\mathrm{EC}}) = \frac{dN_{\mathrm{EC}}}{dM_{\mathrm{EC}}} \propto M_{\mathrm{EC}}^{-\alpha_{\mathrm{ECMF}}}, \tag{2.44}$$

with $\alpha_{\mathrm{ECMF}} = 2$ in the Milky Way (Lada & Lada 2003; Kroupa et al. 2013; Krumholz et al. 2019). This exponent is found to change with metallicity and SFR and varies in extragalactic observations in the range $1.6 \lesssim \alpha_{\mathrm{ECMF}} \lesssim 2.5$ (Schulz et al. 2015, and references therein). A synopsis of the three mass functions is shown in the right panel in Fig. 2.34. The ECMF covers a wide mass range from the smallest coherent and isolated star formation events with mass $M_{\mathrm{EC,\,min}} = 5\,\mathrm{M}_\odot$, up to the most massive plausible clusters with $M_{\mathrm{EC,\,max}} = 10^7\,\mathrm{M}_\odot$ (Pflamm-Altenburg et al. 2013; Schulz et al. 2015; Yan et al. 2017). A larger number of lower-mass clusters systematically under-produces massive stars according to the $M_{*,\,\mathrm{max}}$ relation (Eq. 2.43). In other words, because massive star groups are rarer, the integrated census of massive stars in the Milky Way is also smaller than predicted by a fully stochastic star formation process following the IMF globally. This convolution results in the steeper slope of the ECMF.
It is important to stress that the ECMF is more then only a distribution function of star groups, which go through their entire evolution exclusively as bound embedded clusters. The nomenclature refers to the fact that basically all star groups form in an embedded cluster stage, regardless of their later evolution. This means that the ECMF generally describes the mass distribution of correlated star formation events, which take place spatially within a few pc and temporally on the order of a few Myr (Kroupa et al. 2013, 126, 226). It therefore encompasses the formation of star groups in general, which explicitly also encompasses those which evolve e.g. as open clusters or OB associations.

2.3.3 Superbubbles

In star groups, the radiative, kinetic, and thermal feedback mechanisms from the individual members cumulatively shapes the ISM on a galactic scale. In Sec. 2.2.5, the main contributions were ascribed to stellar winds, UV radiation, and SNe, all of which tend to affect the surroundings isotropically and give rise to spherical structures such as H II regions or wind-blown cavities (cf. Fig. 2.24 and Fig. 2.25 respectively). Since stellar groups are spatially centred, their cumulative feedback has plausibly an isotropic effect, producing bubble-like structures of similar type on

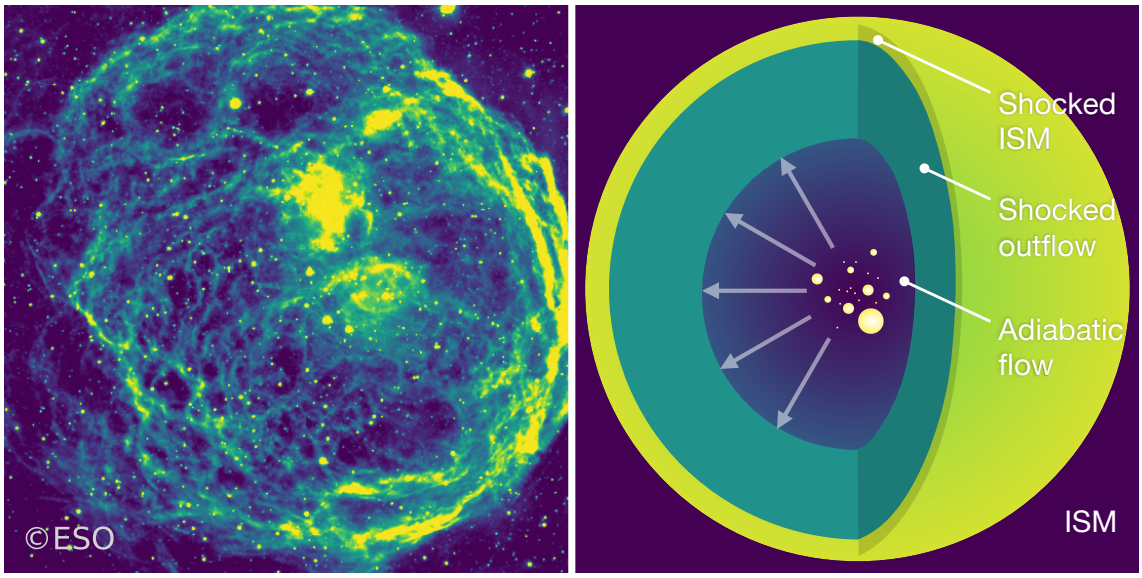

Figure 2.35: *Left:* Optical to near-IR image of the N 70 superbubble in the LMC (Copyright: European Southern Observatory (ESO); https://www.eso.org/public/images/eso9948d/, retrieved March 16, 2020). *Right:* Schematic structure of a superbubble. Adopted as described by Kavanagh (2020) following Weaver et al. (1977).

larger scales. An example is shown in the left panel in Fig. 2.35. Such superbubbles have typically sizes of a few 100 pc and evolve through three phases. This was described in a pioneering paper by Weaver et al. (1977). In the first phase, it is expanding in an adiabatic flow because it is growing so quickly that radiative cooling is too slow to effectively cool the system. Surrounding gas is swept up by this flow which causes a thin shell of interstellar gas to emerge in the second phase. In the third phase, the outer regions of the superbubble are finally significantly slowed down due to radiative losses. A sketch of the emerging superbubble structure is shown in the right panel of Fig. 2.35. Temporally, the evolution goes from a radiation dominated stage via stellar wind dominance to a predominantly SN-driven feedback stage. The radiation pressure is considered to be a main mechanism causing the disruption of massive molecular clouds (Scoville et al. 2001; Fall et al. 2010). Even if SNe are taken into account, radiation pressure may dominate the momentum input in dense clusters especially at the early stages during or short after the majority of star formation occurs (Murray et al. 2010). Since a lot of the ionising radiation is escaping a large part of the galactic ISM beyond molecular clouds gets ionised. The non-ionising photons that are escaping are important for heating the rest of the ISM (Kim et al. 2019). When SN blast waves propagate radially from about the centre through superbubbles, the interior gas is heated to a $\sim 10^6$–10^7 K. The surrounding shell mostly consists of $\sim$ 100 K cool H I or H_2 and the interior is phiotoionised during the first $\sim$ 10 Myr. Under idealised assumptions the outer radius of the superbubble (Weaver et al. 1977; Kavanagh 2020),

$$R_s(t) = \left[\left(\frac{250}{308\pi}\right)\frac{L_\mathrm{W}}{\rho_0}\right]^{\frac{1}{5}} t^{\frac{3}{5}}, \tag{2.45}$$

expands spherically with time as a function of the mechanical luminosity L_W and the density of the surrounding ISM. With an average density of $\rho_0 = 1\,\mathrm{cm}^{-3}$, corresponds to a velocity of typically $\sim 10\,\mathrm{km\,s}^{-1}$(McKee & Ostriker 2007).
A distinct observational signatures of superbubbles are N II far-IR lines (Higdon &

Lingenfelter 2013). These lines are emitted from the shells around ionised superbubbles. Since the bubble interior mostly consists of ionised hydrogen, it can be observed via the H_α Balmer line at 656 nm. In Fig. 2.36, an all-sky map of these H II regions in the Milky Way is shown. The clumpy bubble structure is clearly

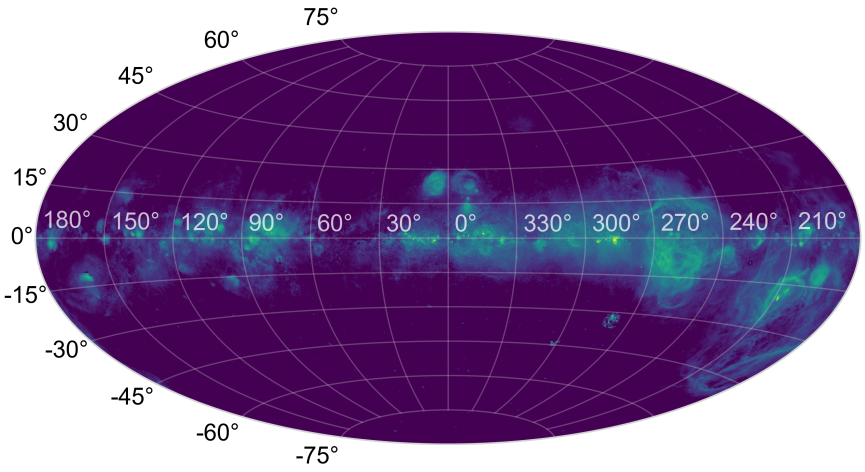

Figure 2.36: H_α all-sky map at 656 nm. The clumpy and bubble-like structure along the Galactic plane shows ionised H II gas around star forming regions.

visible along the Galactic plane. Prominent regions are e.g. the Cygnus OB associations around $(l, b) = (80°, 1°)$, the Scorpius-Centaurus star forming region around $(l, b) = (351, 19)°$, or Barnard's loop in the Orion Molecular Cloud Complex around $(l, b) = (208°, -13°)$. This all-sky map traces the spatial and temporal clustering of star formation regions, OB stars, and subsequent SNe (Higdon & Lingenfelter 2005). Such regions are preferentially formed along the spiral arms, which increase the density of the ISM and cause turbulences when sweeping through the Galactic plane. Melnik & Dambis (2017a) found that the average velocity of OB associations deviates from the overall Galactic motion by 7.2–7.5 $\mathrm{km\,s^{-1}}$. In general, high-mass star forming regions have the tendency to preferentially move towards the Galactic centre. This effect contributes with $\sim 5\,\mathrm{km\,s^{-1}}$ and skews the overall rotation curve of the Milky Way accordingly (Reid et al. 2019). This is because massive star formation occurs in gas that is shocked when it enters the spiral arm at a rather low pitch angle (Roberts 1969).

As a superbubble expands, it accumulates a large amount of neutral H I gas in a large shell surrounding the hot and mostly ionised interior. This gives rise to large H I shells that can be traced by the 21 cm hyperfine structure line emitted due to a spin-flip in neutral hydrogen (e.g. Dickey & Lockman 1990; Hartmann & Burton 1997). A superbubble is defined as combination of such a shell and the ionised interior within which an energy of $E_{\mathrm{SB}} \geq 10^{52}\,\mathrm{erg}$ have been injected due to stellar feedback. These shells reach up to 1.2 kpc in radius and $2 \times 10^7\,\mathrm{M_\odot}$ in mass (Heiles 1979). An all-sky map of the H I emission is depicted in Fig. 2.37. These huge shells are radiatively cooling and decelerating. Recent hydrodynamic simulations of SN- and wind-driven superbubbles show that under more realistic circumstances, cooling, cloud anisotropy, different feedback mechanisms, magnetic fields, or blowouts lead to more complex bubble dynamics (Krause et al. 2013; Krause & Diehl 2014; Krause et al. 2014; Kim et al. 2019; El-Badry et al. 2019; Kavanagh 2020). The efficiency of energy retained in the surrounding ISM per feedback source is usually of the order of 10%. Simulations suggest that the most effective energy injection

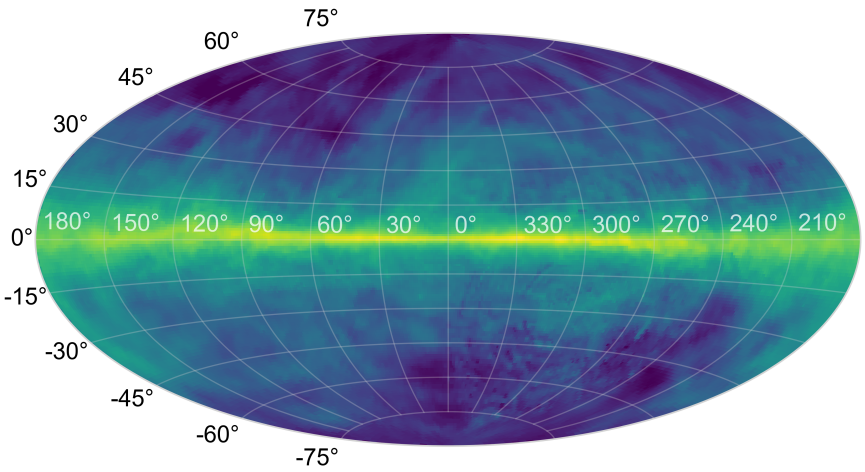

Figure 2.37: HI all-sky map at 21 cm. The hyperfine structure line traces neutral hydrogen swept up in huge arcs and shells surrounding expanding superbubbles.

is due to continuous wind rather than the SN blast wave and it drops significantly after the injection of the first SN in a bubble (Krause et al. 2013). This means that the wind-dominated phase until the first SN is generally decisive for the evolution of a superbubble. At later stages, the cooling mechanisms cause Vishniac instabilities to emerge in the dense hydrogen gas (Vishniac 1983). This leads to clumping of the shell and possibly induces further star formation. In such a picture of triggered star formation, the subsequent generation of stars inherits spatial, kinetic and chemical properties directly from the preceding generation (e.g. Heitsch et al. 2008; Micic et al. 2013; Gong & Ostriker 2015; Krause et al. 2018). Such a feedback dynamic is therefore mainly mediated on the scale of star groups and superbubbles. The timescale on which it takes place is determined by the typical crossing-time of material in these regions, which is $\sim 1\,\mathrm{Myr}$ (Lada & Lada 2003). This is of particular importance for the further argumentation in this thesis because it can be directly associated with the lifetimes of ^{26}Al and ^{60}Fe. Thus, their decay radiation is closely related to the feedback dynamics of star groups. This means that these radioisotopes are unique tracers of nucleosynthesis feedback from star groups and the dynamics of chemical inheritance between stellar generations.

2.3.4 Nearby OB Associations

Blaha & Humphreys (1989) created a catalogue of 91 nearby OB associations within 3.5 kpc around the Sun. Their dynamical properties as well as their partition into associations have been recently updated by Melnik & Dambis (2017a,b). This catalogue is shown in Fig. 2.38. Since these associations are apparently seen in an inclined ring structure around the Sun, they are also called Gould Belt associations. However, recent studies with *Gaia* indicate that this is solely due to a projection effect and does not correspond to an actual prominent physical alignment (Alves et al. 2020). In the following, the four most prominent regions with regard to their ^{26}Al content in the immediate vicinity of the Sun Scorpius-Centaurus, Orion, Cygnus, and Perseus are described in more detail Diehl et al. (2018a). Their position on the sky is shown in Fig. 2.39. As summarized in Tab. 2.7, ^{26}Al has already been detected for the first three which makes them intriguing laboratories of massive star

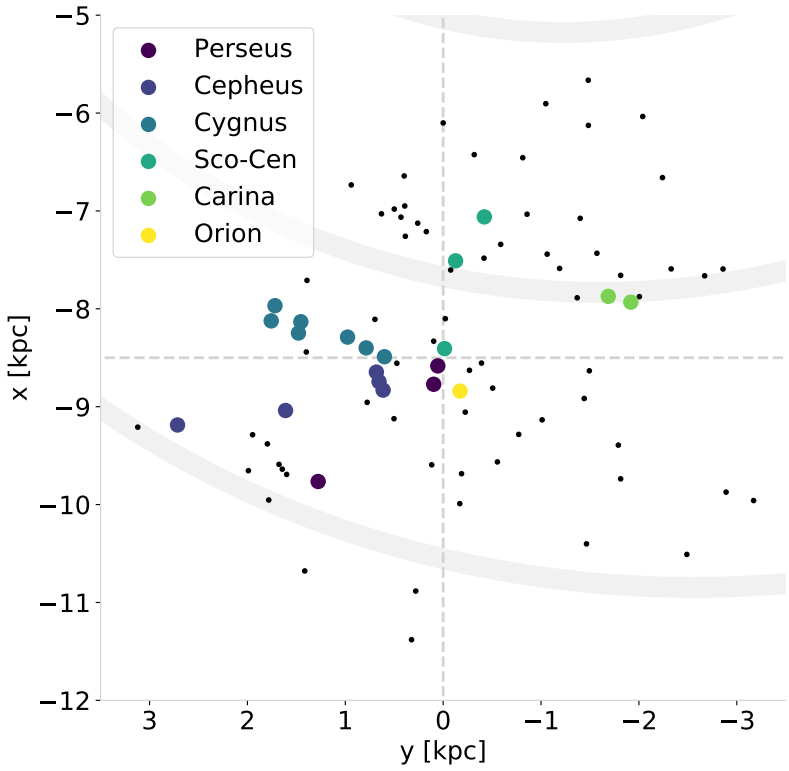

Figure 2.38: Spatial distribution of nearby OB associations within 3.5 kpc in the Galactic plane. Dots denote the positions of OB associations from the *Gaia* catalogue by Melnik & Dambis (2017b). Coloured dots indicate OB associations allocated to prominent massive star regions. The coordinate system is centred at the Galactic centre and the dashed lines define four quadrants around the position of the Sun. Spiral arm tangents are shown in thick grey lines (cf. Sec. 2.4.4).

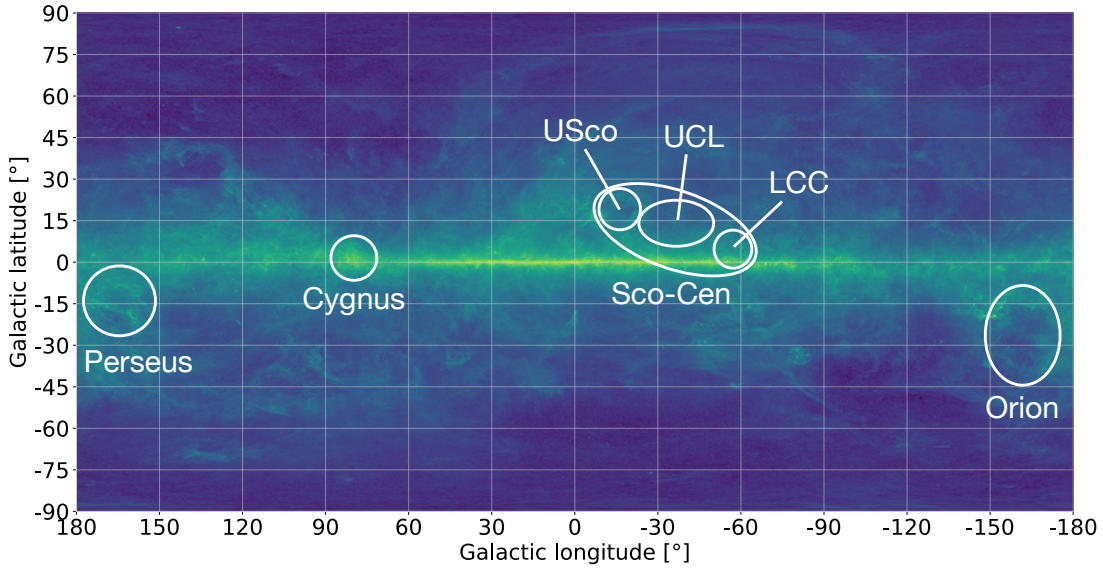

Figure 2.39: Most prominent nearby OB associations on top of a Planck 857 GHz all-sky dust map. For Sco-Cen its subdivision in the three subgroups Upper Scorpius (USco), Upper Centaurus Lupus (UCL), and Lower Centaurus Crux (LCC) is shown. The appearance as ring-like alignment is probably due to a projection effect (Alves et al. 2020).

Table 2.7: ^{26}Al in nearby OB associations measured with INTEGRAL/SPI by Siegert (2017, 173). The flux refers to the nuclear gamma-ray emission line at 1809 keV.

Region	Flux $[10^{-5}\,\mathrm{ph\,cm^{-2}\,s^{-1}}]$	^{26}Al mass $[\mathrm{M_\odot}]$	ΔE_0 [keV]	v_bulk $[\mathrm{km\,s^{-1}}]$
Cygnus	9.28 ± 1.75	154 ± 29	0.00 ± 0.19	0 ± 32
Sco-Cen	7.58 ± 1.43	1.3 ± 0.3	-0.93 ± 0.32	-154 ± 53
Orion	3.65 ± 1.19	5.0 ± 1.6	-0.53 ± 0.47	-88 ± 78

nucleosynthesis feedback.

Scorpius-Centaurus The closest OB association is Sco-Cen at ~ 140 pc from the Sun. It is composed of the three subgroups Upper Scorpius (USco), Upper Centaurus Lupus (UCL), and Lower Centaurus Crux (LCC) (de Zeeuw et al. 1999; Maíz-Apellániz 2001). These seem to correspond to a three-step cascade of triggered star formation with ages between 5 and 17 Myr (Preibisch & Zinnecker 1999; Krause et al. 2018). Star formation in this region stopped and the remaining gas has been accumulated in an H I shell with an angular diameter of about 90° on the sky (Pöppel et al. 2010). Since this superbubble has been shown to be bright in X-rays (Gaczkowski et al. 2015), it is likely that a SN has occurred about 1 Myr ago (Krause & Diehl 2014; Krause et al. 2014). This is in agreement with the fact that the 1.8 MeV line from ^{26}Al has been detected with INTEGRAL/SPI with a flux of $F_{^{26}\mathrm{Al}} = (7.58 \pm 1.43) \times 10^{-5}\,\mathrm{ph\,cm^{-2}\,s^{-1}}$ and an indication for a slight blue-shift (Diehl et al. 2010; Siegert 2017; Krause et al. 2018). This corresponds to an ^{26}Al mass of $\sim 1.3 \times 10^{-4}\,\mathrm{M_\odot}$ which implies feedback from a few massive stars. That is consistent with the estimation of the total initial mass of the entire Sco-Cen region of about $7 \times 10^3\,\mathrm{M_\odot}$ by Krause et al. (2018), with the subgroups USco and UCL both initially containing $2 \times 10^3\,\mathrm{M_\odot}$ and LCC having $3 \times 10^3\,\mathrm{M_\odot}$.

Orion The Orion Nebula is a molecular cloud complex comprising several star forming regions positioned at a distance of ~ 400 pc from the Sun (Menten et al. 2007; Kounkel et al. 2017). The embedded Orion Nebula Cluster is relatively young with an age of 1–2 Myr and a radius of 2.5 pc (Hillenbrand & Hartmann 1998; Da Rio et al. 2017). The cluster feedback contributes to the Orion-Eridanus superbubble structure, which is a large cavity filled with $(0.3\text{–}1.2) \times 10^6$ K hot plasma. It extends ~ 350 pc from the Orion molecular cloud towards the Sun and is sub-structured in several shells that have diameters between 150 and 250 pc. The spatial configuration is shown schematically in Fig. 2.40. Due to over-pressure of the plasma interior, the shells expand with velocities of about $20\,\mathrm{km\,s^{-1}}$(Joubaud et al. 2019). Star formation is still ongoing in this region, indicated by active stellar feedback and the presence of high mass runaway stars (Kroupa et al. 2018; McBride & Kounkel 2019). The dominant group in the Orion region in terms of massive star feedback is the Orion OB1 association composed of four subgroups with ages ≤ 12 Myr (Brown et al. 1994). From the currently present stellar census, Voss et al. (2009, 2010) inferred a number of ~ 550 stars to have formed initially in Orion OB1 with $M_* \geq 2\,\mathrm{M_\odot}$according to the IMF. As will be discussed in Sec. 2.3.5, this is an important estimate in order to model the nucleosynthesis feedback in this region via population synthesis calculations. A direct 1.8 MeV ^{26}Al signal of this feedback was measured with COMPTEL

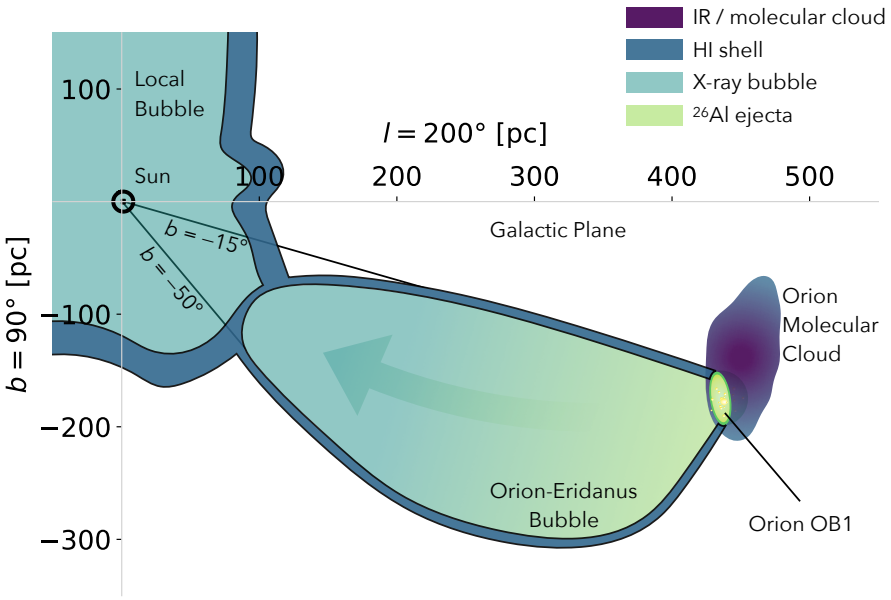

Figure 2.40: Schematic configuration of the Orion-Eridanus superbubble extending between the Orion Molecular Cloud and the Local Bubble. Massive star ejecta from Orion OB1 flowing in the direction away from the Sun are stopped quickly in the dense environment of the Orion Molecular Cloud. Material ejected towards the Sun streams freely into the Orion-Eridanus bubble. The velocity shift seen in ^{26}Al (cf. Tab. 2.7) is therefore dominated by this preferential motion towards the observer. Adopted from Burrows et al. (1993).

(Diehl 2002) and confirmed with high spectral resolution measurements by INTEGRAL/SPI with a line flux of $(3.65 \pm 1.19) \times 10^{-5}\,\mathrm{ph\,cm^{-2}\,s^{-1}}$ (Siegert & Diehl 2017; Siegert 2017). The freshly produced nuclei ejected from Orion OB1 predominantly streams from the association into the Orion-Eridanus cavity and towards the observer. Outflows in the opposite direction are stopped in the dense Orion molecular cloud (cf. Fig. 2.40). This scenario is supported by the fact that ^{26}Al is detected with a spatial offset to the OB association and that the emission line shows a slight blue-shift. This makes the Orion region an excellent touchstone of massive star feedback dynamics.

Cygnus The Cygnus region is composed of at least six OB associations, with Cygnus OB2 being the most prominent, that lie in the Galactic plane around $l = 80°$ and span distances between 0.7 and 2.5 kpc (Plüschke et al. 2002; Reipurth & Schneider 2008). Some of these associations are spatially and temporally related and therefore seem to originate from a similar triggered star formation process as described above for Sco-Cen (Knödlseder et al. 2002). Their ages range between 2.5 and 7.5 Myr and hence within the temporal scope that can be traced by ^{26}Al and ^{60}Fe. In fact, a very clear signal of the 1.8 MeV line with a significance of 10.9σ and an intensity of $(9.28 \pm 1.75) \times 10^{-5}\,\mathrm{ph\,cm^{-2}\,s^{-1}}$from the Cygnus region was measured with INTEGRAL/SPI (Martin et al. 2008, 2009; Siegert 2017). This corresponds to a total amount of $\sim 1.5 \times 10^{-2}\,\mathrm{M_\odot}$ of ^{26}Al. However, Martin et al. (2009) attribute only $\sim 3.9 \times 10^{-5}\,\mathrm{ph\,cm^{-2}\,s^{-1}}$ of the total flux to Cygnus with the rest interpreted as Galactic background. Nevertheless, this is overall consistent with the fact that Cygnus OB2 is an active region that hosts plenty of objects in all stages of massive star evolution, from dense clumps and cores (Cao et al. 2019) to a

variety of massive stars and binary systems (Comerón & Pasquali 2012; Bakış et al. 2014), and a young SN remnant of only 1–2 $\times$ 10^4 yr age (Hester et al. 1994; Blair et al. 2005; Fesen et al. 2018). The region is also associated with a superbubble that emerged over its star formation history of $\sim$ 10 Myr and emits bright in X-rays due to hydrodynamic shocks formed in massive star feedback (Cash et al. 1980; Rauw et al. 2015). Therefore, different ^{26}Al production phases have been probed potentially in the individual sub-populations of the Cygnus region (Plüschke 2001).

Perseus With a distance of about 300 pc and an age of $\sim$ 6 Myr (de Zeeuw et al. 1999), Perseus OB2 is the second closest OB association to the Sun and therefore an ideal candidate for the investigation of massive star nucleosynthesis feedback. It is roughly located at $(l, b) = (165°, -15°)$ with an angular diameter of about 30° and comprises a current census of about 2×10^4 stars in the mass range $0.1 \leq M_* \leq 70\,M_\odot$ (Belikov et al. 2002). These are collectively moving away from the Sun with a velocity of $23.4 \pm 3.9\,\mathrm{km\,s^{-1}}$ (de Zeeuw et al. 1999). At the distance of the association this corresponds to a superbubble of approximately 100 pc diameter seen in 21 cm H I emission to expand with a velocity of $\sim 10\,\mathrm{km\,s^{-1}}$ (Sancisi et al. 1974; Hartmann & Burton 1997). This is expected to show signatures of nucleosynthesis feedback. From COMPTEL observations Knödlseder (1997) estimated a gamma-ray flux of $(3.5 \pm 1.1) \times 10^{-5}\,\mathrm{ph\,cm^{-2}\,s^{-1}}$from a 6° region around the position of Perseus OB2. Bouchet et al. (2015) supported this finding by measurements with INTEGRAL/SPI obtaining a flux of $(5.0 \pm 2.7) \times 10^{-5}\,\mathrm{ph\,cm^{-2}\,s^{-1}}$in the same region around $(l, b) = (161°, -3°)$ with a radial extent of 5°. This was found connected to a larger emission site around $(l, b) = (149°, 8°)$ with a radius of about 11° and a flux of $(8.2 \pm 3.2) \times 10^{-5}\,\mathrm{ph\,cm^{-2}\,s^{-1}}$. In combination with an internal age spread between 1 and 6 Myr, this could be an indication for past triggered star formation events associated with the same parental molecular cloud and therefore a subdivision of the Perseus region into subgroups (Gutermuth et al. 2008; Belikov et al. 2002). In addition, since Perseus OB2 is far from Galactic bulge and little background is expected, this region will be investigated further in Sec. 4.2.2. It will also be utilised observationally as laboratory for probing the ^{26}Al content of massive star groups in Sec. 5.3.

2.3.5 Massive Star Population Synthesis

High-energy astrophysics often has to deal with measurements with comparably low spatial resolution on the order of a few degree. From unresolved systems, such as distant star groups or galaxies, only integrated signals can be observed. An essential tool for investigating the underlying physics of such unresolved systems is population synthesis, sometimes also called population modelling. This is based on the approach of relating the integrated signal of a composite system with the evolutionary properties of its constituents. This goes back to the the pioneering work of Tinsley (1968, 1972) who used a combination of spectral properties according to a stellar birth rate and stellar evolution tracks to infer evolutionary sequences of galaxies. Later, this principle was applied to the evolutionary synthesis of individual stellar populations (Tinsley & Gunn 1976; Tinsley 1980). A recent review of population synthesis methods and applications is given by Cerviño (2013).
The basic principle of a massive star population synthesis is the integration of time

profiles $\psi(M_*, t)$ of stellar properties over the entire mass range of single stars, weighted with the IMF,

$$\Psi(t) = A \int_{M_{*,\,\min}}^{M_{*,\,\max}} \psi(M_*, t)\ \xi(M_*)\ dM_*, \tag{2.46}$$

with the normalisation A according to the total mass of the population. Such a continuous population synthesis is strictly only valid for the limit of stellar populations composed of $N \to \infty$ members (Fouesneau & Lançon 2010; Piskunov et al. 2011). Particularly in small populations, stochastic processes can cause strong deviations from the average obtained by analytical integration over the IMF. In order to take this probabilistic effect into account, usually a discrete population synthesis by Monte Carlo (MC) sampling of the IMF is used (Cerviño & Luridiana 2006). Two currently public codes that are based on this approach are the Stochastically Light Up Galaxies package (SLUG) (da Silva et al. 2012) and the Massive Cluster Evolution and Analysis package (MASSCLEAN) (Popescu & Hanson 2009). In the context of this thesis, the population synthesis model by Voss et al. (2009) (PopSyn) is particularly noteworthy because it is actually specialised for modelling gamma-ray emission and nucleosynthesis feedback from nearby massive star groups. In this code, individual initial mass values for a certain number of stars are sampled according to the IMF by Salpeter (1955). According to this stochastically discretised initial mass distribution stellar evolution models are evaluated. This is done via linear interpolation of an input set of stellar evolution models, e.g. LC06. The resulting stellar profiles are accumulated to obtain the collective effect of the entire group. It can be used for the calculation of kinetic, radiative, and general mass output as well as for the estimation of particular isotopes such as ^{26}Al and ^{60}Fe. It is specifically designed to investigate nearby OB associations and their content of radioactive nucleosynthesis tracers. For this purpose it was successfully applied to model the ^{26}Al emission in the Orion region (Voss et al. 2010) as well as in the Cygnus region (Martin et al. 2010). In this case, the measure for the success of the modelling is the agreement with SPI measurements for the estimated age of the respective group including predictions for ^{60}Fe. This is a strong indication for the validity of both stellar evolution models as well as the population synthesis approach to studying nucleosynthesis feedback.
In Sec. 4.2.1 the optimal sampling population synthesis approach will be discussed. It is based on Approach B described in Sec. 2.3.2 (following Kroupa et al. 2013) and used in PSYCO. This can be understood as a mediating approach between continuous and discrete population synthesis, on the one hand taking into account the boundary conditions arising in small populations, and, on the other hand, avoiding large stochastic deviations from the general IMF shape. It is overall constructed as a refinement of PopSyn to synthesise populations with their total mass as physical input parameter instead of the number of members, and extended in this work to include finer time steps, spatial aspects on global scales, and different SFRs, metallicities, rotation velocities, and explodability models.

Essentials

The initial mass distribution of star groups is described by the ECMF. The cumulative effect of massive star feedback in stellar groups gives rise to large superbubble structures with a few 100 pc diameter in the ISM. Nucleosynthesis feedback from star groups is spatially and dynamically associated with these bubbles and can be modelled via population synthesis calculations.

- How can ^{26}Al be detected from individual groups?
  ⟶ Sec. 3.4
- What is a fast way to model stellar groups of a certain mass?
  ⟶ Sec. 4.2.1
- How strong is the ^{26}Al emission from the Perseus region?
  ⟶ Sec. 5.3

2.4 Galactic Chemical Evolution

The time spans involved seem too long to follow large-scale changes in the Milky Way directly. However, the presence of short-lived radioisotopes in the ISM in particular shows beyond doubt that a chemical evolution is taking place. This mechanism is mainly determined by three interdependent factors: first, how efficiently and frequently do new stars form (cf. Sec. 2.4.2); this is related to how often massive stars end their evolution and release nucleosynthesis products into the surroundings (cf. Sec. 2.4.3); and finally, how effectively are these newly synthesised nuclei mixed and distributed in the interstellar gas (cf. Sec. 2.4.1). Radioactivity in the Milky Way is closely linked to each of these questions. Thus, the investigation of the distribution and the dynamics of radioisotopes and how these are related to the Galactic large scale structure is an excellent approach to study its chemical evolution (cf. Sec. 2.4.4).

2.4.1 Interstellar Medium

The ISM is the medium in which galactic chemical evolution takes place and what mediates the galactic cycle of matter on large scales (cf. Sec. 2.1). Stars are formed from it and it is where they deposit their feedback output. Very generally the ISM consists of matter, cosmic rays, and cosmic rays (e.g. Ferrière 2001; Klessen & Glover 2016). The matter part comprises atomic and molecular gas, as well as dust and can be subdivided into five main thermal components which are summarised in Tab. 2.8. In the temperature range between 250 K and 1000 K, the ISM is sometimes additionally classified as thermally unstable neutral medium (UNM) (Murray et al. 2018). Typical observational tracers of the different ISM phases are e.g. the 21 cm line, the H_α line, or the 2.6 mm line due to rotational transition $J = 1$–0 of $^{12}C^{16}O$. With respect to the total mass of the Milky Way of $\sim 5 \times 10^{11}$–$1 \times 10^{12}\,M_\odot$(Kalberla & Kerp 2009; McMillan 2011, 2017), the fraction of ISM gas is rather low with only $\sim 10^{10}\,M_\odot$ (Kalberla & Kerp 2009). With regards to the mass in the ISM, 70%

Table 2.8: ISM components (adopted from Klessen & Glover (2016) following Caselli et al. (1998), Ferrière (2001), Wolfire et al. (2003), and Jenkins (2013)).

Component	Temperature [K]	Density [cm^{-3}]	Ionisation fraction
Molecular gas	10–20	$> 10^2$	$< 10^{-6}$
Cold neutral medium (CNM)	50–100	20–50	$\sim 10^{-4}$
Warm neutral medium (WNM)	6×10^3–10^4	0.2–0.5	~ 0.1
Warm ionised medium (WIM)	$\sim 8 \times 10^3$	0.2–0.5	1
Hot ionised medium (HIM)	$\sim 10^6$	$\sim 10^{-2}$	1

is accounted for by hydrogen, 28% by helium, and only 2% by heavier elements (Klessen & Glover 2016). Due to the predominance of hydrogen, the ISM phases are often classified according to the chemical state of hydrogen. It is dominated by 75% of neutral H I or molecular H_2 gas. While the latter occupies only 1–2% of the total ISM volume, the 25% ionised H II component is spatially dominant. In addition to the ionisation state, different thermal phases of the ISM are observationally accessible. The H I mass is with 52% mostly WNM and 28% CNM (Murray et al. 2018). McKee & Ostriker (1977) pointed out that especially SN events create large bubbles filled with HIM gas of $T \sim 10^6$ K. This phase, which is therefore closely related to massive star feedback, has a scale height of the order of 1 kpc in the Milky Way (Reynolds 1989). This could be linked to the fact that he Galactic magnetic field quenches the velocity of vertically streaming gas. The magnetic field strength reaches a maximum at ~ 300 pc which causes a pressure gradient acting against the vertically outflowing streams (Evirgen et al. 2019). However, other simulations indicate that magnetic fields may not have such a significant affect on the vertical flow of gas (Hill et al. 2012). The distribution of the molecular component appears to be strongly confined to the Galactic disc with its radial distribution peaking within the central 500 pc correlated with the Galactic bar (Morris & Serabyn 1996).
Even though it is very useful for a general picture, the strict division into distinct phases is deficient with regard to a detailed physical understanding because the ISM is in fact an extremely turbulent medium. Turbulences are mainly driven by thermal instabilities, gas inflow onto the Galactic disk, and stellar feedback. Fig. 2.41 shows the density profile of a magneto-hydrodynamic simulation of the ISM by de Avillez & Breitschwerdt (2005). It includes energy injection due to stellar feedback and illustrates how this gives rise to a chaotic structure of interacting and mixing cavities and dense shells. It is debated what the exact fraction of quantitative effects of the different stellar feedback mechanisms is: While feedback on the scale of individual superbubbles may be driven in large parts by the early wind phases and including the first SN event (Krause et al. 2013; Krause & Diehl 2014), other simulations suggest that on larger scale the contribution due to SNe outweighs the wind component by more than a factor of 10 (Walch & Naab 2015). This underlines that hydrodynamic simulations are an indispensable tool for a self-consistent understanding of how the small scale structures of the ISM are related to galactic dynamics. Recent large scale galactic simulations have shown that the effect of SNe may be overall largely increased because they are expected to occur clustered in very dense cloud environments created by self-gravitational instability (Martizzi 2020). Although stellar feedback is dominated by winds and SNe, stellar radiation is particularly in this respect not negligible. Radiative feedback happens mostly through photoionisation heating and radiative pressure. With respect to the star formation history of a galaxy, this has a significant effect as avoiding the formation of over-dense clusters

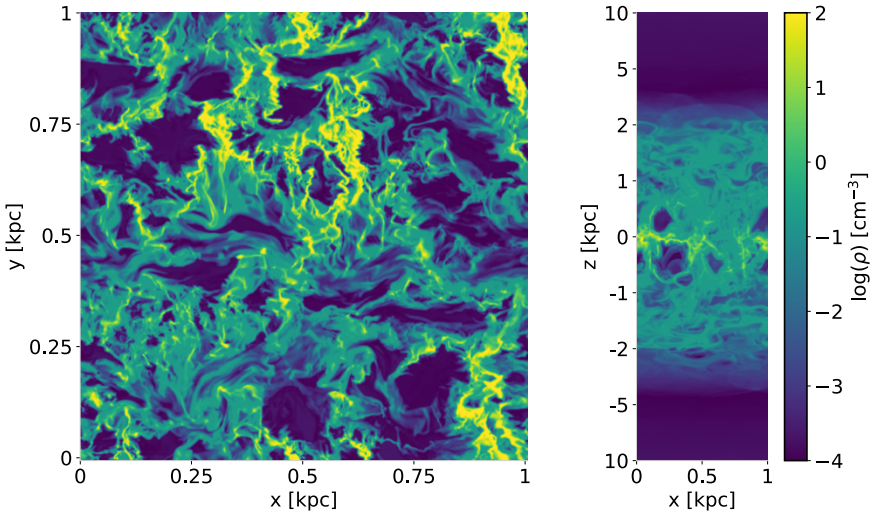

Figure 2.41: Hydrodynamic simulation of the turbulent ISM structure in a three-dimensional data cube by de Avillez & Breitschwerdt (2005) (image reproduced). *Left:* Gas density profile of a 1 kpc^2 two-dimensional cut through the galactic xy-plane. Dense regions following bubble-shaped filaments are shown in bright colours. The hot and diffuse material inside these bubbles is shown in dark colours. *Right:* Gas density profile of a two-dimensional vertical slice through the simulation data cube perpendicular to the galactic plane. It extends to ±10 kpc with a compressed and not uniform axis in z-direction for visibility reasons. Blow-outs and chimneys are visible as openings in the bright bubble walls. Through these material is ejected into the galactic halo as galactic winds.

and thereby preventing highly clustered SNe (Hopkins et al. 2020).
Spherically symmetric models of feedback driven bubbles omit turbulences of the surrounding ISM. However, the detailed density structure plays an important role in the propagation and evolution of such bubbles in turbulent environments. Usually, inhomogeneous density filaments allow for rapid blow-outs which lead to faster and larger expansion of superbubbles in realistic circumstances compared to homogeneous environments (Ohlin et al. 2019). In the expanding interstellar shock waves, particle acceleration is induced, creating high energetic cosmic rays in diffuse shock acceleration (e.g. Urošević et al. 2019). On molecular scale, the turbulences in these shocks also accelerate the growth of dust grains which overall compensates for the higher destruction rate due to SN shocks (Mattsson 2020). Overall on astrophysical scales, the effect of turbulence is twofold. On the galactic scale it prevents overall collapse by counterbalancing the self-gravity field. On smaller scales of GMCs it has the opposite effect of facilitating collapse and star formation (Klessen & Glover 2016). The return of chemically processed material from evolved stars back into the ISM is $\sim$ 1–2 $M_\odot\,yr^{-1}$, which is also mixed mainly due to turbulent motions. The mixing timescale inside a typical superbubble on size scales of 25–500 pc was estimated to be less than 2 Myr. The timescale for complete mixing, i.e. between thermal phases, is longer than the time to reach chemical equilibrium. Thus, the ISM is expected to show an chemical anisotropies. Even in hot regions, the complete mixing process takes on the order of 50 Myr. Because low-level inhomogeneities are continuously maintained by ccSNe on a much shorter timescale, the ISM can be considered as chemically poorly mixed in general. For the estimated SNR of the Galaxy (cf. Sec. 2.4.3), the timescale for erasing also large scale inhomogeneities and reaching compete mixing is about 350 Myr (de Avillez et al. 2002). This is two orders of magnitude longer the lifetime of ^{26}Al and ^{60}Fe. This means that their emission is expected to be inhomogeneously distributed in association with the production sites. It is important to note that the above mentioned typical observational tracers

correspond strictly speaking only to thermal states of the ISM and do not reflect directly distinct underlying physical processes. In this respect, the outstanding role of ^{26}Al and ^{60}Fe, which are the focus of this work, is evident. Their gamma-ray line emission is not biased regarding any thermal or dynamic conditions and is not affected by interstellar gas or dust absorption.

2.4.2 Star Formation Rate

In addition to the dynamic properties of the ISM, which determine the distribution and mixing of new elements within a galaxy, the frequency of star formation is a decisive factor in the chemical evolution of the Milky Way, as it is a major determinant of the total amount of nucleosynthesis. As outlined in Sec. 2.2.1, star formation is a complex process that involves a wide range of physical processes and scales. A phenomenological tool to grasp this highly complex process globally is the star formation rate (SFR) $\dot{M}_*$. It describes how much gas mass in a galaxy is transferred into stars within a unit time. This is, besides the initial gas composition and the IMF, an essential pillar within any framework of galactic chemical evolution (e.g. Kennicutt & Evans 2012; Krumholz 2014).
The consideration of a galactic SFR goes back to Schmidt (1959), who was the first to formulate a power-law correlation between galactic gas content and the rate of star formation. Although the Milky Way is the nearest example, many studies concerning global star formation since then have focussed on extragalactic observations because observations inside the Milky Way face significant problems of stellar distance determinations and selection effects. Thus, Galactic and extragalactic approaches are usually combined to establish a coherent picture of the SFR. The most straight forward approach concerning the rate of star formation in the Milky Way is to count the number of stars of a certain age in order to obtain the mean SFR (Kennicutt & Evans 2012)

$$\langle \dot{M}_* \rangle = \sum_{M_*=M_{*,\,\mathrm{min}}}^{M_{*,\,\mathrm{max}}} \frac{N(M_*, t_*) M_*}{t_*}, \tag{2.47}$$

with the number of stars $N(M_*, t_*)$ of certain mass M_* and lifetime t_*. Counting young stellar objects in the Galactic Legacy Infrared Mid-Plane Survey Extraordinaire (GLIMPSE) survey of the Galactic plane yielded a Galactic SFR in the range $0.68 \leq \dot{M}_* \leq 1.45\,\mathrm{M}_\odot\,\mathrm{yr}^{-1}$ (Robitaille & Whitney 2010). Such an estimations inherits its uncertainties from the determination of the IMF due to its necessarily incomplete observational basis. In particular, corrections have to be applied to account for undetected low mass stars and a duration of star formation has to be assumed. To circumvent this problem, indirect diagnostic methods were developed to determine SFR based on a statistically larger sample of extragalactic measurements. Here, the integrated luminosity in UV, far-IR, or nebular recombination lines is used to infer galactic star formation properties. The respective relations to SFR have ben reviewed by Kennicutt (1998). Especially ionisation due to young and massive stars is closely related to star formation. Therefore, a SFR in the Milky Way can be inferred by simply counting the visible H II regions, extrapolating to lower mass stars, and averaging over the effective lifetime of massive stars. Following this approach, a survey with the Wilkinson Microwave Anisotropy Probe (WMAP) obtained a Galactic

SFR of $\dot{M}_* = (1.3 \pm 0.2)\,\mathrm{M}_\odot\,\mathrm{yr}^{-1}$ (Murray & Rahman 2010). This may be observationally biased because of the relatively small number and short lifetime of high mass stars. The far-IR emission of the Milky Way reflects more the number of lower mass stars and includes a longer timespan. A $100\,\mu$m survey with the Diffuse Infrared Background Experiment (DIRBE) yielded a significantly higher Galactic SFR of $\dot{M}_* = 2.7\,\mathrm{M}_\odot\,\mathrm{yr}^{-1}$ (Misiriotis et al. 2006). Different estimates of the SFR in the Milky Way are summarised in Tab. 2.9. From this overview it becomes clear that it

Table 2.9: Estimates of the average SFR in the Milky Way obtained by using different observational indicators and inferential approaches. Largely following reviews by Chomiuk & Povich (2011) and Kennicutt & Evans (2012).

Source	SFR $[\mathrm{M}_\odot\,\mathrm{yr}^{-1}]$	Physical indicator or method
Miller & Scalo (1979)	5.7 ± 2.3	ISM mass
Güsten & Mezger (1982)	~ 10	Free-free emission
McKee & Williams (1997)	~ 4	Free-free emission
Kennicutt (1998)	~ 1	Lyman continuum
Boissier & Prantzos (1999)	5.2 ± 1.7	Gas surface density
Diehl et al. (2006)	~ 4	1.8 MeV ^{26}Al emission
Misiriotis et al. (2006)	~ 2.7	$100\,\mu$m dust emission
Murray & Rahman (2010)	1.3 ± 0.2	93.5 GHz free-free emission
Robitaille & Whitney (2010)	1.07 ± 0.39	Star counts
Prantzos et al. (2011)	~ 2.3	Galaxy type
Chomiuk & Povich (2011)	1.9 ± 0.4	Meta-analysis
Kennicutt & Evans (2012)	8.25	H I mass (Kalberla & Kerp 2009)
Adams et al. (2013)	$3.6^{+8.3}_{-3.0}$	MC modelling historical SNe
Licquia & Newman (2015)	1.65 ± 0.19	Bayesian meta-analysis

is difficult to set a canonical value of the SFR for the Milky Way since the estimates span an entire order of magnitude between $\sim 1\,\mathrm{M}_\odot\,\mathrm{yr}^{-1}$ and $\sim 10\,\mathrm{M}_\odot\,\mathrm{yr}^{-1}$. Large uncertainties arise due to the fact that basically all SFR estimates rely on underlying theoretical assumptions concerning the IMF, the ECMF, stellar evolution models, or ISM theories linking extragalactic observations to Milky Way properties. Thus, Chomiuk & Povich (2011) applied a meta-analysis of previously performed SFR studies by normalising those underlying assumptions to the same IMF and massive star models. Thereby, they obtained values converging at $\dot{M}_* = (1.9 \pm 0.4)\,\mathrm{M}_\odot\,\mathrm{yr}^{-1}$. However, they find that in particular estimates using absolute counts of the stellar census in low and intermediate mass star groups yield typically a factor of $\sim$ 2–3 higher SFR. Using an entirely different approach of gamma-ray astrophysics Diehl et al. (2006) inferred a Galactic SFR of $\dot{M}_* \sim 4\,\mathrm{M}_\odot\,\mathrm{yr}^{-1}$ from the Galaxy-wide 1.8 MeV emission. With an assumed spatial distribution of ^{26}Al the number of photons is directly linked to the total decaying mass. From assuming a homogeneous exponential disk distribution, the gamma-ray flux was estimated to correspond to a total amount of $(2.8 \pm 0.8)\,\mathrm{M}_\odot$ of ^{26}Al in the Milky Way. The SFR is then obtained as normalisation parameter of the convolution of the IMF with stellar model yields (cf. 2.2.5). However, the IMF as well as in particular the spatial distribution remains a fundamental theoretical input bearing uncertainties. Therefore, in this thesis, a new model approach to improve our understanding of this will be described in Ch. 4.

2.4.3 Supernova Rate

The galactic distribution of ccSN events largely maps the distribution of far-UV radiation. This is due to their progenitors which are moderately massive red supergiants with $M_* \geq 8\,\mathrm{M}_\odot$ in massive star groups close to the spiral arms (Audcent-Ross et al. 2020). This also means that their occurrence rate R_{ccSN} is a global parameter which is selective in particular for the massive star abundance. Since these objects are sparse and the observable depth in the Milky Way is rather limited due to absorption in gas and dust, they were observed only very rarely. The last Galactic ccSN was observed in 1604 and was described by Johannes Kepler (1606). This means that no such event has been observed within the visibility radius in the Milky Way for over 400 yr, so that only a few historically recorded SNe exist. On this sparse basis, Tammann et al. (1994) inferred a Galactic supernova rate (SNR) of $R_{\mathrm{ccSN}} = (2.5^{+0.8}_{-0.5}) \times 10^{-2}\,\mathrm{yr}^{-1}$. An estimate of the SNR based solely on gamma-ray observations within the Galaxy is based on the total mass of ^{26}Al determined as above and is $R_{\mathrm{ccSN}} = (1.9 \pm 1.1) \times 10^{-2}\,\mathrm{yr}^{-1}$ (Diehl et al. 2006).
Since the number of cases observed in the Milky Way is very small, many estimates are based on observations of external galaxies. However, these are subject to various observational biases concerning total mass estimates, detailed morphology, near-IR magnitudes, or bolometric luminosities (Mannucci et al. 2005). Extragalactic estimates of spiral galaxies at low redshift overall agree with the typical estimates of the Galactic SNR range between 1–3 $\times 10^{-2}\,\mathrm{yr}^{-1}$ (cf. Tab. 2.10). Since ccSNe are expected to occur primarily in young and massive star groups, their distribution follows that of star formation. Thus, SNe are also expected to be associated prominently with the Galactic spiral arm structure and their scale height should be associated with that of star forming molecular gas, i.e. $\lesssim 100\,\mathrm{pc}$ (Diehl & Prantzos 2018, 614). In Ch. 4 a new bottom-up MC approach with PSYCO will be outlined to infer the Galactic SNR from the SFR and correlate both to gamma-ray observations of ^{26}Al and ^{60}Fe in the Milky Way. As described in Sec. 2.2.5, the ratio of these isotopes is particularly sensitive to the SNR, which makes it a promising litmus test for stellar nucleosynthesis calculations and in particular explodability models.

Table 2.10: Estimates of the average core-collapse supernova rate (SNR) in the Milky Way obtained by using different inferential approaches.

Source	SNR $[10^{-2}\,\mathrm{yr}^{-1}]$	Physical indicator or method
van den Bergh & Tammann (1991)	3.4 ± 2.0	Radio remnants
Cappellaro et al. (1993)	1.7 ± 0.9	Extragalactic UV luminosity relation
Tammann et al. (1994)	$2.5^{+0.8}_{-0.5}$	Historical records
McKee & Williams (1997)	~ 2	H_α luminosity
Reed (2005)	1.5 ± 0.5	Massive star census
Diehl et al. (2006)	1.9 ± 1.1	1.8 MeV ^{26}Al emission
Prantzos & Boissier (2010)	2.23 ± 0.10	Extragalactic observations
Adams et al. (2013)	$3.2^{+7.3}_{-2.6}$	MC modelling of historical SNe

2.4.4 Large Scale Structure

As the observer is positioned in the Galactic plane, its structure is difficult to observe. In order to nevertheless study the structure, it is crucial to survey the Milky

Way and measure distances to objects that are tracing the large scale structure and then constructing a three dimensional plane-view map. This was first done mostly by observing hydrogen (cf. Fig. 2.37 or Fig. 2.36) or CO (cf. Fig. 2.3) emission (e.g. Georgelin & Georgelin 1976; Dickey & Lockman 1990; Dame et al. 2001; Benjamin et al. 2005). The *Gaia* mission mapped 1.7×10^9 individual stellar sources in the Milky Way and created a view of unprecedented detail (Gaia-Collaboration et al. 2018). The resulting all-sky view of the visible Milky Way is shown in Fig. 2.42. The general structure is characterised by a thin disk of young stars overlaid by dark

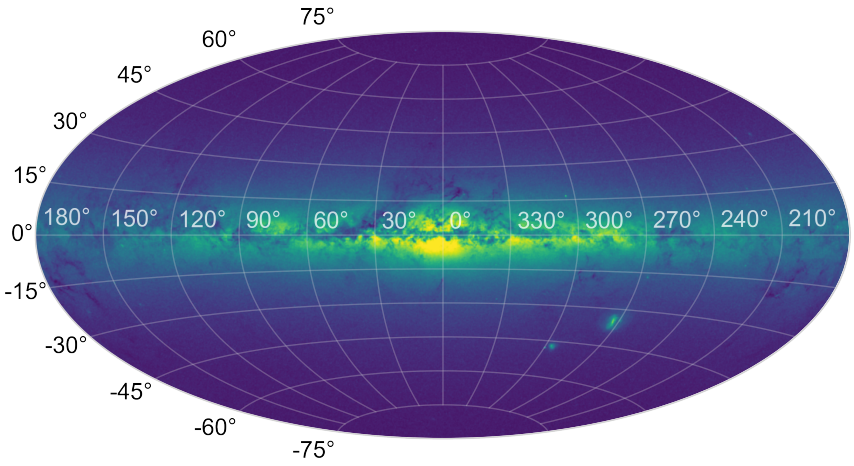

Figure 2.42: Sky map of the total flux measured in four optical filter bands from 1.7×10^9 individual sources in the *Gaia* Data Release 2 (Gaia-Collaboration et al. 2018). The main structure is characterised by a bright thin disc component extending to both sides of a bright bulge. Apart from that, an extended diffuse emission is visible as a thick disk component. The patchy structure is due to absorption of stellar photons in interstellar dust clouds. The LMC and SMC are clearly visible to the lower right.

patches which correspond to occulting interstellar cloud filaments. The emission is centrally concentrated in a bright bulge, with a fainter diffuse component associated with a thick disk populated by old stars. The canonical distance of the Sun to the Galactic centre assigned by the International Astronomical Union (IAU) is $R_{\mathrm{GC}} = 8.5\,\mathrm{kpc}$ (Kerr & Lynden-Bell 1986). Later estimates range between 7 and 9 kpc with a tendency to slightly lower values (Reid 1993).

From the line shift of molecular CO gas emission, a map of the longitudinal distribution of molecular gas velocities in the plane can be obtained (cf. Fig. 2.43, adopted from Dame et al. 2001). Following the CO density, usually a radius for active star formation of $R_{\mathrm{MW}} = 13.5\,\mathrm{kpc}$ is estimated (Kennicutt & Evans 2012). The curved structures in the map are due to Doppler line shifts of emission from material moving in spiral arms. To convert these features into a three-dimensional distribution of objects, the measured velocities can be linked to a model of the rotation of the Milky Way, allowing conclusions to be drawn about distances. The first problem with this is that for a decentralised observer there arises a two-point ambiguity between the close and the far side of the disk. The second difficulty with kinematic distances is that there are clouds of gas and stars that follow peculiar motions that do not follow the overall Galactic circular field exactly. This leads to distance errors typically of the order of the expected spiral arm separations.

A more accurate distance measure are trigonometric parallaxes. In that respect, a main objective are high-mass star forming regions that trace in particular the spiral structure. Friedrich Wilhelm Bessel (1838) used a heliometer to measure a

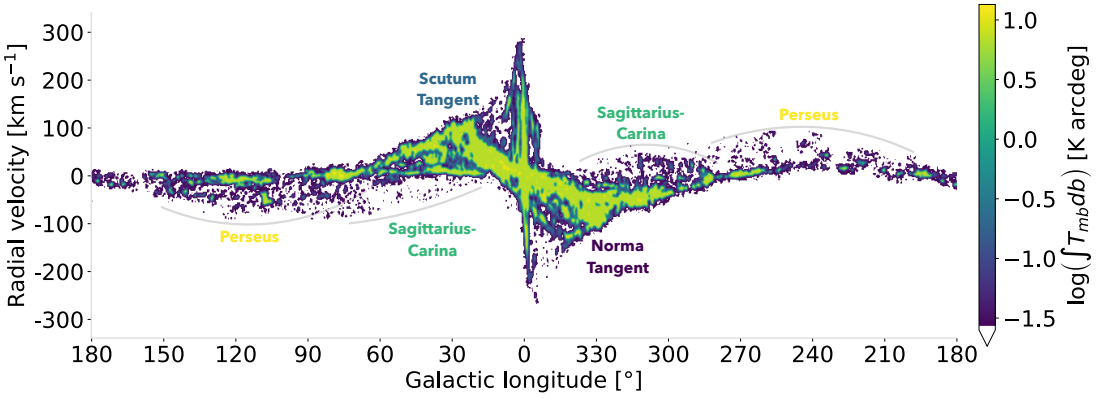

Figure 2.43: Longitude-velocity map of the radial line-of-sight velocity of CO gas in the Milky Way. The colour scale gives the main beam brightness temperature T_{mb} integrated over Galactic latitude b. Prominent features reflecting spiral arms or spiral arm tangents are highlighted in grey and annotated in colours corresponding to the schematic face-on Milky Way spiral structure shown in Fig. 2.44. Crossing the Galactic centre, the diagonal bar is associated with the Galactic Molecular Ring and the vertical spike shows rotation in the Galactic Nuclear Disk. Adopted from Dame et al. (2001).

parallax of 0.314 arcsec of the 61 Cygni binary system with respect to two reference stars and inferred a distance of ~ 3.2 pc. This is impressively close to the current value of ~ 3.5 pc. Using trigonometric parallaxes, this was the first reliable distance measurement of a star other than the Sun. This principle remains to be one of the most reliable distance measures in the Galaxy. Missions that observe in optical wavelengths are restricted to a depth of a few kpc in the Galactic plane because of dust absorption. Radio wavelengths have the advantage that they are not absorbed by dust and can be measured all the way through the Milky Way. In radio, the main objectives are high-mass star forming regions and astrophysical maser sources. The latter radiate due to microwave amplification by stimulated emission of radiation from cloud regions. They are found in the vicinity of young massive stars, red giant stars, and in active galactic nucleus (AGN) accretion disks and have size scales of 10–100 AU with planetary masses. Their collimated radiation outflows make them very good targets for distance estimations (e.g. Zhang et al. 2013). There are currently ~ 200 parallax measurements of massive star regions in the Milky Way (Reid et al. 2014, 2016, 2019). The most distant trigonometric parallax measurement today is obtained with the Very Long Baseline Array (VLBA) for a water maser at a distance $20.4^{+2.8}_{-2.2}$ kpc (Sanna et al. 2017). This traces an active star forming region in the Scutum-Centaurus spiral arm on the far side of the Milky Way. From the observed accumulation of such objects in certain directions spiral arm tangents can be obtained. The inferred structure is shown in a schematic picture in Fig. 2.44 (e.g. Vallée 2008). In the fourth Galactic quadrant, observational data is currently sparse because it can not be observed from the northern hemisphere. Thus, the entire Galactic spiral structure is inferred according to the tangents in the other quadrants. This spiral structure can be also traced by the distance distribution of H II regions (Georgelin & Georgelin 1976). These are associated with Galactic OB associations which show an exponential distribution radially, with scale radius 3.5 kpc (McKee & Williams 1997). Similarly, this spiral structure was also mapped in IR with SIRFT (Benjamin et al. 2003) and Spitzer (Churchwell et al. 2009). With GLIMPSE, a scale radius of $R_* = 3.9 \pm 0.6$ kpc was inferred by modelling the observed mid-IR source distribution with an exponential disk. Also a pronounced

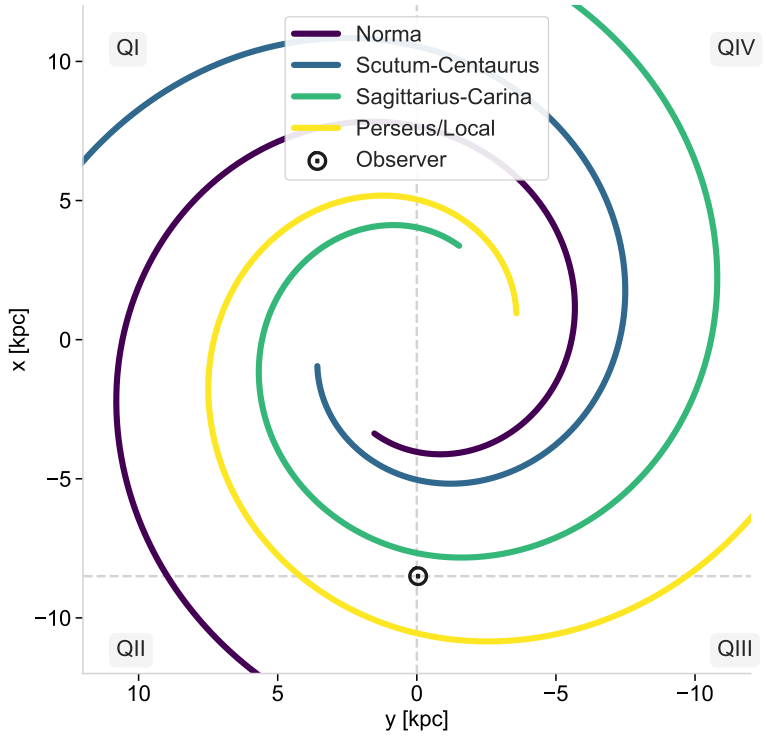

Figure 2.44: Schematic face-on structure of the four spiral arms in the Milky Way. The observer is marked at the position of the Sun $\sim 8.5\,\mathrm{kpc}$ away from the Galactic centre. With respect to this observer, four Galactic quadrants are assigned. The arm locations are denoted according to Faucher-Giguère & Kaspi (2006) and Reid et al. (2019).

east-west asymmetry was found with a strong enhancement of stars at $l = 10°$–$30°$. This is explained by a linear bar structure in the Galactic centre with half-length $R_{\mathrm{bar}} = 4.4 \pm 0.5\,\mathrm{kpc}$, inclined by $\Phi_{\mathrm{bar}} = 44° \pm 10°$ with respect to the axis between the Galactic centre and the Sun (Benjamin et al. 2005). With respect to distance determinations radio pulsars play an important role. Their pulse frequency varies according to the dispersive propagation of the radio signal through the ISM. This means that their signals carry an inherent distance information (Hewish et al. 1968; Taylor & Cordes 1993; Faucher-Giguère & Kaspi 2006).
The Sun revolves with a tangential velocity of $\theta_\odot = 220\,\mathrm{km\,s^{-1}}$ (Kerr & Lynden-Bell 1986) around the Galactic centre and resides in the Local Arm. The latter is also referred to as Orion spur or local spur. This is misleading because it suggests less star formation activity than in an actual spiral arm. However, the density of star forming regions in the Local Arm seems to be similar to that in the Perseus arm. The radial distribution of the SFR in the Milky Way is overall rather constant with an indication for a slight peak of a factor ~ 2 within the inner 500 pc, which corresponds to the Galactic bar region and the Galactic Molecular Ring (Kennicutt & Evans 2012). Besides Galactic introspection, another option to understand the Milky Way structure better is to find other galaxies that resemble certain features we know are present in the Milky Way. Such cases are e.g. UGC 12158, which is sometimes referred to as the closest twin to the Milky Way, or NGC 628, which is seen almost face-on. Optical and radio images of NGC 628 are shown in Fig. 2.45 (for details see e.g. Kreckel et al. 2018; Utomo et al. 2018; Herrera et al. 2020). In the optical, within the central $\sim 2\,\mathrm{kpc}$ a bright bulge region with indications for a bar-like elongation can be seen. There is also a clear structure of two main arms

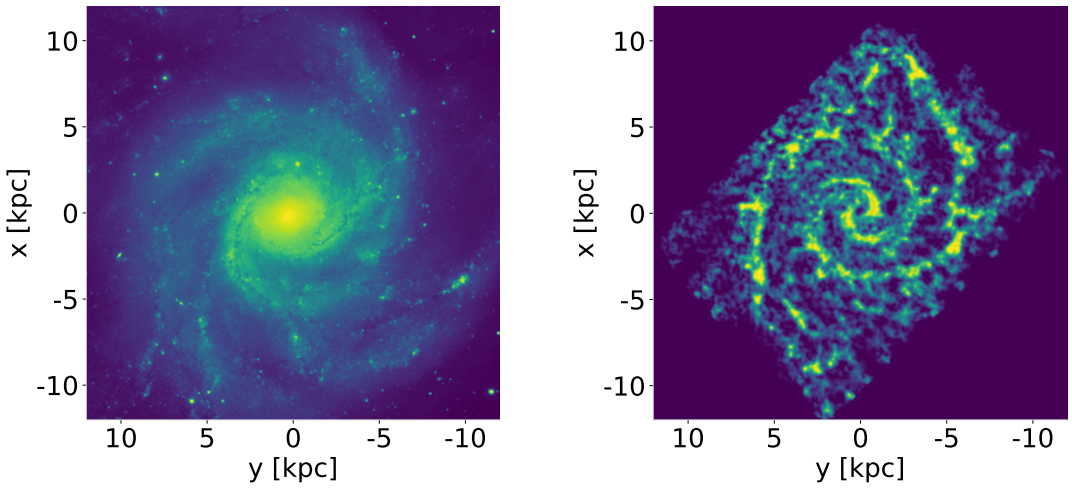

Figure 2.45: Spiral galaxy NGC 628 (M74). *Left:* Optical image taken with the Hubble Space Telescope (copyright: European Space Agency (ESA)/National Aeronautics and Space Administration (NASA)). This represents mostly star light which is seen brightly in the central bulge of the galaxy and associated with a diffuse spiral structure. *Right:* Sub-millimetre image taken with ALMA (copyright: ESO). It shows the emission from cold molecular gas which is strongly correlated with the spiral arms. Additionally, the pronounced bubble structure following the spiral arms shows the characteristically porous nature of the ISM throughout the entire galaxy. Both are reproductions of the original images.

and one secondary arm, which is also assumed for the Milky Way (Vallée 2008). This again underlines the fact that star formation occurs mainly within the spiral arms. Recent investigations of the impact of large scale dynamics on the SFR indicate that it is mostly determined by smaller scale feedback on the scale of GMCs. Large scale events like galactic mergers seem to be of secondary importance for SFR variances (Tress et al. 2020). Simulations show that self-gravitational instabilities are in principle sufficient to form a spiral structure on their own, but more flocculent and not as pronounced as due to intergalactic interactions (e.g. Dobbs et al. 2018; Fujimoto et al. 2018). This indicates that stellar feedback is not solely responsible for the large scale spiral structure of the Milky Way. Instead, it can be induced by a past galactic merger (Tress et al. 2020). The radio emission in the right panel of Fig. 2.45 shows the very pronounced web of giant molecular filaments of $> 100\,\mathrm{pc}$ length. When these are engulfed by a spiral arm, their shape is distorted by the steep spiral arm potential and they are aligned with it (Duarte-Cabral & Dobbs 2017). Since these dense filaments are prominent sites of active star formation, the Galactic superbubble distribution is dominated by the contribution of massive-star clusters formed inside the dense spiral (Higdon & Lingenfelter 2013). Thus, the ISM shows a characteristically porous structure of multiple bubbles predominantly along the spiral arms (Churchwell et al. 2006). This characteristic configuration bears important implications for the dynamics of nucleosynthesis feedback. This is shown schematically in Fig. 2.46. Due to the steep density profile of a spiral arm and the increased higher gas density in the plane, superbubbles preferentially expand in lower-density regimes in the direction ahead of the spiral arm and towards the galactic poles. This implies that massive star ejecta flowing in the opposite direction being stopped quickly due to high-density material in the spiral arm. On the other hand, nucleosynthesis products ejected in the direction ahead of the spiral arm can stream rather freely in the superbubble cavities. This adds overall an additional velocity component to massive star ejecta in the direction of galactic rotation. In the Milky Way, this can be observed as a Doppler line shift excess of the 1.8 MeV

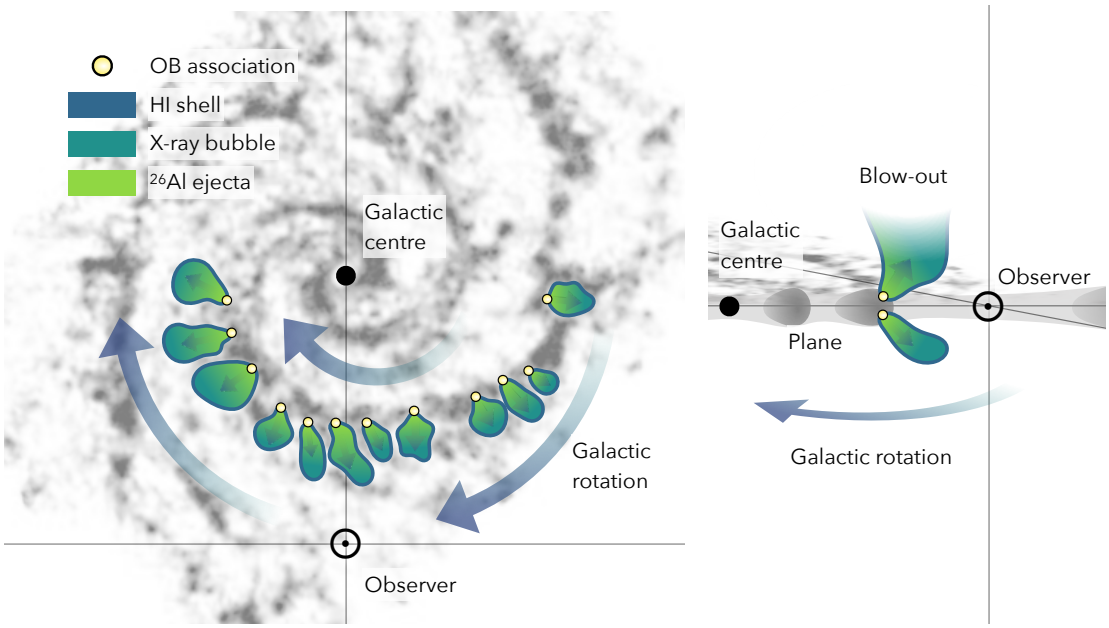

Figure 2.46: Scheme of the superbubble structure in one spiral arm in an face-on (*left*) and an edge-on view (*right*). Plotted on top of a radio image of the spiral galaxy NGC 628 (M74) taken with ALMA (copyright: ESO). A hypothetical observer at a structurally similar position as the Sun is located in the Milky Way faces the spiral arm towards the galactic centre. OB associations form preferentially on the leading edge of a spiral arm. Due to the steep density profile inside the arm, H I shells blown by massive star feedback expand mainly towards less dense material ahead of the arm. Wind and SN ejecta enriched with ^{26}Al are therefore found inside these bubbles streaming mostly in the direction of the overall galactic rotation. This is measured by the hypothetical observer as systematic velocity excess of nucleosynthesis ejecta with respect to the overall CO dust rotation curve. In addition to the in-plane expansion, bubbles also have a preferred direction away from the galactic plane because of a density decrease towards the galactic poles. This leads to higher velocities at larger heights and can even break the shells and blow material out of the plane. This follows the explanatory model introduced by Krause et al. (2015).

gamma-ray line with respect to the overall galactic CO dust rotation curve as shown in Fig. 2.47. Especially when SNe occur highly clustered in dense cloud instabilities, supersonic winds that stream perpendicular to the galactic plane can break up the H I shells and drive galactic fountains as shown in the right panel of Fig. 2.46 (Martizzi 2020). It takes about 200 Myr for gas that is blown out of the disk into the halo to return to the disk again de Avillez et al. (2002), which means that short-lived radioisotopes are suitable to trace the launch of Galactic fountains but not their entire circle.

2.4.5 Galaxy-Wide Nucleosynthesis Feedback Simulations

In order to test dynamical hypotheses about the nucleosynthesis feedback from massive star groups one has to combine the two-dimensional signature from observations of the sky with three-dimensional simulations of the underlying physics. Some of the most recent hydrodynamic simulations of Milky Way type galaxies have been performed e.g. by Hopkins et al. (2018); Buck et al. (2020); Tress et al. (2020); Martizzi (2020). Simulations following the dynamics of Galactic chemical enrichment by tracing the ^{26}Al distribution were done by Fujimoto et al. (2018) and Rodgers-Lee et al. (2019). The latter two are of particular interest in the context of massive star nucleosynthesis feedback. Face-on projections of the ^{26}Al density in both simulated galaxies are shown in Fig. 2.48. Since these two works will be of central importance

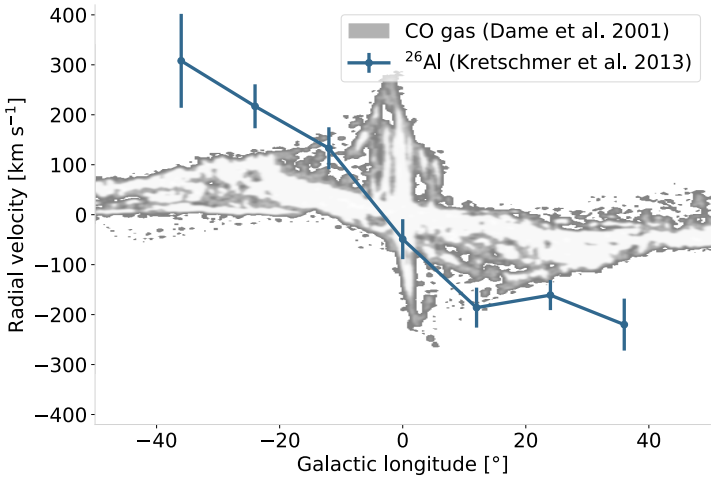

Figure 2.47: Longitude-velocity diagram of radial line-of-sight velocities in the Milky Way. This is for ^{26}Al measured with INTEGRAL/SPI by Kretschmer et al. (2013, *blue* data points), and CO gas measured by Dame et al. (2001, *grey*-scale background as in Fig. 2.43). The velocity excess measured from the 1.8 MeV gamma-ray line shift of ^{26}Al in 12° wide longitude bins with respect to CO gas is explained with superbubble dynamics shown in Fig. 2.46.

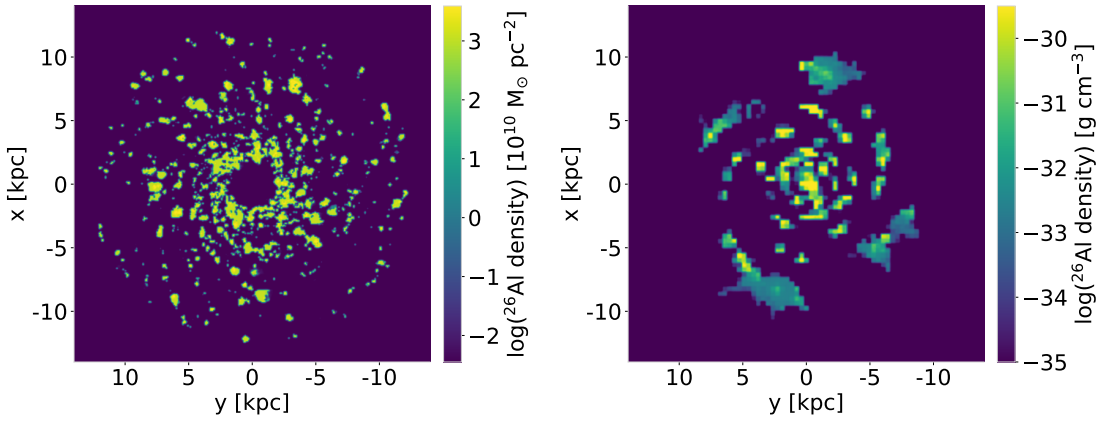

Figure 2.48: Hydrodynamic simulations of ^{26}Al Milky Way like galaxies. *Left:* Galaxy simulation by Fujimoto et al. (2018) (F+18). *Right:* Galaxy simulation by Rodgers-Lee et al. (2019) (R+19).

in this thesis, an abbreviated nomenclature for the galaxy simulation by Fujimoto et al. (2018) (F+18) and the galaxy simulation by Rodgers-Lee et al. (2019) (R+19) will be used in the following.

F+18 performed a high-resolution hydrodynamic galaxy simulation including self-gravity, a fixed axisymmetric logarithmic potential representing the gravity of old stars and dark matter, radiative cooling, photoelectric heating, as well as stellar feedback in the form of photoionisation, stellar winds, and SNe. Overall, they assumed an isolated gas disk orbiting in an otherwise static background potential representing dark matter and a stellar disk component. The dynamics of stellar ^{26}Al and ^{60}Fe are ejecta were followed in order to trace the chemical enrichment of the galaxy. These were calculated via the SLUG population synthesis code using the star-by-star yields taken from Sukhbold et al. (2016). The system evolved for 750 Myr with a maximum spatial resolution of 8 pc. After this runtime, the physical and chemical structure in the simulation reached a statistical equilibrium characterised by a steady large-scale structure of superbubbles filled with the freshly ejected ^{26}Al and

^{60}Fe. In the simulation, a flocculent spiral structure emerged spontaneously.
R+19 presented a hydrodynamic simulation of a galaxy that specifically resembles the Milky Way. Therefore, the gravitational potential includes individual components for the disk, central bulge, dark matter halo, and especially spiral arms following Dobbs et al. (2006). The initial mass density profile was set up using parameters physically relevant for a Milky-Way type galaxy. They included hierarchically clustered star formation, a sub-grid model for modelling stellar group feedback with cumulative energy injection and radiative cooling. Nucleosynthesis yields were inferred to match the massive star population synthesis results from Voss et al. (2009). Superbubbles were injected at the position of maximum spiral arm density at a random radius between 0 and 10 kpc from the galactic centre. This corresponds to a radial decrease of SFR by R^{-1}. The evolution was followed for 121 Myr with a spatial resolution of 125 pc in the plane and 20 pc perpendicular to the plane.
In both simulations the chemical evolution of the galaxy can be seen closely associated with the superbubble structures discussed above. As expected, ^{26}Al fills these ISM cavities but is not mixed fast enough do be significantly passed beyond the dense H I shells before it decays. A major difference lies in the granularity of the respective bubbles. While F+18 generates a large number of bubbles with sizes $\lesssim 500$ pc, R+19 produces fewer and larger cavities up to a few kpc. This discrepancy arises from the fact that galaxy-scale simulations require sub-grid model assumptions for including feedback on the scale of stellar groups which is subject to a plethora of uncertainties (Keller et al. 2014; Fujimoto et al. 2019). The difference in treatment of stellar feedback is also clearly visible in synthetic ^{26}Al sky maps as seen by a hypothetical observer in the respective simulated galaxy. These maps are depicted in Fig. 2.49. These offer an intriguing possibility to test the underlying assumptions

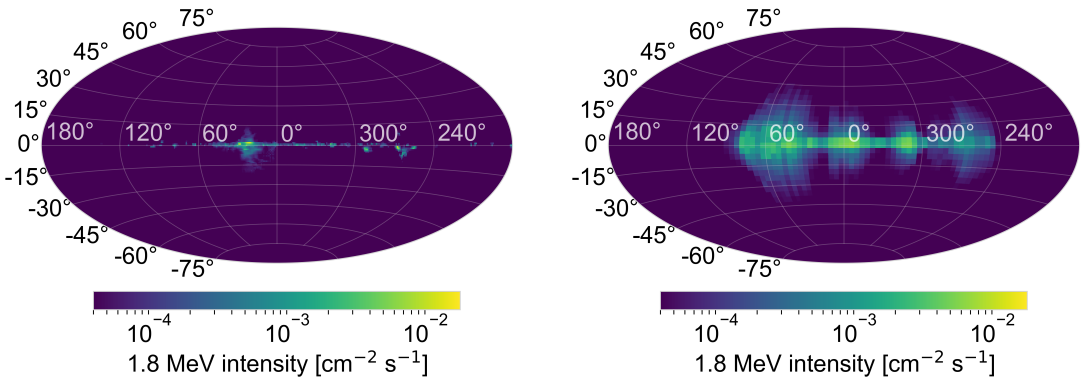

Figure 2.49: Synthetic all-sky maps of galaxy-wide ^{26}Al simulations. *Left:* Galaxy simulation by Fujimoto et al. (2018) (F+18). *Right:* Galaxy simulation by Rodgers-Lee et al. (2019) (R+19).

of nucleosynthesis feedback in the simulations versus observations. Studying the emission morphology on the sky, its intensity, granularity, and extent in longitude and latitude offers a wide range of information about the origin of nucleosynthesis products, their mixing dynamics in the Galaxy as well as their distribution and propagation. The fundamental challenges of such a study as well as new methods including fundamentally informative physical interpretations will be the central topic of this theses and will be presented in Ch. 4 and Ch. 5.

Essentials

The Galaxy-wide structure of the ISM is of turbulent and porous nature. This is mainly driven by feedback from massive star groups. These are associated with superbubbles that follow the overall spiral structure. Modelling this structure is essential to understand Galactic chemical evolution.

- How can the Milky Way be modelled in an effective way on the basis of massive star group nucleosynthesis?
  ⟶ Sec. 4.3
- What can be inferred about the Galactic SFR and SNR from modelling distributed radioactivity?
  ⟶ Sec. 4.4
- What can be inferred from general nucleosynthesis simulations about the Milky Way?
  ⟶ Sec. 5.1
- How can the Galactic signal from ^{26}Al be exploited morphologically?
  ⟶ Sec. 5.4

3 Measuring Radioactivity in the Galaxy

"It is an act of faith to assert that our thoughts have any relation to reality at all."

— Gilbert K. Chesterton (1908)

While observations in the optical or IR produce the probably most staggering astrophysical images, the high-energy regime reveals the likely most staggering astrophysical processes. The most energetic events in the Universe emit photons in this spectral domain beyond a few keV. Nuclear lines in the MeV range play a particularly important role in this respect because they signal the direct interplay between these most high-energetic processes on astrophysical scales with the evolution on smallest nuclear scales. Therefore, measuring the radioactivity in the Galaxy is crucial for understanding the smallest building blocks of the most extreme events. Thus, this chapter focusses on the physical basics of these processes and the technical challenges and methods for their measurement.

3.1 Radioactivity in the Milky Way

Radioactivity refers to the tendency of unstable nuclei to release energy through an internal change in nuclear composition. This can be mediated via ejection of an ^{4}He nucleus in α-decay, emission of a neutron, or the conversion of a nuclear proton due to capture of a shell electron. Additionally, in the context of this thesis, the two most important decay mechanisms are β- and γ-decay. β-decay denotes a weak transition of a neutron n into a proton p via

$$n \longrightarrow p + e^- + \bar{\nu}_e \qquad (\beta^-\text{-decay}), \tag{3.1}$$

under emission of an electron e^- and an electron anti-neutrino $\bar{\nu}_e$; or of a proton into a neutron

$$p \longrightarrow n + e^+ + \nu_e \qquad (\beta^+\text{-decay}), \tag{3.2}$$

under emission of a positron e^+ and an electron neutrino ν_e. If such a decay occurs inside a nucleus, it marks an isobar change of the initial element. This change in the nuclear quantum state usually leaves the daughter nucleus in an excited configuration. In that case an electromagnetic interaction causes the nucleus to transit to energetically lower-lying states. This is referred to as γ-decay

$${}^A_Z\mathrm{X}^*_N \longrightarrow {}^A_Z\mathrm{X}_N + \gamma \qquad (\gamma\text{-decay}) \tag{3.3}$$

of an excited nucleus ${}^A_Z\mathrm{X}^*_N$ in its ground state ${}^A_Z\mathrm{X}_N$ without change in number of neutrons N, protons Z, or mass number $A = N+Z$, but under emission of a gamma-

ray photon γ. This can proceed directly or in cascades via intermediate levels.
All these processes describe the transition from one quantum state to another. This is referred to as decay, because the entity described by the initial state technically ceases to exist. For each individual nucleus, this is an entirely independent stochastic process. In a large sample, the decrease of radioactive atoms relative to their total number $-dN/N$ is proportional to the elapsed time dt according to

$$-\frac{dN}{N} = \lambda\, dt, \tag{3.4}$$

with a characteristic radioactive decay constant λ for each radionuclide. Solving this differential equation gives the exponential radioactive decay law describing the total number of un-decayed atoms

$$N(t) = N_0\, e^{-\lambda t} \equiv N_0\, e^{-\frac{t}{\tau}} \equiv N_0\, e^{-\frac{t}{T_{1/2}\ln(2)}}, \tag{3.5}$$

for an initial amount N_0 at time $t = 0$. Different equivalent formulations with the decay constant λ, characteristic lifetime τ, or radioactive half-life $T_{1/2}$ occur frequently. While the latter gives the time after which N_0 has reduced by a factor $1/2$, the lifetime corresponds to the timespan to reduce it by $1/e$.
The radioactive isotopes ^{26}Al and ^{60}Fe described in Sec. 2.2.3 are examples undergoing a decay sequence of β-decays and subsequent γ-decays:

$$\begin{aligned} {}^{26}_{13}\mathrm{Al}_{13} &\longrightarrow {}^{26}_{12}\mathrm{Mg}^{*}_{14} + e^{+} + \nu_e \\ {}^{26}_{12}\mathrm{Mg}^{*}_{14} &\longrightarrow {}^{26}_{12}\mathrm{Mg}_{14} + \gamma(1809\,\mathrm{keV}) \end{aligned} \tag{3.6a}$$

$$\begin{aligned} {}^{60}_{26}\mathrm{Fe}_{34} &\longrightarrow {}^{60}_{27}\mathrm{Co}_{33} + e^{-} + \bar{\nu}_e \\ {}^{60}_{27}\mathrm{Co}_{33} &\longrightarrow {}^{60}_{28}\mathrm{Ni}^{*}_{32} + e^{-} + \bar{\nu}_e \\ {}^{60}_{28}\mathrm{Ni}^{*}_{32} &\longrightarrow {}^{60}_{28}\mathrm{Ni}_{32} + 2\gamma(1173.2\,\mathrm{keV},\, 1332.5\,\mathrm{keV}). \end{aligned} \tag{3.6b}$$

In Eq. 3.6b, typically an internal conversion of ^{60}Co occurs, which is not mentioned explicitly.

Radioactivity in the Solar System Shortly after its discovery in the 1890s, it became clear that radioactivity is basically present everywhere on Earth. Since then, it has been widely used e.g. in medical diagnosis and treatment, industrial processes for disinfection, filtration, or material and surface treatment, scientific analysis methods, or in nuclear power plants. The economic fact that natural radioactivity, e.g. in the case of ^{235}U used in nuclear power plants, is a non-renewable resource has important cosmological implications. First, elements themselves have an age. Second, because radioactive isotopes are not produced naturally on Earth, their abundance must be either inherited since the formation of the Solar System or scattered onto the Earth as a consequence of cosmic events. Actually, both is the case.
As described in Sec. 2.4.1, along with stable nucleosynthesis products, radioactive nuclei are mixed into the ISM due to stellar feedback. This means, that during the formation of the Solar System, its parental gas cloud was fed with certain radioactive isotopes according to an overall characteristic rate $F_\odot$. This process lasted from the onset of mixing at time t_1 until the parental gas of the Solar System decoupled from the ISM at $t_\odot$. During that time a characteristic Solar System abundance (Clayton

2018)

$$N_{\odot} = \int_{t_1}^{t_{\odot}} \frac{dF_{\odot}}{dt}\, e^{-\left(\frac{t_{\odot}-t}{\tau}\right)}\, dt \tag{3.7}$$

established. If the duration of feeding $t_{\odot} - t_1$ lasted much longer than the lifetime τ of the respective radionuclide, and $dF_{\odot}/dt$ is rather constant during that time, this can be approximated as

$$N_{\odot} = \left(\frac{dF_{\odot}}{dt}\right)_{t_{\odot}} \tau. \tag{3.8}$$

In this case, the number of a certain species of radioactive nuclei present at the formation of the Solar System corresponds to the amount that has been fed into the parental gas during the last mean lifetime of that species. For a given initial abundance at $t_{\odot}$, this can be used as an approximation of what the rate of nucleosynthesis feedback in the Solar System parental cloud was during its collapse.
Since not all of the radioisotopes have decayed since the formation of the Solar System, their abundance can be used for cosmochronology, i.e. to infer the age of astronomical objects and elements. The main assumption to infer elemental ages is that stable isotopes have been produced at the same time as their radioactive isotopes. In general, isotopic ratios are often used as cosmic chronometers. This was done for the first time by Ernest Rutherford (1929), who used the ratio of $(^{235}\mathrm{U}/^{238}\mathrm{U})_{\mathrm{today}} = 7.25 \times 10^{-3}$ along with their different lifetimes to estimate an age of about 4 Gyr for the Solar System. In the same way, with revised values today of $^{235}\mathrm{U}/^{238}\mathrm{U} = 7.25 \times 10^{-3}$, lifetimes $\tau(^{235}\mathrm{U}) = 1.029\,\mathrm{Gyr}$ and $\tau(^{238}\mathrm{U}) = 6.506\,\mathrm{Gyr}$, and the fact that these nuclei decay into the stable isotopes $^{207}\mathrm{Pb}$ and $^{206}\mathrm{Pb}$ respectively, an initial $(^{235}\mathrm{U}/^{238}\mathrm{U})_{\mathrm{init}} = 0.31$ and correspondingly the age of the Earth $T_{\oplus} = 4.57\,\mathrm{Gyr}$ can be calculated (Clayton 2018, 41–44). An important presupposition in this calculation is the production ratio $(^{235}\mathrm{U}/^{238}\mathrm{U})_{\mathrm{prod}} = 1.79$. This is intimately linked to larger scale processes. Depending on whether its nucleosynthesis occurred in a single pre-Solar event or continuously over time, the age of the Milky Way would be about 6.6 Gyr or 13 Gyr respectively (e.g. Cayrel et al. 2001; Frebel et al. 2007; Tissot et al. 2017). Thus, to make such age estimates more precise, a multitude of different tracer nuclei is investigated and nucleosynthesis calculations along with their large scale implications have to be refined (e.g. Dauphas & Chaussidon 2011). This is also the main topic of this thesis.

Radioactive Tracers on Earth Besides the Earth itself, the next further reaching radioactive tracers of pre-Solar origins in the Milky Way are enclosed in dust grains and chondrules in meteoritic material (Groopman et al. 2015; Lugaro et al. 2018). Given the age of the Solar System, in particular such short-lived radioisotopes are basically extinct in such probes. But their abundances can be inferred from radiogenic excess in their daughter nuclei, which are measured mostly via high-precision accellerator mass spectrometry (AMS). For instance, the initial amount of $^{26}\mathrm{Al}$ and $^{60}\mathrm{Fe}$ can be estimated by the increase of $^{26}\mathrm{Mg}/^{24}\mathrm{Mg}$ and $60\mathrm{Ni}/^{58}\mathrm{Ni}$ respectively. Thus, in the early Solar System their isotopic ratio was estimated to be $(^{26}\mathrm{Al}/^{27}\mathrm{Al})_{\mathrm{ESS}} = (5.23 \pm 0.13) \times 10^{-5}$ (Jacobsen et al. 2008) and $(^{60}\mathrm{Fe}/^{56}\mathrm{Fe})_{\mathrm{ESS}} = (1.01 \pm 0.27) \times 10^{-8}$ (Tang & Dauphas 2015).
Dust grains and chondrules contain a cumulative signature of multiple nucleosynthesis events. Time resolved signals from such events individually can be found in sediments of the Earth's deep-sea crust (Wallner et al. 2015, 2016; Feige et al.

2018, for ^{244}Pu ^{60}Fe, and ^{26}Al respectively). As shown in Fig. 3.1, this is consistent with two waves of SN ejecta sweeping across the Earth $\sim 2.5\,\mathrm{Myr}$ and $\sim 6\,\mathrm{Myr}$ ago. Radiogenic excesses from short-lived radioisotopes where also found in fossilised bac-

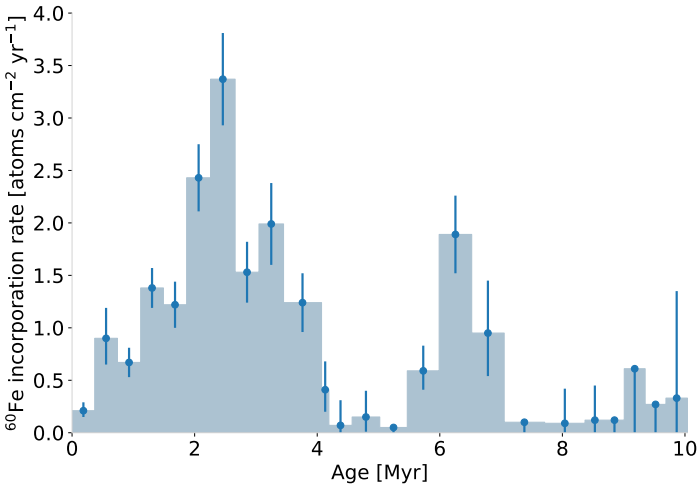

Figure 3.1: ^{60}Fe/Fe-ratios from AMS measurements at the Australian National University (ANU) of 24 for layers of a deep-sea crust. Age estimations are based on ^{10}Be data and statistical uncertainties are estimated using Poisson statistics for small number counts. The signal is consistent with two waves of SN ejecta sweeping across the Earth $\sim 2.5\,\mathrm{Myr}$ and $\sim 6\,\mathrm{Myr}$ ago. First results were released by Wallner et al. (2016). Updated data kindly provided by Anton Wallner (2020, priv. comm.).

teria (Ludwig et al. 2016, ^{60}Fe), on the Moon's surface (Fimiani et al. 2016, ^{60}Fe), or in Antarctic snow (Koll et al. 2019, ^{60}Fe). Another direct evidence of supernova-produced ^{60}Fe was found by Binns et al. (2016), who found 15 ^{60}Fe nuclei in cosmic rays in a measurement period of 17years with the Cosmic Ray Isotope Spectrometer (CRIS). Due to cosmic ray propagation, such a signal reaches $\lesssim 1\,\mathrm{kpc}$. Overall, this not only underlines the importance of investigating radioactivity for a better understanding of the Earth's history, it also vividly illustrates the turbulent past of the Solar System in terms of nucleosynthesis contributions.
In order to reach even further in cosmochronology and to draw a coherent picture of Galactic evolution, the gamma-ray signals from radioactively decaying material in the ISM can be studied. This will be discussed in the following sections.

Essentials

The entirely stochastic phenomenon of radioactivity is present basically everywhere in the Milky Way. Its measurement offers an important window to cosmochronology. A major indicator of near-by tracers are isotopic ratios in pre-Solar dust grains and meteoritic material.

3.2 Cosmic Gamma-Ray Measurements

Most astrophysical observations measure thermal radiation between radio wavelengths from cold molecular clouds up to X-rays from hot interstellar gas. This

means that the electromagnetic energy range 10^{-4}–10^{5} eV carries mainly signals of atomic temperature phases. However, signatures of nucleosynthesis processes are found mostly in isotopic abundances which are not necessarily coupled or restricted to characteristic thermal conditions. On the contrary, in many questions concerning feedback dynamics this is explicitly part of the question, such as: In which ISM phase does ^{26}Al decay? Are there characteristics in mixing of nucleosynthesis products compared to most hydrogen gas? Or does ^{60}Fe largely override the boundaries of hot superbubbles and cold shells, or does it remain diffuse within bubbles? The thermal state is often explicitly in question here and therefore cannot serve as an indicator. To find an answer to such questions, direct information about isotopic properties that are thermally unbiased is required. This is almost exclusively given by nuclear gamma-ray lines, which are observed in the energy range between 0.1 MeV and 10 MeV (Diehl 2018, 20–21). The following sections give a short overview of nuclear line measurements, with a focus on ^{26}Al and INTEGRAL/SPI, which is the instrument of choice in this thesis.

3.2.1 Historic Overview

Burbidge et al. (1957) were the first to introduce the idea that bright emission from type Ia SNe might be due to nuclear energy release from radioactive decay. Although their speculation erroneously relied on fission of ^{254}Cf, this work can be interpreted as wake-up call for gamma-ray astrophysics and the principle of measuring cosmic signals of radioactivity. This was followed by many ambitious observation missions. Diffuse cosmic gamma-rays in the range between 0.07 and 1 MeV were first detected by Metzger et al. (1964) with a caesium iodide scintillator crystals on the *Ranger III* mission. This was followed by several other balloon and satellite missions to detect cosmic gamma-rays (e.g. Clark et al. 1968; Bleeker et al. 1969; Haymes et al. 1969a,b; Vette et al. 1970). Most of them used sodium iodide scintillator crystals as detector material and measured a strong gamma-ray signal at 511 keV from electron-positron annihilation in the direction of the Galactic centre.
The first detection of a interstellar gamma-ray line originating from radioactive decay was achieved by Mahoney et al. (1984). This was a measurement of the 1.8 MeV emission line from ^{26}Al decay with the four high-purity germanium detector crystals of HEAO 3. This confirmed predictions of Ramaty & Lingenfelter (1977) and Arnett (1977) that this isotope should be present in the ISM and provide a gamma-ray signal from ongoing nucleosynthesis. Subsequently galactic ^{26}Al has been measured by several other instruments, e.g. the NaI spectrometer on the Solar Maximum Mission (SMM) (Share et al. 1985), MPI Compton telescope (von Ballmoos et al. 1987), the joint Bell Labs/Sandia Labs balloon flight program (MacCallum et al. 1987), the balloon-borne Gamma-Ray Imaging Spectrometer (GRIS) (Teegarden et al. 1991), or the High Energy X-ray And Gamma-ray Observatory for Nuclear Emissions (HEXAGONE) balloon experiment (Malet et al. 1991).
With COMPTEL aboard the CGRO, the spatial mapping of the ^{26}Al emission with still unrivalled spatial resolution was finally achieved (Diehl et al. 1993a,b; Oberlack et al. 1996). This map vividly demonstrates the astrophysical importance of this isotope and is shown in Fig. 1.1. Since then a multitude of gamma-ray lines from other isotopes such as ^{7}Be (Siegert et al. 2018), ^{44}Ti (Iyudin et al. 1998; Grefenstette et al. 2017), ^{56}Ni (Diehl et al. 2014, 2015), ^{56}Co (Tueller et al. 1990), or ^{60}Fe (Wang et al. 2007, 2020) was found. Nevertheless, 1.8 MeV, as the strongest nuclear gamma-

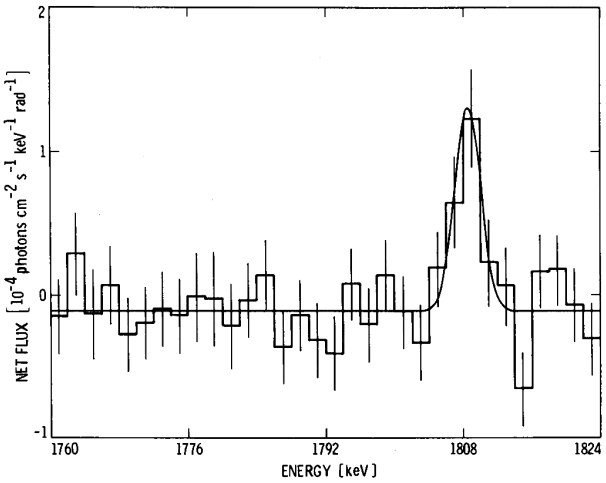

Figure 3.2: First detection of the 1.8 MeV gamma-ray line from interstellar ^{26}Al. It was measured with the detector array of four high-purity germanium detectors of the HEAO 3 instrument by Mahoney et al. (1984).

ray line from the ISM, still remains the most prominent and thus most promising tracer of nucleosynthesis feedback. This currently is still being investigated in detail using gamma-ray spectrometers such as the Compton Spectrometer and Imager (COSI) or INTEGRAL/SPI. The latter is the instrument of choice in this thesis mainly because of its unprecedented high spectral resolution. This instrument is described in more detail below in Sec. 3.3.

3.2.2 Measurement Principles

In order to measure cosmic gamma-rays, two major difficulties must be overcome. On the one hand, the Earth's atmosphere is opaque to gamma-rays. On the other hand, the materials of which telescopes and lenses are usually made are transparent to gamma-rays. This requires satellite-based telescope systems that can operate without focusing optics for photon energies between keV and MeV.

Photon-Matter Interactions Measurements of high-energy photons are based on their three fundamental types of interactions with matter: the photoelectric effect (Einstein 1905b, 145–147), Compton scattering (Compton 1923), and pair production (Blackett & Occhialini 1933). These are shown schematically in Fig. 3.3.
The photoelectric effect is based on the absorption of a photon by a bound electron in some material. If the energy of the photon exceeds the binding energy of the electron, the latter is lifted from the nuclear potential well and escapes as a free particle. The energy surplus from the difference between photon energy and electron binding energy is transferred into kinetic energy of the electron. The cross-section for such an interaction is approximately

$$\sigma_{\mathrm{PE}} = k\frac{Z^n}{E_\gamma^m}, \tag{3.9}$$

which is dependent on the atomic charge number of the material Z, the photon energy E_γ, and a material-specific constant k. With increasing photon energy the

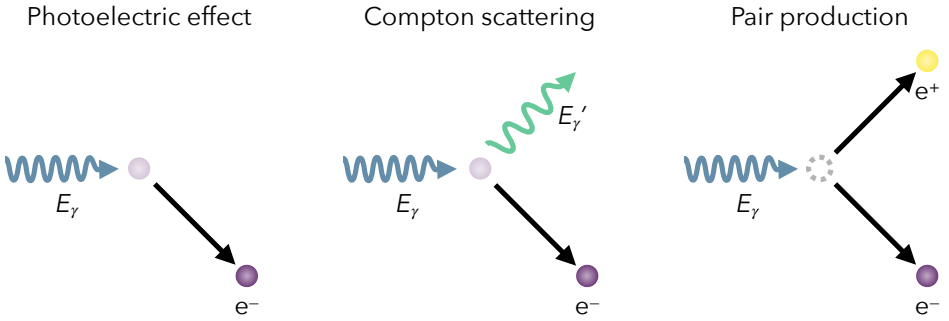

Figure 3.3: Fundamental interactions of gamma-ray photons with matter. The incoming photon with energy E_γ (*blue*) is completely (photoelectric effect) or partially (Compton scattering) transferred to an electron e^-. For $E_\gamma \geq 1022\,\mathrm{keV}$ the production of an e^+e^- pair can occur in the presence of an electric field.

value of the exponent n increases from 4 to 5; on the other hand, m decreases from 3 to 1 in the same course. This variation is due to the fact that with increasing photon energy, electrons can be ejected from shells deeper in the atomic potential well.

While the photoelectric effect dominates at low photon energies, Compton scattering predominates photon-matter interactions from about the electron rest energy of 511 keV. In this case the photons are not completely absorbed, but scatter inelastically on charged particles, mostly electrons. In such interaction, a part of the initial photon energy is transferred to the electron as recoil kinetic energy. On the side of the electron this leads to the Compton effect, i.e. partial energy reduction as well as directional deflection. The differential cross-section for Compton scattering per solid angle element $d\Omega$ is dependent on the scattering angle θ and calculated via the Klein-Nishina formula (Klein & Nishina 1929)

$$\frac{d}{d\Omega}\sigma_{\mathrm{CS}}(\theta) = \frac{r_e^2}{2}\left(\frac{k}{k_0}\right)^2\left[\frac{k}{k_0} + \frac{k_0}{k} - \sin^2\theta\right], \tag{3.10}$$

with $k_0 = \frac{E_\gamma}{m_e c^2}$, $k = \frac{E'_\gamma}{m_e c^2}$, and $r_e = \frac{\alpha\hbar c}{m_e c^2}$, which is the classical electron radius with the fine-structure constant α. The reduced photon energy after the scattering process is

$$E'_\gamma(\theta) = \frac{E_\gamma}{1 + \frac{E_\gamma}{m_e c^2}\,(1 - \cos\theta)} \tag{3.11}$$

Consequently, the kinetic energy of the electron has increased by $E'_e = E_\gamma - E'_\gamma(\theta)$ after scattering. From measuring the energy and direction of the recoil electron, direct conclusions can be drawn about the incident photon. Compton telescopes such as COMPTEL are based on this measuring principle.

If the energy of a photon is $E_\gamma \geq 1022\,\mathrm{keV}$, i.e. at least twice the electron rest energy, the production of an electron-positron pair $\gamma \to e^- + e^+$ can occur due to the photon interaction with an electric field. To ensure energy and momentum conservation during this process, an electromagnetically charged particle as counterpart is required to interact with and which can compensate for the momentum excess. For example, this function can be held by an atom in a material. In a process of basically reversed bremsstrahlung, an e^-e^+ pair can be produced in the interaction of a photon with the Coulomb field exhibited by the atomic nucleus. The pair production cross-section can be approximated for photon energies near the low-energy

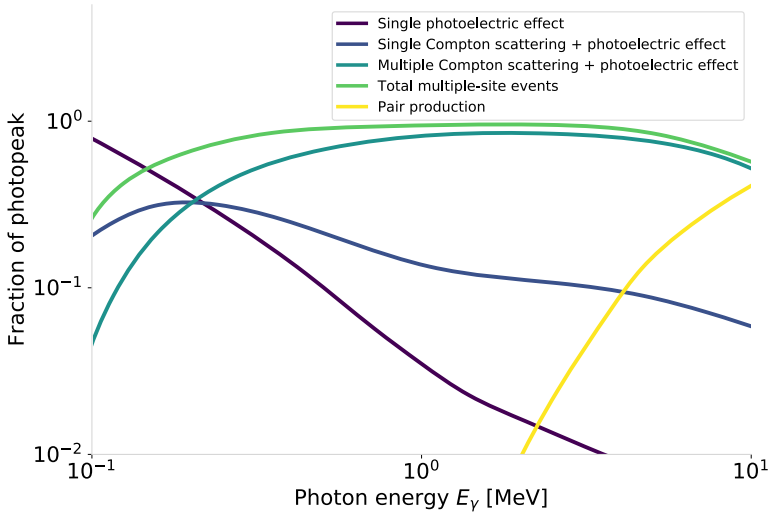

Figure 3.4: Energy dependence of the interaction strength for photon-matter interactions in different channels. Here the example of a cylindrical high-purity Ge detector with a height of 6cm and square cross section is shown. Coloured lines give the fraction of the photo-peak energy, i.e. the full-energy deposition peak, contributed by different energy loss mechanisms. The photoelectric effect dominates up to $\sim 140\,\mathrm{keV}$, pair production from $\sim 3\,\mathrm{MeV}$, and Compton scattering in between. Adopted from Roth et al. (1984).

threshold by (Jauch & Rohrlich 1955)

$$\sigma_{\mathrm{PP}}^{\mathrm{low}} = \frac{1}{12}\alpha\pi r_e^2 Z^2 \left(\frac{E_\gamma}{m_e} - 2\right)^3, \tag{3.12}$$

and in the high-energy limit by

$$\sigma_{\mathrm{PP}}^{\mathrm{high}} = \alpha r_e^2 Z^2 \left[\frac{28}{9}\ln\left(\frac{2E_\gamma}{m_e}\right) - \frac{218}{27}\right]. \tag{3.13}$$

The Z^2 dependence and the monotonic increase with E_γ of the cross-section are particularly noteworthy here. Thus, pair production is especially important within high-Z material and dominates photon-matter interactions at very high photon energies from a few MeV upwards.
The energy dependence in strength of the different energy-loss mechanisms in a 6 cm thick cylindrical Ge detector is shown in Fig. 3.4. This example is very close to the detector type used in the INTEGRAL/SPI instrument, which will be described in more detail in Sec. 3.3.

Gamma-Ray Detection Detectors that utilise the above mentioned interactions of high-energy photons with matter to measure gamma-rays are usually either scintillator-based or semiconductor-based.
In scintillator materials, electrons are excited from the valence band to the conduction band due to the interaction with impinging gamma-rays. When the resulting electron-hole pairs recombine, a photon with lower energy is emitted. This means, so to speak, a translation of the original signal into lower-energy photons. Since the yield of the latter is usually rather low, a scintillation detector is typically composed of a scintillator material coupled to a photomultiplier, which transfers the re-emitted light output into a measurable electronic signal. Besides organic crystals

or plastic scintillators, the most commonly used inorganic scintillator materials are NaI(Tl), CsI(Tl), or $Bi_4Ge_3O_{12}$ bismuth germanate (BGO). The latter has the particular advantage of having a high effective atomic number of $Z_{\text{eff}} = 75$ as well as being one of the densest scintillator materials with $\rho = 7.13\,\text{g}\,\text{cm}^{-3}$. Since the band gap of scintillators is usually of the order of $5 - 9\,\text{keV}$ and therefore their energy resolution reduces to about 10%, they are not suitable for high-resolution gamma-ray spectroscopy. Nevertheless, especially BGO crystals are used for astrophysical measurements as anti-coincidence shield material because of their fast response time (Lichti & Georgii 2001).
The high energy resolution, which is required for gamma-ray spectroscopy, is achieved by semiconductors such as Si or Ge. The latter combines the advantage of a high density of $\rho = 5.33\,\text{g}\,\text{cm}^{-3}$, which increases the photon interaction probability, and a small band gap of 0.67 eV at room temperature, which increases the number of charge carriers per incident photon. This improves the spectral resolution of Ge semiconductors by at least one order of magnitude compared to scintillators. A schematic drawing illustrating the operating principle of a Ge detector is shown in Fig. 3.5.

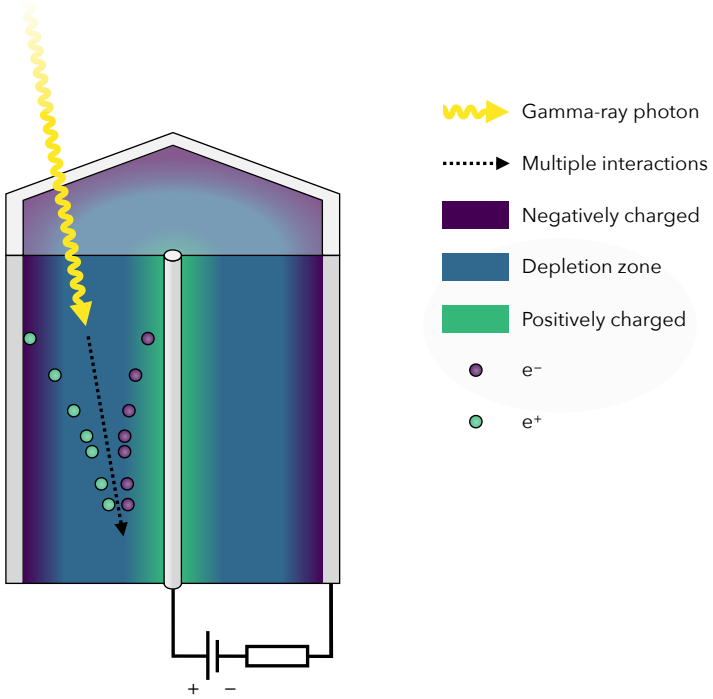

Figure 3.5: Schematic illustration of the operating principle of a Ge detector. An applied reverse voltage creates a depletion zone (*blue*) between the negatively charged (*purple*) anode on the outside and the positively charged anode in a central hole. An incoming photon (*yellow*) creates a multitude of electron-hole pairs which flow to the electrodes and are measured as a voltage pulse proportional to the deposited energy.

In order to use a Ge crystal as detector, an external electric field is applied to generate a zone within the detector, which is overall depleted of charge carriers. This is typically done with a reverse current at high voltage of about $2 - 9\,\text{kV}$. At room temperature electron-hole pairs are thermally excited such that a reverse bias leakage current establishes within the detector diode. In order to avoid such dark current noise, Ge detectors are cooled down to $T \approx 100\,\text{K}$. Gamma-ray photons are preferentially absorbed in the outer regions of the detector by creating a secondary electron. A cylindrical shape of the detector crystal is usually preferred in order to maximise the radiation collection area. As the electron passes through the de-

pletion zone of the detector, it produces a number of electron-hole pairs along its track, which is proportional to the energy of the triggering photon. Because of the applied electric field, the generated electrons and holes drift each in opposite directions to the anode or cathode respectively. In consequence of this flow of charged particles, actual detection is based on the current which is required to re-establish the depletion zone. The accuracy of the signal goes along with the efficiency with which the charges flows to the electrodes. This can be hindered by impurities in the crystal structure caused. As such are induced e.g. by impinging cosmic rays, the charge collection efficiency of space-based detectors in particular degrades over time. Together with other effects, such as the loss of charge carriers or only partial photon energy deposition, this means that a real detector does not reproduce the input spectrum exactly. Instead, the original signal changes due to physical properties of the detector and phonon interactions. The measured signal $D(E)$ therefore corresponds to a convolution of the input signal $S(E)$ with the spectral response function $R(E)$ of the detector,

$$D(E) = S(E) \otimes R(E). \tag{3.14}$$

If the entire energy of the incoming photon is deposited in the detector via the photoelectric effect, it is measured in the photo-peak, i.e. at its exact energy. Nevertheless, each measurement is always additionally blurred according to the intrinsic resolution of the instrument. If, on the other hand, the photon energy is transferred only partly by Compton scattering events to the detector, an energy below the photo-peak is measured. According to Eq. 3.11, this depends on the scattering angle and reaches continuously from $E_{e^-}^{\min} = E_\gamma - E'_\gamma(\theta = 0) = 0$ to a maximum deposited energy

$$E_{e^-}^{\max} = E_\gamma - E'_\gamma(\theta = \pi) = 2E_\gamma \left(\frac{\frac{E_\gamma}{m_e c^2}}{\frac{1}{2} + \frac{E_\gamma}{m_e c^2}} \right). \tag{3.15}$$

In the case of pair production, the detected energy depends in particular on the subsequent interactions of the secondary particles. While they both only deposit their kinetic energy but not their rest mass, the decelerated positron annihilates with an electron in the detector material and thereby produces two gamma-rays at 511 keV each. If these are absorbed, this accounts for the rest masses of the originally produced pair, and the complete photon energy is measured. On the other hand, if one or both of them leave the detector without further interaction, the measured energy is reduced by once or twice $m_e c^2$. This gives rise to a single and double escape peak at 511 keV and 1022 keV below the photo-peak, respectively. The overall resulting spectral features are shown schematically in Fig. 3.6.

Telescope Types In order to construct a gamma-ray telescope from gamma-ray detectors, the latter must be embedded in a system that also provides spatial information in addition to the energy information about incident photons. There are many techniques to achieve this, but the two most used systems are Compton telescopes and coded-mask telescopes. These telescope principles are shown schematically in Fig. ???.

Compton telescopes are based on the kinematics of the Compton effect (cf. Eq. 3.11) and basically composed of two detector modules, a thin and a thick one. Incoming gamma-rays scatter according to the Compton effect in the thin first layer, deposit-

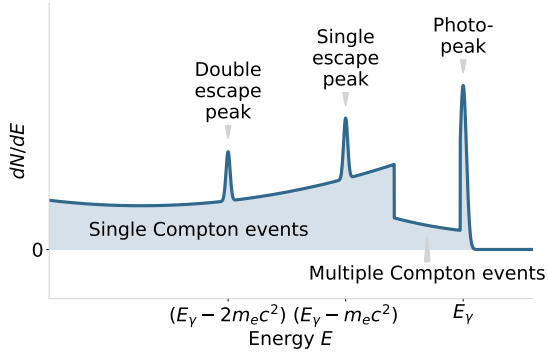

Figure 3.6: Spectral features of a gamma-ray spectrum representing the response of a typical Ge detector. Adopted from Knoll (2010).

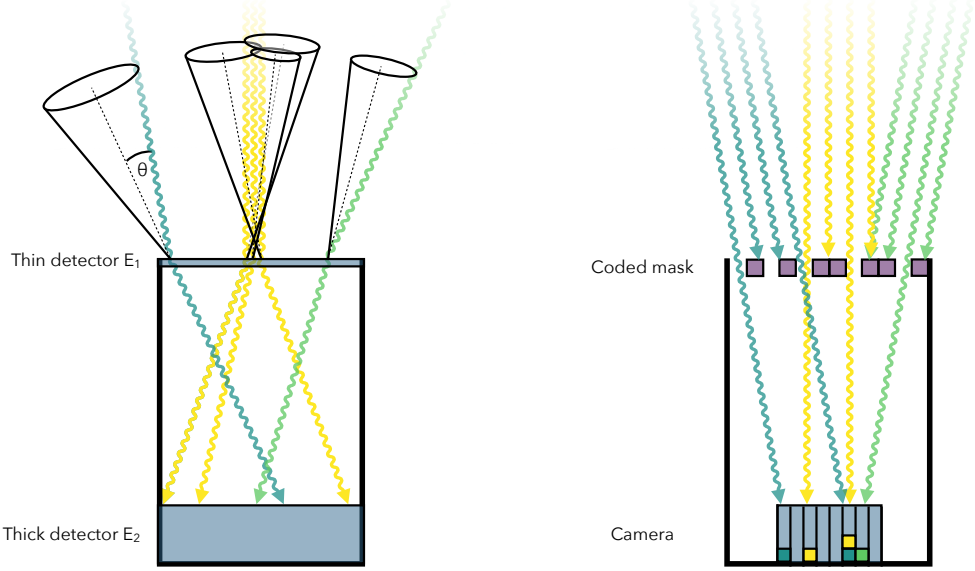

Figure 3.7: Schematic gamma-ray telescope types. *Left:* Compton telescope. It is composed of two detector layers for measuring differential energy E_1 and total energy E_2. From the Compton scattering angle θ a cone for possible photon directions can be projected onto the sky. The intersections of the resulting circles indicate source positions. *Right:* Coded-mask telescope with mask elements shown in *purple*. Sources under different aspect angles cast characteristic shadowgrams onto a position-sensitive camera array. Source positions can be inferred from these characteristic detector patterns, which are shown as counts filling up the camera pixels symbolically with coloured cubes. Photons are represented by wavy lines and detector material is shown in *blue*.

ing energy E_1, and are absorbed in the second module, measuring E_2. Directional information is inferred from the total energy $E_1 + E_2$ and the Compton scattering angle θ. With the limited information of where in the instrument single photons interact, their origins are mapped onto rings on the celestial sphere with each photon having its own directional response. The exceptional advantage of this observational technique lies in the straight-forward imaging information that can be gained from intersections of multiple event circles. With each photon carrying valuable directional information, the large, multi-dimensional data-space can be used for image reconstruction. The most prominent example of this telescope type was COMPTEL aboard the CGRO, with which the first all-sky map of the 1.8 MeV ^{26}Al emission was mapped (cf. Fig. 1.1) with a spectral resolution of $\sim 9\%$ full width at half maximum (FWHM) at 1.3 MeV and an angular resolution between 1° and 2° (Schönfelder et al.

1993; Oberlack et al. 1996; Plüschke et al. 2001). This mission ended in 2000.
The second major telescope type for measuring gamma-rays at MeV energies is based on the coded-mask technique. Such telescopes are mainly composed of a position-sensitive camera and a mask, consisting of a characteristically coded array of transparent and opaque elements. The mask is situated in above the camera inside a shielded collimator tube. Incoming celestial gamma-rays are partially absorbed by the mask and cast a characteristic shadow pattern or shadowgram onto the camera. The latter can be constructed e.g. of an array of individual solid-state detectors. The shadowgram is depending on the source distribution on the sky and the aspect angle of the instrument with respect to these sources. In this way, information about the emission morphology can be reconstructed from the characteristic variations in the shadow pattern. The main advantage of this telescope type is that a high spectral resolution can be achieved by using e.g. cryo-cooled Ge detectors. Currently the only space-based telescope operating in the nuclear line gamma-ray regime is SPI aboard INTEGRAL, which utilises this coded-mask technique. It is used for providing the empirical basis in this thesis and is therefore described in more detail in the following section.

Essentials

Cosmic gamma-ray measurements yield signals of isotopic properties unbiased by thermal and dynamical phases of the ISM. The measurement techniques rely on the photoelectric effect, Compton scattering and pair production. Thereby, the main observational challenges are that the Earth's atmosphere is opaque and the telescope materials are usually mostly transparent to gamma-rays. Thus, space-space based telescopes are necessary.

3.3 INTEGRAL/SPI

The International Gamma Ray Astrophysics Laboratory (INTEGRAL) is a scientific satellite mission by the ESA that was launced on 17 October 2002. It was designed as a follow-up mission to NASA's CGRO to observe the high-energy universe. It can be considered a great success, since it was originally planned with a mission duration of only three years, with a possible two-year extension, and is currently still in service after about 17.5 years and currently extended until 31 December 2021 due to excellent scientific results in the field of gamma-ray astrophysics.
A high-inclination and high-eccentricity orbit of the satellite was chosen in order to minimise the passage time through the Van Allen radiation belts. Particles from Solar winds or cosmic rays are captured by the terrestrial magnetic field and accumulate in these belt-like tori surrounding the Earth. While the inner belt between about 3000 and 6000 km contains mostly protons, mainly electrons form the outer belt, which extends to an altitude of about 25000 km. The enhanced particle densities in these regions increases the radiation-induced damage of instrument detectors and electronic systems. Thus, an elliptical orbit with apogee and perigee of 9000 km and 154000 km was chosen in order to extend the time pent outside these regions. The orbit is inclined by 52.5° with respect to the Earth's rotation axis and it takes the satellite about 72 hours to complete one revolution. This configuration is shown

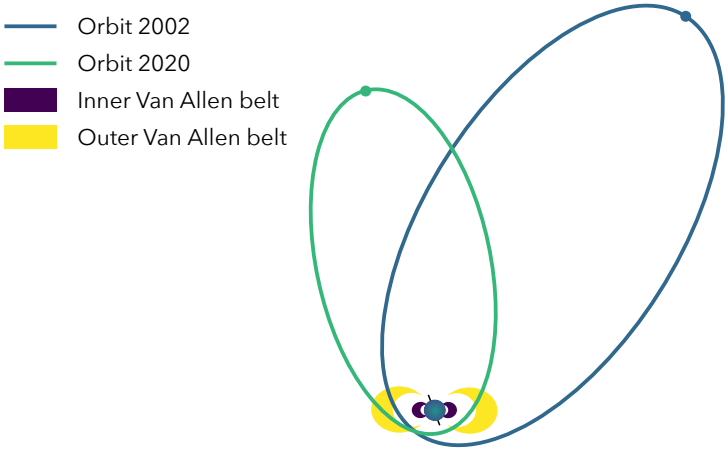

Figure 3.8: Schematic orbit of the INTEGRAL satellite in 2002 (*purple*) and in 2020 (*green*). It is chosen to be highly elliptical in order to reduce the passage time through the Van Allen radiation belts (*purple* and *yellow*).

schematically in Fig. 3.8. Data can typically be taken between orbital phases 0.1 and 0.9, calculated from the perigee as origin. In 2015, after 1500 revolutions, the orbit was reduced to perigee and apogee of 7206 km and 142, 550 km with an orbital period of 64 hours. The inclination has also changed to an almost polar orbit.
The INTEGRAL platform houses four scientific instruments. The gamma-ray Imager on-Board the INTEGRAL Satellite (IBIS), the Joint European X-Ray Monitor (JEM-X), an Optical Monitoring Camera (OMC), and the Spectrometer on INTEGRAL (SPI). Since the analysis in this thesis is based on the latter instrument, the technical description in the following will also be focussed on SPI. A sectional sketch of this instrument is depicted in Fig. 3.9. The critical components for sci-

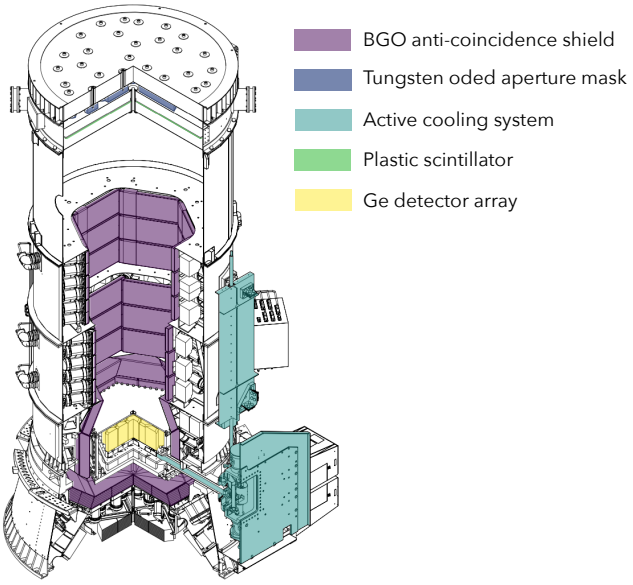

Figure 3.9: Sectional schematic of the SPI instrument. The BGO anti-coincidence shield is composed of collimator rings above the camera as well as side and bottom shields around the detector array. The tungsten coded mask elements have a thickness of about 5 cm with a 3 mm thin plastic scintillator positioned below. The cooling system operates by four Stirling cycle cooling machines tied to passive radiators. This is connected directly with the Ge detectors cold finger and thereby optimally cooled to 85 K. The high-purity Ge detectors have a geometrical area of 500 cm^2 and 7 cm height. Adopted from Mandrou et al. (2002).

entific purposes are the Ge detector array, the tungsten coded mask, and the BGO anti-coincidence shield (ACS), which will be described in Sec. 3.3.1, Sec. 3.3.2, and Sec. 3.3.3 respectively. The main technical characteristics of the spectrometer are summarised in Tab. 3.1.

Table 3.1: Technical characteristics of the SPI instrument. Adopted from Siegert (2017) following Vedrenne et al. (2003), Winkler et al. (2003), Roques et al. (2003), and Siegert et al. (2016).

Property	SPI characteristic
Angular resolution (FWHM)	2.7°
Detectors	19 high-purity Ge detectors ($T \approx 85\,\mathrm{K}$)
Detector area	Geometrical: $508\,\mathrm{cm}^2$; effective: $10 - 100\,\mathrm{cm}^2$
Detector thickness	7 cm
Energy range	$20 - 8000\,\mathrm{keV}$
Field of view	Fully coded: $16° \times 16°$; partially coded: $31° \times 31°$
Power supply	Average: 110 W, Maximum: 385 W
Source location (radius)	10 arcmin
Spectral resolution (FWHM)	2.1 keV at $E_\gamma = 511\,\mathrm{keV}$; 3.16 keV at $E_\gamma = 1809\,\mathrm{keV}$
Total mass	1228 kg

3.3.1 Detector Array

The central element of SPI are 19 individual high-purity Ge detector detectors, which are arranged and combined into one camera array. Each detector has a hexagonal face shape with side length 3.2 cm, which gives a total geometrical are of the camera of $508\,\mathrm{cm}^2$. The height of each detector is 6.94 cm. This results in a total effective area of the SPI camera of $44\,\mathrm{cm}^2$ for photon energies at 1.8 MeV. The arrangement of the detectors is shown in the left panel of Fig. 3.10. They are numbered consecutively from 0 to 18 and for the sake of simplicity accordingly designated as Det00 to Det18. Each charge pulse triggered by a photon is read out individually by separate

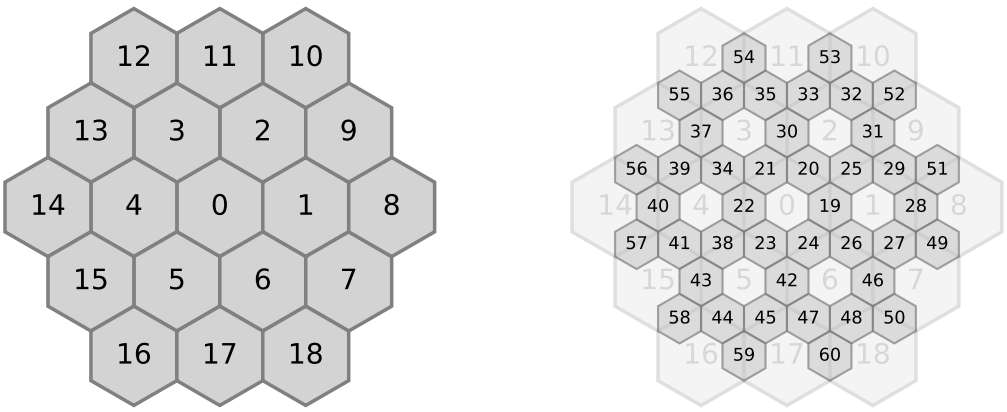

Figure 3.10: Schematic face-on view of the SPI detector array. *Left:* Each hexagon represents on high-purity detector crystal encapsulated in Al and numbered as shown. These physical detectors measure single photon interactions. *Right:* Pseudo-detectors for the measurement of double photon interactions in adjacent detectors. These are conceptual analysis units that result from the virtual interconnection of two adjacent physical detectors, shown in light grey in the back, and are represented by small small hexagons on the respective connecting line.

Table 3.2: SPI detector failures. Given are the IDs of failed single and double detectors and the date of failure as well as the respective instrument time as INTEGRAL Julian Date (IJD) and satellite revolution number. Adopted from Dubath et al. (2015, 55).

Single detector	Double detectors	Date	IJD	Revolution
02	20,25,30,31,32,33	2003-12-06	1435.41635	140
17	45,47,59,60	2004-07-17	1659.46000	214 – 215
05	23,38,42,43,44	2009-02-19	3337.50000	775 – 776
01	19,21,22,24	2010-05-27	3799.66740	929 – 930

readout electronics at each detector. If the photon energy is deposited in one physical detector, this is read out as a single event count. However, photons can also only partially deposit their energy in one detector and then be Compton-scattered into an adjacent detector, where they deposit the remaining energy. In order to be able to use these signals as well, adjacent detector crystals are combined into pseudo detectors that register such double events. This results in 42 double event pseudo-detectors from the combinations of adjacent detectors, which are accordingly numbered from Det19 to Det60, as shown in the right panel of Fig. 3.10. It is important to stress that these are conceptual units of analysis resulting from the virtual combination of adjacent physical detectors.
Constant penetration of the instrument by cosmic rays induces irregularities and defects in the lattice structure of the Ge crystals. This decreases the overall charge collection efficiency and leads to a gradual deterioration of the detectors over time because charge carriers are trapped in material defects and do not reach the electrodes. In order to restore the lattice structure and maintain the high energy resolution, the detector array is heated to 378 K about twice a year (Lonjou et al. 2005; Fahmy et al. 2008). Such an annealing period lasts for about two weeks, during which no scientific data are taken.
During the course of the mission four detectors have ceased to function properly. The detector failures are listed in Tab. 3.2. These detectors are now disabled, which affects the instrument response, since double events are erroneously detected as single events with only a part of the total energy after the failure of one of the physical detectors.

3.3.2 Coded Mask

In order to use the detector array as a gamma-ray telescope, directional information must also be imposed on the incoming photon signals. For this purpose SPI utilises the coded mask technique described in Sec. 3.2.2. Therefore a coded tungsten mask is situated 171 cm above the Ge detector array. It consists of 63 elements made of W with the same hexagonal surface dimensions as the Ge detectors and a thickness of 3 cm. They are arranged in a 120°-rotational symmetric honeycomb structure with 64 omitted elements as shown in Fig. 3.11. The ratio of mask elements to detector pixels, i.e. individual detector determines the angular resolution of SPI of about 2.7° with a point-source location accuracy of $\sim 0.1°$. The mask has a diameter of 72 cm, which leads to a fully-coded field of view of $16° \times 16°$ and a partially-coded field of view of $31° \times 31°$. Since the mask blocks about 50% of the incoming photons, the geometrical detection area is reduced significantly to effectively 10–100 cm^2. This range results from the fact that photons with higher energy also have a higher

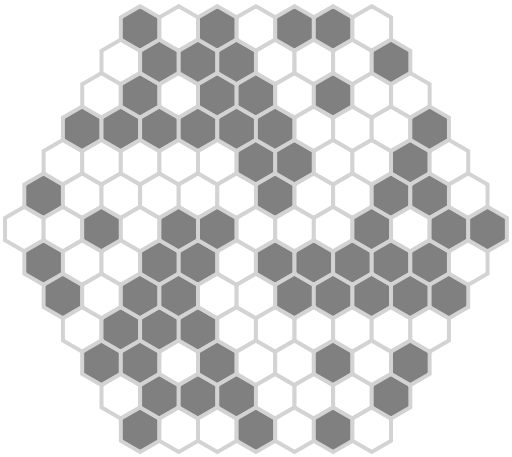

Figure 3.11: SPI coded mask pattern. Grey hexagons represent 63 opaque mask pixels made of 3 cm thick W. They are a arranged in a 120°-rotational symmetric honeycomb structure with 64 transparent pixels.

probability to pass the detector without interaction.

3.3.3 Anti-Coincidence Shield

Since the coded mask only covers a relatively small solid angle, interference signals from high-energy photons and cosmic rays from other directions must be minimized in order to isolate the signal from celestial sources as far as possible. For this purpose, the instrument shielded by an anti-coincidence shield (ACS) made of 91 BGO scintillator crystals. It is composed of a veto shield below the Ge-detector array, a side shield framing the detectors, and two collimator ring assemblies arranged on top of each other above the camera as shown in Fig. 3.9. These sub-units have a varying thickness between 1.6 cm on top and 5 cm at the bottom. BGO has an attenuation cross section for photon energies around 1.8 MeV of $4.7 \times 10^{-2}\,\mathrm{cm^2\,g^{-1}}$ (Berger et al. 2010; Hueso-González et al. 2015). With a density of $\rho = 7.13\,\mathrm{g\,cm^{-3}}$, and an effective atomic number $Z_{\mathrm{eff}} = 75$, this gives a transmission probability through the 5 cm thick SPI side shield for perpendicularly-incident photons of $\sim 18\%$. A comparison of the transmission probabilities for Photons with $E_\gamma = 1809\,\mathrm{keV}$ and $E_\gamma = 511\,\mathrm{keV}$ is shown in Fig. 3.12. This is dependent on the incidence angle and is a maximum for perpendicularly impinging photons.
Each of the BGO crystals is coupled to a photomultiplier tube in order to measure the scintillations induced by incident gamma-rays. The resulting voltage pulses are used to trigger veto-signals within a coincidence window of $\sim 160\,\mu\mathrm{s}$ for photons penetrating the instrument from angles outside the field of view (Roques et al. 2003). Here the count rate ranges between about 5×10^4 and $10^5\,\mathrm{ph\,s^{-1}}$. It follows overall all an intensity variation correlated with the Solar cycle with prominent peaks during Solar flares (Diehl et al. 2018b). Overall, the ACS vetoes counts with a rate of $7 \times 10^4\,\mathrm{s^{-1}}$ versus a count rate of the Ge detectors of about $50\,\mathrm{s^{-1}}$ (Siegert 2017).
Although the ACS provides no further directional information beyond the position of individual crystals, it has a large effective area of $\sim 1\,\mathrm{m^2}$ and a fast response time. Therefore, it can also be used as an independent scientific instrument, for example to detect gamma-ray burst (GRB) signals (von Kienlin et al. 2004; Larsson et al. 2004).

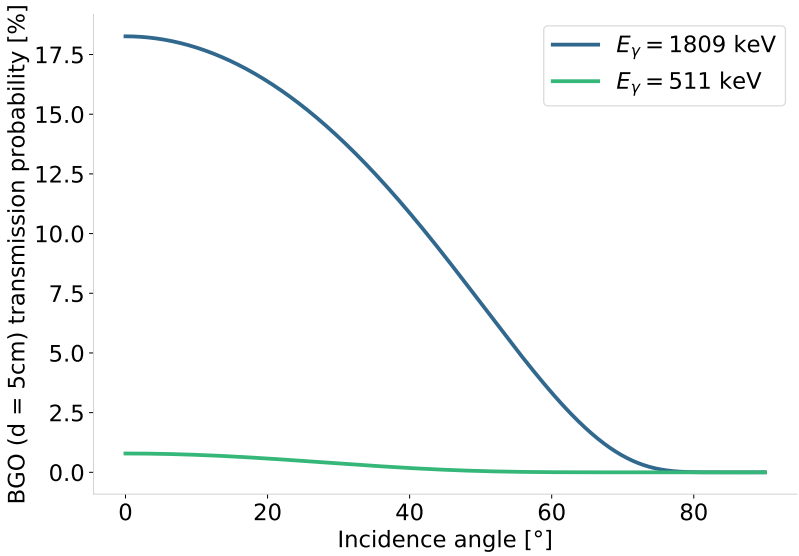

Figure 3.12: Transmission probability of gamma-ray photons with $E_\gamma = 1809\,\mathrm{keV}$ and $E_\gamma = 511\,\mathrm{keV}$ for different incident angles on BGO crystals with thickness $d = 5\,\mathrm{cm}$. A perpendicular incidence angle corresponds to 0°.

In addition to the BGO ACS, the veto system is supplemented by a 0.5 cm thin plastic scintillator assembly as anti-coincidence filter especially for energies near 511 keV. It is installed below the coded mask and provides a modest increase in sensitivity (Vedrenne et al. 2003) of the 511 keV line detection around $5 - 6 \times 10^{-5}\,\mathrm{ph\,cm^{-2}\,s^{-1}}$ for $\sim 1\,\mathrm{Ms}$ of exposure time (Siegert et al. 2016).

Essentials

INTEGRAL/SPI is a coded-mask gamma-ray spectrometer with high spectral resolution of 3.16 keV at 1.8 MeV and a spatial resolution of $\sim 2.7°$. It is currently the only space-based instrument capable of targeted and resolved measuring gamma-rays at MeV energies. Its camera consists of 19 high-purity Ge detectors which are characteristically shadowed by a tungsten mask and shielded by an ACS from cosmic-ray background.

3.4 SPI Data Analysis

In Fig. 3.13, a mission integrated spectrum of the SPI camera is depicted. It shows the total counts measured as single or double detector events over the course of $\sim$ 17.5 yr of operation and 2131 orbit revolutions. This is obtained after pre-processing of the raw data by INTEGRAL's Science Data Centre (ISDC) including an energy calibration and sorting the data in 0.5 keV wide energy bins for each detector. The spectrum represents typically more than 99% instrumental background, even after the counts sorted out by the ACS. The main challenge in SPI data analysis is therefore the separation of comparatively weak celestial sources from an extremely dominant instrumental background. Overall, the data analysis is therefore based on two key assumptions described by Diehl et al. (2018b): First, the signal from celestial

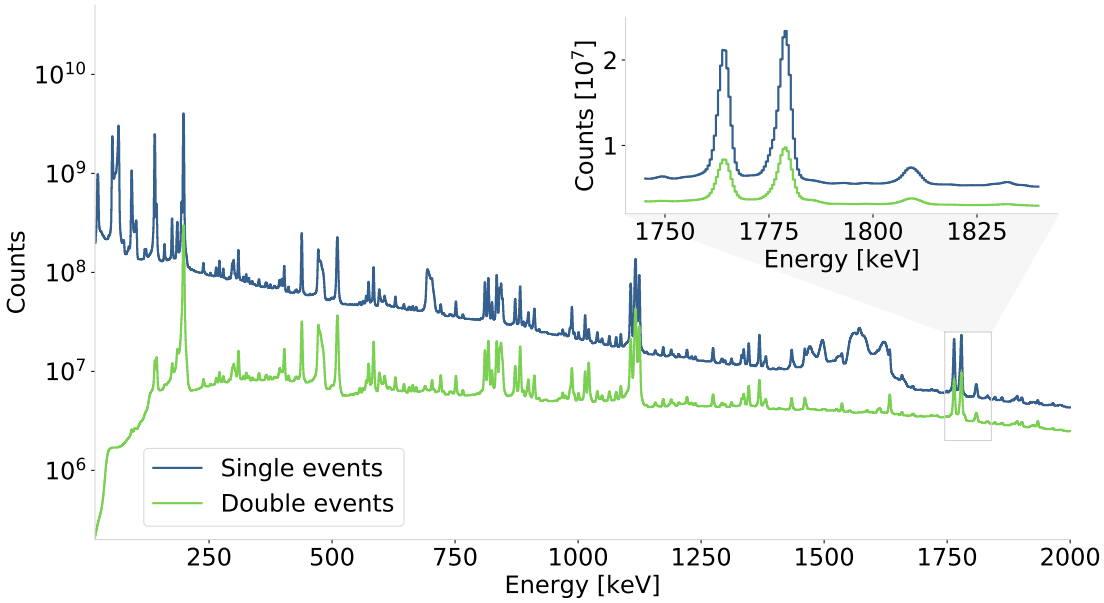

Figure 3.13: Mission integrated spectrum of SPI single (*blue*) and double (*green*) event counts after $\sim$ 17.5 yr of operation and 2131 orbit revolutions. Shown is the low energy range 20–2000 keV with a bin width of 0.5 keV and with an zoomed inset from 1745–1840 around the ^{26}Al emission line on linear scale. A multitude of emission lines can be seen on top of a continuous background. There are overall less double event counts with an increasing fraction towards higher energies. The electronic noise in the region between 1400–1700 keV is more prominent for single than for double events.

sources follows the characteristic mask shadowing pattern which is dependent on the source morphology and which varies with the instrument aspect angle. Second, the background signal is mostly inherent to the instrument, which means that it imprints a intensity pattern on the detectors which is also characteristic but independent of the coded mask and which does not vary with small spacecraft re-orientations. Thus, here the model description

$$m_k = \sum_j R_{jk} \sum_{i=1}^{N_\mathrm{I}} \theta_i M_{ij} + \sum_{i=N_{\mathrm{I}+1}}^{N_\mathrm{I}+N_\mathrm{B}} \theta_i B_{ik} \tag{3.16}$$

is used for the measured instrument counts in each particular energy bin k for N_I sky and N_B background model components (Strong et al. 2003, 2005; Siegert et al. 2019). For each image element j, the celestial source model intensities M_{ij} are convolved with the image response function R_{jk}. The parameters θ_i scale the intensities for all model components i. A detailed description of celestial emission models will be given in Sec. 3.4.2. The background contributions B_{ik} are independent of the mask and the spacecraft orientation but vary on different time scales and over the entire mission due to the solar cycle, nuclear build-up processes, solar flares, and radiation belt transits. A detailed background model taking these variations into account has been obtained from spectral fitting of the entire mission data (Diehl et al. 2018b), which is then adapted to the particular data set subjected to a specific analysis (Siegert et al. 2019). This method of self-consistent background modelling is adopted in this thesis and summarised in Sec. 3.4.1.

3.4.1 Self-Consistent Background Modelling

In SPI observations, typical source intensities are abiyt $10^5\,\mathrm{ph\,cm^{-2}\,s^{-1}}$, which leads to about 2500 source counts within a usual observation period of 1 Ms. In the same time SPI measures on average a total number of $\sim 3 \times 10^7$ event counts (Diehl et al. 2018b). This means that despite the anti-coincidence devices and an electronic pulse-shape discriminator system, SPI data are overlaid by a huge instrumental background. This means that due to statistical limitations simple background subtraction is not feasible for most common source types (Siegert 2017; Siegert et al. 2019). Thus, it is of utmost importance to properly model the huge instrumental background in order to be able to accurately measure celestial sources. Therefore, this thesis follows the self-consistent background modelling approach outlined in detail by Diehl et al. (2018b) and Siegert et al. (2019) following Strong et al. (2005). The background originates mainly from the instrument itself. Particles with energies between MeV and GeV from the Van Allen belts, from the Earth albedo, or cosmic rays penetrate the satellite. Direct interactions with the detectors are vetoed by the ACS or the pulse-shape discrimination system. Nevertheless, a large background signal is caused because these particles also excite atoms and nuclei of the spacecraft materials due to collisions. Thus, secondary causes of delayed gamma-ray emission from excited material arise, such as build-up of long-lived radioactive isotopes of e.g. ^{22}Na, ^{56}Zn, or ^{60}Co. The excitation and subsequent de-excitation or decay of a multitude of radioactive isotopes causes the forest of emission lines in Fig. 3.13. This lies on a continuum which is decreasing towards higher energies. It is mainly produced by bremsstrahlung from secondary particles.

Spectral Description The continuum component is modelled as power-law distribution (Diehl et al. 2018b)

$$C(E; \alpha, c_0) = c_0 \left(\frac{E}{E_m} \right)^{\alpha}, \tag{3.17}$$

normalised to the central energy E_m within the respective region of interest. The emission lines deviate from a regular Gaussian profile

$$G(E; E_0, \sigma) = A_0 \exp \left[-\frac{(E - E_0)^2}{2\sigma^2} \right] \tag{3.18}$$

with amplitude A_0, mean energy E_0, and width σ because of the detector degradation effects mentioned in Sec. 3.3.1. The trapping of charge carriers in defects of the detector crystal's lattice structure can reduce the voltage pulse per event which manifests as the tendency to count photons at lower energies with increasing degradation. This can be described by a convolution of a Gaussian profile with a one-sided exponential

$$T(E; \tau) = \frac{1}{\tau} \exp \left(\frac{E}{\tau} \right) \tag{3.19}$$

with the degradation parameter τ. The instrumental degradation for SPI was estimated by Kretschmer (2011) and Siegert (2017) to be on average $\tau \sim (1.05 \pm 0.03)\,\mathrm{keV}$. This results in an overall description of the emission line shape in SPI

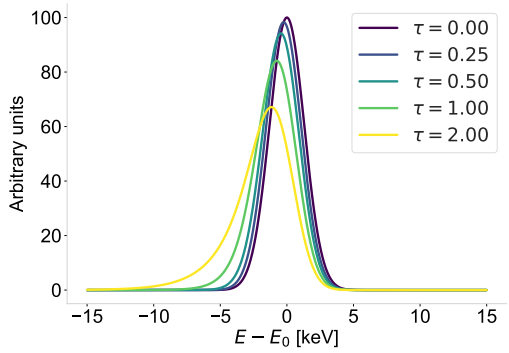

Figure 3.14: Degraded Gaussian line shape according to Eq. 3.20.The peak shift towards lower energies increases with the degradation parameter τ.

measurements as (Kretschmer 2011; Siegert 2017; Diehl et al. 2018b)

$$\begin{aligned} L(E; E_0, \sigma, \tau) &= (G \otimes T)(E) \\ &= \sqrt{\frac{\pi}{2}} \frac{A_0 \sigma}{\tau} \exp\left[\frac{2\tau(E - E_0) + \sigma^2}{2\tau^2}\right] \operatorname{erfc}\left[\frac{\tau(E - E_0) + \sigma^2}{\sqrt{2}\sigma\tau}\right], \end{aligned} \tag{3.20}$$

with the complementary Gaussian error function $\operatorname{erfc}(x) = 1 - \operatorname{erf}(x)$. This shape is shown graphically in Fig. 3.14. An approximation for the resulting peak energy is given by (Siegert 2017)

$$E_{\text{peak}} \approx E_0 - \tau, \tag{3.21}$$

where E_0 is the peak energy of a regular Gaussian. While the regular Gaussian in Eq. 3.18 has a FWHM of $\Gamma = 2\sigma\sqrt{2\ln(2)}$, this changes for the degradation-affected line to (Kretschmer 2011)

$$\Gamma_L \approx \Gamma \left[a_0 + \sqrt{(1 - a_0)^2 + \left(\frac{a_1 \tau}{\Gamma}\right)^2}\right], \tag{3.22}$$

with the fitted constants $a_0 = 0.913735$ and $a_1 = 0.710648$. The intensity of a line with its shape following Eq. 3.20, i.e. the area under the curve, is calculated by (Siegert 2017)

$$F = \int_{-\infty}^{+\infty} L(E)\, dE = \int_{-\infty}^{+\infty} (G \otimes T)(E)\, dE = \int_{-\infty}^{+\infty} G(E)\, dE = \sqrt{2\pi}\, A_0 \sigma, \tag{3.23}$$

which is identical with that of a regular Gaussian line. This means, the total line flux is conserved and does not change due to the degradation. This is the case because the trapping of charge carriers only decreases the measured voltage from a triggering event. However, the pulse as such is retained. In other words, the count number remains the same, only the corresponding energy potentially decreases.
Individual spectral features can be disentangled and identified most clearly in the cumulative spectrum of the entire mission, which is shown in Fig. 3.15 for the region 1745–1840 keV around the ^{26}Al emission line. The spectral features represented according to Eq. 3.17 or Eq. 3.20 and fitted to the cumulative spectrum are shown as well. Associations of individual lines with the decay of radioactive lines follows Diehl et al. (2018b).
Since the measured photon counts follow the Poisson distribution, the likelihood of

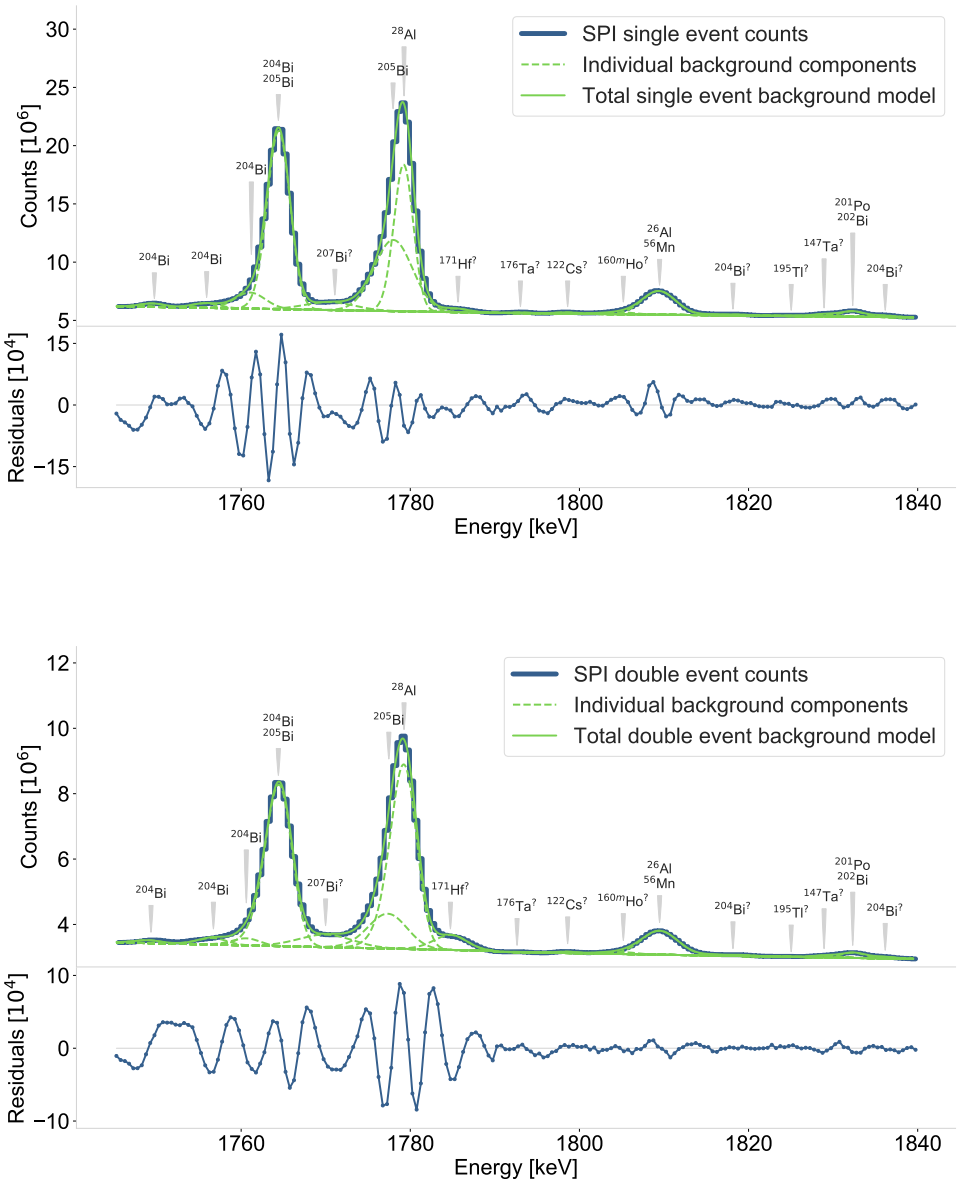

Figure 3.15: *Upper:* SPI instrumental background fit (green solid line) to the total spectrum of single detector counts from 13 yr of the INTEGRAL mission (thick blue line) in the energy range 1745–1840 keV around the ^{26}Al β^+-decay line at 1809 keV. It is composed of nuclear lines on top of a continuum (green dashed line). The fit residuals are shown in the lower part of the figure (thin blue line). Background line identifications with decay lines of radioactive isotopes were obtained following Diehl et al. (2018b). Speculative isotope associations are marked with question marks. *Lower:* Same as upper figure for SPI double detector events.

a set of model parameters θ_i in Eq. 3.16, given a measured data set D with n data points, is calculated by the full Poisson likelihood

$$\mathscr{L}(\boldsymbol{\theta}|D) = \prod_{k=1}^{n} \frac{m_k^{d_k} \exp(-m_k)}{d_k!}, \tag{3.24}$$

where d_k is the measured number of instrument counts and m_k is the model predicted value as described in Eq. 3.16. To determine the parameter set $\boldsymbol{\theta}$ that maximises the likelihood, we use the negative logarithm of the Poisson likelihood dropping the

data-dependent term, which is commonly referred to as Cash statistic (Cash 1979)

$$\log(\mathscr{L}(\boldsymbol{\theta}|D)) \approx -2\sum_{k=1}^{n}[m_k - d_k \log(m_k)]. \tag{3.25}$$

In this thesis, for the first time a detailed treatment of double events is included for the analysis of the 1.8 MeV line. The individual spectral components of double events and single events resemble each other overall. Interestingly, the line shapes seen with double events seem to show an increased degradation compared to that from single events. This phenomenon will be discussed further in Sec. **??**. The overall ratio $R_{S/D}$ of measured single to double events is estimated by the relative line fluxes of the three most prominent line blends at 1764 keV, 1779 keV, and 1810 keV for each annealing period. Fig. 3.16 shows that this ratio increases over the course of the mission from $R_{S/D} \approx 1.7$ in the early phases to $R_{S/D} \approx 2.9$ after 17.5 yr.

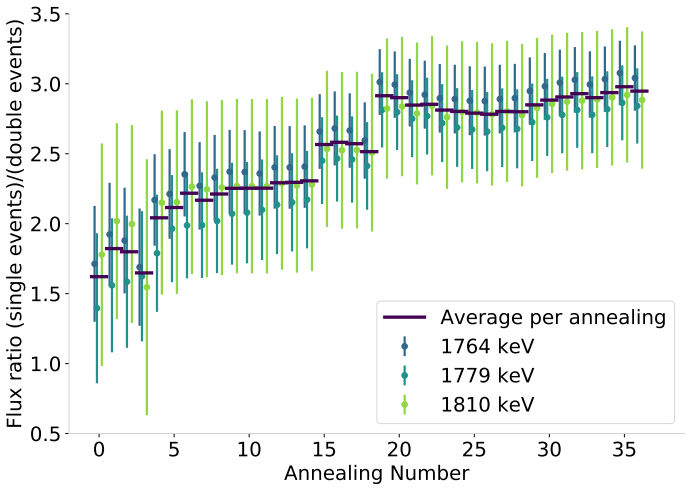

Figure 3.16: Ratio of single to double events per annealing period for the three most prominent background lines at 1763 keV, 1797 keV, and 1810 keV. The colour scale indicates the detector annealing number with a constant fit for each annealing period shown as coloured horizontal line.

Background Detector Pattern The SPI data space has overall four characteristic dimensions: counts per energy, time, and detector. For the differentiation of the background from the sky emission, which is decisive in further data analysis, it is crucial that these two components differ not only in general spectral terms, but show also characteristic variations in time and detector space. The relative intensity ratios of the individual detectors during the first observational epoch, i.e. before the first detector failure during revolution 140, is shown in Fig. 3.17 for the strong blended background line from ^{204,205}Bi at 1764 keV. Detectors in the inner parts of the array show overall lower background line intensities than those on the edges. This clearly reflects the origin of this line in the material surrounding the detectors. Thus, the inner detectors are shielded by the outer ones. The relative intensity variations lie on average in a range between −0.75 and 1.23. In principle a similar background pattern is seen the detected double events shown in the lower panel of Fig. 3.17. This was expected because the background photons originate from the same processes and are only measured via a different interactions in the detectors.

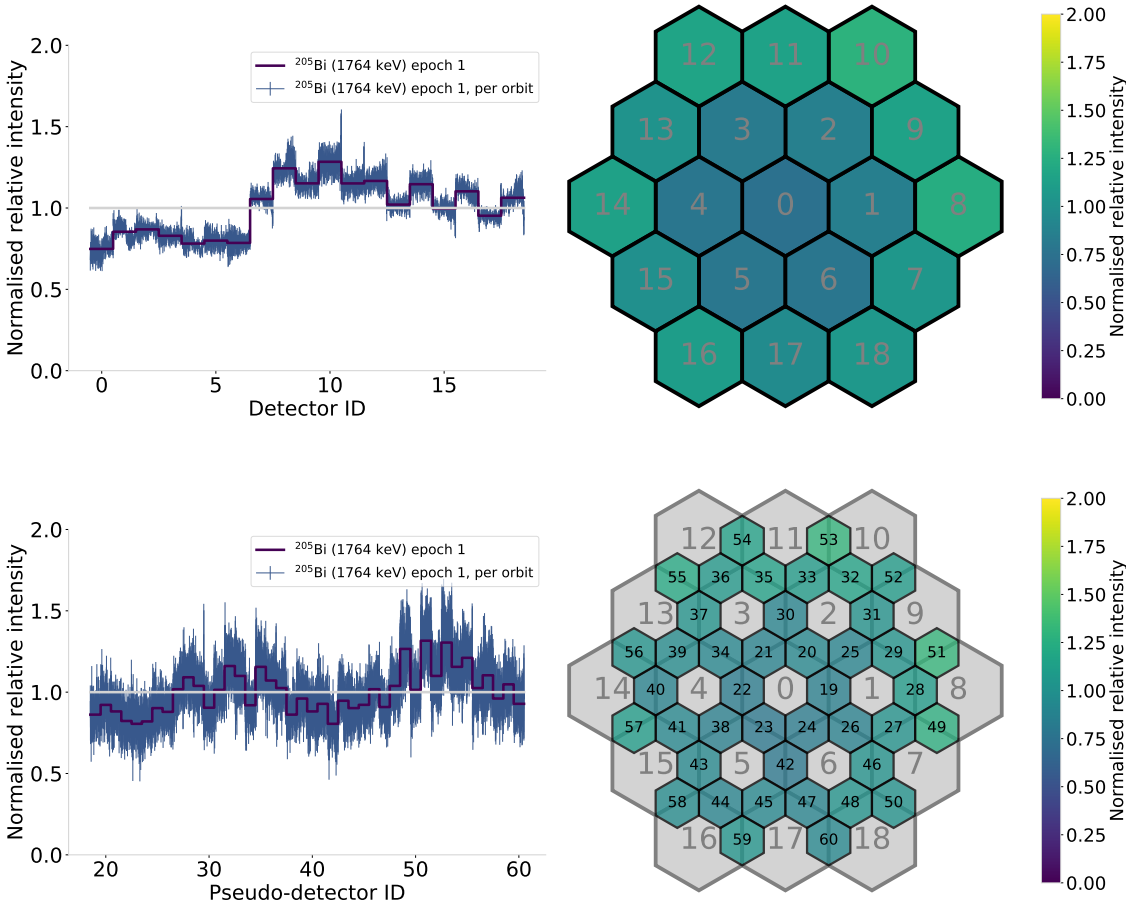

Figure 3.17: SPI detector patterns for the prominent background line from ^{204,205}Bi at 1764 keV. *Upper:* Relative intensity pattern of single Ge detectors. *Lower:* Relative intensity pattern of double-event pseudo detectors.

The relative ratios cover a similar range between 0.80 and 1.32. The comparison of the background intensity pattern projected on a face-on diagram of the detectors on the right side of Fig. 3.17 shows that this generally more smeared out for double than for single events. Additional time information is added to the left graphs in Fig. 3.17 by blue error bars. These indicate the intensity ratios for each revolution between 43–140 in the first epoch individually and are larger for double events because, as shown in the previous paragraph, their count rate is at least a factor of 1.7 lower than that of single events. It illustrates the crucial fact that the relative background detector ratios remain basically constant over time. This is reasonable because of their origin in satellite materials, which also stay spatially constant with respect to the detectors.

Nevertheless, its absolute intensity as well as the particular shape of spectral features changes over longer periods of time reflecting variations due to the Solar cycle, Solar flares, radiation belt transits, radioactive build-up, or detector annealings. Thus, the spectral background model components, as defined from the full-mission spectrum, have to be rescaled on an adequate time scale to properly represent these temporal variations of the background on shorter timescales.

For the ^{26}Al analysis, half-year intervals for the background normalisation corresponding to annealing periods, in addition to detector failure times have been shown by Siegert et al. (2019, Sect. 5.1.2) to be the optimal choice for renormalisation

nodes. Therefore, it is adopted in the analysis for this thesis. Short-term variations are taken into account and modelled according to the saturated detector events tracking these at high statistical precision (e.g. Jean et al. 2003).

3.4.2 Fitting of Celestial Emission Models

The image response function (IRF) of the SPI detectors for celestial signals is characteristically shaped by the coded mask of SPI. It is shown in Fig. 3.18 for photon energies of 1809 keV. It is clearly visible that higher-energetic photons are more

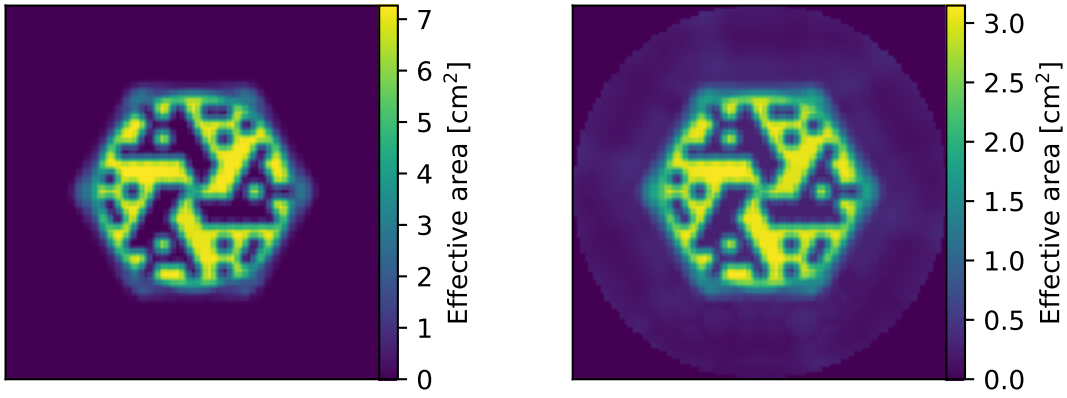

Figure 3.18: SPI IRFs for Det00. *Left:* IRF for photons with $E_\gamma = 509.25$ keV. *Right:* IRF for photons with energy $E_\gamma = 1902.75$ keV.

likely to penetrate through the mask elements and the side shields from outside the field of view. A celestial source, e.g. a point source in the zenith vertically above the detector plane, appears under a different aspect angle for each detector. According to the shadowing of the mask elements, this changes the effective area per detector. This results in a characteristic detector pattern. Since the permeability of the tungsten elements and the detector crystals is energy dependent, this pattern also varies with energy, which is shown in Fig. 3.19. The slice in energy space for $E_\gamma = 1809$ keV is highlighted in the figure. In the first observational epoch, with all detectors working, this leads to a normalized intensity pattern as shown in Fig. 3.20. With a circularly altering pattern of three exposed and three shadowed detectors It clearly represents the direct projection of the innermost mask elements shown in Fig. 3.11 onto the detector array. It shows a much higher contrast between 0.16 and 1.86, which is much higher than for the background detector pattern in Fig. 3.17. The lower panel shows the detector pattern of the 42 double event pseudo-detectors for the same celestial source and with the same overall contrast. It follows overall a similar but flattened pattern, as the contrast between neighbouring detectors levels out in the respective double detector.
SPI typically uses a dithering method for observations, i.e. an observation technique following a 5×5 rectangular grid of pointings on the sky with 2.1° separation between each step. A pointing denotes an observational unit between 30–60 min within which the instrument is oriented towards a particular sky direction. As the satellite changes its orientation, the aspect angle of each detector and therefore the mask

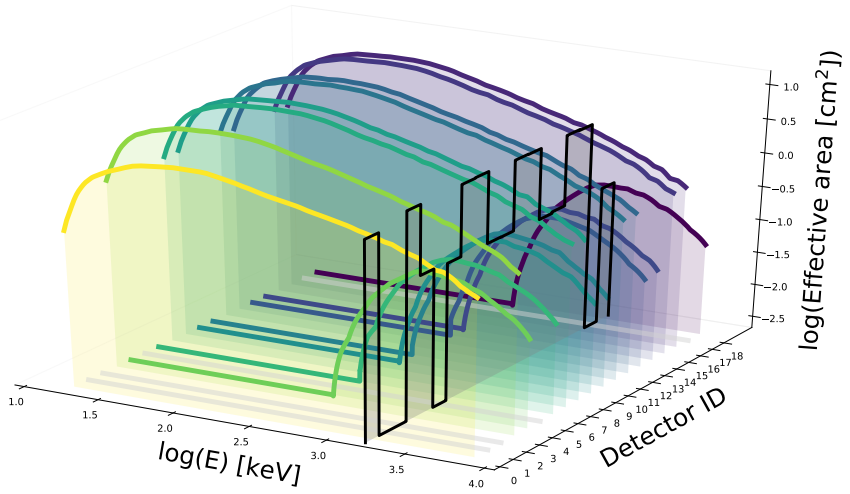

Figure 3.19: Effective area of all 19 SPI detectors for a point source at zenith position above the mask. The difference in pattern between detectors is due to shadowing effects of the coded mask. This implies information about the source position because it varies characteristically with the viewing angle under which the source is observed. A representative slice in energy space shows the effective area detector pattern for photons with 1809 keV energy. Effective areas for shadowed detectors have been flattened to a lowest value of $10^{-2.5}$ cm^2 for better readability. Failed detectors are shown in grey.

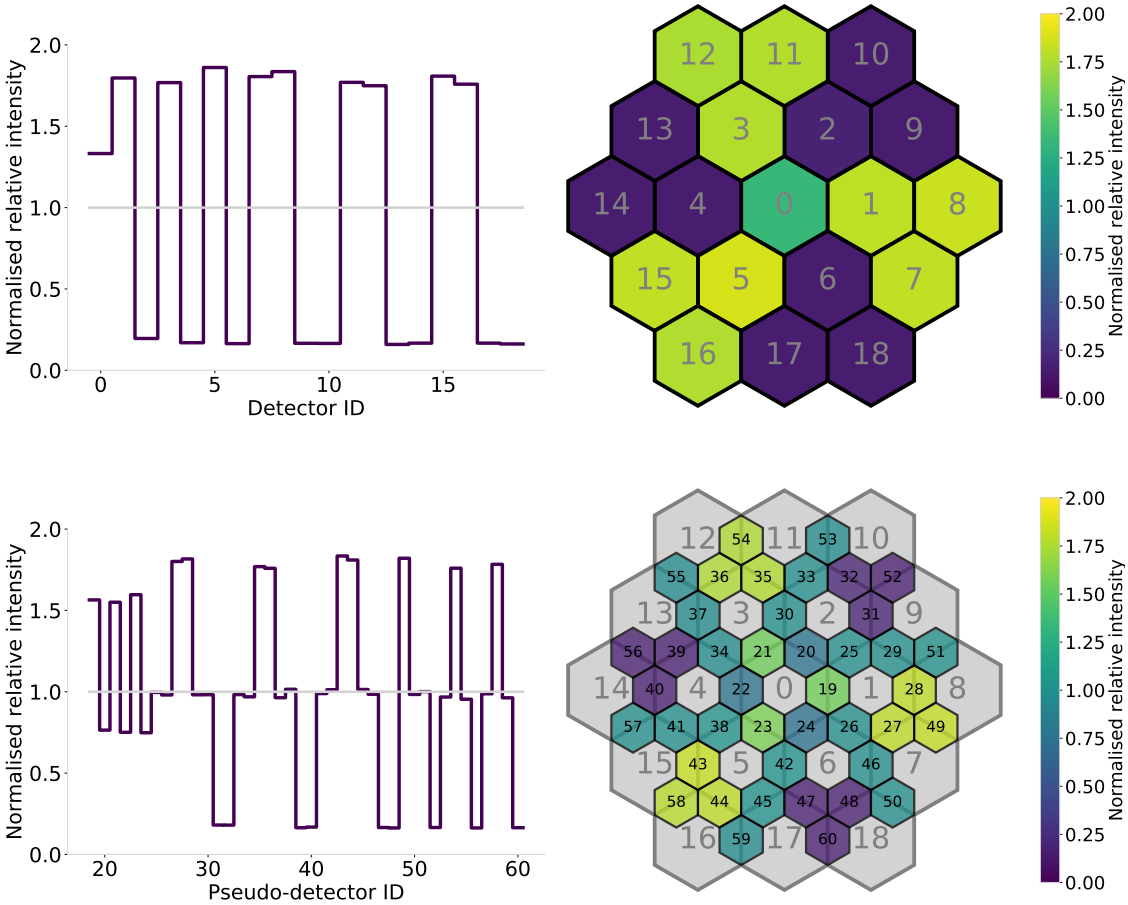

Figure 3.20: SPI detector patterns for a celestial source aligned with the optical axis of the instrument. *Upper:* Relative intensity pattern of single Ge detectors. *Lower:* Relative intensity pattern of double-event pseudo detectors.

pattern shown in Fig. 3.20 changes. This imprints a characteristic time variation of the detector pattern corresponding to the celestial source. The essential point here is that, on the other hand, the background pattern remains constant during this short period of time.
The background modelling approach described in Sec. 3.4.1 relies on the presumption that the data are almost completely composed of background. This only applies if the time span for background determination is chosen long enough for the characteristic source contributions to overall be smeared out. Siegert et al. (2019) showed that for a source that contributes 10% to the total measured spectrum, the cumulative pattern of source and background varies by less than 1% after 20 pointings. Integration over one orbit, which corresponds to typically about 50–90 pointings, is therefore sufficient for the assumption of background dominated data. In this, celestial source contributions can be disentangled from the instrumental background via a simultaneous statistical description of both these components in detector space, due to the fact that the former is variable and the latter constant in time. In the following Sec. 3.4.3, an example of the practical implementation of such an analysis is given based on the full-sky emission at 1.8 MeV.

3.4.3 Application: Full-Sky 1.8 MeV Emission

For the spectral analysis of the full-sky emission from ^{26}Al at 1.8 MeV, a comprehensive SPI dataset from the currently entire mission of 2131 revolutions and 17.5 yr in the energy range from 1790–1840 keV is used. This results in a full-mission dataset comprising observations from 1840 revolutions with 118407 individual pointings and a total exposure time of ~ 255 Ms. The sky coverage of the dataset in time is shown in Fig. 3.21. The patchy structure reflects the observation strategy of INTEGRAL, observing regions of interest separately, rather than performing a uniform full-sky survey.
Scientific data collection started from revolution 43 and additional selection criteria had to be applied. Revolutions during which detector annealings were performed

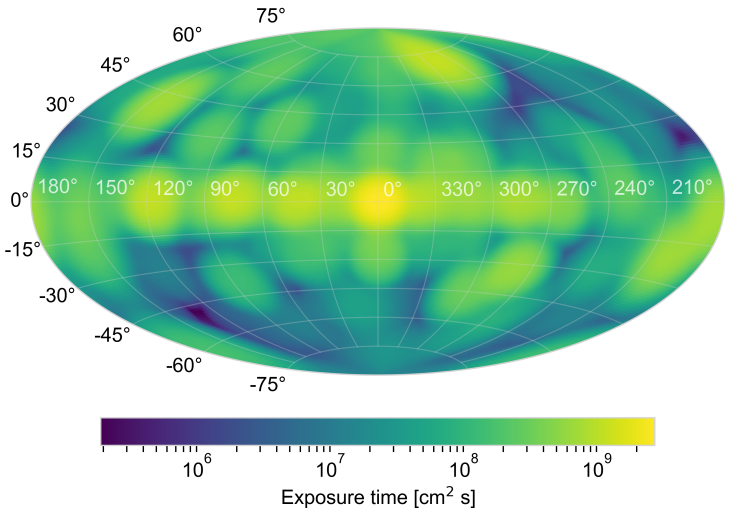

Figure 3.21: SPI full-sky exposure map for 17.5 yr of the INTEGRAL mission with integrated observation time of ~ 255 Ms. The effective area of SPI is 44 cm^2 at 1.8 MeV, accounting for failed detectors (Attie et al. 2003).

are not included, as no scientific data are recorded during these periods. Observations with high event rates exceeding the threshold $\gtrsim 15\,\mathrm{MeV}$ are excluded, because at such high energies the Ge detectors saturate. This indicates particle interactions within the detector, mostly due to mass ejection during Solar flares, for which accurate modelling is not feasible due to their spectral dominance and very short duration. Additionally, 20% of the orbital phase around the perigee are omitted in order to avoid background from particle interactions during passages through the Van Allen radiation belts as illustrated in Fig. 3.8.
The instrumental background was modelled according to the approach outlined in Sec. 3.4.1. The respective background model B_{ik} (cf. Eq. 3.16) was obtained from a spectral fit of the entire mission data as described by Diehl et al. (2018b), which was then adapted to this particular dataset of this analysis following Siegert et al. (2019). For the ^{26}Al analysis, half-year intervals are chosen within which the background normalisation is determined by the fit. This was chosen in such a way that it corresponds to a combination of the observations between two annealings. Detector failures were taken as additional time nodes for background renormalisation, because these change the instrument response considerably. This selection was shown by Siegert et al. (2019, Sect. 5.1.2) to be optimal and therefore adopted in the analysis for this thesis. Short-term variations are taken into account and modelled according to the saturated detector events, tracing the pointing-to-pointing variation at high statistical precision (e.g. Jean et al. 2003).
An additional background source arises due to the fact described in Sec. 3.3.3 that the BGO side shield becomes increasingly transparent for higher photon energies. The transmission probability for photons around 1.8 MeV has been shown to be is about 18% for perpendicularly-incident photons. This would lead to an additional signal mainly when the Galactic disk emission is coming from the side. The transmission probability drops below 1% for incidence angles larger than 69° (cf. Fig. 3.12). The main emission coming from the Galactic ridge corresponds to spacecraft orientations where SPI is pointing towards high Galactic latitudes of $|b| > 21°$. This is the case for 32% of all SPI pointings (Pleintinger et al. 2019). This indicates that the BGO transmissivity at 1.8 MeV does provide additional photons from the sky. Nevertheless, such a celestial background signal is generally included in the background model because the orientation of the satellite usually remains rather constant during one orbit. This means that on that timescale a characteristic and quasi-constant background detector pattern would be imprinted on the camera. Additionally, the contributions from outside the field of produce a weaker detector pattern (cf. Sec. 3.4.2) and because the imaging response does not account for this, these photons are registered in the analysis method as being due to background.
As sky model M_{ij} (cf. Eq. 3.16) for determining the ^{26}Al emission, the maximum entropy map obtained from the entire nine-year COMPTEL mission (Plüschke et al. 2001, Fig. 1.1) is used. This map has an angular resolution of 3.8° and shows a large latitude extent on top of a clumpy structure concentrated towards the inner Galactic disk region as well as an association with spiral arm tangents and nearby massive star regions. Since it is the map with highest spatial resolution obtained from observations of the 1.8 MeV sky from a different instrument, this intensity distribution is chosen as observational cross-reference map and representation of the ^{26}Al sky. In order to translate it into a sky model in SPI's data space, the map is convolved with the IRF for each observational epoch. This gives a prediction of expected counts per detector for each of the 118407 pointings of the dataset. The amplitude of this model is optimised simultaneously with the models for background

lines and continuum using a statistical fit in a maximum likelihood framework to explain the data in each energy bin separately (Strong et al. 2005).
In order to evaluate the performance of the background model, the distribution of residuals $R = (d_p - m_p)/\sqrt{m_p}$ after the fit are shown as histograms in the top panel of Fig. 3.22, where m_p is the model describing the data d_p per pointing p. The figure shows the analysis results for single and double events in parallel on the left and right side respectively. The residuals are displayed both for the fitted background and the entire model including the sky emission. The scatter around 0 follows a normal distribution with $\sigma = 1$. The slight excess of the background model residuals towards positive residuals indicates the remaining sky emission. The fitted and combined full model components describe the data well, exhibiting a Gaussian

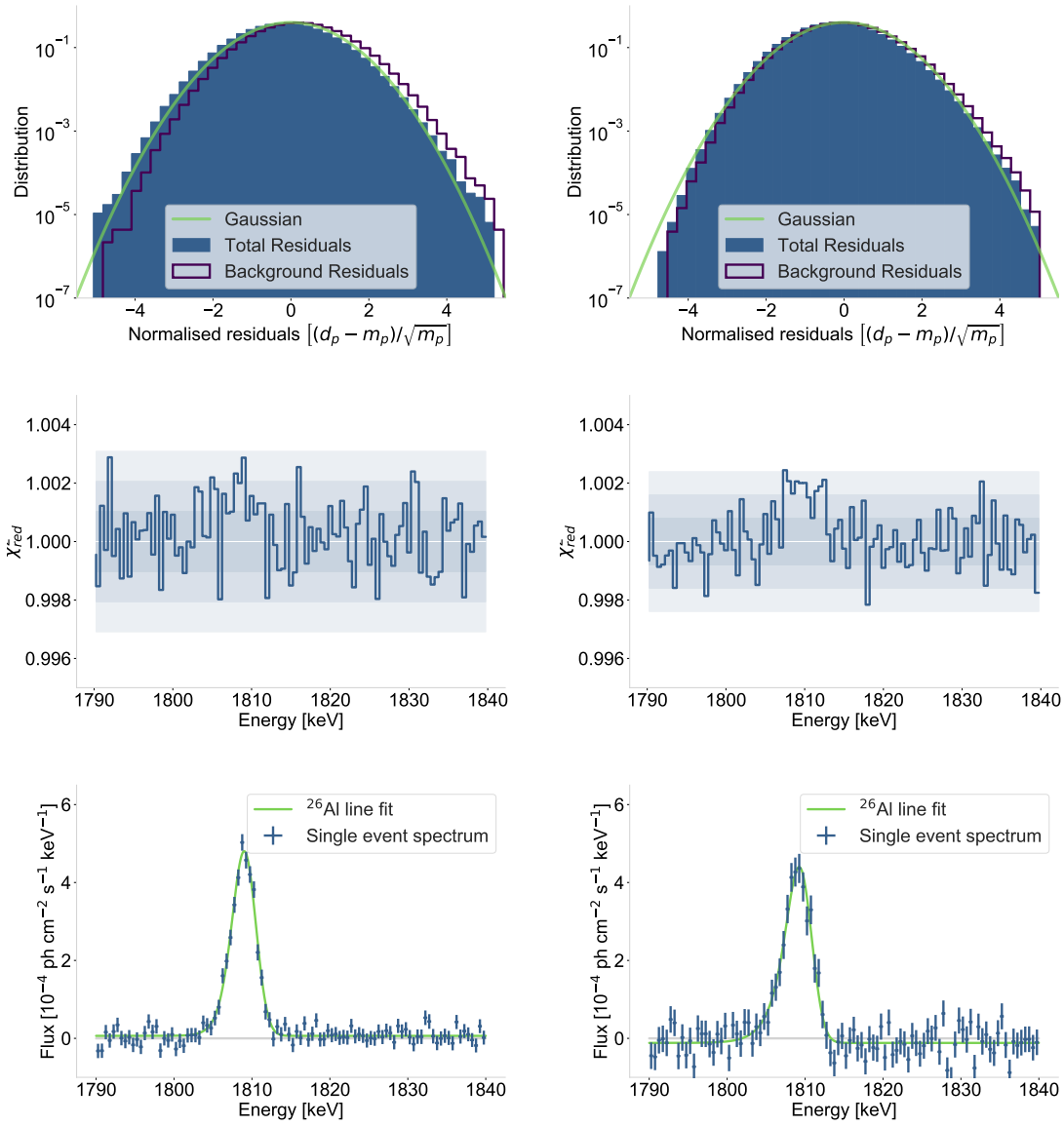

Figure 3.22: SPI data analysis results for single (*left*) and double events (*right*) separately. *Top:* Residuals of the background model overplotted by a normal distribution with width $\sigma = 1$. *Middle:* Model performance measured by χ^2_{red} for each energy bin for the entire SPI camera. The ideal value of $\chi^2_{\mathrm{red}} = 1$ is shown as white line, with 1σ, 2σ, and 3σ uncertainty intervals as shaded grey regions. All points lie within the 3σ band. *Bottom:* Resulting SPI spectra from the amplitude of the sky model fitted in each energy bin. A preliminary degraded Gaussian (cf. Eq 3.20) line fit is shown in *green* to emphasise the line shape and the *grey* line indicates zero flux.

distribution. Additionally, the χ^2-statistics

$$\chi^2 = \sum_{p=1}^{N_{\rm obs}} \frac{(d_p - m_p)^2}{m_p}, \tag{3.26}$$

is used as figure of merit to determine the quality of the simultaneous fit of background and sky model. This can be considered an approximation of the logarithm of the Gaussian likelihood with standard errors of the Poisson distribution $\sigma = \sqrt{m_p}$. This is strictly only valid for data with Gaussian errors, while SPI counts are generally Poisson-distributed. Because the latter can be approximated for large count rates by a normal distribution with standard Poisson errors, the χ^2-statistic can provide a general figure of merit for the fit. In the middle panel of Fig. 3.22 the reduced $\chi^2_{\rm red} = \chi^2/\nu$ is shown, which is normalised to the number of degrees of freedom ν and is optimal for $\chi^2_{\rm red} = 1$. The data points lie all within the 3σ confidence intervals of the χ^2-distribution and scatter around 1, which indicates a statistically sound description of the data over the entire energy range.
The resulting fitted amplitude of the sky model per 0.5 keV energy bin is shown as spectrum in the lower panel of Fig. 3.22. For both, single and double events, the ^{26}Al emission line at 1809 keV is prominently visible. Here, for the first time a detailed analysis of the SPI double events is performed. A preliminary fit of the spectral line shape in Eq. 3.20 to the data by a Levenberg-Marquardt algorithm through χ^2 minimisation shows that both event types yield a consistent line flux of $F_{^{26}\rm Al} = (1.89 \pm 0.05) \times 10^{-3}\,\mathrm{ph\,cm^{-2}\,s^{-1}}$ and $F_{^{26}\rm Al} = (2.09 \pm 0.10) \times 10^{-3}\,\mathrm{ph\,cm^{-2}\,s^{-1}}$ with detection significance of 51σ and 27σ for single and double events, respectively. Interestingly, the signal derived from double events shows larger width with. This will be discussed after further analysis below in this section.
To obtain the best possible signal based on as much data as possible, the two event types are combined and analysed together. Because the average instrumental resolution at 1.8 MeV is 3.17 keV, the photon flux from celestial sources is derived in energy bins finer than the instrumental resolution and the detailed spectral response of the instrument has to be employed in the spectral analysis across a wider energy range (Diehl et al. 2018b). From this analysis method, an instrument spectrum in count space is obtained, i.e. given as number of events that have been measured by the detectors per energy channel. The further analysis aims to investigate the underlying physical properties of the emission.
The spectra in Fig. 3.22 are obtained taking the IRF described in Sec. 3.4.2 into account. This is already included in the standard SPI analysis, which treats each energy bin independently (Strong et al. 2005). Additionally, for a consistent spectral analysis, the energy dispersion of the instrument has to be taken into account. This means, also partial energy deposition of photons due to detector inherent physical effects such as Compton scattering or escaping of secondary photons as shown in Fig. 3.6 has to be included. These effects generally result a redistribution of photons from higher to lower energies. This is described by a redistribution matrix combined in the SPI-specific redistribution matrix file (RMF). It is shown in the left panel of Fig. 3.23 for the energy range 1790–1840 keV. The diagonal elements characterise photon interactions in the photo-peak. The non-zero off-diagonal elements describe the redistribution from the photo-peak into lower-lying energy channels. This means the redistribution of an actual spectral model in physical units of $\mathrm{ph\,cm^{-2}\,s^{-1}\,keV^{-1}}$ into the instrumental analysis channels in units of $\mathrm{counts\,s^{-1}\,keV^{-1}}$. Near the photo-peak, as it is the case in this ^{26}Al analysis, it is almost a fully diagonal matrix with

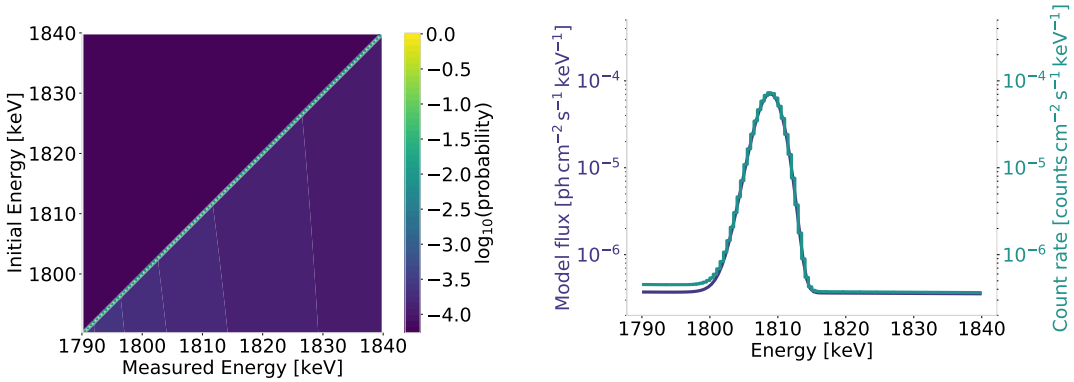

Figure 3.23: *Left:* SPI RMF in the energy range 1790–1840 keV. Non-zero off-diagonal elements quantify the redistribution of photon energies from the photo-peak due to partial energy deposition. *Right:* Effect of the energy redistribution on an exemplary model signal. The initial signal in model space is shown in *blue* and after convolution with the RMF in count space in *green*.

only very weak off-diagonal elements. Fitting a photon model directly to the data in count space would only be valid if the RMF would be perfectly diagonal, i.e. if the response would be entirely linear. The actual effect is illustrated by a convolution of a physical model spectrum with the SPI RMF. As an example, a degraded Gaussian line with a flux of $F_{^{26}\mathrm{Al}} = 1.9 \times 10^{-3}\,\mathrm{ph\,cm^{-2}\,s^{-1}}$, instrumental resolution FWHM $= 3.16\,\mathrm{keV}$, degradation $\tau = 1.05\,\mathrm{keV}$, and Doppler-broadening from the sky of 1.2 keV is shown in the right panel of Fig. 3.23 together with its result in count space. The redistribution of photons from the photo-peak into lower energy channels is visible in the excess of the count rate compared to the original photon model below about 1800 keV. Especially considering the logarithmic sale in Fig. 3.23, it becomes clear that the effect is negligible because statistical effects are one order of magnitude larger than the redistribution effect. Nevertheless, it is included in the following evaluation of the data for consistency.

In order to infer the underlying physical model from the SPI count data, this forward folding approach is applied. The basic procedure is as follows: A physical model $F_\mathrm{i}(E_\mathrm{i};\boldsymbol{\theta})$ with a set of parameters $\boldsymbol{\theta}$ is assumed and convolved with the energy redistribution matrix of SPI $\mathrm{RMF}_\mathrm{SPI}(E_\mathrm{i}, E_\mathrm{m})$, where E_i and E_m are the initial and measured energies respectively. Thereby it is converted into count space, describing the resulting count spectrum

$$F_\mathrm{m}(E_\mathrm{m};\boldsymbol{\theta}) = \int \mathrm{RMF}_\mathrm{SPI}(E_\mathrm{i}, E_\mathrm{m}) F_\mathrm{i}(E_\mathrm{i};\boldsymbol{\theta})\, dE_\mathrm{i}. \tag{3.27}$$

In count space, the initial model spectrum can be statistically compared with the observed counts. The χ^2-statistic is used to perform statistical fits, because the count rates extracted from the fit using the Poisson likelihood are approximately normal distributed. This process is then iterated until the model parameters converge. For this purpose the Python-based Markov chain Monte Carlo (MCMC) ensemble sampler `emcee` (Foreman-Mackey et al. 2019) is used.

As described in Sec. 3.4.1, a typical SPI spectrum consists of a skewed Gaussian $L(E; E_0, \sigma_\mathrm{tot}, \tau)$ described in Eq. 3.20 on top of a power-law shaped continuum emission $C(E; \alpha, c_0)$ following Eq. 3.17. Therefore the total photon model is

$$F_\mathrm{tot}(E; \alpha, c_0, F_{^{26}\mathrm{Al}}, E_0, \sigma, \tau) = C(E; \alpha, c_0) + F_{^{26}\mathrm{Al}} \times L(E; E_0, \sigma, \tau), \tag{3.28}$$

with the integrated line flux of the ^{26}Al line $F_{^{26}\mathrm{Al}}$ and a total width of the line

$$\sigma = \frac{1}{2\sqrt{2\ln 2}}\sqrt{\mathrm{FWHM}_{\mathrm{SPI}}^2 + \mathrm{FWHM}_{\mathrm{sky}}^2}, \tag{3.29}$$

differentiated in instrumental line broadening $\mathrm{FWHM}_{\mathrm{SPI}}$ and line broadening due to Doppler-shift of the signal $\mathrm{FWHM}_{\mathrm{sky}}$, which reflects the actual source dynamics on the sky. This separation is important to avoid confusing instrumental or calibration effects with physical phenomena. In order to set physical constraints on the individual model components, prior probability distributions of the parameters are applied. The approach of using a priori information is based on Bayes' Theorem

$$p(M(\boldsymbol{\theta})|D) = \frac{p(D|M(\boldsymbol{\theta})) \cdot p(M(\boldsymbol{\theta}))}{p(D)}, \tag{3.30}$$

where $p(M(\boldsymbol{\theta})|D)$ is the posterior probability density function of a certain model configuration $M(\boldsymbol{\theta})$ with a set of parameters $\boldsymbol{\theta}$, given an observed dataset D. This is equal to the likelihood function, i.e. the description of the data generating process, $p(D|M(\boldsymbol{\theta}))$, weighted by the marginal likelihood or evidence $p(D)$. The prior probability distribution $p(M(\boldsymbol{\theta}))$ represents either physical plausibility assumptions whose validity is already assumed before the observation and thus independent of the data, or includes independent information about the scales of the system. Accordingly, the following priors on the parameters in Eq. 3.28 are applied in the following analysis:

$$\begin{aligned}
\alpha &\sim \text{normal}(-1.7, 0.5) \\
c_0 &\sim \text{truncated normal}(10^{-6}, 10^{-5}; 0, 1) \\
F_{^{26}\mathrm{Al}} &\sim \text{truncated normal}(1.7 \times 10^{-3}, 8 \times 10^{-5}; 0, 1) \\
E_0 &\sim \text{normal}(1809.78, 0.3) \\
\mathrm{FWHM}_{\mathrm{SPI}} &\sim \text{normal}(3.16, 0.03) \\
\mathrm{FWHM}_{\mathrm{sky}} &\sim \text{truncated normal}(1, 8; 0, 100) \\
\tau &\sim \text{normal}(1.05, 0.01).
\end{aligned} \tag{3.31}$$

The instrument-specific parameters $\mathrm{FWHM}_{\mathrm{SPI}}$ and τ have been well determined in previous studies (Roques et al. 2003; Siegert 2017). Thus, they are chosen in a narrow range around the previously determined values with an inherent uncertainty of $\sim 1\%$. The parameters c_0 and α describing the background continuum were chosen following Kinzer et al. (1999, 2001), where the power-law index was found to be in the range between -1.75 and -1.65. E_0 is estimated according to Eq. 3.21 with an uncertainty corresponding to an overall velocity shift by $50\,\mathrm{km\,s^{-1}}$. The total flux $F_{^{26}\mathrm{Al}}$ was chosen in the range of previous SPI measurements (Siegert 2017; Pleintinger et al. 2019) and predetermined as positive. $\mathrm{FWHM}_{\mathrm{sky}}$ is currently the least constraint parameter in this analysis and therefore only a weak normal prior with a width of 8 keV, i.e. of the order of SN ejecta dynamics, is applied. It is truncated at 100 keV because velocities beyond this value corresponding to $\sim 0.05c$ are not reconcilable with any physically reasonable dynamics of nucleosynthesis ejecta. The MCMC fitting algorithm samples the posterior distribution of each parameter, given these priors and the data, in order to find the optimal set of parameters which maximises the full posterior likelihood distribution. By fitting the parameters together via this approach, it is possible to determine them simultaneously and explore their interdependences. Thus, especially degenerate properties such as σ_{SPI}, σ_{sky} or

τ can be determined individually under the influence of each other in physically reasonable regions of the parameter space.
Fig. 3.24 shows a diagnostic plot of how the spectral fit performs along the different axes of the parameter space. Most parameters follow a symmetric normal

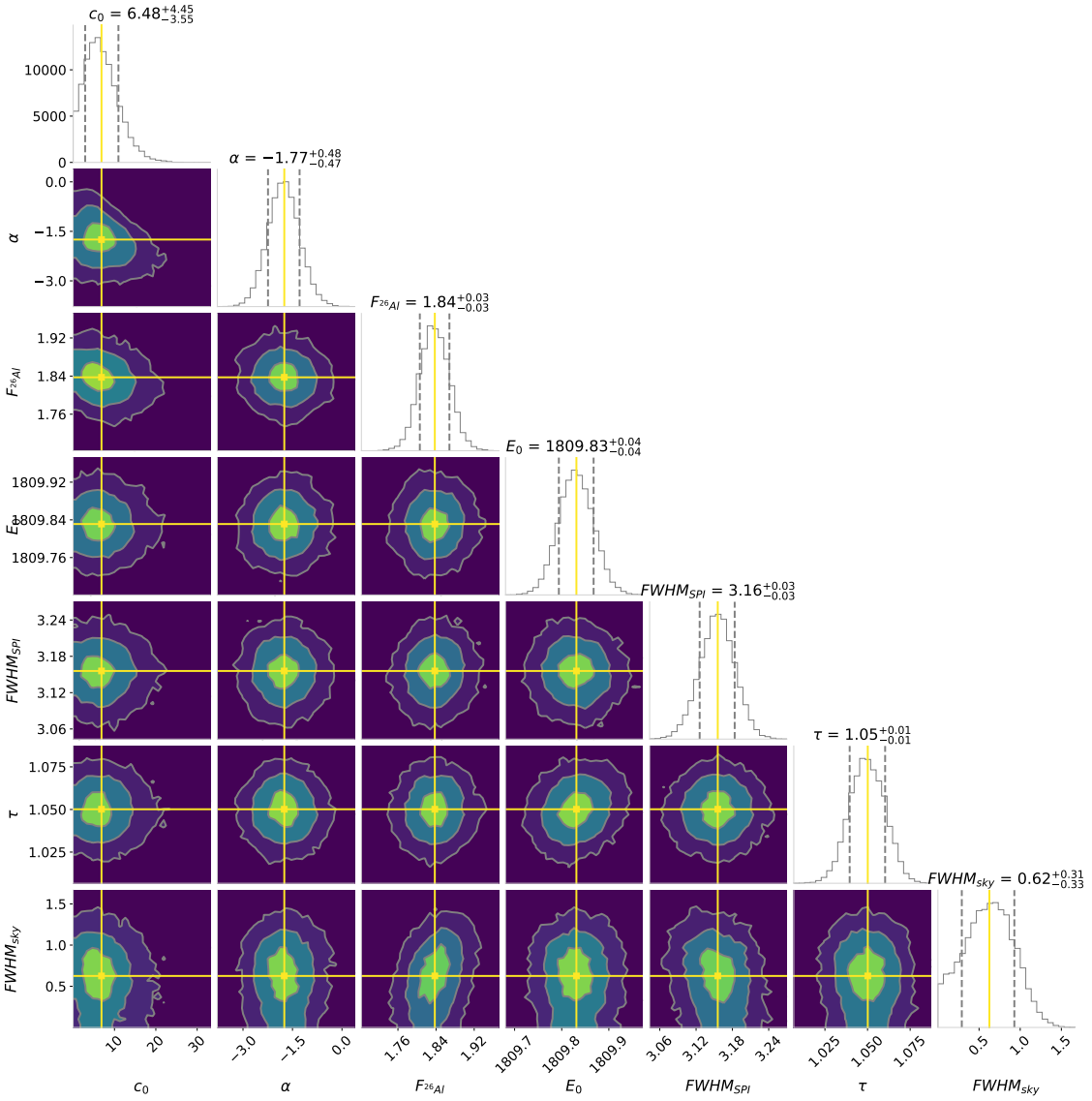

Figure 3.24: Posterior distributions of spectral fit parameters describing the full-sky ^{26}Al signal at 1809 keV measured with SPI according to the photon model in Eq. 3.28. The mean value along each axis is shown in *yellow*. Histograms on the diagonal show marginalised probability distributions along the respective axis with 86th percentiles marked by dashed lines.

distribution. $\mathrm{FWHM_{SPI}}$ and $\mathrm{FWHM_{sky}}$ exhibit slight indications of a negative correlation as expected. While the line centroid of the symmetric Gaussian component is $E_0 = (1809.83 \pm 0.04)\,\mathrm{keV}$, the line width contribution that can be contributed to source dynamics is found to be $\mathrm{FWHM_{sky}} = 0.62^{+0.31}_{-0.33}\,\mathrm{keV}$. This can be converted into Doppler broadening due to an average particle velocity via the relation (Diehl et al. 2006)

$$\bar{v} = \sqrt{\frac{k_\mathrm{B}T}{m_{26}}} = \frac{\mathrm{FWHM}\ \sqrt{3}c}{2\sqrt{2\ln 2}} = 122\,\mathrm{km\,s^{-1}} \times \left(\frac{\mathrm{FWHM}}{1\,\mathrm{keV}}\right), \tag{3.32}$$

where m_{26} is the atomic mass of ^{26}Al. Therefore, the Doppler broadening of the signal corresponds to an average particle velocity of $75.6^{+37.9}_{-40.2}\,\mathrm{km\,s^{-1}}$, which represents the line of sight dynamics of emission sources integrated over the entire sky. Therefore, it is overall smaller than the line shift values obtained by Kretschmer et al. (2013) because the latter exclusively focussed on the emission from the inner Galaxy at $|l| < 50°$.
The full flux of ^{26}Al emission measured from the entire sky is estimated to be $F_{^{26}\mathrm{Al}} = (1.84 \pm 0.03) \times 10^{-3}\,\mathrm{ph\,cm^{-2}\,s^{-1}}$with a total detection significance of 58σ. The flux is slightly higher than previously estimated values e.g. by Siegert (2017, $F_{^{26}\mathrm{Al}} = (1.69 \pm 0.14) \times 10^{-3}\,\mathrm{ph\,cm^{-2}\,s^{-1}}$) or Pleintinger et al. (2019, $F_{^{26}\mathrm{Al}} = (1.71 \pm 0.06) \times 10^{-3}\,\mathrm{ph\,cm^{-2}\,s^{-1}}$).
The overall spectrum of combined single and double events is shown in Fig. 3.25. The SPI spectrum inferred from the simultaneous fit of background and sky model is shown with the total model posterior spectrum with bands of 1σ, 2σ, and 3σ confidence intervals. The probability distributions of the total degraded line shape

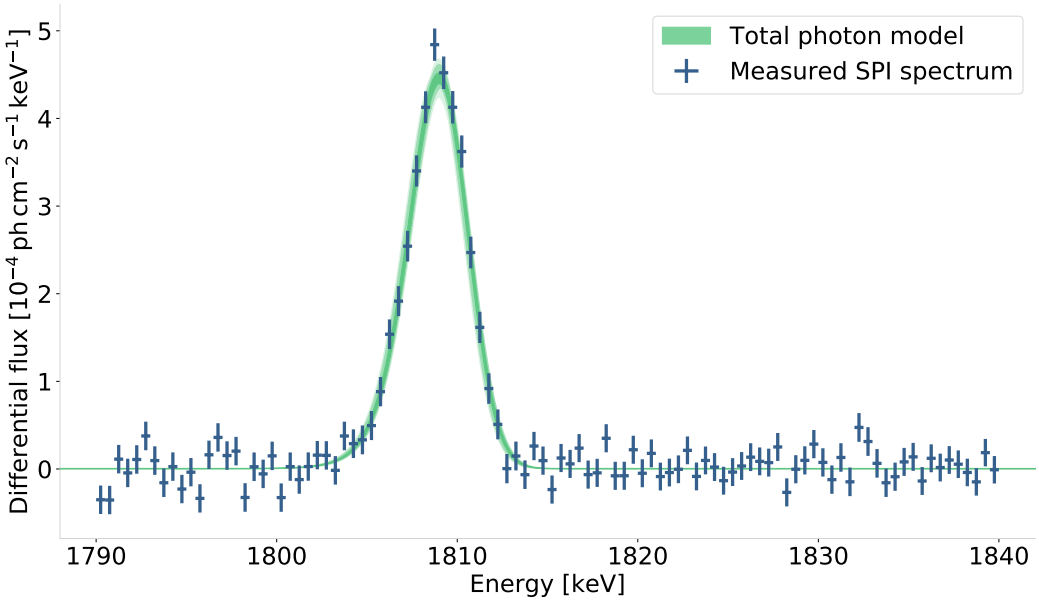

Figure 3.25: SPI spectrum (*blue* data points) of the ^{26}Al full-sky emission at 1809 keV. The best-fitting photon model is shown in bands of 1σ, 2σ, and 3σ confidence intervals in shades of *green* from dark to light. It represents a degraded Gaussian line profile on top of a power-law continuum (cf. Eq. 3.28). Individual spectral parameters are given in Fig. 3.24 and Tab. 3.3. The total flux of the signal is $F_{^{26}\mathrm{Al}} = (1.87 \pm 0.03)\,\mathrm{ph\,cm^{-2}\,s^{-1}}$ with a detection significance of 58σ.

characteristics as described in Sec. 3.4.1 are depicted in Fig. 3.26. The line shows an overall width of $\mathrm{FWHM_{tot}} = 3.23^{+0.07}_{-0.06}\,\mathrm{keV}$ with a shift of the central energy $\Delta E_{\mathrm{cen}} = (0.29 \pm 0.04)\,\mathrm{keV}$ with respect to the rest energy of the ^{26}Al emission line of 1808.73 keV (Endt 1998).In combination with the uncertainty of the energy calibration of about 0.1 keV, this indicates a slight blueshift of the line with a significance of 2.7σ. This would mean a preferential tendency of ^{26}Al moving towards the observer. In principle, this would be consistent with the picture of ^{26}Al being ejected into superbubble cavities along the leading edge of spiral arms as shown in Fig. 2.46. However, this should not be overinterpreted due to the low significance of the effect. A similar MCMC fitting approach is applied to the single and double event spectra shown in Fig. 3.22 separately. The results are summarised in Tab. 3.3 in com-

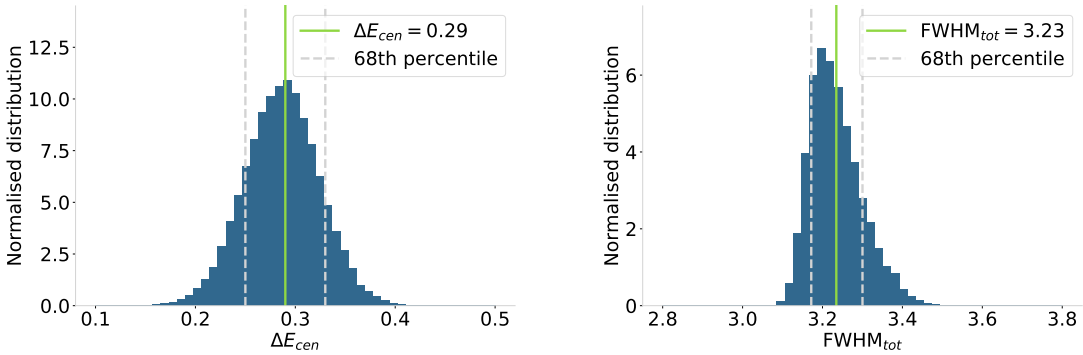

Figure 3.26: Marginalised probability distribution of the central line energy shift $\Delta E_0 = (0.28 \pm 0.04)$ keV with respect to the ^{26}Alemission lab energy of 1808.73 keV and the total line width $\mathrm{FWHM_{tot}} = (3.26 \pm 0.07)$ keV.

Table 3.3: Spectral ^{26}Al line fit parameters of the full photon model in Eq. 3.28 for describing the full-sky emission measured by SPI. The continuum is described by amplitude c_0 at 1000 keV and power-law index α. The centroid energy E_0, and the line width parameters $\mathrm{FWHM_{sky}}$ and $\mathrm{FWHM_{SPI}}$ describe the Gaussian component of the line. The central energy shift ΔE_{cen} and the width $\mathrm{FWHM_{tot}}$ are characteristics of the entire degraded line.

Parameter	Single events	Double events	Singles and doubles	Physical units
c_0	$12.69^{+5.20}_{-4.67}$	$2.25^{+3.42}_{-1.65}$	$6.48^{+4.45}_{-3.55}$	$10^{-6}\,\mathrm{ph\,cm^{-2}\,s^{-1}\,keV^{-1}}$
α	$-1.60^{+0.46}_{-0.46}$	$-1.85^{+0.49}_{-0.48}$	$-1.77^{+0.48}_{-0.47}$	unitless
$F_{^{26}\mathrm{Al}}$	$1.83^{+0.03}_{-0.03}$	$1.79^{+0.05}_{-0.06}$	$1.84^{+0.03}_{-0.03}$	$10^{-3}\,\mathrm{ph\,cm^{-2}\,s^{-1}}$
E_0	$1809.80^{+0.04}_{-0.04}$	$1809.91^{+0.10}_{-0.10}$	$1809.83^{+0.04}_{-0.04}$	keV
ΔE_{cen}	$0.26^{+0.04}_{-0.04}$	$0.36^{+0.08}_{-0.08}$	$0.29^{+0.04}_{-0.04}$	keV
τ	$1.05^{+0.01}_{-0.01}$	$1.04^{+0.10}_{-0.09}$	$1.05^{+0.01}_{-0.01}$	keV
$\mathrm{FWHM_{SPI}}$	$3.15^{+0.03}_{-0.03}$	$3.33^{+0.23}_{-0.25}$	$3.16^{+0.03}_{-0.03}$	keV
$\mathrm{FWHM_{sky}}$	$0.46^{+0.30}_{-0.27}$	$0.76^{+0.56}_{-0.48}$	$0.62^{+0.31}_{-0.33}$	keV
$\mathrm{FWHM_{tot}}$	$3.20^{+0.05}_{-0.05}$	$3.49^{+0.17}_{-0.16}$	$3.23^{+0.07}_{-0.06}$	keV

parison with the combined line characteristics. More detailed analytic plots can be found in the Appendix A in Fig. A.3 and Fig. A.4. The priors for $\mathrm{FWHM_{SPI}}$, $\mathrm{sky_{SPI}}$, τ have been adjusted for the separate treatment of double events. Since the instrument-specific properties regarding this event type have not been determined before, the respective priors have been chosen an order of magnitude wider as $\mathrm{FWHM_{SPI}} \sim \mathrm{normal}(3.16, 1.00)$ and $\tau \sim \mathrm{normal}(1.05, 0.1)$ in order to explore possible effects. On the other hand the sky emission is independent of the event type and therefore $\mathrm{FWHM_{sky}} \sim \mathrm{truncated\ normal}(0.6, 0.3; 0, 100)$ was inherited for the double events from the evaluation of the total signal. All other priors have been applied as in Eq. 3.31. The continuum and line parameters α, $F_{^{26}\mathrm{Al}}$, E_0, or τ are in agreement. This confirms the consistency of the data analysis. Nevertheless, the width of the signal from the two event types shows a tendency towards a higher instrumental $\mathrm{FWHM_{SPI}} = 3.33^{+0.23}_{-0.25}$ keV for doubles than for singles with $\mathrm{FWHM_{SPI}} = 3.15^{+0.03}_{-0.03}$. The line with for single events and the combined signal are in agreement, which shows that the total spectrum is dominated by single events. The other instrument-specific parameter τ, however, is consistent between single and double events. This indicates that the increased line width seen with double

events is not caused by a higher sensitivity of this event type to degradation effects. Instead, this probably results from the spatial distribution of double event interactions within the detectors. These happen preferably in the outer regions of the crystals. Inhomogeneities in the radial field distribution of the applied voltage in the outer areas of the detectors could influence the double events in particular, resulting in a larger detected line width.

Essentials

SPI observations of the ^{26}Al emission across the entire sky during 17.5 yr are analysed.

- Self-consistent background modelling is successfully applied in a simultaneous fit with a sky model in order to disentangle the celestial emission from the large instrumental background.
- The ratio of single to double events is found to be $R_{S/D} \approx 1.7$ in the early and $R_{S/D} \approx 2.9$ in the later mission, mainly due to detector failures.
- The ^{26}Al signal is analysed in a forward modelling approach via an MCMC fitting algorithm including the instrumental RMF.
- A detailed analysis of SPI double events is included for the first time, showing a signal consistent with single event results.
- The total line flux from ^{26}Al emission at 1.8 MeV measured with SPI is $F_{^{26}\mathrm{Al}} = (1.84 \pm 0.03) \times 10^{-3}\,\mathrm{ph\,cm^{-2}\,s^{-1}}$ with a total detection significance of 58σ and a line broadening due to source dynamics of $\mathrm{FWHM_{sky}} = 0.62^{+0.31}_{-0.33}\,\mathrm{keV}$.

4 Modelling Radioactivity in the Galaxy

"Since all models are wrong the scientist must be alert to what is importantly wrong."

— George E. P. Box (1976)

The fundamental question that almost inevitably arises from the previous chapters is how knowledge about the astrophysical phenomena described in Ch. 2 can actually be obtained from measurements as outlined in Ch. 3? This is not in the least a trivial question; on the contrary, it is a contextualised version of one of the main epistemological questions in astrophysics. Size scales are larger, energies are higher, and time spans are longer than can be realised in any conceivable experiment. Therefore, hypothesis tests in this field usually must be carried out without deliberate interference with the investigated processes. In order to bypass this empirical obstruction, theoretical abstraction is commonly used to separate research intentions from their practical realisation. This principle is schematically visualised in Fig. 4.1. It means that an intended cause or manipulation need not be actually

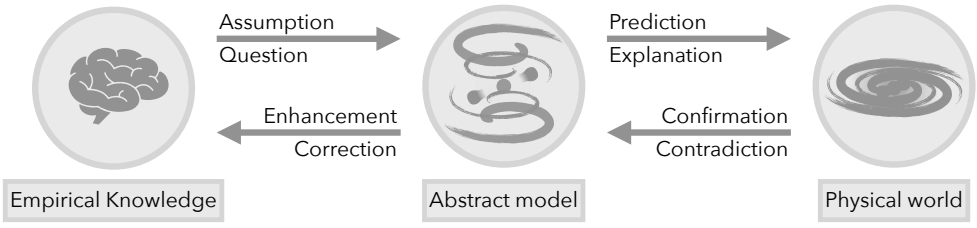

Figure 4.1: Epistemological scheme relying on astrophysical models. Empirical knowledge about astrophysical processes is usually gained by the intermediate step over a theoretical model which abstracts from the practical inaccessibility of the investigated phenomenon.

implemented by physical means to test its effects in an abstract space. The decisive factor here is whether this space correctly internalises the physical properties relevant to the respective problem. Depending on this, coherent abstract models can be formulated that contain theoretical knowledge on the one hand and predict questionable aspects of physical phenomena on the other. The possibility of theoretical execution of otherwise impracticable experiments due to such models makes them indispensable tools for astrophysical investigations. In this chapter, therefore, modelling of the radioactive Galaxy will be presented as abstract tool mediating particularly between the current understanding of massive star physics and cosmic gamma-ray measurements.

4.1 The Galactic Population Synthesis Code PSYCO

Scientific Justification Typically, detailed MHD model calculations are used to simulate astrophysical processes. These follow the evolution of complex systems by solving hydrodynamic and electromagnetic differential equations on a spatial simulation grid over progressing points in time. This is based on physical boundary conditions that describe the understanding of the respective processes as precisely and comprehensively as possible. Such simulations for the specific research about nucleosynthesis feedback have already been presented and discussed in detail in Sec. 2.4.5. For a technical implementation of such simulations, a compromise must always be found between the accuracy of the physical description and computational feasibility. While the former is a priori limited in scientific research due to heuristic simplifications or incomplete knowledge, the latter is usually limited e.g. by the necessary calculation time or available computing power. Minimising the expenditure of time and maximising the technical resources leads, with the means available today, to impressively detailed descriptions of stars, SNe, the ISM, galaxies, or even clusters of galaxies and the cosmic web.
Besides their undoubtedly fascinating richness of detail and enormous scientific potential, such elaborate simulations also have a fundamental weakness. This is that the detail of the description is usually chosen in such a way that one complete instantiation can be calculated within the entire available time period, typically on the order of months. However, a large number of model parameters and boundary conditions are involved in these simulations, all of which are subject to a certain degree of uncertainty or must be treated under simplifying assumptions. Since a simulation can basically be interpreted as an abstract experiment, the parallel to practical experiments illustrates the resulting problem: Suppose a phenomenon is investigated in a laboratory experiment in which a plethora of unknown and interdependent parameters can be controlled but cannot be reduced. A single execution of the experiment with certain boundary conditions therefore corresponds to the test of a single point in the entire parameter space. Thus, even if all the relevant parameters have been considered, neither their mutual influence nor the exact cause of any discrepancies with predictions can be determined on the basis of this single experiment. In addition to this, the influence of stochastic effects cannot be sufficiently considered because the outcome was measured only once. In order to draw scientific conclusions, the experiment must therefore be repeated, either with modified parameters to explore the parameter space or with identical parameters to confirm any results.
The same applies to theoretical simulations. A single instantiation of a simulation describes one case of one certain parameter configuration. To explore the parameter space, to investigate statistical effects, or to validate results with respect to empirical data, the simulation must be repeated. However, this is often technically not possible due to the calculation time required and the costs involved. In order to consider and avoid this issue in simulating radioactivity in the Galaxy repeatedly, a new bottom-up modelling approach is developed and implemented in this thesis.
The main goal of this project is to design an astrophysical model of the radioactive Galaxy in such a way that it can be repeated multiple times in many different parameter configurations and that, at the same time, the scientifically most important and observationally accessible features can be addressed and predicted. This means that the previously mentioned compromise between time expenditure and attention

to detail must also be found, but on the basis of a much shorter time. The aim is to achieve calculation times of minutes instead of months. This is, of course, only possible by considerably simplifying assumptions in the physical description. It is important to emphasize that simplifying assumptions are generally not peculiar to this approach, nor are they fundamentally detrimental to scientific validity. In any theoretical model or simulation, certain simplifications or heuristics must be assumed in order to be able to implement it. This results on the one hand from the computational limits and on the other hand from the limitations of scientific knowledge. In other words, the term model implies simplification. The crucial aspect is to choose these simplifications in such a way that they still allow an adequate treatment of the respective scientific question. Strictly speaking, a scientific question on the other hand is also a considerable simplification in itself, since it implies both canonical assumptions and a sharp delimitation of the subject. It is therefore an important prerequisite in general to coordinate the degree and scope of simplification of both the research question and the model.
The main research question of this thesis has already been narrowed down in Ch. 1: How does nucleosynthesis feedback from massive star groups affect the chemical evolution of the Milky Way and the Solar System?
In the following, the PSYCO model is described, which is specifically tailored to this question and developed in order to address it.

Overall Model Structure The PSYCO framework comprises a pure-Python implementation of an astrophysical model for the particular purpose of investigating the distribution of Galactic radioactivity. Based on stellar population synthesis calculations of individual star groups, it can be seen as expansion of the PopSyn code developed in C++ by Voss et al. (2009), and earlier, similar calculations (Cerviño et al. 2000; Plüschke 2001; Plüschke et al. 2002; Knödlseder et al. 2002; Martin et al. 2008). The basic structure of PSYCO is illustrated in Fig. 4.2.
The essential physical parameter that runs through the model is mass. In this respect, the three basic theoretical assumptions are the distribution of individual stellar masses, given by the IMF (cf. Sec. 2.2.1), the distribution of cluster masses, given by the ECMF (cf. Sec. 2.3.2), and the galactic SFR (cf. Sec. 2.4.2). While the latter, under the assumption of a total model time, defines a global mass constraint, the first two functions divide this mass hierarchically first into stellar clusters and finally individual stars. On that basis, the model type is overall referred to here as a bottom-up approach, since the nucleosynthesis aspect is then built up step by step from the properties of individual stars as basic units of nucleosynthesis feedback by adding various physical assumptions at different levels in order to finally model their large-scale implications. The basic model levels correspond to the physical scales of nucleosynthesis feedback recognised as fundamental and reflected in the structure of Ch. 2. These are in particular single stars, which are referred to here as bottom level, star groups as intermediate level and the large-scale Galactic structure, which represents the top level.

Model Input and Parameters While the nucleosynthesis aspect in PSYCO is built bottom-up, the model input is processed top-down. First, global parameters are selected on the galaxy level; these are the spatial galactic density distribution, the radial galactic metallicity gradient, the SFR, and the model time, i.e. the total time

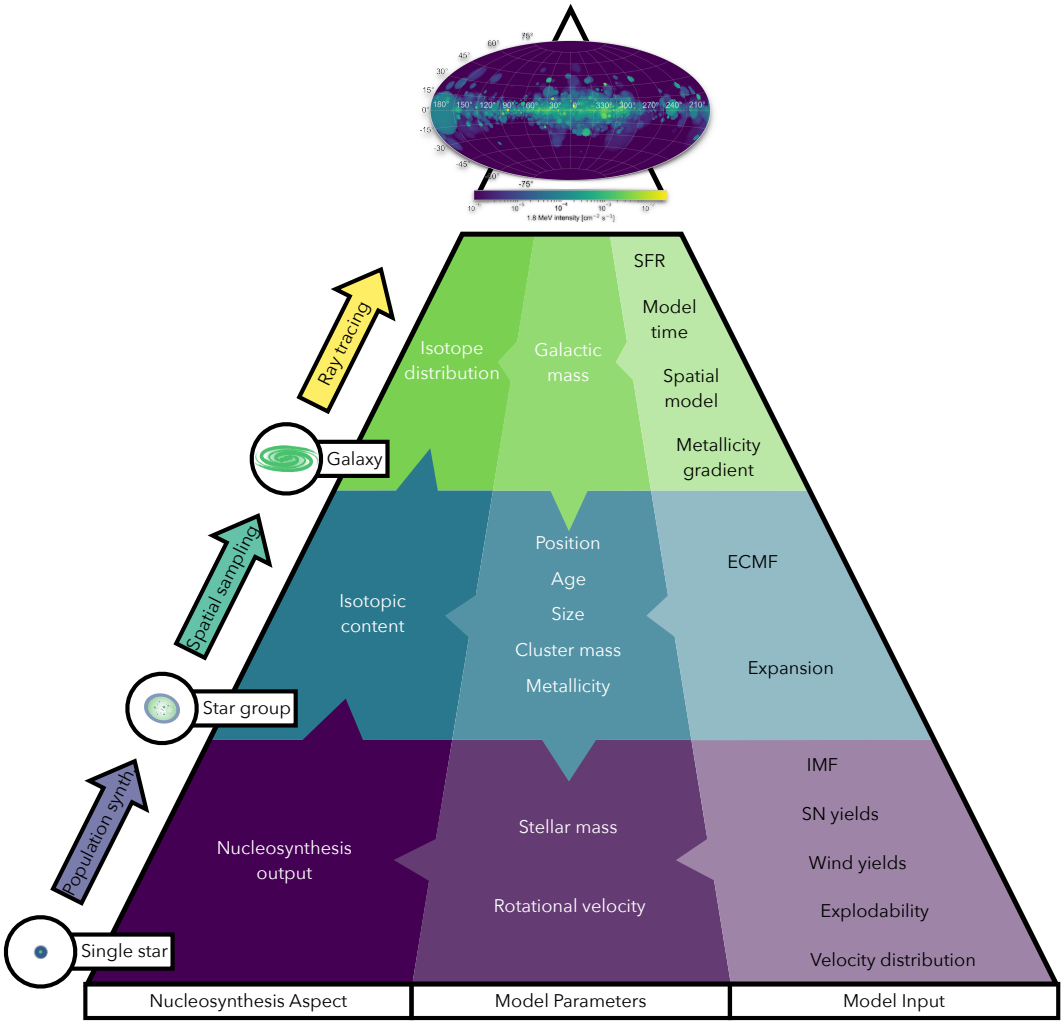

Figure 4.2: Schematic structure of the PSYCO model. It essentially consists of three levels, which correspond to physical size scales: the *bottom* level of single stars, the *intermediate* level of star groups and the *top* level of the entire galaxy. The theoretical model input for each level is shown on the *right*. According to this, the basic model parameters, are determined from top to bottom and indicated in the *middle* of the diagram. Starting with the parameters used to describe the galactic structure, from which the position, age, size, mass and metallicity of star groups are derived, and from which in turn the properties of individual stars are derived. The crucial nucleosynthesis aspect shown on the *left* is then modelled bottom-up. From single star evolution models, population synthesis is used to calculate the nucleosynthesis content of star groups, the spatial distribution of which in turn results from spatial sampling of the galaxy model. Finally, a ray tracing algorithm is used to generate a synthetic full-sky map of the modelled galactic gamma-ray emission.

that the model runs through. The total timespan is determined according to the convergence criterion that the total mass of the isotopes under consideration reaches an equilibrium state between production and decay. As will be described in Sec. 4.3.1 and confirmed in Sec. 4.4.1, this is determined a posteriori to $T_{\mathrm{tot}} = 50\,\mathrm{Myr}$ (cf. also Rodgers-Lee et al. 2019). With these assumptions, the total mass that is converted into stars during this time is determined via $M_{\mathrm{tot}} = \mathrm{SFR} \times T_{\mathrm{tot}}$. A detailed description of these aspects will follow in Sec. 4.3.

This information is inherited at the next deeper level of star groups. Here the ECMF is the building block that governs the distribution of the previously determined total mass to individual clusters. To increase the efficiency of the calculation, the analytic optimal sampling approach is used here, which is explained in Sec. 4.2.1. Under the

assumption of a constant SFR, each cluster is assigned a random age within the total model time. The spatial expansion of the superbubble blown by the stellar feedback from the group is calculated from this age as homogeneously expanding spheres with given mechanical luminosity and ambient density (cf. Sec. 4.3.3). The position of each star group is sampled according to a galactic density distribution and a metallicity is assigned according to a metallicity gradient. Overall, this results in the decisive parameters on this level of cluster position, size, age, metallicity, and mass.
The cluster mass is now distributed to the bottom level of individual stars, assuming the IMF by applying optimal sampling again. Since simultaneous star formation and homogeneous metallicity is assumed within each star group, age and metallicity of single stars resemble the values of the overarching group. The rotational velocity, on the other hand, is an individual star parameter and is randomly sampled according to the observed distribution. Thus, stellar mass, age, metallicity, and rotational velocity are the fundamental parameters of individual stars from which the nucleosynthesis aspect can be built up step by step. The stellar parameters are further explained in Sec. 4.2.3.

Bottom-Up Nucleosynthesis Aspect The previously identified essential astrophysical parameters of single stars determine the choice of stellar models, in particular isotopic wind yields and SN ejecta. The respective stellar evolution models have been described in detail in Sec. 2.2.5. In this way, the total nucleosynthesis output of each single stars is inferred according to the respective model profiles. This is propagated to the next level of star groups, where population synthesis calculations summarise the cumulative nucleosynthesis content of each group. The ejecta are assumed to be homogeneously distributed in the respective superbubble at the position of the stellar group. This is a crucial basic morphological assumption that should be kept in mind as such. Finally, a ray tracing algorithm is implemented to calculate a synthetic sky map of the full-sky gamma-ray emission due to isotopes such as ^{26}Al, ^{60}Fe, or ^{44}Ti on the basis of the emission from each superbubble. This step is described in more detail in Sec. 4.3.4. Due to the modular structure, this approach can easily be extended to other nucleosynthesis phenomena, e.g. regarding events such as novae or also neutron star mergers on longer time scales.

Variety of Model Results Altogether, this model approach facilitates predictions in relation to observable properties of the radioactive Galaxy, such as the gamma-ray fluxes from individual isotopes, the ^{60}Fe/^{26}Al flux ratio, the total galactic mass of the respective isotopes, the 3-dimensional distribution of nucleosynthesis ejecta, the observational depth of nuclear gamma-ray lines, the contribution due to nearby sources, the main source types, or the galactic SNR. On the other hand, it also opens up the possibility of testing theoretical model properties, such as nucleosynthesis yield calculations for single stars, explodability models, spatial aspects of nucleosynthesis feedback on galactic scale, or the global distribution functions IMF and ECMF. The predictive potential and variety of the PSYCO model will be discussed in more detail in Sec. 4.4.
As can already be seen from this description, the simplifications in this model are closely related to the framework provided by the observability of nucleosynthesis feedback features and properties by nuclear gamma-rays. For this reason, the lack

of detail in the physical description compared to MHD simulations is not a real flaw, but rather gives the whole approach a considerable advantage, because it is reduced to features that are actually within the observational scope of current gamma-ray instruments. The finally achieved high iteration speed of the whole model on the order of minutes allows the calculation of a plethora of models including a large number of different parameter configurations. It is important to stress again that PSYCO is not designed to map the physical processes of stellar feedback and the ISM in the greatest possible detail, but as a tool of empirical science, i.e. to address research questions that can actually be addressed by current gamma-ray observations. The latter cover the scale of star groups and the Milky Way as a whole. For this reason, the simplified physical description compared to MHD simulations is effectively applied as considerable advantage. It opens up the possibility to explore the underlying theoretical parameter space and simultaneously relate the results to observations. This will be the particular topic of Sec. 5.4.

Essentials

The PSYCO model is specifically designed as modelling tool to support scientific induction based on observable features of nucleosynthesis feedback by nuclear gamma-rays. It represents a morphological model of a Milky Way-like galaxy, which is constructed bottom-up from theoretically calculated single star yields, through the distribution of star groups, to the total galactic distribution of nucleosynthesis products. The efficient structure and implementation allows a fast calculation of the model and thus a multitude of iterations with a wide range of parameter configurations.

4.2 Population Synthesis

A general description of the massive star population synthesis approach was given in Sec. 2.3.5. To recall the basic principle, this is an integration of stellar evolution profiles weighted according to the IMF and their initial mass. In this way, a synthetic population of stars within a star group is generated, whose collective properties can then be studied. This section is focused on the implementation of population synthesis in the PSYCO code, which follows overall an optimal sampling approach as described in Sec. 4.2.1. The subsequent Sec. 4.2.3 describes the integration of various stellar parameters into the population synthesis calculation. While Sec. 4.2.2 then deals with the modelling of individual star groups, Sec. 4.2.4 examines possible effects of interactions in binary systems.

4.2.1 Sampling Algorithms

As introduced in Sec. 2.3.5, there are two fundamentally diametrical approaches to modelling the mass distribution of single stars emanating from one star formation event. While Approach A was introduced following the approach of treating star formation as entirely stochastic process sampling the IMF, Approach B assumes

star formation being a physically regulated and deterministic process producing the IMF (Kroupa et al. 2013, 131–135). PSYCO follows Approach B in modelling the galactic structure. It will be directly compared to the random sampling technique following Approach A later in this chapter, which is implemented in a sub-routine of PSYCO for investigating star groups individually.

Optimal Sampling The approach is referred to as optimal sampling because it subsumes the discretisation of the continuous IMF in such a way that the resulting sample reproduces its shape as close as possible, i.e. without distortion or gaps. The approach is described in general terms below, as it is not limited to the stellar IMF. First of all, a key feature of the technique is that it is based on the total mass as physical parameter and not the number of stars, which is not a physical quantity. For a mass distribution function that follows a power-law shape

$$\xi(M) = k \left(\frac{M}{M_{\max}} \right)^{-\alpha} \tag{4.1}$$

with normalisation constant k, power-law index α, and $M \in [M_{\min}, M_{\max}]$ (cf. Eq. 2.4–2.6), the total mass of an ensemble is given by

$$M_{\text{tot}} = \int_{M_{\min}}^{M_{\max}} M \; \xi(M) \; dM. \tag{4.2}$$

This physical mass reservoir M_{tot} is optimally distributed over $\xi(M)$ if the accessible mass range is covered with the condition that M would occur exactly once above the physical mass limit $M \in [M_{\max}, M_{\text{trunc}}]$, i.e.

$$1 = \int_{M_{\max}}^{M_{\text{trunc}}} \xi(M) \; dM. \tag{4.3}$$

This assumption implies that there would be one most massive object beyond the physical limit of star formation $M_{\max}$ and below the theoretical truncation of the function M_{trunc}. Since this would be an unphysical object, it is merely a mathematical pivot point that is ultimately removed from the population. This follows the revised optimal sampling approach by Schulz et al. (2015) compared to the approach developed by Kroupa et al. (2013), which is originally based on the most massive physically possible object within the population. Eq. 4.3 in combination with Eq. 4.1 yields the normalisation

$$k = \frac{1-\alpha}{M_{\text{trunc}}^{1-\alpha} \; M_{\max}^{\alpha} - M_{\max}}. \tag{4.4}$$

Applied to Eq. 4.2, this gives for the total mass and the analytical truncation

$$\begin{aligned} M_{\text{tot}} &= \frac{1-\alpha}{2-\alpha} \; \frac{M_{\max}^{2-\alpha} - M_{\min}^{2-\alpha}}{M_{\text{trunc}}^{1-\alpha} - M_{\max}^{1-\alpha}} \\ \Rightarrow \quad M_{\text{trunc}}^{1-\alpha} - M_{\max}^{1-\alpha} &= \frac{1-\alpha}{2-\alpha} \frac{M_{\max}^{2-\alpha} - M_{\min}^{2-\alpha}}{M_{\text{tot}}} \\ \Rightarrow \quad M_{\text{trunc}} &= \left[\frac{1-\alpha}{M_{\text{tot}}(2-\alpha)} (M_{\max}^{2-\alpha} - M_{\min}^{2-\alpha}) + M_{\max^{1-\alpha}} \right]^{\frac{1}{1-\alpha}}. \end{aligned} \tag{4.5}$$

On this basis, the analytic distribution function is discretised by dividing it into separate integrals, each of which fulfils the condition (Schulz et al. 2015)

$$1 = \int_{m_{i+1}}^{m_i} \xi(M)\, dM. \tag{4.6}$$

This means that integration within the limits $m_i > m_{i+1}$ yields exactly one object. Using the previously obtained description of the distribution function, this allows for an iterative determination of the integration limits progressing from largest to the smallest stellar mass via

$$\begin{aligned} 1 &= \int_{m_{i+1}}^{m_i} k \left(\frac{M}{M_{\max}}\right)^{-\alpha} dM = \frac{k}{1-\alpha}\left(m_i^{1-\alpha} - m_{i+1}^{1-\alpha}\right) M_{\max}^{\alpha} \\ \Rightarrow \quad m_{i+1} &= \left(m_i^{1-\alpha} - \frac{1-\alpha}{k M_{\max}^{\alpha}}\right)^{\frac{1}{1-\alpha}}. \end{aligned} \tag{4.7}$$

It is important to stress again, that $m_1 = M_{\max}$ and that mass is decreasing with increasing i. Now the mass of each individual object M_i can be calculated within the integration limits as

$$\begin{aligned} M_i &= \int_{m_{i+1}}^{m_i} M\, \xi(M)\, \mathrm{d}M \\ &= \frac{k}{2-\alpha}(m_i^{2-\alpha} - m_{i+1}^{2-\alpha}) M_{\max}^{\alpha}, \qquad \text{with } \alpha \neq 2. \end{aligned} \tag{4.8}$$

While M_{trunc} constitutes a computational pivot point, $M_{\max}$ is taken as physical boundary which is empirically derived from the overall cluster mass via Eq. 2.43. This inhibits the sampling of unphysically massive stars in small clusters, although the IMF is in principle non-zero over the entire mass range for all mass reservoirs. In this way, the initially continuously described mass distribution is iteratively distributed to discrete objects in such a way that the shape of the input function is reproduced as accurately as possible. This principle can be applied to different formulations of the IMF (cf. Eq. 2.4–2.6) as well as the ECMF (cf. 2.44).

Most objects accumulate at the low-mass end of distributions with $\alpha > 0$. Therefore, the iterative determination of integration limits according to Eq. 4.7 becomes computationally increasingly expensive towards the lower-mass regime. Depending on the mass range relevant for the physical problem, the calculation can therefore be accelerated by defining suitable boundaries in advance. As was extensively explained in Ch. 2, only massive and AGB stars contribute significantly to stellar nucleosynthesis feedback. This means that stars with masses below $M_{\mathrm{cutoff}} = 3\,\mathrm{M}_{\odot}$ incorporate mass during a star formation event but are not expected to eject radioactive nucleosynthesis products. This means, the total mass M_{cut} below this cutoff has to be taken into account with respect to the entire mass processed in a star formation event. On the other hand, it can be waived when it comes to the discretisation, because the individual agents in this mass range show no contribution to the phenomena targeted in this work. The detailed calculation of M_{cut} for different IMF shapes is given in the Appendix B.

An example of an optimally sampled population of stars above M_{cutoff} with a total mass of $10^4\,\mathrm{M}_{\odot}$ is given in Fig. 4.3. It is shown for the three different IMF shapes implemented in PSYCO following Salpeter (1955, S55, cf. Eq. 2.4), Kroupa (2001, K01, cf. Eq. 2.5), and Chabrier (2005, C05, cf. Eq. 2.6). Since S55 includes no flat-

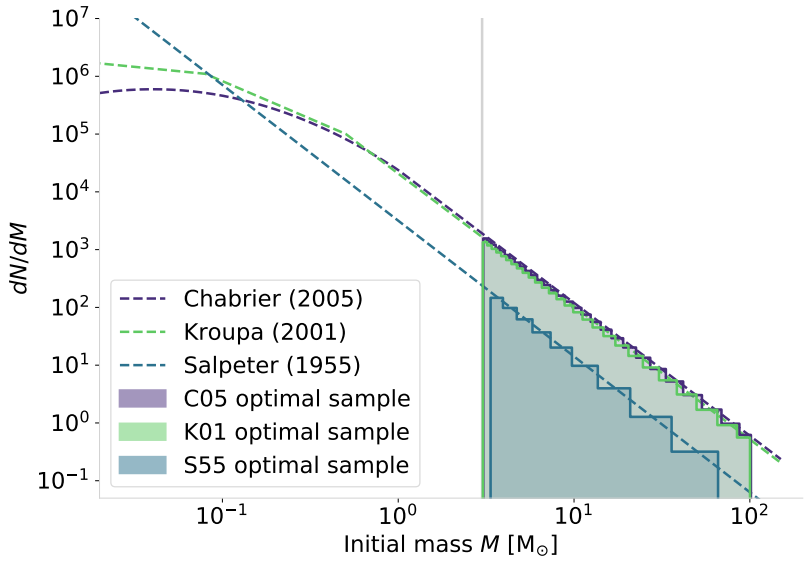

Figure 4.3: Optimally sampled (cf. Eq. 4.8) stellar association with a total mass of $M_{\mathrm{tot}} = 10^4\,\mathrm{M}_\odot$ for three different IMFs. Shown are the slopes of the stellar IMF following Chabrier (2005, C05, *purple*), Kroupa (2001, K01, *green*), and Salpeter (1955, S55, *blue*) as dashed lines. The accordingly sampled sets of individual stellar masses, for which only masses above $M_{\mathrm{cutoff}} = 3\,\mathrm{M}_\odot$ (*grey* solid line) have been taken into account, are shown as histograms. The cutoff is chosen for computational reasons in order to speed up the sampling process while at the same time taking all physically relevant stars for nucleosynthesis feedback into account.

tening for low-mass stars, about 95% of the total mass accumulates in stars below the cutoff mass. For this reason, fewer massive stars are formed according to this function than following K01 or C05. The latter two assign a significantly larger fraction of the total mass to more massive stars, i.e. respectively about 33% and 38% to stars above $M_{\mathrm{cutoff}} = 3\,\mathrm{M}_\odot$, and 20% and 24% to stars above $8\,\mathrm{M}_\odot$. This underlines the importance of integrating a correct shape of the IMF in studies with respect to massive star physics. For that reason, it is implemented as test parameter in PSYCO.

Random Sampling In order to obtain a stochastic and non-deterministic sample from the above mentioned distribution function, random sampling can be applied. Such algorithms are generally based on pseudo random number generators, which generate a sequence of numbers that follow approximately the behaviour of uniformly distributed true random numbers based on some initial random seed value. In order to translate uniformly distributed random numbers into a sample following the specific probability distribution of a simple power-law shaped IMF $\xi(M) \propto M^{-\alpha}$, the inverse transform sampling technique is applied. This is based on the cumulative distribution function (CDF), which is a non-decreasing function that gives the probability of a random variable $u \in [0, 1]$ being less or equal a certain value. The CDF of the IMF in a certain mass range $M \in [M_{\mathrm{l}}, M_{\mathrm{u}}]$ is given by the integral

$$\begin{aligned} F_{\mathrm{IMF}}(u) &= \frac{1}{M_{\mathrm{l}}^{1-\alpha} - M_{\mathrm{u}}^{1-\alpha}} \int_{M_{\mathrm{l}}}^{u} M^{-\alpha}\, dM \\ &= \frac{M_{\mathrm{l}}^{1-\alpha} - u^{1-\alpha}}{M_{\mathrm{l}}^{1-\alpha} - M_{\mathrm{u}}^{1-\alpha}}, \end{aligned} \tag{4.9}$$

with the boundary condition $\alpha \neq 1$ and where the prepended factor accounts for the normalisation to one within the chosen mass range. This gives by inversion

$$\begin{aligned} F_{\mathrm{IMF}}(F_{\mathrm{IMF}}^{-1}(u)) &= u \\ \frac{1}{M_{\mathrm{l}}^{1-\alpha} - M_{\mathrm{u}}^{1-\alpha}} \left[M_{\mathrm{l}}^{1-\alpha} - (F_{\mathrm{IMF}}^{-1}(u))^{1-\alpha}\right] &= u \\ F_{\mathrm{IMF}}^{-1}(u) &= \left[M_{\mathrm{l}}^{1-\alpha} - \frac{u}{M_{\mathrm{l}}^{1-\alpha} - M_{\mathrm{u}}^{1-\alpha}}\right]^{\frac{1}{1-\alpha}}. \end{aligned} \tag{4.10}$$

For a given uniformly distributed random number u between 0–1, the inverse CDF, $F_{\mathrm{IMF}}^{-1}(u)$, describes the translation to a stellar mass value which is distributed according to the IMF. This is shown graphically in Fig. 4.4. This basis of inverse

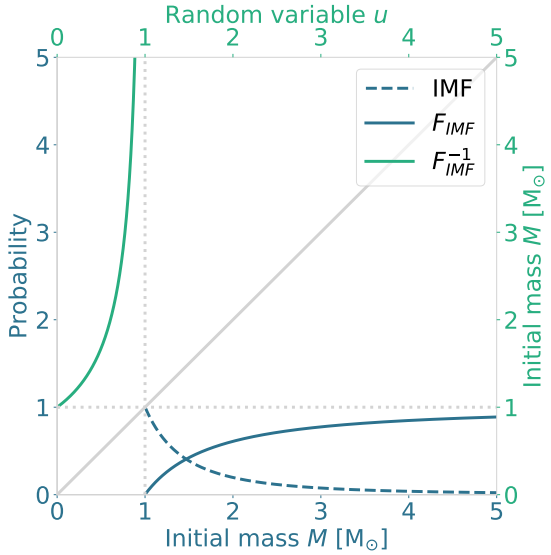

Figure 4.4: Distribution functions for inverse transform sampling the IMF. *Blue* marks quantities related to the probability following a power-law shaped IMF (dashed line) and its CDF F_{IMF} (cf. Eq. 4.9, solid line). *Green* is related to the inverse of the latter, $F_{\mathrm{IMF}}^{-1}(u)$ (cf. Eq. 4.10), which translates a uniformly distributed random variable $u \in [0, 1]$ into stellar mass distributed according to the IMF. For better visibility a single-slope IMF for masses above $1\,\mathrm{M}_\odot$ is used and only displayed up to $5\,\mathrm{M}_\odot$ here. The *grey* solid line indicates the mirror axis of the inversion and the *grey* dotted lines guide the eye to 1 as the maximum value of probability and u.

transform sampling applied to a simple single-slope power law distribution worked through here is applicable to any piecewise monotonically invertible distribution function. Since it will be used later in this thesis, a further example of inverse transform sampling a normal distribution is given in Appendix B.

Usually the number of sampled objects is taken as input for random sampling. However, the bare number of stars is not a physical quantity in the star formation process. Thus, it has to be adjusted to approximately meet a total mass. This can be achieved either by iteratively sampling until the total mass is exceeded or by previously determining the expected number of stars resembling the total cluster mass. The average mass of a star drawn from the simple single-slope IMF in the mass range $M \in [M_{\mathrm{l}}, M_{\mathrm{u}}]$ is given by

$$\langle M \rangle = \int_{M_{\mathrm{l}}}^{M_{\mathrm{u}}} M\ \xi(M)\ \mathrm{d}M = \frac{1-\alpha}{2-\alpha}\ \frac{M_{\mathrm{u}}^{2-\alpha} - M_{\mathrm{l}}^{1-\alpha}}{M_{\mathrm{u}}^{1-\alpha} - M_{\mathrm{l}}^{1-\alpha}}, \tag{4.11}$$

which yields the expected number of stars as $N = M_{\mathrm{tot}}/\langle M \rangle$. If this number of objects is drawn from the IMF, M_{tot} will be obtained on average. However, each individual sample is in particular subject to random variations. This can be seen in Fig. 4.5, which resembles Fig. 4.3 and shows the same exemplary star group of $M_{\mathrm{tot}} = 10^4\,\mathrm{M}_\odot$ now for the random sampling approach. It can be seen that the

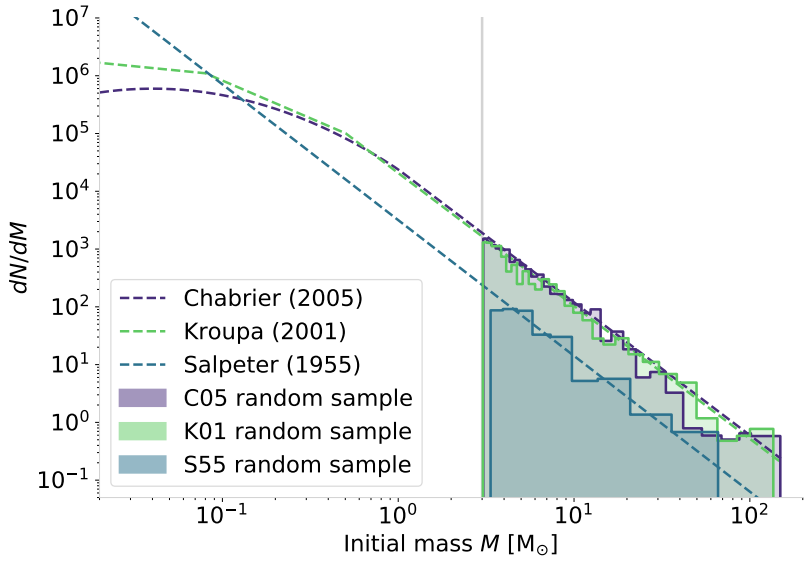

Figure 4.5: Randomly sampled stellar association for three different IMFs with a total mass of $M_{\mathrm{tot}} = 10^4\,\mathrm{M}_\odot$. Same as Fig. 4.3 using a random sampling algorithm instead of an optimal sampling approach.

smaller the sample, the more pronounced the random fluctuations are. It is also apparent that there is a tendency of the random sampling approach to produce more massive stars compared to optimal sampling. This is the case because the latter integrates the relation between the most massive star and the overall cluster mass in Eq. 2.43 while for the former this is omitted.

Application in PSYCO As already mentioned in the introduction to this section, it is an epistemologically delicate question as to which of the sampling techniques should be chosen. In PSYCO, therefore, a flexible combination was chosen to meet the requirements of the respective scientific target level.
For modelling an entire galactic structure on the basis of star groups, the optimal sampling approach is chosen for the following reasons: The main input quantity of mass is coherently reproduced as close as possible, overall physical boundaries of star formation in small groups are included, stochastic deviations from the overall IMF shape are avoided, and the deterministic treatment enables distinctly fast and reproducible computation. The latter point is particularly important for the overall structure of the code. Due to the reproducibility, a set of cluster masses can be discretised systematically and stored in databases. By following this database solution, the determination of mass distributions for typically 10^4–10^6 clusters for each galactic model is accelerated substantially.
The random sampling approach is implemented in a sub-routine for investigating individual star groups. In this way, possible stochastic effects in the process of star formation can be determined and the uncertainty range associated with different stellar parameter variations can be assessed. Additionally, for some observable star

groups the stellar census is known and the number of stars can be used as input in that case. Such associations can be investigated following the approach by Voss et al. (2009).

4.2.2 Modelling Individual Star Groups

With a discrete mass distribution, the foundation for population synthesis of individual stellar associations is laid. Following the general ansatz presented in Sec. 2.3.5, single star evolution models can be combined according to their initial stellar mass in order to calculate collective feedback characteristics as described in Eq. 2.46. The following explanations are limited to the nucleosynthesis aspect of those models relevant in the context of this thesis. Since the evolution models introduced in Sec. 2.2.5 are computationally costly, they are usually provided on irregular time grids and for a sparse number of initial masses. In order to utilize those for a coherent population synthesis, a close-meshed sequence of isochrones has to be established on that basis. Isochrones designate evolutionary tracks on equal time steps. The temporal alignment is done by a sequence of linear interpolations. These are implemented firstly to pin down the original models to equal and narrow time steps, secondly to derive the nucleosynthesis yields for a fine grid of initial masses which are not represented in the original models, and finally to infer the temporal scope in which the ejection occurs for each of those initial masses.
The population synthesis of a full star group is calculated on the basis of these isochrones by combining them according to the sampled set of initial masses. The result for a total cluster mass of $10^4\,M_\odot$, discretised by random sampling the IMF as described in Sec. 4.2.1, is depicted for ^{26}Al and ^{60}Fe ejection in Fig. 4.6. It is shown for the assumptions of instantaneous star formation following three different IMF shapes C05 (cf. Eq. 2.6), K01 (cf. Eq. 2.5), and S55 (cf. Eq. 2.4) and two different stellar yield models LC06 and LC18. For better clarity, the overall behaviour is discussed here in detail only for the case of the standard IMF K01. The remaining cases are similar and summarised in Tab. 4.1.

Table 4.1: ^{26}Al and ^{60}Fe nucleosynthesis feedback results for population synthesis of a $10^4\,M_\odot$ stellar group assuming different IMF shapes (cf. Fig. 4.6). Calculations are based on two different stellar evolution models LC06 and LC18. Times of ejection onset, first, and second peak denote the occurrence after simultaneous star formation. The values give the average from 10^3 MC runs. If two numbers are divided by a slash, the first denotes ^{26}Al and the second ^{60}Fe. The last column gives all the points after star formation where $^{60}\mathrm{Fe}/^{26}\mathrm{Al} = 1$ is crossed towards ^{60}Fe-domination.

Model	IMF	Onset [Myr]	1st peak [Myr]	2nd peak [Myr]	Maximum mass [$10^{-4}\,M_\odot$]	^{60}Fe-domination [Myr]
LC06	S55	2.4 / 3.1	4.0 / 4.4	14.9 / 17.5	1.1 / 1.9	3.2, 15.9
	K01	2.4 / 3.1	4.0 / 4.9	14.9 / 17.7	10.1 / 23.6	3.2, 15.9
	C05	2.4 / 3.1	4.0 / 4.7	14.9 / 17.7	13.3 / 30.2	3.2, 15.9
LC18	S55	1.6 / 7.9	3.4 / 9.8	9.7 / –	0.5 / 0.1	18.3
	K01	1.6 / 7.9	3.4 / 9.7	9.8 / –	4.4 / 1.2	18.3
	C05	1.6 / 7.9	3.4 / 9.7	9.7 / –	5.7 / 1.5	18.3

While ^{26}Al ejection sets in continuously after ~ 2.4 Myr for LC06 and ~ 1.6 Myr for LC18, ^{60}Fe ejection occurs abruptly after ~ 3.1 Myr and ~ 7.9 Myr respectively. The isotopic delay reflects the fact that ^{26}Al is ejected already during the earlier occurring stellar wind phases and ^{60}Fe only in the later stellar explosions. The occurrence of ^{60}Fe is additionally delayed in LC18 due to the model-inherent explodability for

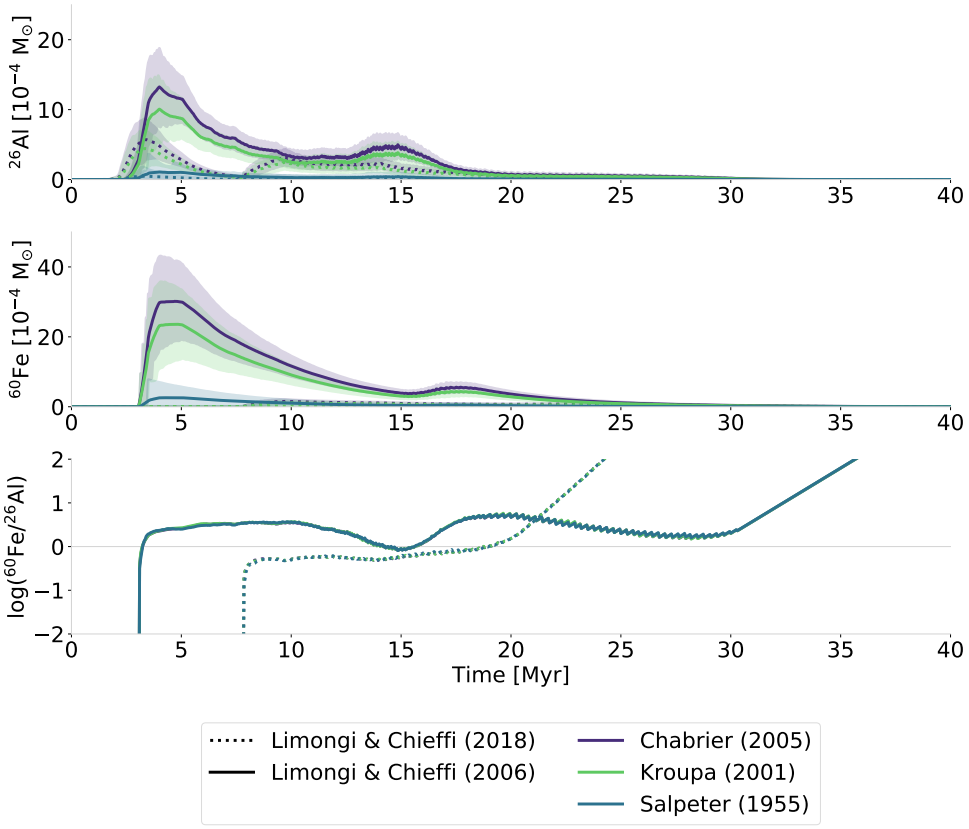

Figure 4.6: Population synthesis of nucleosynthesis ejecta ^{26}Al (*upper*), ^{60}Fe (*middle*), and their average mass ratio (*lower*) in a stellar group with $M_{\mathrm{EC}} = 10^4\,\mathrm{M}_\odot$. It is calculated for two different stellar yield models LC06 as solid and LC18 as dotted lines by assuming concurrent star formation and random sampling three different IMF shapes C05 (*purple*, cf. Eq. 2.6), K01 (*green*, cf. Eq. 2.5), and S55 (*blue*, cf. Eq. 2.4). The shaded regions indicate the 68th percentiles derived from 10^3 MC runs each. Note in particular the different scale for ^{60}Fe. The overall shape shows a structure of two peaks. The first peak is due to strong winds and SN yields from the most massive stars. This is reduced in LC18 because explodability only applies for $M_* = 8$–$25\,\mathrm{M}_\odot$ in this model and thus SN contributions are absent for very massive stars. This is particularly striking for ^{60}Fe. The second peak is due to enhanced explosive burning for $M_* \lesssim 20\,\mathrm{M}_\odot$ in LC06. The mass ratio ^{60}Fe/^{26}Al is generally not affected by the choice of IMF. A detailed account of the differences in shape is given in Tab. 4.1.

$M_* = 8$–$25\,\mathrm{M}_\odot$ only (cf. Sec. 2.2.5). This means that stars with masses higher than $25\,\mathrm{M}_\odot$ are assumed to collapse into black holes directly, without exploding as ccSNe. Thus, SN yields are absent in this stellar mass regime, which would contribute at earlier times. The further time behaviour shows overall two peaks, the first of which is generally higher.

Looking at ^{26}Al from LC06, the first peak reaches up to $1 \times 10^{-3}\,\mathrm{M}_\odot$ and comes from the combined wind and SN ejecta of the most massive stars above $40\,\mathrm{M}_\odot$. Very strong mass loss in this regime reaches down to even the He-core, which leads to efficient transport of ^{26}Al away from hot stellar regions and enhances the yield of this nucleus. In the case of LC18, it arrives only at $0.4 \times 10^{-3}\,\mathrm{M}_\odot$ and slightly earlier, which is mainly due to the fact that it results from solely stellar wind contributions. This first peak of ^{26}Al nucleosynthesis feedback is reached about 4.0 Myr or 3.4 Myr after star formation regarding LC06 and LC18 respectively. The second peak for LC06 occurs after 14.9 Myr and happens due to a shallow dredge-up and weak mass loss phase that are underwent by stars with masses $M_* \lesssim 20\,\mathrm{M}_\odot$. Thus, ^{26}Al from hot-bottom burning resides inside the star when it explodes and these stars show enhanced SN yields. For LC18 the peak is produced after 9.8 Myr by the first SNe from $25\,\mathrm{M}_\odot$ stars.

The ^{60}Fe profile exhibits a similar structure of two peaks for LC06 with the second peak being delayed by about 3 Myr compared to ^{26}Al. The first peak results from the most massive stars within which a fully convective He-burning shell establishes where ^{22}Ne(α,n)^{25}Mg is an efficient neutron source producing ^{60}Fe via ^{59}Fe(n,γ)^{60}Fe at a high rate. Stars terminating between the peaks have masses $\lesssim 40\,\mathrm{M}_\odot$. These experience enhanced mass loss such that the core mass reduces and the convective He-shells are stripped. Thus, mainly the C-burning shell contributes where a decreased reaction rate of ^{22}Ne(α,n)^{25}Mg does not produce neutrons on a large scale for ^{60}Fe to be produced efficiently. However, stars with initial masses of $\lesssim 15\,\mathrm{M}_\odot$ show increased core temperatures due to significant contraction at the end of central O-burning. This increases the temperature in the radiative He-shell such that ^{60}Fe is synthesised. Explosions in this stellar mass regime give rise to the second peak of ^{60}Fe ejection around 17.7 Myr. The LC18 model obtains only a maximum mass of ^{60}Fe of $0.12 \times 10^{-3}\,\mathrm{M}_\odot$ and does not result in a two-peak structure since it only shows contributions of masses $\leq 25\,\mathrm{M}_\odot$.
The general behaviour is overlaid by the half-life times of 0.717 Myr and 2.6 Myr for ^{26}Al and ^{60}Fe, respectively. The longer lifetime of ^{60}Fe is reflected in the fact that it becomes increasingly dominant in the mass ratio ^{60}Fe/^{26}Al at later times. This mass ratio turns out to be an intriguing indicator particularly sensitive to different physical processes and assumptions in stellar evolution models. While ^{60}Fe is dominant right from the beginning of ejection for LC06 at 3.2 Myr with a dip around 15 Myr, it only becomes continuously dominant for LC18 after 18.3 Myr. This is identical for different IMFs because in random sampling the same mass range is accessible for every cluster mass and only the average values are considered here. The sawtooth pattern exhibited by the ^{60}Fe/^{26}Al ratio constitutes a computational artefact because initial stellar masses are taken into account with a precision of $0.1\,\mathrm{M}_\odot$. Since the stellar lifetime is approximately proportional to $M_*^{-2.5}$, this step width yields a larger spread in time between lower mass stars. This leads to a noticeable temporal discretisation particularly for the lower mass regime which contributes at later times.
A direct comparison of optimal vs. random sampling for population synthesis of the previous example star group is shown in Fig. 4.7. As expected, the overall shape is identical. For both stellar evolution models, LC06 and LC18, the main difference arises due to the tendency of random sampling to overproduce massive stars, which was already discussed in Sec. 4.2.1. This manifests in a generally reduced first peak using optimal sampling. Since the latter is deterministic no flattened average is obtained. This makes the effects of individual stars clearly visible as sawtooth patterns in the temporal profiles. Especially the mass ratio of a single group shows strong variations and a high sensitivity to its particular stellar content.
After the previous remarks, it is clear that such population synthesis calculations show the sensitivity of cumulative feedback features in entire clusters to the stellar physics of individual stars. Detailed nuclear and astrophysical processes in stars are reflected in the behaviour of stellar groups and can be inferred from them. This underlines the astrophysical potential of this approach to coherently study nucleosynthesis feedback on different scales.

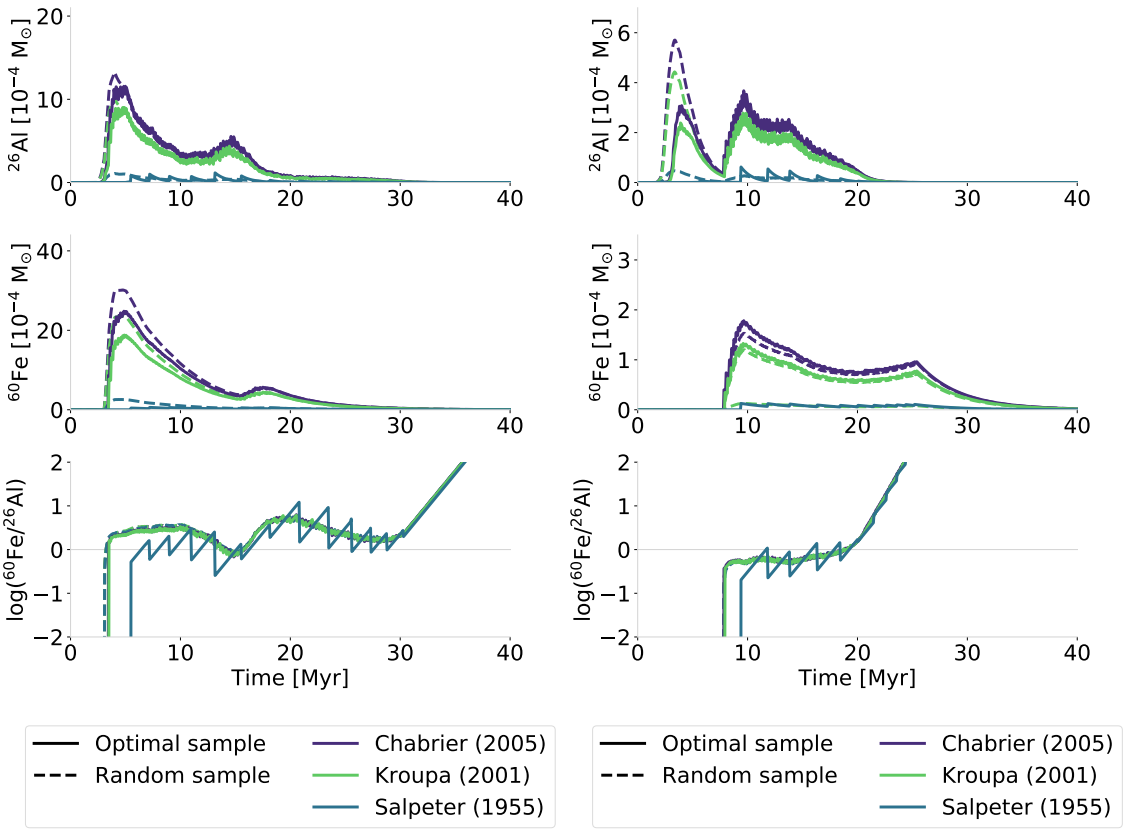

Figure 4.7: Stellar populations synthesis of ^{26}Al and ^{60}Fe nucleosynthesis feedback for a 10^4 M$_\odot$ stellar group using optimal (solid lines) and random sampling (dashed lines) approaches with stellar evolution models LC06 (*left*) and LC18 (*right*). For random sampling the average values of 10^3 MC runs are shown. Colours correspond to different IMF assumptions similar to Fig. 4.6. The main difference is visible as a tendency for overproduction of high-mass stars in random sampling compared to optimal sampling. The prominent sawtooth patterns result from discrete contributions from individual sources.

4.2.3 Stellar Parameters

So far, the only stellar parameter in consideration was the initial stellar mass. As described in Sec. 2.2.5, stellar feedback is dependent on a wide range of physical parameters, in particular explodability, rotational velocity, and metallicity. In this section, the effect of these parameters on nucleosynthesis feedback from stellar associations is investigated. For better clarity, only the standard IMF K01 is used, because the overall physical results are qualitatively independent of the respective choice of IMF. Throughout this section, random sampling is applied for calculating population synthesis in order to estimate the related range of uncertainty in modelling results.

Explodability The general physical groundwork underlying stellar explodability as well as the four theoretical models applied in this thesis were laid out in Sec. 2.2.5 and summarised in Tab. 2.5. Since LC18 holds already a strict model-inherent explodability, the effect of different explodability models are demonstrated using LC06. Nucleosynthesis feedback profiles for a 10^4 M$_\odot$ star group are shown in Fig. 4.8 for the explodability models S09, J12, S+16, and LC18. The explodability models S09, J12, and S+16 show no major deviations and are consistent with each other within uncertainties from MC sampling. As expected, the nucleosynthesis yields are gener-

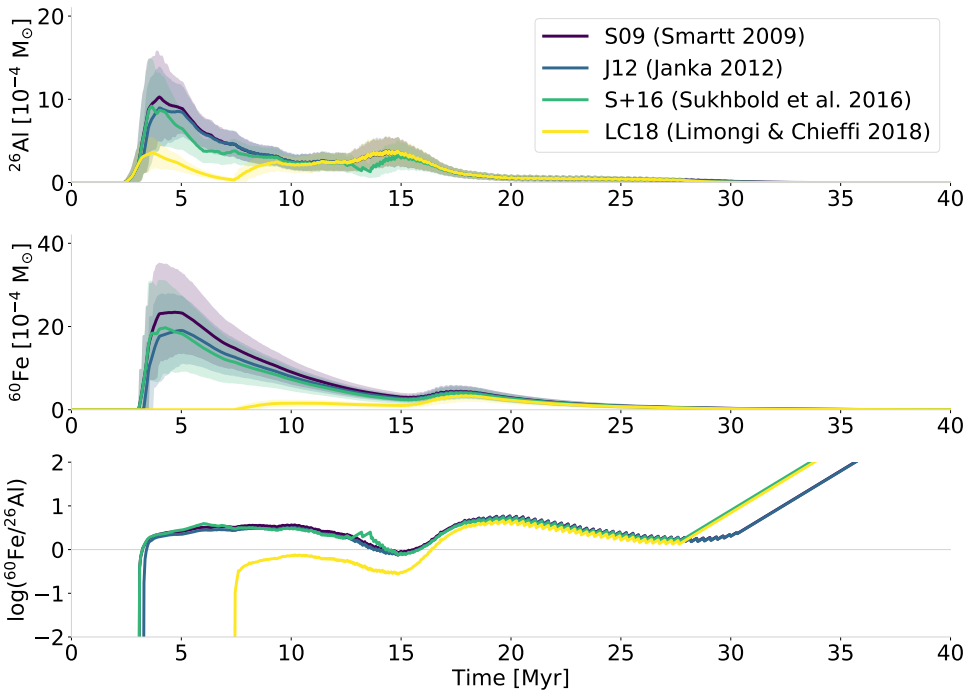

Figure 4.8: Population synthesis of nucleosynthesis feedback from a $10^4\,M_\odot$ star group. Same as Fig. 4.6 for different explodability models S09 (*purple*), J12 (*blue*), S+16 (*green*), and LC18 (*yellow*) using the stellar evolution model LC06 and the fixed IMF K01.

ally smaller if explosions are assumed for fewer stars. The wind component, on the other hand, is not affected by explodability. The disjoint islands of explodability in S+16 (cf. Fig. 2.30) cause distinct features like a small dip in ^{26}Al after around 14 Myr. A significant difference is obtained by applying the explodability LC18, which allows for SNe only for stellar masses below $25\,M_\odot$. While the absence of SN yields from higher-mass stars reduces the first ^{26}Al peak to its stellar wind component, the first ^{60}Fe peak is shifted by ~ 6 Myr to the first explosions of $25\,M_\odot$ stars after about 10.5 Myr. Since ^{60}Fe emerges solely from SNe, it is particularly sensitive to explodability. This is clearly visible in the ^{60}Fe/^{26}Al mass ratio, which is dominated by ^{26}Al for over 16 Myr if very massive star explosions are omitted. Otherwise, this phase only lasts about 3 Myr. Thus, in combination with detailed population synthesis calculations of nucleosynthesis feedback, ^{60}Fe and the mass ratio ^{60}Fe/^{26}Al make promising observational targets for investigating questions concerning massive star explodability. A concise overview over the changes in temporal features is given in Tab. 4.2.

Table 4.2: ^{26}Al and ^{60}Fe nucleosynthesis feedback results for population synthesis of a $10^4\,M_\odot$ stellar group assuming different explodability models (cf. Fig. 4.8). Calculations are based on the stellar evolution model LC06 and standard IMF K01. Properties are the same as in Tab. 4.1.

Explodability	Onset [Myr]	1st peak [Myr]	2nd peak [Myr]	Maximum mass [$10^{-4}\,M_\odot$]	^{60}Fe-domination [Myr]
S09	2.4 / 3.1	4.0 / 4.9	14.9 / 17.7	10.1 / 23.6	3.2, 15.9
J12	2.4 / 3.3	4.0 / 5.0	14.3 / 17.7	9.0 / 19.1	3.4, 15.9
S+16	2.4 / 3.1	3.7 / 4.3	14.9 / 17.7	9.2 / 19.7	3.2, 15.9
LC18	2.4 / 7.5	3.7 / 10.5	14.9 / 17.7	3.8 / 3.4	16.4

Metallicity The Milky Way exhibits a non-uniform metallicity distribution between Solar [Fe/H] = 0 and sub-Solar [Fe/H] = −1 (Cheng et al. 2012). Therefore, in order to develop a consistent picture of stellar feedback across the entire Galaxy, the differences in initial metal enrichment have to be taken into account. The extended model grid of LC18 comprises stellar evolution simulations for different metallicity values and thus its effect can be investigated via population synthesis as well. This is shown for the two considered extreme cases of [Fe/H] = 0 and [Fe/H] = −1 in Fig. 4.9. It can be seen that a change in metallicity leaves the general time evolution

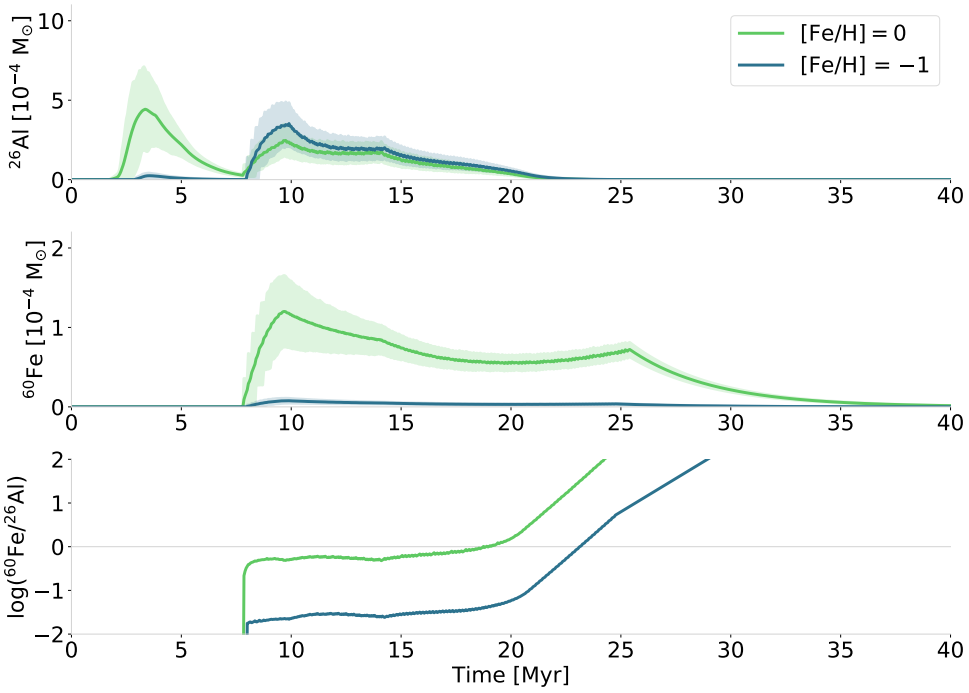

Figure 4.9: Population synthesis of nucleosynthesis feedback from a 10^4 M$_\odot$ star group. Same as Fig. 4.6 for Solar metallicity [Fe/H] = 0 and sub-solar metallicity [Fe/H] = −1 on the basis of stellar evolution models LC18 and standard IMF K01.

of the group unaffected. However, the reduction of metallicity goes along with a significant decrease of the ejected yields. This is the case because the production of ^{26}Al and ^{60}Fe relies heavily on the presence of the initial elements for their synthesis, mainly ^{25}Mg and ^{59}Fe, respectively. This is especially affecting the ^{60}Fe yields since ^{59}Fe is synthesised in a low-metallicity star mainly in the very late central burning phases. Because of the disjunction to neutron rich layers such as for the He- or C-burning shells and the short time scales, only marginal amounts of ^{60}Fe are formed. On the other hand, the opacity of stellar material decreases with metallicity. This counteracts the emergence of large convective zones due to the enhancement of radiative energy transport, which diminishes in particular the convective transport of ^{26}Al towards cooler regions near the stellar surface. Additionally, stellar winds are reduced because the radiation pressure onto the outer stellar material is proportional to its opacity. The two factors lead to a large reduction of ^{26}Al ejection in stellar winds. This is apparent in Fig. 4.9 due to the effective disappearance of the first ^{26}Al peak around 4 Myr in the association with metallicity [Fe/H] = −1. However, the ^{60}Fe production is reduced overall stronger than the ^{26}Al production. Thus, the ^{60}Fe-dominance shifted to a late time after around 23 Myr due to the longer lifetime of ^{60}Fe. The overall effects are summarised together with stellar rotation effects in Tab. 4.3.

Rotational Velocity In Sec. 2.2.2, the rotational velocity was introduced as factor influencing mixing processes in stellar environments. It enhances convective regions and the transports of raw material for nuclear reactions throughout a star and therefore affects nucleosynthesis feedback. The distribution of stellar rotation was observationally determined by Glebocki et al. (2000) for each spectral class individually and updated by Glebocki & Gnacinski (2005). The rotation velocities weighted with the average inclination angle of O and B stars is depicted in Fig. 4.10. The

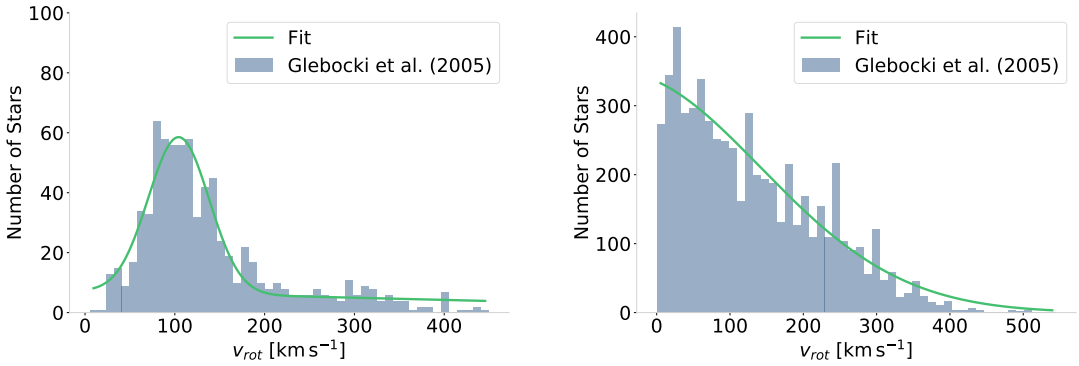

Figure 4.10: Rotational velocity distribution of O (*left*) and B (*right*) stars. The *blue* data points show the observational catalogue by Glebocki & Gnacinski (2005). The *green* line shows the fit of a Gaussian distribution on top of a linear function.

more prominent and shifted peak at $\sim 100\,\mathrm{km\,s^{-1}}$ for O stars can be explained by an interaction between higher momentum transfer due to prolonged accretion during the star formation process and, on the other hand, by its termination at a certain threshold speed. In order to utilize this information in the population synthesis algorithm, an analytic description of the distribution is chosen by fitting a Gaussian on top of a straight line to the catalogue data. This is integrated in an additional MC step by sampling a rotational velocity from these functions depending on their mass, which is assigned to a spectral class according to the classifications in Tab. 2.1. Since only three velocity steps, $0\,\mathrm{km\,s^{-1}}$, $150\,\mathrm{km\,s^{-1}}$, and $300\,\mathrm{km\,s^{-1}}$, are provided in LC18 originally, a finer gradation is obtained by linear interpolations of time and yield. Hereby, rotational velocities limited at $300\,\mathrm{km\,s^{-1}}$ and higher velocities are omitted.

Taking these velocities into account, the nucleosynthesis feedback of a stellar association is affected as illustrated in Fig. 4.11. While the effects on ^{26}Al are restricted to an earlier onset of the wind phase after only 0.6 Myr and a slight prolongation of stellar evolution which delays the second ejection peak by ~ 1 Myr, the implications for ^{60}Fe are striking. Rotation-driven instabilities lead to an increased convective C-burning shell, which means that the region of primary neutron source is enlarged and the phase in which neutrons are massively released is prolonged. This enhances the production of ^{60}Fe in fast spinning stars significantly by a factor of 10. Overall, rotation additionally causes a stretch of stellar evolution in time. The relevant features in the evolution of a star group being affected by stellar rotation are summarised in Tab. 4.3.

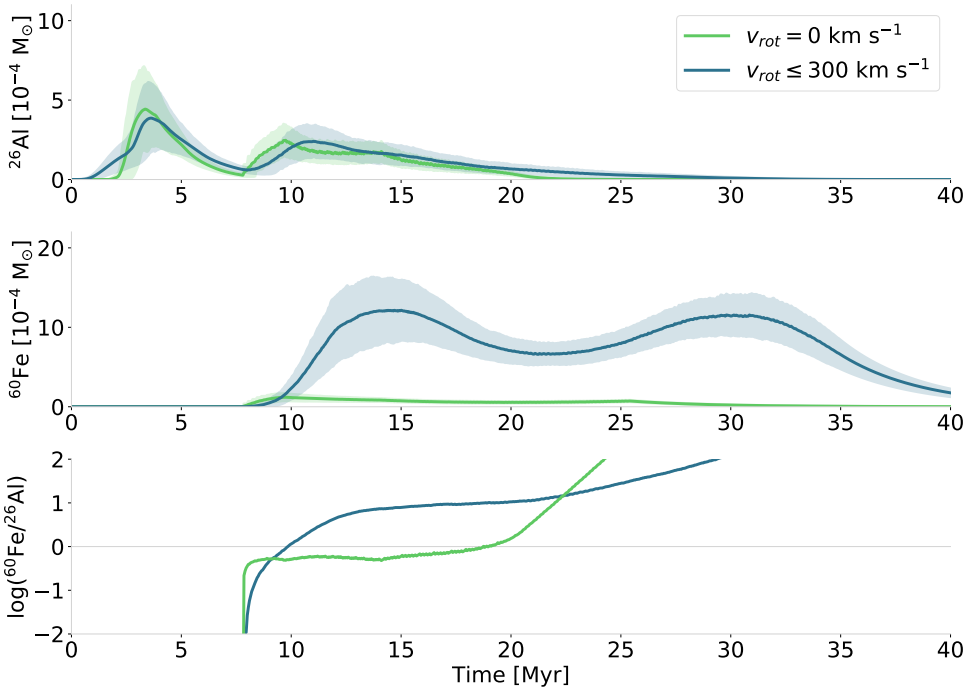

Figure 4.11: Population synthesis of nucleosynthesis feedback from a 10^4 M$_\odot$ star group with Solar metallicity. Same as Fig. 4.6 with (*blue*) and without (*green*) the effects of stellar rotation using the evolution model LC18 and the fixed IMF K01.

Table 4.3: ^{26}Al and ^{60}Fe nucleosynthesis feedback results for population synthesis of a 10^4 M$_\odot$ stellar group and including metallicity [Fe/H] $= -1$ or rotation $v_{\rm rot} \leq 300\,{\rm km\,s^{-1}}$. Calculations are based on the stellar evolution model LC18 and standard IMF K01. Properties are the same as in Tab. 4.1.

Metallicity [Fe/H]	Rotation [km s^{-1}]	Onset [Myr]	1$^{\rm st}$ peak [Myr]	2$^{\rm nd}$ peak [Myr]	Maximum mass [10^{-4} M$_\odot$]	^{60}Fe-domination [Myr]
0	0	1.6 / 7.9	3.4 / 9.7	9.8 / –	4.4 / 1.2	18.3
-1	0	2.9 / 8.1	3.6 / 9.9	9.9 / –	3.5 / 0.08	23.2
0	≤ 300	0.6 / 8.0	3.6 / 15.0	11.0 / 29.8	3.9 / 12.1	9.9

4.2.4 Binary Yield Effects

A frequently discussed issue with regard to nucleosynthesis feedback is the influence of binary interactions. On the one hand, Roche-lobe overflows and tidal interactions can significantly change the chemical composition of binary stars as well as enhance the ejection of material. This leads to equally relevant implications with respect to the stellar end phases, since the composition of SN progenitors is altered or a preferential production white dwarfs occurs. As outlined in Sec. 2.2.5, these effects have so far remained on rather speculative ground, as the theoretical approach proves to be difficult due to the high complexity and parameter diversity of such systems. First binary yield calculations for ^{26}Al have been provided recently by B+19. These feedback profiles have been included in PSYCO in order to narrow down their global impact quantitatively.

To include binarity, an overall binary fraction is assumed. This is done for the currently accepted value of 70% (Sana et al. 2012; Renzo et al. 2019; Belokurov et al. 2020) and an extreme assumption of 90%. In an association that is massive enough, i.e. when the stellar census is large, binarity can be sampled randomly according to that fraction as property of each star independently. This is based on

the assumption that binary stars form just like single stars according to the same IMF. Thus, a particular consideration of combining certain stars into binaries or specifically reproducing the mass ratio can be omitted. The former is redundant because population synthesis generally ignores spatial properties and the latter is irrelevant due to the fully stochastic determination of stellar masses. Since B+19 is restricted to the evolution of the primary star, the secondary component is treated as evolving like a single star due to the lack of additional information in B+19. The stars sampled as single stars are for their part treated as described in the sections above.
B+19 only comprises wind yields, therefore SN ejecta have to be assumed following other models. The yields from single star calculations LC06 or LC18 are used auxiliary due to the lack of particular binary SN yields. The binary wind yields have been calculated in B+19 on a rather sparse and irregular grid of orbital separations and for a maximum initial mass of 60 $M_\odot$. Thus, extensive interpolation is necessary to consistently cover orbital periods between 3 and 100 days. These are sampled uniformly during the population synthesis. Stars with longer periods are treated as single stars. The effects for stars up to 150 $M_\odot$ are extrapolated linearly. In this way a complete grid of binary stars is obtained, which is integrated in the population synthesis. The results for ^{26}Al in an exemplary star group of 10^4 $M_\odot$ including binary yield effects are depicted in Fig. 4.12.

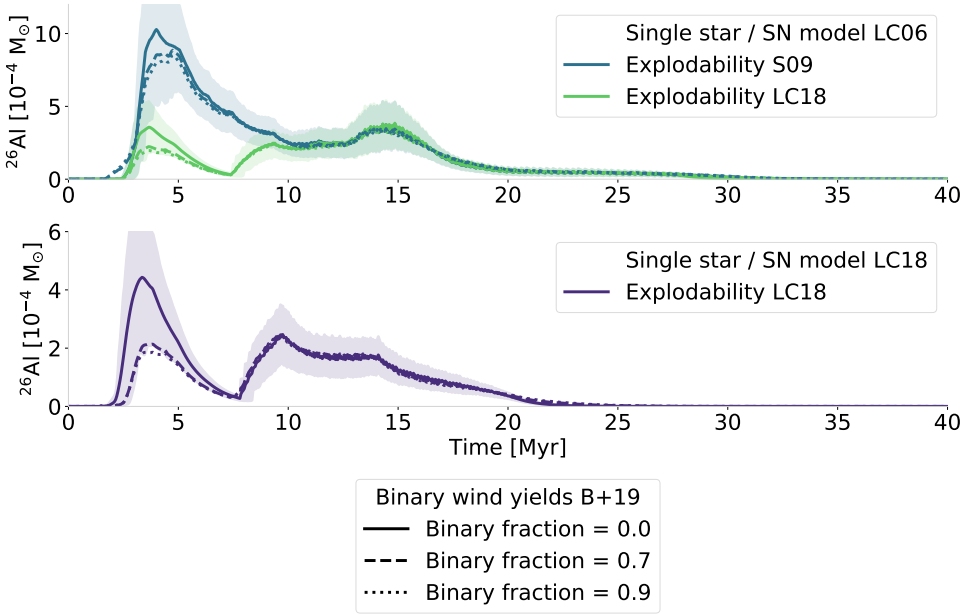

Figure 4.12: Population synthesis of ^{26}Al nucleosynthesis feedback from a 10^4 $M_\odot$ star group taking binary interactions following B+19 into account. Binary systems are included with orbital periods between 3 and 100 days and with an overall fraction of 70% (dashed line) and 90% (dotted line), which is contrasted with an association of only single stars (solid line). Stars with longer periods, i.e. wider separations, and secondary stars are considered to evolve as single stars. The yields for single stars and SNe are taken from LC06 (*upper*) or LC18 (*lower*). Lines indicate the average of 1000 MC runs each. Different colours indicate different explodability models and shaded regions enclose 68% of all MC runs for the group with only single stars.

For LC06 single star evolution models, the two extreme explodability assumptions S09 and LC18 are shown for comparison. Regardless of the choice of SN model, the general effect from binary winds turns out to be rather small, especially for the lower-mass regime, which contributes at later times. The excess in low-mass star wind yields compared to single star models shown in Fig. 2.33 is largely dominated

by SN contributions. Nevertheless, the reduction of wind yields in binary systems with large separation and primary stars of 25–30 $M_\odot$ leads to the tendency of less ^{26}Al ejection after $\sim$ 15 Myr. On the other hand, the increased binary wind yields for stars with masses $\leq$ 20 $M_\odot$ leads to slightly enhanced ejection after $\sim$ 17 Myr. At early stages, the ejection from very massive stars tends to be reduced due to binary interactions. It is important to note that this is to a large part attributed to uncertainties in the necessary extrapolation towards high-mass stars and should not be over-interpreted. Altogether, the changes due to binary interactions lie within the 68th percentile of single star population synthesis results and are therefore considered small. However, this can only serve as rough estimation of such effects since the direct impact on SN progenitors or the detailed evolution of the secondary stars have currently not been modelled properly yet.

Essentials

Population synthesis is an indispensable tool for scaling stellar nucleosynthesis models to phenomena of observable magnitude. Its implementation in PSYCO is expanded to comprise a large variety of physically relevant properties. For the estimation nucleosynthesis feedback in stellar groups, the consideration of

- IMF affects the amplitude of nucleosynthesis feedback, with considerable reduction for S55;
- Explodability changes mainly the contributions from highest-mass stars, with a possibly major decrease at early stages after 3–7 Myr;
- Metallicity mostly lowers ^{26}Al wind contributions at early times and diminishes ^{60}Fe SN yields in later phases of low metallicity associations;
- Rotational velocity slightly stretches stellar evolution in time and significantly increases ^{60}Fe yields due to fast rotating stars;
- Binarity shows overall minor effects with a tendency to reduce wind contributions from the most-massive stars.

4.3 Modelling the Milky Way Structure

Based on the nucleosynthesis properties of stellar groups calculated in the previous Sec. 4.2, the information can be used to scale the model to the galactic level. This corresponds to the transgression from the middle to the top level in Fig. 4.2 and will be described in this section. Therefore, the basic assumption of a galactic SFR discussed in Sec. 4.3.1 is integrated in a spatial galactic model as explained in Sec. 4.3.2 with a temporal aspect developed in 4.3.3. Overall, this aims to obtain a synthetic sky map of galactic radioactivity, which is outlined in Sec. 4.3.4. In principle, this step can be performed to obtain the properties of any type of galaxy. However, the main focus will be on achieving a high similarity with the Milky Way structure in particular, since this is currently the only empirical case with gamma-ray observations of nuclear decay lines accessible.

4.3.1 Galactic Mass

The fundamental physical input in order to model the galactic structure of radioactivity in the PSYCO framework is the total stellar mass, which is indirectly obtained by the choice of a constant SFR (cf. Sec. 2.4.2) over the entire model time. This approach is chosen for three reasons: First, mass is a physical quantity with the rate of star formation phenomenologically characterising an actual physical process. Second, it additionally goes with a temporal information that can be utilised to physically motivate the time evolution of the modelled system. Third, the SFR can be inferred from a variety of observations independent of gamma-ray measurements, which decouples the model from immediately biased assumptions regarding the phenomena under investigation.
Since this thesis is concerned with radioactive isotopes, the overall necessary temporal scope can be estimated by the condition that equilibrium is reached between production and decay. If a constant rate g_i is assumed for the production of isotope i, this is taken into account in Eq. 3.4 by the expression

$$\frac{dN}{dt} = g_i - \lambda_i N. \tag{4.12}$$

If the amount of isotope i at the onset of production $N(t_0) = 0$, the number of atoms at a later time t is then calculated as

$$N(t) = \frac{g_i}{\lambda_i}(1 - e^{-\lambda_i t}). \tag{4.13}$$

For each isotope this approaches asymptotically a characteristic equilibrium value of g_i/λ_i for $t \to \infty$. In the following, sufficient convergence is assumed if 99% of this value is reached. This condition is fulfilled for $t \geq -\frac{\ln 0.01}{\lambda_i}$, which only depends on the decay constant λ_i of the respective isotope and in particular independent of g_i. The latter only determines the absolute amplitude of this radioactive build-up. The time profile of such build-up process for ^{26}Al and ^{60}Fe is shown graphically in Fig. 4.13. For a constant production rate, convergence is reached after 4.7 Myr and 17.3 Myr,

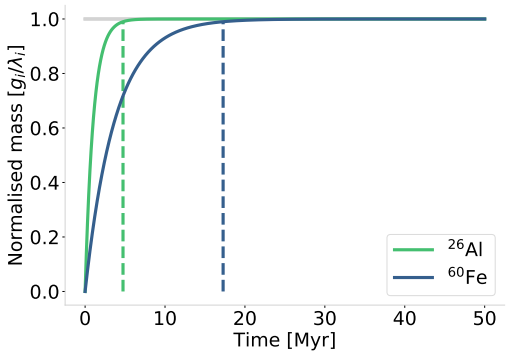

Figure 4.13: Radioactive build-up of ^{26}Al (*green*) and ^{60}Fe (*blue*) for characteristic constant production rate g_i and decay constant λ_i of the respective isotope i. Dashed lines denote the convergence criterion of reaching 99% of the equilibrium value g_i/λ_i (*grey* line).

respectively. Since ^{60}Fe has the longer lifetime, this is the determining factor for the temporal framework. It must be added that in the temporally most extreme case of LC18, the onset of ^{60}Fe ejection occurs only after ~ 10 Myr and is not point-like in time but extended over another ~ 20 Myr (cf. e.g. Fig. 4.11). Taking this offset

into account, convergence of the longest-lived isotope in consideration is expected to be reached in the case of stellar evolution models with the longest stretch in time after $\sim 50\,\mathrm{Myr}$. This serves as an estimation of the total time T_{tot} the model has to evolve in order to develop convergence in mass of the isotopes relevant in the context of this thesis. This will be confirmed by the actual galactic model realisations in Sec. 4.4.1.
The total mass that is transferred into stars over this timespan follows immediately as $M_{\mathrm{tot}} = \mathrm{SFR} \times T_{\mathrm{tot}}$. Since the mass distribution of stellar clusters in the Galaxy follows the ECMF (cf. Sec. 2.3.2), which is similar to the IMF, an analogous approach to the distribution of a total cluster mass to individual stars as described in Sec. 4.2 can be taken. For example, with $\mathrm{SFR} = 2\,\mathrm{M}_\odot\,\mathrm{yr}^{-1}$ a total mass of $M_{\mathrm{tot}} = 10^8\,\mathrm{M}_\odot$ is processed into stars over the course of 50 Myr. Distributing this mass according to the ECMF (cf. Eq. 2.44), a total number of about 8.1×10^4 clusters between $115\,\mathrm{M}_\odot$ and $1.4 \times 10^5\,\mathrm{M}_\odot$ forms. This translates to a cluster formation rate (CFR) of ~ 0.16 per century. The lower-mass threshold for consideration of $115\,\mathrm{M}_\odot$ is chosen because this is the lowest cluster mass to produce a star $\geq 3\,\mathrm{M}_\odot$ in the optimally sampled case. Therefore, less massive clusters are not expected to show any significant signature of radioactivity considering ^{26}Al and ^{60}Fe. As expected, the number of clusters scales linearly with the SFR. On the other hand, due to the logarithmic dependence of the empirical relation of the most massive cluster on SFR, the maximum individual mass remains relatively unaffected (Weidner & Kroupa 2004).
In this way, the rate of cluster formation is derived as galactic property from the SFR, which can be combined with spatial properties of the galactic model in the next step. Thus, a conceptual gateway is opened, to transmit single star properties onto the galactic scale.

4.3.2 Spatial Modelling

Star formation tends to follow regions of high gas densities, which occur in the Milky Way predominantly along spiral arms (cf. Sec. 2.4.4). In order to mimic this physical behaviour, it can be modelled by stochastically placing star formation seeds according to a characteristic density distribution which resembles this large scale structure. However, that also the particular distribution of radioactivity in the Galaxy follows distinctively this morphology is one of the main hypotheses to be tested in this thesis. Therefore, on the one hand, the basic structure of spiral arms is in principle taken into account, while on the other hand leaving the detailed contrast and radial distribution as free parameter of the model.

Galactic Spiral Structure The spatial character of the model is divided into a radial component with respect to the galactic centre and a vertical component with respect to the galactic plane. A detailed discussion of the characteristic Milky Way spiral arm structure was given in Sec. 2.4.4. The large scale spiral structure in the PSYCO framework is based on an implementation of the spiral arms by Beyer (2018) as shown in Fig. 2.44 following mainly Cordes & Lazio (2002) and Vallée (2008). The spiral arm centroids are calculated as logarithmic spirals (e.g. Wainscoat et al.

1992)

$$\theta(R) = k \ \ln\left(\frac{R}{R_0}\right) + \theta_0, \tag{4.14}$$

giving the rotation angle along the radial variable R, with k as constant widening the loop, the inner radius R_0, and the angle at this inner radius θ_0. In order to reproduce a characteristic four-arm spiral, the values in Tab. 4.4 are adopted for the separate arms. This follows mainly Cordes & Lazio (2002) in order to gear towards

Table 4.4: Parameters for centroids of logarithmic spirals (cf. Eq. 4.14) approximating the distribution of ionised gas along the four arms of the Milky Way. Adopted from Wainscoat et al. (1992) and Cordes & Lazio (2002) following Faucher-Giguère & Kaspi (2006). The structure is shown graphically in Fig. 2.44.

Spiral arm	k [rad]	R_0 [kpc]	θ_0 [rad]
Norma	4.25	3.48	3.141
Scutum-Centaurus	4.89	4.90	2.525
Sagittarius-Carina	4.25	3.48	0.000
Perseus/Local	4.89	4.90	5.666

the distribution of free electrons, which are expected to be prominently associated with H II regions around massive star groups (cf. Fig. 2.36). The parameters are based on a Cartesian coordinate system with the origin at the Galactic centre and the position of the Sun at $p_\odot = (x_\odot, y_\odot, z_\odot) = (-8.5, 0.0, 0.01)\,\mathrm{kpc}$ (cf. Sec. 2.4.4). The height of the Sun above the Galactic plane is currently estimated to $5.5 \pm 5.8\,\mathrm{pc}$ (Reid et al. 2019). The large uncertainties of this estimate are due to a possible tilt of the plane. A value of $15 \pm 17\,\mathrm{pc}$ recently obtained with gamma-ray observations confirms this range in height (Siegert 2019).
The spread of stellar groups in the galactic plane around the spiral arm is characterised by a normal distribution centred at the centroid and with a radially increasing width of $\sigma(R) = 0.07 \times R$. This choice is empirically motivated to obtain a physically reasonable distribution close to that of ionised gas in the Milky Way (Faucher-Giguère & Kaspi 2006).
The radial Galactic gravitational potential is usually described by a rather complex combination of a disk-halo, a bulge, and a central nucleus component (e.g. Eq. 1 in Carlberg & Innanen 1987). It has been shown by Yusifov & Küçük (2004) in the context of the pulsar distribution that the effect of this potential can be approximated by a truncated Gaussian distribution. This approximation is adopted in this thesis in order to obtain an easily parametrisable distribution while at the same time maintain a physically reasonable shape. Thus, the radial density distribution is described by

$$\rho(R; R_\mu, \sigma) = \begin{cases} \frac{1}{\sqrt{2\pi}\sigma} \ \exp\left[-\frac{(R-R_\mu)^2}{2\sigma^2}\right], & \text{if } R \in [0, 20] \\ 0, & \text{if } R \notin [0, 20], \end{cases} \tag{4.15}$$

with a maximum at radius R_μ and the width σ. The truncation to $0 \leq R \leq 20\,\mathrm{kpc}$ is chosen towards small radii to avoid overlapping distributions extending to both sides of the galactic centre, and towards large radii to restrict the distribution to a reasonable volume of the Milky Way. The parameters R_μ and σ are parameters PSYCO is designed to test for and are therefore not generally fixed. In order to prevent artificial features at the galactic centre, the polar angle θ is additionally blurred by a stochastic correction angle $\theta_\mathrm{corr} = \theta_\mathrm{rand} \exp(-0.35 \times R)$, with θ_rand being randomly chosen in the range $[0, 2\pi)$ (Faucher-Giguère & Kaspi 2006). Al-

ternative to the Gaussian profile, an optional radial distribution following a simple exponential shape is implemented in order to open up the possibility of generating strongly centrally dominated galactic morphologies.
The vertical density for modelling star formation is homogeneously chosen to follow an exponential distribution $\rho(z; z_0) = z_0^{-1} \exp(-|z|/z_0)$, with the scale height z_0 parametrising the thickness of the galactic disk, which is also implemented as free parameter. Altogether, the position of each star formation seed is essentially chosen stochastically in a four-step process. After the random choice of a spiral arm, the radial coordinate is drawn according to Eq. 4.15, which is translated to a spiral arm centroid position via Eq. 4.14. This position is then altered around the centroid in order to fill out the spiral arm as described above. Finally, the vertical position is exponentially sampled for a given scale height, with equal probability mirrored to the galactic north and south pole.
Five different realisations of such galactic morphologies are shown in Fig. 4.14. They are in order by increasing central dominance and simultaneously decreasing spiral dominance. Accordingly, their nomenclature follows the numbering GM00 to GM04. These are chosen throughout this thesis in order to test different morphological configurations against observational features. The particular parameter configurations characterising those forms are summarised in Tab. 4.5. While GM00, GM01, and

Table 4.5: Galactic radial density profiles. R_μ and σ describe a Gaussian distribution and $R_{\rm exp}$ the scale radius of an exponential profile. The morphologies are visualised in Fig. 4.14.

Morphology	Radial profile	R_μ [kpc]	σ [kpc]	$R_{\rm exp}$ [kpc]
GM00	Gaussian	8.5	3.5	–
GM01	Gaussian	17.03	1.83	–
GM02	Gaussian	5.0	2.5	–
GM03	Exponential	–	–	5.5
GM04	Exponential	–	–	5.5

GM02 are characterised by Gaussian radial profiles, GM03, and GM04 are chosen to be exponentially distributed in radius, which confers a steep profile towards the galactic centre. GM01 follows the distribution of pulsars according to Faucher-Giguère & Kaspi (2006). GM04 is a special case, which is designed as doubly exponential disk without modelling of particular spiral features and thus greatly focussed on the nuclear bulge in the galactic centre.

Galactic Metallicity Gradient The stellar parameter related to the spatial distribution in the galaxy is metallicity. Cheng et al. (2012) derived the radial metallicity gradient in the Milky Way from optical spectra in Sloan Digital Sky Survey (SDSS) data. Different gradients were obtained for four different height levels above the Galactic plane as shown in Fig. 4.15.

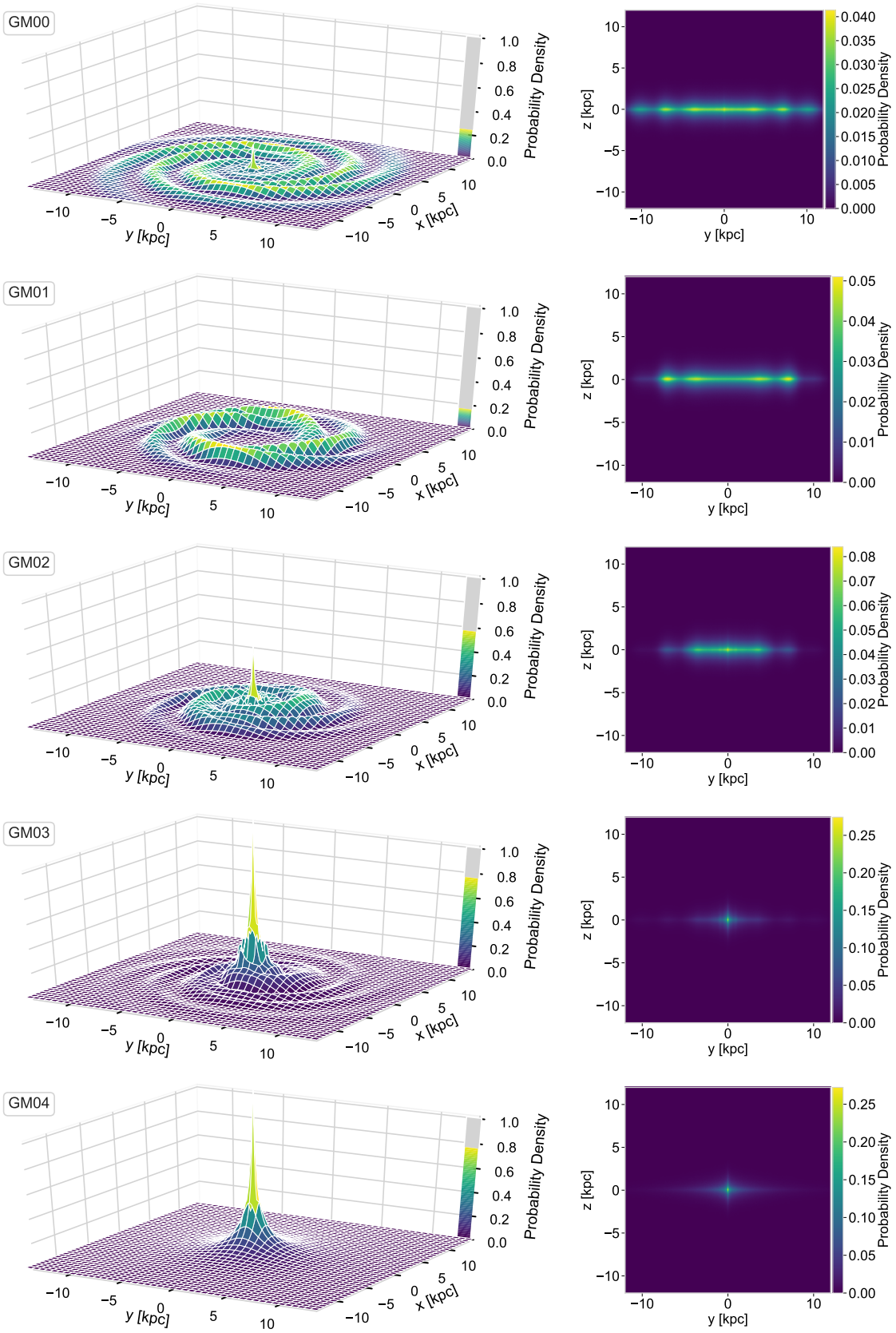

Figure 4.14: Galactic morphologies as implemented in PSYCO. They are ordered from top to bottom by increasing central dominance and simultaneously decreasing spiral dominance. Accordingly, their nomenclature follows the numbering GM00 to GM04. The spiral description follows Eq. 4.14. *Left:* Probability density distributions in the galactic plane with a radial Gaussian profile in the case of GM00, GM01, and GM02, and a exponential profile used for GM03, and GM04. *Right:* Distributions perpendicular to the galactic plane following an exponential profile. GM04 denotes a doubly exponential disk without taking into account any spiral pattern. Parameters of the radial distributions are summarised in Tab. 4.5.

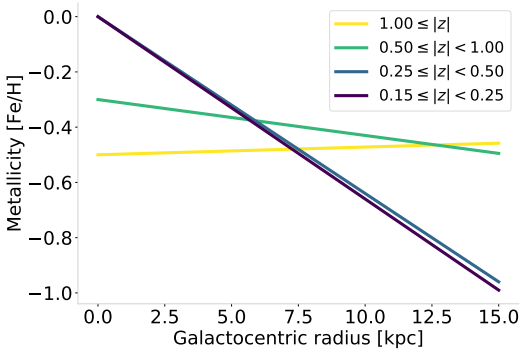

Figure 4.15: Galactic metallicity gradients depending on the height z above the Galactic plane in kpc. Adopted from Cheng et al. (2012).

Table 4.6: Linear parameters of the metallicity gradient in the Milky Way depending on the height z above the Galactic plane.

Height [kpc]	Slope	Intersect
≥ 1.00	-0.0028	-0.5
0.50–1.00	-0.013	-0.3
0.25–0.50	-0.55	0
0.15–0.25	-0.36	0

The respective linear parameters are listed in Tab. 4.6. The overall tendency indicates lower metallicity higher above the plane. This arises due to less turbulences and therefore slower proceeding star formation at large heights and the fact that older objects had more time to drift out of of the plane towards these heights. Young objects are found preferentially near the Galactic centre, where most active star formation sights are situated. These empirical metallicity gradients are utilised in PSYCO to assign metallicity values to stellar associations according to their galactic height and radius. To enable complete sampling, Solar metallicity is fixed in the plane and the gradients are extrapolated to cover the entire model volume.

Nearby Massive-Star Groups As described above, most of the more detailed properties of gamma-ray emission has to be inferred by starting from a rough morphology which can include the Galactic structure, and then refining different regions which are expected to contribute. The properties of gamma-ray emission from parts of the Milky Way are either known beyond this basic level, or can be inferred including further information. According to their level of prior knowledge, stellar associations can be divided into three groups and modelled separately. These will be denoted as known knowns, known unknowns, and unknown unknowns.[1] First, known knowns are stellar groups for which the position, the angular size, and the emission at 1.8 MeV are already known from gamma-ray observations. Second, known unknowns are associations which are observationally known regarding their position and certain spatial characteristics, but unknown with respect to their particular gamma-ray properties. Finally, unknown unknowns are clusters which entirely lack individual observational information and have to be sampled stochastically using the galaxy model as described in the previous paragraphs.
The characteristics of the known knowns are listed in Tab. 4.7. Gamma-ray measurements of individual star groups are essentially limited to the Cygnus region, the Orion-Eridanus superbubble, and the Sco-Cen region (Plüschke 2001; Martin et al. 2009; Siegert 2017). The known unknowns are based on the combined catalogues by Melnik & Efremov (1995) and Melnik & Dambis (2017b). These comprise respectively 88 and 91 nearby OB associations within 0.14–3.50 kpc around the Sun. While positions are adopted according to the new *Gaia* catalogue by Melnik & Dambis (2017b), angular extents are assigned according to Melnik & Efremov (1995) be-

[1] This nomenclature is borrowed from the Johari window, a heuristic model for the analysis of interpersonal relationships in psychological science, developed by Luft & Ingham (1955).

Table 4.7: Properties of nearby OB associations. ^{26}Al masses in parentheses for subgroups are inferred indirectly from their mutual measurement. Information concerning ^{26}Al gamma-ray measurements are mostly adopted from Siegert (2017) and Plüschke (2001), ages from Garmany & Stencel (1992), Bochkarev & Sitnik (1985), Diehl (2002), and Fierlinger (2014), positions from Knödlseder (2000), angular sizes from Bochkarev & Sitnik (1985), Knödlseder (2000), Fierlinger (2014), and Krause et al. (2018), and distances from Ruprecht (1966), Garibdzhanyan et al. (1984), Massey & Thompson (1991), Bochkarev & Sitnik (1985), Diehl et al. (2003), and Krause et al. (2018) following Beyer (2018).

Association	^{26}Al mass $[10^{-4}\,M_\odot]$	Age [Myr]	Position (l, b) [°]	Angular size [°]	Distance [kpc]
Cyg OB1	(17.1)	7.5	$(75.5, 1.7)$	4.0×3.5	1.60
Cyg OB2	(17.1)	2.5	$(80.3, 0.8)$	2.0×2.0	1.70
Cyg OB3	(17.1)	6.5	$(72.6, 2.3)$	3.5×1.5	2.29
Cyg OB4	(17.1)	5.6	$(82.5, -7.3)$	3.0×2.0	1.05
Cyg OB5	(17.1)	5.6	$(67.1, 2.1)$	5.8×9.6	1.60
Cyg OB6	(17.1)	5.6	$(86.0, 1.0)$	6.0×8.0	1.70
Cyg OB7	(17.1)	5.6	$(90.0, 2.1)$	12.0×13.9	0.79
Cyg OB8	(17.1)	3.0	$(77.8, 3.8)$	2.9×3.3	2.25
Cyg OB9	(17.1)	8.0	$(78.0, 1.5)$	2.0×1.4	1.45
Ori OB1	5.0	12.0	$(190.6, -40)$	25.0×34.0	0.40
USco	0.5	7.0	$(351.5, 20.0)$	14.1×14.1	0.15
UCL	0.8	17.0	$(331.0, 12.5)$	45.1×45.1	0.15
LCC	(0.1)	15.0	$(298.5, 5.4)$	25.8×25.8	0.12

cause these are not included in the revised catalogue. Melnik & Dambis (2017b) found an average expansion velocity of OB associations of $v_{\mathrm{exp}} = 6.3\,\mathrm{km\,s^{-1}}$. The typical sphere of influence of an individual star formation event is initially $\sim 2\,\mathrm{pc}$. This is used in combination with the measured angular size to infer the kinematic ages of OB associations (Brown et al. 1997). In this way, ages between 0.24–14.2 Myr are inferred for the known unknowns with an average of $\sim 4.6\,\mathrm{Myr}$. The fact that the associations are rather young results from an observational bias because they continuously drift apart and are therefore harder to observe as coherent units over time. It is important to note that the expansion so far refers to the maximum distances between stars and not the radius of the surrounding superbubbles. The latter is derived from the respective group age as described below in Sec. 4.3.3. The unknown isotopic content of known knowns as well as known unknowns is determined via population synthesis calculations as explained in Sec. 4.2.2 and using the ages as prior knowledge. Since the initially formed stellar mass of each association is unknown, they are modelled as canonical star groups resembling the well studied Orion OB1 association (Voss et al. 2008, 2010). The modelling results for the nearby OB associations will be discussed in Sec. 4.4.4.

4.3.3 Temporal Modelling

The temporal component is introduced in PSYCO by generating star formation seeds according to the formation rate of stellar clusters which was described in Sec. 4.3.1. The total mass that is transformed into stars in each such seed is sampled according to the ECMF. With the assumption of instantaneous star formation, the time evolution of the nucleosynthesis ejection in each association is then followed according to the population synthesis profiles outlined in Sec. 4.2. However, these ejecta are not stationary, but propagate over time. As was discussed in detail in Sec. 2.3.3, this propagation is presumably closely related to the dynamics of interstellar bubbles

surrounding the respective star groups.
Castor et al. (1975) developed an analytical description of a spherically expanding interstellar bubble in a simplified ISM consisting solely of hydrogen with homogeneous density ρ_{ISM}. This was later refined by Weaver et al. (1977), according to which the radius of such bubbles after time t can be approximated by Eq. 2.45. Hydrodynamic ISM simulations by de Avillez & Breitschwerdt (2005) suggest that an isotropic distribution of the hot interior inside these bubbles is reached after $\sim 1\,\mathrm{Myr}$. This is used to determine the distribution of radioactive ejecta around star groups over time (Beyer 2018). The mechanical luminosity of a typical OB association describes their integrated momentum output due to different feedback mechanisms. This was estimated as $L_{\mathrm{W}} = 10^{31}\,\mathrm{J\,s^{-1}}$ in population synthesis calculations by Plüschke (2001). Assuming an average particle density $n \sim 10^2\,\mathrm{cm^{-3}}$ of the swept up ISM gas, L_{W} pushes against the ambient mass density $\rho_{\mathrm{ISM}} = 1.67 \times 10^{-19}\,\mathrm{kg\,m^{-3}}$. The resulting time evolution of the superbubble radius is then given by

$$R_{\mathrm{bubble}}(t) = 0.76 \times \left(\frac{L_{\mathrm{W}} t^3}{\rho_{\mathrm{ISM}}}\right)^{\frac{1}{5}}, \tag{4.16}$$

which is shown graphically for three different ISM particle densities in Fig. 4.16. After a phase of fast expansion in an un-shocked medium, the growth is slowed down due to an increasing density in the swept up shell that counteracts the outward motion. Homogeneously filled with evolving amounts of ^{26}Al and ^{60}Fe, these bubbles dynamically fill out the galactic structure over time. The theoretically further expansion beyond 50 Myr can be omitted in this model because the radioactive content vanishes at late stages which eradicates its visibility in nuclear gamma-rays and therefore any effect on the investigation of radioactivity in this thesis. From the previous population synthesis calculations an interstellar bubble filled with ^{26}Al or ^{60}Fe is expected to be visible by nuclear decay lines for maximum $\sim 25\,\mathrm{Myr}$. During this time the Milky Way rotates by only about 38°. This is short enough that gas and stars can be assumed as approximately co-rotating with the spiral arm, i.e. stars do not drift far from their formation region with respect to the spiral arms. Thus, taking into account further time evolution aspects of cluster positions such as dynamical shifts with respect to an observer or changes between star formation epochs can be omitted. This leaves the morphological aspects of the time evolution of individual bubbles as analytically calculable for any point in time.

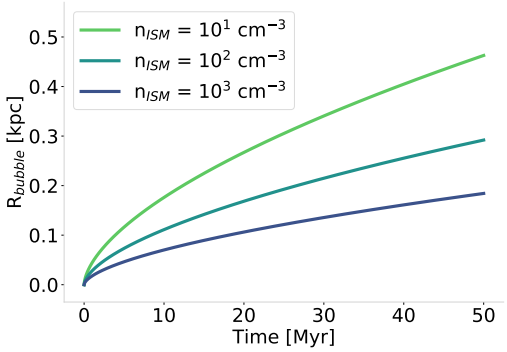

Figure 4.16: Radial time evolution of an expanding interstellar bubble for three different particle densities n_{ISM} of the surrounding ISM according to Eq. 4.16 following Weaver et al. (1977) and Plüschke (2001).

4.3.4 Ray Tracing

In order to translate the previously modelled morphological aspects of galactic radioactivity into a format comparable to gamma-ray observations, synthetic sky maps are calculated. The fundamental building blocks of the spatial structure have been defined in PSYCO as expanding spheres. These emit gamma-rays proportional to their radioactive filling. To infer an omnidirectional map, the emission arriving at a theoretical observer has to be calculated while retaining its directional information on the sky. This is achieved by scanning each bubble with a ray tracing algorithm, the basic principle of which is illustrated for the general case of an emitting spherical shell in Fig. 4.17. This case is described below.

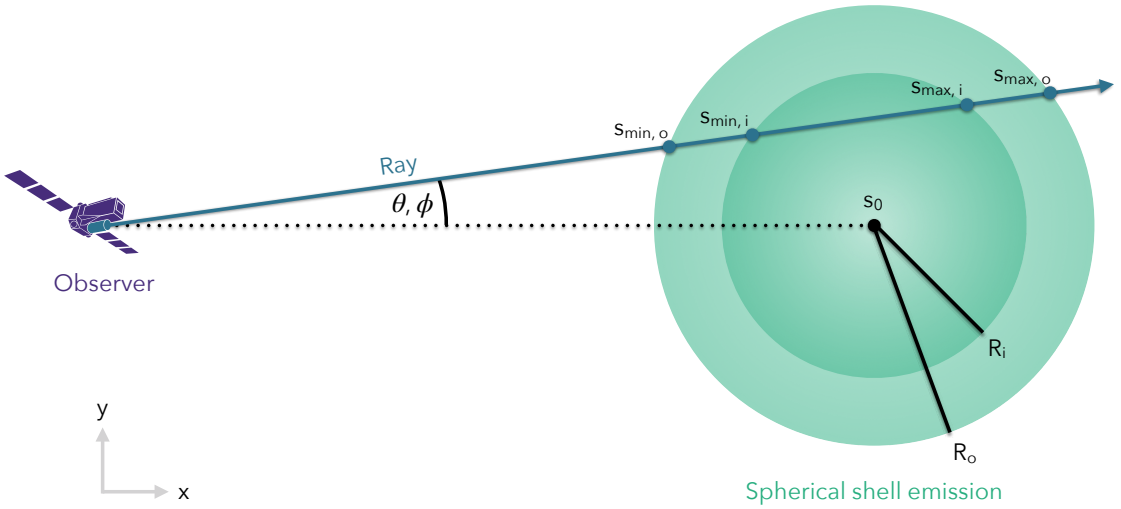

Figure 4.17: Schematic illustration of a ray tracing algorithm for a spherical shell emission in order to obtain a synthetic flux map for a theoretical observer at position $\boldsymbol{p}_0$. It is fundamentally based on the integration between its intersection points (Eq. 4.18) of a conceptual ray $\boldsymbol{s}(\phi, \theta)$ coming from the observer (Eq. 4.17) with a spherical shell at position $\boldsymbol{s}_0$ with inner and outer radii R_i and R_o. The gamma-ray flux arriving at the observer along each ray is proportional to the isotopic mass within the integration boundaries.

Assume the observer's position $\boldsymbol{p}_0 = (0, 0, 0)$ and the centre of the emission sphere $\boldsymbol{s}_0 = (x_0, y_0, z_0)$ with radius R in Cartesian coordinates. The basic idea is now to calculate the incoming emission along each line of sight

$$\boldsymbol{s}(\phi, \theta) = s \cdot \begin{pmatrix} \cos\phi \ \cos\theta \\ \sin\phi \ \sin\theta \\ \sin\theta \end{pmatrix} \tag{4.17}$$

in every direction around the observer with azimuth angle ϕ in the galactic plane and zenith angle θ. In a reversed view, this is called a ray, which conceptually emanates from the observer and is traced along the emitting volume it passes through. Since a spherical shell is described as separated into two shells with different radii and emissivity, the basic task is then to calculate the points of intersection of this ray with each sphere. This is achieved by putting Eq. 4.17 into the analytical formula

of a sphere

$$\begin{aligned}(s\cos\phi\cos\theta - x_0)^2 + (s\sin\phi\cos\theta - y_0)^2 + (s\sin\theta)^2 - R^2 &= 0\\ s^2 - 2s\underbrace{(x_0\cos\phi\cos\theta + y_0\sin\phi\cos\theta + z_0\sin\theta)}_{:=p_0} + \underbrace{x_0^2 + y_0^2 + z_0^2}_{=\boldsymbol{s}_0^2} - R^2 &= 0\\ s^2 - 2sp_0 + \boldsymbol{s}_0^2 - R^2 &= 0,\end{aligned} \tag{4.18}$$

which is solved for the intersections closer and farther from the observer, $s_{\min}$ and $s_{\max}$, by

$$s_{\min}^{\max} = p_0 \pm \sqrt{p_0^2 - \boldsymbol{s}_0^2 + R^2}. \tag{4.19}$$

Now the spherical shell between the outer radius R_o and the inner radius R_i is assumed to be homogeneously filled with density

$$\rho_\mathrm{s}(s) = \begin{cases} 0 & \text{for } 0 \le s \le R_\mathrm{i} \\ \rho_0 & \text{for } R_\mathrm{i} < s \le R_\mathrm{o} \\ 0 & \text{for } R_\mathrm{o} < s \end{cases}, \tag{4.20}$$

Every volume element of the sphere dV emits gamma-ray photons with luminosity of $dL = L_{n,\odot}\rho_0\, dV$, where ρ_0 is the mass density and $L_{n,\odot}$ is the luminosity normalised a unit Solar mass of isotope n in units of $\mathrm{ph\,s^{-1}\,M_\odot{}^{-1}}$. This is calculated for a particular emission line with energy E_γ via

$$L_{n,\odot} := \frac{L_n}{M_\odot} = p_{E_\gamma}\frac{N_{n,\odot}}{\tau_n} = p_{E_\gamma}\frac{1}{\tau_n}\frac{M_\odot}{M_{n,\mathrm{u}}}, \tag{4.21}$$

where p_{E_γ} is the branching probability for the nuclear transition giving rise to the gamma-ray with E_γ, τ_n is the isotopic lifetime, and $N_{n,\odot}$ is the number of atoms which constitute one Solar mass of isotope n. The atom number can be derived from one Solar mass $M_\odot = 1.98892\times10^{30}\,\mathrm{kg}$ divided by the atomic mass $M_{n,\mathrm{u}}$. The latter for the case of ^{26}Al is $M_{26,\mathrm{u}} = 25.986891863\,\mathrm{u} \approx 4.3152\times10^{-26}\,\mathrm{kg}$. This gives a 'standard' luminosity $L_{26,\odot} = 1.44\times10^{42}\,\mathrm{ph\,s^{-1}\,M_\odot{}^{-1}}$ for one Solar mass of ^{26}Al. This can be obtained for any other isotope in a similar way and is summarised in Tab. 4.8 for the three relevant isotopes in this thesis.

Table 4.8: Standard luminosities $L_{n,\odot}$ of one Solar mass of ^{26}Al, ^{60}Fe, and ^{44}Ti (cf. Eq. 4.21) for different emission lines with photon energies E_γ and the respective transition probability p_{E_γ}. The properties characterising isotope n are its lifetime τ_n and atomic mass $M_{n,\mathrm{u}}$. The last column gives the power output of the respective isotope normalised to a mass of $10^{-5}\,\mathrm{M_\odot}$.

Isotope	τ_n [yr]	$M_{n,\mathrm{u}}$ [u]	E_γ [keV]	p_{E_γ} [%]	$L_{n,\odot}$ [$\mathrm{ph\,s^{-1}\,M_\odot{}^{-1}}$]	P_γ [$\mathrm{erg\,s^{-1}}$]
^{26}Al	1.04×10^6	25.99	1808.73	99.7	1.40×10^{42}	4.05×10^{31}
			1129.67	0.3	4.22×10^{39}	7.63×10^{28}
^{44}Ti	89	43.96	67.88	94.4	9.65×10^{45}	1.05×10^{34}
			78.34	96	9.32×10^{45}	7.92×10^{33}
			1157.03	99.9	9.70×10^{45}	1.80×10^{35}
^{60}Fe	3.8×10^6	59.93	58.60	2.1	3.50×10^{39}	3.28×10^{27}
			1173.24	99.9	1.67×10^{41}	3.13×10^{30}
			1332.50	100	1.67×10^{41}	3.56×10^{30}

The incoming flux on a particular ray is proportional to the luminosity of the intersected volume. To convert this to flux arriving at an observer, this has to be weighted by $1/(4\pi s^2)$ to take the omnidirectional emission of every volume element

at distance s into account. In order to computationally grasp this, the sky is divided into a regular grid of quadratic pixels with angular side length δ. Each ray is then chosen to go through the centre (ϕ_0, θ_0) of one such pixel and covering the solid angle corresponding to the pixel size. Integration along a ray and over the projected area $dA = s^2\, d\omega = s^2\, \sin\theta\, d\theta\, d\phi$ of the differential solid angle $d\omega$ onto a sphere with radius s then yields

$$\begin{aligned} F(\phi_0, \theta_0) &= \iiint_V \frac{L_{n,\odot}\rho_\mathrm{s}(s)}{4\pi s^2}\, ds\, dA \\ &= \frac{L_{n,\odot}}{4\pi} \int_{\phi_\mathrm{min}}^{\phi_\mathrm{max}} \int_{\theta_\mathrm{min}}^{\theta_\mathrm{max}} \int_0^\infty \rho_\mathrm{s}(s) \sin\theta\, ds\, d\theta\, d\phi \\ &= \frac{L_{n,\odot}}{4\pi}\, \delta \left[\cos\left(\theta_0 - \frac{\delta}{2}\right) - \cos\left(\theta_0 + \frac{\delta}{2}\right)\right] \left(\int_{s_{\mathrm{min,\,o}}}^{s_{\mathrm{min,\,i}}} \rho_0\, ds + \int_{s_{\mathrm{max,\,i}}}^{s_{\mathrm{max,\,o}}} \rho_0\, ds\right) \\ &= \frac{L_{n,\odot}}{2\pi}\, \rho_0 \left(\sqrt{p_0^2 - \boldsymbol{s}_0^2 + R_\mathrm{o}^2} - \sqrt{p_0^2 - \boldsymbol{s}_0^2 + R_\mathrm{i}^2}\right) \cdot 2\delta\, \sin\theta_0\, \sin\left(\frac{\delta}{2}\right). \end{aligned} \tag{4.22}$$

The final description is based the luminosity normalised to one Solar mass, $L_{n,\odot}$, in order to achieve an equation that is easily scalable by an isotope specific factor. This is implemented in a vectorised version in order to cover a full grid of sky pixels, which are chosen usually with a size of $1^\circ \times 1^\circ$ on a 360×180 grid.

Deviations from spherical shell symmetry are achieved by applying the matrix representation of a three-dimensional ellipsoid instead of the spherical description in Eq. 4.18. This will be used in particular to model the observationally known shapes of nearby OB associations and can also be applied e.g. to take galactic density gradients in certain directions into account.

With the total isotopic mass of a source M_n obtained from population synthesis calculations (cf. Sec. 4.2), the density is easily obtained as $\rho_0 = \frac{3}{4\pi} M_n R^{-3}$ for a homogeneously filled sphere with radius R. Together with the isotopic luminosity (cf. Tab. 4.8) a flux map of gamma-ray emission from a modelled superbubble is obtained with physical units of $\mathrm{ph\,cm^{-2}\,sr^{-1}\,s^{-1}}$. This is repeated for each group and finally summed into a full-sky map of the entire galactic emission as obtained from the full model.

To save computational resources, emission sites can be treated as point-like if they are small enough or sufficiently distant to the observer. This applies to sources that violate the condition

$$\arctan\left(\frac{R}{d}\right) > \frac{\delta}{\sqrt{2}}, \tag{4.23}$$

with the source radius R, its distance to the observer d, and the pixel side length δ. The condition is also illustrated in Fig. 4.18 with $\alpha = \arctan(R/d)$. Sources with radii below this threshold are hit by one ray at most. In that case, its emission is combined as point like in the pixel within which its centre $(\phi_\mathrm{s}, \theta_\mathrm{s})$ lies with respect to the observer. The flux calculation then reduces to $F(\phi_\mathrm{s}, \theta_\mathrm{s}) = \frac{M_n L_{n,\odot}}{4\pi d^2}$, with the total mass M_n in units of Solar masses of isotope n within the source.

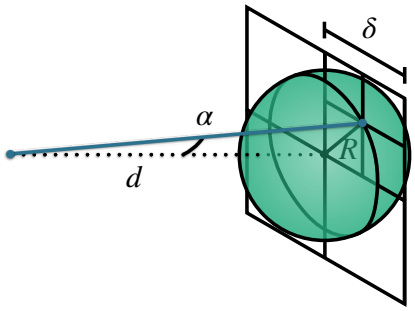

Figure 4.18: Schematic illustration of the condition for assuming point-like emission (cf. Eq. 4.23).

Essentials

- In order to model the galactic structure of radioactivity in PSYCO, star groups are sampled on the basis of a four-arm density distribution in space and according to a cluster formation rate inferred from the SFR in time.
- Nearby OB associations can be treated separately to include prior knowledge about them. Otherwise, each association develops a homogeneously filled superbubble which is expanding in an isotropic ISM.
- The evolution of the isotopic content over time is introduced by populations synthesis of each group according to their initial masses.
- Synthetic sky maps of the overall resulting gamma-ray emission is calculated by ray tracing of each of these bubbles.

4.4 Model Results

The simulation of an entire galaxy requires the inclusion of a large number of physical parameters. An adequate consideration therefore also requires the allowance for a certain variance in each of these parameters. The great advantage of the PSYCO model described above is that it allows exactly this by limiting it to the empirically most important predictor variables as listed in Tab. 4.9. With 100 MC runs for each parameter configuration, a total number of 180000 full galactic model realisations is

Table 4.9: Full parameter grid used in this thesis for constructing 180000 realisations of PSYCO models. For each configuration in model space 100 MC runs are performed to cover stochastic variations. Explodability variations are only mapped onto the stellar model LC06 because LC18 already bears a model inherent explodability. The last column gives cross-references for further explanations of each parameter within this thesis.

Parameter	Values	Cross-reference
SFR $[\mathrm{M}_\odot\,\mathrm{yr}^{-1}]$	$1, 2, 4, 8$	Sec. 2.4.2, Tab. 2.9
IMF	S55, K01, C05	Sec. 2.2.1, Fig. 2.5
Radial morphology	GM00, GM01, GM02, GM03, GM04	Sec. 4.3.2, Fig. 4.14, Tab. 4.5
Scale height [kpc]	$0.1, 0.2, 0.3, 0.5, 0.7$	Sec. 4.3.2, Fig. 4.14
Stellar model	LC06, LC18	Sec. 2.2.5, Fig. 2.28, Fig. 2.29
Explodability	S09, J12, S+16, LC18	Sec. 2.2.5, Fig. 2.30, Tab 2.5

obtained as basis for the analysis in this thesis. This provides the decisive opportunity to specify model results with intrinsic uncertainty. The stellar models used here were chosen because, on the one hand, they offer full time profiles for a relatively complete set of stellar masses and, on the other hand, they are easily comparable due to their similar model structure.
The parameter space is not entirely symmetric because different explodability models can only be mapped onto the stellar model LC06, since LC18 already bears a model inherent explodability model. For better clarity and readability the following presentation of results is condensed to the most significant parameter configurations. Therefore, e.g. model assumptions following S09 and LC18 are interpreted as extreme cases for explodability, and the standard IMF K01 is used if not stated otherwise.

4.4.1 Mass of ^{26}Al and ^{60}Fe

The total simulated mass of radioactive isotopes is expected to reach an equilibrium state between production and decay as described in Sec. 4.3.1. The actual temporal evolution of the galactic ^{26}Al and ^{60}Fe mass in the PSYCO model is shown in Fig. 4.19 for the case of SFR $= 4\,\mathrm{M}_\odot\,\mathrm{yr}^{-1}$ and the two stellar evolution models LC06 and LC18. As expected, convergence is reached in all cases after 50 Myr. This a

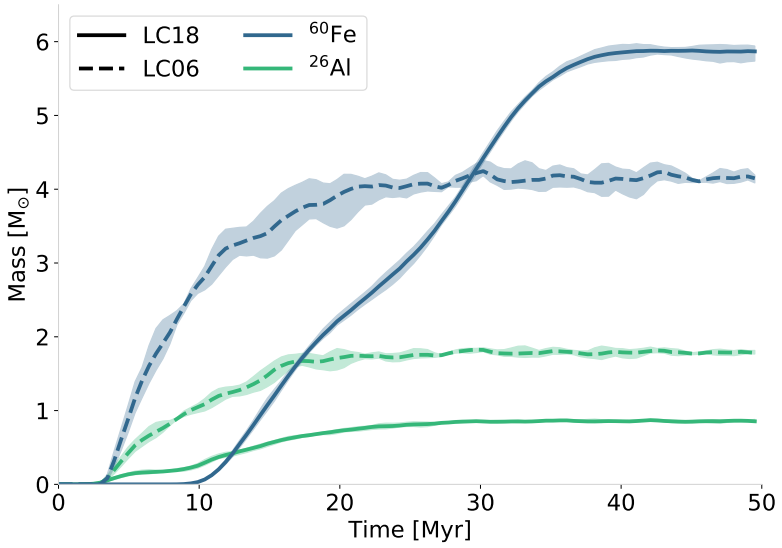

Figure 4.19: Time evolution of the total ^{60}Fe (*blue*) and ^{26}Al (*green*) mass for PSYCO models with SFR $= 4\,\mathrm{M}_\odot\,\mathrm{yr}^{-1}$ and the standard IMF K01. Shown are the results based on stellar models LC06 (solid lines) and LC18 (dashed lines) with explodability S09 and LC18 applied respectively. After 50 Myr convergence is reached with both models and for both isotopes. Shaded regions denote the 68th percentile of 100 model instantiations.

posteriori justifies the initial choice of the overall model time as proposed in Sec. 4.1. Thus, in the following, the models are all analysed after 50 Myr because at that time their physical properties have converged and vary by statistical effects of the MC sampling processes only. This is the case independent of the particular choice of SFR because a change in SFR scales only the amplitude of the curves in Fig. 4.19 but does not lead to time variations. Since the time evolution beyond stochastic

effects is described analytically, the final morphological evaluation can be limited to the calculation of one point in time after convergence. This is a crucial aspect because it reduces the computation time significantly for each model realisation. It further supports the originally intended approach to calculate a large number of instantiations of the model.
As outlined in Sec. 4.4.1, the total isotopic mass scales almost linearly with SFR as the main physical input parameter. This is illustrated in Fig. 4.20 for ^{26}Al and ^{60}Fe. The choice of IMF significantly changes the resulting nucleosynthesis yields.

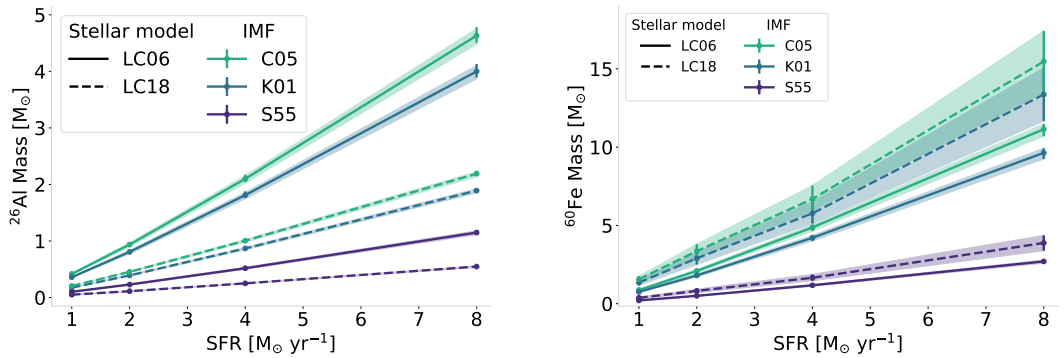

Figure 4.20: Total galactic amount of ^{26}Al (*left*) and ^{60}Fe (*right*) as a function of SFR for different IMFs C05 (*green*), K01 (*blue*), and C05 (*purple*). The results vary strongly with the choice of stellar evolution model LC06 (solid lines) or LC18 (dashed lines) with explodability S09 and LC18 applied respectively. Shaded regions and errorbars indicate the 68th percentile of 2500 MC runs for each model configuration.

In particular, S55 shows a low production of radioactive isotopes because of the absence of a power-law break for low mass stars. On the other hand, K01 and C05 lead to similar results due to a comparable mitigation of low-mass star production. Compared to the high-mass power law index, the break for low mass stars is shown to be the more important factor for galactic chemical evolution with respect to the IMF shape. The larger uncertainty regions for LC18 results from the higher variability of this model taking also metallicity and stellar rotation into account.
The ^{60}Fe/^{26}Al mass ratio exhibits no significant variation with the choice of IMF. This is equivalent to what was found for individual star groups in Sec. 4.2.3. Further, it is independent of the galactic SFR and yields $\sim$ 2.3 and $\sim$ 7.1 for LC06 and LC18 respectively. Overall, a strong variation with different stellar models is apparent. In Fig. 4.20, this is amplified by different explodability assumptions S09 and LC18 applied to the stellar evolution models LC06 and LC18 respectively. The particular variance with explodability can be studied in Fig. 4.21 for the case of LC06 with standard IMF K01. While the ^{26}Al mass varies by a factor of $\sim$ 1.5 with explodability, this is more severe for ^{60}Fe with a factor of 3.5–4.5 due to its exclusive SN origin. Additionally, the striking difference between stellar evolution models becomes clear. The same explodability model LC18 applied to stellar models LC06 and LC18 yields a factor of $\sim$ 6.2 difference in ^{60}Fe mass. Taken together, the right panels of Fig. 4.20 and Fig. 4.21 indicate that the uncertainties inherent to stellar evolution models in predicting ^{60}Fe output supersede those effects due to the IMF or the explodability. With a factor $\sim$ 1.3, this effect seems less significant for the case of ^{26}Al. Overall, this emphasizes the importance of multivariate analyses for understanding nucleosynthesis feedback.
A weak dependence of the ^{60}Fe/^{26}Al mass ratio on SFR corresponding to the resulting proportion of massive-star production is found as shown in Fig. 4.22. As expected, explodability has a major effect on this ratio because ^{60}Fe is proportion-

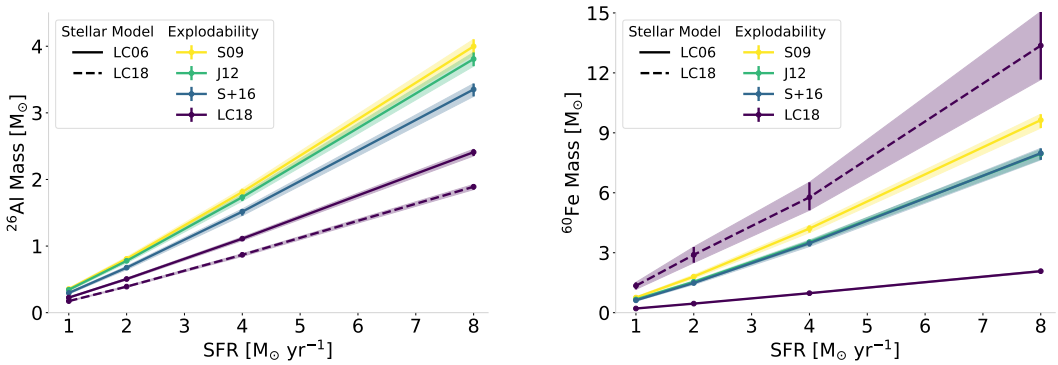

Figure 4.21: Total galactic amount of ^{26}Al (*left*) and ^{60}Fe (*right*) as a function of SFR for different explodability models S09 (*yellow*), J12 (*green*), S+16 (*blue*), and LC18 (*purple*) based on stellar evolution models LC06. LC18 (dashed line) bears an intrinsic explodability and is shown for comparison. Shaded regions and errorbars indicate the 68th percentile of 2500 MC runs for each model configuration.

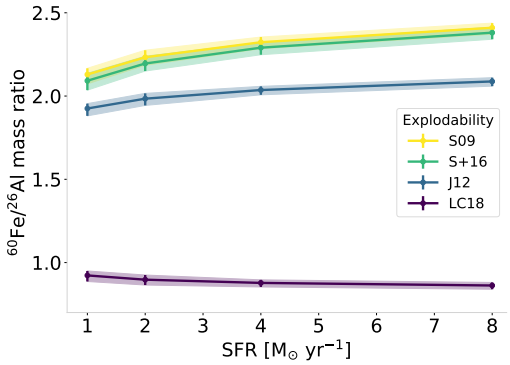

Figure 4.22: Galactic mass ratio ^{60}Fe/^{26}Al as a function of SFR for different explodability models S09 (*yellow*), J12 (*green*), S+16 (*blue*), and LC18 (*purple*) based on stellar evolution models LC06. For comparison, LC18 yields a ratio of 7.1 ± 0.8. Shaded regions and errorbars indicate the 68th percentile of 2500 MC runs for each model configuration.

ally reduced with fewer massive stars reaching explosions. Again, this seems to be outweighed by the particular nature of nucleosynthesis yield calculations because for explodability LC18, the stellar models LC06 and LC18 arrive at $^{60}\mathrm{Fe}/^{26}\mathrm{Al} = 0.9 \pm 0.2$ and $^{60}\mathrm{Fe}/^{26}\mathrm{Al} = 7.1 \pm 0.8$, respectively.

Diehl et al. (2006) estimated a total galactic amount of ^{26}Al of $(2.8 \pm 0.8)\,\mathrm{M}_\odot$ based on the intensity of the 1.8 MeV gamma-ray line. According to the model results presented here, such a mass requires SFR $\geq 4\,\mathrm{M}_\odot\,\mathrm{yr}^{-1}$. For a reduced explodability such as LC18, this even suggests SFR $\geq 6.5\,\mathrm{M}_\odot\,\mathrm{yr}^{-1}$. Nevertheless, this should be interpreted with caution, especially since the basic measure of total flux and its spatial implications and its conversion to a total ^{26}Al mass is not straight-forward because the geometry is more complicated than a double exponential disk (Fujimoto et al. 2018; Rodgers-Lee et al. 2019, e.g.) and will be discussed further in the context of PSYCO models in Sec. 4.4.3.

4.4.2 Supernova Rate

As described in Sec. 2.4.3, the galactic SNR is an important conceptual linkage within the context of massive-star physics. This quantity can be easily studied in the PSYCO framework by counting the explosions that occur during the course of

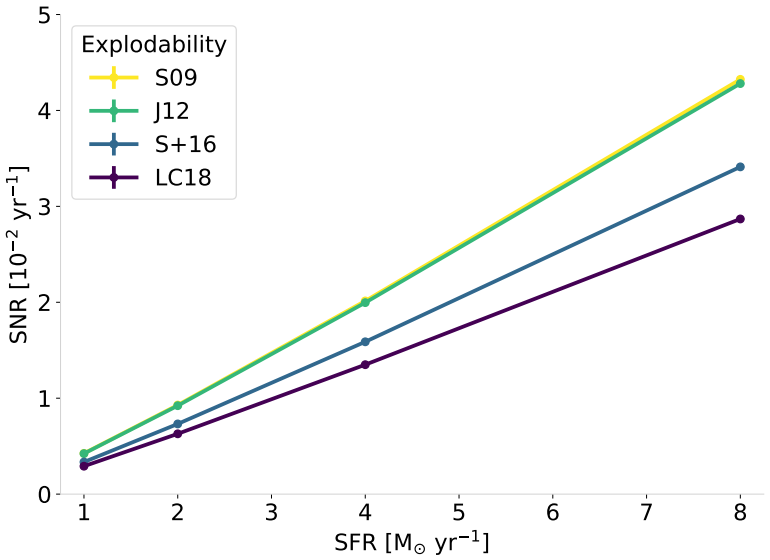

Figure 4.23: Rate of galactic ccSNe per century as a function of SFR for different explodability models S09 (*yellow*), J12 (*green*), S+16 (*blue*), and LC18 (*purple*) assuming the standard IMF K01. The scatter is determined from 2500 MC runs for each model configuration, the 1σ region of which lies within the line width.

50 Myr. The SNR depends mainly on two model parameters, namely the SFR and the explodability. This interdependence is illustrated in Fig. 4.23. In the case of S09, about 50% of all SNe theoretically occur for stars more massive than $20\,\mathrm{M}_\odot$. This essentially determines the order of magnitude for the influence of explodability assumptions.
Empirically from different observational tracers inferred values of the SNR in the Milky Way lie roughly in the range 1.5–3.5 per century (cf. Tab. 2.10). This implies a SFR $\geq 3\,\mathrm{M}_\odot\,\mathrm{yr}^{-1}$ according to the presented models. Here, SFR $= 4\,\mathrm{M}_\odot\,\mathrm{yr}^{-1}$ results in a SNR of 1.4–2.0 per century, depending on explodability. This range consistently covers what is expected from observations. Thus, the analysis so far indicates a preferential tendency towards higher star formation rates with respect to empirically grounded parameter boundaries.

4.4.3 Gamma-Ray Flux

The most decisive inferred model quantity with regard to a phenomenological analysis is the received gamma-ray flux. In the PSYCO framework, this is obtained for a theoretical observer within the galaxy model at the coordinates of the Sun. Examples of synthetic differential full-sky flux maps of the gamma-ray emission obtained with different galactic morphologies are depicted in Fig. 4.24 and Fig. 4.25 for the stellar evolution models LC06 and LC18, respectively. These flux maps are constructed via ray tracing as explained in Sec. 4.3.4 and include 3-dimensional information about the distribution of individual flux contributors on top of the 2-dimensional information about the spatial emission morphology in the sky. Panels on the left show emission from ^{26}Al decay and on the right from ^{60}Fe. Each row, in the joint consideration of Fig. 4.24 and Fig. 4.25, depicts one consistent MC run. The general appearance reflects the increasing central domination from GM00 to GM04 as expected from the input morphologies (cf. Fig. 4.14). While the overall

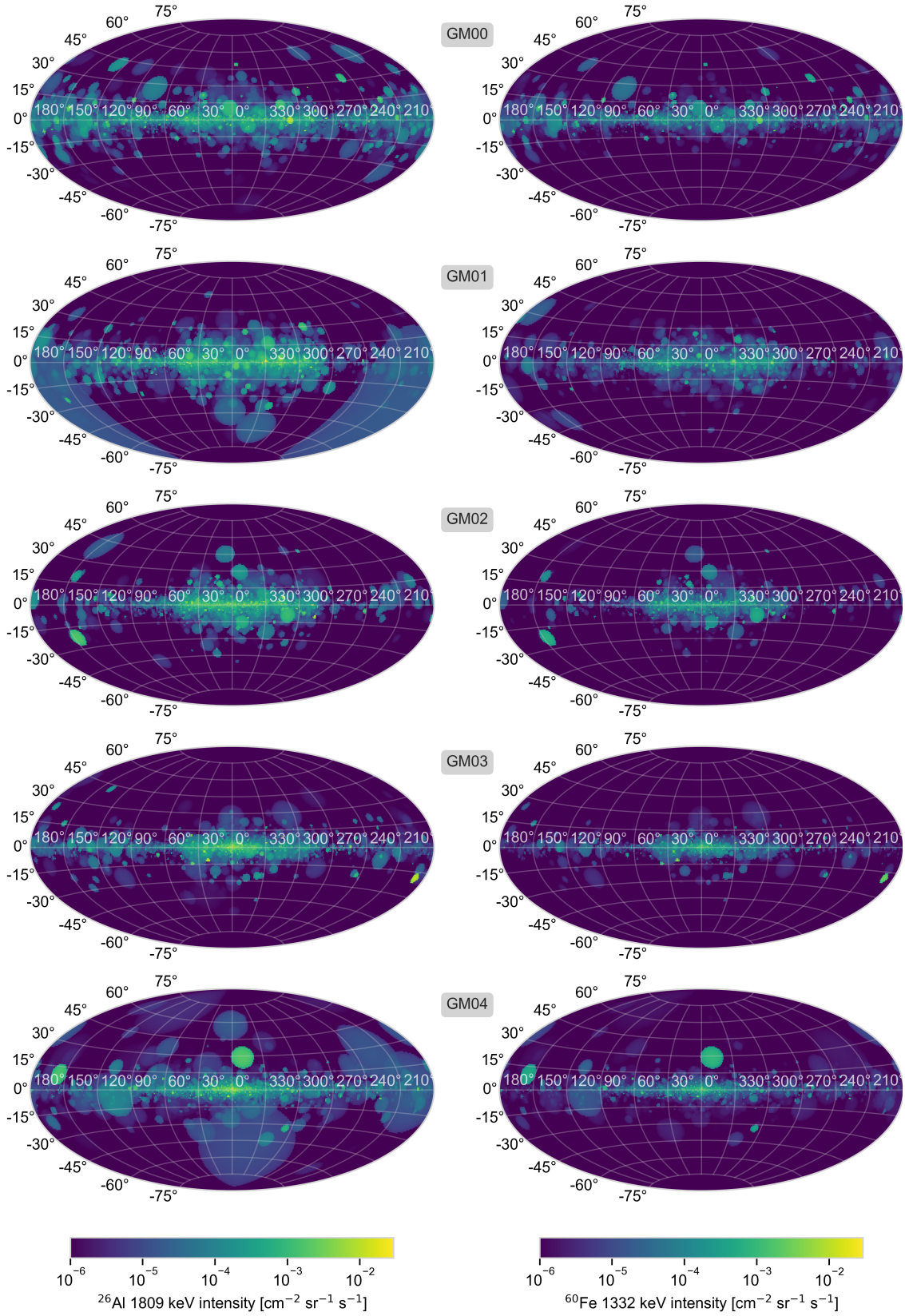

Figure 4.24: Synthetic full-sky gamma-ray maps of the 1.8 MeV line from ^{26}Al decay (*left*) and the 1.3 MeV line from ^{60}Fe decay constructed with PSYCO. Each row represents an individual MC run based on a different radial galactic density distribution as indicated in grey boxes (for the nomenclature cf. Sec. 4.3.2) with a consistent scale height of 300 pc. Nucleosynthesis yields are based on LC06 stellar evolution models with S09 explodability for the K01 IMF.

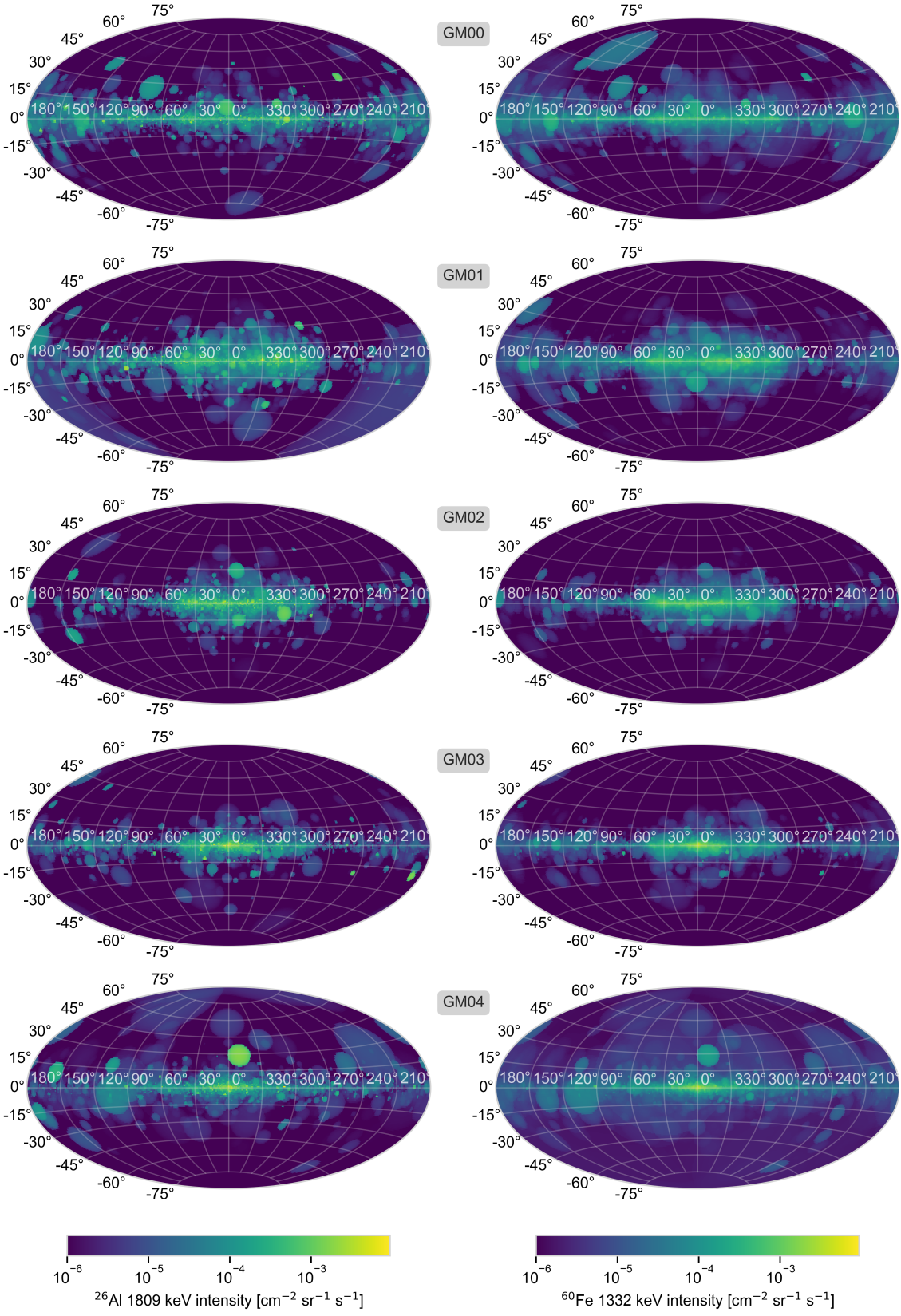

Figure 4.25: Same as Fig. 4.24 for LC18 stellar evolution models with the inherent explodability. Note also the different range of the colour scheme compared to Fig. 4.24.

vertical distribution is symmetric towards the galactic poles, the inclusion of spiral arms leads to an east-west asymmetry. This manifests most clearly in reduced emission around $l = 240°$–$270°$, which corresponds to the tangential gap between the trailing ends of the Sagittarius-Carina arm and the Local arm. Accordingly, a relatively sharp emission edge around $l = 280°$ indicates the trailing Sagittarius-Carina spiral arm tangent. On the other hand, its leading tangent appears at a smaller angle around $l = 50°$ since the spiral turns narrower in that direction. Towards larger longitudes, this is followed by an increasing emission from the approaching Local arm, which fades again beyond $l \sim 180°$. The central galactic region is generally characterised by a bright ridge. Additionally, GM02 and GM03 show a luminous bulge emission concentrated at $(l, b) = (0°, 0°)$. Here and also in the following, for the sake of simplicity, the concentrated emission from the spatial region associated with the bulge in the Milky Way is referred to as such, although there is no explicit modelling of the Galactic bulge involved. GM04, the doubly exponential disk, is to be highlighted as a morphologically special case in this list, because it shows none of the spiral arm-specific properties, since these are not included in the corresponding galaxy model.
The overall shape is overlaid by an irregular structure due to individual or clustered groups. It is important to stress that the latter is an entirely stochastic phenomenon and barely indicates actual physical correlations. The sometimes large extents and scatter towards high latitudes of these prominent groups are nearby emission sites. While their vertical scatter is of purely stochastic nature, their latitudinal frequency shows a bimodal distribution. They occur more frequently towards the galactic centre and towards the galactic anti-centre. Very nearby groups can lead to largely extended emissions (cf. e.g. Fig. 4.24 ^{26}Al for GM01 at $l \approx 145°$–$245°$ and $b \approx -75°$–$20°$) or even omnidirectional contribution in the case positioning inside a radioactively filled bubble (cf. Fig. 4.25 ^{60}Fe for GM04).
^{60}Fe appears overall fainter due to its lower activity compared to ^{26}Al. The isotopic contrast is especially salient for LC06 since this model additionally comprises lower ^{60}Fe production rates. The reduced emission leads to a distribution that appears more concentrated in the central galactic region. For LC18, on the other hand, increased ^{60}Fe production leads to a more even emission level for both isotopes. This also brings out another important morphological aspect more clearly. Due to the longer half-life of ^{60}Fe, it occurs preferentially in older bubbles and therefore appears more diffuse than ^{26}Al. This effect is enhanced in LC18 because in that case ^{60}Fe ejection is additionally delayed due to stellar rotation.

Integrated Flux The total flux arriving at the observer is compared for different spatial models in Fig. 4.26. Here, the focus is on the radial distribution and different scale heights are combined, which makes a set of 500 model realisations for each parameter configuration. The latter is limited for better clarity of the presentation to a paradigmatic choice of the standard IMF K01 and stellar models LC06 with explodability S09 and LC18 with its inherent explodability. Other stellar model configurations scale accordingly with the total isotopic mass they produce (cf. Fig. 4.20 or Fig. 4.21).
The graphs in Fig. 4.26 underline the previously mentioned aspect that the nuclear line from ^{26}Al is overall more intense than ^{60}Fe emission lines. Nevertheless, it is particularly striking that the intensity levels show only weak variations with galactic morphology. The maximum is obtained with GM01 and the minimum with GM03.

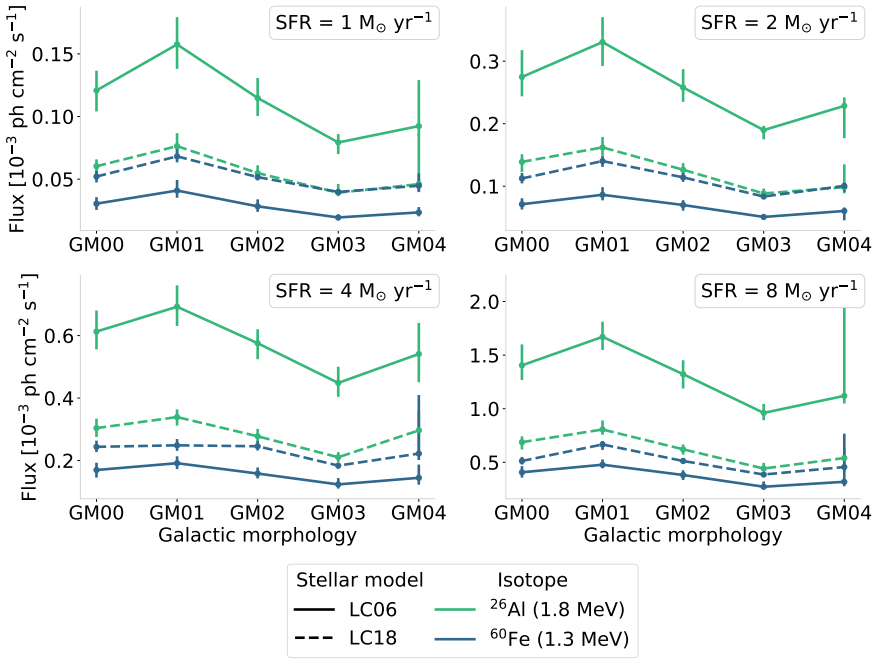

Figure 4.26: Total flux of gamma-ray photons from modelled ^{26}Al (*green*) and ^{60}Fe (*blue*) decay as observed by a theoretical observer at the position of the Sun within the different galactic morphologies given in Fig. 4.14. The results for different stellar models LC06 and LC18 are given for the two extreme explodability assumptions S09 and LC18 respectively. Different panels correspond to different assumptions about the galactic SFR as indicated. The standard IMF K01 is applied in all of the displayed cases. The uncertainties represent the 68th percentile of 500 model instantiations per parameter configuration.

The specific feature of GM01 is a particularly prominent Sagittarius-Carina arm directly in front of the observer towards the galactic centre. This indicates that a significant proportion of the high total flux results from an emphasis on this nearby structure. On the other hand, GM03 is characterised by an exponential radial density decrease combined with the spiral structure, which places the observer between two spiral arms. Both aspects of GM03 reduce the local probability density for star formation in the vicinity of the observer. This suggests that the low flux in this case is also closely linked to local characteristics.
If the investigation is restricted to the inner galactic region between $|l| \leq 30°$ and $|b| \leq 10°$ the picture changes to a maximum for GM02 and a minimum for GM00. This is shown in Fig. A.5 in the appendix. Since the integrated flux varies weakly with galactic morphology, it can be approximated by constant values for each SFR. This is summarised in Tab. 4.10. The ^{26}Al values for the full sky lie consistently

Table 4.10: ^{60}Fe and ^{26}Al gamma-ray flux in units of $10^{-4}\,\mathrm{ph\,cm^{-2}\,s^{-1}}$.

Spatial scope		Full sky				Inner galaxy			
SFR $[\mathrm{M_\odot\,yr^{-1}}]$		1	2	4	8	1	2	4	8
LC06	^{26}Al	1.2	2.6	5.7	13.0	0.4	1.0	2.1	5.0
	^{60}Fe	0.3	0.7	1.6	3.7	0.1	0.3	0.6	1.4
LC18	^{26}Al	0.5	1.2	2.9	6.2	0.2	0.5	1.0	2.4
	^{60}Fe	0.5	1.1	2.3	5.1	0.2	0.5	1.0	2.2

below the observationally obtained value of $F^{\mathrm{full}}_{^{26}\mathrm{Al}} = (1.84 \pm 0.03) \times 10^{-3}\,\mathrm{ph\,cm^{-2}\,s^{-1}}$ (cf. Sec. 3.4.3), even for a very high SFR $= 8\,\mathrm{M_\odot\,yr^{-1}}$ or a galactic ^{26}Al mass of $\sim 4\,\mathrm{M_\odot}$. On the other hand, the observational ^{60}Fe flux $F_{^{60}\mathrm{Fe}} = (0.31 \pm 0.06) \times 10^{-3}\,\mathrm{ph\,cm^{-2}\,s^{-1}}$ is met on average by model configurations with SFR $\geq 4\,\mathrm{M_\odot\,yr^{-1}}$

or $\gtrsim 4\,\mathrm{M}_\odot$ of ^{60}Fe. This indicates a general discrepancy between modelling ^{26}Al and ^{60}Fe.

On average, about 40% of the total flux originates from the inner galactic region. This means that it is typically dominated by emission from $|l| > 30°$ and $|b| > 10°$. Particularly the high latitude sites are located nearby. The proportion of flux from the inner galaxy shows a minimum of $\sim 23\%$ in the cases GM00 and GM01. A maximum contribution from that region of $\sim 50\%$ is seen for GM02 and GM03. This is an important morphological indicator since a restriction to the inner galactic region is used observationally in order to focus on the concentrated high-intensity emission from that area in combination with long instrument exposure (e.g. Diehl et al. 2006; Siegert 2017).

A comparison of the observational full-sky flux of ^{26}Al obtained in Sec. 3.4.3 with the flux from the inner Galaxy $F^{\mathrm{inner}}_{^{26}\mathrm{Al}} = (2.89 \pm 0.07) \times 10^{-4}\,\mathrm{ph\,cm^{-2}\,s^{-1}}$ measured by Siegert (2017) gives an even lower proportion of $\sim 16\%$ from the central Galaxy. Interestingly, the observed flux from this region is reached by average model results from SFR $\approx 5\,\mathrm{M}_\odot\,\mathrm{yr}^{-1}$ or $\sim 2\,\mathrm{M}_\odot$ of ^{26}Al. This indicates a rough agreement between certain model configurations and observations for the inner galactic region. It also points out that the main source of deviation between model results and observations apparently lies outside this spatial range.

The differentiation of galactic models according to different scale heights is shown in Fig. 4.27. It can be seen that large parts of the uncertainties given in Fig. 4.26 arise from different assumptions in scale height. In general, larger scale heights result in lower total flux. This is the case because scale height increases the average source distance to the observer. This effect is stronger for galaxy models with increased local prevalence, i.e. GM00, GM01, and GM04. Nevertheless, a mere reduction of the galactic height is not sufficient to compensate for the discrepancy to the observed ^{26}Al flux.

Here, an interplay between galactic evolution and stellar evolution models can be seen for the case of LC18. Delayed ^{60}Fe ejection due to stellar rotation preferentially fills old and large bubbles. If this intrinsically more diffuse emission is additionally spread vertically, the r^{-2} dependence of flux amplifies the scale height effect for ^{60}Fe significantly. Other than that, Fig. 4.27 indicates that the vertical galactic scale height appears to be a morphological parameter of minor significance with respect to the total flux.

Spatial Distribution of Flux Contributions So far, the 2-dimensional information of gamma-ray flux projected onto the sky around the observer has been considered. The model environment also includes the 3-dimensional distribution of the respective flux contributions. To judge the visibility of such flux contributions, an order of magnitude estimation based on SPI is used. With a total observation time of $\sim 255\,\mathrm{Ms}$ a flux of about $1 \times 10^{-6}\,\mathrm{ph\,cm^{-2}\,s^{-1}}$ is required for a 1σ signal of the 1.8 MeV emission line above the background. This is taken as rough lower limit for the flux necessary in order to be potentially visible. However, visibility is a cumulative matter along the line of sight. In order to visualise this, adaptive spatial binning (Cappellari & Copin 2003) is used to obtain Voronoi tessellations, each of which consistently contributes a flux of $10^{-6}\,\mathrm{ph\,cm^{-2}\,s^{-1}}$ at the position of the observer. This is shown Fig. 4.28 for a projection of ^{26}Al and ^{60}Fe flux contributors onto the galactic plane. The case for SFR $= 4\,\mathrm{M}_\odot\,\mathrm{yr}^{-1}$ and stellar model LC06 with explodability S09 is shown. The same representation for SFR $= 2\,\mathrm{M}_\odot\,\mathrm{yr}^{-1}$ and

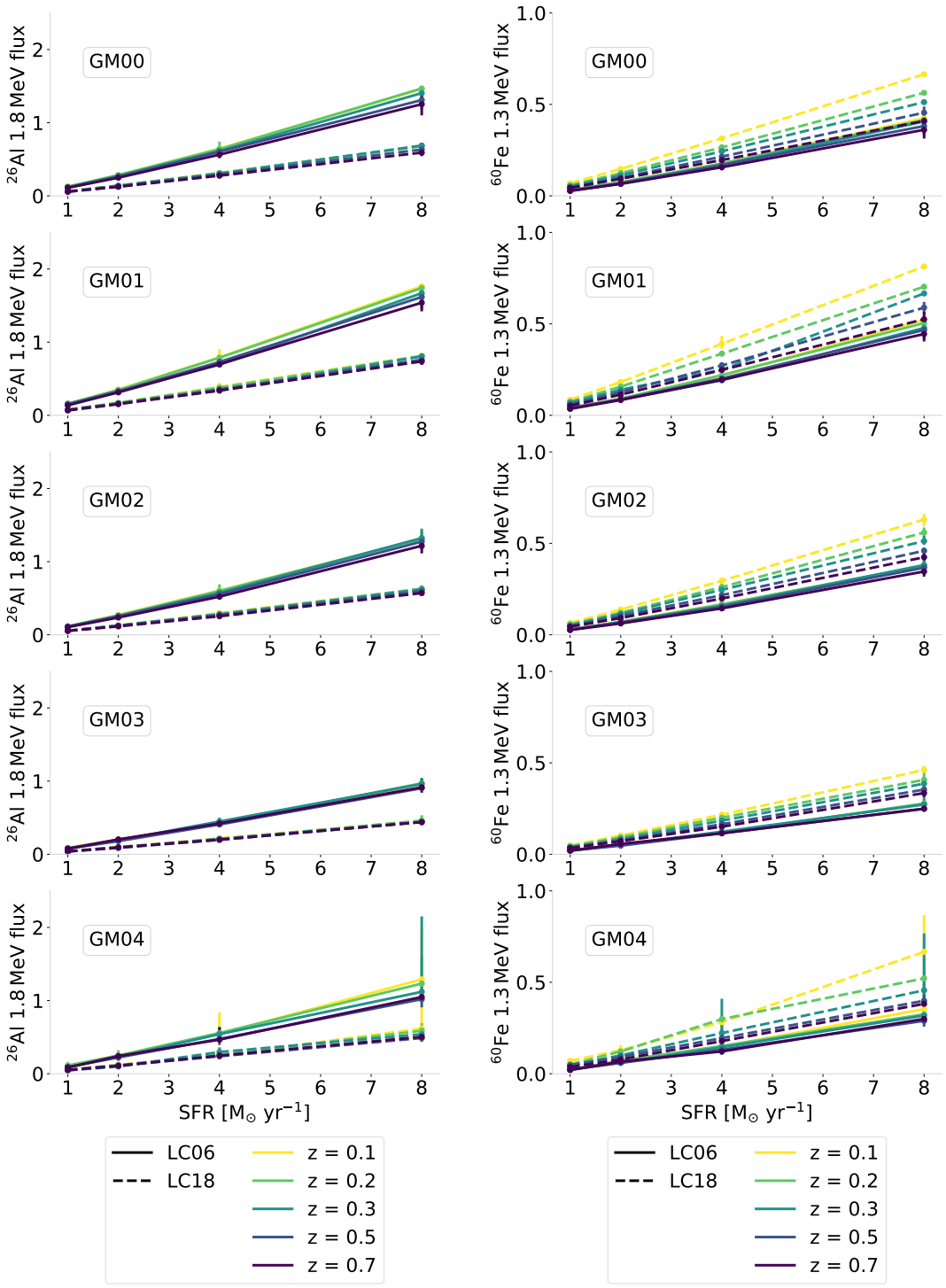

Figure 4.27: Total flux in units of 10^{-3} ph cm^{-2} s^{-1}in units of 10^{-3} ph cm^{-2} s^{-1} of gamma-ray photons from modelled ^{26}Al (*left*) and ^{60}Fe (*right*) decay as observed by a theoretical observer at the position of the Sun within different galactic morphologies as indicated in grey boxes. Different colours indicate the variation of the vertical galactic scale height z for each model, which is labelled in units of kpc. This is given for two stellar evolution models LC06 (solid lines) and LC18 (dashed lines). The uncertainty regions denote the 68th percentile of 100 MC runs each.

SFR $= 8\,\mathrm{M}_\odot\,\mathrm{yr}^{-1}$ is depicted in the appendix in Fig. A.7 and Fig. A.8 respectively. Each spatial bin contributes the same flux to the observer. The colour-coding denotes the size of the region which is necessary to accumulate that flux. Therefore, bright areas indicate regions with a high density of visible flux contributors. For the mostly spiral-arm dominated morphologies, these are found in close vicinity to the

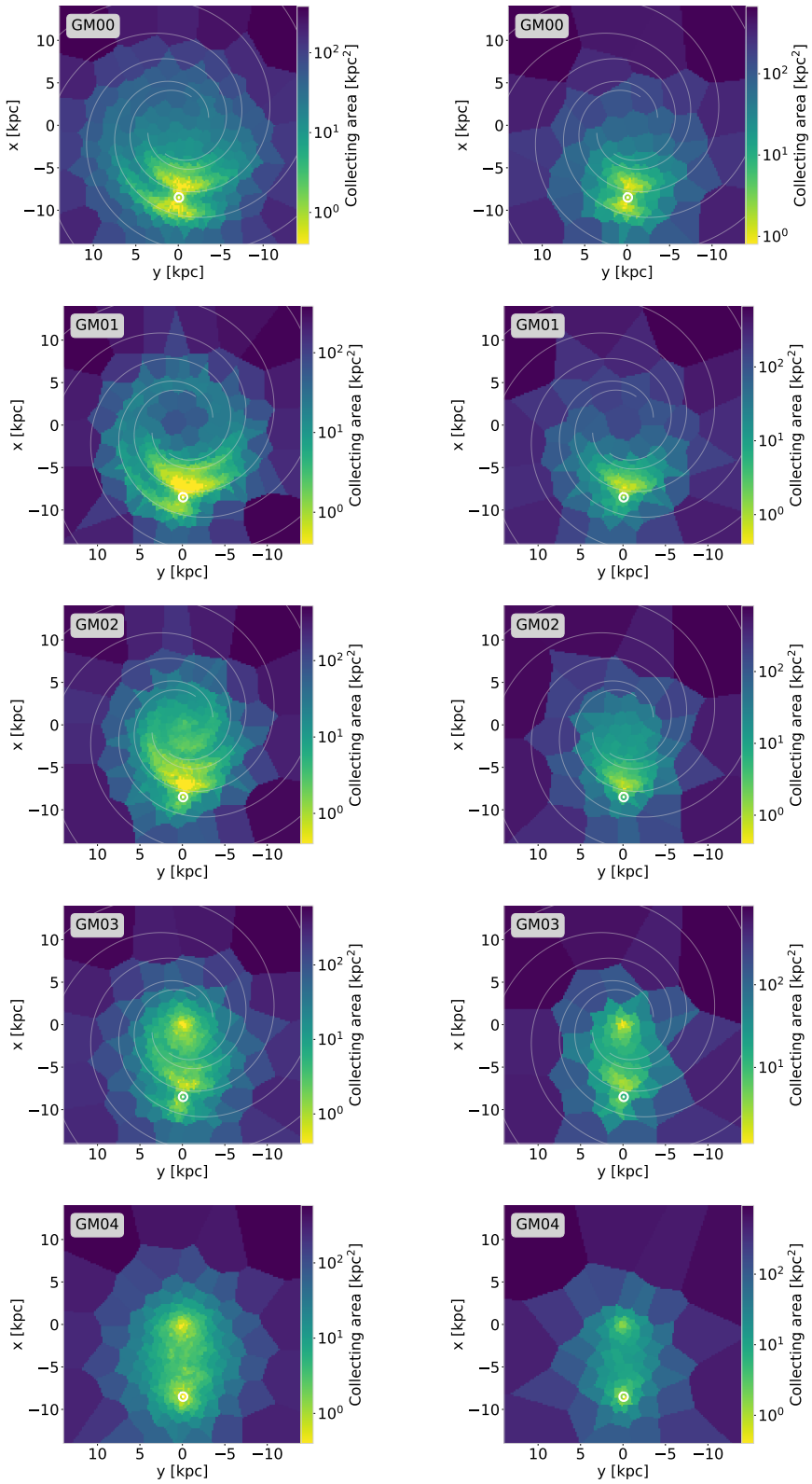

Figure 4.28: Radial distribution of modelled flux contributions for a theoretical observer (*white*) from ^{26}Al (*left*) and ^{60}Fe (*right*) decay. Each row represents average results of 500 model instantiations based on spatial models as denoted in grey boxes (for the nomenclature cf. Sec. 4.3.2). The fundamental model assumptions are stellar evolution models LC06, explodability S09, IMF K01, and SFR $= 4\,\mathrm{M}_\odot\,\mathrm{yr}^{-1}$. The latter corresponds to a total mass of $(1.81 \pm 0.07)\,\mathrm{M}_\odot$ and $(4.21 \pm 0.18)\,\mathrm{M}_\odot$ of ^{26}Al and ^{60}Fe respectively. Adaptive spatial binning (Cappellari & Copin 2003) was used to obtain Voronoi tessellations as spatial bins, each of which consistently contributes a flux of $10^{-6}\,\mathrm{ph\,cm^{-2}\,s^{-1}}$ for the observer. The colour scale refers to the collecting area covered by each such pixel. The galactic centre lies at $(x, y) = (0, 0)$ and the spiral arm centroids are indicated by *grey* lines (cf. Fig. 2.44). The distributions for SFR $= 2\,\mathrm{M}_\odot\,\mathrm{yr}^{-1}$ and SFR $= 8\,\mathrm{M}_\odot\,\mathrm{yr}^{-1}$ are shown in the appendix in Fig. A.7 and Fig. A.8 respectively.

observer. This confirms the previous indications that local emission is of particular importance for the explanation of the overall sky. Especially the leading edge of the Sagittarius-Carina arm directly in front of the observer towards the galactic centre appears prominently if such a structure is included. On the other hand, the Local arm towards the galactic anti-centre is significantly less prominent except for the flat distribution in the GM00 case. For the two centrally dominated morphologies GM03 and GM04, a strong flux component arises concentrated from the galactic centre. GM04 also shows a rather pooled local component. This is due to the fact that the doubly exponential disk goes smoothly with radius and omits a spiral arm gap around the observer. Overall, the ^{26}Al and ^{60}Fe gamma-ray flux follows similar distributions. However, since ^{60}Fe emission has lower intensity, it is more concentrated towards the prominent features just discussed.
The cumulative flux arriving at the observer position from within a certain radius is shown in Fig. 4.29. The first thing to note here is that in all cases, on average 50% of the entire emission are received from within 6 kpc maximum for the shallowest increase in GM03. For GM00 and GM01, a radius of only ~ 2.8 kpc already contains half the total flux. These radii exclude especially the galactic centre at a distance of 8.5 kpc. On average, $\sim 30\%$ of the entire flux is enclosed within 2 kpc, which is about the distance to the Local arm tangent. Particularly noteworthy is also the large scatter at small distances. In 0.3% of all cases, 90% of the total flux originates from within a radius of 6 kpc around the observer. This means in these cases the local component outweighs the overall galactic emission by far.
In order to assess the morphological adequacy of the PSYCO models, the cumulative flux distribution obtained for the hydrodynamic simulation by Rodgers-Lee et al. (2019) is added as grey lines for comparison. The four graphs correspond to four different observer positions on the Solar circle within the simulated galaxy. This simulation appears generally rather centrally dominated and is thus resembled closest by GM03. The observer positions show a large intrinsic scatter in the received flux with an indication for a strong component from the Local arm distance. In that case, spiral-arm dominated morphologies like GM01 are closest the shape from the hydrodynamic simulation. Overall, the degeneracy between local and galactic emission seems also to be found in the hydrodynamic simulation. This is covered by PSYCO using the canonical choice of morphologies in Sec. 4.14. Overall, this shows the promising possibility of a combined approach by a prepending detailed MHD simulation of the large-scale stellar feedback dynamics as done e.g. by Rodgers-Lee et al. (2019) or Fujimoto et al. (2018) and, morphologically based on that, a subsequent modelling by PSYCO to test the important model parameters through a large number of instantiations.
Looking at the four galactic quadrants as defined in Fig. 2.44, an asymmetry is apparent for models including spiral arms. As expected, in GM04 this asymmetry is absent. The largest flux is received from QIV, i.e. $270° < l < 360°$. This reflects the trailing side of the Sagittarius-Carina arm which is is passing by closely in this quadrant. It outshines the leading arm side in QI, i.e. at $0° < l < 90°$. In the direction of the galactic anti-centre, the main contribution originates from the Local arm seen by an excess in QII, i.e. from $90° < l < 180°$. For the case of an enhanced Local arm such as in GM00, this quadrant even dominates entirely within a radius of 4.5 kpc. Such an enhanced flux of QI seems inconsistent with Milky Way observations (cf. e.g. Diehl et al. 2018a, 466). Nevertheless, a general observational indication of more emission from QIV (cf. e.g. Fig. 1.1 or Kretschmer et al. 2013; Bouchet et al. 2015) would be consistent with a pronounced contribution from the

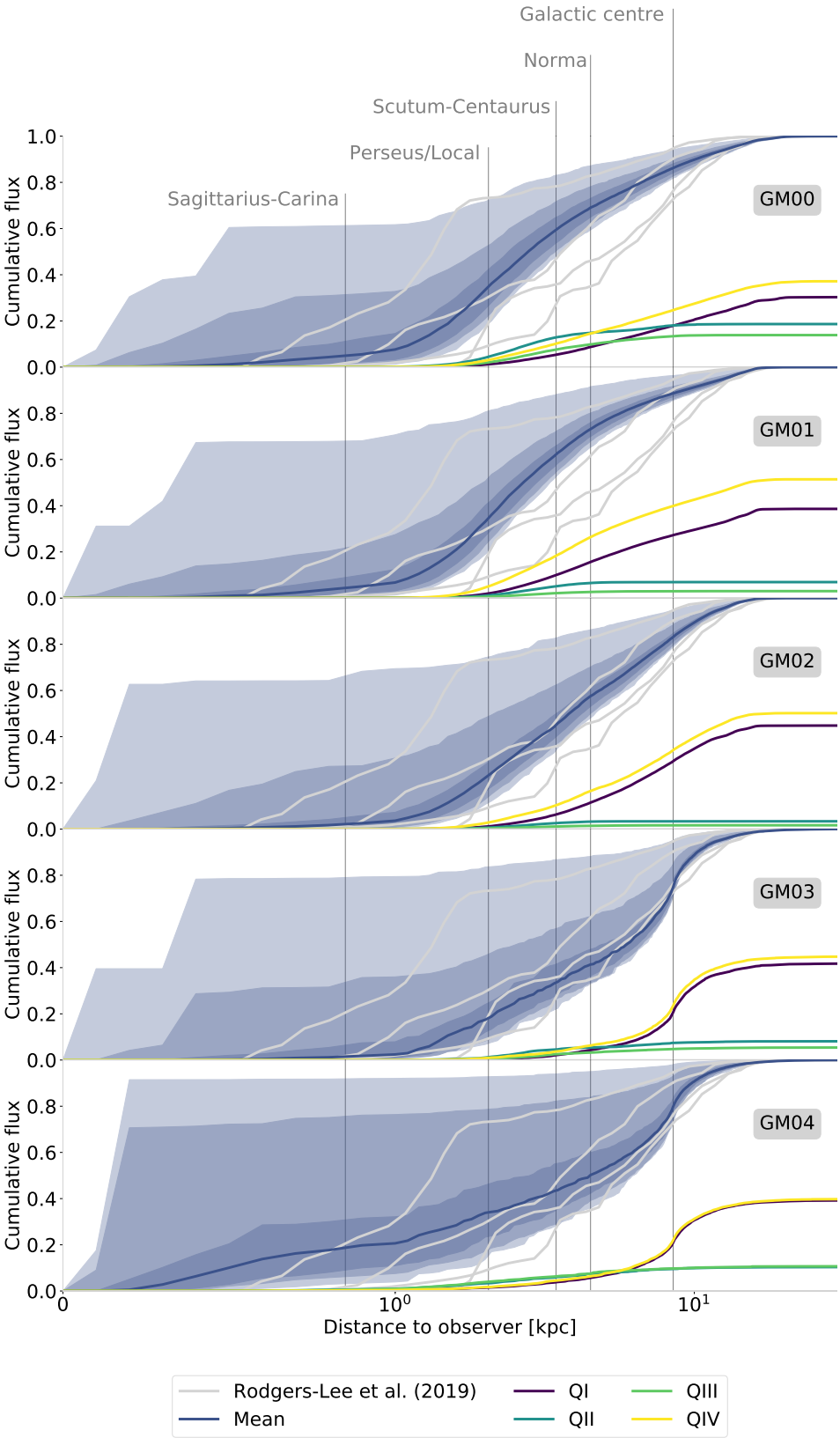

Figure 4.29: Cumulative 1.8 MeV flux as a function of the radial distance to the observer. Each panel corresponds to a different spatial model as indicated in the grey boxes. The mean contribution inside a certain radius is given as *blue* line. Shaded regions give the 68th, 95th, and 99.7th percentile around the mean derived from 500 models each. The model basis is composed of LC06 stellar models, S09 explodability, and K01 IMF. Contributions from individual quadrants follows the definition in Fig. 2.44 and are given without uncertainties in *purple*, *cyan*, *green*, and *yellow*. All flux values are normalised to the average total flux. As comparison, results from four different observer positions in the hydrodynamic simulations by Rodgers-Lee et al. (2019) are added as *light grey* lines. Distances to spiral arm centroids and the galactic centre are indicated as *dark grey* vertical lines and labelled above. Note that between 0 and 1 the distance scale is linear.

Sagittarius-Carina arm in front of the observer.
A general shift of superbubbles filled with nucleosynthesis ejecta with respect to the spiral arm centroids is widely discussed in literature as outlined in Sec. 2.4.4. Such a shift can be investigated in the PSYCO framework by rotating the canonical spiral arms by a certain angle in the galactic plane. To estimate the maximum effect of this, one instantiation of the morphology with the most salient nearby spiral features, GM01, is fully rotated clockwise with respect to the projections in Fig. 4.28 by 360° in steps of 0.25°. The variation of the total flux as a function of the rotation angle of the galaxy model is depicted in Fig. 4.30. Starting in a dip at 0°,

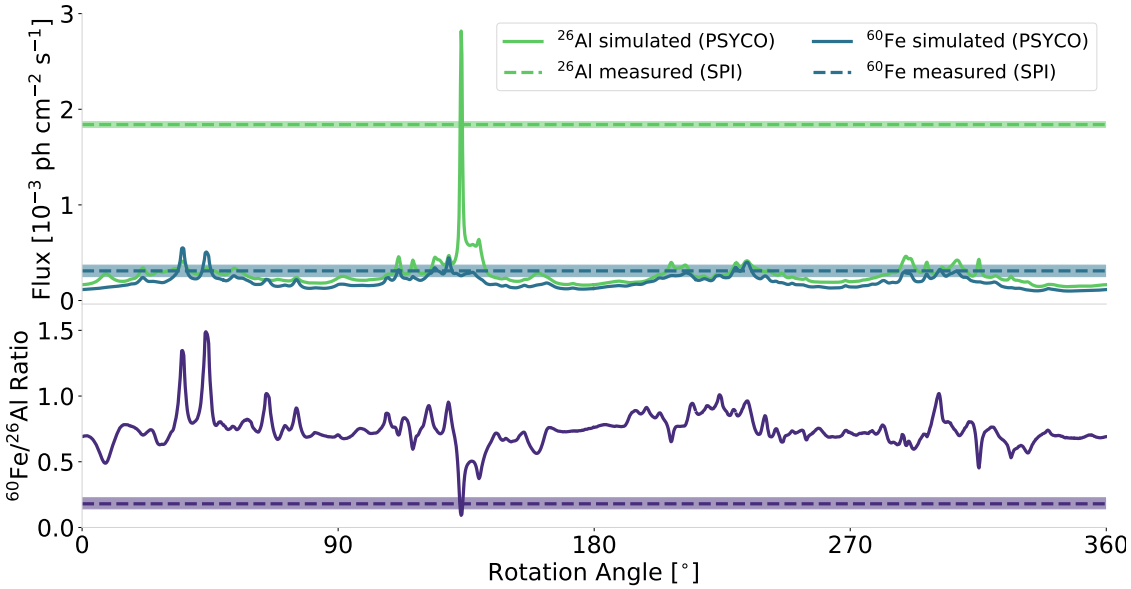

Figure 4.30: *Upper:* Total gamma-ray flux from ^{26}Al (*green*) and ^{60}Fe (*blue*) as a function the rotation angle of the spatial PSYCO model in the galactic plane. Rotation is clockwise for the projections in Fig. 4.28. The flux values $F_{^{60}\mathrm{Fe}} = (0.31 \pm 0.06) \times 10^{-3}\,\mathrm{ph\,cm^{-2}\,s^{-1}}$ (Wang et al. 2020) and $F_{^{26}\mathrm{Al}} = (1.84 \pm 0.03) \times 10^{-3}\,\mathrm{ph\,cm^{-2}\,s^{-1}}$ (cf. Sec. 3.4.3) are shown as dashed lines with shaded uncertainty regions. The model configuration is characterised by morphology GM01 with 300 pc, stellar model LC18, IMF K01, and SFR $= 2\,\mathrm{M_\odot\,yr^{-1}}$. *Lower:* Same as above for the ^{60}Fe/^{26}Al flux ratio.

the overall received flux shows a regular pattern about $\sim 90°$ as expected from the global structure of four spiral arms. Maxima are reached after around 30°, 120°, 210°, and 300°, which correspond to the passages through the four spiral arms. This indicates that for an overall offset of radioactively filled superbubbles of $\sim 15°$–$45°$ preceding the spiral arms the total measured flux increases on average by a factor of about 2. On top of the overall sinusoidal shape there is an additional variation in distinct and locally restricted peaks. These features arise from incidentally bright foreground sources and therefore accumulate preferentially in regions where the observer is placed close to or inside a spiral arm. One particularly striking instance of such features stands out around rotation angle 134° as a prominently bright peak of ^{26}Al emission. This will be discussed separately in the next paragraph.
The ^{60}Fe emission in this model configuration seems overall consistent with measurements by Wang et al. (2020) in the case of such an offset. However, this is to be interpreted with caution because of the large degeneracy between different model variables, such as SFR, IMF, yield model, or explodability. Their impact can easily exceed a factor of 2. On the other hand, the general discrepancy between modelled and measured ^{26}Al emission spans about an order of magnitude, which is, according to the previous discussion, on average not accountable by any model configuration,

except for a unreasonably high SFR.

Outliers The striking peak of ^{26}Al emission in Fig. 4.30 indicates that certain incidental spatial model configurations can vary the modelled flux by up to an order of magnitude. Flux maps from the respective region are depicted in Fig. 4.31 as spatial sequence of 1° steps around 133.5°. It is characterised by the direct passage

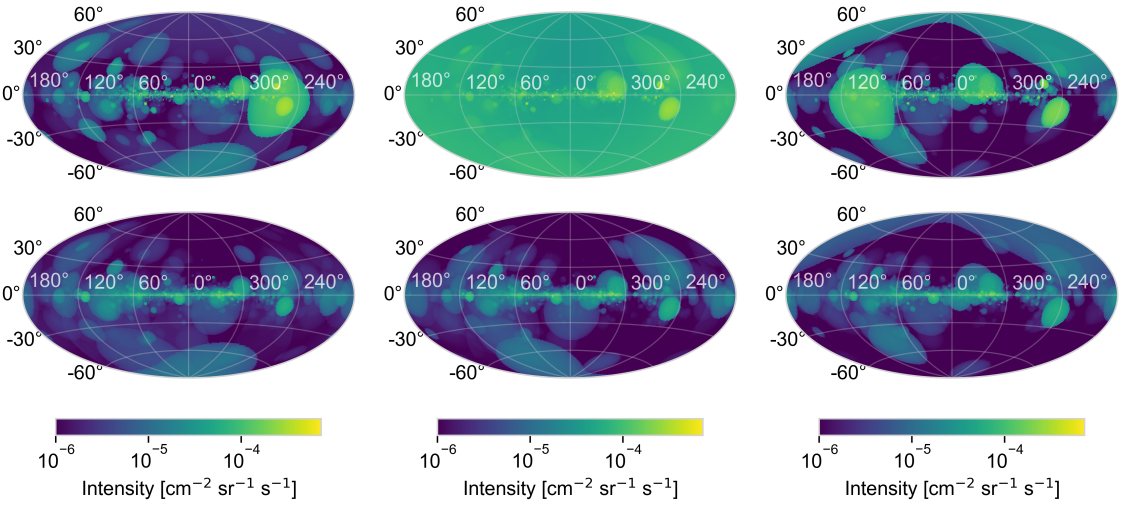

Figure 4.31: Gamma-ray sky maps of the galactic model described in Fig. 4.30 for the spatial sequence of model rotation angles 132.5° (*left*), 133.5° (*middle*), and 134.5° (*right*). *Upper:* 1809 keV emission along the three spatial steps. It shows the passage through a superbubble filled with $5.6 \times 10^{-4}\,\mathrm{M}_\odot$ ^{26}Al emerging from a 6.9 Myr old stellar group with a total mass of $3.7 \times 10^4\,\mathrm{M}_\odot$. The total flux reaches a maximum of $2.81 \times 10^{-3}\,\mathrm{ph\,cm^{-2}\,s^{-1}}$ in the upper middle panel. *Lower:* 1332 keV emission. The young and bright ^{26}Al bubble contains only negligible amount of ^{60}Fe.

through a superbubble densely filled with ^{26}Al. In this model realisation, this particular bubble originates from a 6.9 Myr old stellar group with a total stellar mass of $3.7 \times 10^4\,\mathrm{M}_\odot$. Due to its young age, it contains $5.6 \times 10^{-4}\,\mathrm{M}_\odot$ of ^{26}Al from massive-star winds and only negligible amounts of ^{60}Fe. Its centre passes the observer with a minimum distance of only 33 pc about 20 pc below the galactic plane in the direction of the galactic anti-centre. Due to the radial extent of 89 pc of the superbubble, the observer is fully encased at that point. This results in an omnidirectional emission with a slight anisotropic excess towards the bubble centre, which is located at $(l, b) = (180°, -65°)$ (cf. upper middle panel in Fig. 4.31). Here, the 1809 keV flux from this group only reaches a maximum of $2.40 \times 10^{-3}\,\mathrm{ph\,cm^{-2}\,s^{-1}}$, which dominates the total flux of $2.81 \times 10^{-3}\,\mathrm{ph\,cm^{-2}\,s^{-1}}$ by far. On the other hand, this bubble is basically dark in 1332 keV emission since it is too young to have produced significant amounts of ^{60}Fe. Thus, this feature is not seen in the lower panels of Fig. 4.31. Besides the spatial peculiarity, this additional temporal configuration consistently reduces the ^{60}Fe/^{26}Al flux ratio. Altogether, this incidental arrangement results in a remarkable coincidence with values from observing the Milky Way from the Solar System concerning the ^{26}Al flux, the ^{60}Fe flux, as well as the ^{60}Fe/^{26}Al flux ratio as shown in Fig. 4.30. Against this background, a potential importance of such outliers is highlighted.

In order to assess the relative frequency of such outliers, the full distribution of model samples is considered in Fig. 4.32. The histograms show the total fluxes from 500 model realisations for each combination of stellar model LC06 or LC18,

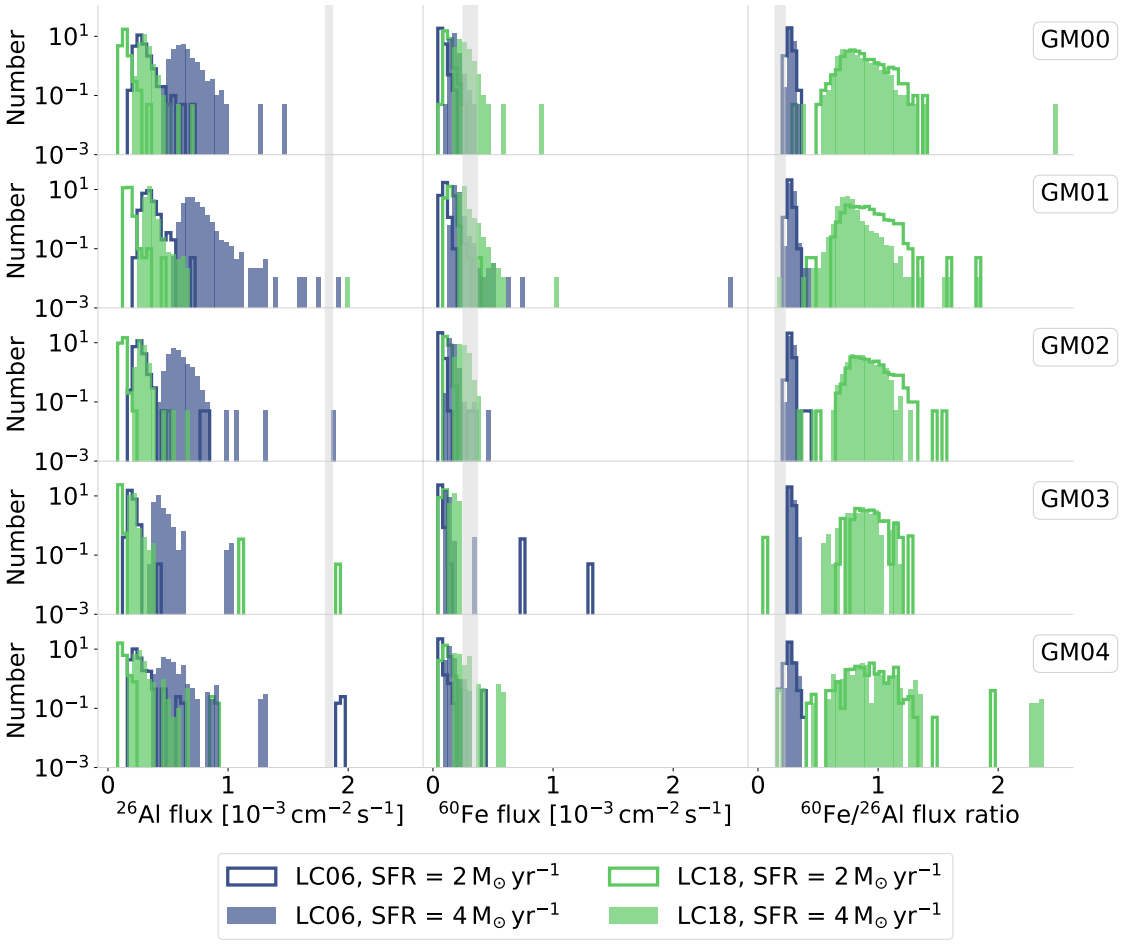

Figure 4.32: Total flux histograms for 500 PSYCO model realisations for each combination of stellar model LC06 (*blue*) or LC18 (*green*), SFR = $2\,\mathrm{M}_\odot\,\mathrm{yr}^{-1}$ (unfilled steps) or SFR = $4\,\mathrm{M}_\odot\,\mathrm{yr}^{-1}$(filled bars), and the five galactic morphologies GM00–GM04 (cf. Fig. 4.14). The vertically filled *grey* regions indicate the observational values from the Milky Way for $F_{^{26}\mathrm{Al}} = (1.84 \pm 0.03) \times 10^{-3}\,\mathrm{ph\,cm^{-2}\,s^{-1}}$ (cf. Sec. 3.4.3, *left*), $F_{^{60}\mathrm{Fe}} = (0.31 \pm 0.06) \times 10^{-3}\,\mathrm{ph\,cm^{-2}\,s^{-1}}$ (Wang et al. 2020, *middle*), and their ratio *right*.

SFR = $2\,\mathrm{M}_\odot\,\mathrm{yr}^{-1}$ or SFR = $4\,\mathrm{M}_\odot\,\mathrm{yr}^{-1}$, and all five galactic morphologies. The overall picture was already discussed in the context of Fig. 4.26. The histogram visualisation now allows to emphasize the exceptional cases, i.e. in particular configurations with high 1.8 MeV flux close to the observed Milky Way value. Such configurations occur regardless of the galactic morphology, SFR, or stellar model with a probability on the order of 10^{-3}–10^{-2}. They seem to be more frequent in the case of GM01 because this morphology emphasizes on the Sagittarius-Carina arm and therefore nearby components. The probability of outliers increases for higher SFR since more stellar associations are produced. Additionally, LC06 yields generally a higher ^{26}Al mass than LC18. As already mentioned, an additional temporal configuration is required to coherently also produce a low ^{60}Fe/^{26}Al flux ratio consistent with the Milky Way value. This occurs in only about 10^{-3} of all cases which is therefore considered a very rare event.

Considering the isolated flux from the inner galaxy with $|l| \leq 30°$ and $|b| \leq 10°$ (cf. Fig. A.6 in the appendix), the frequency of outliers reduces strongly. This underlines the findings earlier in this section that this region is mostly influenced by average galaxy-wide emission. Since most of the galactic mass lies within the inner galaxy region and the 1.8 MeV Milky Way flux value is on average reproduced for SFR = $4\,\mathrm{M}_\odot\,\mathrm{yr}^{-1}$ and LC06, which is only weakly dependent on the specific spatial

configuration, an overall Galactic ^{26}Al mass of $M_{^{26}\mathrm{Al}} \gtrsim 1.8\,\mathrm{M}_\odot$ indicates a reasonable estimate for the Milky Way. Within the statistical uncertainties, this is in agreement with the previously found estimation of $(2.8 \pm 0.8)\,\mathrm{M}_\odot$ by Diehl et al. (2006) with a tendency towards the lower range. On the other hand, this nevertheless emphasizes the importance of local flux contributions in the vicinity of the Solar System.
It is important to note that the multiplicity of model parameters can lead to a certain degree of degeneracy which cannot be addressed by the total gamma-ray flux or ratios alone. A more distinguished analysis to assess the adequacy and importance of individual parameters towards a more profound understanding of this complex system is elaborated in Sec. 5.4 using 17.5 yr of SPI full-sky data.

4.4.4 Nearby OB Associations

The importance of nearby emission emerged consistently in the previous considerations and modelling results. Since this has also been suggested from observations in the particular case of the Milky Way, this flux contribution can be modelled separately on the basis of the prior empirical knowledge. In Sec. 4.3.2, the basic properties of the nearby associations have been outlined and the characteristics of the known knowns been summarised in Tab. 4.7. The latter category of stellar groups is associated with observationally determined extents, ages, distances, and ^{26}Al fluxes. The missing ^{60}Fe information can be estimated assuming a canonical star group of the type of the well studied Orion region (Voss et al. 2010) and using population synthesis. The results are listed in Tab. 4.11. This indicates poten-

Table 4.11: ^{60}Fe gamma-ray flux in units of $10^{-4}\,\mathrm{ph\,cm^{-2}\,s^{-1}}$ estimated for known knowns (cf. Tab. 4.7) by using population synthesis with different stellar model configurations for a canonical stellar association of the type of Orion OB1, i.e. 640 stars in the range 8–120 $\mathrm{M}_\odot$ (Voss et al. 2010). Statistical uncertainties are inferred from 10^3 MC runs.

Stellar model	Explodability	Cyg OB1–9	Ori OB1	USco	UCL	LCC
LC06	S09	$1.0^{+0.2}_{-0.2}$	$0.5^{+0.1}_{-0.1}$	$10.5^{+3.2}_{-3.9}$	$2.9^{+0.7}_{-0.9}$	$3.0^{+0.6}_{-0.8}$
	J12	$0.8^{+0.1}_{-0.2}$	$0.5^{+0.1}_{-0.1}$	$8.9^{+2.8}_{-3.5}$	$2.8^{+0.7}_{-0.9}$	$2.7^{+0.5}_{-0.7}$
	S+16	$0.7^{+0.1}_{-0.2}$	$0.4^{+0.1}_{-0.1}$	$7.9^{+2.9}_{-3.8}$	$2.6^{+0.7}_{-0.9}$	$2.4^{+0.6}_{-0.7}$
	LC18	0.0	$0.1^{+0.1}_{-0.1}$	0.0	$2.0^{+0.7}_{-0.8}$	$1.0^{+0.2}_{-0.2}$
LC18	LC18	0.0	$0.8^{+0.3}_{-0.4}$	0.0	$7.4^{+1.8}_{-2.2}$	$12.1^{+2.8}_{-4.1}$

tial test fields for observational studies of SN yields. Their combined ^{26}Al flux is $F_{^{26}\mathrm{Al}} = 2.9 \times 10^{-4}\,\mathrm{ph\,cm^{-2}\,s^{-1}}$(Siegert 2017).
In order to assess the known unknown star groups, a combined OB association catalogue from Melnik & Efremov (1995) and Melnik & Dambis (2017b) is used. This includes a radius of ~ 3.5 kpc around the observer. With documented positions, extents, and inferred ages, the bubble size and the isotopic content for each of these groups is estimated via population synthesis. For this purpose, dynamic ages are applied as described in Sec. 4.3.2. Both components are finally combined into sky maps for the isolated consideration of known nearby OB associations. These are depicted in Fig. 4.33 as average over 10^3 MC instantiations on the basis of LC06 as well as LC18. Both, in ^{26}Al and ^{60}Fe emission they are dominated by the three known regions Cygnus, Sco-Cen, and Orion. The Cygnus region around $l = 80°$ appears particularly bright and Sco-Cen and Orion extend to relatively large heights. The detailed total contributions including the known unknowns are listed in Tab. 4.12. Altogether, the nearby OB associations within ~ 3.5 kpc localised by observations

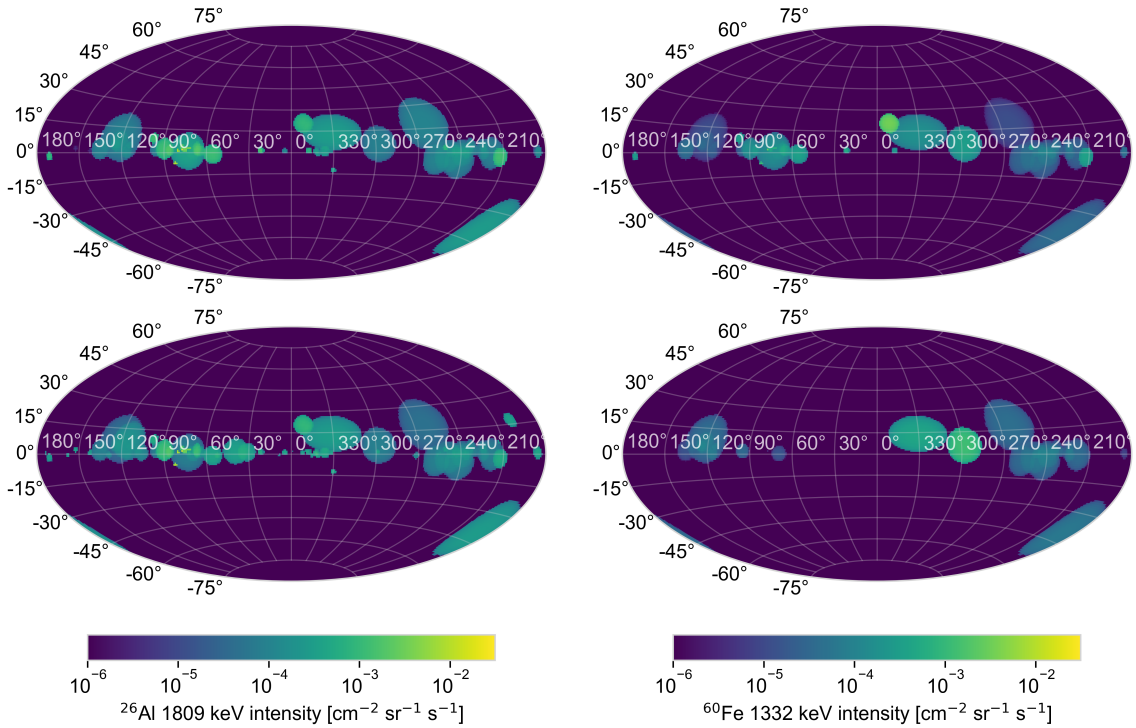

Figure 4.33: Full-sky maps of the ^{26}Al (*left*) and ^{60}Fe(*right*) emission from known nearby OB associations modelled with PSYCO using their characteristic properties as described in Sec. 4.3.2. The *upper* maps represent modelling based on stellar models LC06 and the *lower* on LC18.

Table 4.12: Gamma-ray flux from known unknown star groups and the combined contribution of known knowns and unknowns (nomenclature see Sec. 4.3.2) in units of $10^{-4}\,\mathrm{ph\,cm^{-2}\,s^{-1}}$. Estimates are based on 10^3 population synthesis calculations for canonical Orion-like star groups.

		Known unknowns		Combined	
Stellar model	Explodability	^{60}Fe	^{26}Al	^{60}Fe	^{26}Al
LC06	S09	$0.6^{+0.2}_{-0.3}$	$2.1^{+0.6}_{-0.9}$	$2.4^{+0.5}_{-0.7}$	$5.0^{+0.6}_{-0.9}$
	LC18	$0.04^{+0.01}_{-0.01}$	$1.1^{+0.3}_{-0.5}$	$0.3^{+0.1}_{-0.1}$	$4.0^{+0.3}_{-0.5}$
LC18	LC18	$0.3^{+0.1}_{-0.1}$	$1.6^{+0.6}_{-0.8}$	$2.3^{+0.5}_{-0.6}$	$4.5^{+0.6}_{-0.8}$

can account for 20%–30% of the total measured ^{26}Al emission in the Milky Way. This sets a lower limit as model constraint for the ^{26}Al gamma-ray flux from this domain. As was found in Fig. 4.29, this is reproduced by all galactic morphologies used with PSYCO in this thesis. However, model results have to be interpreted with caution in this respect since the used kinematic OB association catalogues show an observational bias towards smaller and therefore younger groups. Older and chemically more enriched groups may be missed by those catalogues. The particular consideration of nearby associations already exceeds the average total ^{26}Al flux obtained for SFR $= 2\,\mathrm{M_\odot\,yr^{-1}}$ modelled with PSYCO. This indicates that a higher SFR is required in the model in order to obtain sufficiently dense clustering of OB associations in the vicinity of the observer. On the other hand, the ^{60}Fe gamma-ray flux from nearby OB associations is rather uncertain due to the strong dependence on the assumed explodability model. This underlines the importance of studying the nucleosynthesis processes of SNe in order to obtain a coherent picture of the galactic chemical evolution. To address this particular issue, PSYCO has been extended by the option to model short-lived radioisotopes ejected directly from stellar explosions. This will be explained in a short excursus in the following Sec. 4.4.5 for

the example of ^{44}Ti.

4.4.5 Short-Lived Radioactivity: ^{44}Ti

The decay radiation of short-lived radioisotopes constitutes a direct tracer of nucleosynthesis processes due to prompt stellar explosion mechanisms. These processes are subject to intensive simulation work in order to model and understand the complex dynamics of ccSNe (e.g. Janka 2012; Burrows et al. 2018). An observationally important isotope produced in such events is ^{44}Ti. Its explosive nucleosynthesis yields have been theoretically estimated e.g. by Limongi & Chieffi (2018) or Timmes et al. (1996) within the range 10^{-5}–$10^{-4}\,\mathrm{M}_\odot$. This is of the same order as the longer-lived isotopes ^{26}Al and ^{60}Fe. Due to the more than four orders of magnitude smaller lifetime of only 89 yr, individual ccSNe are expected to be bright in nuclear ^{44}Ti gamma-rays lines with energies of 68 keV, 78 keV, and 1157 keV. On the other hand, the short lifetime strongly limits this emission both spatially and temporally. Therefore, these gamma-ray sources are restricted to their immediate production site and appear point-like rather than extended in observations. As confirmed in a recent study by Weinberger et al. (2020) using SPI, about 1–2 such sources are detectable from the Solar System above a detection limit of $\sim 1 \times 10^{-5}\,\mathrm{ph\,cm^{-2}\,s^{-1}}$(cf. also Grebenev et al. 2012; Boggs et al. 2015; Tsygankov et al. 2016; Grefenstette et al. 2017). This observational frequency can be used to test the theoretical model yields. For this purpose, the PSYCO framework is extended to also model the galactic distribution of short-lived isotopes from ccSNe. Since the standard temporal binning of 5×10^4 yr is too coarse in order to cover phenomena on timescales on the order of 10^1–10^2 yr, a separate approach is implemented for those. For each ccSN event per regularly sampled star group, the ^{44}Ti yield and the exact time of explosion is collected. The remaining mass after 50 Myr is then calculated for each source via the radioactive decay law. The resulting gamma-ray flux is finally inferred by assuming a point-like emission at the sampled distance of the respective stellar association. In this way, a full-sky gamma-ray flux map of modelled ^{44}Ti emission is constructed on the basis of LC18 SN yields as shown in Fig. 4.34. As expected, only few sources appear as bright individual pixels near the galactic plane. Due to the rareness of the events considered, the only clear morphological characteristic that can be read off such sky map is a concentration towards the galactic plane in the direction of the galactic centre.

The number of detectable sources depends on the instrumental detection threshold. This is shown in Fig. 4.35. For SFR $= 2\,\mathrm{M}_\odot\,\mathrm{yr}^{-1}$ the number of on average detectable ccSNe in ^{44}Ti gamma-rays above a flux threshold of $10^{-5}\,\mathrm{ph\,cm^{-2}\,s^{-1}}$ is ~ 0.6 and therefore below the observationally indicated range. Nevertheless, this is in agreement within the statistical 1σ scatter of the galaxy models of ± 1 which is calculated from 100 MC instantiations for each of the model configurations and is omitted in Fig. 4.35 for better readability. This scatter is the case independent of the specific choice of galactic morphology. Assuming SFR $= 4\,\mathrm{M}_\odot\,\mathrm{yr}^{-1}$, an average number of 1.4 ± 1.1 detectable ^{44}Ti sources is produced, which matches the measurements from the Milky Way. Considering the relation between SFR and SNR shown in Fig. 4.23, this is points to a galactic rate of ccSNe of 1.4 ± 1.1 per century. A reduction of the detection threshold with future instruments would increase the number of SN remnants for which short-lived nucleosynthesis studies will be made possible and therefore benefit the accuracy of such estimates. Nevertheless, this

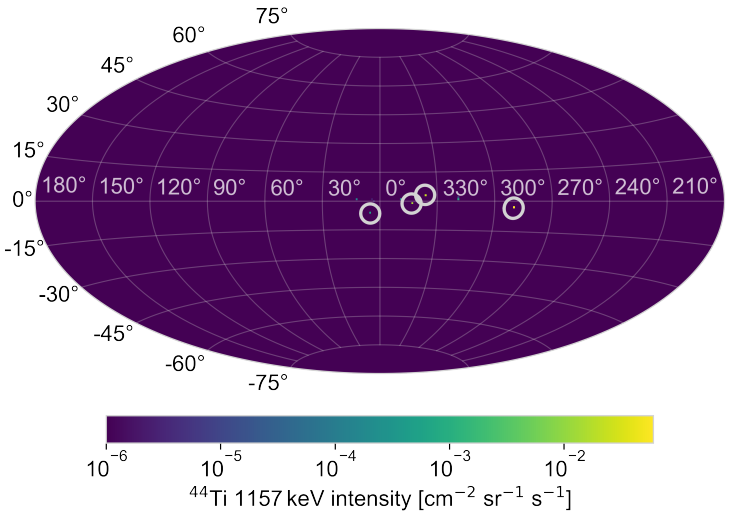

Figure 4.34: Galactic sky-map of ^{44}Ti gamma-ray sources modelled with PSYCO on the basis of LC18, SFR = $4\,M_\odot\,yr^{-1}$, and spatial model GM01. As expected, only few individual pixels near the galactic plane appear bright, the four brightest of which are highlighted by grey circles.

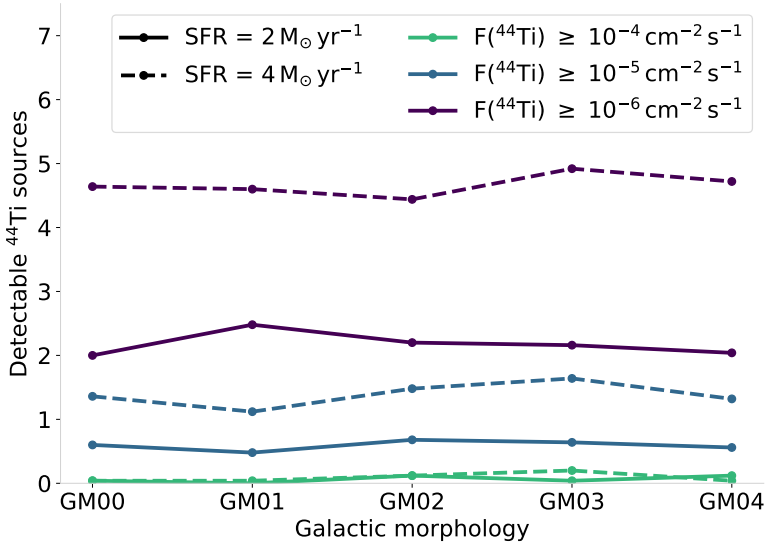

Figure 4.35: Number of detectable ^{44}Ti point sources in the Milky Way for different galactic morphologies and using the LC18 nucleosynthesis yields with the K01 IMF. Colours correspond to different gamma-ray detection thresholds. Solid lines indicate connect values for SFR = $2\,M_\odot\,yr^{-1}$ and dashed lines for SFR = $4\,M_\odot\,yr^{-1}$. Each point gives the average of 100 MC runs with a 1σ scatter of about ±1, which is omitted in the figure for better readability.

result affirms and extends the consistency of the PSYCO modelling approach for galactic nucleosynthesis feedback also on the basis of short-lived radioisotopes.

Essentials

- A total number of 180000 realisations of the PSYCO model is used to analyse a parameter grid comprising SFR, IMF, galactic radial morphology, scale height, stellar nucleosynthesis yields, and explodability models.
- Nearly-linear relationships between SFR and total galactic ^{26}Al and ^{60}Fe content have been found for a variety of model configurations with a tendency towards larger SFR $\geq 4\,M_\odot\,yr^{-1}$ being consistent with global flux observations.
- A link between SFR and SNR based on ^{26}Al and ^{60}Fe is presented with 1.4–2.0 ccSNe per century for SFR $= 4\,M_\odot\,yr^{-1}$.
- The modelled nuclear gamma-ray line flux shows a prominently irregular structure from nearby superbubbles on top of a galactic component mainly reflecting the close-by spiral structure. ^{60}Fe appears more diffuse than ^{26}Al. The measured flux from the inner galaxy is on average reproduced by some model configurations, while the full-sky flux of 1.8 MeV is systematically underestimated, probably owing to foreground emission.
- Particularly striking outlier models incidentally reproduce measured gamma-ray characteristics in ^{26}Al, ^{60}Fe, as well as ^{60}Fe/^{26}Al flux ratio by very nearby and young star groups which are bright in ^{26}Al and dark in ^{60}Fe emission.
- Currently known nearby OB associations within ~ 3.5 kpc account for about 20%–30% of the total measured 1.8 MeV flux.
- The number of 1–2 ccSN remnants observable by ^{44}Ti decay in the Milky Way are modelled consistent with SNR $\sim 1.4 \pm 1.1$ per century.

5 Comparing Models to Gamma-Ray Measurements

"We have become trapped by our capacity for abstraction: it provides us with accurate descriptive information, but serves to undermine our belief in the utility and meaning of existence."

— Jordan B. Peterson (1999, 19)

The analysis of the nucleosynthesis signature in the Milky Way and the Solar System in the course of this thesis has now arrived at a conceptual configuration with empirical measurements on the one hand (cf. Ch. 3) and theoretical models on the other hand (cf. Ch. 4). As will first be explained in Sec. 5.1, these two components are undoubtedly separated by an ontological chasm. The remainder of this chapter will therefore be devoted to the task of conceptually bridging this gap and nonetheless combining these two essentially different components in a scientifically fruitful way. This concludes the investigatory course of this thesis by a comprehensive consideration of the three astrophysical scales of the nucleosynthesis feedback processes, which were discussed in Ch. 2 as fundamental, namely from individual sources in Sec. 5.2, over groups of stars in Sec. 5.3, up to the entire Galaxy in Sec. 5.4. This will be summarised in a discussion and outlook in Sec. 5.5.

5.1 An Epistemological Impasse in Comparisons?

As visualised in Fig. 4.1, the indirect route of astrophysical inquiry via theoretical models in principle presupposes their conceptual compatibility with empirical data. This is a cornerstone of astrophysical research which is often questioned indirectly or even disregarded. Objections in this regard come both from observers and theorists and can be subsumed under the flippantly formulated allegation that apples are compared with oranges. Since this chapter is explicitly concerned with the comparison between models and data, it is important to give a short outline of the general lines of argumentation in this respect.

The criticism of observers is usually that models and simulations are under-determined in relation to actually measured physical systems; the components, which are therefore fundamentally different, would thus be supposedly incompatible. The inverse extreme of overly detailed models compared to limited experimental possibilities boils down to a similar point of criticism. This aspect has already been discussed in detail in Sec. 4.1. It is important to repeat that this is a delicate argument, because it can be used in a very general way as an argument against any scientific assessment of general laws and regularities. On the other hand, however,

it is of great importance in order to direct the focus of simulated properties to observationally relevant features.
The criticism on the part of theory follows mostly one of two arguments (Ellis & Silk 2014). One is that observations may be too poorly resolved or too strongly affected by measurement uncertainties to allow for a well-founded evaluation of the simulation. A second line of argument is based on the statement that any particular simulation represents a realization of a general case, while the measurements may be limited to a few unique cases. Although a basic comparability would be granted, it is casually argued that this would generally not be meaningful, since the two components are obviously different in nature.
On closer examination, these arguments can strictly speaking not serve as general objections against the comparability of models and data, but as practical rejections of the respective model. This can be fundamentally assessed by a recourse to the axiomatic primacy of empirical measurements in physical science. This means that the functionality of theoretical models is actually limited to their comparability with empirical data. In other words, a simulation or model that cannot be properly evaluated due to insufficient data is simply not a tool of empirical science.
To refer to the often used proverb of the impasse of comparing apples and oranges mentioned at the beginning of this section, it should be noted that this is generally neither a valid nor a helpful objection. Pointing out the essential difference between entities like apples and oranges can be reduced to the trivial statement that something is not something else. Alluding to their suspected incomparability is a rhetoric shortcut avoiding the fact that comparability is a matter of perspective. If it is possible to find a transformation of object properties into a common space, the respective objects are ultimately made comparable in that space. And since each object under consideration must represent an empirical phenomenon in order to be scientific, they must be comparable according to the aspects of their respective phenomenology. In this regard, even a comparison yielding fundamental differences is not at all invalid but in fact informative.
Overall, this particular section is therefore, following the argument by Ellis & Silk (2014), which is intended to support the primacy of empiricism in physical science. These very general remarks are made here, since such objections affect the field of gamma-ray astrophysics in particular, due to the difficult measurements. Based on this short presentation, it can be stated that there is actually no general epistemological impasse in comparisons. On the contrary, precisely because of the challenging data situation, the fullest possible exploitation of these data with reference to theoretical models promises the greatest possible scientific progress. This principle will therefore be applied in the following sections at the fundamental levels for research about nucleosynthesis feedback. Stellar evolution models are compared to gamma-ray measurements of an individual stellar system, γ^2 Velorum, population synthesis calculations are probed against the signature from the Perseus OB associations, and a detailed morphological analysis method is developed to exploit the full Galactic gamma-ray signal with recourse to full galaxy simulations.

Essentials

To retain the functionality of theoretical simulations and models as tools of empirical science, comparability with measurements must be ensured in an informative way.

5.2 Individual Source: γ^2 Velorum

According to Sec. 2.2, single stars are the driving agents of nucleosynthesis feedback. A fundamental understanding of these processes is therefore best based on a detailed investigation of these individual objects. Therefore, the measurement of the nuclear ^{26}Al line is investigated here from the binary star system γ^2 Velorum which is the source most likely to be suitable for this purpose due to its proximity to Earth.

5.2.1 Object Characteristics

The spectroscopic binary star system γ^2 Velorum is positioned at Galactic coordinates $(l, b) = (262.8°, -7.7°)$ in the Vela OB2 association (van Leeuwen 2007) and was first described by Sahade (1955). It consists of a O7-type star and a WC8 star. Due to the latter, the system is also designated WR 11, referring to its WR characteristics. The distance of the system with respect to the Solar System is determined as 336^{+8}_{-7} pc (North et al. 2007), moving away from the observer with a radial velocity of $(15 \pm 3)\,\mathrm{km\,s^{-1}}$ (Gontcharov 2006). Other distance determinations yield values between 258^{+41}_{-31} pc (Schaerer et al. 1997) and 480 pc (Pozzo et al. 2000). Despite the considerable uncertainty, this makes WR 11 the closest WR-type star to Earth. In combination with the expected emission of fresh nucleosynthesis products due to the WR nature, this system is perfectly suited as a test object of an individual nucleosynthesis source.
Current estimates of the mass ratio determine the WR component with $M_{\mathrm{WR}} = (9.0 \pm 0.6)\,\mathrm{M_\odot}$ and radius $R_{\mathrm{WR}} = (6 \pm 3)\,\mathrm{R_\odot}$ as secondary star accompanying the O7 star with $M_{\mathrm{O}} = (28.5 \pm 1.1)\,\mathrm{M_\odot}$ and radius $R_{\mathrm{O}} = (17 \pm 2)\,\mathrm{R_\odot}$ as primary component of γ^2 Velorum (De Marco et al. 2000; North et al. 2007). Earlier mass estimates yielded an inverted ratio with $M_{\mathrm{WR}} = (30 \pm 2)\,\mathrm{M_\odot}$ and $M_{\mathrm{O}} = 9^{+2.5}_{-1.5}\,\mathrm{M_\odot}$ (Schmutz et al. 1997). This would imply a reversed attribution with a primary WR star and a secondary O-type star. Despite this tentativeness, the total mass of the system is obtained consistently with $\sim 40\,\mathrm{M_\odot}$. According to star cluster models, this suggests that the system originates from a cluster with at least $\geq 500\,\mathrm{M_\odot}$ since otherwise such a massive object would not occur (Mapelli et al. 2015, cf. also Sec. 4.2). The binary components orbit each other with a period of $P_{\mathrm{orb}} = 78.53 \pm 0.01$ days and an eccentricity $e = 0.334 \pm 0.003$ (North et al. 2007). The broad line characteristic of the Wolf-Rayet component indicates strong mass loss with a rate of $\dot{M}_{\mathrm{WR}} = 2.5 \times 10^{-5}\,\mathrm{M_\odot\,yr^{-1}}$ (Benaglia et al. 2019) and escape wind velocities of $v_\infty = 2.5 \times 10^3\,\mathrm{km\,s^{-1}}$ (De Marco & Schmutz 1999) ejected from WR 11. Although the companion O7 star usually ejects about one order of magnitude less dense winds, it is launched with a similar velocity. The opposing material flows collide and give rise to a wind collision region (Eichler & Usov 1993). Thus, the system is also classified as a colliding wind binary.
Measurements of the UV and X-ray radiation from this region revealed radiatively driven instabilities in shocked high-temperature material surrounding a pronounced wind cavity around the O star (St Louis et al. 1993; Willis et al. 1995). Due to the interaction of the winds with stellar magnetic fields and relativistic particles in the collision region, gamma-ray emission in the GeV range is expected from this source (Werner et al. 2013). A luminosity of $L_{\gamma^2\,\mathrm{Vel}} = (3.7 \pm 0.7) \times 10^{31}\,\mathrm{erg\,cm^{-2}\,s^{-1}}$ of the system in the 0.1–100 GeV range is inferred by Pshirkov (2016) from a flux excess

detected with the *Fermi* Large Area Telescope (LAT) from the direction of γ^2 Velorum. However, this detection covers about 10^2 arcmin, which encloses a multitude of candidate sources. While radio interferometric data at 1.4 and 2.5 GHz confirmed WR 11 as possible gamma-ray producer, seven other possible candidates were also confirmed in the same region (Benaglia 2016). Recently found evidence for a variability of the γ-ray emission in agreement with the period of γ^2 Velorum supports an origin from this system (Martí-Devesa et al. 2020). Overall, the spectral index of WR 11 is consistent with thermal emission, which may indicate that suspected synchrotron radiation from colliding winds is in large parts absorbed in the stellar photospheres due to their close separation (Benaglia et al. 2019).
The binary γ^2 Velorum is part of the γ Velorum sub-cluster of the Vela OB2 association. This cluster is in turn again divided into two kinematically separable subdivisions that lie along the line of sight from the Solar System and differ by about 1–2 Myr in age (Franciosini et al. 2018). This indicates a sequential star formation event driven by stellar feedback in the past. The sub-cluster contains many lithium-rich pre-main sequence stars and is therefore considered relatively young between 10–20 Myr (Jeffries et al. 2009, 2017). Spectroscopic radial velocities obtained with *Gaia* revealed significant expansion of the sub-cluster as well as the entire Vela OB2 group, which specifies it as an unbound association (Armstrong et al. 2020). With an age of only between (3.5 ± 0.4) Myr (De Marco & Schmutz 1999; North et al. 2007) and (5.5 ± 1.1) Myr (Eldridge 2009), γ^2 Velorum itself is estimated to be even younger than the field average. This age is around the onset of ^{26}Al ejection as expected from stellar evolution models. Additionally, the object is characterised by an extensive mass-loss rate. Therefore, it constitutes an intriguing observational target for the investigation of nuclear gamma-ray lines and thereby testing stellar model calculations. The age determinations are also around the boundary at which the system is supposed to have already experienced binary interaction in the form of a mass transfer event (Eldridge 2009). This makes it additionally a target for probing the specific case of possibly enhanced nucleosynthesis wind yields due to rotational mixing and mass transfer in binary systems. These aspects will be pursued further in the following Sec. 5.2.2.
Two other objects in the vicinity are explicitly considered in the following analysis, i.e. the two putative SN remnants Vela Junior and the Vela Supernova Remnant. Vela Junior is situated at $(l, b) = (266.3°, -1.2°)$ with an angular diameter of $\sim 2°$ (Green 2014). The age of the remnant is determined to $\lesssim 1500$ yr and was initially assumed to lie about 200 pc away from the Solar System (Aschenbach 1998; Iyudin et al. 1998). More recent estimations yield a larger distance of $\gtrsim 0.5$ kpc (Allen et al. 2015). The object was discovered due to its ^{44}Ti gamma-ray emission by Iyudin et al. (1998) with COMPTEL. The central stellar remnant inside the explosion debris is identified as neutron star (Pavlov et al. 2001).
The position of the Vela Supernova Remnant is $(l, b) = (263.9°, -3.4°)$ and extends over 4.25° in the sky (Green 2014). While its distance is with (250 ± 30) pc (Cha et al. 1999) comparable to that of Vela Junior, it is about ten times older with an age of 1.1×10^4 yr (Taylor et al. 1993). The central object is the Vela Pulsar, which is a fast rotating neutron star (Fey et al. 2004). However, the actual nature of this object being a SN remnant is still debated (e.g. Acero et al. 2016).

5.2.2 ^{26}Al Signal from γ^2 Velorum

Due to the WR nature and the unique proximity to the Solar System, γ^2 Velorum is particularly suitable for studying the ^{26}Al gamma-ray signal from a single stellar source. This was first investigated by Oberlack et al. (2000) using COMPTEL. The authors did not detect the 1.8 MeV gamma-ray line and provided a 2σ upper flux limit of $1.1 \times 10^{-5}\,\mathrm{ph\,cm^{-2}\,s^{-1}}$. Based on the distance estimation of $258^{+2.1}_{-1.4}\,\mathrm{pc}$, this also sets a limit of $\left(6.3^{+2.1}_{-1.4}\right) \times 10^{-5}\,\mathrm{M_\odot}$ on the ^{26}Al yield from γ^2 Velorum. This was followed up by Mowlavi et al. (2004, 2005) using 1.8 Ms of INTEGRAL/SPI measurements, which yielded an upper flux limit of $2.6 \times 10^{-5}\,\mathrm{ph\,cm^{-2}\,s^{-1}}$.
Since then, the observation time of SPI at the position of γ^2 Velorum has increased by about a factor of 2.5. Here, the full accumulated data of single and double events in the energy range 1745–1840 keV from a $16° \times 16°$ field around the position of γ^2 Velorum is used to revise the previously determined limits. This comprises an total observation time of ~ 6.2 Ms from a total number 2076 instrument pointings. Taking detector failures and deadtime corrections into account, this corresponds to an effective mean lifetime of 5.5 Ms for single detectors and 4.7 Ms for double detectors. The spatial sky coverage of the data set is depicted in the exposure map in Fig. 5.1. The general approach of SPI data analysis has already been discussed in

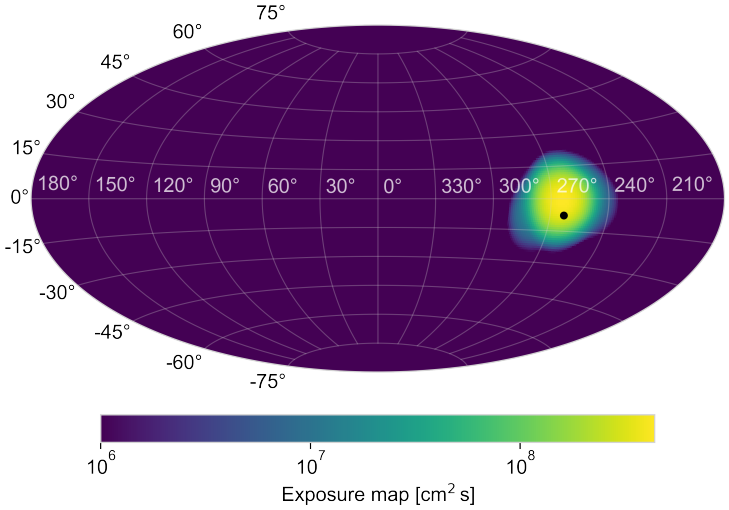

Figure 5.1: SPI exposure map for the ^{26}Al analysis of γ^2 Velorum (*black* dot). It comprises an integrated observation time of $\sim$ 6.2 Ms from 2076 instrument pointings. The effective area of SPI is $44\,\mathrm{cm^2}$ at 1.8 MeV, accounting for failed detectors (Attie et al. 2003).

detail in Sec. 3.4.3 for the full-sky 1.8 MeV emission. It is now also applied to the case of γ^2 Velorum using a point source representation as celestial emission model. Additionally, the Vela Supernova Remnant and Vela Junior are included in order to account for additional background signals owing to those sources. The performance of the respective background model is evaluated in Fig. 5.2 for single and double events separately. The residuals follow a normal distribution around zero with width 1. This is the case for both, the full model description as well as the background model only. This indicates that the data are already well described solely by background. The χ^2-statistic (cf. Eq. 3.26) in the middle panels shows a scatter around the optimum $\chi^2_{\mathrm{red}} = 1$ as expected from variance of the χ^2 distribution, within 3σ. This confirms that the data are described by the combined sky and background model over the entire energy range in a statistically sound way. Parallel to this, the

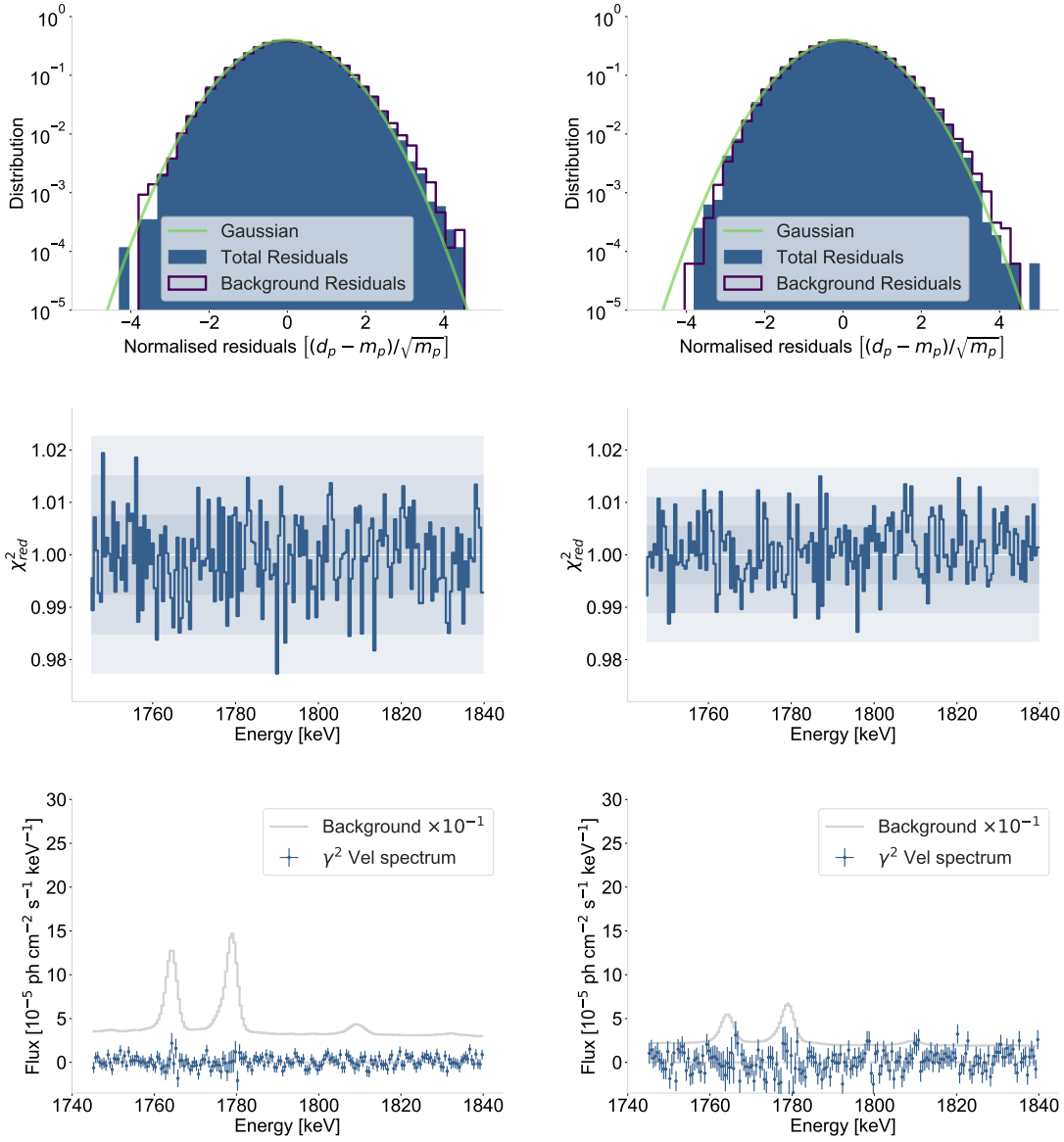

Figure 5.2: SPI data analysis results of the ^{26}Al emission from γ^2 Velorum for single (*left*) and double events (*right*) separately. *Top:* Residuals of the background model overplotted by a standard normal distribution with width $\sigma = 1$. *Middle:* Model performance measured by χ^2_{red} for each energy bin for the entire SPI camera. The ideal value of $\chi^2_{\mathrm{red}} = 1$ is shown as white line, with 1σ, 2σ, and 3σ intervals of the χ^2 distribution as shaded grey regions. All points lie within the 3σ band. *Bottom:* Resulting SPI spectra from the amplitude of the point source model fitted in each 0.5 keV wide energy bin in the range 1745–1840 keV. The full background counts scaled by a factor 10^{-1} are shown for comparison as *grey* solid line and a *grey* dashed line guides the eye to zero flux.

same evaluation for a combined fit of single and double events is shown in Fig. A.9 in the appendix. It shows the same statistical properties as the separate treatment of event types, which confirms the consistency of the general approach.

The resulting spectra for single and double events with a bin width of 0.5 keV both appear to be stochastically scattered around zero flux. As expected this scatter is higher and with larger statistical uncertainties around the strong background lines at 1764 keV or 1779 keV associated with ^{28}Al and ^{204,205}Bi.

In order to determine the possible nuclear line contribution in the data, the event types are combined into one spectrum. The total photon model for the ^{26}Al emission line as described in Eq. 3.28 is then forward folded through the SPI instrument response and fitted via MCMC ensemble sampling as outlined in Sec. 3.4.3. Statistical

priors are adopted as listed in Eq. 3.31, except for the line parameters, which are chosen according to the upper limit found by Mowlavi et al. (2004) as

$$\begin{aligned} F_{^{26}\mathrm{Al}} &\sim \text{truncated normal}(2.6 \times 10^{-5}, 1 \times 10^{-4}; 0, 1) \\ E_0 &\sim \text{uniform}(1808.0, 1810.0), \end{aligned} \tag{5.1}$$

with a uniform prior for the line centroid since a potential line shift is ultimately in question. The resulting posterior distributions of the line fit parameters are depicted in Fig. 5.3. The final spectrum of combined single and double events is

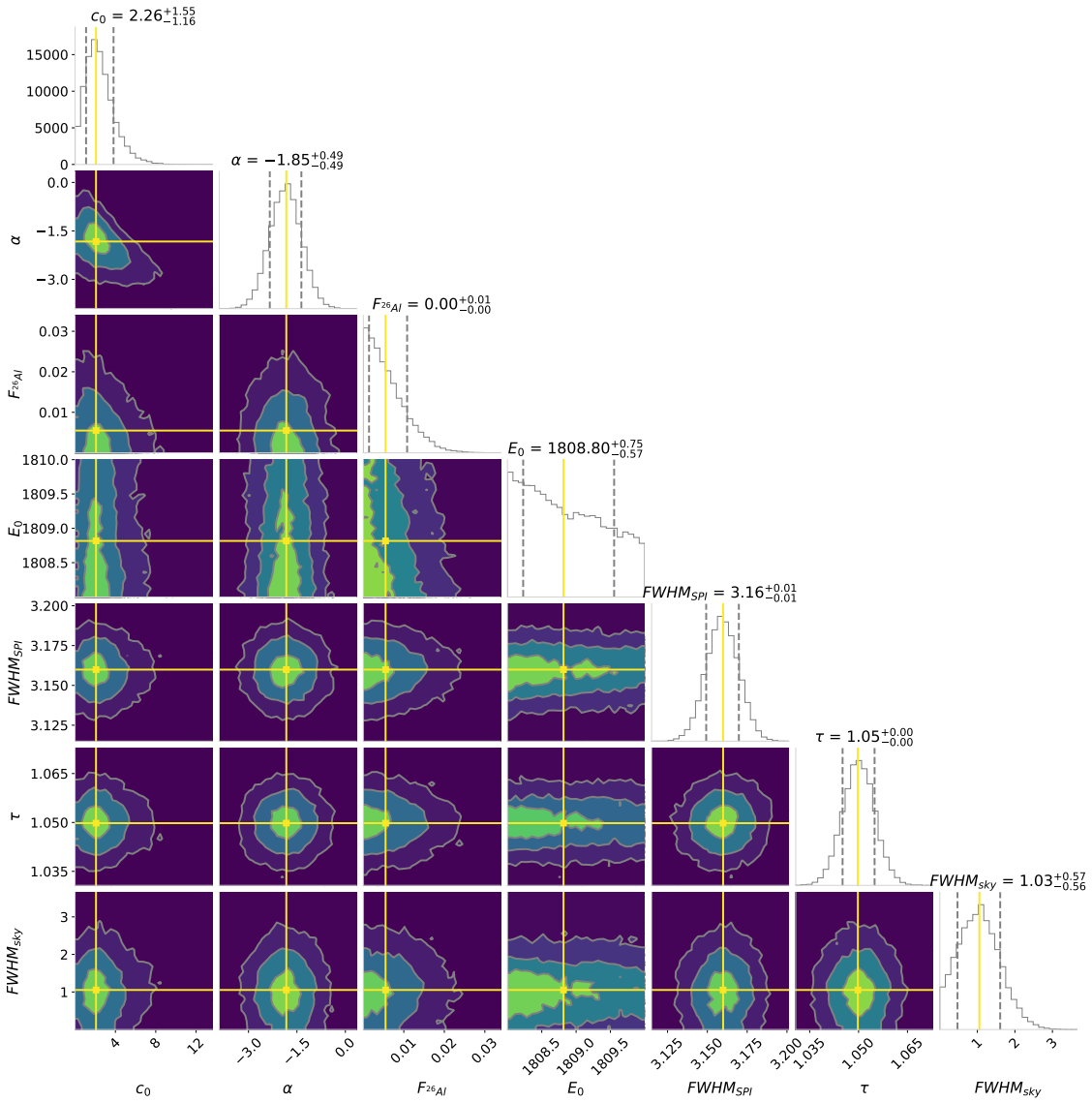

Figure 5.3: Posterior distributions of spectral fit parameters describing the ^{26}Al signal from γ^2 Velorum at 1809 keV measured with SPI according to the photon model in Eq. 3.28. The mean value along each axis is shown in *yellow*. Histograms on the diagonal show marginalised probability distributions along the respective axis with 68th percentiles marked by dashed lines.

displayed in Fig. 5.4, together with the fitted total model for ^{26}Al emission. The spectrum is clearly dominated by the single events (cf. lower panels in Fig. 5.2) and larger statistical uncertainties are recognisable around strong background lines due to the higher background count rates in those spectral domains. Nevertheless, the continuum and even strong and distinct background features are accounted for in the background model and therefore smoothly erased. The line fit yields a non-

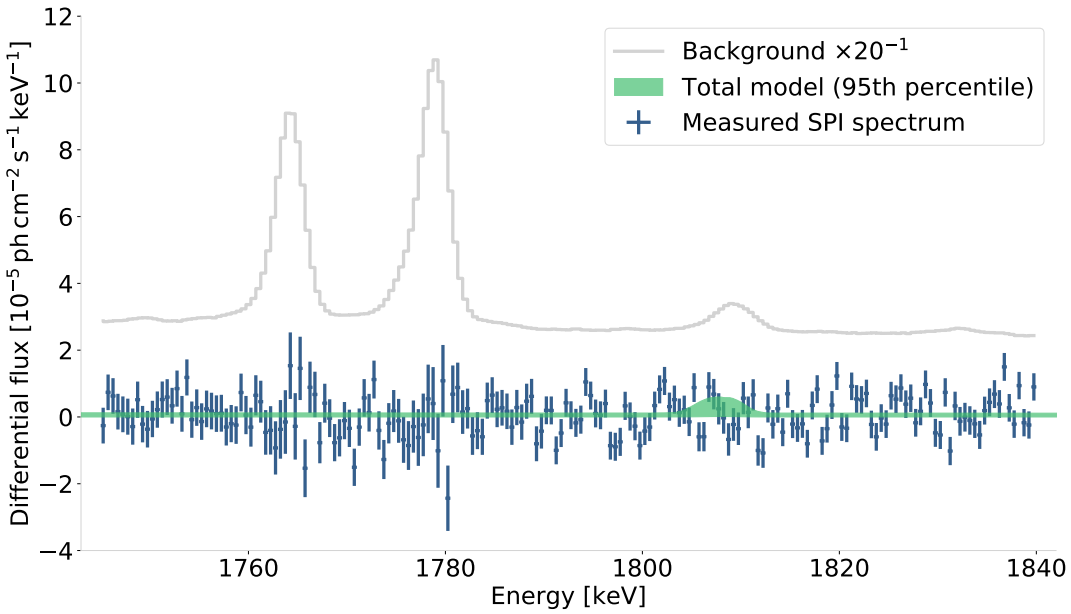

Figure 5.4: SPI spectrum (*blue* data points) of the ^{26}Al emission at 1809 keV from γ^2 Velorum for a separate treatment of single and double events. The best-fitting photon model is shown in a band of the 2σ confidence interval in *green*. It represents a degraded Gaussian line profile on top of a power-law continuum (cf. Eq. 3.28). The posterior distributions of individual fit parameters are shown in Fig. 5.3 in the appendix. The spectrum shows no ^{26}Al signal at 1.8 MeV with a 2σ upper flux limit of 1.7×10^{-5} ph cm^{-2} s^{-1}. The scaled instrumental background is shown in *grey*. The detailed association of background lines with radioactive isotopes is given in Fig. 3.15.

detection of the 1.8 MeV ^{26}Al emission line and results in a 2σ upper flux limit of 1.7×10^{-5} ph cm^{-2} s^{-1}. This means that due to the extended data situation, the upper limit obtained with SPI is reduced by 65% compared to the determination by Mowlavi et al. (2004) using an effective observation time of 1.8 Ms. For comparison, the spectral analysis results for the combined treatment of single and double events are shown in the appendix with the resulting spectrum in Fig. A.9 and posterior distributions of the spectral fit parameters in Fig. A.10. This yields overall consistent results.

For the current distance estimate of 336 pc, the flux limit corresponds to an 2σ upper ^{26}Al mass limit of 1.6×10^{-4} M$_\odot$ ejected and currently present around γ^2 Velorum. Considering the uncertainties arising from different distance estimates, this varies between 1.0×10^{-4} M$_\odot$ at 258 pc and 2.9×10^{-4} M$_\odot$ at 450 pc.

5.2.3 Comparison with Stellar Evolution Models

The initial mass of WR 11 is estimated as $M_{\mathrm{WR}}^{\mathrm{initial}} = 57 \pm 15\,\mathrm{M}_\odot$ (Schaerer et al. 1997). This rather wide mass range provides the basis for a comparison of the upper ^{26}Al mass limit found in Sec. 5.2.2 with the stellar evolution models introduced in Sec. 2.2.5. Therefore, Solar metallicity is assumed for γ^2 Velorum in the following. Oberlack et al. (2000) based their analysis on the rather near distance of 258^{+41}_{-31} pc by Schaerer et al. (1997). The following investigations are normalised to the updated distance of 336^{+8}_{-7} pc obtained by North et al. (2007).

A compilation of the observed limits from COMPTEL and SPI with the predicted

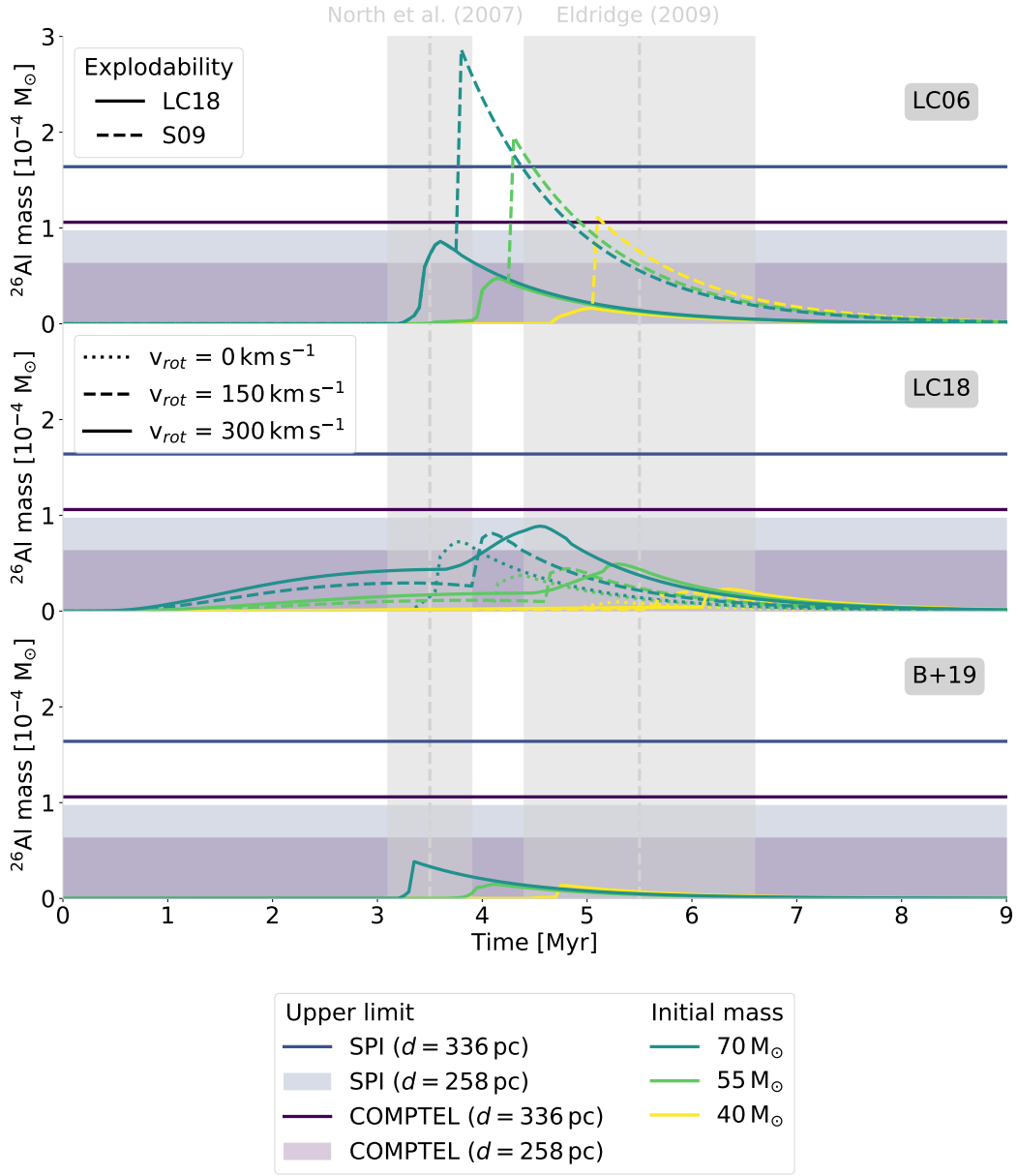

Figure 5.5: Comparison of single star model predictions with observational limits of γ^2 Velorum measured with SPI (*blue*) and COMPTEL (Oberlack et al. 2000, *purple*). The limits are given for a source distance of 258 pc (Schaerer et al. 1997, shaded regions) and 336 pc (North et al. 2007, solid lines). The cases of three different stellar initial masses corresponding to the boundaries of the estimate $M_{\mathrm{WR}}^{\mathrm{initial}} = 57 \pm 15\,\mathrm{M}_\odot$ by Schaerer et al. (1997) are depicted. The panels correspond to single star models LC06 (*upper*), LC18 (*middle*), and binary models B+19 (*lower*). Different stellar model parameters are represented in line styles as indicated in the legend of the respective panel. Age estimates of γ^2 Velorum are given as *grey* shaded regions. The predicted values lie mostly just below the upper limits.

stellar tracks modelled by LC06, LC18, and B+19 in the considered initial mass range is shown in Fig. 5.5. Two explodability alternatives are given for LC06. In this respect, S09 could yield ^{26}Al with an amount exceeding the observational limits due to ejecta from a past SN of a $M_{\mathrm{WR}}^{\mathrm{initial}} > 50\,\mathrm{M}_\odot$ star. Since no remnant of such event is known observationally in the system, this scenario is excluded. In the case of explodability LC18, the flux limit obtained by Oberlack et al. (2000) with COMPTEL excludes an initial mass $M_{\mathrm{WR}}^{\mathrm{initial}} \gtrsim 60\,\mathrm{M}_\odot$ at 258 pc and evolutionary age of (3.5 ± 0.4) Myr (North et al. 2007). At $d = 336$ pc the stellar mass is only constrained to $M_{\mathrm{WR}}^{\mathrm{initial}} \lesssim 80\,\mathrm{M}_\odot$. The SPI measurements constrain this to

$M_{\mathrm{WR}}^{\mathrm{initial}} \lesssim 100\,\mathrm{M}_{\odot}$. The consideration of LC06 provides also an upper limit on the age of γ^2 Velorum of $< 5\,\mathrm{Myr}$. For older objects, the stellar evolution would be completed and a SN remnant would be predicted.
In the case of LC18, stellar tracks for three different rotation velocities are assumed. As in the previous case, the stellar model predictions lie mostly right below the detectability thresholds. The revised SPI upper limit is consistent with an initial WR mass of $M_{\mathrm{WR}}^{\mathrm{initial}} < 77\,\mathrm{M}_{\odot}$ at a distance of $d \geq 258\,\mathrm{pc}$ in the case of a fast rotating star. The age constraint obtained with LC06 can not be confirmed on the basis of LC18.
The binary ^{26}Al wind yields from B+19 are generally reduced compared to the previously considered single star yields. Their predicted amount of ^{26}Al lies a factor of 2–4 below the upper limits provided by gamma-ray measurements. This means that gamma-ray observations are not in tension with stellar model predictions. Since ^{60}Fe and ^{44}Ti are only ejected in SNe, their presence is currently not expected around the still evolving γ^2 Velorum.
This investigation provides excellent motivation for future gamma-ray missions. It shows that with a sensitivity increase of about one order of magnitude γ^2 Velorum would be an important target for follow-up gamma-ray investigations. The direct measurement of stellar properties such as rotation or binarity affecting the nucleosynthesis feedback of a single star might then be possible using this promising source.

Essentials

The ^{26}Al signal of the binary WR star γ^2 Velorum is investigated with SPI and compared to stellar evolution models.

- The measurements show no detection of the 1.8 MeV line with a 2σ upper flux limit of $1.7 \times 10^{-5}\,\mathrm{ph\,cm^{-2}\,s^{-1}}$.
- The corresponding upper ^{26}Al mass limit of $1.6 \times 10^{-4}\,\mathrm{M}_{\odot}$ in the system at a distance of 336 pc is close to, but does not constrain current stellar evolution models.

5.3 Massive Star Group: Perseus

Massive star groups form the next level of physical entities suitable for studying nucleosynthesis feedback if individual sources are observationally inaccessible. Thus, the most nearby stellar associations are subject to extensive studies and the most prominent examples have already been outlined in Sec. 2.3.4. The specific aspect of ^{26}Al emission has been studied in particular for Cygnus (Kretschmer et al. 2000; Knödlseder 2000; Knödlseder et al. 2001; Martin et al. 2008, 2010), Sco-Cen (Diehl et al. 2010; Ohlendorf et al. 2010), Carina (Voss et al. 2012), and the Orion-Eridanus region (Voss et al. 2010). It has been shown that these studies provide both significant contributions to a consistent understanding of the dynamics of massive-star ejecta, as well as excellent test cases for model assumptions.
With respect to SPI measurements, the second closest young OB association to the Sun, i.e. Perseus OB2 (Per OB2), was relatively scarcely observed, e.g. compared to

the Orion or Sco-Cen regions. In order to improve this data situation and to be able to study this promising group, a SPI observation proposal of Per OB2 was granted 3 Ms of observation time during this thesis. This is used here to study the ^{26}Al signal of Per OB2 in Sec. 5.3.2 and to compare it with population synthesis models in Sec. 5.3.3.

5.3.1 Perseus Superbubble Characteristics

The main properties of the Per OB2 association have already been outlined in Sec. 2.3.4. It generally shows a lower number of massive stars compared to Orion, Vela, or Sco-Cen (Zari et al. 2018). However, 12 dust shells with radii between 0.1–3 pc have been found that require mass-loss rates of at least 10^{-8}–$10^{-6}\,M_\odot\,yr^{-1}$. At least two of these shells are supposed to be driven by high-mass stars. (Arce et al. 2011). A number of 66 AGB stars have been found embedded in the molecular could region by infrared observations (Azimlu et al. 2015). Thus, strong stellar feedback activity is expected.
From an age of 6 Myr today, an initial census of $\sim 2 \times 10^4$ stars is estimated to have formed according to the IMF between 0.1–120 $M_\odot$ in the Per OB2 association (Bally et al. 2008). This corresponds to about ~ 75 stars more massive than 4 $M_\odot$. Since the radial velocity of the stars is $\sim 15\,km\,s^{-1}$ faster than the the mean velocity of field stars in the local vicinity, this could have occurred in a triggered star formation event (Steenbrugge et al. 2003). Per OB2 has blown a superbubble cavity of ~ 100 pc in diameter, which is seen as a $\sim 20°$ H I shell in the sky (Bally et al. 2008). The contour of this bubble configuration is sketched in Fig. 5.6 on top of the COMPTEL map (left panel, Plüschke 2001) and the SPI map (right panel, Bouchet et al. 2015) of the 1.8 MeV emission. Two adjacent shells around Orion OB 1 (Ori OB1) and

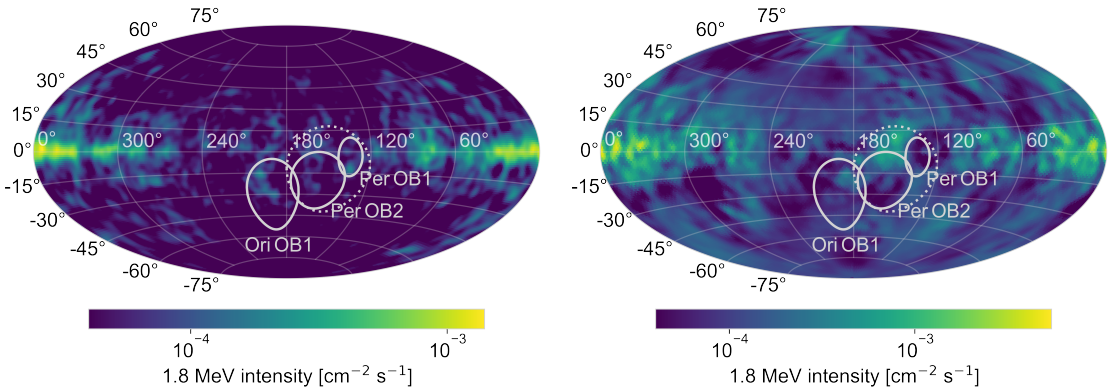

Figure 5.6: COMPTEL (*left*, Plüschke 2001) and SPI (*right*, Bouchet et al. 2015) full-sky maps of the ^{26}Al emission. Light *grey* ellipses denote superbubble shells associated with prominent OB associations as indicated. The regions relevant for the SPI analysis is marked as dotted *grey* circle. Note that the maps are centred towards the Galactic anti-centre.

Perseus OB1 (Per OB1) are seen next to the bubble around Per OB2. The Orion-Eridanus superbubble is positioned at a distance of ~ 400 pc and might actually be physically related to the Perseus molecular cloud complex. The exact configuration of this bubble is difficult to determine due to projection effects, but overall Ori OB1 appears to be embedded in a large and highly elongated H I shell with $20° \times 45°$ (Bally 2008; Pon et al. 2014). However, the bubble boundaries traced by magnetic field lines constrain a slightly smaller area of about $35° \times 25°$ (Soler et al. 2018; Joubaud et al. 2019). Additionally, a complex system of nested shells was found

expanding in the Orion-Eridanus bubble with distances of 150–250 pc (Ochsendorf et al. 2015; Joubaud et al. 2019).
On the other hand, the Per OB1 association lies (2.34 ± 0.05) kpc away from the Sun and is therefore close to Per OB2 only in projection at $(l, b) = (134.7°, -3.2°)$ (Slesnick et al. 2002). It has a radial velocity of $-43.3\,\mathrm{km\,s^{-1}}$ and therefore moves in the opposite direction as Per OB2 (Melnik & Dambis 2009). This also indicates association with a large-scale star formation mechanism. With an age of (13 ± 1) Myr, Per OB1 is also a rather young association that shows a peculiar bulk motion out of the Galactic plane. Additionally, the region seems not to be associated with a GMC in its direct vicinity. This spatial configuration is interpreted as produced by a previously expanding superbubble that accelerated the molecular cloud gas outward. The stars of Per OB1 formed and were simultaneously stripped of the surrounding gas in this event. Additionally, abundance anomalies found in the spectra of two Per OB1 members suggest that mixing of chemically enriched material occurred in the initial star-forming cloud gas (Kendall et al. 1996). There are also younger O-type stars at higher latitudes and very young stellar objects in cloud remnants associated with Per OB1 at rather large heights of 280–400 pc above the Galactic plane (Lee & Lim 2008). This supports a scenario of triggered star formation. Since the vicinity of Per OB1 is particularly depleted of molecular gas, it is associated with a large H I shell of 350×550 pc (Cappa & Herbstmeier 2000), which is also shown in Fig. 5.6.
A third OB association in the Perseus region, Per OB3, is situated 170–200 pc away from the Sun. With ~ 50 Myr, it is significantly older than Per OB1 or Per OB2 (de Zeeuw et al. 1999). Thus, although it is in close proximity to the Sun, it is not expected to still contain significant amounts of ^{26}Al. This association might constitute an interesting test case for ^{60}Fe decay at late evolutionary stages.
On the one hand, this shows that the entire Perseus region has great astrophysical potential for investigating the Galactic Cycle of Matter. On the other hand, however, it is also clear that the size, gamma flux and morphological configuration of nucleosynthesis ejecta is difficult to estimate in advance because the stellar census is insufficiently known and interacting shell dynamics complicate the picture.

5.3.2 ^{26}Al Signal from Perseus

The COMPTEL map as well as the SPI map of the 1.8 MeV line both show emission features in the direction of the Perseus region (cf. Fig. 5.6). While the COMPTEL map exhibits only tenuous patterns, the SPI map contains a more salient structure in this area. Therefore, the first important issue to note in this context is that both maps show a significant difference towards the Perseus region. This is probably due to the irregular exposure patterns in SPI and a general difference in the exposure between COMPTEL and SPI.
For a section of 6° around $(l, b) = (168.5°, -6.5°)$, Knödlseder (1997) estimated a gamma-ray flux of $(5.3 \pm 1.1) \times 10^{-5}\,\mathrm{ph\,cm^{-2}\,s^{-1}}$ with COMPTEL and related it to Per OB2. The more recent measurements with SPI by Bouchet et al. (2015) revealed two rather extended emission spots in this area. The weaker one was found around $(l, b) = (161°, -3°)$ with a radius of $\sim 5°$ and a 1.8 MeV flux of $(5.0 \pm 2.7) \times 10^{-5}\,\mathrm{ph\,cm^{-2}\,s^{-1}}$. The coordinates coincide with the boundaries of the H I shell around Per OB2. A brighter emission site was found around $(l, b) = (149°, 8°)$ with a flux of $(8.2 \pm 3.2) \times 10^{-5}\,\mathrm{ph\,cm^{-2}\,s^{-1}}$ within a radius of 11°. This spot is located between both OB associations with a considerable offset towards the

Northern Galactic hemisphere and is located in the direction of the Taurus molecular cloud.
The total observation time of SPI in the chosen data set within a radius of 30° around $(l, b) = (150°, -12°)$ is $\sim$ 15.5 Ms from 5561 instrument pointings with a mean lifetime of 12.8 Ms and 9.3 Ms for single and double detectors respectively. Its spatial coverage is shown in the exposure map in Fig. 5.7. In order to investigate

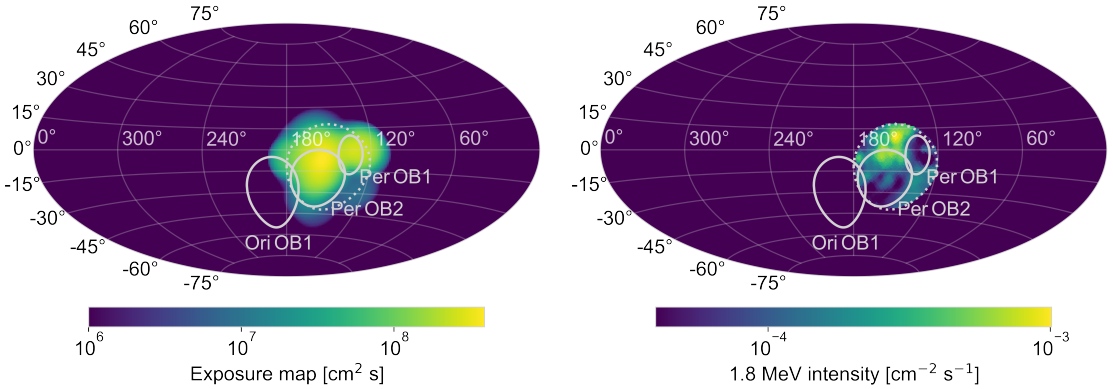

Figure 5.7: *Left:* SPI exposure map of the data set used for the analysis of Perseus with pointings inside the dotted circle. It comprises 5561 instrument pointings with a total of $\sim$ 15.5 Ms observation time. *Right:* Circular region of the SPI map with a radius of 30° used as emission model for the maximum likelihood fitting. Light *grey* ellipses denote superbubble shells associated with prominent OB associations as indicated. The regions relevant for the SPI analysis is marked as dotted *grey* circle. Note that the map is centred towards the Galactic anti-centre.

this region, the analysis outlined in Sec. 3.4.3 is applied to this data set in the energy range 1790–1840 keV. As a first approach, a circular region with a radius of 30° of the sky maps in Fig. 5.6 serve as representations of the emission morphology in this area (cf. right panel in Fig. 5.7). These celestial representations are used as sky models. Therefore, they are convolved with the coded mask pattern of SPI and fitted to the data simultaneously with the self consistent background model.
The COMPTEL map is characterised only by rather undefined and faint filamentary structures with low intensity gradients in the Perseus region. This leads to a weak and rather uniform detector gradients describing the celestial emission in the SPI instrument space. Thus, a degeneration of the fit between sky and background model occurs. The results are therefore mainly dominated by statistical fluctuations. Thus, the COMPTEL map proves to be an unsuitable model for the particular case of studying the Perseus region.
The more pronounced intensity gradients in the SPI map yield an adequate fit (cf. Fig. A.11 in the appendix). Based on the normally distributed residuals and the scattering of the χ^2-statistic around $\chi^2_{\mathrm{red}} = 1$, the combined sky and background model describes the data well. The resulting spectrum of combined single and double events is shown in Fig. 5.8. The spectral line fit is obtained by the MCMC fitting algorithm (cf. Sec. 3.4.3) using the statistical priors as listed in Eq. 3.31, except for a lower line flux of

$$F_{^{26}\mathrm{Al}} \sim \text{truncated normal}(1.3 \times 10^{-4}, 1 \times 10^{-4}; 0, 1) \tag{5.2}$$

as expected from the previous SPI measurements in this region. The resulting full posterior distributions of the spectral fit are depicted in Fig. 5.9. A rather high 1.8 MeV line flux of $F_{^{26}\mathrm{Al}} = (3.6 \pm 0.4) \times 10^{-4}\,\mathrm{ph\,cm^{-2}\,s^{-1}}$ is obtained with a detection significance level of $\sim 8.5\sigma$. This would correspond to a mass of $M_{^{26}\mathrm{Al}} = (2.96 \pm 0.33) \times 10^{-3}\,\mathrm{M_\odot}$ at the Per OB2 distance of 310 pc. This is about a factor of 2.7 more than what was expected from the estimates by Bouchet et al.

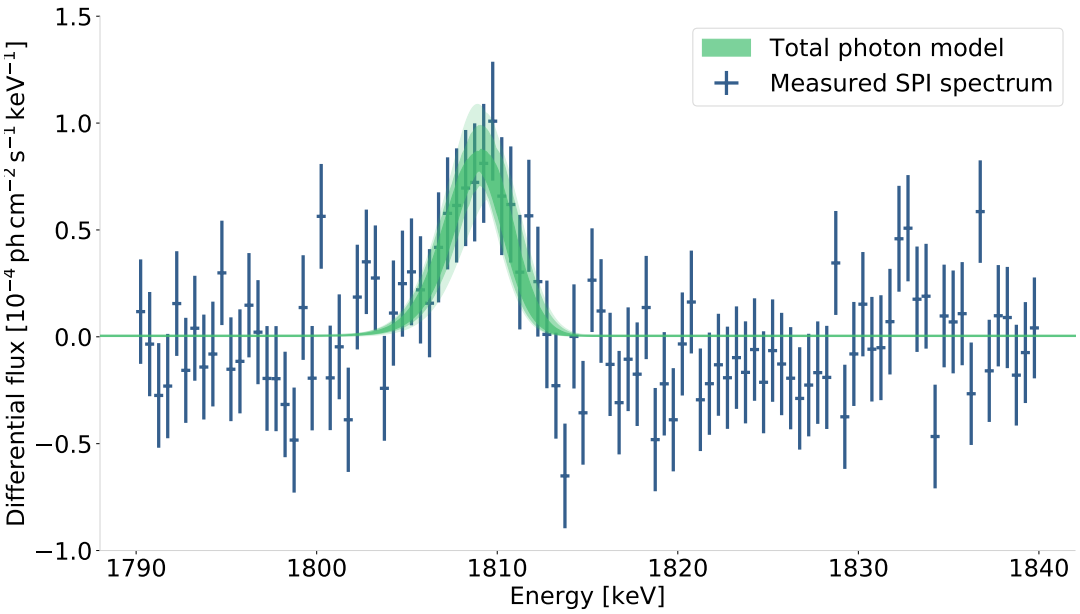

Figure 5.8: SPI spectrum (*blue* data points) of the ^{26}Al emission at 1809 keV from Perseus region for combined single and double events. It is obtained by fitting a cut-out of the SPI map (Bouchet et al. 2015) with radius 30° as sky model. The 1σ, 2σ, and 3σ confidence regions of the best-fitting photon model are shown in shades of *green*. It represents a degraded Gaussian line profile on top of a power-law continuum (cf. Eq. 3.28). The posterior distributions of individual fit parameters are shown in Fig. 5.9. The spectrum shows an 8.5σ detection of the ^{26}Al signal at 1.8 MeV with a flux of $(3.6 \pm 0.4) \times 10^{-4}$ ph cm^{-2} s^{-1}.

(2015). This is due to the fact that the features that are particularly prominent in the map were examined in spatially narrow domains. The present study uses a comparatively large area of 30° for the analysis in order to obtain an overall picture of this region. A more detailed investigation of the flux from only the Per OB2 association is described below. The line parameters $\mathrm{FWHM_{SPI}}$ and τ reflect the characteristic instrumental properties of SPI as discussed in Sec. 3.4.3. The line appears to be slightly above the instrumental resolution due to the dynamics of the emission sites by $\mathrm{FWHM_{sky}} = (1.13 \pm 0.55)$ keV. This corresponds to a Doppler broadening due to wind velocity and turbulences of (140 ± 60) km s^{-1} along the line of sight. This is about a factor of 2 larger than what was found for the integrated emission over the entire sky which indicates that ^{26}Al is in a comparatively turbulent state in the direction of Perseus when observed. As depicted in Fig. 5.10, the line additionally shows a shift of the central energy $\Delta E_{\mathrm{cen}} = (0.34 \pm 0.22)$ keV with respect to the ^{26}Al emission line laboratory energy. This indicates a blue shift from nucleosynthesis ejecta streaming preferentially towards the observer as would be expected from a spatial configuration with the OB association being located in front of the dense molecular cloud (cf. Sec. 2.4.4). However, the line shift remains too uncertain to draw definite conclusions about a global flow of material.
In order to determine the individual contribution of Per OB2 as isolated as possible, a parameterised model for its spatial representation is chosen. For this purpose, a homogeneously filled and emitting sphere centred at the position of Per OB2 serves as approximation of the typical distribution of ejecta in the superbubble around the stellar group. By varying the bubble radius, the fit performance tracks the accuracy of the model for describing the ^{26}Al distribution in the surroundings of the association. The flux is integrated between 1805–1813 keV to obtain the entire

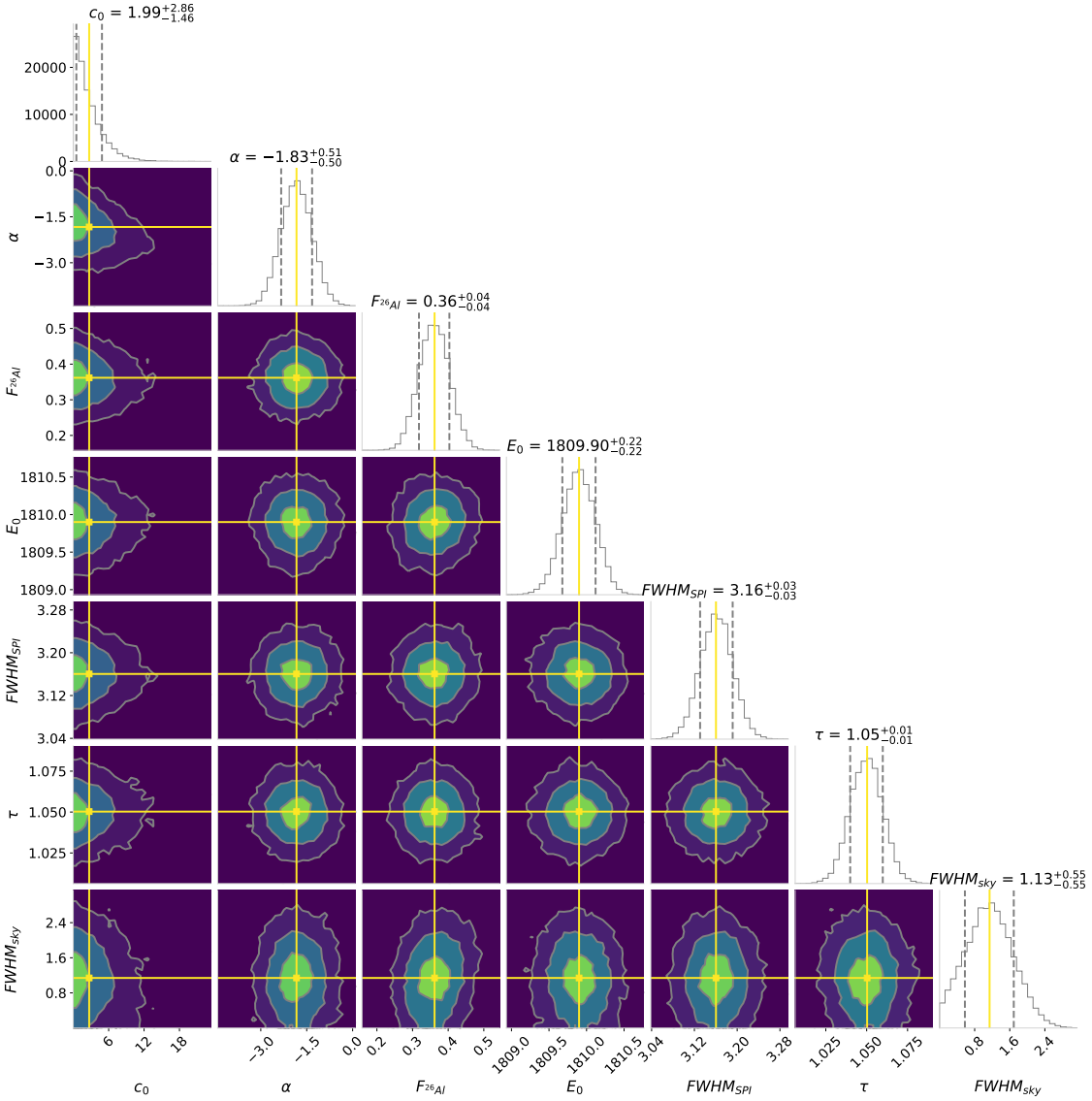

Figure 5.9: Posterior distributions of spectral fit parameters describing the ^{26}Al signal at 1809 keV from the Perseus region as measured with SPI according to the photon model in Eq. 3.28. The underlying data is obtained by a combined treatment of single and double events (cf. Fig. A.11). The flux is given in 10^{-4} ph cm^{-2} s^{-1} and the other line shape parameters in keV. The mean value along each axis is shown in *yellow*. Histograms on the diagonal show marginalised probability distributions along the respective axis with 86th percentiles marked by dashed lines. The respective spectrum is shown in Fig. 5.8.

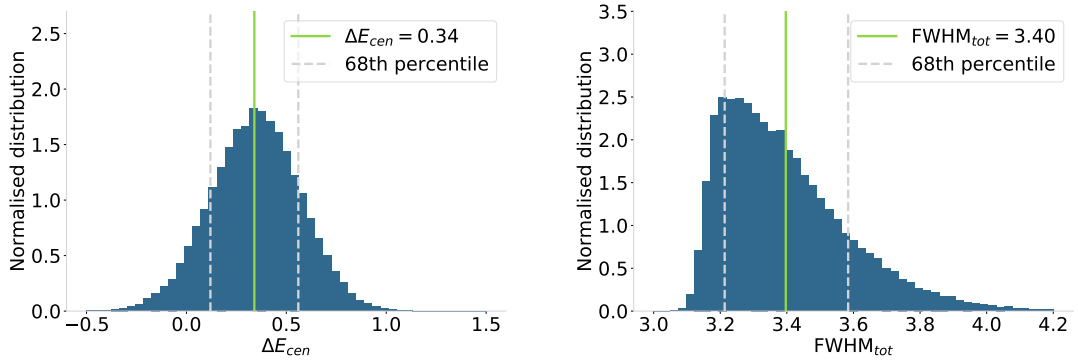

Figure 5.10: Marginalised probability distribution of the central line energy shift $\Delta E_0 = (0.34 \pm 0.22)$ keV with respect to the ^{26}Alemission lab energy of 1808.73 keV and the total line width $\mathrm{FWHM_{tot}} = 3.40^{+0.18}_{-0.19}$ keV.

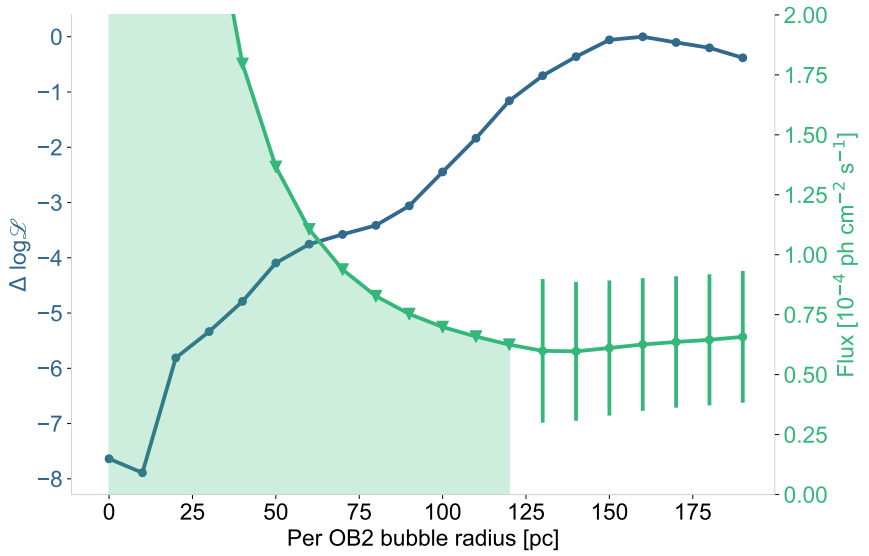

Figure 5.11: Radial superbubble extent of a spherical model describing the emission in the direction of Per OB2 as measured with SPI. The likelihood for different radii are shown in *blue* on the left axis relative to the maximum likelihood for $R = 160\,\mathrm{pc}$. $R = 0\,\mathrm{pc}$ denotes a point source. The plateau around 60–90 pc is comparable to the H I bubble radius associated with Per OB2. The right axis denotes the resulting flux for each bubble radius in *green*. Upper limits are obtained in the shaded *green* region and marked by triangles. Flux values with a significance $\geq 2\sigma$ are shown as *green* dots with error bars.

1.8 MeV emission in one energy bin. The results are depicted in Fig. 5.11. The model approaches a maximum likelihood value for a bubble radius $R = (160 \pm 60)\,\mathrm{pc}$. Additionally, a plateau is seen around 60–90 pc. This is comparable to the H I shell radius associated with Per OB2. However, the 1.8 MeV fluxes for smaller radii are below the detection limit of SPI and only upper limits could be obtained. In general, this study indicates that there is an ^{26}Al structure on the order of $\gtrsim 100\,\mathrm{pc}$ present around Per OB2, which is in agreement with the neutral hydrogen shell as boundary. Nevertheless, a notable amount of the 1.8 MeV emission originates from areas beyond that region, in particular from the galactic plane and other foreground emission from the Local Arm in the galactic anti-centre (cf. Sec. 5.3.3). This matches the morphology found by Bouchet et al. (2015), which is shown in the right panel of Fig. 5.7.

As the bubble radius is assumed beyond 120 pc, it increasingly includes areas associated with Per OB1 and the region rather brightly seen in the direction of Taurus in the SPI map. For such larger radii, the spherical model yields a flux of $(6.3 \pm 2.8) \times 10^{-5}\,\mathrm{ph\,cm^{-2}\,s^{-1}}$, which is in agreement with the Per OB2 values found previously with SPI and COMPTEL. This flux implies an ^{26}Al mass of $(5.1 \pm 2.2) \times 10^{-4}\,\mathrm{M_\odot}$ in Per OB2, which will be discussed in the following Sec. 5.3.3 in more detail.

These findings are consistent with the morphology seen in the SPI map in the direction of Perseus which however was constructed with less exposure in this region of the sky. A major amount of 1.8 MeV photons is emitted from a region which is currently interpreted not to be associated with Per OB2. Since the region is far from the Galactic bulge towards the Galactic anti-centre, and also below the Galactic plane, this is affected by only weak Galactic background components. The considerably large flux measured from the overall Perseus region in Fig. 5.8 is also unlikely to be solely accounted for by the additional contribution of Per OB1. This would require $\sim 0.13\,\mathrm{M_\odot}$ of ^{26}Al at the group's distance of 2.3 kpc, which is far above what could be expected from population synthesis models. This means the Perseus region is

more complex than including only the above-discussed known stellar associations. In the following, the flux of $(6.3 \pm 2.8) \times 10^{-5}\,\mathrm{ph\,cm^{-2}\,s^{-1}}$ will be used to discuss the implication for population synthesis models as conservative limit.

5.3.3 Comparison with Population Synthesis Models

In order to predict the expected amount of ^{26}Al in the Per OB2 region, the population synthesis approach outlined in Sec. 4.2 is applied. These predictions can then be compared with the observed values determined in Sec. 5.3.2.
For an instantaneous star formation event of $\sim 2 \times 10^4$ stars, the population synthesis results for this association are shown in Fig. 5.12. The general shape of the

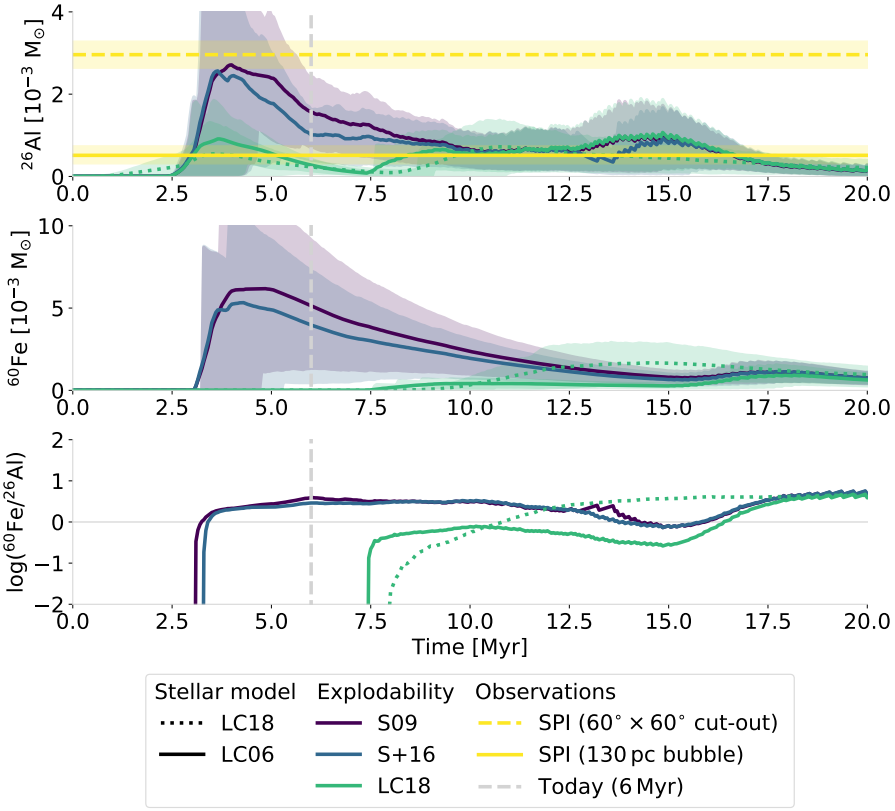

Figure 5.12: Population synthesis profiles of the ^{26}Al (*upper*) and ^{60}Fe (*middle*) ejecta from a stellar group representing the Per OB2 association with 2×10^4 members in the mass range 0.1–120 M$_\odot$ formed according to the S55 IMF. The calculations are based on the evolution stellar models LC06 (solid lines) and LC18 (dotted lines). Different explodability models S09 (*purple*), S+16 (*blue*), and LC18 (*green*) are applied to the LC06 tracks. Shaded 68% uncertainty regions are obtained from 1000 MC runs for each configuration. The *lower* panel gives the predicted ^{60}Fe/^{26}Al mass ratio. The observed ^{26}Al mass values estimated at the distance 310 pc of Per OB2 are shown in *yellow*. The two values are based on a section with 30° radius of the SPI 1.8 MeV map (cf. right panel in Fig. 5.6 Bouchet et al. 2015) representing the overall emission from the Perseus region (dashed line) or a spherical bubble model with radius $R = 130$ pc at the position of Per OB2 individually (solid line). The *grey* dashed line marks the age of Per OB2 of 6 Myr.

temporal evolution and the influences of different stellar parameters have already been described in Sec. 4.2.3. The mean values of all model configurations consistently underestimate the overall mass of $M_{^{26}\mathrm{Al}} = (2.96 \pm 0.33) \times 10^{-3}\,\mathrm{M_\odot}$ inferred from the overall emission from the circular region with a radius 30° in the direction and distance of Per OB2; for an association age of 6 Myr, the age of Per OB2, this is underestimated by at least a factor of 2. The comparatively low expected mass for

Per OB2 underlines the suggestion that the measured emission does not come from this association alone but from a cumulative effect of different contributing sites. The mass $M_{^{26}\mathrm{Al}} = (5.1 \pm 2.2) \times 10^{-4}\,\mathrm{M}_\odot$ that can be attributed to a sphere with radius $R = (160 \pm 60)\,\mathrm{pc}$ at the position of Per OB2 is met for all model configurations within 68% of the cases. However, the explodability model S09 would over-predict the mass by more than a factor of 3. Models with inhibited explosions for the most massive stars tend to approach the observed value of Per OB2 more closely with $(10 \pm 6) \times 10^{-4}\,\mathrm{M}_\odot$ for S+16 or $(2.3 \pm 1.5) \times 10^{-4}\,\mathrm{M}_\odot$ for LC18 explodability. This is the case regardless of the specific underlying evolution model LC06 or LC18. This indicates that the direct effect of not having explosions of high-mass stars is measured by the relatively faint appearance of Per OB2 in the nuclear 1.8 MeV line. Furthermore, the population synthesis calculations, especially for explodability LC18, agree well with the gamma-ray measurements by both COMPTEL and SPI from the Per OB2 region. On the one hand, this can be seen as a further confirmation of the modelling approach. On the other hand, this provides observational support for stellar evolution models including restrained SN occurrence for massive stars in the domain beyond $25\,\mathrm{M}_\odot$.
For the hypothesis of low explodability for high mass stars, no measurable ^{60}Fe emission would be expected from Per OB2 (cf. middle panel in Fig. 5.12).
Another important issue for future investigations remains the Perseus ^{26}Al puzzle. The high total 1.8 MeV flux from the entire Perseus region is difficult to explain by the sole contribution of the three Perseus OB associations. Additionally, as also indicated in the SPI map, its major part appears to originate from a region considerably displaced from those regions. A future gamma-ray telescope with improved spatial sensitivity would be needed to solve this puzzle and map this emission to its physical origin.

Essentials

The ^{26}Al signal from the Perseus region is investigated with SPI and compared to population synthesis predictions.

- Fitting a section of the SPI map with a radius of 30° obtains a total 1.8 MeV flux of $F_{^{26}\mathrm{Al}} = (3.6 \pm 0.4) \times 10^{-4}\,\mathrm{ph\,cm^{-2}\,s^{-1}}$ from the entire Perseus region.
- Exclusively to this group, an ^{26}Al gamma-ray flux of $F_{^{26}\mathrm{Al}} = (6.3 \pm 2.8) \times 10^{-5}\,\mathrm{ph\,cm^{-2}\,s^{-1}}$ can be attributed by evaluating spherical emission models with $R = (160 \pm 60)\,\mathrm{pc}$ at the position of Per OB2. This corresponds to an ^{26}Al mass of $(5.1 \pm 2.2) \times 10^{-4}\,\mathrm{M}_\odot$ at a distance 310 pc.
- Population synthesis calculations of Per OB2 can match the amount of ^{26}Al inferred from the observations, but only for a reduced explodability of high mass stars beyond $25\,\mathrm{M}_\odot$. This underlines the consistency between the measurements and the modelling approach and provides observational support explodability models with absent explosions for the most massive stars.

5.4 Milky Way Morphology

Morphological aspects of Galactic radioactivity are particularly relevant on the global scale. As outlined in Sec. 2.4, the distribution of radioisotopes, especially ^{26}Al and ^{60}Fe, provides information about active sites of nucleosynthesis, Galactic chemical enrichment, as well as dynamics and feeback processes in the ISM. Besides recent hydrodynamic simulations which were described in Sec. 2.4.5, empirical models also have a long history in order to describe and understand diffuse radioactivity in the Galactic ISM (Prantzos 1993; Prantzos & Diehl 1995; Knödlseder et al. 1996; Lentz et al. 1999; Sturner 2001; Drimmel 2002; Alexis et al. 2014). Comparisons of those with data have previously been done heuristically by identifying morphological similarities between the 1.8 MeV emission from ^{26}Al decay and multi-wavelength tracers or geometric emission models (e.g. Hartmann 1994; Prantzos & Diehl 1995; Diehl et al. 1997; Knödlseder et al. 1999; Diehl et al. 2004; Kretschmer et al. 2013). The astrophysical implications for the understanding of Galactic radioactivity are hereby inferred from the respective tracer. Direct comparative measures, on the other hand, promise unbiased access to the particular properties that characterise nucleosynthesis feedback and its large scale implications. To achieve such an approach, simulations or models that are based on astrophysical assumptions have to be cross-checked with observations. This is particularly challenging on the galactic scale because the Milky Way is one particular realisation of a galaxy and any given hydrodynamic simulation will not necessarily match it perfectly. This issue has already been discussed in Sec. 5.1. This section is now based on the proposition described there that also objects that do not belong to the exact same category are comparable if they can be projected to a common parameter space. Based on this, a range of approaches for comparing synthetic sky maps and 1.8 MeV gamma-ray data measured with SPI is described in this section. The potential and limitations of a direct likelihood comparison of models with data will be outlined in Sec. 5.4.1. This motivates a more generic scale height approach in Sec. 5.4.2 which was developed by Pleintinger et al. (2019) and is applied to the case of hydrodynamic simulations F+18. Finally, the PSYCO models described in Sec. 4.3 are fully exploited by applying the newly developed morphological analysis in conjunction with SPI data in Sec. 5.4.3.

5.4.1 Direct Likelihood Comparison

In search for a way to compare a simulated sky map with observational data, the probably most straightforward approach is to examine how well the map actually describes the data. Therefore, the simulation must be designed in such a way that it models the measurements in some respect. As outlined in Sec. 5.1, this should be granted in any case in order to be empirically useful. Nevertheless, in a direct comparison clear discrepancies can be expected a priori due to the specific morphological features of the Milky Way. These are mostly dominated by random effects of the particular distribution of feedback-driven superbubbles. An individual instantiation of a simulation is not expected to match these particular structures in detail. This inevitably arises from the nature of the two analysis components in the case of a very limited number of simulations of a comparatively over-complex physical system on the one hand and statistically limited measurements from a particular

perspective on the other.
For a direct comparison, a synthetic sky map is used as emission model M in Eq. 3.16 for describing the 1.8 MeV sky. The image is transferred into SPI instrument space by convolving it with the coded mask pattern. A maximum likelihood optimisation according to Eq. 3.25 is then performed to fit the model to the full-sky data set in detector space. The general procedure has been described in detail already in Sec. 3.4.3. This results in a likelihood value for each fitted synthetic emission map. However, this does not provide an absolute goodness of fit. A direct evaluation on the basis of the obtained likelihoods therefore is omitted. Instead, only a relative measure of the fit quality of different sky models can be obtained. For this purpose, the test statistic (Pleintinger et al. 2019)

$$TS = \log(\mathscr{L}(M_0|D)) - \log(\mathscr{L}(M_1|D)) \tag{5.3}$$

is used, which characterises a likelihood-ratio test (Neyman & Pearson 1928) of a celestial model M_1 describing the sky emission on top of the instrumental background versus the null-model M_0 which includes only the background description of the data D. TS is then interpreted as the likelihood of model M_1 given the data D relative to the null-hypothesis M_0. In order to probe the statistical validity of TS and qualitatively classify its numeric values, the probability of M_1 occurring by chance in D is evaluated by drawing a sample of 1000 Poisson datasets containing background only. A sky model M_1 and the null-hypothesis M_0 are subsequently fitted to all synthetic data sets, obtaining a TS value each. The respective distribution of TS is shown in the histograms in Fig. 5.13. Six simulated sky maps from F+18 corresponding the

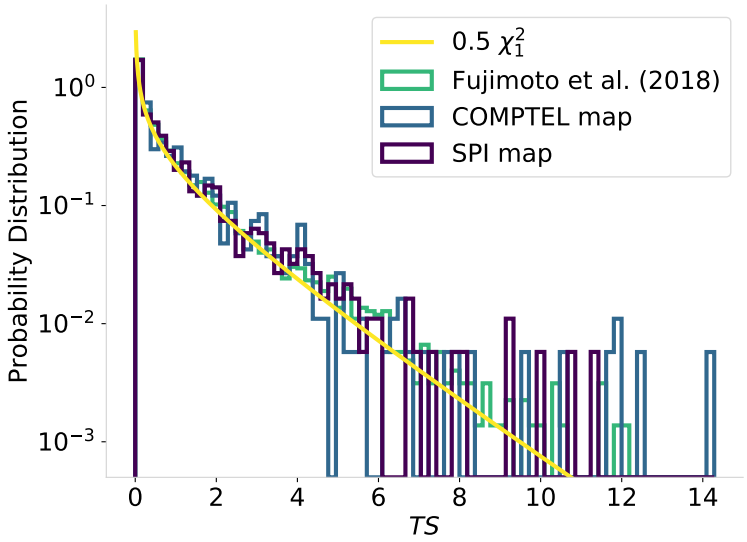

Figure 5.13: Distribution of the likelihood-ratio test statistic TS according to Eq. 5.3 inferred from fitting different emission models to 1000 synthetic SPI Poisson datasets. The observational 1.8 MeV maps by COMPTEL (Plüschke et al. 2001, cf. Fig. 1.1, *blue*) and SPI (Bouchet et al. 2015, cf. right panel in Fig. 5.6, *purple*) as well as six simulated sky maps by Fujimoto et al. (2018, cf. Fig. 2.48, *green*) serve as sky models M_1 which are tested against the null-model M_0 of background only. The sky maps by Fujimoto et al. (2018) correspond to the observer positions at 10°, 70°, 110°, 120°, 250°, and 260° in the simulated galaxy which are combined in one histogram. TS follows a $\chi^2/2$-distribution as shown by the *yellow* line. Adopted from Pleintinger et al. (2019).

observer positions at 10°, 70°, 110°, 120°, 250°, and 260° (cf. e.g. Fig. 2.48) in the simulated galaxy serve as synthetic sky models. Additionally, the COMPTEL map (cf. Fig. 1.1) and the SPI map (cf. right panel in Fig. 5.6) are used as observation based celestial emission models. For all the maps TS is clearly $\chi^2/2$-distributed. The factor 1/2 results from the fact that the Poisson distribution is constrained to

only positive values. Thus, the negative half of the otherwise symmetric normal distribution is omitted (e.g. Mattox et al. 1996). This examination makes it possible to associate the test statistic TS values with the probability for occurrence by chance of a sky model in the SPI dataset. Thus, in the following a higher values of TS are defined as designation for better fitting models and smaller values of TS corresponding to worse fitting models. Absolute values of TS can be evaluated down to a lower limit of 10^{-3}.

Application to Synthetic Sky Maps The direct model comparison with respect to the measured SPI full-sky dataset is shown in Fig. 5.14. Here again an evaluation of the COMPTEL map and the SPI map as sky models was included as observation-based point of reference. The analysis includes the determination of the ^{26}Al signal in one energy band from 1805–1813 keV for two different spatial realms. In a first case, it is restricted to measurements of the inner Galactic region with $|b| \leq 10°$ and $|l| \leq 30°$. This reflects an isolated treatment of the regions with highest gamma-ray intensity and longest instrument exposure time. In a second approach, the analysis includes the 1.8 MeV emission from the entire sky. In both cases, the two different observation-based TS values lie close to each other, which was expected since they are obtained from the same observational target only with different instruments. However, this underlines the consistency between COMPTEL and SPI measurements in general. They only differ by 2 for the full sky and 7 for the inner Galaxy and are therefore treated as qualitatively identical in the following.
Taking only the inner Galaxy into account, the TS values of the simulated sky maps fall mostly below the observation-based reference. However, the morphologies obtained from certain sight-lines in the simulation are as unlikely to occur by chance in the dataset as the maximum entropy reconstructions from observations. This

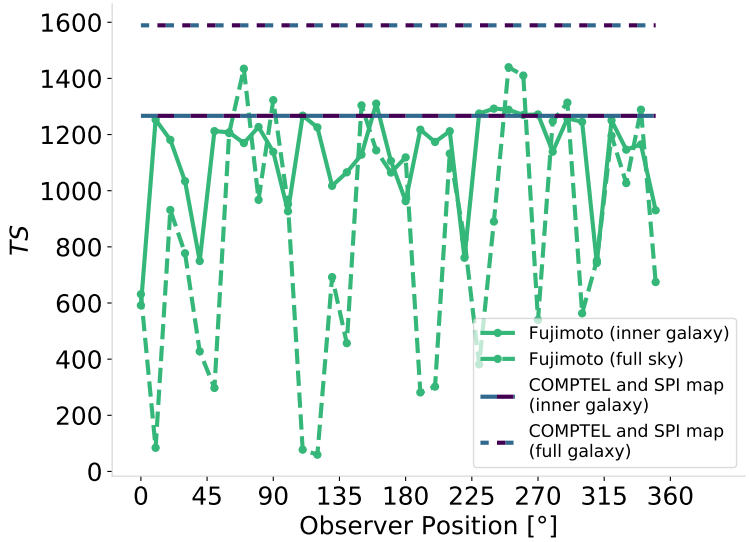

Figure 5.14: Likelihood ratio of the synthetic F+18 sky maps relative to the likelihood of a background-only fit (cf. Eq. 5.3). TS values are obtained for fitting the full-sky emission (solid lines) or only the inner Galactic region (dashed lines) in the the energy range 1805–1813 keV as measured with SPI. Higher values of TS generally indicate a lower probability for chance occurrence in the measured dataset (cf. Fig. 5.13). Values for the COMPTEL and SPI maps serve as observation-based points of reference. Since these would be graphically indistinguishable, they are shown combined in single lines (*blue/purple*). The values for the F+18 simulation correspond to synthetic maps constructed from 36 different observer positions in the simulated galaxy as given by the bottom axis. Adopted from Pleintinger et al. (2019).

manifests as TS values close to or even above the observational reference. In these cases, the simulation is interpreted to describe the inner Galactic emission well. This is represented well by the generic hydrodynamic simulation. Interestingly, there are values for synthetic sky maps even above the observational reference. This means that some observer positions yield sky maps which fit the SPI data better than the observational maximum entropy maps. There are some indications that this may be mainly a result of the particular geometric alignment of superbubble structures seen in the direction of the Galactic centre. This issue will be discussed further in Sec. 5.4.2.
For the case of the full-sky emission, the TS values for the observation-based maps are higher, which corresponds to a reduced probability of chance occurrence of the respective emission features measurements of the entire sky. On the other hand, values based on F+18 are in the same range as for the inner Galaxy and thus significantly lower overall. Thus, the synthetic sky maps fit the gamma-ray measurements worse than the observation based maps. This means that high latitude components are particularly relevant for a significant divergence of simulations from maximum entropy maps concerning the full sky. This is expected to be mostly affected by the characteristic foreground emission of the Milky Way. Since the particular structure of the prominent emission regions such as Cygnus, Sco-Cen, or Orion (cf. e.g. 4.7), as well as characteristic spiral arm tangents have been omitted in F+18, this was expected. On the other hand, the COMPTEL and SPI maps include these features due to their observational nature and therefore provide a better fit to the SPI data. Overall, the direct likelihood comparison between gamma-ray measurements and galaxy-scale simulations is limited due to the dependence on morphological peculiarities especially in high-latitude regions. However, an important finding is that the numerical simulations F+18 overall miss large parts of the particular spatial structure of the 1.8 MeV gamma-ray sky as measured from Earth.

5.4.2 Scale Height Analysis

The direct comparison of the ^{26}Al gamma-ray emission and galaxy-wide nucleosynthesis feedback simulations performed in Sec. 5.4.1 was limited by the specific configuration of morphological peculiarities in the Galaxy. Thus, a more general comparison method using scale height decompositions has been developed by Pleintinger et al. (2019).
The following evaluations rely on maximum likelihood estimations of emission models. Commonly used morphological analysis techniques such as expansion in wavelets or spherical harmonics are highly sensitive to the initial assumptions for image reconstruction. Already a simple rotation on the sky results in an infinite number of celestial representations by spherical harmonics for each combination of degree and mode. This does not constitute a viable approach with respect to SPI measurements because in this case each realisation of such an analytic model would have to be tested individually. This is overall impracticable. Instead, for this purpose, exponential scale height models are chosen as common representations of measurements and simulations. This has the advantage that on the one hand it contains basic morphological information and on the other hand individual realisations can be fitted to SPI data. Additionally, it is physically motivated by the fact that the density of young massive stars shows an exponential decrease with Galactic radius (cf. Sec. 2.4.4). This makes the assumption of a similarly shaped ^{26}Al density phys-

ically reasonable. A doubly exponential disk model

$$\rho(r,z) = A_0 \exp\left[-\left(\frac{r}{r_0} + \frac{|z|}{z_0}\right)\right], \tag{5.4}$$

with the galactocentric radius $r^2 = x^2 + y^2$, the amplitude of the disk A_0, the height above the disk z, scale radius r_0, and scale height z_0 is assumed as first-order model for the three-dimensional distribution of the galactic ^{26}Al emissivity in units of $\mathrm{ph\,cm^{-3}\,s^{-1}}$. A projection of this emission model onto the celestial sphere in galactic longitude l and latitude b is obtained by line-of-sight integration, which yields the two-dimensional flux distribution

$$F(l,b) = \frac{1}{4\pi} \int_{s_\mathrm{min}}^{s_\mathrm{max}} \rho(x_\mathrm{s} + s \cdot u_x, y_\mathrm{s} + s \cdot u_y, z_\mathrm{s} + s \cdot u_z)\ \mathrm{d}s. \tag{5.5}$$

This is obtained for the relative position of the Sun with respect to the Galactic centre $\vec{p}_\mathrm{s} = (x_\mathrm{s}, y_\mathrm{s}, z_\mathrm{s}) = (8.5, 0, 0)\,\mathrm{kpc}$ along the vector

$$\vec{u} = \begin{pmatrix} u_x \\ u_y \\ u_z \end{pmatrix} = \begin{pmatrix} \cos(l)\cos(b) \\ \sin(l)\cos(b) \\ \sin(b) \end{pmatrix}. \tag{5.6}$$

The integration is confined to the volume of the Milky Way by setting the boundaries s_min and s_max. An example of a double exponential disk model with scale radius $r_0 = 5.5\,\mathrm{kpc}$ and scale height $z_0 = 0.7\,\mathrm{kpc}$ is depicted in Fig. 5.15.

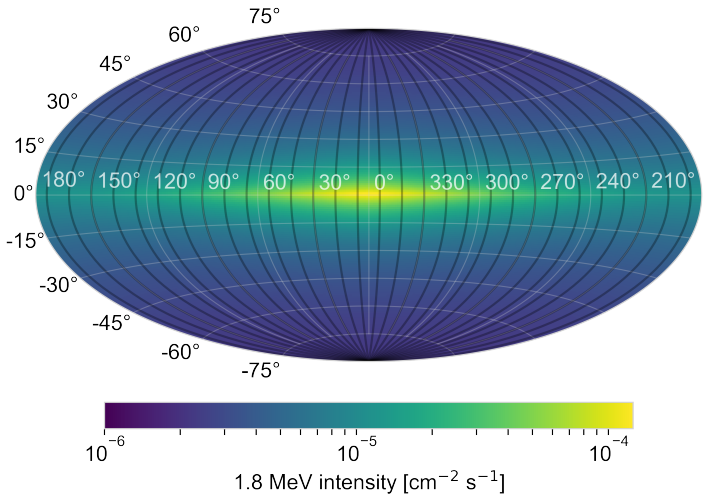

Figure 5.15: Flux distribution of a double exponential disk emission model (Eq. 5.4) with scale radius $r_0 = 5.5\,\mathrm{kpc}$ and scale height $z_0 = 0.7\,\mathrm{kpc}$ projected onto the celestial sphere (Eq. 5.5). *Grey* lines denote the 30 latitude bins of 12° width used for the scale height distribution analysis in this thesis.

Uniform Scale Height The galaxy-wide scale height and scale radius can be determined as global measure of the ^{26}Al distribution in the Milky Way. Therefore, 2048 exponential disk models are constructed for combinations of 32 scale radii and 64 scale heights. The scale height ranges from 10–475 pc in 15 pc steps and from 500–2050 pc in 50 pc steps. The scale radius is consistently spaced by 250 pc steps in the range 0.5–8.25 kpc (Siegert 2017). Each combination of scale height and scale radius is then fitted individually as sky model to the SPI dataset. Thus, for each

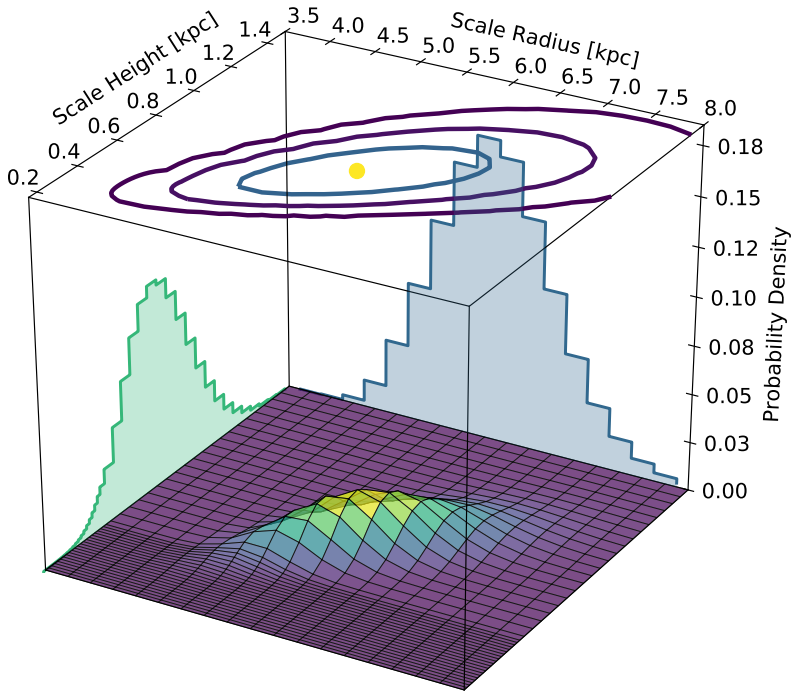

Figure 5.16: Probability density distribution for exponential disk models describing the full-sky ^{26}Al emission measured with SPI in combinations of exponential scale height and radius (cf. Eq. 5.4). The contour plot on top gives the 1, 2, and 3σ uncertainty boundaries around the best fit value of $r_0 = 5.81 \pm 0.64$ kpc and $z_0 = 0.77 \pm 0.17$ kpc (*yellow* dot). Shaded histograms on the side panels give the likelihood profiles of each parameter separately. Adopted from Pleintinger et al. (2019).

grid point a Poisson likelihood value is obtained from which the probability density distribution of scale height and radius for the Galactic 1.8 MeV emission can be inferred. This distribution is shown in Fig. 5.16. The best-fitting exponential disk parameters for characterising Galaxy-wide ^{26}Al emission are $r_0 = 5.81 \pm 0.64$ kpc and $z_0 = 0.77 \pm 0.17$ kpc (Pleintinger et al. 2019). Estimates from the COMPTEL all-sky survey suggested a smaller scale height of 150–170 pc (Oberlack 1997; Diehl et al. 1997). Earlier studies concerning the ^{26}Al scale height with SPI were restricted to the long exposed inner Galaxy with $|l| \leq 30°$ and $|b| \leq 10°$. For a fixed scale radius of 4 kpc, tthese investigations obtained smaller scale heights between 60 and 250 pc (Diehl et al. 2006; Wang et al. 2009). The spatial restriction to the inner Galaxy apparently causes a bias towards smaller values of z_0 since it particularly leaves out features at large scale heights.

The scale height analysis can now serve as basis for evaluating galaxy-scale simulations. By fitting the same grid of emission models to the synthetic sky maps obtained from simulations, the morphology of both gamma-ray measurements and simulations can be compared. In order to take the temporal and spatial inhomogeneity of the SPI sky coverage into account, the synthetic sky maps have to be weighted by the SPI exposure map (cf. Fig. 3.21). Thereby, the sky maps are transferred into count space projected onto the sky with the same dynamical range as in SPI observations. A Pearson's χ^2 optimisation is performed to determine the best-fitting amplitude for each exponential disk model with respect to the sky maps. The minimum χ^2 values denote the scale height and radius combinations which best describe the simulated emission morphology.

In order to use this approach for an evaluation of F+18 simulations, 36 synthetic sky maps have been constructed corresponding to different viewing angles in the simulated galaxy with a spacing of 10°. By applying the fitting method to all the

sky maps as described, an average of $r_0 = 3.02\,\mathrm{kpc}$ and $z_0 = 0.07\,\mathrm{kpc}$ is obtained. The order of the scale radius is therefore generally consistent with observations. On the other hand, the scale height is overall underestimated by about a factor of 10 by F+18. However, the observer position at 100° yields the maximum scale height value of $z_0 = 0.7\,\mathrm{kpc}$. Apparently, this marks a rather unique position in the simulation which is in agreement with what was found from Milky Way observations in terms of scale height. This position in the simulation is characterised by a localisation of the observer directly inside a superbubble with $\sim 1\,\mathrm{kpc}$ radius and the alignment of two rather close-by high star formation clumps in the direction of the galactic centre. This could be an indication that the Sun is located at such a special place in the Milky Way and that the measured scale height is a result of similar local contributions inside the Local Bubble.
Although the global scale height constitutes a rather rough measure, this approach establishes a comparability between observations and models that can be used for scientific inference.

Scale Height Distribution In order to obtain spatially resolved information about the granularity and patchiness of the galactic 1.8 MeV emission, the scale height analysis is subdivided into separate regions of interest (ROIs). Their dimensions are chosen to achieve a compromise between spatial resolution and intensity of the contained ^{26}Al signal. Thus, 30 longitude bins are defined along the galactic plane with 180° in latitude and 12° width in longitude (Kretschmer et al. 2013). These ROIs are marked in grey in Fig. 5.15.
A scale height estimation as described in the previous case for the galaxy-wide emission is now applied to each ROI separately. In this case, only the scale height z_0 is retained as free parameter by fixing the scale radius to $r_0 = 5.5\,\mathrm{kpc}$. On the other hand, the range of the scale height is extended to cover values from 10 pc to 5 kpc. The step size is adopted similar to the case described in the previous paragraph with 50 pc between 0.5–5 kpc. This results in a total of 123 exponential disk emission models with different scale heights which are fitted in each of the 30 ROIs. It must be taken into account that observations from two adjacent regions overlap, since SPI has a field of view of $16° \times 16°$. To take this into account, the evaluation was repeated for 12 different sets of ROIs, each shifted by 1° in longitude.
The scale heights of the ^{26}Al distribution derived from SPI measurements and simulations for the 30 bins along Galactic longitude are depicted in Fig. 5.17. Measurement uncertainties are represented by the average width of the $\log(\mathscr{L})$-profile in each ROI. It is important to keep in mind that neighbouring data points from adjacent longitude bins are not independent. Therefore, the error bars in longitude are depicted to include a symmetric spread by 8° to both sides. Additionally, the data points are grouped together alternately in order to interpret possible trends.
SPI measurements yield intermediate-to-very-large-scale heights on the order of kpc in the regions around the Galactic centre at $|l| < 60°$. This reaches even up to 5 kpc, which is the maximum possible value considered in this analysis. Towards outer regions with $|l| > 60°$, mainly small scale heights around $\sim 10\,\mathrm{pc}$ with a few intermediately large heights up to a few kpc are found. Because of the average vertical flow velocity of nucleosynthesis products in combination with the lifetime of ^{26}Al, large scale heights can be generally interpreted as contributions dominated by nearby or even local emission sites around the Sun. Small scale heights, on the other hand, indicate emission dominated by photons originating from the Galactic

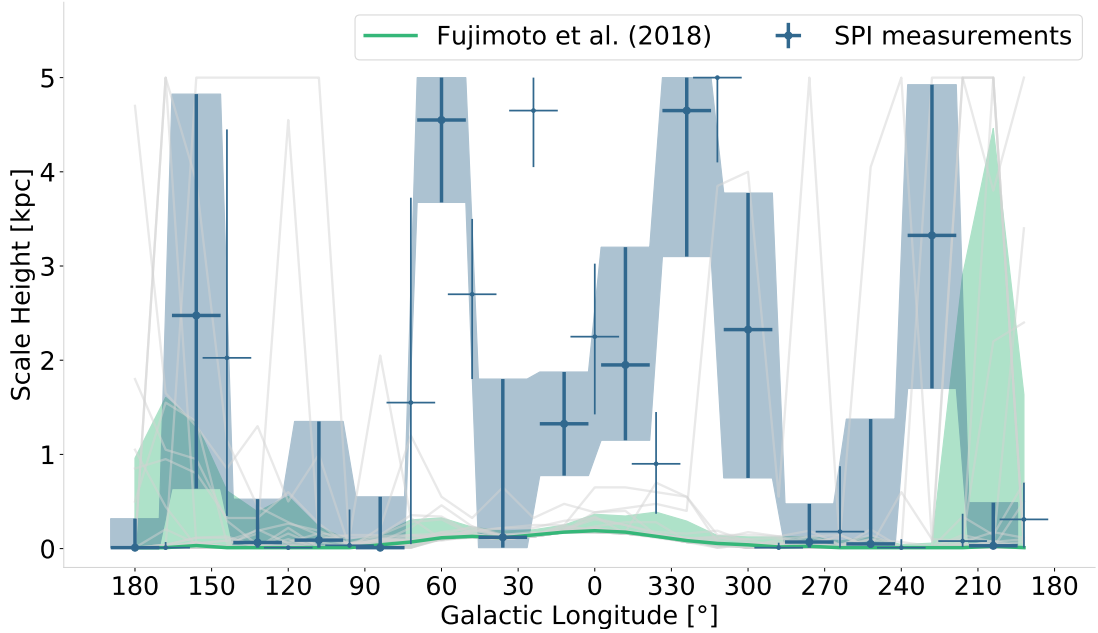

Figure 5.17: Best-fitting scale height for 30 individual longitude bins along the galactic plane. Each bin is 12° wide as shown in Fig. 5.15. Maximum likelihood results from SPI observations of the Milky Way are shown in *blue* with error bars in y-direction representing the average width of the $\log(\mathscr{L})$-profile in each longitude bin. The analysis is restricted to a maximum value of 5 kpc. Because adjacent regions overlap observationally as a result of the SPI field of view, each bin width is increased symbolically by 8° to both sides in longitude. Additionally, data points are represented alternately with bold and thin markers to group mostly-independent data points together. The shaded region is based on only the bold data points in order to guide the eye for a possible trend. The median value obtained for 36 simulated maps from F+18 are marked *green* with 68% lying within the shaded region. *Grey* lines show the individual results for each simulated sky map. Adopted from Pleintinger et al. (2019).

disk. Therefore, the distribution measured in Fig. 5.17 indicates a strong component from nearby emission around $|l| < 60°$ and, in contrast, a predominance of galactic emission at $|l| > 60°$. This is consistent with what would be expected due to foreground emission e.g. from Sco-Cen around $l = 350°$ (e.g. Krause et al. 2018). The analysis yields consistently smaller scale heights between 10 pc and 100 pc in the galactic centre direction $|l| < 60°$ for F+18. The separate graphs of the 36 individual simulated maps do not show any outliers that would account for this divergence compared to the observed distribution. This difference with respect to gamma-ray measurements shows that the simulation generally underestimate the local star formation component as seen by observations of the Milky Way. Another reason could be an underestimation of the vertical flow of material in the simulation. In particular the clustering and merging effects of superbubbles lead to an increased flow of nucleosynthesis products in larger cavities out of the galactic plane (von Glasow et al. 2013). Insufficient consideration of this effect could lead to the reduced scale heights. Towards larger latitudes with $|l| > 60°$ F+18 and SPI measurements converge at small height values of ~ 10 pc. In this regions, some observer positions yield also the intermediate or large scale heights on the order of kpc in accordance with observations. This indicates that the effect of the stochastic star formation process that occurs globally in the galaxy is dominant in SPI data in this spatial domain.

In general, this shows that due to the spatially resolved scale height distribution comparison between theory and observation is facilitated in both directions.

Scale Height Spectrum While the scale height distribution obtained in Fig. 5.17 already constitutes a generalised comparative method, it is still mainly characterised by the particular spatial configuration of the specific observer perspective in the Milky Way. However, due to the decomposition into regular longitude bins and the reduction to a single parameter, a further level of abstraction is now possible which is even independent of the particular galactic configuration in longitude. The distribution can be condensed to a scale height frequency spectrum, as shown in Fig. 5.18. The uncertainty regions for SPI measurements represent 68% of the results obtained from the 12 different sets of longitude bins each of which is shifted by 1°. This accounts for the arbitrary placement of ROIs. The spectrum inferred from gamma-ray measurements exhibits a major contribution in small scale height features of about $z_0 \sim 10\,\mathrm{pc}$. A second, fairly shallow and constant component is shown for larger scale heights even up to 5 kpc. This shows a bimodal contribution from two rather distinct emission features in the Milky Way. It also shows a posteriori that the global scale height description discussed earlier in the context of Fig. 5.16 apparently constitutes an insufficient generalisation of the actual emission morphology. This means that the actual ^{26}Al sky is insufficiently represented by an exponential disk. The granularity caused by superbubble structures makes a decisive contribution in this respect.

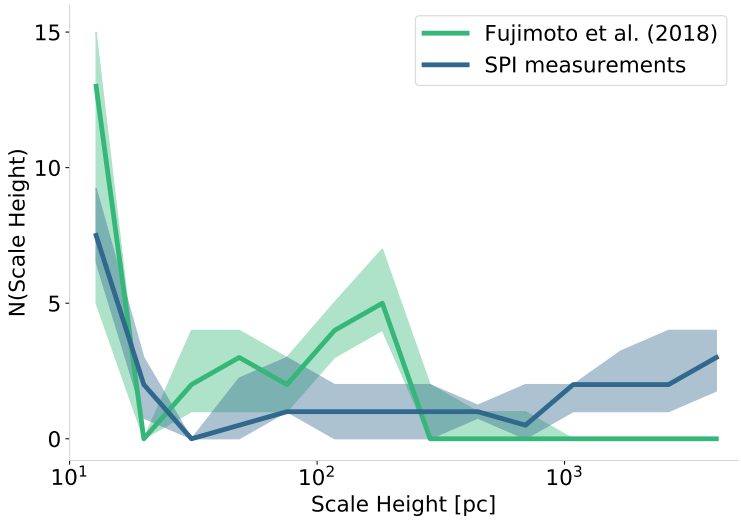

Figure 5.18: Frequency spectrum of best-fitting scale heights obtained for the ^{26}Al distribution in 30 12° wide longitude bins from SPI gamma-ray measurements (*blue*) and 36 synthetic sky maps constructed from the F+18 simulation (*green*). The *blue* shaded region marks the 68th percentile of SPI observations for 12 different sets of longitude bins shifted by 1° each. The *green* shaded region denotes 68% of the results obtained for the 36 different observer positions in the simulated galaxy. Adopted from Pleintinger et al. (2019).

The scale height spectrum obtained for the 36 observer positions in the F+18 simulation shows an excess of small scale heights in agreement with what was found for the Milky Way within 68% of the cases. On the other hand, the constant contribution of larger latitude extents is apparently not reproduced. Instead, a second component peaks around $z_0 \sim 100\,\mathrm{pc}$. This means that the galaxy-wide disk contributions are captured by the simulation and the nearby large scale height components are underestimated. The latter are on the order of a few hundred pc which does not reflect the observed morphology.

Overall, the scale height decomposition of the 1.8 MeV gamma-ray emission provides important information about the detailed geometry of nucleosynthesis feedback in the Milky Way. The particularly large scale heights seen in observations and their

comparatively low frequency in synthetic sky maps, points to a more coarse-grained superbubble structure in the Galaxy than obtained by hydrodynamic modelling. The importance of a prominent bubble structure is supported by a subsequent study by Fujimoto et al. (2019) suggesting that the pre-SN feedback stage was implemented too weak in F+18. The granularity found in Fig. 5.17 as well as in the bimodal shape of the scale height spectrum in Fig. 5.18 have also implications for previously determined scale heights of the Galactic 1.8 MeV emission. It underlines a significant deviation of the actual ^{26}Al sky from a simple doubly exponential disk model. A large global ^{26}Al scale height is therefore the result of strong local foreground emission. The predominance of the latter indicates that the 1.8 MeV emission contains a significant contribution from nearby superbubble structures, e.g. from Sco-Cen or regions along the spiral arm tangents (e.g. del Rio et al. 1996; Diehl et al. 2010; Krause et al. 2018). The strong foreground contribution could also indicate the signature of an ^{26}Al-filled superbubble that may have overrun the Solar System in the past. This would lead to a surrounding emission that dominates in regions with only comparatively weak Galactic disk emission (Pleintinger et al. 2019). However, current estimates of the total ^{26}Al mass in the Milky Way rest on the assumption of a consistent global scale height. The described results show that the uncertainties in these estimates are large and that the local foreground has to be taken into account more detailed (Diehl et al. 2006).
As outlined in Sec. 5.1, the general scientific benefit of such a phenomenological analysis can now be confirmed as twofold: On the one hand, based on agreement of observations and simulated predictions, conclusions about the three-dimensional distribution of nucleosynthesis products can be drawn and a general physical interpretation of the observed emission features can be made. On the other hand, the differences facilitate corrections or updates of the understanding of the nucleosynthesis and feedback processes underlying the theoretical implementation. In this way, the scale height approach has already inspired refinements in the feedback treatment used in F+18 that were implemented in a follow-up simulation by Fujimoto et al. (2020). This underlines the scientific richness of this morphological analysis. The scale height distribution and the scale height spectrum have therefore proved to be effective analytical approaches for exploiting theoretical models in conjunction with current gamma-ray measurements as empirical astrophysical tools. This is not at all limited to the specific case of hydrodynamic simulations considered in this section, but is applicable to models of all kinds and therefore points beyond this particular case. In the following section the analysis of the PSYCO models in Sec. 4.4 is complemented by a similar morphological consideration.

5.4.3 Morphological Exploitation of PSYCO Models

The PSYCO model (cf. Ch. 4) is perfectly suited to test a plethora of morphological hypotheses about the Galactic distribution of ^{26}Al. This is mainly due its flexibility in astrophysical parameters, computational resource efficiency, and diverse viability. The bottom-up modelling approach is particularly suited for the explicit investigation of the special case of the Milky Way because the stochasticity of the modelled structures can be included from a multitude of MC instantiations. Therefore, the phenomenological analysis methods outlined in Sec. 5.4.1 and Sec. 5.4.2 are applied to a subset of 30000 PSYCO model instantiations from the parameter grid in Tab. 4.9. The total number of originally 180000 models is reduced by only

taking into account the canonical IMF K01 and omitting SFR $= 1\,\mathrm{M}_\odot\,\mathrm{yr}^{-1}$ as physically unreasonable. Additionally, the explodability model J12 is left out due to its similarity to S+16. The analysis in this section will be similar to the previous two sections, with the PSYCO model structure allowing for a more comprehensive and Milky Way-specific interpretation.

Direct Likelihood Comparison Each of the 30000 synthetic sky maps modelled with PSYCO is taken as emission model M_1 and fitted to the full-sky SPI data set as described in Sec. 3.4.3. In order to reduce the computation time, the resolution of the maps is reduced to $2^\circ \times 2^\circ$. This is still below the spatial resolution of SPI and therefore does change the fit quality only negligibly by $\Delta \log \mathscr{L} \approx 0.2$. The maximum likelihood fits are performed for one energy bin between 1805–1813 keV, encompassing the integrated 1.8 MeV line emission. This further minimises computing time. In this way, a total time for map convolution and maximum likelihood fit of ~ 30 min per sky map is achieved. Subsequently, test statistic values TS can be calculated according to Eq. 5.3. This gives an likelihood ratio test for each of the 30000 modelled morphologies. The corresponding average results are shown in Fig. 5.19 in comparison with the observational reference values obtained from the COMPTEL and SPI 1.8 MeV maximum entropy maps.
There are no major changes in the fit quality for different SFR assumptions. This shows that there are no decisive morphological changes with SFR between 2–8 $\mathrm{M}_\odot\,\mathrm{yr}^{-1}$. The SFR mainly change the total mass and therefore the integrated flux in the map. During the maximum likelihood fit, the amplitude and therefore the total flux of the emission model is optimised. On the other hand, the results show variations for different galactic morphologies. Exponential density distributions, i.e. GM03 and GM04, yield on average lower TS values than Gaussian profiles. This is independent of an additional spiral structure, which is included in GM03. Thus, the cause of this variation is the central bulge component. This is very prominent in exponential profiles, whereas it is much fainter in the more spiral-dominated morphologies GM00, GM01, and GM02. This indicates that a particularly bright ^{26}Al emission detected from the central Galactic bulge region is absent in the Milky Way measurements.
On average, the highest TS values are obtained with GM02, and also with the smallest statistical variations. GM02 is characterised by a pronounced and homogeneous emission from the galactic ridge region associated with the nearby spiral arm in the direction of the galactic centre. Local emission sites in the vicinity of the observer are particularly rare in this morphology because the density maximum lies ~ 2.5 kpc away towards the galactic centre and the observer is also placed in the lower-density gap between two spiral arms. This leads to smaller stochastic fluctuations. The lowest average TS from a Gaussian density profile is obtained with GM01. The latter is characterised by a particularly steep density maximum ~ 1.5 kpc away from the observer towards the galactic centre. This leads to the absence of a galactic bulge component and a pronounced contrast between the Sagittarius-Carina arm and the Local Arm, the former being particularly salient and the latter comparatively weak. A flatter gradient between the two spiral arms describes the data better than such a steep gradient.
Variations with scale height underline the importance of nearby sites of star formation. The vertical extent of the galactic distribution, expressed by the scale height, affects the global fit quality of models with a tendency of larger scale heights fitting the data worse. An increased scale height increases the average distance to stellar

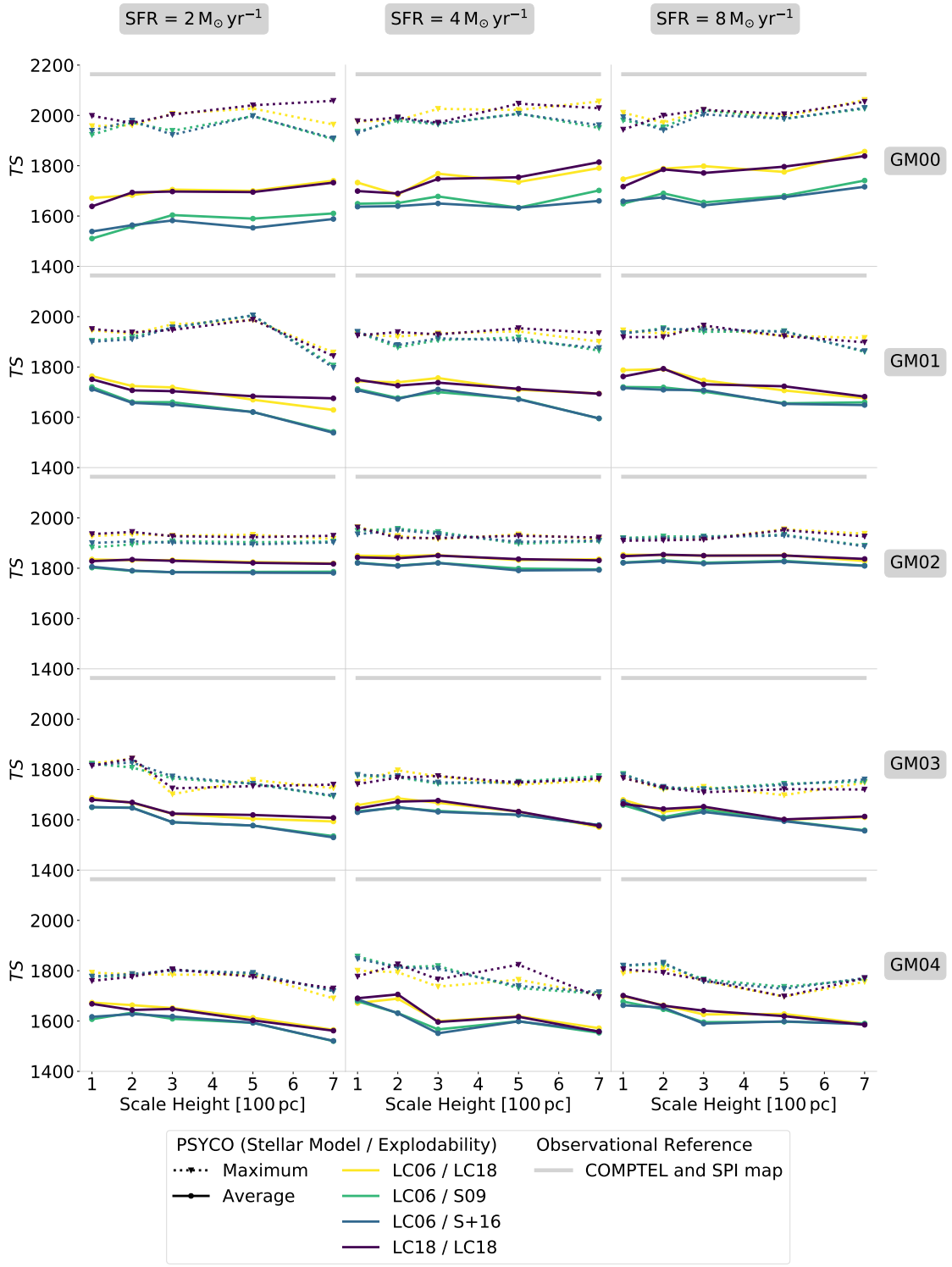

Figure 5.19: Likelihood ratio of 30000 sky maps modelled with PSYCO relative to the likelihood of a background-only fit with the SPI full-sky data set (cf. Eq. 5.3). Model results are differentiated in panels for three different SFRs (columns) and five different radial galactic morphologies (rows, cf. Fig. 4.14 for the nomenclature). Dots and solid lines denote the average values from 100 instantiations for five different scale height assumptions. The colours correspond to stellar model configuration as noted in the legend. Triangles mark the maximum TS value obtained from the 100 MC samples for each model configuration. The thick *grey* line denotes the combined observational reference value obtained with the COMPTEL and SPI maps (cf. Tab. 5.1 for numeric values).

associations. Accordingly, this reduces the average measured superbubble extent as well as the overall prominence of foreground emission. The improvement of the fit quality of GM00 with increasing scale height indicates that in the observations

of the Milky Way a strong contribution from high latitudes is measured from the direction of the Galactic anti-centre. GM00 is the only morphology that shows fit improvements for both higher SFRs and larger scale heights. SFR $= 2\,\mathrm{M_\odot\,yr^{-1}}$ yields only on the order of 0.5–1 $\mathrm{M_\odot}$ of ^{26}Al. A higher total mass is required to fully develop the galactic characteristics of GM00 because it is the widest morphology extending even beyond a radius of 15 kpc. This explains the improvements with SFR. Additionally, the radial distribution in GM00 is rather flat. Thus, a variation of scale height leads to a similar effect towards the galactic centre and anti-centre. In the other distributions, however, a change in scale height widens regions in the direction of the Galactic centre. The improvement of the fit quality of GM00 with increasing scale height thus indicates that in the observations of the Milky Way a comparatively strong contribution from high latitudes is measured from the direction of the Galactic anti-centre.

Regarding the different stellar models, there is a tendency of explodability LC18 yielding systematically higher TS values than the other explodability models. This indicates an overall increased size of superbubbles. Based on LC18 explodability, the majority of ^{26}Al ejection generally occurs at later times because SN yields from early exploding high mass stars are inhibited. This implies that bright superbubbles are older and therefore larger. In this case, the size of superbubbles is on average $\sim 300\,\mathrm{pc}$ in diameter. This is about a factor of 2 smaller for S09 or S+16. The model fits therefore show that ^{26}Al is preferentially found in superbubbles on the order of $\gtrsim 300\,\mathrm{pc}$. The preference for such large structures also points to the effect of frequent bubble merging, which would increase the average cavity size significantly.

Fig. 5.19 only addresses morphological properties of the synthetic sky maps. This means that the actual predicted flux per model is not yet taken into account, since the amplitude of the sky model is optimised during the maximum likelihood fit. The respective fitted scaling parameters are given in Fig. 5.20. A scaling parameter of 1 implies that no better fit is obtained by changing the amplitude of the sky model. Larger values indicate a corresponding upscaling and smaller values a downscaling of the original synthetic sky map as result the fit in order to better describe the data. Model configurations yielding scaling parameter close to 1 have a consistent Galactic ^{26}Al mass of 1.7–1.9 $\mathrm{M_\odot}$. This is the case for LC06 with full explodability S09 and SFR $= 4\,\mathrm{M_\odot\,yr^{-1}}$ as well as for stellar models LC18 with SFR $= 8\,\mathrm{M_\odot\,yr^{-1}}$(cf. Fig. 4.20). This supports a galactic ^{26}Al mass in the Milky Way in the range 1.7–1.9 $\mathrm{M_\odot}$, surprisingly independent of the underlying morphology. As expected, for models with SFR $= 2\,\mathrm{M_\odot\,yr^{-1}}$ an average upscaling between about a factor of 2 and more than an order of magnitude is necessary to best fit the SPI data. This means, the actual flux of the most salient gradients is accordingly underestimated with respect to what is measured for the Milky Way. Less scaling is required towards higher SFRs or stellar models with larger explodability for the most massive stars, i.e. S09 or S+16. This is consistent with the trend found in Fig. 4.26 that low SFRs and explodability LC18 generally underestimate the overall 1.8 MeV gamma-ray flux measured in Sec. 3.4.3. For stellar models LC06 with explodabilities S09 or S+16 and SFR $= 8\,\mathrm{M_\odot\,yr^{-1}}$, on average downscaling by a factor down to 1/3 is obtained. This means that while SFR $= 8\,\mathrm{M_\odot\,yr^{-1}}$ most likely results in a total flux close to the observed $(1.84 \pm 0.03) \times 10^{-3}\,\mathrm{ph\,cm^{-2}\,s^{-1}}$ (cf. Fig. 4.26), the underlying spatial distribution does not necessarily match the measurements of the Milky Way.

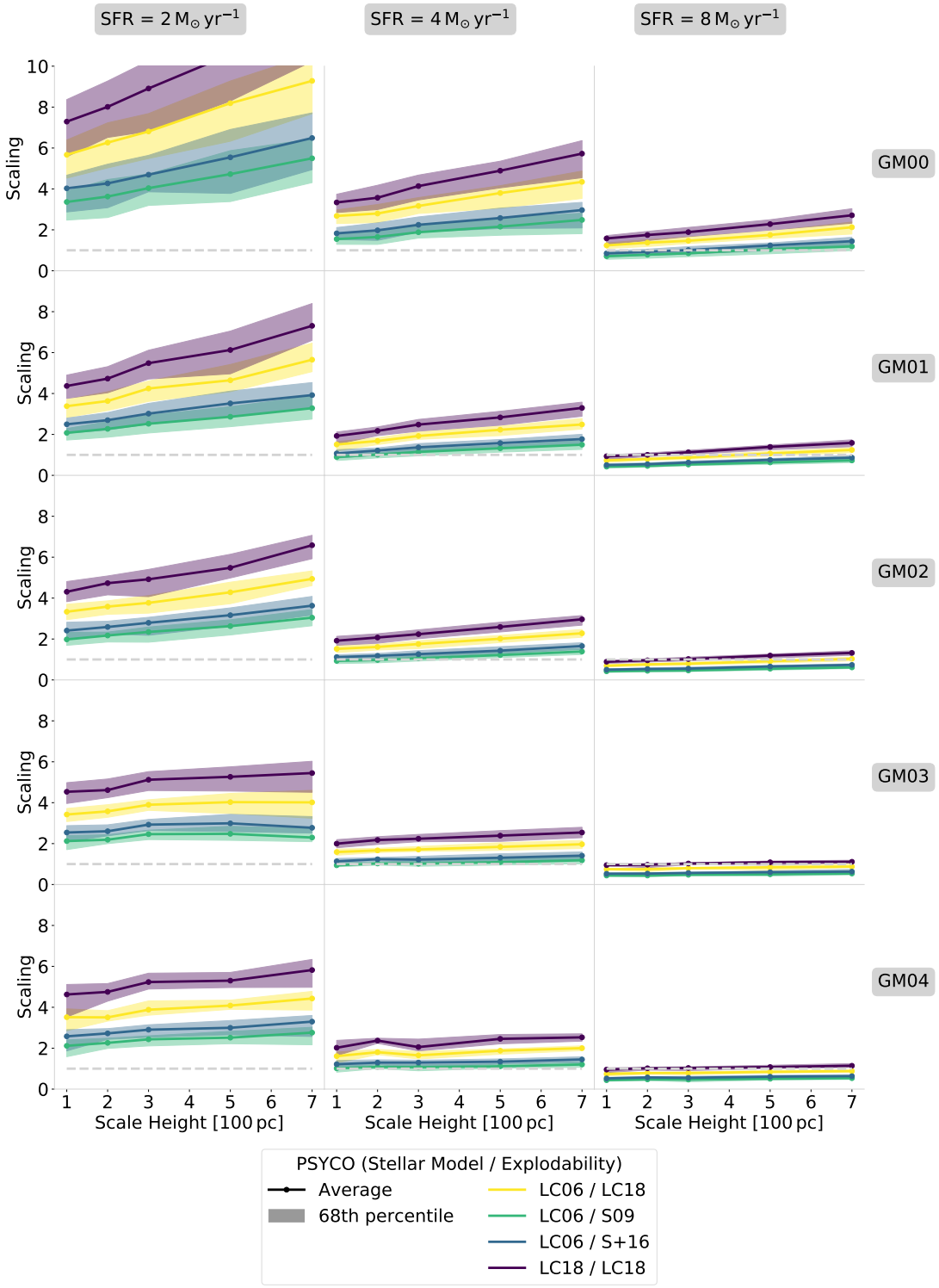

Figure 5.20: Scaling parameters obtained for 30000 sky maps modelled with PSYCO by fitting them to the SPI full-sky dataset (cf. also Fig. 5.19). Shaded regions denote the 68th percentile calculated from 100 MC instantiations for each model configuration. The dashed *grey* line marks the scaling parameter 1. Larger values indicate a corresponding upscaling and smaller a downscaling of the original synthetic sky map as result of the fit to SPI data.

Best-Fitting Maps The best fitting individual sky map with $TS = 2061$ is obtained for GM00 and a scale height of 700 pc with SFR $= 8\,\mathrm{M}_\odot\,\mathrm{yr}^{-1}$, stellar models LC06, and explodability LC18. This model is depicted in Fig. 5.21. Although it constitutes the best fitting synthetic map, its TS value is still about $\Delta TS = 100$ lower than the observational reference maps (cf. Tab. 5.1). The fit residuals are projected from

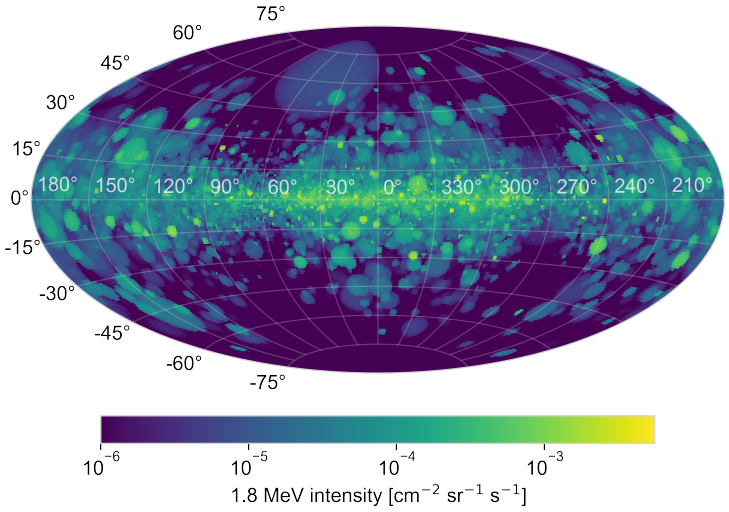

Figure 5.21: Best fitting sky map with $TS = 2061$ (cf. Eq. 5.3) out of 30000 PSYCO models (cf. Fig. 5.19). It is based on GM00 with 700 pc scale height and SFR $= 8\,\mathrm{M}_\odot\,\mathrm{yr}^{-1}$, IMF K01, stellar models LC06, and explodability LC18.

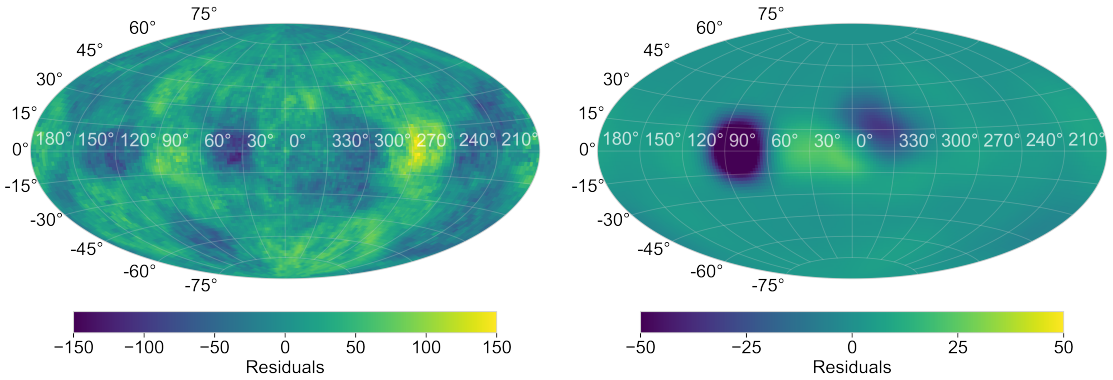

Figure 5.22: *Left:* Backprojection of the residuals obtained from the best fitting PSYCO map (cf. Fig. 5.21) onto the celestial sphere. Residuals are given in units of number of photons. *Right:* Relative change in backprojected residuals if known knowns (cf. Tab. 4.7) are added manually to the map.

SPI detector space through the coded mask back onto the sky. This is shown in the left panel of Fig. 5.22. Bright regions, i.e. positive residuals, indicate areas in the sky where the measured Milky Way emission is underestimated by the synthetic sky map. The reverse applies for dark regions or negative residuals. Positive residuals align in a ring-like structure with a diameter of 120°–180° and centred near the Galactic centre. This can be partly attributed to prominent foreground emission sites in the Milky Way. To estimate this influence, the three known associations (cf. Tab. 4.7), i.e. Cygnus, Sco-Cen, and Orion, are added to the map in Fig. 5.21 and the fit is repeated. It is important to note that this reduces the investigation to a purely phenomenological analysis since the stochastic properties of the original galaxy model are overrun. Including the known associations, the fit slightly improves to $TS = 2077$. The spatial distribution to which this improvement can be attributed is shown in the right panel of Fig. 5.22. The emission from the Cygnus and Sco-Cen region are captured better by the sky map with this feature included. On the other hand, for the Orion-Eridanus region, no notable change results from its explicit consideration. However, this can not account for the entire aforementioned ring-like structure seen in the backprojected residuals. Thus, the origin of

this residual structure is still to be clarified.
A composite sky map of the best-fitting models (cf. Fig. 5.23) is assembled. These are defined by $TS \geq 2000$. 49 maps fulfil this condition, 47 of which are based on GM00 and 2 on GM01. Those are normalised and combined in one average sky map displayed in Fig. 5.23. The composite map yields $TS = 2123$. This means it

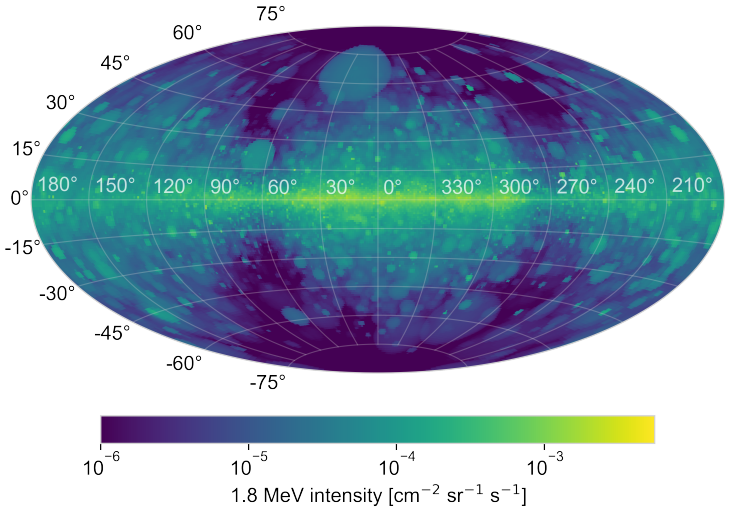

Figure 5.23: Composite synthetic sky map from the 49 best fitting PSYCO models, i.e. with $TS \geq 2000$. It is normalised to an integrated flux of 1.84×10^{-3} ph cm^{-2} s^{-1}.

fits the data better than any of the underlying maps individually. Its most striking characteristic is a pronounced bimodal distribution. On top of the disk component, a rather homogeneous emission originates from within $\sim 60°$ around the Galactic centre as well as the anti-centre. These areas are sharply separated by rather empty regions along the spiral arm tangents. Apart from that, this map is characterized by a striking homogeneity of the emission. As previously obtained with the individual best fitting map, the manual inclusion of the known knowns leads to an improvement of the fit on the same order to $TS = 2134$. An overview over fit results of the separately considered maps is summarised in Tab. 5.1. This compilation demon-

Table 5.1: Likelihood ratios TS (cf. Eq. 5.3) of the best fitting PSYCO model (cf. Fig. 5.21) and the best fitting composite model (cf. Fig. 5.23). Both are evaluated with and without the manual inclusion of known knowns (cf. Tab. 4.7). The observational reference values obtained for the COMPTEL and SPI map are given for comparison.

Map	Known knowns	TS
SPI		2166
COMPTEL		2160
Best model composite	✓	2134
Best model composite	×	2123
Best model	✓	2077
Best model	×	2061

strates a systematic improvement due to the manual inclusion of known knowns (cf. Tab. 4.7). On the other hand, an inclusion of known unknowns (cf. Sec. 4.3.2) yields no further improvement of the fit. This shows that those associations within 3.5 kpc in the Milky Way are already captured by the overall properties of the galactic model.
However, the backprojection of the residuals of the composite best model map in-

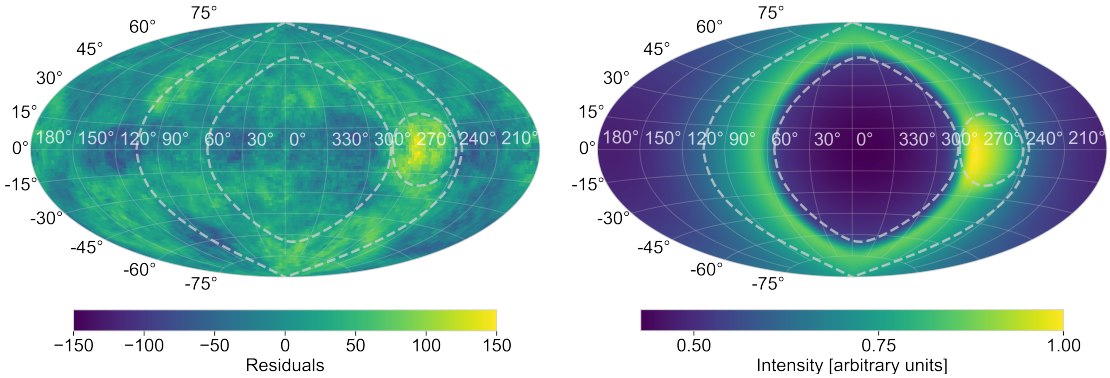

Figure 5.24: *Left:* Backprojection of the residuals obtained from the best fitting composite PSYCO model (cf. Fig. 5.23) including known knowns onto the celestial sphere. Residuals are given in units of number of photons. Dashed *grey* lines guide the eye to prominent residual features. *Right:* Representation of residual features by two components. First, the observer is positioned inside a shell with distance to its centre of 500 pc, with an inner shell radius of 400 pc, and an outer radius of 800 pc. This yields a large ring-like structure. Second, a spherical emission site at the distance of Vela OB 1 of 0.8 kpc (Allen et al. 2015) with a radius of 80 pc.

cluding known knowns in the left panel of Fig. 5.24 yields similar features as in Fig. 5.22. Residuals without known knowns as well as the relative improvement due to their inclusion are depicted in Fig. A.12 in the appendix. The ring-like feature in the residuals can be explained by locating the observer directly inside a ^{26}Al-filled spherical shell, e.g. at a distance of 500 pc with an outer radius of 800 pc and a shell thickness of 400 pc (cf. right panel in Fig. 5.24). Another line of argument can attribute the residuals to missing emission along the spiral arm tangents due to the strongly bimodal model configuration mentioned before. Thus, the gap between the spiral arms in the Milky Way would be less pronounced as suggested by GM00.
A bright emission feature occurs rather concentrated in the Galactic plane within a radius of $\sim 22°$ around $l = 270°$. This is in the direction of the Vela OB1 association at $l = 265°$. Thus, missing foreground emission from the Vela region can explain the large residuals in this area. This is represented by a spherical emission with 80 pc radius at the distance of Vela OB1 of 0.8 kpc in the right panel of Fig. 5.24. Another explanation for the flux excess at $l = 270°$ could be that ^{26}Al-filled superbubbles generally precede the spiral arm (cf. Fig. 2.46). Such configuration would extend the emission from the Sagittarius-Carina arm towards latitudes $< 300°$ and thereby increase the emission around $l = 270°$. Further tests for different spiral arm orientations have to be performed with PSYCO in order to clarify the origin of this residual feature.

Scale Height Analysis The scale height distributions (cf. Sec. 5.4.2) of the 30000 PSYCO models are depicted in Fig. 5.25. Here, the average values from 100 instantiations for each model configuration are given for better visualisation. As expected, the overall shape of the scale height distributions does not vary strongly for different underlying SFRs. The large scale heights up to ~ 5 kpc seen in SPI observations are not reached by any of the model configurations on average. This points to a peculiar position of the Solar System as also suggested in Sec. 4.4.3 from a pure model approach. Generally, the observed scale height distribution shows a rather bimodal configuration of large scale heights of a few kpc towards Galactic centre and anti-centre, and small scale heights on the order of ~ 0.1 kpc in between (cf. discussion in Sec. 5.4.2). A similar structure is found only for the spiral dominated

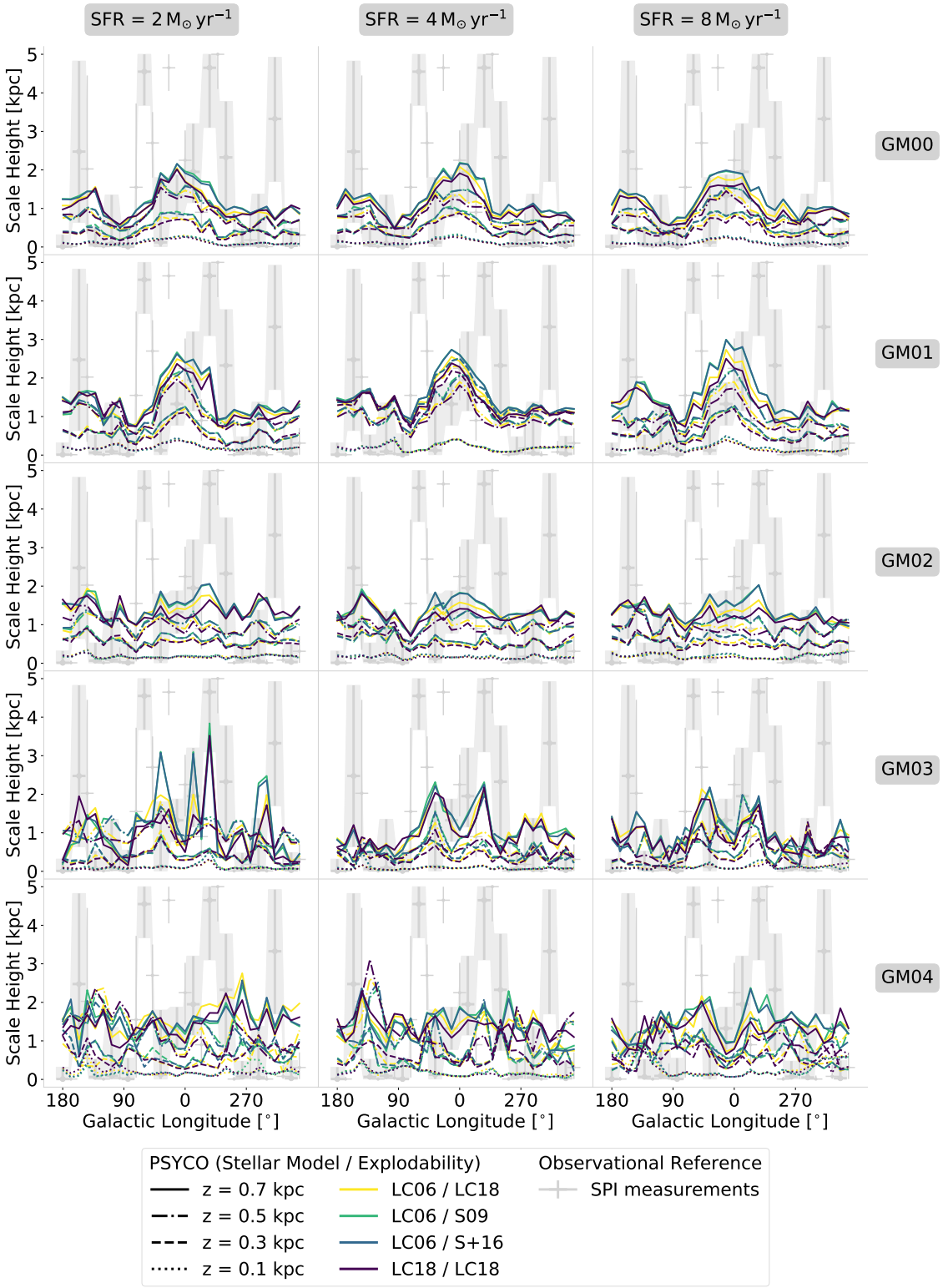

Figure 5.25: Scale height distributions of 30000 PSYCO models for 30 individual longitude bins along the galactic plane. Each bin is 12° wide as shown in Fig. 5.15. The model grid has already been described in the context of Fig. 5.19. Maximum likelihood results from SPI observations of the Milky Way are shown for comparison in *grey* with error bars in y-direction representing the average width of the $\log(\mathscr{L})$-profile in each longitude bin. The analysis is restricted to a maximum value of 5 kpc. Because adjacent regions overlap observationally as a result of the SPI field of view, each bin width is increased symbolically by 8° to both sides in longitude (cf. Pleintinger et al. 2019). For better visibility, only the mean values obtained for 100 MC instantiations per model configuration are displayed. Colours mark different stellar models and line styles denote varying scale height assumptions of the galactic models.

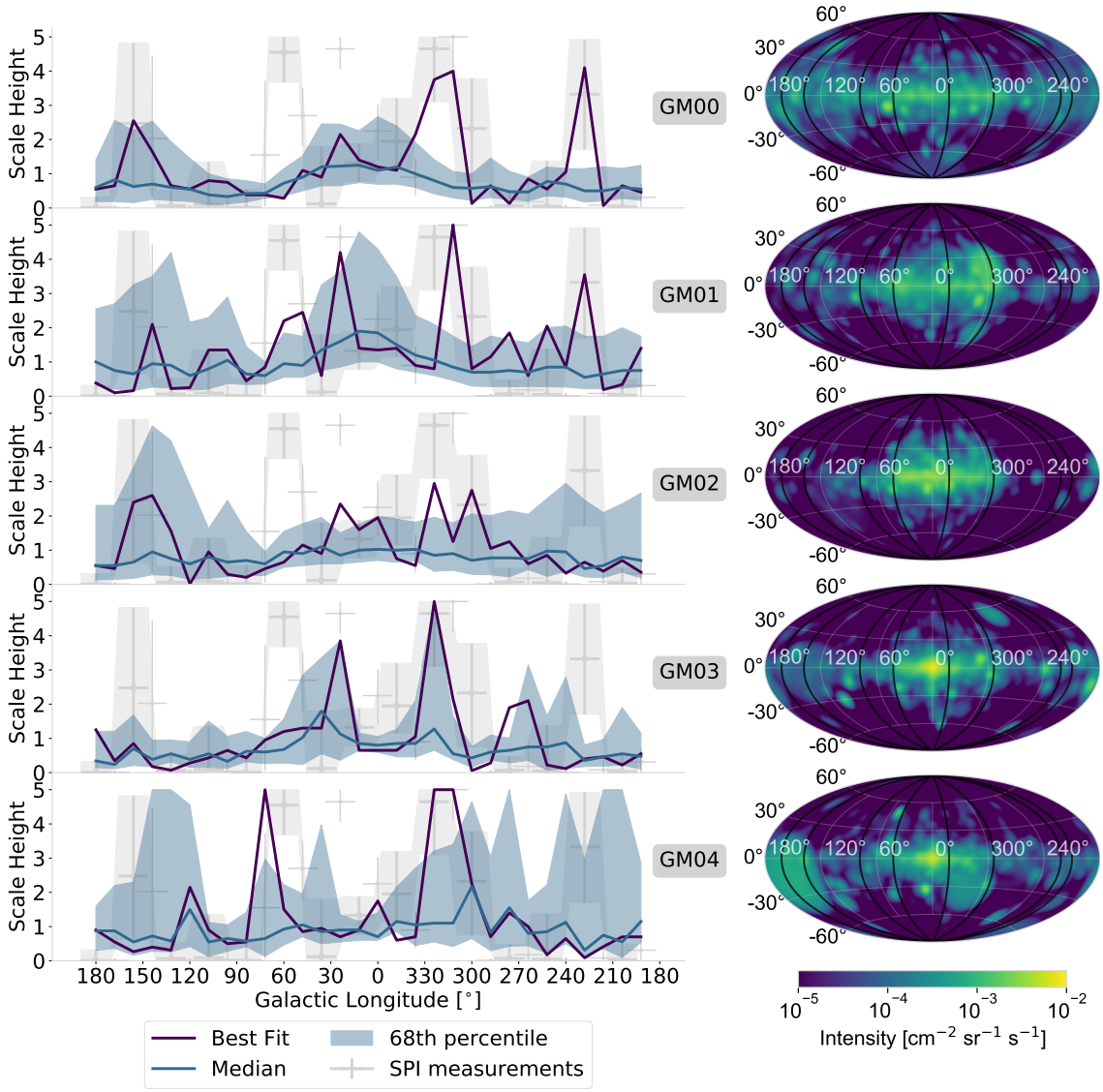

Figure 5.26: *Left:* Best fitting scale height distributions (*purple*) with respect to SPI measurements (*grey*) obtained from 6000 PSYCO models for each radial galactic morphology (cf. Fig. 4.14). In each case, the best fit is obtained with scale heights 0.7 kpc and stellar models LC18. The median of the 300 models using the respective model configuration is shown in *blue* with 68% lying within the *blue* shaded region. *Right:* Sky maps corresponding to the best fitting scale height distribution in the left panel. The maps are normalised to the observed total flux and smoothed with a Gaussian filter of 2° width to emphasize the general characteristics over smaller details. Regions yielding large scale height in SPI measurements are marked by *black* lines.

morphologies GM00 and GM01. Central dominated morphologies on the other hand yield rather uniform distributions. With increasing model scale height the structure becomes more bimodal. However, in order to reproduce the large observed scale heights, the overall model scale height cannot be increased arbitrarily. This also raises the general baseline, which leads to configurations that no longer meet the small scale height contributions. This means that the observed structure could be explained either by a generally high scale height with individual outliers to smaller ones, or vice versa a generally small scale height with high outliers. This will be discussed further below in the context of considering the scale height spectra.

The best fitting scale height distributions for each radial galactic morphology are calculated on the basis of a χ^2 distance determination and shown in Fig. 5.26. The best fitting profile for each galactic morphology is obtained with scale height 0.7 kpc and stellar model LC18. This has twofold implications. On the one hand, it favours

large scale heights if particularly associated with the Local Arm. On the other hand, it prefers larger ^{26}Al bubbles based on the preference for LC18. The 68th percentile of the respective model configuration in Fig. 5.26 indicates an East-West asymmetry arising from the spiral structure in GM00, GM01, and GM02. Within this statistical scatter, the observed feature around $l = 150°$ is included. This means that large scale heights and strong emission from the direction of the Perseus region can also be explained as overall Galactic emission resulting from a prominent Local Arm. On the other hand, the observed scale height peak around $l = 230°$ can not be explained in that way. The latter points to a foreground interpretation, e.g. by the Orion-Eridanus region located near that domain.
The striking dominance of the Sagittarius-Carina arm towards the Galactic centre in GM01 leads to a peak at $l = 0°$ up to 5 kpc within 68%. This contradicts the observed profile in this area, which rather shows a dip flanked by two peaks at $l \sim -40°$ and $l \sim 60°$. This central structure is on average best represented by GM03. The latter is central dominated with a widened galactic ridge emission due to a weak spiral component. The other morphology with a exponential radial density profile, GM04, shows a similar dip, but less pronounced. The statistical scatter is largest for this morphology because the local star formation density in the vicinity of the observer is also largest.
In particular, the observed peak around $l = 60°$ can be explained as a foreground feature, since it is not captured within 68% by any model. As this position differs from the location of Cygnus by about twice the bin size in longitude, it is not directly linked to this region. Instead, this increase in scale height can be explained as associated with the tangent of the spiral arm gap in that direction, where a widely extended foreground component dominates over the galaxy-wide emission.
The entire set of scale height profiles in Fig. 5.25 is translated to scale height spectra in Fig. 5.27. Since in the previous analysis the scale height distributions remained basically constant for SFRs above $2\,\mathrm{M_\odot\,yr^{-1}}$, this parameter is no longer explicitly considered in this representation. As expected from the previous scale height investigations, on average none of the model configurations exactly reflects the observed structure. With increasing scale height the spectrum becomes more concentrated with a large scale height peak. In this case small scale height features occur less frequently. Agreement between models and observations is found for the amount of longitude bins with very small scale heights from GM03 and GM00 within 68% for a galactic scale height of 0.1 kpc. This agreement goes along with a similarity of the spectra to what was obtained for F+18 by Pleintinger et al. (2019) as shown in Fig. 5.18. While Pleintinger et al. (2019) studied only one realisation of the hydrodynamic simulation, the many instances of the PSYCO model also allow to investigate the effect of statistical outliers and spatial peculiarities in this thesis.
For this purpose, the scale height spectra that are closest to the observed spectrum are listed for each galactic morphology in Fig. 5.28. These are obtained for model scale height assumptions of 0.2 kpc, 0.7 kpc, 0.7 kpc, 0.2 kpc, and 0.2 kpc for GM00, GM01, GM02, GM03 and GM04 respectively. This indicates that the observed granularity of the Milky Way can be produced generally by any scale height configuration and for any of the considered galactic morphologies. The overall smallest χ^2 value is obtained for the case of GM00 with $z_0 = 0.2\,\mathrm{kpc}$ and $\mathrm{SFR} = 8\,\mathrm{M_\odot\,yr^{-1}}$. This map (cf. upper right panel in Fig. 5.28) is characterised by a rather thin and continuous disk component, including prominent and broader emission from the Local Arm towards the Galactic anti-centre. On top of that, few rather bright superbubbles are seen as outliers at high latitudes. The contrast between these two components

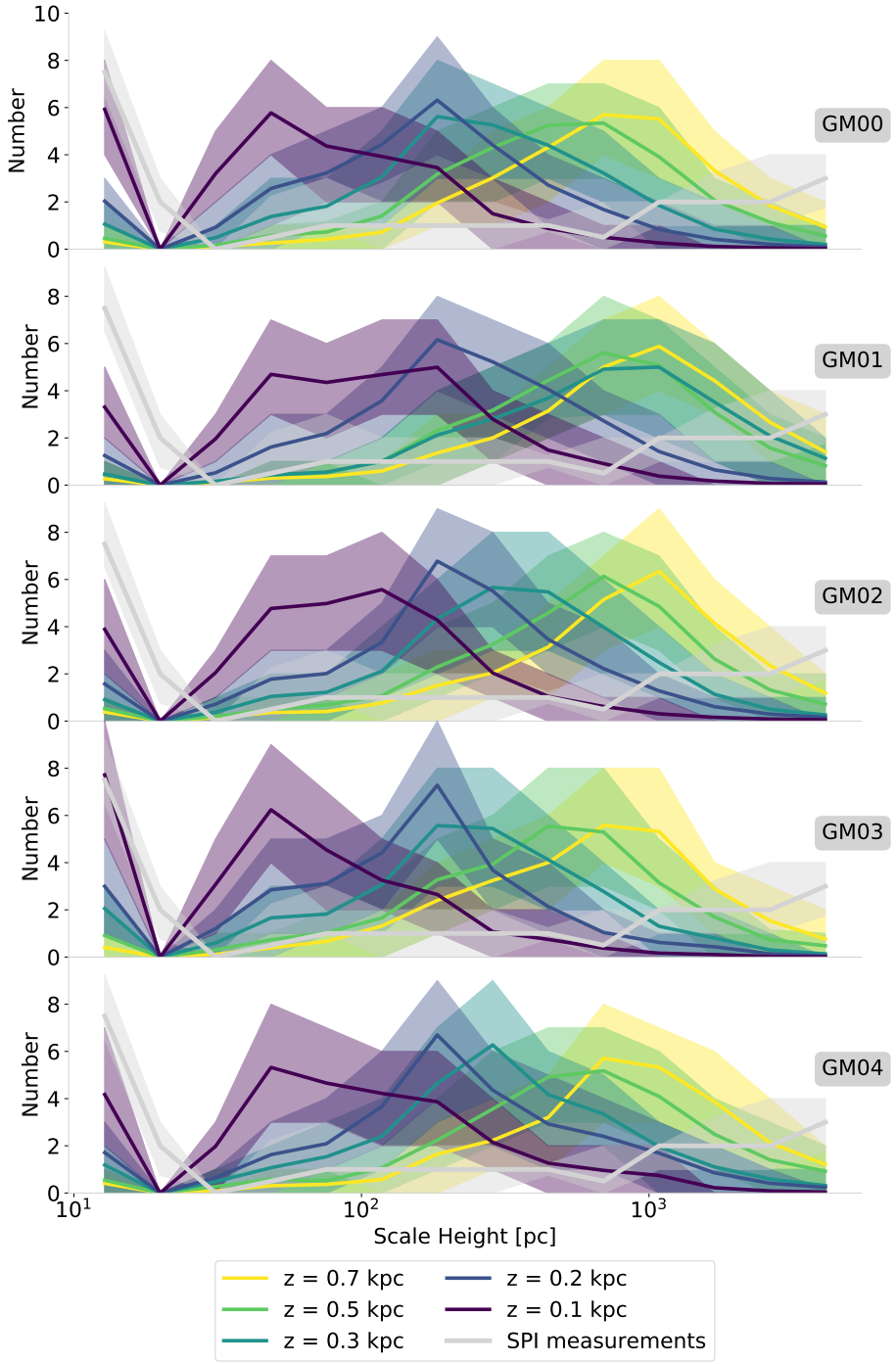

Figure 5.27: Scale height spectra of 6000 PSYCO models for each galactic radial morphology as denoted in *grey* boxes per panel. Colours mark different scale height assumptions with solid lines giving the median of 1200 model instantiations for each scale height configuration. Shaded regions assign the respective 68th percentiles. The *grey* line and shaded region marks the scale height spectrum of the Milky Way as measured with SPI (cf. Pleintinger et al. 2019, or Sec. 5.4.2).

gives rise to the observed bimodal distribution between the small scale height peak and the flat large scale height component. The presence of bright star groups that are located nearby and seen under a large latitude angle of $|b| > 30°$ is generally striking in the sky maps in the right panel of Fig. 5.28. These features are decisive to explain the observed granularity of the 1.8 MeV sky.

This investigation indicates that while large scale height features can be equally represented by either a large overall galactic scale height or individual nearby sites

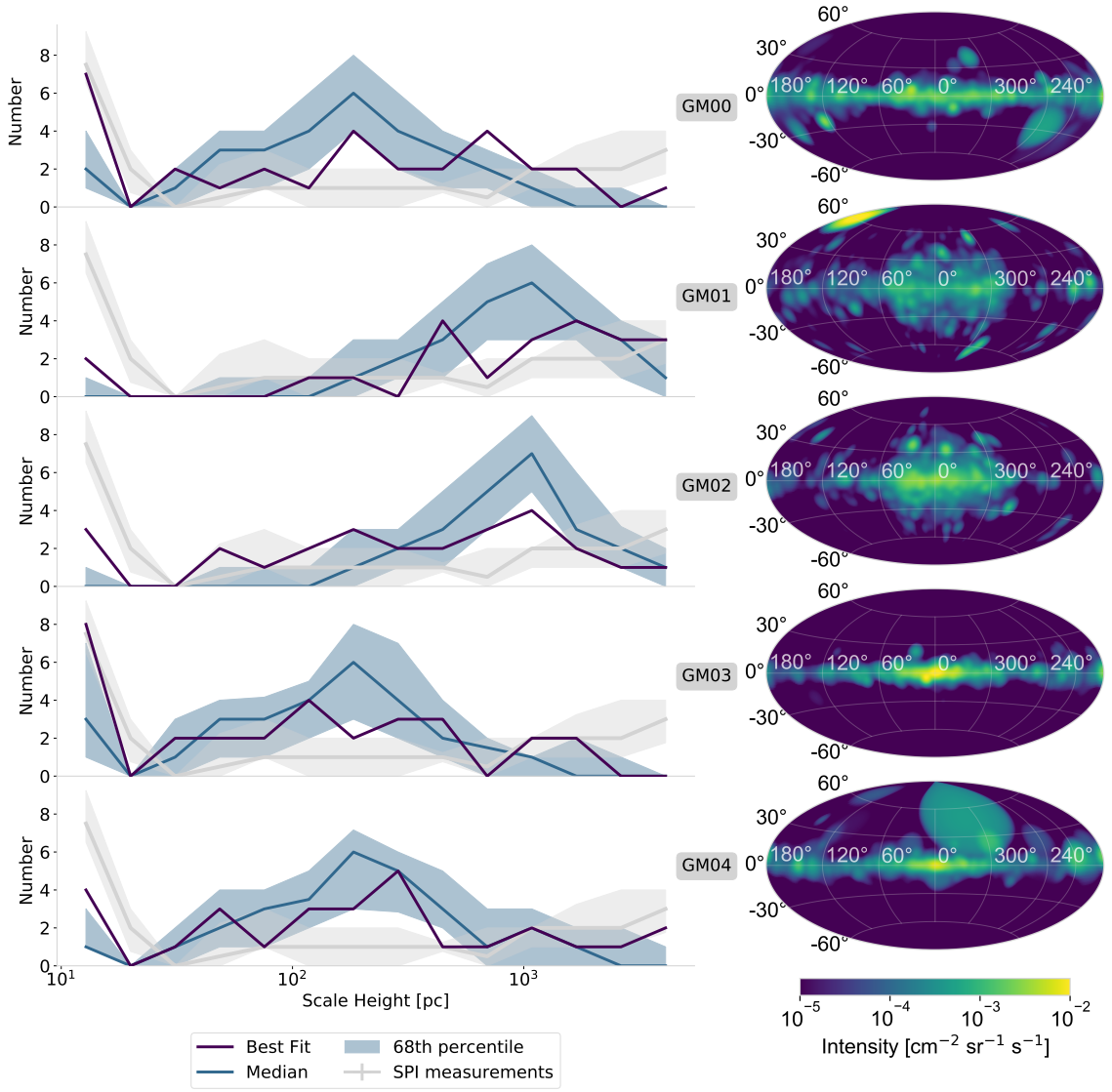

Figure 5.28: *Left:* Best fitting scale height spectra (*purple*) with respect to SPI measurements (*grey*) obtained from 6000 PSYCO models for each radial galactic morphology as denoted in the *grey* boxes per panel (cf. Fig. 4.14). The best fitting spectra are obtained with model scale heights 0.2 kpc, 0.7 kpc, 0.7 kpc, 0.2 kpc, and 0.2 kpc for GM00, GM01, GM02, GM03 and GM04 respectively. The median of 300 models using the respective model configuration in each panel is shown in *blue* with 68% lying within the *blue* shaded region. The maps are normalised to the observed total flux and smoothed with a Gaussian filter of 2° width to emphasize the general characteristics over smaller details.

at high latitudes, the small scale height peak is more likely explained by a small galaxy-wide scale height than by bright foreground features located in the galactic plane. This clarifies the previously mentioned quandary of which component is galactic and which foreground. Overall, the evaluation of scale height spectra favours an overall thin galaxy-wide scale height distribution, which is overlaid by a few prominent foreground emission sites at high latitudes.
A comprehensive and conclusive discussion of the analysis in Ch. 5 with reference to the complete picture of this thesis is presented separately in the following Sec. 5.5.

Essentials

The ^{26}Al signal from the entire Galaxy measured with SPI is exploited morphologically by comparing it to synthetic sky maps from the hydrodynamic simulation by Fujimoto et al. (2018) and 30000 PSYCO models.

- The uniform exponential disk parameters best fitting the global Galactic ^{26}Al emission are $r_0 = 5.81 \pm 0.64\,\mathrm{kpc}$ and $z_0 = 0.77 \pm 0.17\,\mathrm{kpc}$.
- Scale height distribution and the scale height spectrum are established as comparative tools for investigating the Galactic morphology seen with nuclear gamma-ray lines.
- A bimodal scale height spectrum from SPI observations indicates a strong nearby emission component which is on average not represented in F+18.
- The evaluation of the PSYCO models indicates the absence of a particularly bright bulge emission and the presence of a relatively prominent Local Arm towards the galactic anti-centre seen in 1.8 MeV from the Milky Way.
- Discrepancies between PSYCO models and SPI observations indicate a missing prominent emission component from the direction of the Carina region in the models and overall suggest that the average bubble size is larger than currently assumed, which could be an indication of frequent bubble merging.
- The galactic distribution of ^{26}Al that consistently appears to closest reproduce the observed morphology of the Milky Way is GM00, which is characterized by a particularly homogeneous emphasis on the spiral arms.

5.5 Conclusion and Discussion

This section provides a conclusion of the key results of this thesis concerning nucleosynthesis feedback of massive star groups and their implications for the global chemical evolution of the Milky Way. The astrophysical and galactic parameters presented in Ch. 2 are discussed with recourse to measurements in Sec. 3.4.3, modelling in Ch. 4, and their cross-evaluation in the previous part of this Ch. 5.

SFR and SNR The correlation between SFR and SNR is mainly modulated by stellar explodability (cf. Fig. 4.23). According to the PSYCO modelling results, this gives rise to a linear relation $\mathrm{SNR} = \varepsilon \times \mathrm{SFR}$, with $\varepsilon = (0.36\text{–}0.56) \times 10^{-2}\,{\mathrm{M}_\odot}^{-1}$ within the range of SFR of 1–8 $\mathrm{M}_\odot\,\mathrm{yr}^{-1}$, depending on explodability. This constitutes an important link within the Galactic Cycle of Matter (cf. Fig. 2.2) as it quantifies the mass that is recycled in SNe to 1/3–2/3 of the total stellar mass. There is a preference towards smaller values of ε because a low explodability in the high-mass regime, such as e.g. LC18, is suggested by multiple indicators throughout this thesis. With regard to the modelling of star formation dynamics described by the IMF, it has been found that the low-mass break of the IMF proves to be decisive for galactic

chemical evolution. The high-mass slope is of less importance (cf. Fig. 4.20). Concerning radioactivity tracers, the low-mass break is modelled consistently by both K01 and C05.
From the consideration of SFRs in the range 1–8 $M_\odot\,yr^{-1}$, also a linear relation is inferred for the formation rate of stellar clusters. It can be described as CFR = $6 \times SFR \times 10^{-4}\,[yr^{-1}]$, which yields a CFR of about 0.16 or 0.29 per century for SFR = $2\,M_\odot\,yr^{-1}$ or SFR = $4\,M_\odot\,yr^{-1}$ respectively (cf. Sec. 4.3.1). This constitutes a heuristic connection between the formation of individual stars and the emergence of large scale structures.
In order to obtain a total Galactic ^{26}Al mass of $(2.8 \pm 0.8)\,M_\odot$ as determined by Diehl et al. (2006), a SFR $\gtrsim 4\,M_\odot$ is required in the PSYCO modelling framework. This required mass increases with decreasing explodability for high-mass stars. The PSYCO model calculations in connection with gamma-ray observations are incompatible with the commonly assumed SFR of about 1.5–3.5 $M_\odot\,yr^{-1}$ (cf. Sec. 2.4.2). Instead, a higher SFR $\gtrsim 4\,M_\odot\,yr^{-1}$ is suggested. SFR = $4\,M_\odot\,yr^{-1}$ implies a rate of 1.4–2.2 SNe per century, which is consistent with the determinations for the Milky Way (cf. Tab. 2.10). The observed ^{60}Fe line intensity of $F_{^{60}\mathrm{Fe}} = (0.31 \pm 0.06) \times 10^{-3}\,ph\,cm^{-2}\,s^{-1}$ (Wang et al. 2020) is obtained for the global assumption of SFR $\gtrsim 4\,M_\odot\,yr^{-1}$, which yields an average galactic ^{60}Fe mass of $\gtrsim 4\,M_\odot$ (cf. Fig. 4.26 or Fig. 4.32).
For the case of ^{26}Al a larger Galactic SFR is confirmed on the basis of the isolated treatment of the inner Galaxy emission from $|l| \leq 30°$ and $|b| \leq 10°$. This spatial confinement is necessary because only this area is dominated by galaxy-wide emission, while higher latitudes and longitudes exhibit strong contamination by foreground emission. The 1.8 MeV emission from this region is modelled with SFR $\sim 5\,M_\odot\,yr^{-1}$ or $M(^{26}\mathrm{Al}) \sim 2\,M_\odot$(cf. Sec. 4.4.3 or Fig. A.6). However, this is still influenced by the remaining prominent foreground emission from ^{26}Al. The abundance of nearby massive-star regions is also underestimated for SFR = $2\,M_\odot\,yr^{-1}$. Besides a generally larger SFR, this also indicates that the local star formation is underestimated and the clustering of star formation events is more prominent than currently assumed in PSYCO.
About 1–2 SN remnants are observable by their ^{44}Ti gamma-ray emission. This number is modelled in the PSYCO framework by assuming SFR = $4\,M_\odot\,yr^{-1}$, which yields on average 1.4 ± 1.1 SN remnants detectable by their ^{44}Ti decay signature with current instruments. This confirms the higher estimate of the SFR.

Stellar Yields and Explodability Explodability, rotation, and metallicity are the crucial parameters for stellar nucleosynthesis feedback. Their implications for star groups have been discussed in detail in Sec. 4.2.3. Stellar rotation and metallicity mainly affect the temporal profile and contrast between wind and SN yields. ^{60}Fe shows the strongest variations between nucleosynthesis models. Thus, the $^{60}\mathrm{Fe}/^{26}\mathrm{Al}$ mass ratio is strongly dependent on those model assumptions, yielding 2.3 or 7.1 for LC06 or LC18 respectively. The flux ratio of 0.17 ± 0.04 observed with SPI in the Milky Way (cf. Wang et al. 2020, or Sec. 3.4.3), is reached closer by models based on LC06 yield calculations.
A decrease in explodability is accompanied by a reduction of the amount of stellar material that is reprocessed in a subsequent Cycle of Matter. In other words, explodability primarily determines the leakage of this cycle. Since this parameter is selective towards explosive nucleosynthesis mechanisms and consequently SN yields,

it reduces ^{60}Fe more than ^{26}Al. While the former is ejected only in SNe, the latter is also present in stellar wind ejecta. Thus, it also strongly affects the time profile of the ^{60}Fe/^{26}Al mass ratio in stellar groups.
Concerning the entire Milky Way, the Galactic 1.8 MeV flux of $(1.84 \pm 0.03) \times 10^{-3}\,\mathrm{ph\,cm^{-2}\,s^{-1}}$ (cf. Sec. 3.4.3) is on average underestimated by PSYCO models, even for extreme assumptions such as SFR $= 8\,\mathrm{M_\odot\,yr^{-1}}$. This indicates generally underestimated nucleosynthesis yields or a peculiar observer position in the Milky Way. Additionally, the fit of galactic PSYCO models to full-sky measurements of the Milky Way yields a preference for explodability LC18. Since in this case ^{26}Al is found on average in superbubbles that tend to be older and therefore larger, this is also linked to a spatial effect. Particularly on the galactic level, a degeneracy between stellar evolution models and spatial configurations is present.
The investigation of individual sources is constrained by the sensitivity limit of current gamma-ray telescopes. SPI measurements of the most promising WR source, γ^2 Velorum, yield a 2σ upper flux limit of $1.7 \times 10^{-5}\,\mathrm{ph\,cm^{-2}\,s^{-1}}$ (cf. Sec. 5.2). This limit is in agreement with current stellar models.
While previous investigations of individual stellar associations mainly covered Cygnus, Sco-Cen, and Orion (cf. Sec. 2.3.4 or Tab. 4.7), this was extended in this thesis by exploiting newly obtained SPI measurements of the Perseus region (cf. Sec. 5.3). A 1.8 MeV flux of $F_{^{26}\mathrm{Al}} = (6.3 \pm 2.8) \times 10^{-5}\,\mathrm{ph\,cm^{-2}\,s^{-1}}$ and accordingly an ^{26}Al mass of $M(^{26}\mathrm{Al}) = (5.1 \pm 2.2) \times 10^{-4}\,\mathrm{M_\odot}$ was attributed to the Per OB2 association. This is consistent with earlier studies using COMPTEL (Knödlseder 1997) and SPI observations (Bouchet et al. 2015). A comparison with population synthesis calculations, adapted to Per OB2, shows that this mass value is best modelled with stellar yields including the reduced explodability for high mass stars, LC18 (cf. Fig. 5.12). Assuming a higher explodability, e.g. S09, a 2–3 times larger mass would be expected. Therefore, the Per OB2 measurements confirm LC18.
A rather high total 1.8 MeV emission of $(3.6 \pm 0.4) \times 10^{-4}\,\mathrm{ph\,cm^{-2}\,s^{-1}}$ is measured from within a larger 30° radius in the Perseus region. This leads to the Perseus ^{26}Al puzzle: This large flux cannot be accounted for by a simple superposition of the three Perseus OB associations. Therefore, either a currently unnoticed strong foreground source is present, or a larger structure along the line of sight in the Local Arm creates this flux excess cumulatively.
An explanation would be the enhancement of wind yields due to binary interactions in the mass range $M_* \leq 25\,\mathrm{M_\odot}$. In Sec. 4.2.4, first modelling attempts of binary wind yields by Brinkman et al. (2019) were integrated into the population synthesis. The results showed no significant increase in yields due to these effects. However, the change in chemical composition of SN progenitors remains a crucial uncertainty in this respect.

Isotopic Mass and Galactic Distribution The crucial measurement for the determination of the Galactic ^{26}Al mass is the total 1.8 MeV emission of $F_{^{26}\mathrm{Al}} = (1.84 \pm 0.03) \times 10^{-3}\,\mathrm{ph\,cm^{-2}\,s^{-1}}$ measured from the entire sky with SPI in Sec. 3.4.3. This is consistently underestimated by PSYCO models. This can be attributed either to a generally underestimated ^{26}Al mass or a mismatched spatial configuration.
The isotopic mass scales linearly with the SFR (cf. Fig. 4.20). SFR $= 4\,\mathrm{M_\odot\,yr^{-1}}$ yields total ^{26}Al and ^{60}Fe masses in the range 0.9–1.8 $\mathrm{M_\odot}$ and 1.0–5.8 $\mathrm{M_\odot}$ respectively, depending on the underlying stellar evolution and explodability models. Only the most extreme model case in this respect with SFR $= 8\,\mathrm{M_\odot\,yr^{-1}}$ and explodabil-

ity S09 reaches the observed flux for certain galactic morphologies (cf. Fig. 4.26). This is a physically unreasonably high SFR for the Milky Way. Additionally, the fit of modelled full-sky distributions to SPI measurements suggests a total ^{26}Al mass of 1.7–1.9 $M_\odot$. In this case, accurately modelled intensity gradients are indicated by a scaling parameter of 1 (cf. Fig. 5.20). This mass range is also obtained by the investigation of the gamma-ray flux that originates from the inner Galaxy region within $|l| \leq 30°$ and $|b| \leq 10°$ (cf. Tab. 4.10 or Fig. A.6). This confirms the total Galactic ^{26}Al mass of $\sim 2\,M_\odot$, independent of the underlying assumptions of the SFR or stellar models. Therefore, the modelled, low flux is probably the result of a spatial configuration in the Milky Way which is on average not captured by the assumed spatial distributions.
A variety of morphological assumptions have been tested concerning the distribution of ^{26}Al and ^{60}Fe in the Milky Way (cf. Fig. 4.14 and Tab. 4.9). Certain model configurations produce a total flux similar to observations. The flux is scaled linearly with SFR (cf. Fig. 4.26 and Fig. 4.27). In observations, 16% of the entire 1.8 MeV gamma-ray flux originates from the inner Galaxy region (cf. Siegert 2017, and Sec. 3.4.3). This ratio varies in PSYCO models between 40% and 23% for central and spiral arm dominated galactic morphologies, respectively (cf. Sec. 4.4.3). On the one hand, this points to a spiral arm dominated distribution in the Milky Way. On the other hand, the observed, low ratio also points towards an additional strong local component at high latitudes or a particularly prominent Local Arm in the direction of the Galactic anti-centre. A bright spiral arm component in the Milky Way is supported by a general latitudinal asymmetry receiving the largest part from QIV, i.e. $-90° < l < 0°$ (Kretschmer et al. 2013; Bouchet et al. 2015). This is achieved by the inclusion of a prominent Sagittarius-Carina arm (cf. Fig. 4.29).
About 50% of the total ^{26}Al line flux originates from within a radius between 2.8–6.0 kpc. If strong foreground sources are present, this proportion can even increase up to 90%. This means that only a minor contribution is expected from the Galactic bulge region within ~ 2 kpc around the Galactic centre (cf. Fig. 4.28).
The best fitting parameters for describing the full-sky emission of the Milky Way by a homogeneous doubly exponential disk are scale radius of $r_0 = (5.81 \pm 0.64)$ kpc and scale height $z_0 = (0.77 \pm 0.17)$ kpc (cf. Fig. 5.16). A comparison with the MHD simulation by Fujimoto et al. (2018) and the large number of PSYCO models shows that this large scale height is mainly due to prominent foreground emission at high latitudes. Beyond that, a more detailed analysis of the galactic morphology is possible with the new approach of scale height decomposition in conjunction with PSYCO models. The observed scale height distribution reveals that a pronounced and highly contrasted granularity is characteristic for the ^{26}Al sky (cf. Fig. 5.17). Thus, a doubly exponential disk constitutes a physically inaccurate representation. Instead, the model comparisons point to a small scale height in the order of 0.1 kpc, which in some regions is overlaid by nearby emission at large scale heights up to 5 kpc. This is supported by direct fits of PSYCO models to SPI data. These, on average, deteriorate for increasing scale heights and with identical radial distributions (cf. Fig. 5.19). Dominant nearby components occur preferentially in the direction of the Galactic centre around $|l| < 60°$. This gives rise to a characteristically bimodal scale height spectrum of the Milky Way peaking around 0.1 kpc (cf. Fig. 5.18). This is best reflected by a prominent spiral structure, which causes a high contrast between extended emission from the arms and the gap between them (cf. Fig. 5.21). In contrast, a mainly exponential morphology produces a flat scale height distribution. No predominance of the Sagittarius-Carina arm is found. Instead, a significant

contribution of the 1.8 MeV flux also originates also from the Local Arm.
The direct comparison of 180000 PSYCO models to measurements, their scale height distributions, and their scale height frequency spectra show that the radial morphology GM00 (cf. upper panel in Fig. 4.14) best describes the 1.8 MeV gamma-ray measurements from the entire sky (cf. Sec. 5.4.3). Its main characteristics are an equal emphasis on the two closest spiral arms and the absence of strong emission from the Galactic bulge region (cf. upper panel in Fig. 4.28). For an accurate description of the SPI data, a characteristic configuration of foreground sources is required to account for the measured flux from high latitudes.

Superbubble Size and Merging PSYCO models based on explodability LC18 describe the 1.8 MeV SPI data on average better than the same models using a different explodability (cf. Fig. 5.19). This is correlated with a tendency to fill superbubbles with the bulk of ^{26}Al at later times. Therefore, larger bubbles appear brighter in this case. The average diameter of superbubble structures filled with ^{26}Al in the Milky Way is determined to > 300 pc. This is in agreement with the distribution of ^{26}Al around Per OB2, which is found within a maximum likelihood radius of (160 ± 60) pc (cf. Sec 5.11). Regarding the age of around 6 Myr of Per OB2, this is slightly larger than expected from the approximation for spherical expansion in Eq. 4.16 (cf. also Fig. 4.16).
The underestimation in models of both the 1.8 MeV local foreground components and the average bubble size indicates that the actual local star formation density in the vicinity of the Solar System is larger and that it occurs overall more clustered than currently assumed. This is also supported by the full-sky morphology of the Milky Way ^{26}Al emission, which appears more coarse-grained than suggested in the simulation by Fujimoto et al. (2018). Clustered star formation would release kinetic energy through stellar feedback processes spatially more concentrated. This would increase the average size of the cavities. Such a mechanism could also account for the more salient granularity in the observed scale height distribution of the Milky Way.
The increased bubble size also points to a frequent merging of superbubble structures. This was already suggested e.g. by Krause et al. (2013, 2015), or Rodgers-Lee et al. (2019). Shells break up frequently and open up into previously blown cavities. Thus, they grow larger as a consequence of the feedback contributions from multiple star groups. This is supported by the fact that ^{26}Al is found in a rather turbulent state in Per OB2 with a velocity dispersion of $(140 \pm 60)\,\mathrm{km\,s^{-1}}$ and an indication for an overall blue-shift (cf. Sec. 5.3.2). This indicates material streaming freely in the preferred direction of a lower-density ambient medium and away from dense molecular gas structures.

The Solar System as Galactic Outlier? Considering the history of astrophysics, it is undoubtedly a delicate hypothesis to suggest a spatially or temporally special position of the Solar System. However, the gamma-ray measurements of ^{26}Al indicate both. In this respect, the crucial results from PSYCO models and the MHD simulation by Fujimoto et al. (2018) together with 1.8 MeV SPI observations are: a consistently underestimated total 1.8 MeV flux, an omitted prominent emission at very high latitudes, an underestimated ^{60}Fe/^{26}Al gamma-ray flux ratio, a morphological deviation from the overall scale height distribution as well as from the high bimodal contrast

in the respective scale height frequency spectrum. Although these properties are missed by the modelled galactic average, they are met for certain outlier configurations (cf. Fig. 4.32, Fig. 5.26, and Fig. 5.28).
The comparison of the MHD simulation by Fujimoto et al. (2018) with SPI shows convergence for a spatial configuration in the simulation where the observer is situated near or even inside prominent ^{26}Al-filled bubbles (cf. Pleintinger et al. 2019, or Sec. 5.4.2). In addition to such a spatial alignment, the low ^{60}Fe/^{26}Al gamma-ray flux ratio compared to observations points also to a peculiar temporal configuration. On the basis of current stellar nucleosynthesis calculations, this can generally not be obtained by the galactic average but only by a nearby young association that is rich in ^{26}Al due to very-massive star winds and poor in ^{60}Fe due to an absence of SN ejecta.
A serendipitous example of such a case is found by the 360° rotation of a modelled galaxy shown in Fig. 4.30. Here, the agreement of modelled and observed ^{26}Al and ^{60}Fe flux coincides with the direct passage through a superbubble filled with ^{26}Al by an only 6.9 Myr old stellar group (cf. also Fig. 4.31). If the observer is situated directly inside such an ^{26}Al-filled superbubble, the contribution due to this omnidirectional source can reach up to $\sim 85\%$ of the entire line flux. Such a configuration generally agrees with the picture of the the Solar System as indicated by isotopic abundance studies of ^{60}Fe signatures in deep-sea sediments on the Earth by Wallner et al. (2016, cf. Fig. 3.1). This study shows that material enriched with ^{60}Fe swept over the Solar System about 3 Myr and 6 Myr ago. According to population synthesis calculations, ^{60}Fe ejection within a stellar association starts about 3–8 Myr after its formation. Assuming an additional propagation duration on the order of ~ 1 Myr, measurements of the deep-sea crust would be compatible with the contribution from a 10–15 Myr old association. The ^{60}Fe/^{26}Al gamma-ray flux ratio from such a group would be in agreement with the observed Milky Way value assuming LC18 evolution models (cf. Fig. 4.6 and Sec. 4.2.3). This means that gamma-ray measurements would be compatible with the hypothesis that the Solar System was overrun by a chemically enriched shell in the past and is currently located inside a feedback-driven superbubble enriched in ^{26}Al.
For such a configuration, an omnidirectional emission of 1.8 MeV gamma-ray photons would be expected. Since the coded-mask detection principle of SPI relies on rather small-scale intensity gradients, a homogeneous emission across the entire sky is particularly difficult to measure. However, an indirect signature of such a rather diffuse foreground emission might be found in the scale height distribution of the Milky Way (cf. Fig. 5.17). The particularly large scale heights near $l \approx 60°$ and $l \approx 300°$ can not be attributed unambiguously to known foreground sites. Instead, these scale heights could arise because the galaxy-wide emission concentrated in the disk is particularly weak along the spiral arm gaps in these directions. This in turn leads to a predominance of an omnidirectional emission component especially in these areas.
In order to quantify the chance occurrence of such a local configuration, it can be assigned a probability of on the order of 10^{-2}–10^{-3} within the PSYCO framework (cf. Fig. 4.32). Since there is currently only one observable case, the Milky Way, this is not ultimately assessable. These results should therefore generally only be interpreted with caution and validated with next generation telescopes.

Outlook Gamma-ray measurements constitute an essential basis for empirical research about nucleosynthesis feedback in the Milky Way. The strong dependence on the underlying single star yield calculations emphasises the importance of further studies in the field of massive-star evolution (Higgins & Vink 2019; Szécsi et al. 2020). It has been shown that especially their explosion mechanisms are currently a research field of crucial importance for providing a coherent picture of nucleosynthesis feedback and galactic chemical evolution (Burrows et al. 2019; Suwa et al. 2019; Ebinger et al. 2019, 2020; Agrawal et al. 2020; Chan et al. 2020). There are many indications that binary interactions and their implications for SN progenitors play a decisive role in this respect. While further investigations of the binary wind yields, such as Brinkman et al. (2019), are necessary in order to obtain a comprehensive picture, the population synthesis calculations in this work show that the direct wind enhancement is of secondary importance compared to the general alteration of SN progenitor properties. Recent studies on this field show that the stripping of stellar envelopes in close binary systems can significantly change the evolutionary path of a star as bare He-core and respectively alter the explosive nucleosynthesis yields (Prentice et al. 2019; Woosley 2019; Ertl et al. 2020; Götberg et al. 2020). In the field of binary population synthesis (e.g. Chrimes et al. 2020; Woosley et al. 2020; Mandel et al. 2020; Patton & Sukhbold 2020), an important and promising future effort is to establish an adequate mapping of stripped He-core masses and their respective explosion yields onto current single star evolution models. This will adjust the calculations for altered terminal phases due to binary interactions.
Superbubble dynamics and in particular their merging and mixing properties have been shown to be decisive for the large-scale distribution of nucleosynthesis ejecta. To study these complex processes in detail, elaborate MHD simulations are indispensable (cf. e.g. Rodgers-Lee et al. 2019; Beniamini & Hotokezaka 2020; Fujimoto et al. 2018, 2019, 2020; Krause et al. 2020). Since these are also very expensive and difficult to compare with measured gamma-ray data, a combined approach with semi-analytic models such as PSYCO is suggested in order to make effective scientific use of them.
The chemical history of the Solar System is not entirely understood, but continues to be an intriguing field of research (cf. eg. Breitschwerdt et al. 2016; Fields et al. 2019; Fimiani et al. 2016; Hyde & Pecaut 2018; Ludwig et al. 2016; Lugaro et al. 2018; Melott et al. 2017; Melott & Thomas 2019; Schulreich et al. 2017, 2018; Wallner et al. 2016). Future cosmic gamma-ray measurements will be an essential part within a consistent framework of multi-messenger observations. An important aspect will be to measure omnidirectional emission as a potential consequence of direct embedding of the Solar System in an ^{26}Al-filled superbubble. This is difficult with the current coded-mask instrument SPI. A possible signature of such an emission could be obtained by occultation studies using passages of the Earth or the Moon through the field of view. Assuming a flux of $10^{-3}\,\mathrm{ph\,cm^{-2}\,s^{-1}}$, as could be expected from a surrounding $\sim 10\,\mathrm{Myr}$ young and therefore about 100 pc sized bubble, SPI would be able to detect such a contribution by 4 Ms of occultation observations. In 18 yr of the INTEGRAL mission, only 0.26 Ms had been devoted to Earth observations, so that such an endeavour seems out of reach. The detection principle of a Compton telescope with a larger field of view would have less difficulties in measuring particularly such an omnidirectional source, which would therefore be a suitable technology for a future instrument investigating such a phenomenon. Solutions to these issues beyond the results found in this thesis thus point towards scientifically rich measurements with future gamma-ray telescopes.

6 Summary

This thesis was devoted to the general research question: How does nucleosynthesis feedback from massive star groups affect the chemical evolution of the Milky Way and the Solar System? In order to assess this question, on the empirical side, measurements of the cosmic gamma-ray emission of decaying ^{26}Al in the Milky Way were utilised through measurements with INTEGRAL/SPI. On the theoretical side, a galactic population synthesis model, PSYCO, for the large-scale impacts of stellar nucleosynthesis feedback was developed. These two components were finally combined in a newly devised comparison in order to exploit them as fully as possible for studying stellar feedback from massive star groups and their nucleosynthesis implications in the Galaxy.

The hierarchical process of galactic chemical enrichment was investigated observationally on the three essential spatial scales characterising the cosmic Cycle of Matter in our Galaxy to obtain a complete experimental picture. This included measurements of the nuclear 1.8 MeV gamma-ray line from the individual stellar source γ^2 Velorum, the star group Perseus OB2, and the Milky Way as a whole. For the individual source, an upper flux limit of $1.7 \times 10^{-5}\,\mathrm{ph\,cm^{-2}\,s^{-1}}$ was obtained, fully consistent with model calculations. The Perseus OB2 group was associated with an ^{26}Al mass of $(5.1 \pm 2.2) \times 10^{-4}\,\mathrm{M_\odot}$. In combination with population synthesis calculations, this provides an important constraint for stellar evolution models, indicating reduced or inhibited SN explosions for stars with masses $M_* \geq 25\,\mathrm{M_\odot}$. The currently most complete use of the SPI data archive including double detector events with 17.5 yr of full-sky observations yielded an ^{26}Al line flux of $(1.84 \pm 0.03) \times 10^{-3}\,\mathrm{ph\,cm^{-2}\,s^{-1}}$. This is the most precise measurement of the ^{26}Al line so far. Overall, a coherent empirical approach to the connection between the nuclear fusion reactions occurring within massive stars and the subsequent processing of the respective products on galactic scales was achieved.

To investigate this very process from a theoretical perspective, it was modelled bottom-up with PSYCO. In this framework, simulations of single stars are utilised in population synthesis calculations of massive star groups to model the spatial aspects of nucleosynthesis ejecta in an entire galaxy. This constitutes a versatile and flexible modelling approach for the specific purpose of determining nucleosynthesis properties of the Milky Way in conjunction with gamma-ray observations. Consistent modelling results were obtained for a global SNR of 1.4 ± 1.1 per century and a Galactic SFR of $\sim 4\,\mathrm{M_\odot\,yr^{-1}}$, which is larger than the current canonical value of the Milky Way.

The general epistemological challenge in astrophysics concerning the comparability of generic theoretical models with unique empirical data was assessed by translating both components into a common parameter space. By determining the characteristic exponential scale height as a function of Galactic longitude, a coherent analysis was performed in data and model space. On that basis, the two closest spiral arms, the Sagittarius-Carina Arm and the Local Arm, have been identified as the major Galactic contributors to the 1.8 MeV full-sky emission. Additionally, a prominent

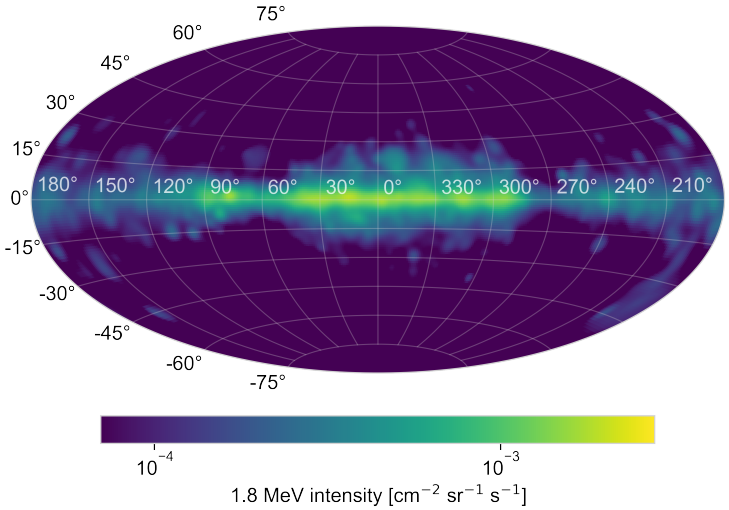

Figure 6.1: Best-fitting composite full-sky map of the 1.809 MeV emission from ^{26}Al decay modelled with PSYCO. It is composed of the average of the 49 best-fitting model instantiations including the known foreground associations Cygnus, Sco-Cen, and Orion. A Gaussian filter of 2° width was applied to adjust the original map to the spatial resolution of SPI. The modelling procedure underlying this map was described in detail in Sec. 5.4.3.

^{26}Al foreground source surrounding the Solar System was disentangled from the overall Galactic emission. Taking this foreground contamination into account, the entire Galactic mass of ^{26}Al was estimated in the range of $(1.4 \pm 0.5)\,M_\odot$. For ^{60}Fe, a Galactic mass in the range 3.5–6.0 $M_\odot$ was inferred. The newly developed ansatz of scale height decomposition was therefore effectively applied as a functional and scientifically fruitful approach in order to bridge the conceptional gap between detailed simulations and state-of-the-art gamma-ray observations.

Based on the extensive exploitation of measurements and models of radioactivity in the Galaxy, this thesis is integrated in the larger endeavour of understanding how the chemical composition of the Milky Way and the Solar System came about. From the specific perspective of gamma-ray astrophysics, this work contributed to integrate the theory of nucleosynthesis in stars into a coherent galaxy-wide picture. This is represented in Fig. 6.1. It depicts the full-sky map obtained within the PSYCO framework which best describes the SPI data. The similarities with the reconstructed image by COMPTEL in Fig. 1.1 shown in the introduction can therefore be associated with detailed astrophysical properties. This includes essential stellar evolution characteristics, their linkage to massive star cluster dynamics, a variety of overall galactic parameters, and the underlying three-dimensional distribution. Besides a pronounced nearby spiral-arm structure and the absence of intense 1.8 MeV emission from the Galactic centre, the general spatial distribution of nucleosynthesis ejecta was confirmed to be associated with superbubble structures, the average extent of which appears larger than usually assumed. Accordingly, ^{26}Al is found to preferentially expand in cavities of > 300 pc and exhibits an overall turbulent state which is confirmed through Doppler broadening measurements. This points to a highly dynamic state of the ISM which leads to sequentially triggered and clustered star formation as well as frequent merging of feedback-driven interstellar bubbles. Altogether, the observed 1.8 MeV map contains crucial details about the geometry of massive star feedback in the Milky Way, some of which were uncovered throughout this thesis.

Concerning the particular chemical composition of the Solar System, indications

have been found that it is situated directly inside an ^{26}Al-filled superbubble. This means that the Solar System is currently directly affected by nearby massive-star activity and therefore chemically enriched in fresh and radioactive nucleosynthesis products compared to the Galactic average. This study demonstrates the importance of exploiting measurements of cosmic gamma-rays, and in particular of ^{26}Al, in order to comprehend the evolution of matter in the Milky Way and the Solar System. In order to confirm the special position of the latter and its embedding inside a radioactive bubble, this readily underlines the necessity of future gamma-ray telescope missions.

In a figurative sense, the measurements in this thesis may help to determine the place of the Solar System, the Earth, and finally of humanity in the overarching cosmic Cycle of Matter. However, this is not the place to conclusively clarify if this helps to alleviate the cosmological one of the narcissistic wounds of humanity. The field of tension in which man finds himself undoubtedly persists: on the one hand to look alienated at objective nature and on the other hand to be nevertheless at home in it. But perhaps it is precisely the experience of this tension that drives an astonished engagement with nature within the natural sciences. From this perspective it is at least certainly possible also for an astrophysicist to call the Galaxy by conviction *our* Milky Way.

A Additional Figures and Tables

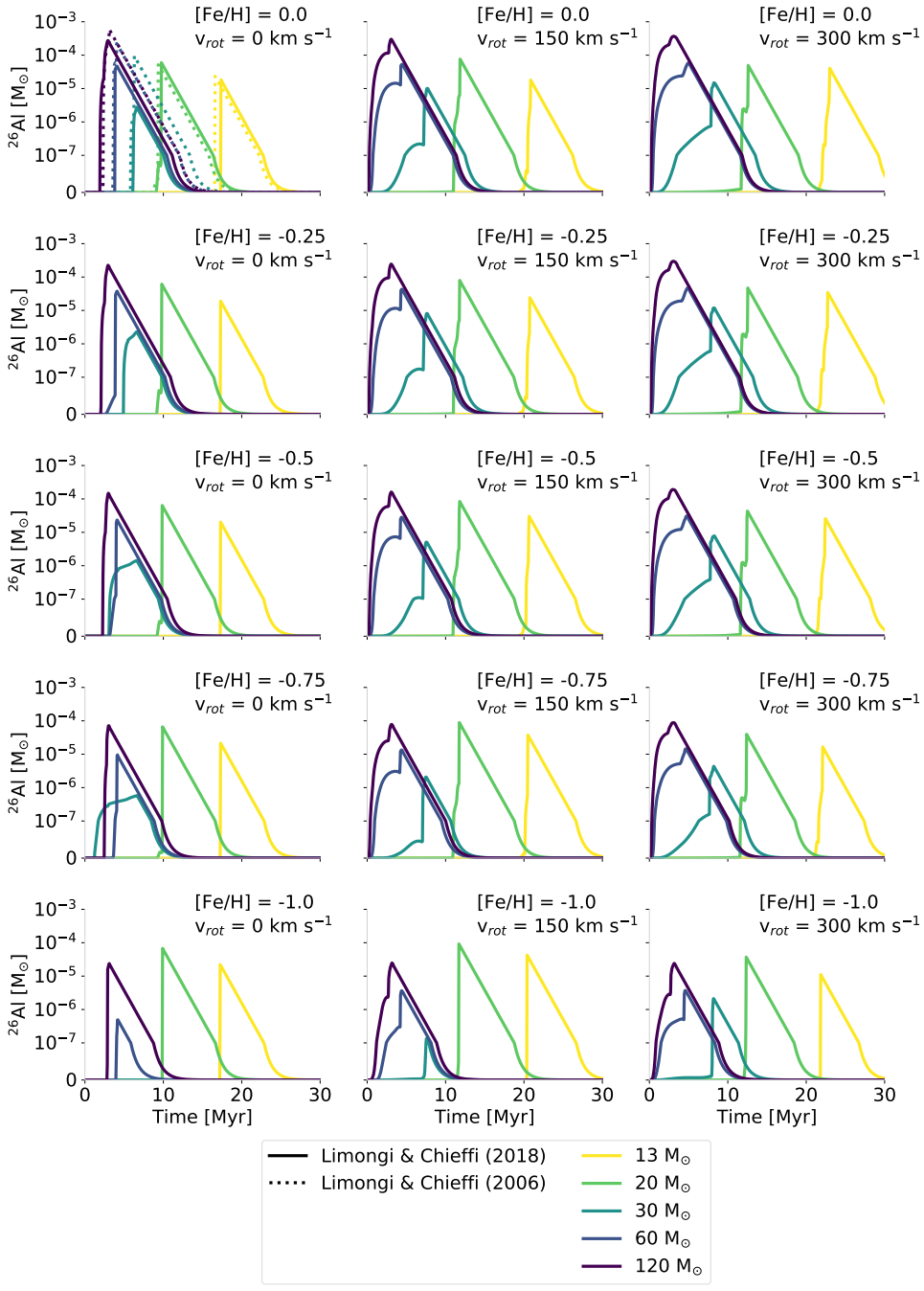

Figure A.1: ^{26}Al nucleosynthesis feedback profiles from LC18 and LC06 for individual stars with different metallicities and rotational velocities.

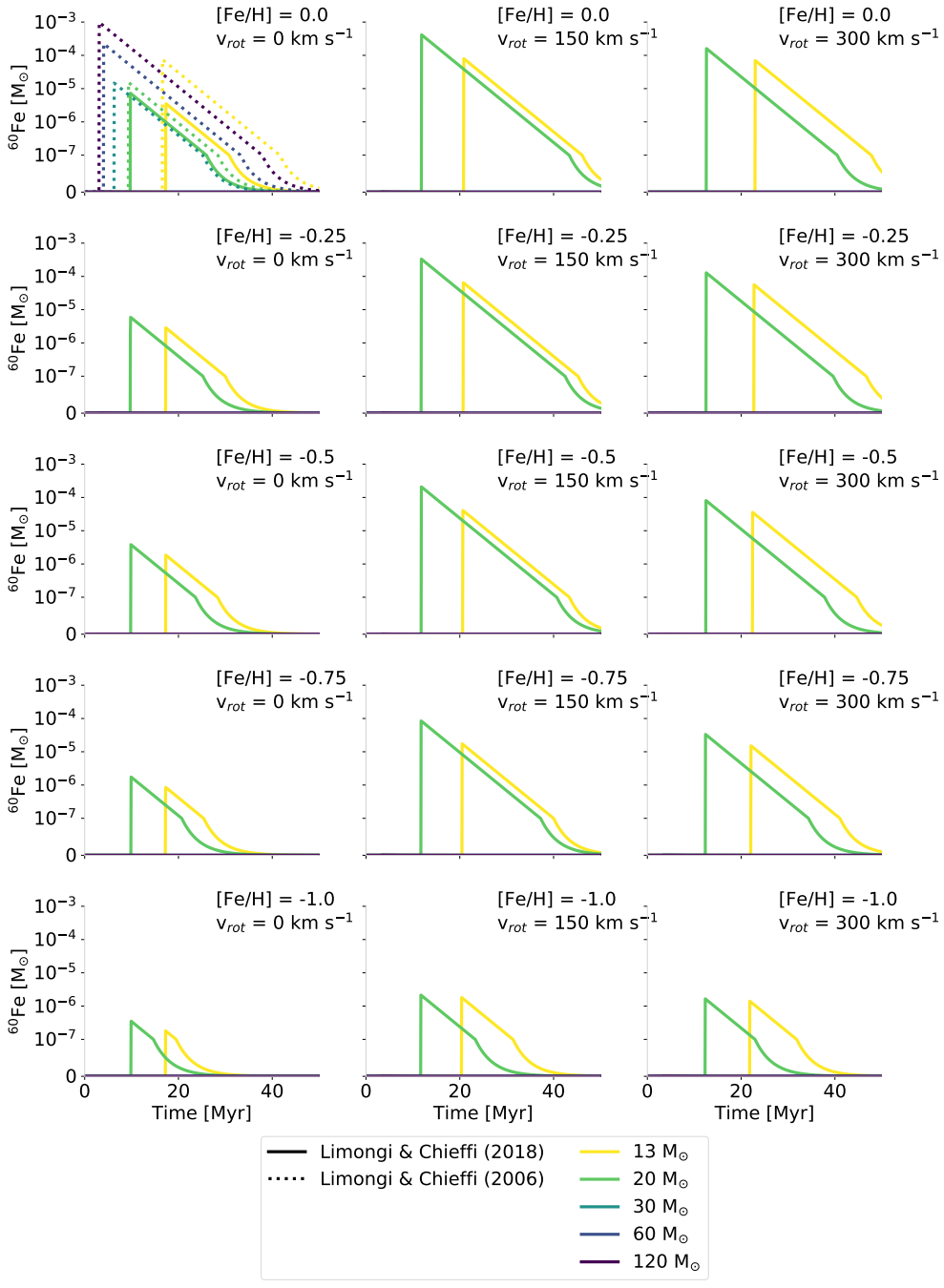

Figure A.2: ^{60}Fe nucleosynthesis feedback profiles from LC18 and LC06 for individual stars different metallicities and rotational velocities.

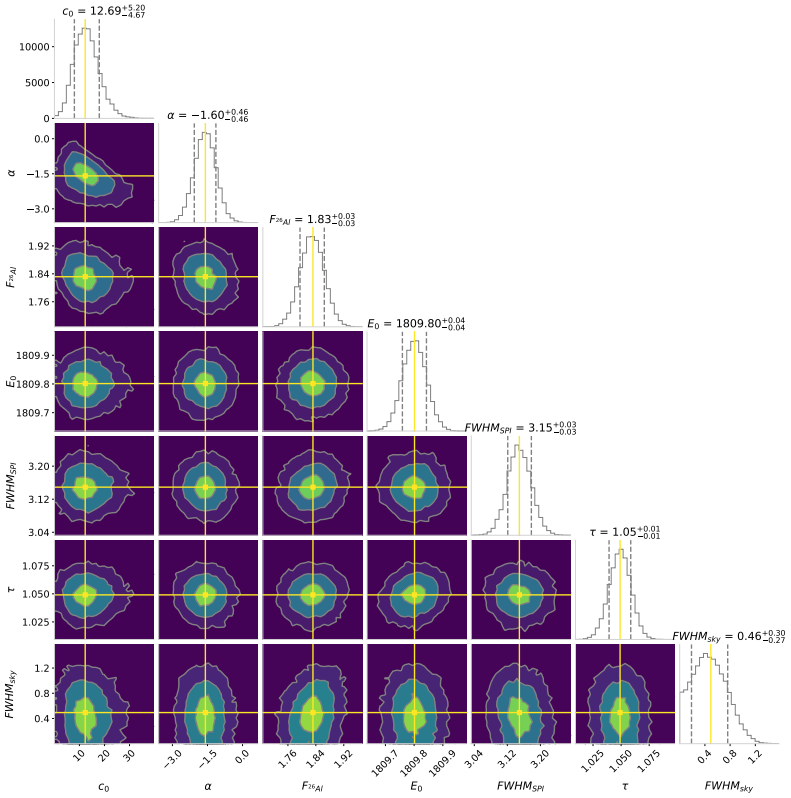

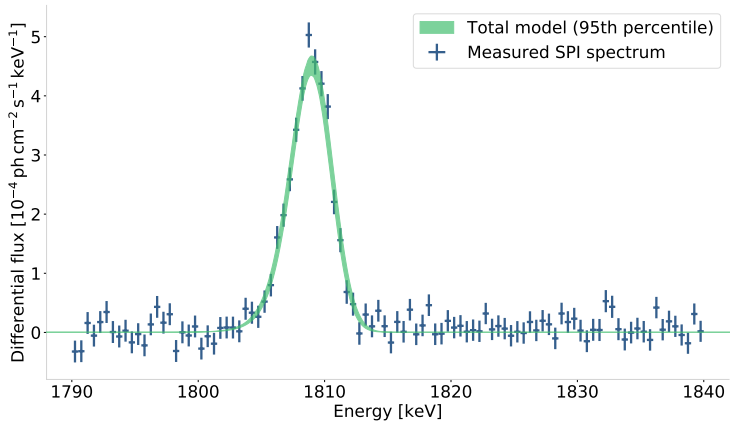

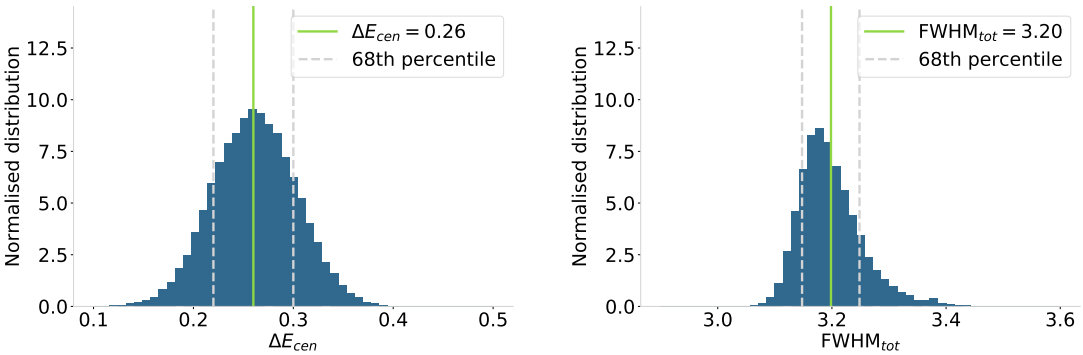

Figure A.3: Spectral MCMC fit results for the full-sky emission of ^{26}Al at 1809 keV measured with SPI single events separately. *Upper:* Equivalent to Fig. 3.24. *Middle:* Equivalent to Fig. 3.25. *Lower:* Equivalent to Fig. 3.26.

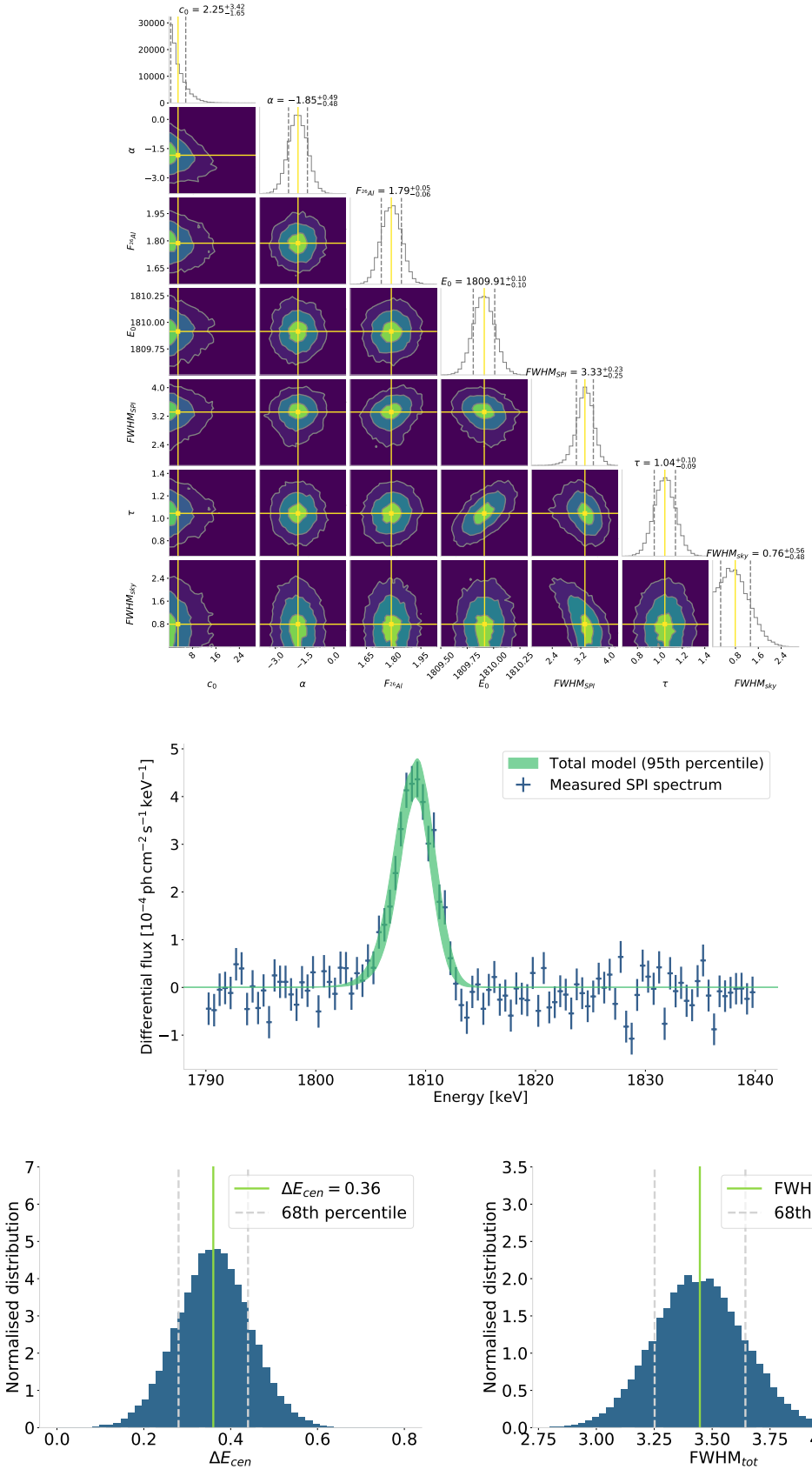

Figure A.4: Spectral MCMC fit results for the full-sky emission of ^{26}Al at 1809 keV measured with SPI double events separately. *Upper:* Equivalent to Fig. 3.24. *Middle:* Equivalent to Fig. 3.25. *Lower:* Equivalent to Fig. 3.26.

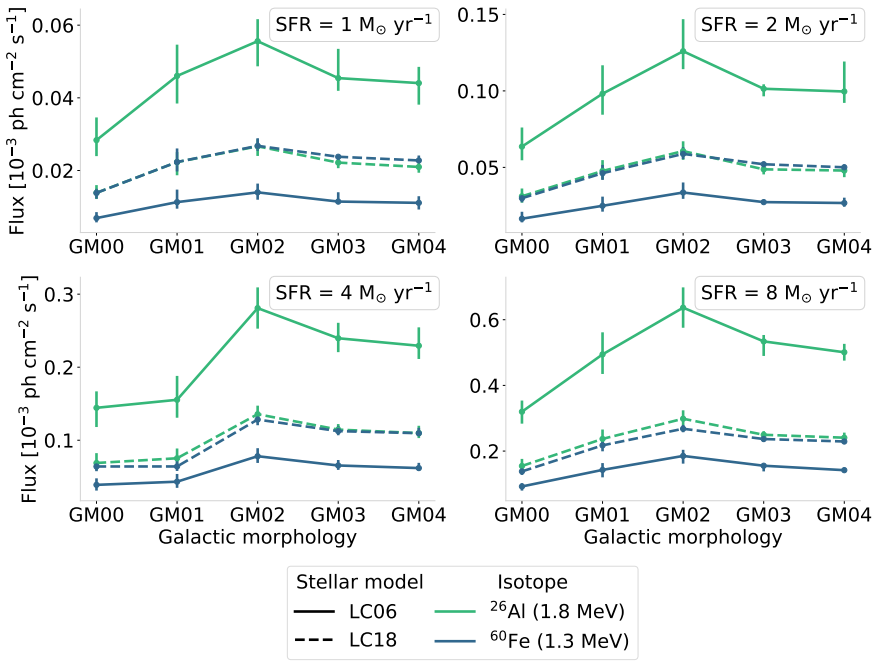

Figure A.5: Same as Fig. 4.26 for consideration of only the inner galactic region with $|l| \leq 30°$ and $|b| \leq 10°$.

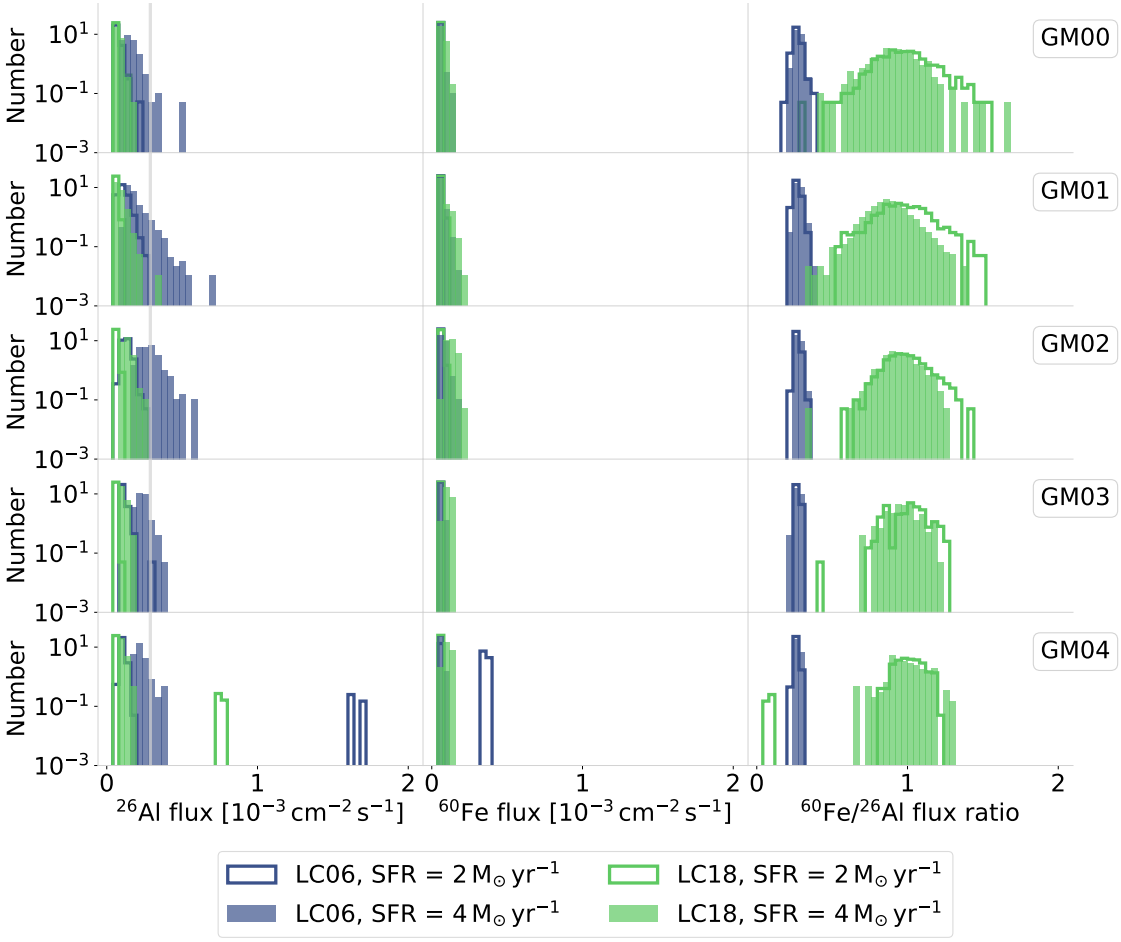

Figure A.6: Same as Fig. 4.32 for consideration of only the inner galactic region with $|l| \leq 30°$ and $|b| \leq 10°$. The observational flux value of ^{26}Al $F_{26} = (2.89 \pm 0.07) \times 10^{-4}$ ph cm^{-2} s^{-1}is adopted from Siegert (2017) and shown in *grey* in the left panel.

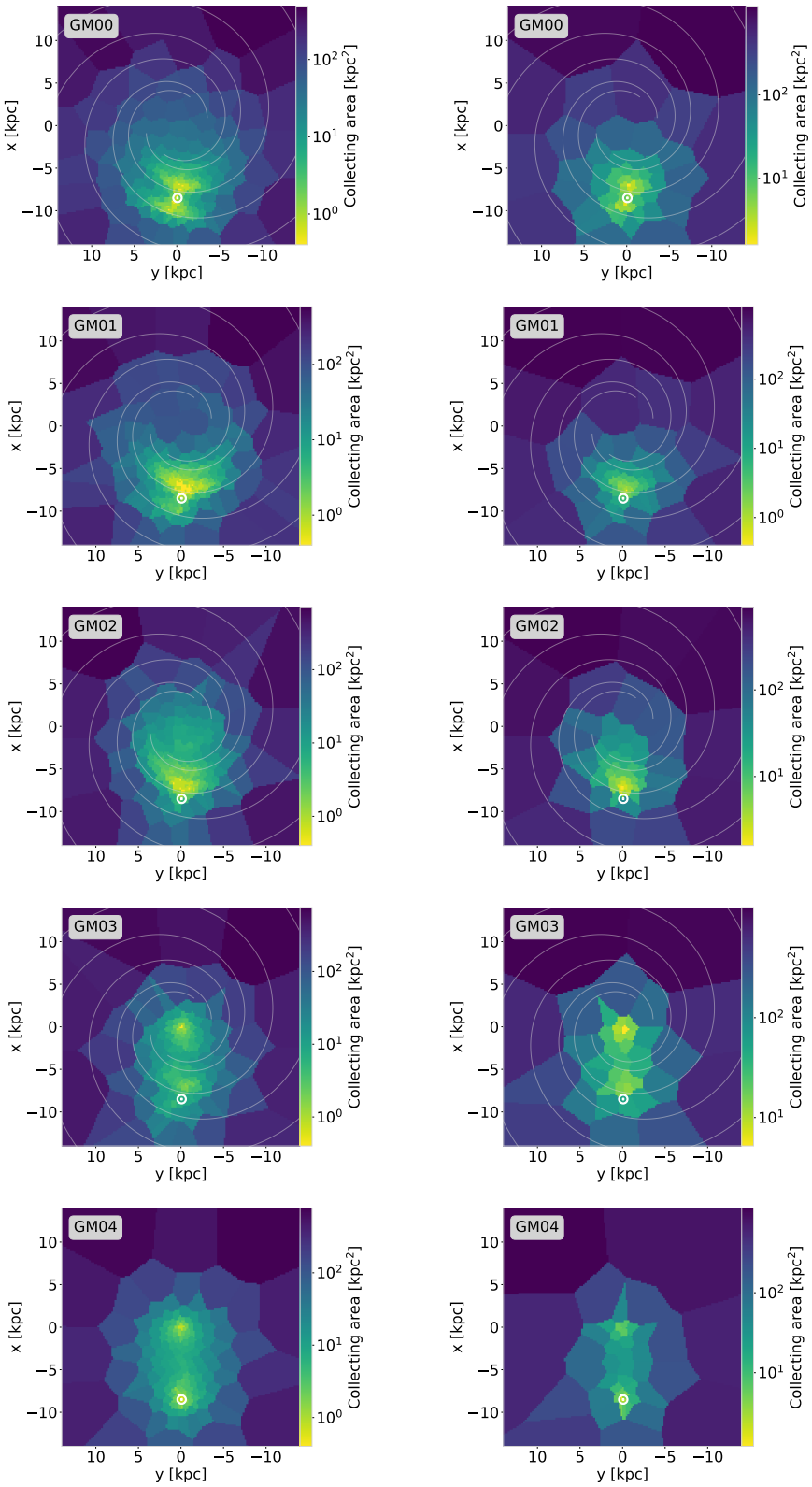

Figure A.7: Same as Fig. 4.28 for SFR $= 2\,\mathrm{M}_\odot\,\mathrm{yr}^{-1}$, which corresponds to a total mass of $(0.81 \pm 0.03)\,\mathrm{M}_\odot$ and $(1.80 \pm 0.09)\,\mathrm{M}_\odot$ of ^{26}Al and ^{60}Fe respectively.

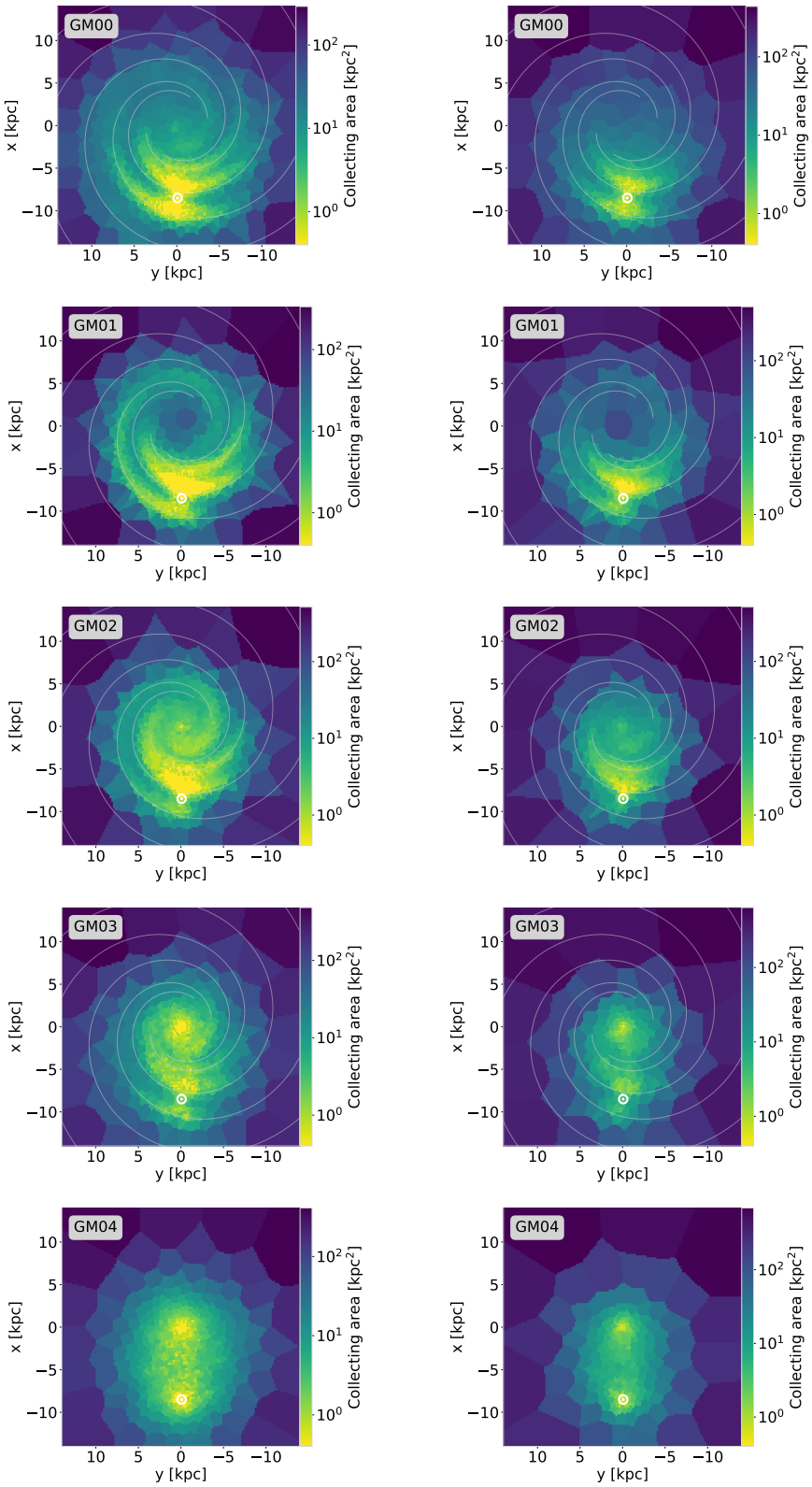

Figure A.8: Same as Fig. 4.28 for SFR $= 8\,\mathrm{M}_\odot\,\mathrm{yr}^{-1}$, which corresponds to a total mass of $(4.00 \pm 0.12)\,\mathrm{M}_\odot$ and $(9.64 \pm 0.35)\,\mathrm{M}_\odot$ of ^{26}Al and ^{60}Fe respectively.

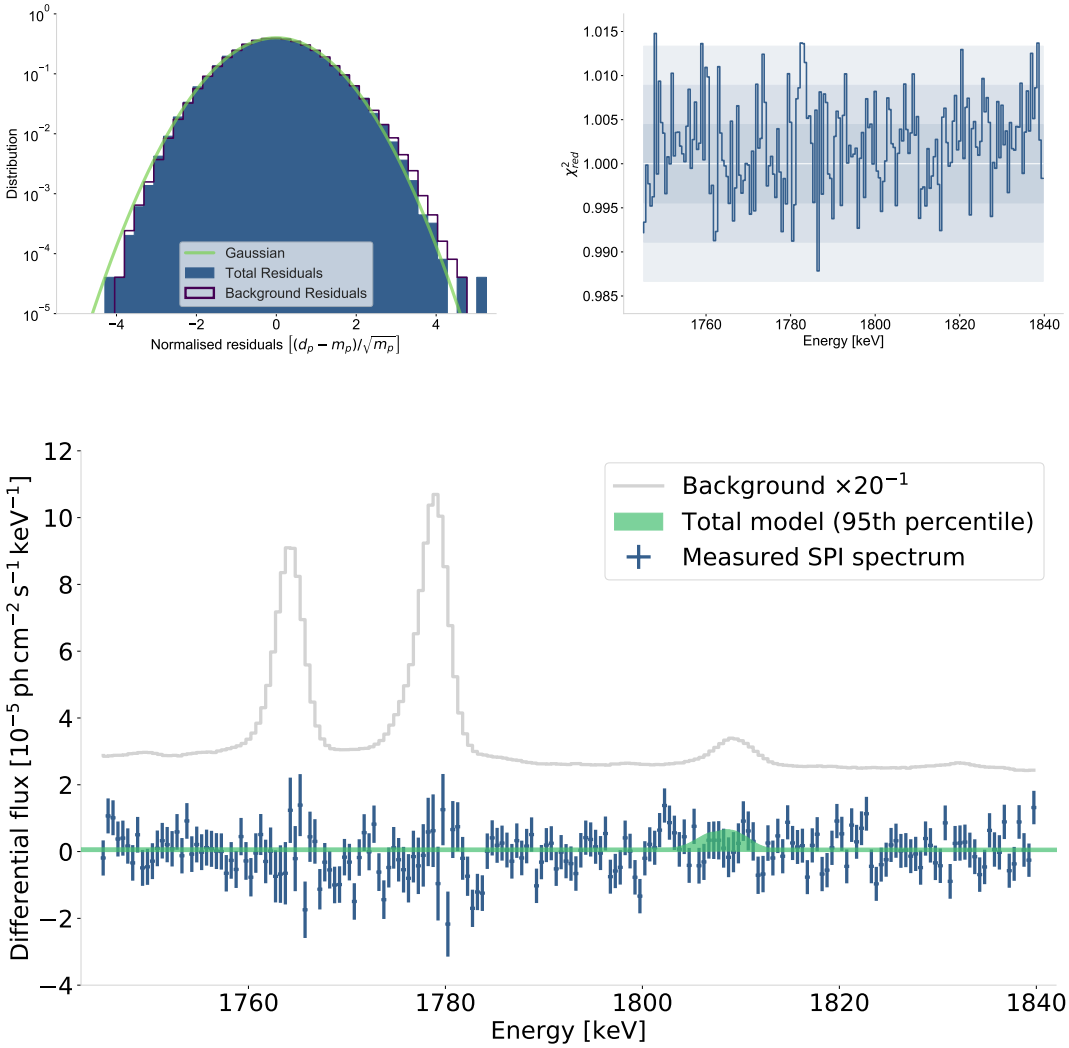

Figure A.9: SPI data analysis results of the ^{26}Al emission from γ^2 Velorum for a combined treatment of single and double events. *Top left:* Residuals of the background model overplotted by a normal distribution with width $\sigma = 1$. *Top right:* Model performance measured by χ^2_{red} for each energy bin for the entire SPI camera. The ideal value of $\chi^2_{\mathrm{red}} = 1$ is shown as white line, with 1σ, 2σ, and 3σ uncertainty intervals as shaded grey regions. All points lie within the 3σ band. *Lower:* SPI spectrum (*blue* data points) of the ^{26}Al emission at 1809 keV from γ^2 Velorum for a combined treatment of single and double events. The best-fitting photon model is shown in a band of the 2σ confidence interval in *green*. It represents a degraded Gaussian line profile on top of a power-law continuum (cf. Eq. 3.28). The posterior distributions of individual fit parameters are shown in Fig. A.10. The spectrum shows a non-detection of the ^{26}Al signal at 1.8 MeV with a 2σ upper flux limit of 2.3×10^{-5} ph cm^{-2} s^{-1}.

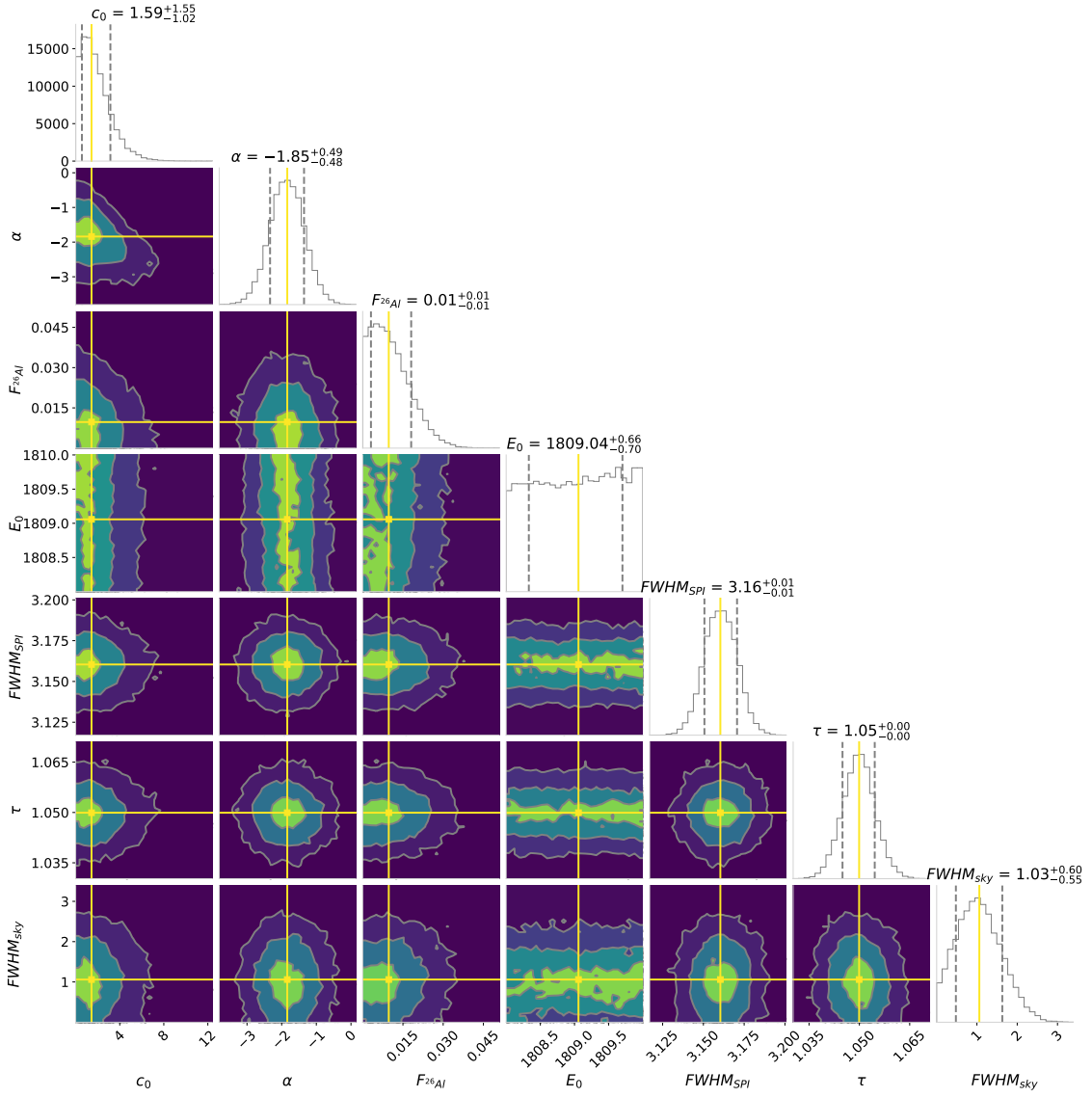

Figure A.10: Posterior distributions of spectral fit parameters describing the ^{26}Al signal at 1809 keV from γ^2 Velorum as measured with SPI according to the photon model in Eq. 3.28. The underlying data are obtained by a combined treatment of single and double events. The mean value along each axis is shown in *yellow*. Histograms on the diagonal show marginalised probability distributions along the respective axis with 86th percentiles marked by dashed lines. The respective spectrum is shown in Fig. A.9.

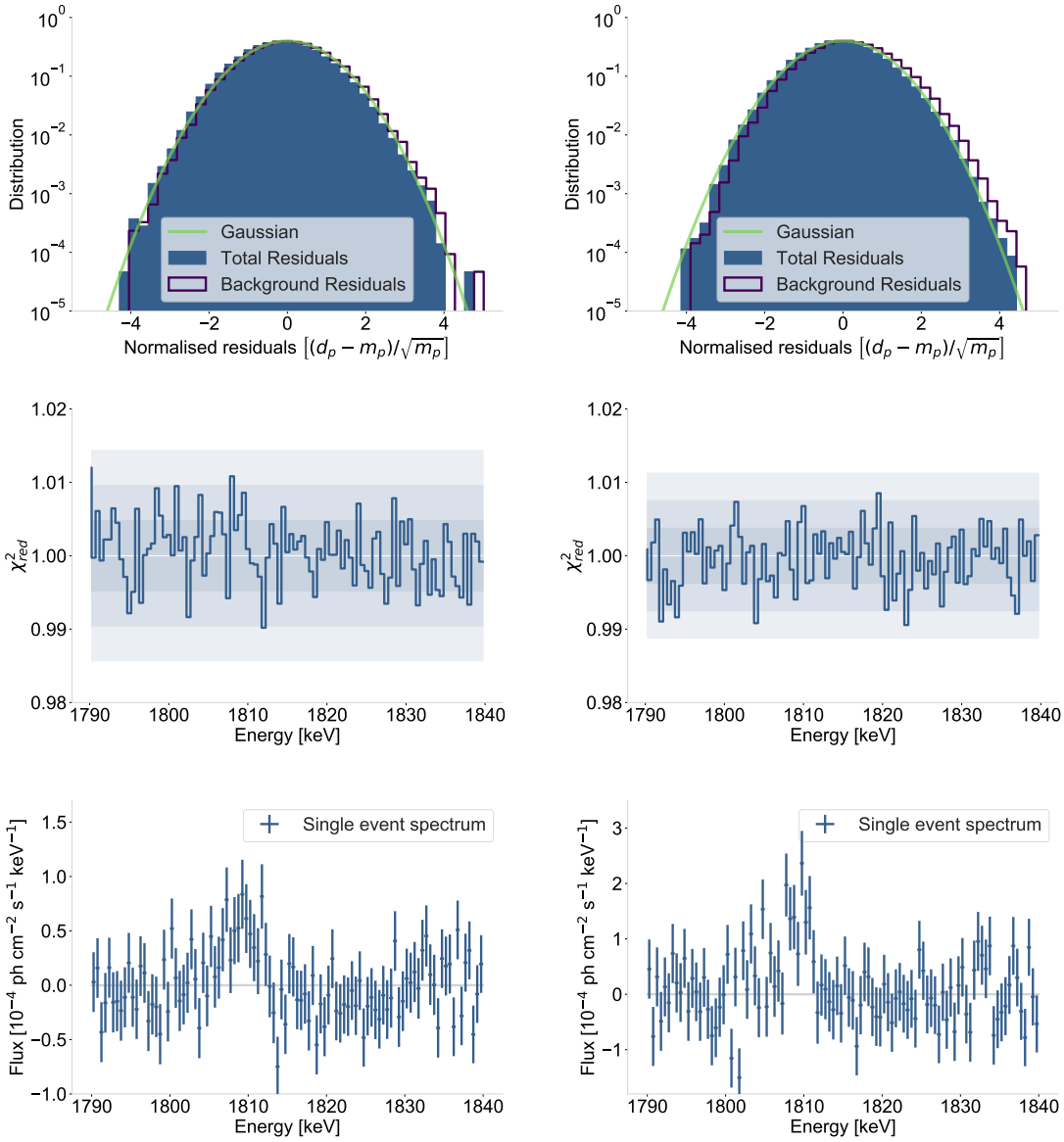

Figure A.11: SPI data analysis results of the ^{26}Al emission from the Perseus region for fitting a 30° radius cut-out of the SPI ^{26}Al map (Bouchet et al. 2015) to single (*left*) and double events (*right*) separately. *Top:* Residuals of the background model overplotted by a normal distribution with width $\sigma = 1$. *Middle:* Model performance measured by χ^2_{red} for each energy bin for the entire SPI camera. The ideal value of $\chi^2_{\mathrm{red}} = 1$ is shown as white line, with 1σ, 2σ, and 3σ uncertainty intervals as shaded grey regions. All points lie within the 3σ band. *Bottom:* Resulting SPI spectra from the amplitude of the SPI map region fitted in each 0.5 keV wide energy bin in the range 1745–1840 keV. A *grey* dashed line guides the eye to zero flux.

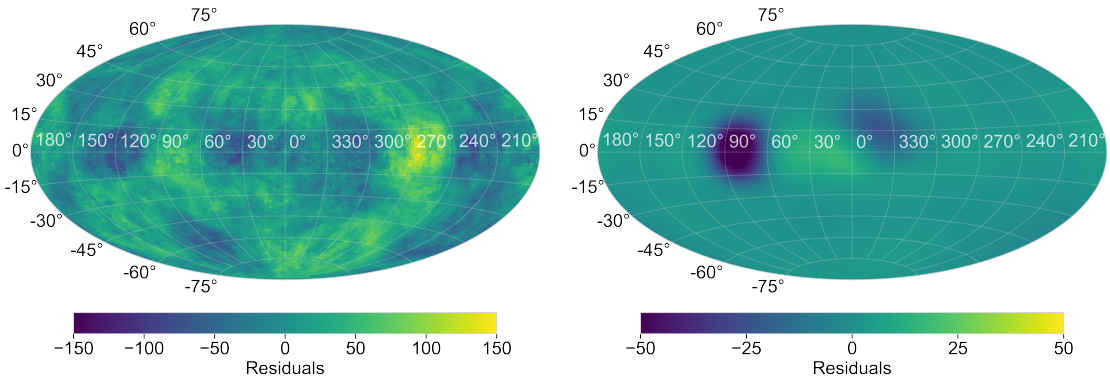

Figure A.12: *Left:* Backprojection of the residuals obtained from the best fitting composite PSYCO model (cf. Fig. 5.23) without the inclusion of known knowns onto the celestial sphere. Residuals are given in units of number of photons. *Right:* Relative change in backprojected residuals if known knowns (cf. Tab. 4.7) are added to the map.

B Additional Equations and Derivations

IMF Cutoff Mass

In order to computationally accelerate the optimal sampling process described in Sec. 4.2.1, the mass M_{cut} below a physically reasonable cutoff mass M_{cutoff} can be waived in the iterative discretisation according to Eq. 4.7. In the following, the calculation of M_{cut} is given for different shapes of the stellar IMF.

Salpeter (1955)

The IMF by Salpeter (1955) was defined in Eq. 2.4. For $M \in [M_{\text{min}}, M_{\text{max}}]$ and normalisation constant A, it yields a total stellar mass

$$M_{\text{tot}} = A \int_{M_{\text{min}}}^{M_{\text{max}}} M \; \xi_{\text{S55}}(M) \; dM = \frac{A}{2-\alpha} \left(M_{\text{max}}^{2-\alpha} - M_{\text{min}}^{2-\alpha} \right).$$

The proportion below a certain mass threshold $M_{\text{min}} < M_{\text{cutoff}} < M_{\text{max}}$ is

$$M_{\text{cut}} = A \int_{M_{\text{min}}}^{\text{cutoff}} M \; \xi_{\text{S55}}(M) \; dM = \frac{M_{\text{tot}}}{(M_{\text{max}}^{2-\alpha} - M_{\text{min}}^{2-\alpha})} \left({M_{\text{cutoff}}}^{2-\alpha} - M_{\text{min}} \right).$$

Kroupa (2001)

The IMF by Kroupa (2001) was defined in Eq. 2.5. The three mass regimes are characterised by power-law index $\gamma = 0.3$ for $M \leq M_1$, index $\beta = 1.3$ for $M_1 < M \leq M_2$, and index $\alpha = 2.3$ for $M > 0.5\,\text{M}_\odot$. The boundaries are $M_1 = 0.08\,\text{M}_\odot$ and $M_2 = 0.5\,\text{M}_\odot$. The individual normalisations for the first and second mass range are $k_0 = \frac{0.08^{-\beta} k_1}{0.08^{-\gamma}}$ and $k_1 = \frac{0.5^{-\alpha}}{0.5^{-\beta}}$ respectively. For $M \in [M_{\text{min}}, M_{\text{max}}]$ and overall normalisation constant A, it yields a total stellar mass

$$\begin{aligned} M_{\text{tot}} &= A \int_{M_{\text{min}}}^{M_{\text{max}}} M \; \xi_{\text{K01}}(M) \; dM \\ &= A \underbrace{\left[\frac{k_0}{2-\gamma} (M_1^{2-\gamma} - M_{\text{min}}^{2-\gamma}) + \frac{k_1}{2-\beta} (M_2^{2-\beta} - M_1^{2-\beta}) + \frac{1}{2-\alpha} (M_{\text{max}}^{2-\alpha} - M_2^{2-\alpha}) \right]}_{:=\Gamma}. \end{aligned}$$

This gives a normalisation $A = M_{\text{tot}}/\Gamma$. The proportion below a certain mass

threshold $1\,\mathrm{M}_\odot < M_{\mathrm{cutoff}} < M_{\mathrm{max}}$ is then

$$\begin{aligned} M_{\mathrm{cut}} &= A \int_{M_{\mathrm{min}}}^{\mathrm{cutoff}} M\ \xi_{\mathrm{K01}}(M)\ dM \\ &= \frac{M_{\mathrm{tot}}}{\Gamma} \left[\frac{k_0}{2-\gamma}(M_1^{2-\gamma} - M_{\mathrm{min}}^{2-\gamma}) + \frac{k_1}{2-\beta}(M_2^{2-\beta} - M_1^{2-\beta}) + \frac{1}{2-\alpha}(M_{\mathrm{cutoff}}^{2-\alpha} - M_2^{2-\alpha}) \right]. \end{aligned}$$

Chabrier (2003, 2005)

The IMF by Chabrier (2005) was defined in Eq. 2.6 with high-mass power-law index $\alpha = 2.3$ and break at $M_1 = 1\,\mathrm{M}_\odot$. For $M \in [M_{\mathrm{min}}, M_{\mathrm{max}}]$ and normalisation constant A, it yields a total stellar mass

$$\begin{aligned} M_{\mathrm{tot}} &= A \int_{M_{\mathrm{min}}}^{M_{\mathrm{max}}} M\ \xi_{\mathrm{C05}}(M)\ dM \\ &= A \underbrace{\left\{ \sqrt{\frac{\pi}{2}}\mu^2 \left(-e^{2\sigma^2}\right) \sigma \left[\mathrm{erf}\left(\frac{\log\mu + 2\sigma^2 - \log M_1}{\sqrt{2}\sigma} \right) - \mathrm{erf}\left(\frac{\log\mu + 2\sigma^2 - \log M_{\mathrm{min}}}{\sqrt{2}\sigma} \right) \right] + \frac{k}{2-\alpha}\left(M_{\mathrm{cutoff}}^{2-\alpha} - M_1^{2-\alpha}\right) \right\}}_{:=\Gamma}. \end{aligned}$$

This gives a normalisation $A = M_{\mathrm{tot}}/\Gamma$. The proportion below a certain mass threshold $1\,\mathrm{M}_\odot < M_{\mathrm{cutoff}} < M_{\mathrm{max}}$ is then

$$\begin{aligned} M_{\mathrm{cut}} = \frac{M_{\mathrm{tot}}}{\Gamma} \Bigg\{ &-\sqrt{\frac{\pi}{2}}\mu^2 e^{2\sigma^2} \sigma \left[\mathrm{erf}\left(\frac{\log\mu + 2\sigma^2 - \log M_1}{\sqrt{2}\sigma} \right) - \mathrm{erf}\left(\frac{\log\mu + 2\sigma^2 - \log M_{\mathrm{min}}}{\sqrt{2}\sigma} \right) \right] \\ &+ \frac{k}{2-\alpha}\left(M_{\mathrm{cutoff}}^{2-\alpha} - M_1^{2-\alpha}\right) \Bigg\}. \end{aligned}$$

Inverse Transform Sampling of a Gaussian

In order to transform a uniformly distributed random variable $u \in [0, 1]$ into a truncated Gaussian distribution in the range $x \in [a, b]$, the following inverse transform sampling technique is applied throughout this thesis. The Gaussian

$$g(x) = Ae^{-\frac{(x-\mu)^2}{2\sigma^2}}$$

is normalised by

$$\begin{aligned} G(x) &= \int_a^b g(x)\ dx = \int_a^b Ae^{-\frac{(x-\mu)^2}{2\sigma^2}}\ dx \\ &= A\sqrt{\frac{\pi}{2}}\sigma \left\{ \mathrm{erf}\left[\sqrt{\frac{1}{2\sigma^2}}(b-\mu) \right] - \mathrm{erf}\left[\sqrt{\frac{1}{2\sigma^2}}(a-\mu) \right] \right\} := A \cdot N. \end{aligned}$$

The respective CDF is accordingly given by

$$F(x) = \frac{1}{N}\sqrt{\frac{\pi}{2}}\sigma \left\{ \operatorname{erf}\left[\sqrt{\frac{1}{2\sigma^2}}(x-\mu)\right] - \operatorname{erf}\left[\sqrt{\frac{1}{2\sigma^2}}(a-\mu)\right]\right\}.$$

This is now taken to give u by inversion, which gives the wanted relation

$$\begin{aligned} F\left(F^{-1}(u)\right) &= u \\ u &= \frac{1}{N}\sqrt{\frac{\pi}{2}}\sigma \left\{ \operatorname{erf}\left[\sqrt{\frac{1}{2\sigma^2}}\left(F^{-1}(u)-\mu\right)\right] - \operatorname{erf}\left[\sqrt{\frac{1}{2\sigma^2}}(a-\mu)\right]\right\} \\ F^{-1}(u) &= \sqrt{2\sigma^2}\operatorname{erf}^{-1}\left\{ u\frac{N}{\sigma}\sqrt{\frac{2}{\pi}} + \operatorname{erf}\left[\frac{1}{2\sigma^2}(a-\mu)\right]\right\} + \mu. \end{aligned}$$

C Bibliography

Abbott, D. C. 1982, ApJ, 259, 282
Acero, F., Ackermann, M., Ajello, M., et al. 2009, yCat, J/ApJS/224/8
Acero, F., Ackermann, M., Ajello, M., et al. 2016, ApJ Suppl. Ser., 224, 8
Adams, S. M., Kochanek, C. S., Beacom, J. F., Vagins, M. R., & Stanek, K. Z. 2013, ApJ, 778, 164
Agrawal, P., Hurley, J., Stevenson, S., Szécsi, D., & Flynn, C. 2020, arXiv e-prints, arXiv:2005.13177
Alexis, A., Jean, P., Martin, P., & Ferrière, K. 2014, A&A, 564, A108
Allen, G. E., Chow, K., DeLaney, T., et al. 2015, ApJ, 798, 82
Alves, J., Zucker, C., Goodman, A. A., et al. 2020, Nature, 578, 237
Ambartsumian, V. A. 1949, Astronomicheskii Zhurnal, 26, 3
Angulo, C., Arnould, M., Rayet, M., et al. 1999, Nuclear Physics A, 656, 3
Arce, H. G., Borkin, M. A., Goodman, A. A., Pineda, J. E., & Beaumont, C. N. 2011, ApJ, 742, 105
Armstrong, J. J., Wright, N. J., Jeffries, R. D., & Jackson, R. J. 2020, MNRAS, 494, 4794
Arnett, W. D. 1977, Eight Texas Symposium on Relativistic Astrophysics, 302, 90
Arnett, W. D., Bahcall, J. N., Kirshner, R. P., & Woosley, S. E. 1989, IN: Annual review of astronomy and astrophysics. Volume 27 (A90-29983 12-90). Palo Alto, 27, 629
Aschenbach, B. 1998, Nature, 396, 141
Asplund, M., Grevesse, N., Sauval, A. J., & Scott, P. 2009, Annu. Rev. Astron. Astrophys., 47, 481
Attie, D., Cordier, B., Gros, M., et al. 2003, A&A, 411, L71
Audcent-Ross, F. M., Meurer, G. R., Audcent, J. R., et al. 2020, MNRAS, 492, 848
Audi, G., Wapstra, A. H., & Thibault, C. 2003, Nuclear Physics, 729, 337
Azimlu, M., Martínez-Galarza, J. R., & Muench, A. A. 2015, AJ, 150, 95
Bakış, V., Hensberge, H., Bilir, S., et al. 2014, AJ, 147, 149
Bally, J. 2008, Handbook of Star Forming Regions, I, 459
Bally, J., Walawender, J., Johnstone, D., Kirk, H., & Goodman, A. 2008, Handbook of Star Forming Regions, I, 308
Bastian, N., Covey, K. R., & Meyer, M. R. 2010, Annu. Rev. Astron. Astrophys., 48, 339
Bate, M. R. 2000, MNRAS, 314, 33
Bate, M. R., Bonnell, I. A., & Bromm, V. 2002, MNRAS, 332, L65
Bazan, G., Brown, L. E., Clayton, D. D., et al. 1993, AIP Conf. Proc., 280, 47
Beals, C. S. 1929, MNRAS, 90, 202
Belikov, A. N., Kharchenko, N. V., Piskunov, A. E., Schilbach, E., & Scholz, R. D. 2002, A&A, 387, 117
Belokurov, V., Penoyre, Z., Oh, S., et al. 2020, MNRAS, 496, 1922
Benaglia, P. 2016, PASA, 33, e017
Benaglia, P., del Palacio, S., Ishwara-Chandra, C. H., et al. 2019, A&A, 625, A99

Beniamini, P. & Hotokezaka, K. 2020, MNRAS, 496, 1891
Benjamin, R. A., Churchwell, E., Babler, B. L., et al. 2003, Publ. Astron. Soc. Pac., 115, 953
Benjamin, R. A., Churchwell, E., Babler, B. L., et al. 2005, ApJ, 630, L149
Berger, M. J., Hubbell, J. H., Seltzer, S. M., et al. 2010, XCOM: Photon Cross Section Database. NIST Standard Reference Database 8 (XGAM)
Beringer, J., Arguin, J. F., Barnett, R. M., et al. 2012, Physical Review D, 86, 010001
Bessel, F. W. 1838, Astronomische Nachrichten, 16, 65
Beyer, A. 2018, Bachelor's thesis, ^{26}Al Emission from Massive Star Groups in the Milky Way (Garching bei München: Technische Universität München)
Bihr, S., Beuther, H., Linz, H., et al. 2015, A&A, 579, A51
Binns, W. R., Israel, M. H., Christian, E. R., et al. 2016, Science, 352, 677
Blaauw, A. 1964, Annu. Rev. Astron. Astrophys., 2, 213
Blackett, P. M. S. & Occhialini, G. P. S. 1933, in Proceedings of the Royal Society of London. Series A (The Royal Society London), 699–720
Blaha, C. & Humphreys, R. M. 1989, Astronomical Journal (ISSN 0004-6256), 98, 1598
Blair, W. P., Sankrit, R., & Raymond, J. C. 2005, AJ, 129, 2268
Bleeker, J. A., Burger, J. J., Deerenberg, A. J., et al. 1969, PRL, 22, 1325
Blondin, J. M., Borkowski, K. J., & Reynolds, S. P. 2001, ApJ, 557, 782
Bochanski, J. J., Hawley, S. L., Covey, K. R., et al. 2010, AJ, 139, 2679
Bochkarev, N. G. & Sitnik, T. G. 1985, Astrophysics and Space Science (ISSN 0004-640X), 108, 237
Boggs, S. E., Harrison, F. A., Miyasaka, H., et al. 2015, Science, 348, 670
Bohlin, R. C., Savage, B. D., & Drake, J. F. 1978, ApJ, 224, 132
Boissier, S. & Prantzos, N. 1999, Monthly Notices, 307, 857
Bok, B. J. 1934, Harvard College Observatory Circular, 384, 1
Böker, T., Sarzi, M., McLaughlin, D. E., et al. 2004, AJ, 127, 105
Bond, J. R., Arnett, W. D., & Carr, B. J. 1984, ApJ, 280, 825
Bonnell, I. A. & Bate, M. R. 2005, MNRAS, 362, 915
Bonnell, I. A. & Larson, R. B. 2007, Protostars and Planets V, 149
Bouchet, L., Jourdain, E., & Roques, J.-P. 2015, ApJ, 801, 142
Box, G. E. P. 1976, Journal of the American Statistical Association, 71, 791
Boyd, D. F. A. & Whitworth, A. P. 2005, A&A, 430, 1059
Breitschwerdt, D., Feige, J., Schulreich, M. M., et al. 2016, Nature, 532, 73
Briceño, C., Preibisch, T., Sherry, W. H., et al. 2007, Protostars and Planets V, 345
Brinkman, H. E., Doherty, C. L., Pols, O. R., et al. 2019, ApJ, 884, 38
Bromm, V., Kudritzki, R. P., & Loeb, A. 2001, ApJ, 552, 464
Brown, A. G. A., Blaauw, A., Hoogerwerf, R., de Bruijne, J. H. J., & de Zeeuw, P. T. 1999, in The Origin of Stars and Planetary Systems (Dordrecht: Springer, Dordrecht), 411–440
Brown, A. G. A., de Geus, E. J., & de Zeeuw, P. T. 1994, A&A, 289, 101
Brown, A. G. A., Dekker, G., & de Zeeuw, P. T. 1997, MNRAS, 285, 479
Buck, T., Obreja, A., Macciò, A. V., et al. 2020, MNRAS, 491, 3461
Burbidge, E. M., Burbidge, G. R., Fowler, W. A., & Hoyle, F. 1957, Rev. Mod. Phys., 29, 547
Burgasser, A. J., Reid, I. N., Siegler, N., et al. 2007, Protostars and Planets V, 427
Burrows, A., Marley, M., Hubbard, W. B., et al. 1997, ApJ, 491, 856
Burrows, A., Radice, D., & Vartanyan, D. 2019, MNRAS, 485, 3153

Burrows, A., Radice, D., Vartanyan, D., et al. 2020, MNRAS, 491, 2715
Burrows, A., Vartanyan, D., Dolence, J. C., Skinner, M. A., & Radice, D. 2018, Space Science Reviews, 214, 33
Burrows, D. N., Singh, K. P., Nousek, J. A., Garmire, G. P., & Good, J. 1993, ApJ, 406, 97
Cao, Y., Qiu, K., Zhang, Q., et al. 2019, ApJ Suppl. Ser., 241, 1
Cappa, C. E. & Herbstmeier, U. 2000, AJ, 120, 1963
Cappellari, M. & Copin, Y. 2003, MNRAS, 342, 345
Cappellaro, E., Turatto, M., Benetti, S., et al. 1993, A&A, 273, 383
Carlberg, R. G. & Innanen, K. A. 1987, Astronomical Journal (ISSN 0004-6256), 94, 666
Caselli, P., Walmsley, C. M., Terzieva, R., & Herbst, E. 1998, ApJ, 499, 234
Cash, W. 1979, ApJ, 228, 939
Cash, W., Charles, P., Bowyer, S., et al. 1980, ApJ, 238, L71
Cassinelli, J. P. 1979, In: Annual review of astronomy and astrophysics. Volume 17. (A79-54126 24-90) Palo Alto, 17, 275
Castor, J., McCray, R., & Weaver, R. 1975, ApJ, 200, L107
Cayrel, R., Hill, V., Beers, T. C., et al. 2001, Nature, 409, 691
Cerviño, M. 2013, New Astronomy Reviews, 57, 123
Cerviño, M., Knödlseder, J., Schaerer, D., von Ballmoos, P., & Meynet, G. 2000, A&A, 363, 970
Cerviño, M. & Luridiana, V. 2006, A&A, 451, 475
Cha, A. N., Sembach, K. R., & Danks, A. C. 1999, ApJ, 515, L25
Chaboyer, B., Demarque, P., & Pinsonneault, M. H. 1995, ApJ, 441, 865
Chaboyer, B. & Zahn, J. P. 1992, A&A, 253, 173
Chabrier, G. 2001, ApJ, 554, 1274
Chabrier, G. 2003, PASP, 115, 763
Chabrier, G. 2005, The Initial Mass Function 50 years later. Edited by E. Corbelli and F. Palle, 327, 41
Chabrier, G., Baraffe, I., Allard, F., & Hauschildt, P. 2000, ApJ, 542, L119
Chabrier, G., Baraffe, I., & Plez, B. 1996, Astrophysical Journal Letters v.459, 459, L91
Chabrier, G., Gallardo, J., & Baraffe, I. 2007, A&A, 472, L17
Chan, C., Müller, B., & Heger, A. 2020, MNRAS, 495, 3751
Cheng, J. Y., Rockosi, C. M., Morrison, H. L., et al. 2012, ApJ, 746, 149
Chesterton, G. K. 1908, in The Collected Works of G. K. Chesterton, 236
Chieffi, A. & Limongi, M. 2013, ApJ, 764, 21
Chiosi, C. & Maeder, A. 1986, IN: Annual review of astronomy and astrophysics. Volume 24 (A87-26730 10-90). Palo Alto, 24, 329
Chomiuk, L. & Povich, M. S. 2011, AJ, 142, 197
Chrimes, A. A., Stanway, E. R., & Eldridge, J. J. 2020, MNRAS, 491, 3479
Churchwell, E., Babler, B. L., Meade, M. R., et al. 2009, PASP, 121, 213
Churchwell, E., Povich, M. S., Allen, D., et al. 2006, ApJ, 649, 759
Clark, G. W., Garmire, G. P., & Kraushaar, W. L. 1968, ApJ, 153, L203
Clark, P. C., Bonnell, I. A., Zinnecker, H., & Bate, M. R. 2005, MNRAS, 359, 809
Clayton, D. D. 2018, Astrophysics with Radioactive Isotopes, 453, 29
Coc, A. 2016, J. Phys.: Conf. Ser., 665, 012001
Comerón, F. & Pasquali, A. 2012, A&A, 543, A101
Compton, A. H. 1923, Physical Review, 21, 483
Conti, P. S. 1978, In: Annual review of astronomy and astrophysics. Volume 16.

(A79-14551 03-88) Palo Alto, 16, 371
Cordes, J. M. & Lazio, T. J. W. 2002, arXiv e-prints, arXiv:astro
Covey, K. R., Greene, T. P., Doppmann, G. W., Lada, C. J., & Wilking, B. A. 2005, Astronomische Nachrichten, 326, 886
Covey, K. R., Hawley, S. L., Bochanski, J. J., et al. 2008, AJ, 136, 1778
Cyburt, R. H., Fields, B. D., Olive, K. A., & Yeh, T.-H. 2016, Rev. Mod. Phys., 88, 015004
Da Rio, N., Tan, J. C., Covey, K. R., et al. 2017, ApJ, 845, 105
da Silva, R. L., Fumagalli, M., & Krumholz, M. R. 2012, ApJ, 745, 145
Daffern-Powell, E. C. & Parker, R. J. 2020, MNRAS
Dale, J. E. 2015, New Astronomy Reviews, 68, 1
Dame, T. M., Hartmann, D., & Thaddeus, P. 2001, ApJ, 547, 792
Darwin, C. 1859, On the Origin of Species by Means of Natural Selection, Or the Preservation of Favoured Races in the Struggle for Life (London: John Murray)
Dauphas, N. & Chaussidon, M. 2011, Annual Review of Earth and Planetary Sciences, 39, 351
de Avillez, M. A. & Breitschwerdt, D. 2005, A&A, 436, 585
de Avillez, M. A., Mac Low The Astrophysical Journal, M. M., & 2002. 2002, ApJ, 581, 1047
De Marco, O. & Schmutz, W. 1999, A&A, 345, 163
De Marco, O., Schmutz, W., Crowther, P. A., et al. 2000, A&A, 358, 187
de Mink, S. E., Pols, O. R., & Hilditch, R. W. 2007, A&A, 467, 1181
de Zeeuw, P. T., Hoogerwerf, R., de Bruijne, J. H. J., Brown, A. G. A., & Blaauw, A. 1999, AJ, 117, 354
del Rio, E., von Ballmoos, P., Bennett, K., et al. 1996, A&A, 315, 237
Dib, S. 2014, MNRAS, 444, 1957
Dickey, J. M. & Lockman, F. J. 1990, IN: Annual review of astronomy and astrophysics. Vol. 28 (A91-28201 10-90). Palo Alto, 28, 215
Diehl, R. 2002, New Astronomy Reviews, 46, 547
Diehl, R. 2018, Astrophysics with Radioactive Isotopes, 453, 3
Diehl, R., Bennett, K., Bloemen, H., et al. 1993a, A&A Suppl. Ser., 97, 181
Diehl, R., Collmar, W., Lichti, G., et al. 1993b, AIP Conf. Proc., 280, 40
Diehl, R., Halloin, H., Kretschmer, K., et al. 2006, Nature, 439, 45
Diehl, R., Hartmann, D. H., & Prantzos, N. 2018a, Astrophysics with Radioactive Isotopes, 453, 427
Diehl, R., Knödlseder, J., Lichti, G. G., et al. 2003, A&A, 411, L451
Diehl, R., Kretschmer, K., Lichti, G., et al. 2004, in Proceedings of the th INTEGRAL Workshop on the INTEGRAL Universe, 27–32
Diehl, R., Lang, M. G., Martin, P., et al. 2010, A&A, 522, A51
Diehl, R., Oberlack, U., Knödlseder, J., et al. 1997, in Proceedings of the fourth compton symposium (AIP), 1114–1118
Diehl, R. & Prantzos, N. 2018, Astrophysics with Radioactive Isotopes, 453, 581
Diehl, R., Siegert, T., Greiner, J., et al. 2018b, A&A, 661, A12
Diehl, R., Siegert, T., Hillebrandt, W., et al. 2014, Science, 345, 1162
Diehl, R., Siegert, T., Hillebrandt, W., et al. 2015, A&A, 574, A72
Dobbs, C. L., Bonnell, I. A., & Pringle, J. E. 2006, MNRAS, 371, 1663
Dobbs, C. L., Pettitt, A. R., Corbelli, E., & Pringle, J. E. 2018, MNRAS, 478, 3793
Drimmel, R. 2002, New Astronomy Reviews, 46, 585
Duarte-Cabral, A. & Dobbs, C. L. 2017, MNRAS, 470, 4261
Dubath, P., Kreykenbohm, I., Ferrigno, C., et al. 2015, SPI Analysis Unser Manual,

10th edn., INTEGRAL Science Data Centre, ISDC/OSA-UM-SPI
Duchêne, G. & Kraus, A. 2013, Annu. Rev. Astron. Astrophys., 51, 269
Ebinger, K., Curtis, S., Fröhlich, C., et al. 2019, ApJ, 870, 1
Ebinger, K., Curtis, S., Ghosh, S., et al. 2020, ApJ, 888, 91
Eddington, A. S. 1920, The Observatory, 43, 341
Edgar, R. & Clarke, C. 2004, MNRAS, 349, 678
Eggleton, P. P. 1983, ApJ, 268, 368
Eichler, D. & Usov, V. 1993, ApJ, 402, 271
Einstein, A. 1905a, Annalen der Physik, 323, 639
Einstein, A. 1905b, Annalen der Physik, 322, 132
Ekström, S., Georgy, C., Eggenberger, P., et al. 2012, A&A, 537, A146
El-Badry, K., Ostriker, E. C., Kim, C.-G., Quataert, E., & Weisz, D. R. 2019, MNRAS, 490, 1961
Eldridge, J. J. 2009, Monthly Notices of the Royal Astronomical Society: Letters, 400, L20
Ellis, G. & Silk, J. 2014, arXiv e-prints, 516, 321
Elmegreen, B. G. 1979, ApJ, 231, 372
Elmegreen, B. G. 1994, ApJ, 433, 39
Elmegreen, B. G. 1997, ApJ, 486, 944
Elmegreen, B. G. 1999, ApJ, 527, 266
Elmegreen, B. G. 2000, ApJ, 539, 342
Elmegreen, B. G. 2009, The Evolving ISM in the Milky Way and Nearby Galaxies, 14
Elmegreen, B. G. & Scalo, J. 2006, ApJ, 636, 149
Endal, A. S. & Sofia, S. 1978, ApJ, 220, 279
Endt, P. M. 1990, Nuclear Physics A, 521, 1
Endt, P. M. 1998, Nuclear Physics, 633, 1
Ertl, T., Woosley, S. E., Sukhbold, T., & Janka, H.-T. 2020, ApJ, 890, 51
Evirgen, C. C., Gent, F. A., Shukurov, A., Fletcher, A., & Bushby, P. J. 2019, MNRAS, 488, 5065
Fahmy, S., Schmidt, M., Cordero, F., & Roques, J.-P. 2008, ESA and EUMETSAT
Fall, S. M., Chandar, R., & Whitmore, B. C. 2005, ApJ, 631, L133
Fall, S. M., Krumholz, M. R., & Matzner, C. D. 2010, ApJ, 710, L142
Faucher-Giguère, C.-A. & Kaspi, V. M. 2006, ApJ, 643, 332
Feige, J., Wallner, A., Altmeyer, R., et al. 2018, PRL, 121, 221103
Ferrière, K. M. 2001, Rev. Mod. Phys., 73, 1031
Fesen, R. A., Weil, K. E., Cisneros, I. A., Blair, W. P., & Raymond, J. C. 2018, MNRAS, 481, 1786
Fey, A. L., Ma, C., Arias, E. F., et al. 2004, AJ, 127, 3587
Fields, B. D., Ellis, J. R., Binns, W. R., et al. 2019, arXiv e-prints, arXiv:1903.04589
Fierlinger, K. 2014, PhD thesis, Ludwig-Maximilians-Universität, München
Figer, D. F. 2005, Nature, 434, 192
Fimiani, L., Cook, D. L., Faestermann, T., et al. 2016, PRL, 116, 151104
Firestone, R. B., Ekstrom, L. P., & Chu, S. Y. F. 1999, American Physical Society, CE.13
Foreman-Mackey, D., Farr, W. M., Sinha, M., et al. 2019, JOSS, 4, 1864
Fouesneau, M. & Lançon, A. 2010, A&A, 521, A22
Franciosini, E., Sacco, G. G., Jeffries, R. D., et al. 2018, A&A, 616, L12
Frebel, A., Christlieb, N., Norris, J. E., et al. 2007, ApJ, 660, L117
Freud, S. 1917, Imago. Zeitschrift für Anwendung der Psychoanalyse auf die Geis-

teswissenschaften, 5, 1
Fujimoto, Y., Chevance, M., Haydon, D. T., Krumholz, M. R., & Kruijssen, J. M. D. 2019, MNRAS, 487, 1717
Fujimoto, Y., Krumholz, M. R., & Inutsuka, S.-i. 2020, arXiv e-prints, arXiv:2006.03057
Fujimoto, Y., Krumholz, M. R., & Tachibana, S. 2018, MNRAS, 480, 4025
Gaczkowski, B., Preibisch, T., Stanke, T., et al. 2015, A&A, 584, A36
Gaia-Collaboration, Brown, A. G. A., Vallenari, A., et al. 2018, A&A, 616, A1
Garibdzhanyan, A. T., Gasparyan, K. G., & Oganesyan, R. K. 1984, ApJ Suppl. Ser., 20, 129
Garmany, C. D. & Stencel, R. E. 1992, A&A Suppl. Ser., 94, 211
Geen, S., Hennebelle, P., Tremblin, P., & Rosdahl, J. 2016, MNRAS, 463, 3129
Gehrz, R. D., Truran, J. W., Williams, R. E., & Starrfield, S. 1998, Publ. Astron. Soc. Pac., 110, 3
Georgelin, Y. M. & Georgelin, Y. P. 1976, A&A, 49, 57
Gies, D. R. 1987, Astrophysical Journal Supplement Series (ISSN 0067-0049), 64, 545
Glebocki, R. & Gnacinski, P. 2005, VizieR On-line Data Catalog, 3244
Glebocki, R., Gnacinski, P., & Stawikowski, A. 2000, Acta Astronomica, 50, 509
Goethe, J. W. 1808, Faust. Eine Tragödie. (J. G. Cotta'sche Buchhandlung)
Gong, M. & Ostriker, E. C. 2015, ApJ, 806, 31
Gontcharov, G. A. 2006, Astronomy Letters, 32, 759
Götberg, Y., Korol, V., Lamberts, A., et al. 2020, arXiv e-prints, arXiv:2006.07382
Gratton, R., Bragaglia, A., Carretta, E., et al. 2019, Astron Astrophys Rev, 27, 8
Grebenev, S. A., Lutovinov, A. A., Tsygankov, S. S., & Winkler, C. 2012, Nature, 490, 373
Green, D. A. 2014, arXiv e-prints
Grefenstette, B. W., Fryer, C. L., Harrison, F. A., et al. 2017, ApJ, 834, 19
Groopman, E., Zinner, E., Amari, S., et al. 2015, ApJ, 809, 31
Güsten, R. & Mezger, P. G. 1982, Vistas in Astronomy, 26, 159
Gutermuth, R. A., Myers, P. C., Megeath, S. T., et al. 2008, ApJ, 674, 336
Hartmann, D. & Burton, W. B. 1997, Atlas of Galactic Neutral Hydrogen, 243
Hartmann, D. H. 1994, AIP Conf. Proc., 304, 176
Haymes, R. C., Ellis, D. V., Fishman, G. J., Glenn, S. W., & Kurfess, J. D. 1969a, ApJ, 157, 1455
Haymes, R. C., Ellis, D. V., Fishman, G. J., Glenn, S. W., & Kurfess, J. D. 1969b, ApJ, 155, L31
Heftrich, T., Bichler, M., Dressler, R., et al. 2015, Phys. Rev. C, 92, 015806
Heger, A. & Langer, N. 1998, A&A, 334, 210
Heger, A., Langer, N., & Woosley, S. E. 2000, ApJ, 528, 368
Heger, A., Woosley, S. E., Fryer, C. L., & Langer, N. 2003, in From Twilight to Highlight: The Physics of Supernovae (Berlin/Heidelberg: Springer, Berlin, Heidelberg), 3–12
Heiles, C. 1979, ApJ, 229, 533
Heitsch, F. & Burkert, A. 2002, ASP Conf. Ser., 285, 13
Heitsch, F., Burkert, A., Hartmann, L. W., Slyz, A. D., & Devriendt, J. E. G. 2005, ApJ, 633, L113
Heitsch, F., Hartmann, L. W., Slyz, A. D., Devriendt, J. E. G., & Burkert, A. 2008, ApJ, 674, 316
Herbig, G. H. 1962, Advances in Astronomy and Astrophysics, 1, 47

Herrera, C. N., Pety, J., Hughes, A., et al. 2020, A&A, 634, A121
Hester, J. J., Raymond, J. C., & Blair, W. P. 1994, ApJ, 420, 721
Hewish, A., Bell, S. J., Pilkington, J. D. H., Scott, P. F., & Collins, R. A. 1968, Nature, 217, 709
Higdon, J. C. & Lingenfelter, R. E. 2005, ApJ, 628, 738
Higdon, J. C. & Lingenfelter, R. E. 2013, ApJ, 775, 110
Higgins, E. R. & Vink, J. S. 2019, A&A, 622, A50
Hill, A. S., Joung, M. R., Mac Low, M.-M., et al. 2012, ApJ, 750, 104
Hillenbrand, L. A. & Hartmann, L. W. 1998, ApJ, 492, 540
Hirschi, R., Meynet, G., & Maeder, A. 2004, A&A, 425, 649
Höfner, S. & Olofsson, H. 2018, Astron Astrophys Rev, 26, 1
Hopkins, P. F., Grudić, M. Y., Wetzel, A., et al. 2020, MNRAS, 491, 3702
Hopkins, P. F., Wetzel, A., Kereš, D., et al. 2018, MNRAS, 480, 800
Howarth, I. D. & Prinja, R. K. 1989, Astrophysical Journal Supplement Series (ISSN 0067-0049), 69, 527
Hoyle, F. 1946a, MNRAS, 106, 384
Hoyle, F. 1946b, MNRAS, 106, 255
Hoyle, F. 1946c, MNRAS, 106, 343
Hoyle, F. 1954, Astrophysical Journal Supplement, 1, 121
Hoyle, F. & Fowler, W. A. 1960, ApJ, 132, 565
Huang, W. & Gies, D. R. 2006, ApJ, 648, 580
Hueso-González, F., Biegun, A. K., Dendooven, P., et al. 2015, J. Inst., 10, P09015
Hurley, J. R., Pols, O. R., & Tout, C. A. 2000, MNRAS, 315, 543
Hyde, M. & Pecaut, M. J. 2018, Astronomische Nachrichten, 339, 78
Iliadis, C. 2015, Nuclear Physics of Stars, 2nd edn. (Weinheim: Viley-VCH)
Iliadis, C., Champagne, A., Chieffi, A., & Limongi, M. 2011, The Astrophysical Journal Supplement, 193, 16
Isern, J., Hernanz, M., & Jose, J. 2018, Astrophysics with Radioactive Isotopes, 453, 287
Iyudin, A. F., Schönfelder, V., Bennett, K., et al. 1998, Nature, 396, 142
Jacobsen, B., Yin, Q.-z., Moynier, F., et al. 2008, E&PSL, 272, 353
Janka, H.-T. 2012, Annual Review of Nuclear and Particle Science, 62, 407
Janka, H.-T., Hanke, F., Hüdepohl, L., et al. 2012, Progress of Theoretical and Experimental Physics, 2012, 01A309
Jauch, J. & Rohrlich, F. 1955, Theory of Photons and Electrons (Addison-Wesley Publishing)
Jean, P., Vedrenne, G., Roques, J.-P., et al. 2003, A&A, 411, L107
Jeans, J. H. 1902, Philosophical Transactions of the Royal Society A: Mathematical, Physical and Engineering Sciences, 199, 1
Jeffries, R. D., Jackson, R. J., Franciosini, E., et al. 2017, MNRAS, 464, 1456
Jeffries, R. D., Naylor, T., Walter, F. M., Pozzo, M. P., & Devey, C. R. 2009, MNRAS, 393, 538
Jenkins, E. B. 2013, ApJ, 764, 25
Jerabkova, T., Zonoozi, A. H., Kroupa, P., et al. 2018, arXiv e-prints, arXiv:1809.04603
Jose, J. & Hernanz, M. 1998, ApJ, 494, 680
Joubaud, T., Grenier, I. A., Ballet, J., & Soler, J. D. 2019, A&A, 631, A52
Jun, B.-I., Jones, T. W., & Norman, M. L. 1996, Astrophysical Journal Letters v.468, 468, L59
Jung, C. G. 1954, in C. G. Jung - Gesammelte Werke IX/1 (Zürich: Eranos-

Jahrbuch), §88
Kahn, F. D. 1974, A&A, 37, 149
Kalberla, P. M. W. & Kerp, J. 2009, Annu. Rev. Astron. Astrophys., 47, 27
Kapteyn, J. C. 1914, ApJ, 40, 43
Karakas, A. I. & Lattanzio, J. C. 2014, PASA, 31, e030
Kavanagh, P. J. 2020, Astrophysics and Space Science, 365, 6
Keller, B. W., Wadsley, J., Benincasa, S. M., & Couchman, H. M. P. 2014, MNRAS, 442, 3013
Kendall, T. R., Dufton, P. L., & Lennon, D. J. 1996, A&A, 310, 564
Kennicutt, R. C. & Evans, N. J. 2012, Annu. Rev. Astron. Astrophys., 50, 531
Kennicutt, R. C. J. 1998, Annu. Rev. Astron. Astrophys., 36, 189
Kepler, J. 1606, De Stella Nova in Pede Serpentarii (Prague: Paul Sessius)
Kerr, F. J. & Lynden-Bell, D. 1986, Monthly Notices of the Royal Astronomical Society (ISSN 0035-8711), 221, 1023
Kholopov, P. N. 1959, Soviet Astronomy, 3, 291
Kim, C.-G., Ostriker, E. C., & Raileanu, R. 2017, ApJ, 834, 25
Kim, J.-G., Kim, W.-T., & Ostriker, E. C. 2016, ApJ, 819, 137
Kim, J.-G., Kim, W.-T., & Ostriker, E. C. 2019, ApJ, 883, 102
Kim, W.-T. & Ostriker, E. C. 2002, ApJ, 570, 132
Kim, W.-T., Ostriker, E. C., & Stone, J. M. 2002, ApJ, 581, 1080
Kinzer, R. L., Milne, P. A., Kurfess, J. D., et al. 2001, ApJ, 559, 282
Kinzer, R. L., Purcell, W. R., & Kurfess, J. D. 1999, ApJ, 515, 215
Kippenhahn, R., Weigert, A., & Weiss, A. 2012, Stellar structure and evolution, Springer-Verlag, Berlin Heidelberg
Kirk, H. & Myers, P. C. 2011, ApJ, 727, 64
Klein, O. & Nishina, T. 1929, Zeitschrift für Physik, 52, 853
Klessen, R. S. & Glover, S. C. O. 2016, Star Formation in Galaxy Evolution: Connecting Numerical Models to Reality, 43, 85
Knödlseder, J. 1997, PhD thesis, Université Paul Sabatier - Toulouse III
Knödlseder, J. 2000, A&A, 360, 539
Knödlseder, J., Bennett, K., Bloemen, H., et al. 1999, A&A, 344, 68
Knödlseder, J., Cerviño, M., Le Duigou, J. M., et al. 2002, A&A, 390, 945
Knödlseder, J., Cerviño, M., Schaerer, D., von Ballmoos, P., & Meynet, G. 2001, in Proceedings of the Fourth INTEGRAL Workshop, 47–50
Knödlseder, J., Prantzos, N., Bennett, K., et al. 1996, arXiv e-prints, 9604053
Knoll, G. F. 2010, Radiation Detection and Measurement (University of Michigan: John Wiley & Sons)
Koen, C. 2006, MNRAS, 365, 590
Koll, D., Korschinek, G., Faestermann, T., et al. 2019, PRL, 123, 072701
Kounkel, M., Hartmann, L., Loinard, L., et al. 2017, ApJ, 834, 142
Krause, M., Burkert, A., Diehl, R., et al. 2018, A&A, 619, A120
Krause, M. & Diehl, R. 2014, ApJ, 794, L21
Krause, M., Diehl, R., Bagetakos, Y., et al. 2015, A&A, 578, A113
Krause, M., Diehl, R., Böhringer, H., Freyberg, M., & Lubos, D. 2014, A&A, 566, A94
Krause, M., Fierlinger, K., Diehl, R., et al. 2013, A&A, 550, A49
Krause, M., Offner, S. S. R., Charbonnel, C., et al. 2020, Space Science Reviews, 216, 64
Kreckel, K., Faesi, C., Kruijssen, J. M. D., et al. 2018, ApJ, 863, L21
Kretschmer, K. 2011, PhD thesis, Technische Universität München, Garching, bei

München
Kretschmer, K., Diehl, R., Krause, M., et al. 2013, A&A, 559, A99
Kretschmer, K., Plüschke, S., Diehl, R., & Hartmann, D. H. 2000, Astronomische Gesellschaft Meeting Abstracts, 17, 77
Kroupa, P. 2001, MNRAS, 322, 231
Kroupa, P. & Boily, C. M. 2002, MNRAS, 336, 1188
Kroupa, P., Jerabkova, T., Beccari, G., & Yan, Z. 2018, arXiv e-prints, A74
Kroupa, P. & Weidner, C. 2003, ApJ, 598, 1076
Kroupa, P., Weidner, C., Pflamm-Altenburg, J., et al. 2013, in Planets, Stars and Stellar Systems (Dordrecht: Springer, Dordrecht), 115–242
Krumholz, M. R. 2014, Physics Reports, 539, 49
Krumholz, M. R., Bate, M. R., Arce, H. G., et al. 2014, Protostars and Planets VI, 243
Krumholz, M. R., Klein, R. I., & McKee, C. F. 2005, Massive star birth: A crossroads of Astrophysics, 227, 231
Krumholz, M. R. & Matzner, C. D. 2009, ApJ, 703, 1352
Krumholz, M. R., Matzner, C. D., & McKee, C. F. 2006, ApJ, 653, 361
Krumholz, M. R., McKee, C. F., & Bland-Hawthorn, J. 2019, Annu. Rev. Astron. Astrophys., 57, 227
Lada, C. J. & Lada, E. A. 2003, Annu. Rev. Astron. Astrophys., 41, 57
Langer, N. 1998, A&A, 329, 551
Larson, R. B. 1969, MNRAS, 145, 271
Larson, R. B. 1981, MNRAS, 194, 809
Larson, R. B. 2003, arXiv e-prints, 1651
Larsson, S., Ryde, F., Borgonovo, L., et al. 2004, in Proceedings of the 5th INTEGRAL Workshop on the INTEGRAL Universe (ESA SP-552). 16-20 February 2004, 649–
Lee, H.-T. & Lim, J. 2008, ApJ, 679, 1352
Lentz, E. J., Branch, D., & Baron, E. 1999, ApJ, 512, 678
Li, Z. Y. & Nakamura, F. 2005, Protostars and Planets V, 8289
Lichti, G. & Georgii, R. 2001, The universe in gamma rays, 27
Licquia, T. C. & Newman, J. A. 2015, ApJ, 806, 96
Limongi, M. & Chieffi, A. 2003, ApJ, 592, 404
Limongi, M. & Chieffi, A. 2006, ApJ, 647, 483
Limongi, M. & Chieffi, A. 2018, ApJ Suppl. Ser., 237, 13
Liszt, H. S. 1993, ApJ, 411, 720
Lombardi, M., Bouy, H., Alves, J., & Lada, C. J. 2014, A&A, 566, A45
Lonjou, V., Roques, J.-P., von Ballmoos, P., et al. 2005, Nuclear Instruments and Methods in Physics Research Section A, 554, 320
Low, C. & Lynden-Bell, D. 1976, MNRAS, 176, 367
Ludwig, P., Bishop, S., Egli, R., et al. 2016, in Proceedings of the National Academy of Sciences, Physik Department, Technische Universität München, 85748 Garching, Germany (National Academy of Sciences), 9232–9237
Luft, J. & Ingham, H. 1955, Proceedings of the Western Training Laboratory in Group Development
Lugaro, M. & Chieffi, A. 2018, in Astrophysics with Radioactive Isotopes (Cham: Springer, Cham), 91–172
Lugaro, M., Ott, U., & Kereszturi, Á. 2018, Progress in Particle and Nuclear Physics, 102, 1
Luhman, K. L. 2012, Annu. Rev. Astron. Astrophys., 50, 65

Luhman, K. L. & Potter, D. 2006, ApJ, 638, 887
Mac Low, M.-M. & Klessen, R. S. 2004, Rev. Mod. Phys., 76, 125
MacCallum, C. J., Huters, A. F., Stang, P. D., & Leventhal, M. 1987, ApJ, 317, 877
Maeder, A. 1987, A&A, 178, 159
Maeder, A. 1992, A&A, 264, 105
Maeder, A. 2009, Physics, Formation and Evolution of Rotating Stars (Berlin Heidelberg: Springer)
Maeder, A. & Meynet, G. 2000, Annu. Rev. Astron. Astrophys., 38, 143
Mahoney, W. A., Ling, J. C., Jacobson, A. S., & Lingenfelter, R. E. 1982, ApJ, 262, 742
Mahoney, W. A., Ling, J. C., Wheaton, W. A., & Jacobson, A. S. 1984, ApJ, 286, 578
Maíz-Apellániz, J. 2001, ApJ, 560, L83
Maíz-Apellániz, J. 2008, ApJ, 677, 1278
Maíz-Apellániz, J., Walborn, N. R., Morrell, N. I., Niemela, V. S., & Nelan, E. P. 2007, ApJ, 660, 1480
Malet, I., Niel, M., Vedrenne, G., et al. 1991, in AIP Conf. Proc., Centre d'Étude Spatiale des Rayonnements, Toulouse, France (AIP), 123–128
Mandel, I., Müller, B., Riley, J., et al. 2020, arXiv e-prints, arXiv:2007.03890
Mandrou, P., Roques, J.-P., & Schönfelder, V. 2002, Science Performance Report, Tech. Rep. SPI-NS-0-9758-CESR, CESR
Mannucci, F., Della Valle, M., Panagia, N., et al. 2005, A&A, 433, 807
Mapelli, M., Vallenari, A., Jeffries, R. D., et al. 2015, A&A, 578, A35
Martí-Devesa, G., Reimer, O., Li, J., & Torres, D. F. 2020, A&A, 635, A141
Martin, P., Knödlseder, J., Diehl, R., & Meynet, G. 2009, A&A, 506, 703
Martin, P., Knödlseder, J., & Meynet, G. 2008, New Astronomy Reviews, 52, 445
Martin, P., Knödlseder, J., Meynet, G., & Diehl, R. 2010, A&A, 511, A86
Martizzi, D. 2020, MNRAS, 492, 79
Massey, P. 2003, Annual Review of Astronomy &Astrophysics, 41, 15
Massey, P. & Hunter, D. A. 1998, ApJ, 493, 180
Massey, P. & Thompson, A. B. 1991, Astronomical Journal (ISSN 0004-6256), 101, 1408
Mattox, J. R., Bertsch, D. L., Chiang, J., et al. 1996, ApJ, 461, 396
Mattsson, L. 2020, MNRAS, 491, 4334
Matzner, C. D. 2002, ApJ, 566, 302
McBride, A. & Kounkel, M. 2019, ApJ, 884, 6
McKee, C. F. & Holliman, J. H. I. 1999, ApJ, 522, 313
McKee, C. F. & Ostriker, E. C. 2007, Annu. Rev. Astron. Astrophys., 45, 565
McKee, C. F. & Ostriker, J. P. 1977, ApJ, 218, 148
McKee, C. F. & Williams, J. P. 1997, ApJ, 476, 144
McMillan, P. J. 2011, MNRAS, 414, 2446
McMillan, P. J. 2017, MNRAS, 465, 76
Melnik, A. M. & Dambis, A. K. 2009, MNRAS, 400, 518
Melnik, A. M. & Dambis, A. K. 2017a, MNRAS, 472, 3887
Melnik, A. M. & Dambis, A. K. 2017b, Vizier On-line Data Catalog: Kinematic data for stars in OB-associations
Melnik, A. M. & Efremov, Y. N. 1995, Astronomy Letters, 21, 10
Melott, A. L. & Thomas, B. C. 2019, The Journal of Geology, 127, 475
Melott, A. L., Thomas, B. C., Kachelrieß, M., Semikoz, D. V., & Overholt, A. C. 2017, ApJ, 840, 105

Menten, K. M., Reid, M. J., Forbrich, J., & Brunthaler, A. 2007, A&A, 474, 515
Metzger, A. E., Anderson, E. C., Van Dilla, M. A., & Arnold, J. R. 1964, Nature, 204, 766
Meynet, G., Arnould, M., Prantzos, N., & Paulus, G. 1997, A&A, 320, 460
Meynet, G., Hirschi, R., Maeder, A., & Ekström, S. 2006, EAS Publications Series, 19, 85
Micic, M., Glover, S. C. O., Banerjee, R., & Klessen, R. S. 2013, MNRAS, 432, 626
Miller, G. E. & Scalo, J. 1978, PASP, 90, 506
Miller, G. E. & Scalo, J. 1979, ApJ Suppl. Ser., 41, 513
Misiriotis, A., Xilouris, E. M., Papamastorakis, J., Boumis, P., & Goudis, C. D. 2006, A&A, 459, 113
Morris, M. & Serabyn, E. 1996, Annu. Rev. Astron. Astrophys., 34, 645
Mowlavi, N., Knödlseder, J., Dubath, P., et al. 2004, in Proceedings of the 5th INTEGRAL Workshop on the INTEGRAL Universe (ESA SP-552). 16-20 February 2004, 39–
Mowlavi, N., Knödlseder, J., Meynet, G., et al. 2005, Nuclear Physics A, 758, 320
Mowlavi, N. & Meynet, G. 2000, A&A, 361, 959
Murray, C. E., Stanimirović, S., Goss, W. M., et al. 2018, ApJ Suppl. Ser., 238, 14
Murray, N., Quataert, E., & Thompson, T. A. 2010, ApJ, 709, 191
Murray, N. & Rahman, M. 2010, ApJ, 709, 424
Neugent, K. F. & Massey, P. 2011, ApJ, 733, 123
Neyman, J. & Pearson, E. S. 1928, London Oxford University Press, 20A, 175
Norman, C. & Silk, J. 1980, ApJ, 238, 158
North, J. R., Tuthill, P. G., Tango, W. J., & Davis, J. 2007, MNRAS, 377, 415
Nugis, T. & Lamers, H. J. G. L. M. 2000, A&A, 360, 227
Oberlack, U. 1997, PhD thesis, Technische Universität München, Garching bei München
Oberlack, U., Bennett, K., Bloemen, H., et al. 1996, A&A Suppl. Ser., 120, 311
Oberlack, U., Wessolowski, U., Diehl, R., et al. 2000, A&A, 353, 715
Ochsendorf, B. B., Brown, A. G. A., Bally, J., & Tielens, A. G. G. M. 2015, ApJ, 808, 111
Oey, M. S. & Clarke, C. J. 2005, ApJ, 620, L43
Ohlendorf, H., Diehl, R., Lang, M., et al. 2010, in "Proceedings of the 11th Symposium on Nuclei in the Cosmos. 19-23 July 2010. Heidelberg, 146
Ohlin, L., Renaud, F., & Agertz, O. 2019, MNRAS, 485, 3887
Oliphant, M. L., Harteck, P., & Rutherford. 1934a, Nature, 133, 413
Oliphant, M. L. E., Harteck, P., & Rutherford, L. 1934b, Proceedings of the Royal Society A: Mathematical, Physical and Engineering Sciences, 144, 692
Osterbrock, D. E. & Ferland, G. J. 2006, Astrophysics of Gaseous Nebulae and Active Galactic Nuclei, 2nd edn. (Sausalito, California: University Science Books)
Padoan, P. & Nordlund, Å. 2004, ApJ, 617, 559
Palacios, A., Meynet, G., Vuissoz, C., et al. 2005, A&A, 429, 613
Palme, H., Lodders, K., & Jones, A. 2014, in Treatise on Geochemistry (Elsevier), 15–36
Parikh, A., José, J., Karakas, A., Ruiz, C., & Wimmer, K. 2014, Phys. Rev. C, 90, 038801
Parker, E. N. 1966, ApJ, 145, 811
Patton, R. A. & Sukhbold, T. 2020, arXiv e-prints, arXiv:2005.03055
Pavlov, G. G., Sanwal, D., Kızıltan, B., & Garmire, G. P. 2001, ApJ, 559, L131
Peterson, J. B. 1999, Maps of Meaning: The Architecture of Belief (New York:

Routledge)
Petrovic, J., Langer, N., & van der Hucht, K. A. 2005, A&A, 435, 1013
Pfalzner, S. 2009, A&A, 498, L37
Pflamm-Altenburg, J., González-Lópezlira, R. A., & Kroupa, P. 2013, MNRAS, 435, 2604
Pflamm-Altenburg, J. & Kroupa, P. 2008, Nature, 455, 641
Pflamm-Altenburg, J., Weidner, C., & Kroupa, P. 2007, ApJ, 671, 1550
Pignatari, M., Herwig, F., Hirschi, R., et al. 2016, ApJ Suppl. Ser., 225, 24
Pinsonneault, M. 1997, Annu. Rev. Astron. Astrophys., 35, 557
Pinsonneault, M. H., Deliyannis, C. P., & Demarque, P. 1991, ApJ, 367, 239
Piskunov, A. E., Kharchenko, N. V., Röser, S., Schilbach, E., & Scholz, R. D. 2006, A&A, 445, 545
Piskunov, A. E., Kharchenko, N. V., Schilbach, E., et al. 2011, A&A, 525, A122
Planck-Collaboration, Ade, P. A. R., Aghanim, N., et al. 2014, A&A, 571, A16
Pleintinger, M. M. M., Siegert, T., Diehl, R., et al. 2019, A&A, 632, A73
Plummer, H. C. 1911, MNRAS, 71, 460
Plüschke, S. 2001, PhD thesis, Technische Universität München, Garching bei München
Plüschke, S., Cerviño, M., Diehl, R., et al. 2002, New Astronomy Reviews, 46, 535
Plüschke, S., Diehl, R., Schönfelder, V., et al. 2001, in Proceedings of the Fourth INTEGRAL Workshop, ed. B. Battrick, A. Giménez, V. Reglero, & C. Winkler, ESA Publications Division, ESA SP-459, Alicante, Spain, 55–58
Pols, O. R., Cote, J., Waters, L. B. F. M., & Heise, J. 1991, A&A, 241, 419
Pon, A., Johnstone, D., Bally, J., & Heiles, C. 2014, MNRAS, 444, 3657
Popescu, B. & Hanson, M. M. 2009, AJ, 138, 1724
Pöppel, W. G. L., Bajaja, E., Arnal, E. M., & Morras, R. 2010, A&A, 512, A83
Portegies Zwart, S. F., McMillan, S. L. W., & Gieles, M. 2010, Annu. Rev. Astron. Astrophys., 48, 431
Pozzo, M., Jeffries, R. D., Naylor, T., et al. 2000, MNRAS, 313, L23
Prantzos, N. 1993, AIP Conf. Proc., 280, 52
Prantzos, N., Boehm, C., Bykov, A. M., et al. 2011, Rev. Mod. Phys., 83, 1001
Prantzos, N. & Boissier, S. 2010, Progenitors and Environments of Stellar Explosions, 77
Prantzos, N. & Diehl, R. 1995, Advances in Space Research, 15, 99
Prantzos, N. & Diehl, R. 1996, Physics Reports, 267, 1
Preibisch, T. & Zinnecker, H. 1999, AJ, 117, 2381
Prentice, S. J., Ashall, C., James, P. A., et al. 2019, MNRAS, 485, 1559
Pshirkov, M. S. 2016, Monthly Notices of the Royal Astronomical Society: Letters, 457, L99
Puls, J., Vink, J. S., & Najarro, F. 2008, Astron Astrophys Rev, 16, 209
Ramaty, R. & Lingenfelter, R. E. 1977, ApJ, 213, L5
Rauw, G., Nazé, Y., Wright, N. J., et al. 2015, ApJ Suppl. Ser., 221, 1
Reed, B. C. 2005, AJ, 130, 1652
Rees, M. J. 1976, MNRAS, 176, 483
Reid, I. N., Gizis, J. E., & Hawley, S. L. 2002, AJ, 124, 2721
Reid, M. J. 1993, In: Annual review of astronomy and astrophysics. Vol. 31 (A94-12726 02-90), 31, 345
Reid, M. J., Dame, T. M., Menten, K. M., & Brunthaler, A. 2016, ApJ, 823, 77
Reid, M. J., Menten, K. M., Brunthaler, A., et al. 2019, ApJ, 885, 131
Reid, M. J., Menten, K. M., Brunthaler, A., et al. 2014, ApJ, 783, 130

Reipurth, B. & Schneider, N. 2008, Handbook of Star Forming Regions, I, 36
Renzo, M., Zapartas, E., de Mink, S. E., et al. 2019, A&A, 624, A66
Reynolds, R. J. 1989, ApJ, 339, L29
Roberts, W. W. 1969, ApJ, 158, 123
Robitaille, T. P. & Whitney, B. A. 2010, ApJ, 710, L11
Rodgers-Lee, D., Krause, M., Dale, J., & Diehl, R. 2019, MNRAS, 490, 1894
Roques, J.-P., Schanne, S., von Kienlin, A., et al. 2003, A&A, 411, L91
Rosen, A. L., Lopez, L. A., Krumholz, M. R., & Ramirez-Ruiz, E. 2014, MNRAS, 442, 2701
Roth, J., Primbsch, J. H., & Lin, R. P. 1984, IEEE Transactions on Nuclear Science, 31, 367
Rugel, G., Faestermann, T., Knie, K., et al. 2009, PRL, 103, 072502
Ruprecht, J. 1966, Bulletin of the Astronomical Institute of Czechoslovakia, 17, 33
Rutherford, E. 1929, Nature, 123, 313
Sackmann, I. J., Boothroyd, A. I., & Kraemer, K. E. 1993, Astrophysical Journal v.418, 418, 457
Sahade, J. 1955, PASP, 67, 348
Sallaska, A. L., Iliadis, C., Champange, A. E., et al. 2013, ApJ Suppl. Ser., 207, 18
Salpeter, E. E. 1955, ApJ, 121, 161
Sana, H., de Mink, S. E., de Koter, A., et al. 2012, Science, 337, 444
Sancisi, R., Goss, W. M., Anderson, C., Johansson, L. E. B., & Winnberg, A. 1974, A&A, 35, 445
Sanders, D. B., Scoville, N. Z., Tilanus, R. P. J., Wang, Z., & Zhou, S. 1993, AIP Conf. Proc., 278, 311
Sanna, A., Reid, M. J., Dame, T. M., Menten, K. M., & Brunthaler, A. 2017, Science, 358, 227
Scalo, J. 1986, Fundamentals of Cosmic Physics (ISSN 0094-5846), 11, 1
Schaerer, D., Schmutz, W., & Grenon, M. 1997, ApJ, 484, L153
Schmidt, M. 1959, ApJ, 129, 243
Schmutz, W., Schweickhardt, J., Stahl, O., et al. 1997, A&A, 328, 219
Schönfelder, V., Aarts, H., Bennett, K., et al. 1993, Astrophysical Journal Supplement Series (ISSN 0067-0049), 86, 657
Schootemeijer, A. & Langer, N. 2018, A&A, 611, A75
Schulreich, M., Breitschwerdt, D., Feige, J., & Dettbarn, C. 2018, Galaxies, 6, 26
Schulreich, M. M., Breitschwerdt, D., Feige, J., & Dettbarn, C. 2017, A&A, 604, A81
Schulz, C., Pflamm-Altenburg, J., & Kroupa, P. 2015, A&A, 582, A93
Scoville, N. Z., Polletta, M., Ewald, S., et al. 2001, AJ, 122, 3017
Share, G. H., Kinzer, R. L., Kurfess, J. D., et al. 1985, ApJ, 292, L61
Shenar, T., Gilkis, A., Vink, J. S., Sana, H., & Sander, A. A. C. 2020, A&A, 634, A79
Shingles, L. J., Doherty, C. L., Karakas, A. I., et al. 2015, MNRAS, 452, 2804
Shu, F. H., Adams, F. C., & Lizano, S. 1987, Annu. Rev. Astron. Astrophys., 25, 23
Siegert, T. 2017, PhD thesis, Technische Universität München, Garching bei München, Online available at: https://mediatum.ub.tum.de/1340342
Siegert, T. 2019, A&A, 632, L1
Siegert, T., Coc, A., Delgado, L., et al. 2018, A&A, 615, A107
Siegert, T. & Diehl, R. 2017, in JPS Conf. Proc. (Journal of the Physical Society of Japan), 14–020305
Siegert, T., Diehl, R., Vincent, A. C., et al. 2016, A&A, 595, A25

Siegert, T., Diehl, R., Weinberger, C., et al. 2019, A&A, 626, A73
Sieverding, A., Martínez-Pinedo, G., Langanke, K., & Heger, A. 2017, in Proceedings of the 14th International Symposium on Nuclei in the Cosmos (NIC2016), Technical University of Darmstadt, Institute for Nuclear Physics, Schlossgartenstr. 2, 64289 Darmstadt, Germany (Journal of the Physical Society of Japan), 020701
Slesnick, C. L., Hillenbrand, L. A., & Massey, P. 2002, ApJ, 576, 880
Smartt, S. J. 2009, Annu. Rev. Astron. Astrophys., 47, 63
Smith, N. 2013, MNRAS, 434, 102
Soler, J. D., Bracco, A., & Pon, A. 2018, A&A, 609, L3
St Louis, N., Willis, A. J., & Stevens, I. R. 1993, ApJ, 415, 298
Stark, A. A. & Lee, Y. 2006, ApJ, 641, L113
Steenbrugge, K. C., de Bruijne, J. H. J., Hoogerwerf, R., & de Zeeuw, P. T. 2003, A&A, 402, 587
Steigman, G. 2007, Ann. Rev. Nucl. Part. Sci., 57, 463
Strong, A. W., Bouchet, L., Diehl, R., et al. 2003, A&A, 411, L447
Strong, A. W., Diehl, R., Halloin, H., et al. 2005, A&A, 444, 495
Sturner, S. J. 2001, in Proceedings of the Fourth INTEGRAL Workshop, 101–104
Sukhbold, T., Ertl, T., Woosley, S. E., Brown, J. M., & Janka, H.-T. 2016, ApJ, 821, 38
Suwa, Y., Tominaga, N., & Maeda, K. 2019, MNRAS, 483, 3607
Szécsi, D., Wünsch, R., Agrawal, P., & Langer, N. 2020, arXiv e-prints
Tammann, G. A., Loeffler, W., & Schroeder, A. 1994, ApJ Suppl. Ser., 92, 487
Tanabashi, M., Hagiwara, K., Hikasa, K., et al. 2018, Physical Review D, 98, 030001
Tang, H. & Dauphas, N. 2015, ApJ, 802, 22
Taylor, J. H. & Cordes, J. M. 1993, Astrophysical Journal - Part 1 (ISSN 0004-637X), 411, 674
Taylor, J. H., Manchester, R. N., & Lyne, A. G. 1993, Astrophysical Journal Supplement Series (ISSN 0067-0049), 88, 529
Teegarden, B. J., Barthelmy, S. D., Gehrels, N., et al. 1991, in AIP Conf. Proc., NASA/Goddard Space Flight Center (AIP), 116–122
Thielemann, F.-K., Diehl, R., Heger, A., Hirschi, R., & Liebendoerfer, M. 2018, Astrophysics with Radioactive Isotopes, 453, 173
Thielemann, F.-K., Nomoto, K., & Hashimoto, M.-A. 1996, Astrophysical Journal v.460, 460, 408
Timmes, F. X., Woosley, S. E., Hartmann, D. H., & Hoffman, R. D. 1996, Astrophysical Journal v.464, 464, 332
Timmes, F. X., Woosley, S. E., Hartmann, D. H., et al. 1995, Astrophysical Journal v.449, 449, 204
Tinsley, B. M. 1968, ApJ, 151, 547
Tinsley, B. M. 1972, A&A, 20, 383
Tinsley, B. M. 1980, Fundamentals of Cosmic Physics, 5, 287
Tinsley, B. M. & Gunn, J. E. 1976, ApJ, 203, 52
Tissot, F. L. H., Dauphas, N., & Grove, T. L. 2017, Geochimica et Cosmochimica Acta, 213, 593
Tress, R. G., Smith, R. J., Sormani, M. C., et al. 2020, MNRAS, 492, 2973
Tsygankov, S. S., Lutovinov, A. A., Krivonos, R. A., et al. 2016, MNRAS, 457, 258
Tueller, J., Barthelmy, S., Gehrels, N., et al. 1990, ApJ, 351, L41
Tur, C., Heger, A., & Austin, S. M. 2010, ApJ, 718, 357
Uberseder, E., Adachi, T., Aumann, T., et al. 2014, PRL, 112, 211101

Uberseder, E., Reifarth, R., Schumann, D., et al. 2009, PRL, 102, 151101
Ugliano, M., Janka, H.-T., Marek, A., & Arcones, A. 2012, ApJ, 757, 69
Umeda, H. & Nomoto, K. 2002, ApJ, 565, 385
Unsöld, A. & Bascheck, B. 2002, Der neue Kosmos, 7th edn. (Berlin Heidelberg: Springer Verlag)
Urošević, D., Arbutina, B., & Onić, D. 2019, Astrophysics and Space Science, 364, 185
Utomo, D., Sun, J., Leroy, A. K., et al. 2018, ApJ, 861, L18
Vallée, J. P. 2008, AJ, 135, 1301
van den Bergh, S. 1966, Astronomical Journal, 71, 990
van den Bergh, S. & Tammann, G. A. 1991, IN: Annual review of astronomy and astrophysics. Vol. 29 (A92-18081 05-90). Palo Alto, 29, 363
van Leeuwen, F. 2007, A&A, 474, 653
Vanbeveren, D., Van Bever, J., & Belkus, H. 2007, ApJ, 662, L107
Vedrenne, G., Roques, J.-P., Schönfelder, V., et al. 2003, A&A, 411, L63
Verschueren, W. & David, M. 1989, A&A, 219, 105
Vette, J. I., Gruber, D., Matteson, J. L., & Peterson, L. E. 1970, ApJ, 160, L161
Vink, J. S. & de Koter, A. 2005, A&A, 442, 587
Vink, J. S., de Koter, A., & Lamers, H. J. G. L. M. 2000, A&A, 362, 295
Vishniac, E. T. 1983, ApJ, 274, 152
von Ballmoos, P., Diehl, R., & Schönfelder, V. 1987, ApJ, 318, 654
von Glasow, W., Krause, M., Sommer-Larsen, J., & Burkert, A. 2013, MNRAS, 434, 1151
von Kienlin, A., Rau, A., Beckmann, V., & Deluit, S. 2004, Max-Planck-Institut für extraterrestrische Physik, Garching bei München, Germany (AIP), 622–625
Voss, R., Diehl, R., Hartmann, D. H., Cerviño, M., & Vink, J. S. 2008, in Proceedings of the th INTEGRAL Workshop, 27
Voss, R., Diehl, R., Hartmann, D. H., et al. 2009, A&A, 504, 531
Voss, R., Diehl, R., Vink, J. S., & Hartmann, D. H. 2010, A&A, 520, A51
Voss, R., Martin, P., Diehl, R., et al. 2012, A&A, 539, A66
Wainscoat, R. J., Cohen, M., Volk, K., Walker, H. J., & Schwartz, D. E. 1992, Astrophysical Journal Supplement Series (ISSN 0067-0049), 83, 111
Walch, S. & Naab, T. 2015, MNRAS, 451, 2757
Wallner, A. 2020, Table of 60Fe AMS measurements at ANU, publication in review, priv. comm. (17.04.2020)
Wallner, A., Faestermann, T., Feige, J., et al. 2015, Nat Commun, 6, 1
Wallner, A., Feige, J., Kinoshita, N., et al. 2016, Nature, 532, 69
Wanajo, S., Müller, B., Janka, H.-T., & Heger, A. 2018, ApJ, 852, 40
Wang, W., Harris, M. J., Diehl, R., et al. 2007, A&A, 469, 1005
Wang, W., Lang, M. G., Diehl, R., et al. 2009, A&A, 496, 713
Wang, W., Siegert, T., Dai, Z. G., et al. 2020, ApJ, 889, 169
Ward-Thompson, D., André, P., Crutcher, R., et al. 2007, Protostars and Planets V, 33
Weaver, R., McCray, R., Castor, J., Shapiro, P., & Moore, R. 1977, ApJ, 218, 377
Weidner, C. & Kroupa, P. 2004, MNRAS, 348, 187
Weidner, C. & Kroupa, P. 2005, ApJ, 625, 754
Weidner, C., Kroupa, P., & Bonnell, I. A. D. 2010, MNRAS, 401, 275
Weidner, C., Kroupa, P., Pflamm-Altenburg, J., & Vazdekis, A. 2013, MNRAS, 436, 3309
Weinberger, C., Diehl, R., Pleintinger, M. M. M., Siegert, T., & Greiner, J. 2020,

A&A, 638, A83
Werner, M., Reimer, O., Reimer, A., & Egberts, K. 2013, A&A, 555, A102
Whitmore, B. C., Chandar, R., & Fall, S. M. 2007, AJ, 133, 1067
Whitworth, A., Bate, M. R., Nordlund, Å., Reipurth, B., & Zinnecker, H. 2007, Protostars and Planets V, 459
Willis, A. J., Schild, H., & Stevens, I. R. 1995, A&A, 298, 549
Winkler, C., Courvoisier, T. J. L., Di Cocco, G., et al. 2003, A&A, 411, L1
Wolf, C. J. E. & Rayet, G. 1867, CRAS, 65, 292
Wolf, R. A. 1965, Physical Review, 137, 1634
Wolfire, M. G., McKee, C. F., Hollenbach, D., & Tielens, A. G. G. M. 2003, ApJ, 587, 278
Woosley, S. E. 2019, ApJ, 878, 49
Woosley, S. E., Arnett, W. D., & Clayton, D. D. 1973, Astrophysical Journal Supplement, 26, 231
Woosley, S. E. & Heger, A. 2007, Physics Reports, 442, 269
Woosley, S. E., Heger, A., & Weaver, T. A. 2002, Rev. Mod. Phys., 74, 1015
Woosley, S. E., Sukhbold, T., & Janka, H.-T. 2020, ApJ, 896, 56
Woosley, S. E. & Weaver, T. A. 1995, Astrophysical Journal Supplement v.101, 101, 181
Yan, Z., Jerabkova, T., & Kroupa, P. 2017, A&A
Yorke, H. W. & Sonnhalter, C. 2002, ApJ, 569, 846
Yusifov, I. & Küçük, I. 2004, A&A, 422, 545
Zari, E., Hashemi, H., Brown, A. G. A., Jardine, K., & de Zeeuw, P. T. 2018, A&A, 620, A172
Zhang, B., Reid, M. J., Menten, K. M., et al. 2013, ApJ, 775, 79
Zinnecker, H. & Yorke, H. W. 2007, Annu. Rev. Astron. Astrophys., 45, 481